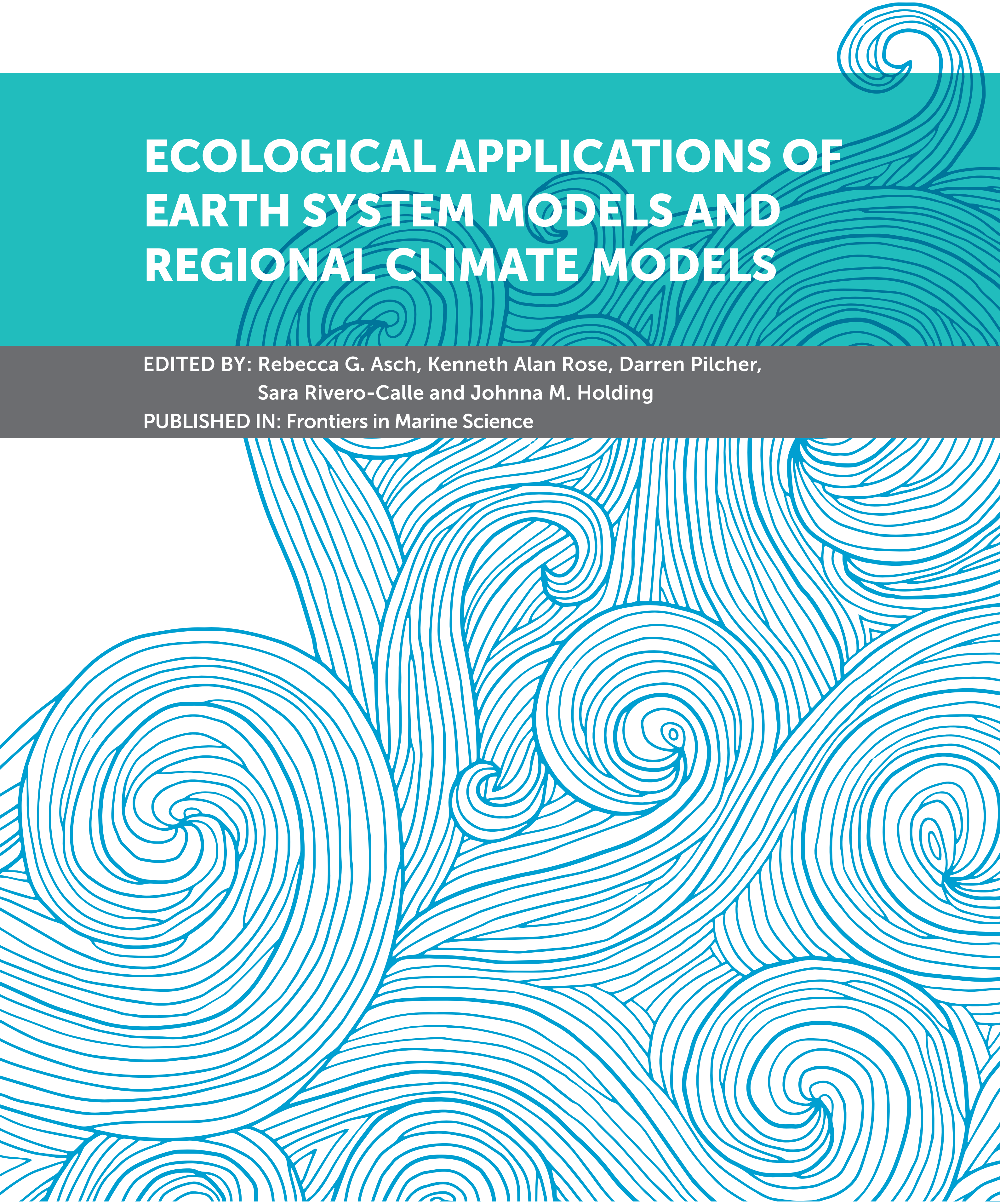

ECOLOGICAL APPLICATIONS OF EARTH SYSTEM MODELS AND REGIONAL CLIMATE MODELS

EDITED BY: Rebecca G. Asch, Kenneth Alan Rose, Darren Pilcher,
Sara Rivero-Calle and Johnna M. Holding

PUBLISHED IN: Frontiers in Marine Science

frontiers Research Topics

ISSN 1664-8714
ISBN 978-2-88971-755-2
DOI 10.3389/978-2-88971-755-2

About Frontiers

Frontiers is more than just an open-access publisher of scholarly articles: it is a pioneering approach to the world of academia, radically improving the way scholarly research is managed. The grand vision of Frontiers is a world where all people have an equal opportunity to seek, share and generate knowledge. Frontiers provides immediate and permanent online open access to all its publications, but this alone is not enough to realize our grand goals.

Frontiers Journal Series

The Frontiers Journal Series is a multi-tier and interdisciplinary set of open-access, online journals, promising a paradigm shift from the current review, selection and dissemination processes in academic publishing. All Frontiers journals are driven by researchers for researchers; therefore, they constitute a service to the scholarly community. At the same time, the Frontiers Journal Series operates on a revolutionary invention, the tiered publishing system, initially addressing specific communities of scholars, and gradually climbing up to broader public understanding, thus serving the interests of the lay society, too.

Dedication to Quality

Each Frontiers article is a landmark of the highest quality, thanks to genuinely collaborative interactions between authors and review editors, who include some of the world's best academicians. Research must be certified by peers before entering a stream of knowledge that may eventually reach the public - and shape society; therefore, Frontiers only applies the most rigorous and unbiased reviews.
Frontiers revolutionizes research publishing by freely delivering the most outstanding research, evaluated with no bias from both the academic and social point of view. By applying the most advanced information technologies, Frontiers is catapulting scholarly publishing into a new generation.

What are Frontiers Research Topics?

Frontiers Research Topics are very popular trademarks of the Frontiers Journals Series: they are collections of at least ten articles, all centered on a particular subject. With their unique mix of varied contributions from Original Research to Review Articles, Frontiers Research Topics unify the most influential researchers, the latest key findings and historical advances in a hot research area! Find out more on how to host your own Frontiers Research Topic or contribute to one as an author by contacting the Frontiers Editorial Office: frontiersin.org/about/contact

ECOLOGICAL APPLICATIONS OF EARTH SYSTEM MODELS AND REGIONAL CLIMATE MODELS

Topic Editors:
Rebecca G. Asch, East Carolina University, United States
Kenneth Alan Rose, University of Maryland Center for Environmental Science (UMCES), United States
Darren Pilcher, University of Washington and NOAA/PMEL, United States
Sara Rivero-Calle, University of Georgia, United States
Johnna M. Holding, Aarhus University, Denmark

Citation: Asch, R. G., Rose, K. A., Pilcher, D., Rivero-Calle, S., Holding, J. M., eds. (2021). Ecological Applications of Earth System Models and Regional Climate Models. Lausanne: Frontiers Media SA. doi: 10.3389/978-2-88971-755-2

Table of Contents

frontiers in Marine Science

EDITORIAL
published: 08 October 2021
doi: 10.3389/fmars.2021.773443

Editorial: Ecological Applications of Earth System Models and Regional Climate Models

Rebecca G. Asch[1]*, **Johnna M. Holding**[2], **Darren J. Pilcher**[3,4], **Sara Rivero-Calle**[5] and **Kenneth A. Rose**[6]

[1] Department of Biology, East Carolina University, Greenville, NC, United States, [2] Department of Bioscience & Arctic Research Centre, Aarhus University, Aarhus, Denmark, [3] Cooperative Institute for Climate, Ocean, and Ecosystem Studies (CICOES), University of Washington, Seattle, WA, United States, [4] Pacific Marine Environmental Laboratory (PMEL), National Oceanic and Atmospheric Administration (NOAA), Seattle, WA, United States, [5] Skidaway Institute of Oceanography, University of Georgia, Athens, GA, United States, [6] Horn Porn Laboratory, University of Maryland Center for Environmental Science (UMCES), Cambridge, MD, United States

Keywords: earth system model, regional climate model, climate change, ocean acidification, marine ecosystems, biogeochemistry, fisheries

Editorial on the Research Topic

Ecological Applications of Earth System Models and Regional Climate Models

Edited and reviewed by:
Matthias Gröger,
Leibniz Institute for Baltic Sea Research (LG), Germany

****Correspondence:***
Rebecca G. Asch
aschr16@ecu.edu

Specialty section:
This article was submitted to Global Change and the Future Ocean, a section of the journal Frontiers in Marine Science

Received: *09 September 2021*
Accepted: *14 September 2021*
Published: *08 October 2021*

Citation:
Asch RG, Holding JM, Pilcher DJ, Rivero-Calle S and Rose KA (2021) Editorial: Ecological Applications of Earth System Models and Regional Climate Models. Front. Mar. Sci. 8:773443. doi: 10.3389/fmars.2021.773443

Earth system models (ESMs) that couple sub-models describing atmospheric and oceanic dynamics with models of the cryosphere and biosphere are increasingly used to project climate change. Regional climate models (RCMs) function similarly but focus on regional scales with finer resolution. Due to the inclusion of lower trophic levels in ESMs (phytoplankton, zooplankton), these models are increasingly applicable for addressing ecological questions. While ESMs and RCMs do not typically represent higher trophic levels, they provide insights through: (1) coupling with mechanistic upper trophic level models, and (2) providing outputs to parameterize statistical, habitat-based models. Both types of analyses are increasingly used to forecast the dynamics of commercially and ecologically important species for management (Payne et al., 2017; Tommasi et al., 2017; Jacox et al., 2020). There are challenges related to using ESMs to explore ecological questions due to their coarse spatial and taxonomic resolution and a lack of understanding by many ecologists of the structural differences among different ESMs (Kearney et al., 2021). This Research Topic (RT) emerged as a result of the 2014 Ecological Dissertations in Aquatic Sciences Symposium, which led to a manuscript (Asch et al., 2016) and a session at the 2019 Aquatic Sciences Meeting entitled "Ecological Applications of ESMs and RCMS." The RT includes papers from the 2019 conference session and additional contributions from the community.

REGIONS

In **Figure 1**, we grouped the papers in this RT based on region, trophic level, oceanic drivers of changes, and modeling approach. Five papers focused on the Northeast Pacific (California Current, Gulf of Alaska), three the Northeast Atlantic, two the Western Pacific, and three presented global analyses (**Figure 1A**). Studies from the southern hemisphere were underrepresented. This is a pattern common to meta-analyses of marine global change biology (Mackas et al., 2012; Poloczanska et al., 2013). Also not represented was the Western Atlantic; these gaps might reflect regional research priorities and the availability of well-developed RCMs.

MODELING APPROACHES

Contributions were evenly distributed between global ESMs and RCMs (**Figure 1D**). Some papers (Holdsworth et al.; Pozo Buil et al.) integrated across these models by using dynamical downscaling of global models to inform boundary conditions at the edges of RCMs. Within the ESM and RCM analyses, papers used diverse approaches to examine how physical and biogeochemical forcing impacts marine ecosystems (**Figure 1E**). Some studies, such as Birkmanis et al., used species distribution modeling to statistically link environmental drivers with changes in habitat suitability. Other papers used a more mechanistic approach, such as trait-based models to investigate functional group dynamics (Petrik et al.) or an individual-based approach to examine larval dispersal or animal movement (Fiechter et al.; Norton et al.). Other papers conducted model experiments where simulations of different scenarios were run to evaluate organismal responses (Bahl et al.; Bednaršek et al.). Two papers investigated coupled natural-human systems; Suh and Pomeroy used changes in fish catch to parameterize an economic model and Fiechter et al. considered fleet dynamics when modeling Pacific sardine.

Coupling ESMs and RCMs to ecological analyses offers several key advantages:

(1) Emergent properties of the coupled physical and ecological systems can be identified, revealing underlying dynamics that could be difficult to tease out via observations or experiments. For example, Bahl et al. identified biogeochemical variables that exhibit linear vs. non-linear responses to radiative forcing. Petrik et al. investigated the "pelagicification" of ocean ecosystems whereby the biomass of large pelagic fishes declines under climate change due to their increasing metabolic demands combined with decreased secondary productivity. Norton et al. followed the environmental exposure history of individual crab larvae, which would be impossible to track with solely observations.

(2) Projection of responses to future conditions (temperature, ocean acidification, hypoxia, stratification) are well-grounded by the use of ESMs and RCMs. Such analyses also allow the separation of effects due to individual stressors that often co-occur. Bednaršek et al. differentiated between changes in aragonite saturation due to rising CO_2 and eutrophication by using model scenarios to separate these effects. Boyd et al. differentiated between multiple drivers affecting Atlantic mackerel and concluded that fishing mortality had a larger effect than climate change.

(3) Model simulations can identify rapidly changing locations or organisms at risk. Reygondeau et al. identified no-analog biogeochemical provinces that emerged under climate change. How organisms will adapt and acclimate to these novel conditions is unknown and modeling results could help ensure ecological monitoring is in place to detect such responses.

INTEGRATING OCEAN OBSERVATIONS AND MODELS

In situ observations are often the most reliable measure of a variable. However, they can be costly to obtain and may lack resolution in space or time. Satellite products are useful for increasing coverage, but rely on calibration with *in situ* measurements (Behrenfeld and Falkowski, 1997). Although using satellite data requires additional training, integrating *in situ* and satellite approaches with modeling is a logical step forward and is illustrated with two papers on the North Sea. This focus on the North Sea may reflect its historical wealth of observations and heterogeneous oceanography, which is difficult for models to capture. North Sea mixing is controlled by tidal influence along the coast and convective forcing offshore, both of which affect biogeochemistry and phytoplankton biomass. Mészáros et al. integrated satellite, *in situ*, and model observations to describe more accurately the dynamic nature of the region and project changes in primary productivity. Biogeochemistry of the coastal North Sea is also highly influenced by terrestrial run-off. Xu et al. showed coastal and offshore sites had different historical trends in chlorophyll *a*, with decreasing concentrations offshore and increasing trends along the coast despite a decrease in nutrient supply. This result was counterintuitive, leading them to conclude that satellite and modeling data should be used together to reassess *in situ* monitoring locations.

SPECIES AND CLIMATE DRIVERS

Climate change is a multifaceted phenomenon that causes changes in diverse physico-chemical ocean characteristics. Papers covered a wide range of oceanic drivers affected by climate change that impact marine ecosystems (**Figure 1C**). The most common drivers examined were changes in temperature and primary and secondary productivity. Notably missing were studies examining sea level rise, which has a substantial effect on habitat availability and coastal ecosystem functioning (Oppenheimer et al., 2019). This gap likely reflects that ESMs and RCMs operate at broader geographic scales than most analyses of sea level rise that focus on nearshore environments.

Papers were nearly evenly distributed among examining nutrients and biogeochemical dynamics, primary production, and upper trophic levels (**Figure 1B**). Several papers also investigated the dynamics of zooplankton, benthos, and fisheries. The few examples focused on zooplankton may reflect that they tend to be poorly represented in both nutrient-phytoplankton-zooplankton-detritus models and upper trophic level models (Rose et al., 2010).

Six papers projected the responses of fish and crabs to future climate (**Figure 1B**). Use of Representative Concentration Pathway 8.5 was common across all analyses; several studies also included other Representative Concentration Pathways. These papers showed that the response of upper trophic levels to future

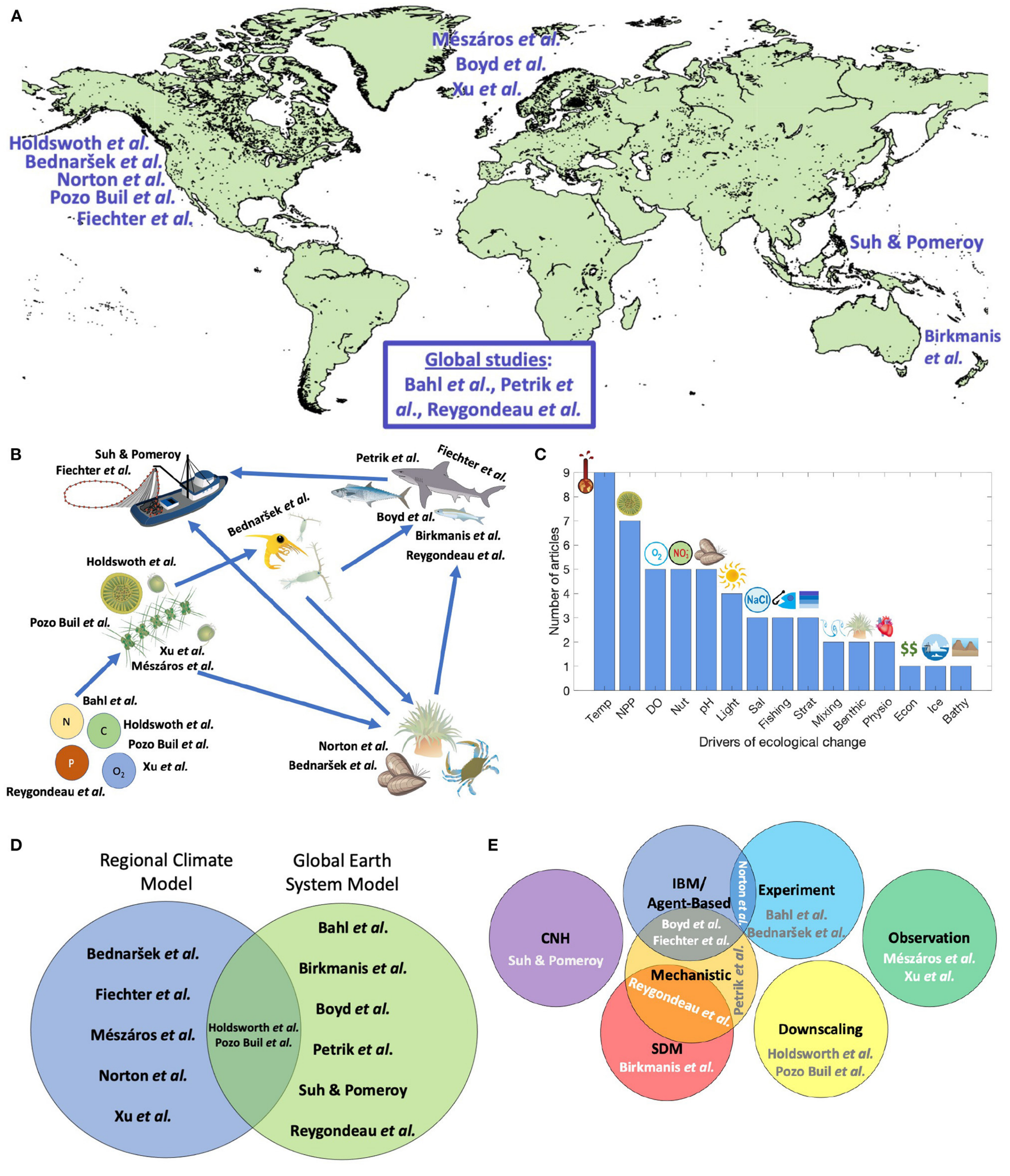

FIGURE 1 | Shared characteristics of papers in this Research Topic (RT). **(A)** Geographic distribution of studies. **(B)** Trophic level examined. This diagram contains pictorial representations of nutrients, primary producers, zooplankton, benthic organisms, top predators, and fisheries. Arrows depict flows between these trophic levels. If a study considered primary production mainly as a driver of ecological change at higher trophic levels, then this study is represented in this diagram as focusing on higher trophic levels rather than primary producers. **(C)** Drivers of ecological change examined in this RT. Temp, temperature; NPP, net primary production.

(Continued)

FIGURE 1 | This also includes studies examining chlorophyll concentration or secondary production; DO, dissolved oxygen; Nut, nutrients; pH, includes all studies examining ocean acidification and the carbonate chemistry system; Light, includes studies examining changes in turbidity or euphotic depth; Sal, salinity; Strat, stratification. This includes studies examining changes in mixed layer depth (MLD) since MLD is often measured as a function of stratification; Mixing, includes upwelling and mixing by eddies; Physio, includes physiological and metabolic rates; Econ, economic drivers; Bathy, bathymetry. If phytoplankton dynamics are examined by a study as the primary ecological variable of interest, then primary producers are classified as a response variable and not the underlying driver of change. **(D)** Venn diagram indicating how many studies utilized regional climate models (RCMs) and global earth system models (ESMs). The intersection between these categories includes dynamical downscaling studies that used outputs from ESMs to simulate future changes in regional climate. Studies that utilized RCMs but where downscaling was not a major focus of the manuscript were placed solely in the RCM category. **(E)** Venn diagram of modeling and observational approaches used in each manuscript. SDM, species distribution model; IBM, individual-based model; CNH, coupled natural-human system. Mechanistic models refer to the ecological component of the model and not the underlying ESM or RCM. Classifications are based on a study's primary modeling approach. Illustrations are from ian.umces.edu/media-library and freepik.com.

climate was not a simple decline or poleward shift following optimal temperatures. Projected responses were complicated, including positive and negative responses in abundance that were accompanied by changes in the location and shape of spatial distributions. For example, Petrik et al. predicted general declines in their fish functional groups within an ESM under climate change but groups differed in how closely they tracked the climate-induced changes in productivity and their prey. Birkmanis et al. predicted opposite responses of two different shark species, while Boyd et al. and Fiechter et al. predicted long-term increases in their study species.

Overall, RT papers were diverse in terms of modeling approach, focal ecosystems, and species examined. The research approaches described provide examples of how ESMs and RCMs can be coupled to models to address ecological questions related to climate change. Some missing topics include paleo-ecological studies, data assimilation, integration of data from autonomous observational platforms (Chai et al., 2020), and examination of climate variability. The recent publication of the 6th Assessment Report by the Intergovernmental Panel on Climate Change will provide additional impetus to continue the application of ESMs and RCMs to answer pressing ecological questions.

AUTHOR CONTRIBUTIONS

All authors contributed to writing and editing this editorial. **Figure 1** was prepared by RGA.

FUNDING

RGA was supported by the East Carolina University Department of Biology and an Alfred P. Sloan Foundation Research Fellowship. SR-C was supported by the University of Georgia Skidaway Institute of Oceanography. JH was supported by European Commission H2020 project INTAROS (Grant No. 727890). DP was supported by the Cooperative Institute for Climate, Ocean, and Ecosystem Studies (CICOES) under NOAA Cooperative Agreement NA20OAR4320271. This is CICOES contribution #2021-1160, PMEL contribution #5308, and Eco-FOCI-1017.

ACKNOWLEDGMENTS

We would like to acknowledge the organizers of the 2014 Ecological Dissertations in Aquatic Sciences Symposium since this RT is a product of dialogues initiated at that symposium. Symposium sponsors include the Association for the Sciences of Limnology and Oceanography, the University of Hawaii at Manoa, and the Center for Microbial Oceanography: Research and Education. Several of the papers included here were originally presented at the 2019 Aquatic Science Meeting in San Juan, Puerto Rico, which was also sponsored by the Association for the Sciences of Limnology and Oceanography. Lastly, we thank all contributors to this RT.

REFERENCES

Asch, R. G., Pilcher, D. J., Rivero-Calle, S., and Holding, J. (2016). Demystifying models: answers to ten common questions that ecologists have about earth system models. *Limnol. Oceanogr. Bull.* 25, 65–67. doi: 10.1002/lob.10113

Behrenfeld, M. J., and Falkowski, P. G. (1997). Photosynthetic rates derived from satellite-based chlorophyll concentration. *Limnol. Oceanogr.* 42, 1–20. doi: 10.4319/lo.1997.42.1.0001

Chai, F., Johnson, K. S., Claustre, H., Xing, X., Wang, Y., Boss, E., et al. (2020). Monitoring ocean biogeochemistry with autonomous platforms. *Nat. Rev. Earth Env.* 1, 315–326. doi: 10.1038/s43017-020-0053-y

Jacox, M. G., Alexander, M. A., Siedlecki, S., Chen, K., Kwon, Y. O., Brodie, S., et al. (2020). Seasonal-to-interannual prediction of North American coastal marine ecosystems: forecast methods, mechanisms of predictability, and priority developments. *Prog. Oceanogr.* 183:102307. doi: 10.1016/j.pocean.2020.102307

Kearney, K. A., Bograd, S. J., Drenkard, E., Gomez, F. A., Haltuch, M., Hermann, A. J., et al. (2021). Using global-scale earth system models for regional fisheries applications. *Front. Mar. Sci.* 8:622206. doi: 10.3389/fmars.2021.622206

Mackas, D. L., Greve, W., Edwards, M., Chiba, S., Tadokoro, K., Eloire, D., et al. (2012). Changing zooplankton seasonality in a changing ocean: comparing time series of zooplankton phenology. *Prog. Oceanogr.* 97–100, 31–62. doi: 10.1016/j.pocean.2011.11.005

Oppenheimer, M., Glavovic, B. C., Hinkel, J., van de Wal, R., Magnan, A. K., Abd-Elgawad, A., et al. (2019). "Sea level rise and implications for low-lying islands, coasts and communities," in *IPCC Special Report on the Ocean and Cryosphere in a Changing Climate*, eds H. O. Pörtner, D. C. Roberts, V. Masson-Delmotte, P. Zhai, M. Tignor, E. Poloczanska, et al. (Cambridge: Cambridge University Press), 321–445.

Payne, M. R., Hobday, A. J., MacKenzie, B. R., Tommasi, D., Dempsey, D. P., Fässler, S. M. M., et al. (2017). Lessons from the first generation of marine ecological forecast products. *Front. Mar. Sci.* 4:289. doi: 10.3389/fmars.2017.00289

Poloczanska, E. S., Brown, C. J., Sydeman, W. J., Kiessling, W., Schoeman, D. S., Moore, P. J., et al. (2013). Global imprint of climate change on marine life. *Nat. Clim. Change* 3, 919–925. doi: 10.1038/nclimate1958

Rose, K. A., Allen, J. I., Artioli, Y., Barange, M., Blackford, J., Carlotti, F., et al. (2010). End-to-end models for the analysis of marine ecosystems: challenges, issues, and next steps. *Mar. Coast. Fish*. 2, 115–130. doi: 10.1577/C09-059.1

Tommasi, D., Stock, C. A., Hobday, A. J., Methot, R., Kaplan, I. C., Eveson, P. J., et al. (2017). Managing living marine resources in a dynamic environment: the role of seasonal to decadal climate forecasts. *Prog. Oceanogr*. 152, 15–49. doi: 10.1016/j.pocean.2016.12.011

Conflict of Interest: The authors declare that the research was conducted in the absence of any commercial or financial relationships that could be construed as a potential conflict of interest.

frontiers
in Marine Science

ORIGINAL RESEARCH
published: 25 February 2020
doi: 10.3389/fmars.2020.00102

The Importance of Environmental Exposure History in Forecasting Dungeness Crab Megalopae Occurrence Using J-SCOPE, a High-Resolution Model for the US Pacific Northwest

Emily L. Norton[1]*, Samantha Siedlecki[2], Isaac C. Kaplan[3], Albert J. Hermann[1,4], Jennifer L. Fisher[5], Cheryl A. Morgan[5], Suzanna Officer[6], Casey Saenger[1], Simone R. Alin[4], Jan Newton[7], Nina Bednaršek[8] and Richard A. Feely[4]

[1] Joint Institute for the Study of the Atmosphere and Ocean, University of Washington, Seattle, WA, United States, [2] Department of Marine Sciences, University of Connecticut Groton, Groton, CT, United States, [3] Conservation Biology Division, Northwest Fisheries Science Center, National Marine Fisheries Service, National Oceanic and Atmospheric Administration, Seattle, WA, United States, [4] Pacific Marine Environmental Laboratory, National Oceanic and Atmospheric Administration, Seattle, WA, United States, [5] Cooperative Institute for Marine Resources Studies, Oregon State University, Newport, OR, United States, [6] Whitman College, Walla Walla, WA, United States, [7] Applied Physics Laboratory, University of Washington, Seattle, WA, United States, [8] Southern California Coastal Water Research Project, Costa Mesa, CA, United States

OPEN ACCESS

Edited by:
Kenneth Alan Rose,
University of Maryland Center for Environmental Science (UMCES), United States

Reviewed by:
Halley Elizabeth Froehlich,
University of California, Santa Barbara, United States
Felisa Rey,
University of Aveiro, Portugal

****Correspondence:***
Emily L. Norton
emilyln@uw.edu

Specialty section:
This article was submitted to Global Change and the Future Ocean, a section of the journal Frontiers in Marine Science

Received: *10 October 2019*
Accepted: *07 February 2020*
Published: *25 February 2020*

Citation:
Norton EL, Siedlecki S, Kaplan IC, Hermann AJ, Fisher JL, Morgan CA, Officer S, Saenger C, Alin SR, Newton J, Bednaršek N and Feely RA (2020) The Importance of Environmental Exposure History in Forecasting Dungeness Crab Megalopae Occurrence Using J-SCOPE, a High-Resolution Model for the US Pacific Northwest. Front. Mar. Sci. 7:102. doi: 10.3389/fmars.2020.00102

The Dungeness crab (*Metacarcinus magister*) fishery is one of the highest value fisheries in the US Pacific Northwest, but its catch size fluctuates widely across years. Although the underlying causes of this wide variability are not well understood, the abundance of *M. magister* megalopae has been linked to recruitment into the adult fishery 4 years later. These pelagic megalopae are exposed to a range of ocean conditions during their dispersal period, which may drive their occurrence patterns. Environmental exposure history has been found to be important for some pelagic organisms, so we hypothesized that inclusion of recent environmental exposure history would improve our ability to predict inter-annual variability in *M. magister* megalopae occurrence patterns compared to using "*in situ*" conditions alone. We combined 8 years of local observations of *M. magister* megalopae and regional simulations of ocean conditions to model megalopae occurrence using a generalized linear model (GLM) framework. The modeled ocean conditions were extracted from JISAO's Seasonal Coastal Ocean Prediction of the Ecosystem (J-SCOPE), a high-resolution coupled physical-biogeochemical model. The analysis included variables from J-SCOPE identified in the literature as important for larval crab occurrence: temperature, salinity, dissolved oxygen concentration, nitrate concentration, phytoplankton concentration, pH, aragonite, and calcite saturation state. GLMs were developed with either *in situ* ocean conditions or environmental exposure histories generated using particle tracking experiments. We found that inclusion of exposure history improved the ability of the GLMs to predict megalopae occurrence 98% of the time. Of the six swimming behaviors used to simulate megalopae dispersal, five behaviors generated GLMs with superior fits to the observations, so a biological ensemble of these models was constructed. When the biological ensemble was used for forecasting, the model showed skill in predicting megalopae occurrence (AUC = 0.94). Our results highlight the importance of including exposure history in larval occurrence modeling and help provide a method for predicting pelagic megalopae occurrence. This work is a step toward developing a forecast product to support management of the fishery.

Keywords: *Metacarcinus magister*, megalopae, particle tracking, simulated larval behaviors, exposure history, habitat modeling, J-SCOPE, GLM

INTRODUCTION

The Dungeness crab fishery is one of the most economically important fisheries on the US West Coast, totaling over \$200M in 2017 (Pacific States Marine Fisheries Commission, 2019). However, this fishery experiences wide inter-annual fluctuations in catch size. For example, in Washington and Oregon, the lowest commercial crab catches were reported in the early 1980s ($<$1300 metric tons in Washington; $<$2300 metric tons in Oregon), and record high catches, nearly 10-fold higher, were reported in the 2004–2005 season ($>$11,300 metric tons in Washington; $>$15,000 metric tons in Oregon), with moderate variability observed even across consecutive years.[1], [2] Variable catch rates have been accompanied by large swings in ex-vessel landing values, e.g. from \$33.9M in the 2013–2014 season to \$74.2M in the 2017–2018 season in Oregon. These large fluctuations have the potential to affect management strategies, fishermen's livelihoods, and local economies (Botsford et al., 1983; Methot, 1986). Due to consistently high fishing effort, it is thought that variable annual catch rates reflect changes in adult Dungeness crab population sizes. The precise causes of this variability are not completely understood but have long been a subject of research (Methot and Botsford, 1982; Botsford and Hobbs, 1995; Higgins et al., 1997).

One factor that has been linked to variability in the *Metacarcinus magister* fishery is the abundance of the final pelagic larval stage, the megalopal stage, 4 years prior (Shanks and Roegner, 2007; Shanks et al., 2010; Shanks, 2013). Shanks (2013) reported a significant, parabolic relationship between megalopae abundance in coastal habitats and recruitment into the adult *M. magister* fishery four years later: recruitment into the fishery was maximized at intermediate megalopae abundances, and otherwise was limited either by population levels (low abundance) or density-dependent effects (high abundance).

Abundance of *M. magister* megalopae is influenced by ocean conditions on small and large scales. For example, survival and condition of *M. magister* larvae have been shown to be negatively impacted by exposure to low pH (Descoteaux, 2014; Miller et al., 2016); steep calcite saturation state gradients (Bednaršek et al., 2020); extreme temperatures (Wild, 1980; Pauley et al., 1989; Sulkin et al., 1996); low salinities (Reed, 1969; Brown and Terwilliger, 1999); low oxygen conditions (Bancroft, 2015; Gossner, 2018); and poor-quality or scarce food (Bigford, 1977; Harms and Seeger, 1989; Sulkin et al., 1998; Casper, 2013). Additionally, megalopae abundance has been significantly correlated with large-scale oceanographic features, such as the phase of the Pacific Decadal Oscillation (PDO; Shanks, 2013), wind-induced currents (Hobbs et al., 1992), and the timing of the spring transition of the California Current (Shanks and Roegner, 2007). The spring transition marks the onset of seasonal upwelling, which is a primary driver of ocean variability in this region.

Every summer the coastline of the Pacific Northwest experiences a shift in wind direction that promotes upwelling of "corrosive" deep water, which is low in oxygen, pH, and calcium carbonate saturation states, to habitat on the continental shelf (Huyer et al., 1979; Feely et al., 2008, 2016; Hickey and Banas, 2008). Though these winds vary in intensity and duration, hypoxia ($O_2 < 1.4$ ml l^{-1}; 61 μmol kg^{-1}; 62 mmol m^{-3}) has increasingly developed over portions of the continental shelf in recent years, with occasional severe hypoxia ($O_2 \sim 0.5$ ml l^{-1}; 22 μmol kg^{-1}; 22 μmol kg^{-1}) occurring in *M. magister* habitat (Grantham et al., 2004; Chan et al., 2008; Connolly et al., 2010). Low pH conditions, sometimes as low as 7.6, and other carbonate chemistry parameters (e.g. delta calcite, pCO_2, aragonite and calcite saturation states), accompany this low oxygen water, providing an additional stress to organisms (Feely et al., 2008, 2012, 2016; Harris et al., 2013; Busch and McElhany, 2016; Hodgson et al., 2016; Miller et al., 2016; Siedlecki et al., 2016; Bednaršek et al., 2017, 2020).

Summer upwelling conditions have been simulated by an experimental ocean model, JISAO's Seasonal Coastal Ocean Prediction of the Ecosystem (J-SCOPE; Siedlecki et al., 2016). J-SCOPE is a high-resolution (1.5 km horizontal resolution; 40 vertical layers), Regional Ocean Modeling System (ROMS)-based, biogeochemical model for Washington and Oregon shelf waters.[3] J-SCOPE has demonstrated measurable skill for ocean conditions on seasonal timescales (Siedlecki et al., 2016), and environmental variables from this model have been used to predict habitat for sardines (*Sardinops sagax*; Kaplan et al., 2016) and hake (*Merluccius productus*; Malick et al., in prep). Additionally, by pairing the J-SCOPE model system with a particle tracking model and simulated behaviors, environmental exposure history has been shown to influence pteropod survival (Bednaršek et al., 2017). When run in hindcast-mode, J-SCOPE simulates realistic historical ocean conditions and benefits from physical forcing (e.g. boundary conditions, atmospheric forcing, rivers, and tides) that is data-assimilated. These hindcasts, spanning years 2009–2017, output variables specifically relevant to *M. magister* megalopae, and are used in this study.

---

[1] https://www.dfw.state.or.us/MRP/shellfish/commercial/crab/landings.asp

[2] https://wdfw.wa.gov/fishing/commercial/crab/coastal/about

[3] http://www.nanoos.org/products/j-scope/home.php

With the right combination of prognostic ocean conditions, *M. magister* megalopae occurrence and habitat could be forecast over a large spatial scale and variable conditions, supplementing field surveys of megalopae (Shanks et al., 2010) and improving forecasting for management applications. Current management relies on pre-season monitoring of crab conditions and real-time catch rates. By incorporating the megalopal stage into management, Dungeness crab fisheries managers in Washington and Oregon would benefit from an ocean model-based tool that would forecast catch with a lead time of >4 years, a timescale that is useful for coordinating state, tribal, and federal managers to develop realistic long-term management strategies, and for fishermen to anticipate changes in the resource (Hobday et al., 2016).

Our aim is to develop a statistical model driven by modeled ocean conditions to predict megalopae occurrence. We tested the hypothesis that occurrence of *M. magister* megalopae is affected by exposure to both concurrent *and* recent environmental conditions that are predictable on seasonal timescales. We propose that exposure history may influence megalopae occurrence patterns because prior exposure to lethal or sub-optimal environmental conditions would either increase megalopae mortality or potentially spur avoidance behaviors (which have been observed during settlement, e.g. Sobota and Dinnel, 2000), ultimately resulting in a decreased probability of occurrence. Thus, we investigated whether inclusion of recent exposure history would improve our ability to model megalopae occurrence over using only environmental conditions concurrent with sampling. Hence, simulated ocean conditions over an 8 year period were used to model the occurrence of megalopae within generalized linear models (GLMs) that included two distinct suites of predictor variables: (1) "*in situ*" GLMs were developed with physical and biogeochemical variables extracted from the ocean model at the times and locations concurrent with megalopae sampling and (2) "exposure history" GLMs included physical and biogeochemical variables extracted along simulated megalopae trajectories from six distinct dispersal experiments. We found that exposure history did improve our ability to model megalopae occurrence, and we assembled a "biological ensemble" of GLMs to generate a superior forecast for megalopae occurrence. An ancillary outcome of this study was the identification of ocean conditions that may influence spatial heterogeneity of *M. magister* megalopae, identified as the environmental variables that were included as predictors in the occurrence GLMs. The framework developed in this study could be applied to other pelagic species to assess the influence of exposure history on their habitat.

MATERIALS AND METHODS

Our methods rely on a range of interdisciplinary tools and procedures. We provide a flow chart to clarify the order of operations and linkages therein for the methods and results in this paper (**Figure 1**).

Metacarcinus magister Megalopae Collection

Metacarcinus magister larvae were collected on surveys conducted by NOAA Northwest Fisheries Science Center (NOAA/NWFSC) as part of a larger study of juvenile salmonids and associated nekton (Morgan et al., 2019) at 37 unique stations off of the Washington and Oregon coasts from 2009 to 2017 (**Table 1** and **Supplementary Table 1**). Surveys were conducted during the daytime in late May and/or June for approximately week-long periods. Larvae were collected using a 0.6 m bongo net with 335 μm mesh size. Plankton nets were towed obliquely by letting out 60 m of cable and immediately retrieving it at a rate of 30 m/min while being towed at two knots. Thus, nets were fished from a maximum depth of 20–30 m to the surface, spanning a large portion of the expected depth habitat of megalopae (see details below). Samples were immediately preserved in 5% buffered formalin/seawater solution and returned to the laboratory for analysis. In the laboratory, plankton samples were rinsed and then sorted based on larval developmental stage and enumerated. For more details on field and laboratory methods, see Morgan et al. (2005). For this study, we modeled megalopae occurrence, characterized as presence or absence of megalopae at each sampling station.

Modeled Ocean Conditions

J-SCOPE Historical Ocean Simulations

Historical ocean simulations (i.e. hindcasts) were used in lieu of empirical measurements because they provide spatially and temporally continuous ocean conditions. We have conducted extensive model evaluation with ocean observations for all the variables considered here (see Siedlecki et al., 2016, and results below). Modeled environmental variables, obtained from the J-SCOPE ocean model (Siedlecki et al., 2016), were used to develop the GLMs to predict megalopae occurrence. Environmental conditions were extracted from historical ocean simulations for 2009–2016 corresponding to either the megalopae collection times and locations (*in situ* GLM) or along backtracking particle trajectories (exposure history GLMs; more details below). Historical ocean simulations for 2017 were reserved for GLM performance testing.

J-SCOPE Variable Skill Assessment

Validation of J-SCOPE's historical ocean simulations was performed for a wider range of environmental variables than in previous work (e.g. Siedlecki et al., 2015, 2016; Year in Review webpages at http://www.nanoos.org/products/j-scope/). Additionally, assessments were performed for distinct depth intervals (**Table 2**) to investigate the skill of particular ocean conditions as they were experienced by *in situ* or exposure history particles, since the skill of these predictor variables may be relevant to the subsequent performance of the megalopae occurrence GLMs. To accomplish this, empirical observations were matched temporally and spatially to modeled variables.

Ocean Observational Data

Observational data were compiled from regional moorings and surveys conducted from 2009 to 2017 (**Figure 2** and

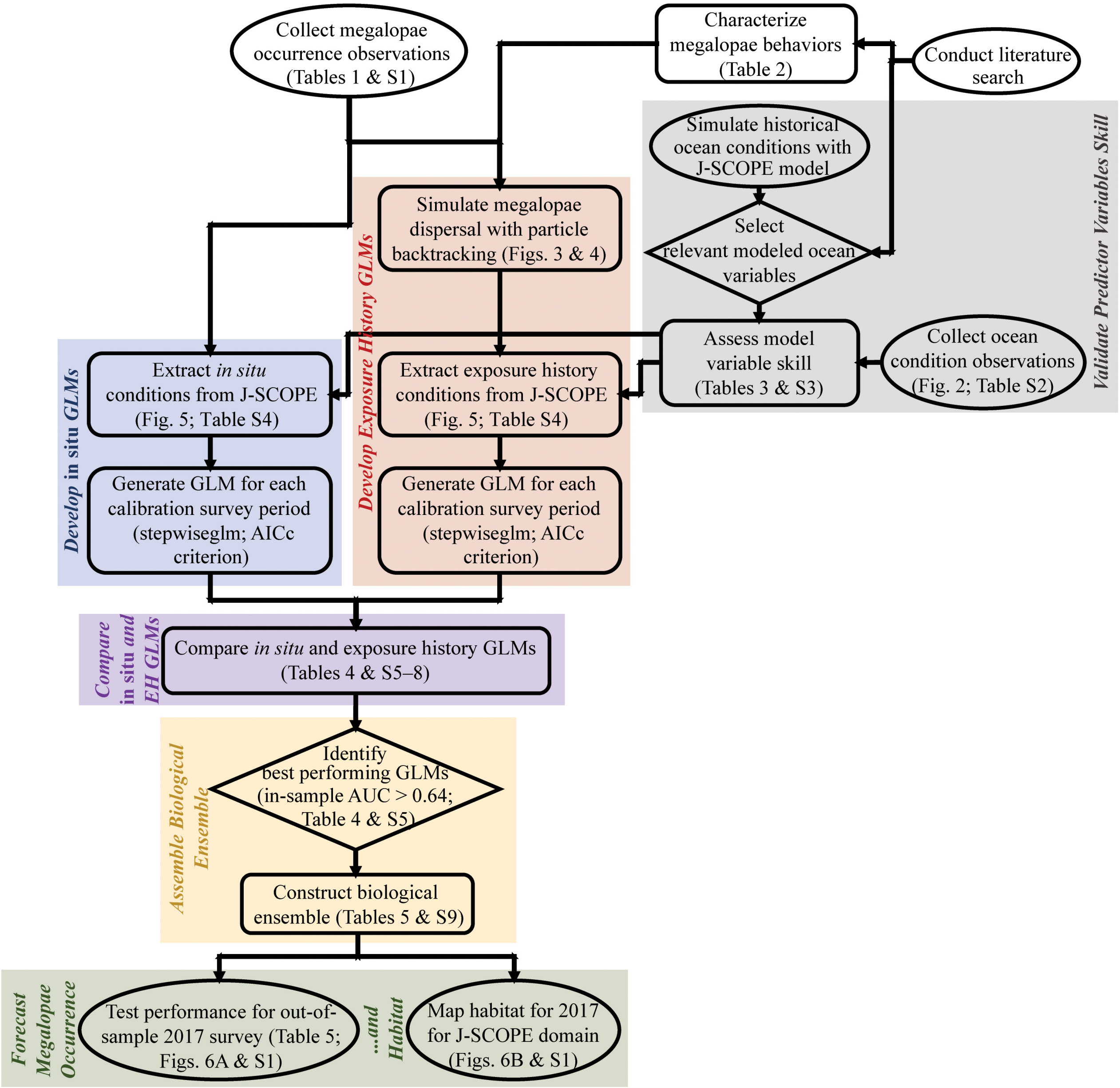

FIGURE 1 | Flowchart summarizing the main methods and results of this paper, including validation of predictor variables skill (gray); development of *in situ* (blue) and exposure history (red) generalized linear models (GLMs); comparison of *in situ* and exposure history GLMs (purple); assembly of the biological ensemble (yellow); and forecasting of megalopae occurrence and habitat (green). Start and end nodes are in ovals, process steps are in boxes, and decision points are in diamonds. Table SX refers to **Supplementary Tables (1–9)**. AICc = Akaike information criterion corrected for small sample size; AUC = area under the receiver operating characteristic (ROC) curve; EH = exposure history; GLM = generalized linear model; J-SCOPE = JISAO's Seasonal Coastal Ocean Prediction of the Ecosystem.

Supplementary Table 2). CTD-based measurements of temperature, salinity, oxygen, and phytoplankton (measured as fluorescence) were made ∼1–2 times per month from 2009 to 2017 at seven stations across the continental shelf and slope along the Newport Hydrographic Line (NHL; 44.6517°N). Surface nitrate data were also collected along the NHL. NOAA/NWFSC Groundfish bottom trawl surveys measured bottom temperature on the continental shelf and slope from 2009 to 2014. Nitrate was also measured at surface and sub-surface locations during the NOAA/NWFSC Northern California Current survey in 2011. In addition to megalopae sampling conducted by NOAA/NWFSC Juvenile Salmon surveys, nitrate was measured at 3 m depth at 37 stations off the Washington and Oregon coasts from 2009 to 2014. Temperature and oxygen were observed at surface and sub-surface locations ∼1–2 times per month from 2009 to 2017 at the Cape Elizabeth mooring in the Olympic Coast National Marine Sanctuary (OCNMS). Temperature, oxygen, salinity, nutrients (i.e. nitrate, phosphate, and silicate), dissolved inorganic carbon

TABLE 1 | Megalopae sampling survey information, including sampling date, number of stations where megalopae were present and absent, and total number of stations sampled (see **Figure 4A** for map; see **Supplementary Table 1** for sampling location information).

Survey	Year	Sampling dates	Megalopae present (# Stns)	Megalopae absent (# Stns)	Total # Stns sampled
1	2009	5/23–5/28	15	15	30
2	2009	6/24–6/30	11	23	34
3	2010	5/21–5/27	17	12	29
4	2010	6/22–6/28	5	31	36
5	2011	5/21–5/26	13	16	29
6	2011	6/21–6/27	9	26	35
7	2012	5/30–6/3	5	20	25
8	2012	6/22–6/28	11	24	35
9	2013	6/21–6/27	13	23	36
10	2014	6/21–6/27	18	17	35
11	2015	6/22–6/28	5	28	33
12	2016	6/23–6/29	5	27	32
13	2017	6/22–6/28	5	28	33

Sampling was conducted with a bongo net fished from a maximum depth of 30 m to the ocean surface. Surveys from 2009 to 2016 were used in generalized linear model development, while the 2017 survey was reserved for out-of-sample model performance testing.

TABLE 2 | Environmental condition extractions for *in situ* (row 1) and particle tracking (rows 2–7) experiments, including (when relevant) where environmental conditions were extracted, the behavior simulated for particles, the depth at which particles were initialized, and the core depth habitat.

Experiment	Environmental exposure extractions	Particle behavior	Start depth (m)	Core depth habitat (m)
In situ	Sampling station locations	N/A	N/A	0–30
EH-DVM30	Particle tracking	0–30 m DVM	30	0–30
EH-DVM60	Particle tracking	0–60 m DVM	60	0–60
EH-S1	Particle tracking	Surface-following	1	0–5
EH-P1	Particle tracking	Passive	1	40–50
EH-P30	Particle tracking	Passive	30	55–70
EH-D15P	Particle tracking	0–30 m DVM for 15 days, then passive	30	0–30

EH = exposure history simulation; DVM = diel vertical migration behavior; S = surface-following behavior; P = passive behavior.

(DIC), and total alkalinity (TA) were measured at surface and sub-surface locations on Pacific Coast Ocean Observing System (PaCOOS) annual surveys in 2009 and 2010. Temperature, oxygen, salinity, nutrients, phytoplankton, DIC, and TA were also measured at surface and sub-surface locations on West Coast Ocean Acidification (WCOA) surveys conducted in 2011, 2012, 2013, and 2016. For all surveys with temperature, salinity, phosphate, silicate, DIC, and TA measurements, values of pH (at *in situ* temperature, salinity, and pressure, on the total scale) and aragonite (Ω_{ar}) and calcite saturation states (Ω_{ca}) were calculated in CO2SYS (Pelletier et al., 2007), using carbonate dissociation constants from Lueker et al. (2000), salinity to boron ratios from Uppström (1974), bisulfate equilibrium constants from Dickson (1990), and the "seacarb" option for fluoride (i.e. Perez and Fraga, 1987 when $33 > T > 10$ [°C] and $40 > S > 10$ [PSU], otherwise Dickson and Riley, 1979). Additionally, empirical relationships using the proxy variables oxygen and temperature were developed to estimate carbonate chemistry variables for the region encompassed by the model domain based on calibration data sets collected on all WCOA surveys following the methods described in Alin et al. (2012; Eqs. 1–3):

$$pH = 7.2587 + 0.0021314 \times \mathrm{O} + 0.018633 \times \mathrm{T} \quad (1)$$

$$\Omega_{ar} = 0.990759 + 0.04372 \times (\mathrm{T} - T_r) + 0.0043285 \times (\mathrm{O} - O_r) + 0.0006399 \times (\mathrm{T} - T_r) \times (\mathrm{O} - O_r) \quad (2)$$

$$\Omega_{ca} = -20.343 + 1.8719 \times \mathrm{T} + 0.0082364 \times \mathrm{O} + 69.047 \div \mathrm{T} - 0.046982 \times \mathrm{T}^2 \quad (3)$$

where $T_r = 8.1903$ and $O_r = 144.441$ are reference values based on the calibration data set, and T = temperature (°C) and O = oxygen (μmol kg^{-1}) are modeled or observed values. These equations were applied at sites where both temperature and oxygen data were available. For phytoplankton observations (measured as either fluorescence or chlorophyll), units were converted following the methods of Davis et al. (2014) prior to comparison with the modeled phytoplankton variable (mmol m^{-3}).

Statistical Skill Calculations

Observations and modeled data were paired within a given depth interval (**Table 2**), and two statistics were calculated to assess model variable skill: (1) the Pearson correlation coefficient (r), ranging from −1 (negative correlation) to 1 (positive correlation), indicates the degree of linear correlation between the observed and modeled variables; and (2) normalized root-mean-square error (NRMSE) estimates the magnitude of the difference between the observed and modeled variables, with the sign indicating the direction of model bias (positive sign indicates model overestimate; negative sign indicates model underestimate; see **Supplementary Equations 1, 2**).

Variable Selection for Habitat Models

In situ Variables

To assemble a suite of potential predictor variables for developing the GLM, we selected physical and biogeochemical variables identified in the biological literature as important for the development and survival of *M. magister* megalopae or a closely related organism, and that exist or can be derived from the J-SCOPE historical ocean simulations. We omitted synthetic or summary variables, such as the PDO or upwelling indices, despite their reported correlations with megalopae abundance (Hobbs et al., 1992; Shanks and Roegner, 2007; Shanks, 2013) because we strive for a mechanistic understanding of how fundamental ocean conditions characterize megalopae habitat—e.g. is it the cooler water temperatures, lower oxygen levels, or more acidified conditions of the upwelled waters that influence habitat? Thus, a total of eight potential predictor variables were

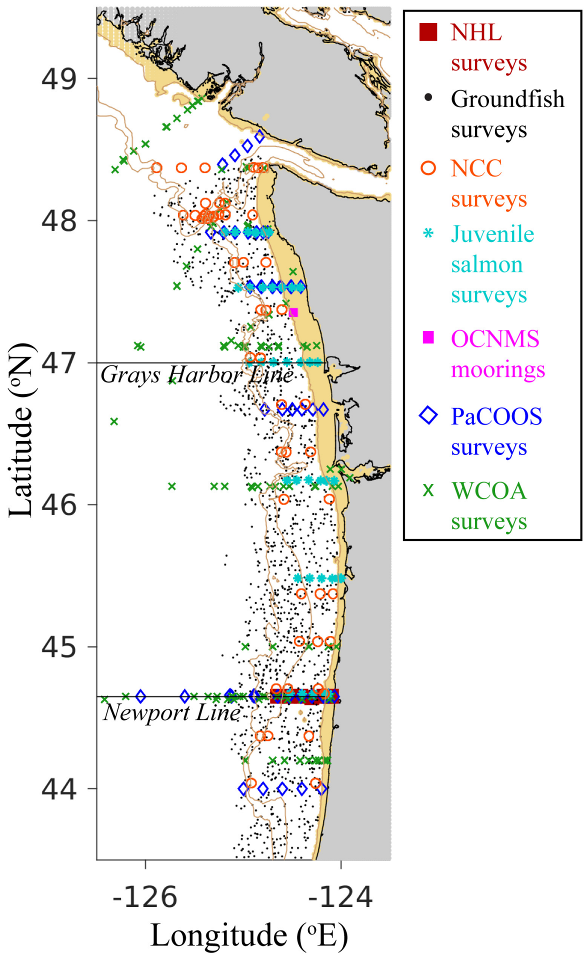

FIGURE 2 | Empirical observation sampling locations used to assess the skill of J-SCOPE modeled ocean variables. Survey and mooring symbols correspond to the figure legend, with tiny black dots representing groundfish survey locations. The Grays Harbor Line and the Newport Line, two common hydrographic transects, are plotted for reference. The 200 and 500 m isobaths are indicated by light brown contours, and depths shallower than 50 m are shaded light brown. Land is shaded gray. NHL = Newport Hydrographic Line; NCC = Northern California Current; OCNMS = Olympic Coast National Marine Sanctuary; PaCOOS = Pacific Coast Ocean Observing System; WCOA = West Coast Ocean Acidification. See **Supplementary Table 2** for additional information on sampling dates, depths, and measured parameters.

considered for inclusion in our statistical models: temperature, salinity, dissolved oxygen concentration, nitrate concentration, phytoplankton concentration, pH, aragonite saturation state (Ω_{ar}), and calcite saturation state (Ω_{ca}). Temperature was chosen because it is thought to influence *M. magister* larval development duration (Moloney et al., 1994; Sulkin and McKeen, 1996; Sulkin et al., 1996) and to be an indicator of advective processes (Ferrari and Ferreira, 2011). Due to the high abundance of *M. magister* megalopae observed within Columbia River plume fronts, salinity was selected as there is substantial salinity variability within the plume (Morgan et al., 2005), and *M. magister* larvae are reportedly sensitive to changes in salinity (Pauley et al., 1989). Dissolved oxygen was selected because *M. magister* megalopae and juveniles experience negative metabolic effects and high mortality rates, respectively, in hypoxic conditions (Bancroft, 2015; Gossner, 2018). In addition to temperature, nitrate concentration is a strong indicator of upwelling, indicating both nutrient sources for primary productivity and offshore Ekman transport (Hales et al., 2005; Palacios et al., 2013). Phytoplankton concentration was selected as an indicator of cross-shelf and alongshore currents and retentive features, and as a proxy for food availability (Largier et al., 2006; Kudela et al., 2008). pH was included because Miller et al. (2016) found that exposure of *M. magister* larvae to low pH conditions increased mortality and slowed development rates. We selected Ω_{ca} as a potential predictor because the *M. magister* megalopae exoskeleton contains calcite (Bednaršek et al., 2020; Boßelmann et al., 2007; Neues et al., 2007). Although Ω_{ar} may not directly affect the condition of the megalopal exoskeleton, we chose to include this variable as a potential predictor because of the impacts it has on the pelagic food web that may influence megalopae development and survival (Riebesell et al., 2000; Fabry et al., 2008).

Five variables (temperature, salinity, dissolved oxygen concentration, nitrate concentration, and phytoplankton concentration) were extracted directly from the J-SCOPE historical ocean simulations at the stations where megalopae were sampled, and then averaged over the upper 30 m of the water column, the sampling depth of the megalopae collections. The remaining three variables (pH, Ω_{ar}, Ω_{ca}) were calculated with empirically derived formulae that used dissolved oxygen concentration and temperature at the station locations from the J-SCOPE historical ocean simulations (see equations above); these were then averaged over the surface 30 m.

Exposure History Variables

Simulated megalopae dispersal

To test our hypothesis that recent environmental exposure history is important in determining megalopae occurrence, we used particle tracking to simulate virtual megalopae dispersal. Since megalopal stage duration is approximately 30 days for temperatures in this region (Poole, 1966; Ebert et al., 1983) and physical uncertainty in the particle trajectories due to unresolved vertical and horizontal advection and diffusion becomes large over approximately the same time span (sensitivity analyses not shown), particles were tracked backward in time for a period limited to 30 days. Future studies may incorporate earlier larval developmental stages (e.g. zoeae) or run full lifecycle individual-based models, but the current study focuses on whether the environmental exposure over the course of the 30 days prior to megalopae collection can be used to improve megalopae occurrence modeling. Thus, we simulated megalopae dispersal with an offline particle tracking model, the Larval TRANSport Lagrangian model (LTRANSv2b; North et al., 2008, 2011; Schlag and North, 2012), driven by external physical forcing, random displacement, and directed swimming behaviors as prescribed by the user. To account for stochasticity, 100 particles were initialized at each of the 37 sampling stations on the last day of each survey (**Table 1**). Ocean velocities from J-SCOPE hourly historical ocean simulations were "reversed" (i.e. negated) to force particle advection backward in time, and particle behavior was imposed.

Although researchers have used observations of the horizontal and vertical distribution of larvae to infer swimming behavior, these behaviors have not been precisely characterized. Thus, six particle back-tracking experiments were run to simulate the depth habitats occupied and the range of behaviors potentially exhibited by *M. magister* megalopae in the 30 days prior to collection (**Table 2**). In the first two simulations, particles exhibited diel vertical migration (DVM) behavior to daytime depths of either 30 m ("EH-DVM30") or 60 m ("EH-DVM60"), per depth variations reported in the literature (Hobbs and Botsford, 1992). These behaviors simulated active swimming down to the maximum depth at dawn, maintaining that depth throughout the day (∼16 h), swimming up to the water's surface at dusk, and maintaining the near surface habitat for the remainder of the night (∼8 h; swimming speed = 10 cm/s; Fernandez et al., 1994; Rasmuson, 2013; Rasmuson and Shanks, 2014). In the third simulation, particles sustained a near-surface habitat by constantly swimming upward ("EH-S1") to mimic anecdotal reports of surface aggregations of megalopae in swarms or attached to flotsam (Lough, 1976; Shenker, 1988). Although DVM and surface-following behaviors are most commonly reported in the biological literature for megalopae, we ran two additional simulations that allowed particles to disperse passively (i.e. no swimming behavior) after being initialized either at the surface ("EH-P1") or at 30 m depth ("EH-P30"), which represent the vertical limits of the plankton collection tows. Passive behavior was simulated for two reasons: (1) because the collected organisms were identified to developmental stage (i.e. megalopae) but their precise age was unknown, organisms that had recently molted from the last zoeal stage would have exhibited reduced swimming abilities commensurate with the earlier life stage (Jacoby, 1982) for potentially a large portion of the back-tracking period, which would be more closely approximated by passive dispersal; and (2) to investigate the effects of behavior on environmental exposure history, passive dispersal served as a null model for comparison with the active behaviors. The passive dispersal simulations included a backward random walk in the vertical direction, whose magnitude was calculated at each time step based on the stored local value of vertical diffusion calculated by the J-SCOPE historical ocean simulation. Finally, to account for megalopae who may have molted from the final zoeal stage mid-way through the 30-day period prior to collection, we simulated a behavior for which the particle exhibited DVM (0–30 m depth) for the first 15 days of the back-tracking simulation, followed by passive dispersal for the second half of the simulation ("EH-D15P"). For all behaviors, simulated dispersal trajectories were updated every 60 s, and particle locations and ambient environmental conditions were recorded hourly.

Prior to calculating exposure history for the particle tracks, we removed records of particles that had exited the model boundaries, which included particles located in the Columbia River and Salish Sea, due to a lack of confidence in the biogeochemical modeling in those areas (i.e. particles located at longitude > −123.9°E or < −126.5°E or latitude > 49.5°N or < 43.5°N; 12.2% of exposure history records). Additionally, we removed any particle exposure data that had unrealistic negative values due to extrapolation errors when a particle was located either at the ocean surface or just above the seafloor (0.29% of exposure history records).

Exposure history variable calculations

Two types of exposure history statistics were calculated for each particle and then averaged across all particles ($N = 100$) initialized at each station. (1) *Average environmental conditions* for all variables (temperature, salinity, dissolved oxygen concentration, nitrate concentration, phytoplankton concentration, pH, Ω_{ar}, and Ω_{ca}) were calculated by extracting the ambient environmental field from the J-SCOPE historical ocean simulations along the particle trajectory and then averaging over the entire 30-day simulation. (2) *Severity indices* ("SI"), which are a combined metric of the intensity and duration of exposure to stressful conditions, were calculated for a subset of environmental variables (oxygen, pH, Ω_{ar}, and Ω_{ca}) by multiplying the duration of time (in days) and magnitude beyond an environmental threshold that a particle was exposed to a stressful condition, and then summed over the 30-day backtracking simulation (Hauri et al., 2013; Bednaršek et al., 2017; **Supplementary Equations 3, 4**). Environmental thresholds for the severity indices were defined as oxygen < 1.4 ml l^{-1} ($O_2 < 62$ mmol m^{-3}; 61 μmol kg^{-1}; i.e. hypoxia), pH < 7.75 (Feely et al., 2008, 2016; Hodgson et al., 2016; Miller et al., 2016), $\Omega_{ar} < 1$ (i.e. physical threshold for aragonite dissolution), and $\Omega_{ca} < 1$ (i.e. physical threshold for calcite dissolution).

Developing a Habitat Model for Megalopae

GLM Development

A GLM was used to identify the modeled environmental variables that best explain the temporal and spatial heterogeneity in *M. magister* megalopae occurrence in coastal Washington and Oregon waters. Although life stage processes and population dynamics are assumed to be non-linear, linear models are often used to approximate these processes in fisheries science (e.g. Ricker, 1973; Austin and Cunningham, 1981; Guisan et al., 2002; Venables and Dichmont, 2004), and GLMs have been used successfully to predict probability of occurrence for a wide range of species (Brotons et al., 2004; MacLeod et al., 2008; Krigsman et al., 2012; Froehlich et al., 2015). A GLM is a statistical model that relates a combination of predictor variables (i.e., modeled ocean variables) to a response variable (i.e. megalopae occurrence characterized as presence or absence at each sampling station). Because our response variable had a binomial distribution (i.e. megalopae were either "present" or "absent"), we used a logit link function (Eq. 4; Fisher, 1954),

$$f(\mu) = log\left(\frac{\mu}{1-\mu}\right) \tag{4}$$

where

$$\mu = \frac{e^{X_b}}{1 + e^{X_b}} \tag{5}$$

where X_b is a linear combination of predictor variables (Eq. 5).

To examine the hypothesis that exposure history is an important driver of megalopae occurrence, a suite of potential GLMs were developed using environmental variables from one of two types of experiments (**Table 2**): (1) "*in situ*" ocean conditions extracted from the model at the times and locations where megalopae were sampled; and (2) exposure history statistics for ocean conditions were extracted along particle trajectories from six distinct particle behavior simulations. We included modeled variables from all 12 surveys (2009–2016; i.e. the "calibration survey period") during GLM development. The automated GLM forward and backward stepwise function in Matlab (R2018b; stepwiseglm) was used to evaluate all possible combinations of the suite of predictor variables (eight variables for the *in situ* models; 12 variables for the exposure history models), and to add and/or remove variables until the best GLM with the lowest Akaike information criterion corrected (AICc) score for small sample size was derived (Burnham and Anderson, 2002). Non-significant and/or potentially collinear predictors were retained in GLMs if their removal resulted in an increased AICc score, indicating that they contributed to model fit despite their lack of statistical significance and/or independence from other predictors in the model. AICc scores attempt to balance the inclusion of additional predictor variables that improve model fit but result in increased model complexity by imposing a penalty for variable inclusion to prevent over-fitting and subsequent declines in model prediction performance (Wilks, 1995). AICc scores were used to compare GLMs developed using *in situ* and exposure history experiments.

To investigate the impacts of year effects due to inter-annual variation in environmental conditions in the northeast Pacific Ocean (e.g. El Nino-Southern Oscillation and an anomalous "marine heatwave" in 2014–2016; Bond et al., 2015; Fisher et al., 2015; Thompson et al., 2018) and variability in J-SCOPE model skill (e.g. Year in Review pages at http://www.nanoos.org/products/j-scope/) on GLM model development, we conducted a modified sliding window analysis to develop additional GLMs. Here, we modified the calibration survey period to include only 10 of the 12 surveys available between 2009 and 2016 during GLM development, i.e. all combinations of 10 out of 12 surveys [mathematically, $C(12,10)$] were used to develop an additional 66 GLMs for the *in situ* and exposure history experiments, following the methods described above.

Biological Ensemble Assembly

Since the primary aim of this study was to generate the best model for forecasting inter-annual megalopae occurrence patterns, we relied on a model performance metric, the in-sample AUC value, to identify high-performance GLMs across experiments (i.e. *in situ* or exposure history behaviors). The in-sample AUC value ["area under the receiver operating characteristic (ROC) curve," see Fielding and Bell, 1997] measures model performance on the data used to develop the model. AUC is calculated by comparing the GLM output probability to the observed presence/absence for megalopae at each station. AUC ranges from 0 to 1, with AUC < 0.5 indicating no model skill, and $0.5 <$ AUC ≤ 1 indicating skill above random chance.

Due to the high performance of several individual GLMs across exposure history experiments, we selected multiple GLMs to form a "biological ensemble" to represent a range of simulated megalopae behaviors for forecasting applications (see below). We used a criterion of in-sample AUC ≥ 0.64 to identify a cluster of top-performing GLMs to include in the biological ensemble. Each member GLM was weighted equally. To evaluate potential collinearity of variables in the final biological ensemble, correlation coefficients were calculated for predictor variables in each member GLM.

Applying the Habitat Model

Biological Ensemble Performance Evaluation

To quantify the biological ensemble's ability to forecast megalopae occurrence, the ensemble was used to predict megalopae occurrence for the out-of-sample 2017 survey. Each member GLM of the biological ensemble was individually evaluated for 2017, and then the forecasted megalopae occurrence probabilities were averaged across the member GLMs to obtain the biological ensemble forecast for 2017. Specifically, particle simulations using J-SCOPE modeled ocean conditions for 2017 were conducted for each behavior represented by the GLMs in the biological ensemble. Exposure histories for each behavior were incorporated into the relevant member GLM to generate five independent forecasts of megalopae occurrence probabilities for each sampling site. These five sets of probabilities were then averaged (with equal weighting of each member GLM) to forecast megalopae occurrence probabilities for the biological ensemble as a whole. Ultimately, an AUC value was calculated by comparing the biological ensemble's forecasted megalopae probabilities to megalopae occurrence observed on the 2017 survey.

Habitat Forecasting

Finally, megalopae habitat throughout the J-SCOPE model domain was forecast for 2017 using the biological ensemble. Habitat prediction simulations were run for each behavior represented by the GLMs in the biological ensemble, using particles initialized over a grid throughout the *x*/*y* domain of the J-SCOPE ocean model. As described above, the particle exposure histories were incorporated into the individual GLMs comprising the ensemble, and then those output probabilities of megalopae occurrence were averaged across the member GLMs to generate a spatially comprehensive forecast of megalopae habitat for the biological ensemble for 2017.

RESULTS

Generalized linear models predicting megalopae occurrence based on the experiments outlined in **Table 2** were constructed using modeled ocean conditions from either *in situ* megalopae sampling locations or exposure history simulations based on particle tracking experiments with unique behavior and initialization depth. Comparing these GLMs allowed us to

TABLE 3 | Skill assessment of J-SCOPE historical ocean simulation variables that will be considered as potential predictor variables during megalopae occurrence GLM development.

Experiment	Depth habitat (m)	Temperature (°C)	Salinity	Oxygen (mmol m^{-3})	Nitrate (mmol m^{-3})	Phytoplankton (mmol m^{-3})	pH	Ω_{ar}	Ω_{ca}
In situ/EH-DVM30/EH-D15P	0–30	0.88	0.76	0.71	0.61	0.10	0.71	0.75	0.78
		0.58	−0.66	0.79	1.01	1.56	−0.77	−0.70	0.67
		(8391)	(8391)	(8189)	(860)	(8105)	(7516)	(7516)	(7516)
EH-DVM60	0–60	0.91	0.79	0.75	0.62	0.09	0.75	0.77	0.80
		0.51	−0.63	0.82	1.19	−1.30	0.78	0.73	0.68
		(14832)	(14832)	(14482)	(906)	(14398)	(13287)	(13287)	(13287)
EH-S1	0–5	0.82	0.74	0.50	0.62	0.50	0.56	0.72	0.76
		0.76	−0.70	−0.92	−0.84	2.71	−0.88	−0.72	−0.69
		(1335)	(1335)	(1302)	(625)	(1255)	(1195)	(1195)	(1195)
EH-P1	40–50	0.87	0.66	0.71	0.75	0.04	0.72	0.73	0.77
		−0.59	−0.85	−0.94	2.63	−1.14	−0.90	−0.84	−0.77
		(2403)	(2403)	(2348)	(33)	(2353)	(2165)	(2165)	(2165)
EH-P30	55–70	0.89	0.61	0.54	N/A	0.09	0.58	0.56	0.72
		−0.51	−0.92	−1.25		−1.57	−1.13	−1.13	−0.88
		(2729)	(2729)	(2665)	(0)	(2689)	(2409)	(2409)	(2409)

Environmental variables were validated in May and June from 2009 to 2017 and binned by megalopae depth habitat, corresponding to distinct exposure history particle dispersal simulations or "in situ" habitat (0–30 m). Variable skill was assessed by computing statistical comparisons of modeled and observed values at the time and location where observations were collected. Within each box, Pearson's correlation coefficient (r) is on top, the normalized root-mean-square error (NRMSE) where the sign indicates the direction of bias of the model (see ***Supplementary Equations 1, 2****) is in the middle, and the number of observations (n) used for model validation is shown parenthetically at the bottom. Shading indicates significant skill of the J-SCOPE modeled variable: blue indicates $r > 0.5$; green indicates $-1 < NRMSE < 1$. See* ***Table 2*** *for details of in situ and exposure history behaviors.*

investigate the hypothesis that exposure history is important for characterizing megalopae occurrence. Because these GLMs are built from modeled ocean variables, we begin by reporting skill assessments for these variables to understand their influence on GLM fit and performance.

J-SCOPE Variable Skill Assessment

Environmental variables from J-SCOPE historical ocean simulations performed well (as indicated by *r* and *NRMSE*; **Table 3**) within the depth habitats dictated by the simulated megalopae behaviors (**Table 2**) and during the time period when particle dispersal was simulated (May–June). All but one of the variables (phytoplankton) had a significant correlation with the observations at all depth habitats ($r > 0.5$), and variable performance generally improved with depth. Phytoplankton did not perform as well as the other variables, except near the ocean surface (0–5 m). Year-round model validation showed similar patterns as seen in the May–June validations (**Supplementary Table 3**).

Environmental Exposure of Megalopae

The exposure histories generated by the particle tracking experiments were driven predominantly by the particle depth habitats, which were determined by particle behavior and initialization depth (**Figures 3–5**; ANOVA results shown in **Supplementary Table 4**). On average, particles exhibiting passive dispersal initialized at 30 m depth (EH-P30) inhabited significantly deeper waters (mean particle depth = 47.1 ± 13.3 m (mean ± std); **Figure 3** and **Supplementary Table 4**) and originated farther offshore (mean particle ending isobath = 572 ± 455 m; **Figure 4**) than particles in any other experiment. The properties of the simulated ocean conditions that these particles were exposed to were ultimately different because of their unique depth habitat (**Figure 5** and **Supplementary Table 4**). Exposure histories for these passive particles were characterized by significantly lower temperature, dissolved oxygen concentration, phytoplankton concentration, pH, Ω_{ar}, and Ω_{ca}, and significantly higher salinity and nitrate concentrations than particles in other exposure history simulations. Consequently, particles in this experiment were exposed to the most severe hypoxic stress and corrosive waters [severity index (SI) for oxygen = 2.14 ± 3.23 hypoxia-days; SI pH = 1.88 ± 1.45 days with pH < 7.75; SI Ω_{ar} = 2.90 ± 2.37 undersaturation-days; SI Ω_{ca} = 1.69 ± 2.13 undersaturation-days). In contrast, the surface-following particles (EH-S1) had a tightly constrained depth habitat within ∼5 m of the ocean surface (mean particle depth = 2.39 ± 0.04 m), which was significantly shallower than any of the other experiments (**Figure 3**). Their exposure histories were characterized by significantly higher temperature, oxygen, phytoplankton, pH, Ω_{ar}, and Ω_{ca}, and significantly lower salinity and nitrate concentrations (**Figure 5** and **Supplementary Table 4**). Thus, these surface-following particles experienced minimal exposure to hypoxic and corrosive waters (SI Oxygen = 0.02 ± 0.06 hypoxia-days; SI pH = 0.07 ± 0.15 days below 7.75 pH; SI Ω_{ar} = 0.10 ± 0.20 undersaturation-days; SI Ω_{ca} = 0.002 ± 0.004 undersaturation-days). Particles in other experiments were exposed to intermediate environmental conditions at intermediate depth habitats. Passive particles initialized at the surface (EH-P1; mean particle depth = 20.4 ± 20.7 m) had exposure histories most similar to particles in the 30 m DVM experiment (EH-DVM30; mean particle depth = 20.3 ± 1.2 m)

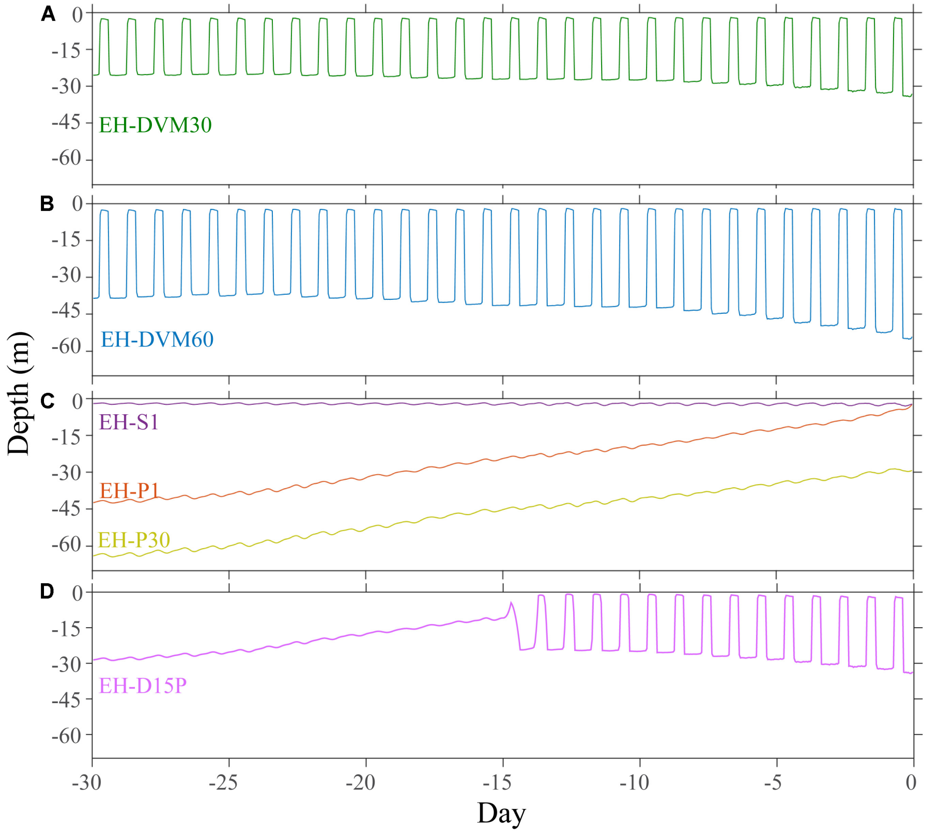

FIGURE 3 | Average depth and variability over time was driven by simulated particle behavior and initialization depth. Particles exhibiting DVM behaviors were tightly constrained between 30 m (EH-DVM30; **A**) or 60 m depths (EH-DVM60; **B**) and the surface. **(C)** Passive particles initialized at 1 m (EH-P1) and at 30 m depths (EH-P30) originated from deeper depths and traveled up in the water column over time, while surface-following particles (EH-S1) experienced a tightly constrained depth habitat near the surface. **(D)** These particles spent the first 15 days of the simulation exhibiting DVM between the surface and 30 m depth, and then they transitioned to passive dispersal (EH-D15P).

and the experiment where particles transitioned from DVM to passive dispersal (EH-D15P; mean particle depth = 20.7 ± 7.3 m). Passive dispersal particles initialized at 30 m (EH-P30; mean particle depth = 47.1 ± 13.3 m) experienced conditions most similar to the 60 m DVM particles (EH-DVM60; mean particle depth = 30.8 ± 2.4 m). *In situ* extracted conditions were most similar to those experienced by passively dispersing particles initialized at the surface (EH-P1).

GLM Comparisons: *In situ* Versus Exposure History

Inclusion of environmental exposure history during GLM development improved our ability to predict megalopae occurrence. The *in situ* GLM had the worst model fit (i.e. highest AICc score) and worst in-sample model performance (i.e. lowest AUC) compared to the exposure history models (**Table 4**; see additional statistics in **Supplementary Table 5**). Sliding window analyses that were used to evaluate the influence of individual surveys on GLM fit and performance (**Supplementary Table 6**) provided further support that, independent of the calibration survey period used to develop the GLM, the *in situ* model was out-performed by the exposure history models in 65 out of 66 cases (98% of cases).

Among the exposure history GLMs, model fit and in-sample performance were affected by the type of simulated behavior and the depth at which the particles were initialized (**Table 4** and **Supplementary Table 6**). Simulations that included passive dispersal (EH-P1, EH-D15P, and EH-P30) had the best model fit (i.e. lowest AICc scores), followed by DVM behaviors (EH-DVM30 and EH-DVM60), and then the surface-following behavior (EH-S1). These rankings of model fit based on simulated behavior were supported by the sliding window analyses as well (**Supplementary Table 6**). In-sample model performance, however, showed a different pattern of GLM rankings. When all surveys from 2009 to 2016 were used for GLM development, in-sample AUC indicated highest model performance for the EH-P1 GLM, followed by EH-D15P, EH-DVM60, EH-S1, EH-DVM30, and finally EH-P30 GLMs (**Table 4**). The sliding window analysis showed similar results, such that the EH-P1, EH-D15P, and EH-DVM60 GLMs generally had the highest performance, but on average, the EH-DVM30 and EH-P30 GLMs performed better than the EH-S1 GLMs (**Supplementary Tables 6, 7**).

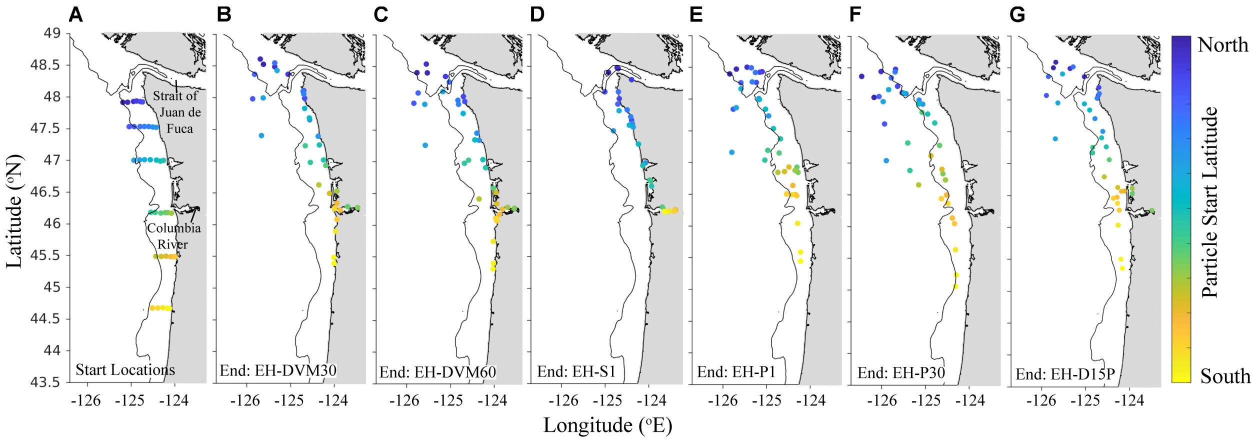

FIGURE 4 | Particle start **(A)** and average back-tracked origination locations **(B–G)** after 30-day simulated backtracking for particle exposure history simulations (2009–2017) that varied by behavior and initialization depth: DVM behavior from the surface to 30 m (EH-DVM30; **B**) and 60 m depths (EH-DVM60; **C**); the surface-following behavior (EH-S1; **D**); passive particles initialized at 1 m (EH-P1; **E**) and at 30 m depths (EH-P30; **F**); and DVM transitioning to passive dispersal at day 15 (EH-D15P; **G**; see **Table 2** for details about exposure history experiments). Particles were initialized at the same 37 sampling stations. Back-tracked origination locations were averaged for all 100 particles initialized at each station, which sometimes resulted in the average origination location being on land; these particles were moved to the nearest shoreline. Initialization locations are uniquely colored for improved resolution of differing dispersal patterns across the spatial domain. Land is shaded gray, and the 200 m isobath is shown for reference.

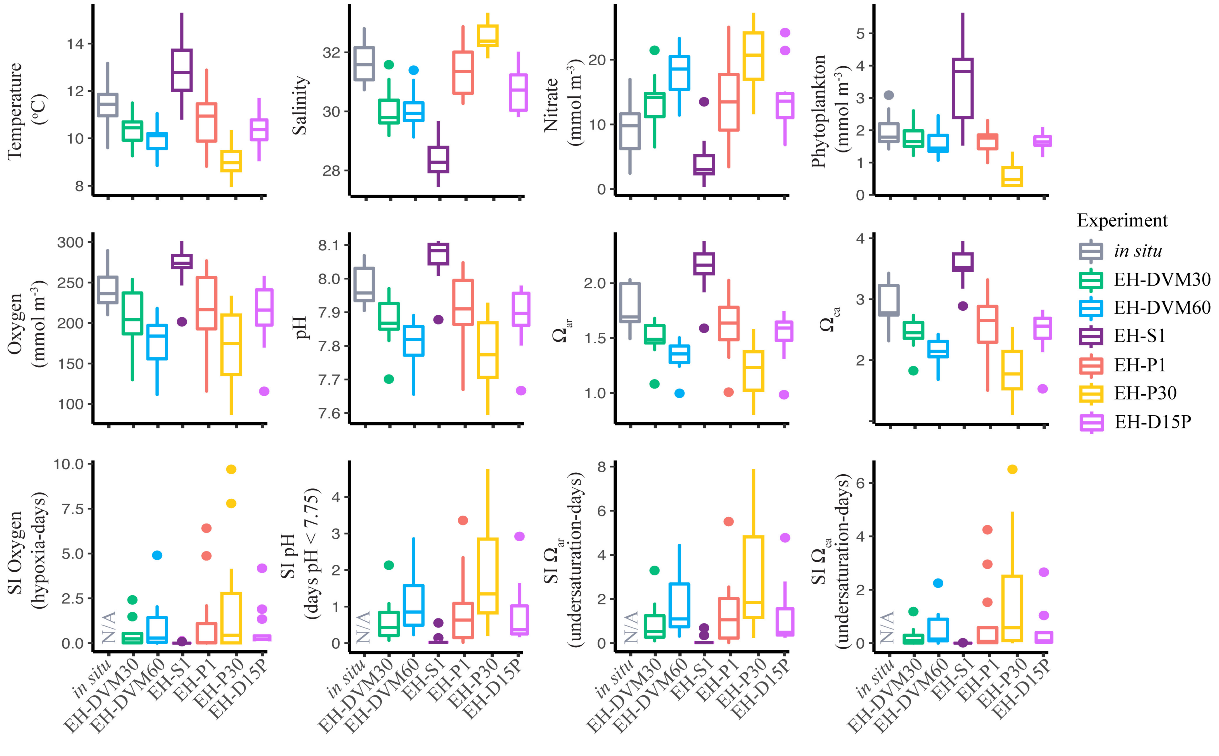

FIGURE 5 | *In situ* conditions and particle tracking exposure histories differed among years and among simulations with different particle behaviors and initialization depths. These box and whisker plots show the interquartile range (bounds of the box) with a horizontal line at the median, ends of the vertical lines at the fifth and 95th percentiles, and outliers represented by dots. Averages were calculated across all particles within an *in situ* extraction or particle tracking simulation, and statistics were calculated across survey averages to show variability over time (2009–2017; see **Supplementary Table 4** for ANOVA results).

The GLMs contained different significant predictors depending on whether or not exposure history was included, and which particle tracking behavior was simulated (**Table 4**). The predictors included in the GLMs calibrated with all surveys from 2009 to 2016 were oxygen (three occurrences), salinity (two), nitrate (two), SI for Ω_{ca} (one), phytoplankton (one), SI for Ω_{ar}

TABLE 4 | Predictor variables [significant predictors in bold ($p < 0.05$)] and their direction of correlation to megalopae occurrence for generalized linear models (GLMs) developed using surveys from 2009 to 2016 (see **Supplementary Table 5** for additional statistics and **Supplementary Tables 6, 7** for results from the sliding window analysis).

Experiment	Predictor variables (bold $p < 0.05$)	ΔAICc	In-sample AUC
In situ	−**N**	11.8	0.602
EH-DVM30	+**O**	4.7	0.644
EH-DVM60	+**S**, +**O**	5.3	0.650
EH-S1	−T, −**N**, −SI Ω_{ca}	7.9	0.645
EH-P1	+**S**, +**O**	0.0	0.658
EH-P30	+P, −**SI** $\boldsymbol{\Omega_{ar}}$	1.9	0.625
EH-D15P	**+pH**	1.7	0.657

*Metrics for relative model fit (ΔAICc; low values are superior) and in-sample model performance (AUC; high values are superior) are shown. N = nitrate; O = oxygen; P = phytoplankton; S = salinity; T = temperature; SI Ω_{ar} = severity index for aragonite saturation state; and SI Ω_{ca} = severity index for calcite saturation state. See **Table 2** for details about in situ and exposure history experiments.*

TABLE 5 | A biological ensemble of GLMs [significant predictors in bold ($p < 0.05$)] assembled from models with strong in-sample performance (AUC (2009–2016) ≥ 0.64; see **Table 4** for all models considered).

Experiment	Equation (bold $p < 0.05$)	2017 AUC
EH-DVM30	−3.01 + 0.109***O**	0.814
EH-DVM60	−6.42 + 0.132***S** + 0.00988***O**	0.936
EH-S1	1.77 − 0.157*T − 0.0994***N** − 79.5*(SI Ω_{ca})	0.757
EH-P1	−11.0 + 0.248***S** + 0.0111***O**	0.914
EH-D15P	−34.9 + 4.32***pH**	0.779
Biological ensemble:		0.943

*Out-of-sample model performance was evaluated for the 2017 survey for each model individually, and for the biological ensemble as a whole when probabilities from all five models were averaged to predict megalopae occurrence. O = oxygen (mmol m^{-3}); S = salinity; T = temperature (°C); N = nitrate (mmol m^{-3}); and SI Ω_{ca} = severity index for calcite saturation state (undersaturation-days). See **Table 2** for details about exposure history experiments.*

(one), temperature (one), and pH (one). Although the sliding window analysis indicated that the calibration survey period used to develop the GLM had some influence on which predictors were included in the GLMs (**Supplementary Tables 6, 8**), the relative frequency of the most common predictors was similar to that observed in the GLMs developed using all surveys: oxygen (194 occurrences), salinity (161), nitrate (146), Ω_{ca} (76), SI for Ω_{ca} (66), phytoplankton (60), Ω_{ar} (38), SI for Ω_{ar} (36), and temperature (35; **Supplementary Table 8**).

Biological Ensemble Formation

Due to the overall high performance of several GLMs and slight variations in their relative performance when different calibration survey periods were used (**Supplementary Table 6**), we decided to select multiple models to generate a biological ensemble that we expect to be more robust to interannual variability than any single model (**Table 5**). The biological ensemble is comprised of five GLMs with the highest overall in-sample model performance (i.e. AUC ≥ 0.64) from the following exposure history behaviors: 30 m DVM (EH-DVM30), 60 m DVM (EH-DVM60), surface-following (EH-S1), passive dispersal initialized at 1 m depth (EH-P1), and DVM transitioning to passive dispersal (EH-D15P). For the biological ensemble, megalopae abundance was positively correlated with salinity, oxygen, and pH, and negatively correlated with temperature, nitrate, and the SI for Ω_{ca}. Correlation coefficients calculated for pairwise comparisons of predictor variables within a single GLM indicated low dependency among variables (**Supplementary Table 9**).

Habitat Model Performance and Predictions

When model performance was tested for the biological ensemble using the out-of-sample 2017 survey, the ensemble performed better than random (AUC > 0.5), indicating skill in predicting megalopae occurrence (**Table 5**). Each member of the biological ensemble performed better than random (AUC > 0.5; **Supplementary Figure 1**), and the ensemble as a whole performed better than any individual member (AUC = 0.94). An AUC value of 0.94 means that for 94% of the stations where megalopae were found to be present, the model predicted a higher probability of megalopae occurrence than for randomly sampled stations where megalopae were observed to be absent.

Finally, when we simulated dispersal of megalopae initialized throughout the J-SCOPE model domain, and applied their environmental exposure histories within the biological ensemble, we were able to generate a spatially explicit habitat model for Washington and Oregon (**Figure 6**). Over this larger domain, the biological ensemble predicted relatively high probabilities of megalopae occurrence seaward of the continental shelf break. Additionally, megalopae occurrence probabilities tended to increase with latitude. Markedly low probabilities of megalopae occurrence were predicted near the mouth of the Columbia River and near the Strait of Juan de Fuca.

DISCUSSION

Importance of Exposure History

Model fit and performance (indicated by AICc and AUC, respectively) improved when megalopae exposure history was used to develop the GLM compared to the *in situ* GLM, regardless of the type of particle behavior used to simulate megalopae dispersal. This suggests that prior environmental exposure is important to include in addition to *in situ* conditions when predicting megalopae occurrence. While behavior affected the exposure history of the particles, the type of behavior did not influence the GLM performance as much as the decision to include exposure history itself. A biological ensemble of five top performing exposure history GLMs was created to capture the range of behaviors that best predicted megalopae occurrence. Within the biological ensemble, megalopae occurrence was positively correlated with dissolved oxygen concentration, salinity, and pH, and negatively correlated with temperature, nitrate concentration, and the SI for Ω_{ca}. These predictor variables suggest that megalopae are less common in nutrient-rich environments, potentially generated by upwelling of deep waters that are corrosive and hypoxic, or inflow from terrestrial

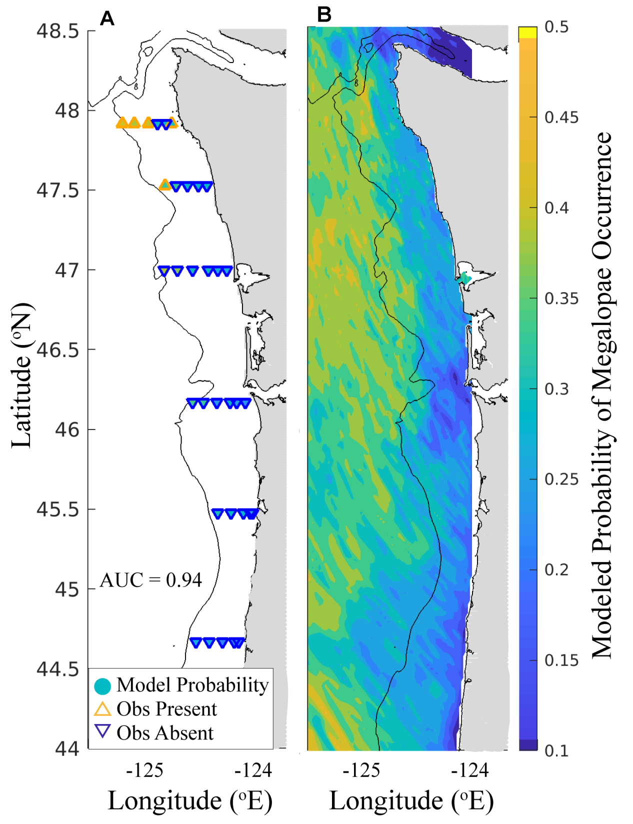

FIGURE 6 | Biological ensemble model forecast for the out-of-sample 2017 survey. **(A)** Comparison of ensemble-predicted and observed megalopae occurrence at 33 stations. Markers located at the megalopae sampling stations are filled (see color bar) according to the probability of megalopae occurrence as predicted by the biological ensemble (see **Table 5**). The outline color and orientation of the triangle indicates whether megalopae were observed to be present (orange, upward-pointing triangles) or absent (blue, downward-pointing triangles) at that station. **(B)** Probability of megalopae occurrence throughout the J-SCOPE *x*, *y* model domain forecasted by the biological ensemble (see color bar). Land is shaded gray, and the 200 m isobath is shown.

sources, such as the Columbia River or the Strait of Juan de Fuca, characterized by warmer temperatures and low salinities (Fiedler and Laurs, 1990; Davis et al., 2014).

Below, we discuss in more detail (1) why a biological ensemble was assembled to encompass the range of potential behaviors exhibited by *M. magister* megalopae, (2) how the predictor variables in the biological ensemble generate a picture of the preferred habitat for *M. magister* megalopae, and (3) what the limitations of this work are and how they can be addressed in future studies.

Multiple Behaviors in the Biological Ensemble

The biological ensemble consists of the top performing GLMs which represent the breadth of possible behaviors that forecast megalopae occurrence most skillfully (**Table 5**). Due to the uncertainty of the precise age of the megalopae at collection, potential life history changes over the 30 days prior to collection may explain why passive, DVM, and surface-following behavior models produced GLMs with strong model fit and performance (**Tables 4**, **5**). *M. magister* larvae may spend as few as ∼7 days or as many as ∼33 days in the megalopal stage (Poole, 1966; Ebert et al., 1983; Sulkin et al., 1996), so our 30-day backtracking experiments may have spanned a period when larvae had reduced swimming abilities as zoeae (Jacoby, 1982), or our DVM behaviors may have overestimated their swimming speeds (Hobbs and Botsford, 1992). Including a GLM with a combination of passive and DVM behavior (EH-D15P) only increased the performance of the ensemble as a whole. Additionally, the surface-following model (EH-S1) may have simulated reported phenomena of megalopae attaching to flotsam or forming swarms near the water's surface during the daytime (Lough, 1976; Shenker, 1988; Roegner et al., 2003). Thus, we hypothesize that realistic megalopae behaviors may be more accurately represented through a combination of passive, DVM, and surface-following simulations compared to any one behavior alone.

Modeled Megalopae Habitat Conditions

The biological ensemble, when used to forecast megalopae habitat for the entire J-SCOPE domain and compared to the out-of-sample 2017 survey, performed very well (**Table 5** and **Figure 6**). This spatially explicit model showed increasing probabilities of megalopae occurrence seaward of the continental shelf break. This modeled habitat pattern aligns with reports from the literature that *M. magister* larvae disperse offshore during early development before traveling back to the continental shelf to settle (Johnson et al., 1986; Pauley et al., 1989; Hobbs et al., 1992; Morgan and Fisher, 2010). On regional scales, low probabilities for megalopae occurrence were predicted near the mouth of the Columbia River, in the Strait of Juan de Fuca, and for near-shore areas in Oregon. Finally, high variability in megalopae occurrence was predicted on kilometer scales. The predictor variables identified in the biological ensemble may provide insight into the environmental conditions that create suitable (and unsuitable) habitat for *M. magister* megalopae.

The biological ensemble member GLMs can be divided into two depth habitat groups characterized by unique predictor variables. Four of the five models in the biological ensemble were defined by megalopae swimming behaviors that resulted in intermediate depth habitats, in which a small portion of dispersal time was spent at the ocean surface and the majority of time was spent at depth (EH-DVM30, EH-DVM60, EH-P1, and EH-D15P; **Tables 2**, **5** and **Figure 3**). In these GLMs, megalopae occurrence was positively correlated with oxygen concentration and/or salinity, or pH. These predictor variables may indicate that megalopae in mid-water depth habitats are sensitive to low oxygen or low pH conditions characteristic of upwelled waters and/or low salinities indicative of terrestrial sources, such as the Columbia River plume or the Strait of Juan de Fuca waters. Preferences for environments characterized by high oxygen, pH, and salinity are generally consistent with the habitat requirements for *M. magister* described in the literature (e.g. Reed, 1969; Sulkin and McKeen, 1989; Brown and Terwilliger, 1999;

Curtis and McGaw, 2012; Descoteaux, 2014; Miller et al., 2016; Gossner, 2018). For example, negative impacts, such as increased mortality, decreased growth, and increased respiration rates, have been demonstrated when *M. magister* megalopae and juveniles are exposed to hypoxic conditions (Bancroft, 2015; Gossner, 2018). Prior laboratory experiments have also shown increased mortality of *M. magister* zoeae and megalopae when exposed to low salinity conditions (Reed, 1969; Brown and Terwilliger, 1999), and avoidance of adult crabs to low salinity conditions, except when starved (Curtis and McGaw, 2012). The positive correlation between pH and megalopae occurrence is consistent with reports that *M. magister* larvae are negatively impacted by exposure to low pH (Descoteaux, 2014; Miller et al., 2016).

In contrast to the intermediate depth habitat models discussed above, the fourth member GLM of the biological ensemble corresponds to megalopae occurrence in near-surface habitats (i.e. the surface-following behavior model, EH-S1). In surface waters, where oxygen concentrations and salinity are relatively consistent across temporal and spatial domains (**Figure 5**), alternative predictors were identified to characterize preferred habitat, such as minimal exposure to calcite-undersaturated conditions, relatively cool temperatures, and low nutrient concentrations (**Table 5**). These habitat preferences again may signal avoidance of upwelled waters, characterized by low Ω_{ca} and rich in nutrients, or terrestrial inputs, with warm temperatures and high nutrient concentrations. The negative correlation between SI for Ω_{ca} and megalopae occurrence is supported by recent work by Bednaršek et al. (2020) which showed that *M. magister* megalopae may experience external carapace dissolution due to prolonged exposure to more severe calcite saturation state gradients. Several studies have also highlighted the importance of temperature on larval development and survival in *M. magister* (Sulkin and McKeen, 1989; Sulkin and McKeen, 1996; Sulkin et al., 1996; Brown and Terwilliger, 1999), and our results indicate a preference for relatively cool temperatures in shallow habitats where thermal stress may be more common than at depth (**Figure 5**). If megalopae occurrence is linked to exposure history via a mortality mechanism, then our results may suggest that megalopae experience lethal temperatures in shallow habitats over the 30-day particle tracking simulations. To our knowledge, no studies have investigated the direct effects of nitrate concentrations on megalopae survival or development. We propose that low nutrient concentrations may indirectly define megalopae habitat by serving as a proxy for preferred downwelling regimes (Hales et al., 2005; Palacios et al., 2013) outside of freshwater plumes, or may indicate the presence of food sources (such as phytoplankton and zooplankton), causing a draw-down of nutrients.

A novel approach taken by this study was to evaluate the skill of modeled variables within the specific depth range and season relevant to our study species. Since the skill of the ocean variables influences the skill of the GLMs to predict megalopae occurrence, and ultimately to model preferred habitat, differences in variable skill may help explain differences in predictive power of GLMs developed with exposure histories from unique behavior simulations. Overall, our model validation showed that ocean variable skill generally improved with depth (**Table 3**), consistent with prior work by Siedlecki et al. (2016), but variables with strong skill in surface waters also generated GLMs capable of good model performance (e.g. EH-S1 GLM in **Table 5**). Notably, the 0–30 m DVM exposure history experiment (EH-DVM30), the DVM transitioning to passive behavior (EH-D15P), and the *in situ* model all used ocean variables within ~0–30 m depth range, and thus the J-SCOPE variable skill was similar for all GLMs, yet both exposure history GLMs had better fit (lower AICc) and higher predictive skill (higher AUC) than the *in situ* GLMs (**Table 4** and **Supplementary Tables 6, 7**). This finding further supports our conclusion that exposure to recent environmental conditions is important to include in modeling megalopae occurrence.

Model Limitations and Future Work

In this study, the suite of potential predictor variables was limited to (1) variables that were included in the J-SCOPE historical ocean simulations, (2) variables whose skill could be assessed using observational data, and (3) variables, or threshold values for severity indices, identified in the published literature as being important for *M. magister* megalopae or related species. For example, only microzooplankton concentration is modeled in J-SCOPE, a class of zooplankton which is not the main food source for brachyuran crab larvae (Bigford, 1977; Harms and Seeger, 1989; Sulkin et al., 1998; Casper, 2013), so we omitted this variable from consideration. Regarding the severity indices, we used thresholds to characterize stressful conditions that may not be biologically relevant for *M. magister* megalopae, due to limited availability of published scientific studies (see discussions in Hettinger et al., 2012; Waldbusser et al., 2015). Given the importance of temperature and salinity on modeling megalopae occurrence, severity indices for these conditions could also be developed if critical thresholds were identified.

Here, we assembled the five best-performing GLMs into a biological ensemble with equal weighting of its members, due to a lack of information about realistic larval behaviors in wild populations. Future *in situ* behavioral studies of *M. magister* late-stage zoeae and early-stage megalopae would help shape realistic larval behavior in particle tracking simulations and inform the relative weighting of member GLMs in the biological ensemble.

Application of the biological ensemble for modeling megalopae habitat is best applied during the temporal and spatial window of the megalopae observations used in this study—namely, late May (2009–2012) and late June (2009–2017) over the continental shelves of Washington and Oregon. Since marine conditions typically become more stressful as the upwelling season evolves, beginning in ~mid-April (Austin and Barth, 2002; Hales et al., 2006; Hauri et al., 2015), our model may weight exposure to more stressful conditions more heavily given the relative under-representation of the earlier (May) sampling period in recent years. Additionally, because all megalopae sampling stations were located over the continental shelf, but we applied the biological ensemble to forecast habitat over the entire J-SCOPE model domain, evaluation of the model's prediction of high-quality megalopae habitat in offshore areas would be essential to utilizing the predicted habitat fields offshore.

Finally, this study laid the groundwork for future forecasting of megalopae abundance. To model more complex dynamics, such as abundance, we will apply either generalized linear mixed models (GLMMs), delta-GLMs, or generalized additive models (GAMs), which have relaxed constraints on the types of relationships allowed between the predictor and response variables (Guisan et al., 2002; Venables and Dichmont, 2004; Brodie et al., 2019). Additionally, we will rely on J-SCOPE seasonal forecasts to predict megalopae abundance on seasonal timescales. Since megalopae abundance is correlated with recruitment into the *M. magister* fishery 4 years later (Shanks and Roegner, 2007; Shanks et al., 2010; Shanks, 2013), improved forecasts of megalopae abundance, generated without arduous field sampling, would extend the management time horizon from seasonal to more than 4 years in advance, potentially promoting increased long-term planning and stability in the fishery (Hobday et al., 2016; Tommasi et al., 2017).

CONCLUSION

Inclusion of environmental exposure history improved our ability to predict megalopae occurrence. Ultimately, a biological ensemble was generated from GLMs developed with multiple behaviors to encompass biologically relevant variations in megalopae dispersal. This biological ensemble showed superior predictive performance (high AUC) relative to individual GLMs. The biological ensemble identified positive correlations between megalopae occurrence and oxygen concentration, salinity, and pH, and negative correlations with temperature, nitrate concentration, and the SI for Ω_{ca}. When considered together, these variables indicate that megalopae habitat is characterized by downwelling conditions seaward of terrestrial inputs, such as Columbia River plume or the Strait of Juan de Fuca waters.

DATA AVAILABILITY STATEMENT

The datasets analyzed in this study are included in this article, in the **Supplementary Material**, or can be found online (see **Supplementary Table 2**).

AUTHOR CONTRIBUTIONS

EN was the principal author of the manuscript, designed and performed backtracking experiments with guidance from SS and AH and conducted habitat modeling with input from SS, IK, and CS. Model skill was evaluated by EN, SO, and SS. JF and CM collected and analyzed biological and environmental samples. SA and RF collected ocean condition observations. SA derived ocean acidification formulae. EN, SS, SO, IK, JF, CM, AH, SA, RF, CS, JN, and NB contributed to the writing and editing of the manuscript.

FUNDING

We thank the NOAA Ocean Acidification Program for funding this work. Funding for this study was provided by the Bonneville Power Administration (Project 1998-014-00) and the NOAA Northwest Fisheries Science Center, NOAA National Marine Fisheries Service. Portions of this work were supported by NOAA Climate Program Office MAPP (Grant # NA17OAR4310112). SO was supported by the JISAO Summer Internship Program. The contributions of SA and RF were supported by NOAA Pacific Marine Environmental Laboratory (PMEL) and the NOAA Ocean Acidification Program. This is PMEL contribution number 5006. This publication is partially funded by the Joint Institute for the Study of the Atmosphere and Ocean (JISAO) under NOAA Cooperative Agreement NA15OAR4320063, Contribution No. 2019-1020.

ACKNOWLEDGMENTS

We greatly appreciate the many people who contributed to this project over the years, including the captains and crews who operated vessels, especially the *F/V Frosti*, and the many scientists who helped collect the samples.

SUPPLEMENTARY MATERIAL

The Supplementary Material for this article can be found online at: https://www.frontiersin.org/articles/10.3389/fmars.2020.00102/full#supplementary-material

REFERENCES

Alin, S. R., Feely, R. A., Dickson, A. G., Hernandez-Ayon, J. M., Juranek, L. W., Ohman, M. D., et al. (2012). Robust empirical relationships for estimating the carbonate system in the southern California current system and application to CalCOFI hydrographic cruise data (2005–2011). *J. Geophys. Res.* 117, :C05033. doi: 10.1029/2011JC007511

Austin, J. A., and Barth, J. A. (2002). Variation in the position of the upwelling front on the Oregon shelf. *J. Geophys. Res.* 107:3180. doi: 10.1029/2001JC000858

Austin, M. P., and Cunningham, R. B. (1981). Observational analysis of environmental gradients. *Proc. Ecol. Soc. Aust.* 11, 109–119.

Bancroft, M. P. (2015). *An Experimental Investigation of the Effects of Temperature and Dissolved Oxygen on the Growth of Juvenile English Sole and Juvenile Dungeness Crab*. master's thesis., Oregon State University, Corvallis, OR.

Bednaršek, N., Feely, R. A., Beck, M. W., Alin, S. R., Siedlecki, S. A., Calosi, P., et al. (2020). Exoskeleton dissolution with mechanoreceptor damage in larval Dungeness crab related to severity of present-day ocean acidification vertical gradients. *Sci. Total Environ.* [Epub ahead of print].

Bednaršek, N., Feely, R. A., Tolimieri, N., Hermann, A. J., Siedlecki, S. A., Pörtner, H. O., et al. (2017). Exposure history determines pteropod vulnerability to ocean acidification along the US West Coast. *Sci. Rep.* 7, :4526. doi: 10.1038/s41598-017-03934-z

Bigford, T. E. (1977). Effect of several diets on survival, development time, and growth of laboratory-reared spider crab *Libinia emarginata*, larvae. *Fish. Bull. U. S.* 76, 59–64.

Bond, N. A., Cronin, M. F., Freeland, H., and Mantua, N. (2015). Causes and impacts of the 2014 warm anomaly in the NE Pacific. *Geophys. Res. Lett.* 43, 3414–3420. doi: 10.1002/2015GL063306

Botsford, L. W., and Hobbs, R. C. (1995). Recent advances in the understanding of cyclic behavior of Dungeness crab (*Cancer magister*) populations. *ICES Mar. Sci. Symp.* 199, 157–166.

Botsford, L. W., Methot, R. D. Jr., and Johnston, W. E. (1983). Effort dynamics of the Northern California Dungeness crab (*Cancer magister*) fishery. *Can. J. Fish. Aquat. Sci.* 40, 337–346. doi: 10.1139/f83-049

Boßelmann, F., Roman, P., Fabritius, H., Raabe, D., and Epple, M. (2007). The composition of the exoskeleton of two crustaceans: the American lobster *Homarus americanus* and the edible crab *Cancer pagurus*. *Thermochim. Acta* 463, 65–68. doi: 10.1016/j.tca.2007.07.018

Brodie, S., Thorson, J. T., Carroll, G., Hazen, E. L., Bograd, S., and Selden, R. L. (2019). Trade-offs in covariate selection for species distribution models: a methodological comparison. *Ecography* 42, 1–14.

Brotons, L., Thuiller, W., Aruajo, M. B., and Hirzel, A. H. (2004). Presence-absence versus presence-only modelling methods for predicting bird habitat suitability. *Ecography* 27, 437–448. doi: 10.1111/j.0906-7590.2004.03764.x

Brown, A. C., and Terwilliger, N. B. (1999). Developmental changes in oxygen uptake in *Cancer magister* (Dana) in response to changes in salinity and temperature. *J. Exp. Mar. Biol. Ecol.* 241, 179–192. doi: 10.1016/S0022-0981(99)00071-4

Burnham, K. P., and Anderson, D. R. (2002). *Model Selection and Multimodel Inference: A Practical Information-Theoretic Approach*, 2nd Edn. New York, NY: Springer.

Busch, D. S., and McElhany, P. (2016). Estimates of the direct effect of seawater pH on the survival rate of species groups in the California current ecosystem. *PLoS One* 118:e0160669. doi: 10.1371/journal.pone.0160669

Casper, N. J. (2013). *Nutritional Role of Microalgae in the Diet of First Stage Brachyuran Crab Larvae*. Bellingham, WA: Western Washington University Graduate School Collection.

Chan, F., Barth, J. A., Lubchenco, J., Kirincich, A., Weeks, H., Peterson, W. T., et al. (2008). Emergence of anoxia in the California Current large marine ecosystem. *Science* 319, :920. doi: 10.1126/science.1149016

Connolly, T. P., Hickey, B. M., Geier, S. L., and Cochlan, W. P. (2010). Processes influencing seasonal hypoxia in the northern California current system. *J. Geophys. Res.* 115, :C03021. doi: 10.1029/2009JC005283

Curtis, D. L., and McGaw, I. J. (2012). Salinity and thermal preference of Dungeness crabs in the lab and in the field: effects of food availability and starvation. *J. Exp. Mar. Biol. Ecol.* 413, 113–120. doi: 10.1016/j.jembe.2011.12.005

Davis, K. A., Banas, N. S., Giddings, S. N., Siedlecki, S. A., MacCready, P., Lessard, E. J., et al. (2014). Estuary-enhanced upwelling of marine nutrients fuels coastal productivity in the U.S. Pacific Northwest. *J. Geophys. Res. Oceans* 119, 8778–8799. doi: 10.1002/2014JC010248

Descoteaux, R. (2014). *Effects of Ocean Acidification on Development of Alaskan Crab Larvae*. Fairbanks, AK: University of Alaska.

Dickson, A. G. (1990). Standard potential of the reaction: AgCl (s) + 1/2H2(g) = Ag (s) + HCl (aq), and the standard acidity constant of the ion HSO4- in synthetic sea water from 273.*15* to 318.15 K. *J. Chem. Thermodyn.* 22, 113–127. doi: 10.1016/0021-9614(90)90074-z

Dickson, A. G., and Riley, J. P. (1979). The estimation of acid dissociation constants in seawater media from potentiometric titrations with strong base, I. The ionic product of water – KW. *Mar. Chem.* 7, 89–99. doi: 10.1016/0304-4203(79)90001-x

Ebert, E. E., Haseltine, A. W., Houk, J. L., and Kelly, R. O. (1983). Laboratory cultivation of the Dungeness crab, *Cancer magister*. *Fish. Bull.* 172, 259–309.

Fabry, V. J., Seibel, B. A., Feely, R. A., and Orr, J. C. (2008). Impacts of ocean acidification on marine fauna and ecosystem processes. *ICES J. Mar. Sci.* 65, 414–432. doi: 10.1093/icesjms/fsn048

Feely, R. A., Alin, S. R., Carter, B., Bednaršek, N., Hales, B., Chan, F., et al. (2016). Chemical and biological impacts of ocean acidification along the west coast of North America. *Estuar. Coast. Shelf Sci.* 183, 260–270. doi: 10.1016/j.ecss.2016.08.043

Feely, R. A., Klinger, T., Newton, J. A., and Chadsey, M. (2012). *Scientific Summary of Ocean Acidification in Washington State Marine Waters*. Seattle, WA: Pacific Marine Environmental Laboratory.

Feely, R. A., Sabine, C. L., Hernandez-Ayon, J. M., Ianson, D., and Hales, B. (2008). Evidence for upwelling of corrosive "acidified" water onto the continental shelf. *Science* 320, 1490–1492. doi: 10.1126/science.1155676

Fernandez, M., Iribarne, O. O., and Armstrong, D. A. (1994). Swimming behavior of Dungeness crab, *Cancer magister* Dana, megalopae in still and moving water. *Estuaries* 17, 271–275.

Ferrari, R., and Ferreira, D. (2011). What processes drive the ocean heat transport? *Ocean Model.* 38, 171–186. doi: 10.1038/srep44011

Fiedler, P. C., and Laurs, R. M. (1990). Variability of the Columbia River plume observed in visible and infrared satellite imagery. *Int. J. Remote Sensing.* 11, 999–1010. doi: 10.1080/01431169008955072

Fielding, A. H., and Bell, J. F. (1997). A review of methods for the assessment of prediction errors in conservation presence/absence models. *Environ. Conserv.* 24, 38–49. doi: 10.1017/s0376892997000088

Fisher, J. L., Peterson, W. T., and Rykaczewski, R. R. (2015). The impact of El Niño events on the pelagic food chain in the northern California current. *Global. Change. Biol.* 21, 4401–4414. doi: 10.1111/gcb.13054

Fisher, R. (1954). The analysis of variance with various binomial transformations. *Biometrics* 10, 130–139.

Froehlich, H. E., Hennessey, S. M., Essington, T. E., Beaudreau, A. H., and Levin, P. S. (2015). Spatial and temporal variation in nearshore macrofaunal community structure in a seasonally hypoxic estuary. *Mar. Ecol. Progr. Ser.* 520, 67–83. doi: 10.3354/meps11105

Gossner, H. M. (2018). *Quantifying Sensitivity and Adaptive Capacity of Shellfish in the Northern California Current Ecosystem to Increasing Prevalence of Ocean Acidification and Hypoxia*. master's thesis., Oregon State University, Corvallis, OR.

Grantham, B. A., Chan, F., Nielsen, K. J., Fox, D. S., Barth, J. A., Huyer, A., et al. (2004). Upwelling-driven nearshore hypoxia signals ecosystem and oceanographic changes in the northeast Pacific. *Nature* 429, 749–754. doi: 10.1038/nature02605

Guisan, A., Edwards, T. C. Jr., and Hastie, T. (2002). Generalized linear and generalized additive models in studies of species distributions: setting the scene. *Ecol. Model.* 157, 89–100. doi: 10.1016/s0304-3800(02)00204-1

Hales, B., Karp-Boss, L., Perlin, A., and Wheeler, P. A. (2006). Oxygen production and carbon sequestration in an upwelling coastal margin. *Global. Biogeochem. Cycles* 20, :GB3001. doi: 10.1029/2005GB002517

Hales, B., Moum, J. N., Covert, P., and Perlin, A. (2005). Irreversible nitrate fluxes due to turbulent mixing in a coastal upwelling system. *J. Geophys. Res.* 110:C10S11. doi: 10.1029/2004JC002685

Harms, J., and Seeger, B. (1989). Larval development and survival in seven decapod species (Crustacea) in relation to laboratory diet. *J. Exp. Mar. Biol. Ecol.* 133, 129–139. doi: 10.1016/0022-0981(89)90162-7

Harris, K. E., DeGrandpre, M. D., and Hales, B. (2013). Aragonite saturation state dynamics in a coastal upwelling zone. *Geophys. Res. Lett.* 40, 1–6.

Hauri, C., Gruber, N., McDonnell, A. M. P., and Vogt, M. (2013). The intensity, duration, and severity of low aragonite saturation state events on the California continental shelf. *Geophys. Res. Lett.* 40, 3424–3428. doi: 10.1002/grl.50618

Hauri, C., Gruber, N., Plattner, G.-K., Alin, S., Feely, R. A., Hales, B., et al. (2015). Ocean acidification in the California current system. *Oceangraphy* 22, 60–71. doi: 10.5670/oceanog.2009.97

Hettinger, A., Sanford, E., Hill, T. M., Russell, A. D., Sato, K. N., Hoey, J., et al. (2012). Persistent carry-over effects of planktonic exposure to ocean acidification in the Olympia oyster. *Ecology* 93, 2758–2768. doi: 10.1890/12-0567.1

Hickey, B. M., and Banas, N. S. (2008). Why is the Northern end of the California current system so productive? *Oceanography* 21, 90–107. doi: 10.5670/oceanog.2008.07

Higgins, K., Hastings, A., Sarvela, J. N., and Botsford, L. W. (1997). Stochastic dynamics and deterministic skeletons: population behavior of Dungeness crab. *Science* 276, 1431–1435. doi: 10.1126/science.276.5317.1431

Hobbs, R. C., and Botsford, L. W. (1992). Diel vertical migration and timing of metamorphosis of larvae of the Dungeness crab *Cancer magister*. *Mar. Biol.* 112, 417–428. doi: 10.1007/bf00356287

Hobbs, R. C., Botsford, L. W., and Thomas, A. (1992). Influence of hydrographic conditions and wind forcing on the distribution and abundance of Dungeness crab, *Cancer magister*, larvae. *Can. J. Fish. Aquat. Sci.* 49, 1379–1388. doi: 10.1139/f92-153

Hobday, A. J., Spillman, C. M., Eveson, J. P., and Hartog, J. R. (2016). Seasonal forecasting for decision support in marine fisheries and aquaculture. *Fish. Oceanogr.* 25, 45–56. doi: 10.1111/fog.12083

Hodgson, E. E., Essington, T. E., and Kaplan, I. C. (2016). Extending vulnerability assessment to include life stages considerations. *PLoS One* 11:e0158917. doi: 10.1371/journal.pone.0158917

Huyer, A. E., Sobey, E. J. C., and Smith, R. L. (1979). The spring transition in currents over the Oregon continental shelf. *J. Geophys. Res.* 84, 6995–7011.

Jacoby, C. (1982). Behavioral responses of the larvae of *Cancer magister* Dana (1852) to light, pressure and gravity. *Mar. Behav. Physiol.* 8, 267–283. doi: 10.1080/10236248209387024

Johnson, D. F., Botsford, L. W., Methot, R. D. Jr., and Wainwright, T. C. (1986). Wind stress and cycles in Dungeness crab (*Cancer magister*) catch off California, Oregon, and Washington. *Can. J. Fish. Aquat. Sci.* 43, 838–845. doi: 10.1139/f86-103

Kaplan, I., Williams, G., Bond, N., Hermann, A., and Siedlecki, S. A. (2016). Cloudy with a chance of sardines: forecasting sardine distributions using regional climate models. *Fish. Oceanogr.* 25, 15–27. doi: 10.1111/fog.12131

Krigsman, L. M., Yoklavich, M. M., Dick, E. J., and Cochrane, G. R. (2012). Models and maps: Predicting the distribution of corals and other benthic macro-invertebrates in shelf habitats. *Ecosphere* 3, 1–16. doi: 10.1890/ES11-00295.1

Kudela, R. M., Banas, N. S., Barth, J. A., Frame, E. R., Jay, D. A., Largier, J. L., et al. (2008). New insights into the controls and mechanisms of plankton productivity in coastal upwelling waters of the northern California current system. *Oceanography* 21, 54–59.

Largier, J. L., Lawrence, C. A., Roughan, M., Kaplan, D. M., Dever, E. P., Dorman, C. E., et al. (2006). WEST: a northern California study of the role of wind-driven transport in the productivity of coastal plankton communities. *Deep- Sea Res. II* 53, 2833–2849. doi: 10.1016/j.dsr2.2006.08.018

Lough, R. G. (1976). Larval dynamics of the Dungeness crab, *Cancer magister*, off the central Oregon coast, 1970–71. *Fish. Bull.* 74, 353–376.

Lueker, T. J., Dickson, A. G., and Keeling, C. D. (2000). Ocean pCO2 calculated from dissolved inorganic carbon, alkalinity, and equations for K1 and K2: validation based on laboratory measurements of CO2 in gas and seawater at equilibrium. *Mar. Chem.* 70, 105–119. doi: 10.1016/s0304-4203(00)00022-0

MacLeod, C. D., Mandleberg, L., Schweder, C., Bannon, S. M., and Pierce, G. J. (2008). A comparison of approaches for modelling the occurrence of marine animals. *Hydrobiologia* 612, 21–32. doi: 10.1016/j.prevetmed.2012.11.005

Methot, R. D. Jr. (1986). "Management of Dungeness crab fisheries," in *North Pacific Workshop on Stock Assessment and Management of Invertebrates*, eds G. S. Jamieson, and N. Bourne (Ottawa: Deptartment of Fisheries and Oceans), 326–334.

Methot, R. D. Jr., and Botsford, L. W. (1982). Estimated preseason abundance in the California Dungeness crab (*Cancer magister*) fisheries. *Can. J. Fish. Aquat. Sci.* 39, 1077–1083. doi: 10.1139/f82-145

Miller, J. J., Maher, M., Bohaboy, E., Friedman, C. S., and McElhany, P. (2016). Exposure to low pH reduces survival and delays development in early life stages of Dungeness crab (*Cancer magister*). *Mar. Biol.* 163, :118.

Moloney, C. L., Botsford, L. W., and Largier, J. L. (1994). Development, survival and timing of metamorphosis of planktonic larvae in a variable environment: the Dungeness crab as an example. *Mar. Ecol. Prog. Ser.* 113, 61–79. doi: 10.3354/meps113061

Morgan, C. A., Beckman, B. R., Weitkamp, L. A., and Fresh, K. L. (2019). Recent ecosystem disturbance in the Northern california current. *Fisheries* 44, 465–474. doi: 10.1002/fsh.10273

Morgan, C. A., De Robertis, A., and Zabel, R. W. (2005). Columbia River plume fronts. I. Hydrography zooplankton distribution, and community composition. *Mar. Ecol. Prog. Ser.* 2009, 19–31. doi: 10.3354/meps299019

Morgan, S. G., and Fisher, J. L. (2010). Larval behavior regulates nearshore retention and offshore migration in an upwelling shadow and along the open coast. *Mar. Ecol. Prog. Ser.* 404, 109–126. doi: 10.3354/meps08476

Neues, F., Ziegler, A., and Epple, M. (2007). The composition of the mineralized cuticle in marine and terrestrial isopods: a comparative study. *CrystEngComm* 9, 1245–1251.

North, E. W., Adams, E. E., Schlag, S., Sherwood, C. R., He, R., and Socolofsky, S. (2011). Simulating oil droplet dispersal from the Deepwater Horizon spill with a Lagrangian approach. *Geophys.ical Monograph. Series.* 195, 217–226. doi: 10.1029/2011gm001102

North, E. W., Schlag, Z., Hood, R. R., Li, M., Zhong, L., Gross, T., et al. (2008). Vertical swimming behavior influences the dispersal of simulated oyster larvae in a coupled particle-tracking and hydrodynamic model of Chesapeake Bay. *Mar. Ecol. Prog. Ser.* 359, 99–115. doi: 10.3354/meps07317

Pacific States Marine Fisheries Commission. (2019). *Species Report: Commercial Land Catch: Metric-Tons (mt), Revenue, and Price-per-pound (Price/Lbs)*. Portland, OR: Pacific States Marine Fisheries Commission.

Palacios, D. M., Hazen, E. L., Schroeder, I. D., and Bograd, S. J. (2013). Modeling the temperature-nitrate relationship in the coastal upwelling domain of the California current. *J. Geophys. Res. Oceans* 118, 3223–3239. doi: 10.1002/jgrc.20216

Pauley, G. B., Armstrong, D. A., Van Citter, R., and Thomas, G. L. (1989). *Species Profiles: Life Histories and Environmental Requirements of Coastal Fishes and Invertebrates (Pacific Southwest)–Dungeness Crab*. Washington, DC: U.S. Army Corps of Engineers.

Pelletier, G., Lewis, E., and Wallace, D. (2007). *CO2SYS.XLS: A Calculator for the CO2 System in Seawater for Microsoft Excel/VBA*. Olympia, WA: Washington State Department of Ecology.

Perez, F. F., and Fraga, F. (1987). Association constant of fluoride and hydrogen ions in seawater. *Mar. Chem.* 21, 161–168. doi: 10.1016/0304-4203(87)90036-3

Poole, R. L. (1966). A description of laboratory-reared zoeae of *Cancer magister* Dana, and megalopae taken under natural conditions (Decapoda Brachyura). *Crustaceana* 11, 83–97. doi: 10.1163/156854066x00487

Rasmuson, L. K. (2013). The biology, ecology and fishery of the Dungeness crab, *Cancer magister*. *Advances. in Marine. Biology.* 65, 95–148. doi: 10.1016/B978-0-12-410498-3.00003-3

Rasmuson, L. K., and Shanks, A. L. (2014). *In situ* observations of Dungeness crab megalopae used to estimate transport distances by internal waves. *Mar. Ecol. Progr. Ser.* 511, 143–152. doi: 10.3354/meps10926

Reed, P. H. (1969). Culture methods and effects of temperature and salinity on survival and growth of Dungeness crab (*Cancer magister*) larvae in the laboratory. *J. Fish. Res. Board Can.* 26, 389–397. doi: 10.1139/f69-037

Ricker, W. E. (1973). Linear regressions in fishery research. *J. Fish. Res. Board Can.* 30, 409–434. doi: 10.1139/f73-072

Riebesell, U., Zondervan, I., Rost, B., Tortell, P. D., Zeebe, R. E., and Morel, F. M. M. (2000). Reduced calcification of marine plankton in response to increased atmospheric CO2. *Nature* 407, 364–367. doi: 10.1038/35030078

Roegner, G. C., Armstrong, D. A., Hickey, B. M., and Shanks, A. L. (2003). Ocean distribution of Dungeness crab megalopae and recruitment patterns to estuaries in southern Washington state. *Estuaries* 26, 1058–1070. doi: 10.1007/bf02803363

Schlag, Z. R., and North, E. W. (2012). *Lagrangian TRANSport model (LTRANS v.2) User's Guide*. Cambridge, MD: University of Maryland Center for Environmental Science.

Shanks, A. L. (2013). Atmospheric forcing drives recruitment variation in the Dungeness crab (*Cancer magister*), revisited. *Fish. Oceangr.* 22, 263–272. doi: 10.1111/fog.12020

Shanks, A. L., and Roegner, G. C. (2007). Recruitment limitation in Dungeness crab populations is driven by variation in atmospheric forcing. *Ecology* 88, 1726–1737. doi: 10.1890/06-1003.1

Shanks, A. L., Roegner, G. C., and Miller, J. (2010). Using megalopae abundance to predict future commercial catches of Dungeness crabs (*Cancer magister*) in Oregon. *Calif. Coop. Ocean. Fish. Investig. Rep.* 51, 106–118.

Shenker, J. M. (1988). Oceanographic association of neustonic larval and juvenile fishes and Dungeness crab megalopae off Oregon. *Fish. Bull.* 86, 299–319.

Siedlecki, S. A., Banas, N., Davis, K. A., Giddings, S., Hickey, B. M., MacCready, P., et al. (2015). Seasonal and interannual oxygen variability on the Washington and Oregon continental shelves. *J. Geophys. Res. Oceans* 120, 608–633. doi: 10.1002/2014JC010254

Siedlecki, S. A., Kaplan, I. C., Hermann, A. J., Nguyen, T. T., Bond, N. A., Newton, J. A., et al. (2016). Experiments with seasonal forecasts of ocean conditions for the Northern region of the California Current upwelling system. *Sci. Rep.* 6, :27203. doi: 10.1038/srep27203

Sobota, J. L., and Dinnel, P. (2000). Settlement behavior of Dungeness crab (*Cancer magister* Dana 1852) megalopae in the presence of the shore crab, *Hemigrapsus* (Decapoda, Brachyura). *Crustaceana* 73, 223–234. doi: 10.1163/156854000504174

Sulkin, S., Lehto, J., Strom, S., and Hutchinson, D. (1998). Nutritional role of protists in the diet of first stage larvae of the Dungeness crab *Cancer magister*. *Mar. Ecol. Prog. Ser.* 169, 237–242. doi: 10.3354/meps169237

Sulkin, S. D., and McKeen, G. L. (1989). Labarotory study of survival and duration of individual zoeal stages as a function of temperature in the brachyuran crab *Cancer magister*. *Mar. Biol.* 103, 31–37. doi: 10.1007/bf00391062

Sulkin, S. D., and McKeen, G. L. (1996). Larval development of the crab *Cancer magister* in temperature regimes simulating outer-coast and inland-water habitats. *Mar. Biol.* 127, 235–240. doi: 10.1007/bf00942108

Sulkin, S. D., Mojica, E., and McKeen, G. L. (1996). Elevated summer temperature effects on megalopal and early juvenile development in the Dungeness crab, *Cancer magister*. *Can. J. Fish. Aquat. Sci.* 53, 2076–2079. doi: 10.1139/cjfas-53-9-2076

Thompson, A. R., Schroeder, I. D., Bograd, S. J., Hazen, E. L., Jacox, M. G., Leising, A., et al. (2018). State of the California current 2017–2018: still not quite normal in the North and getting interesting in the South. *Calif. Coop. Ocean. Fish. Investig. Rep.* 59:66.

Tommasi, D., Stock, C. A., Hobday, A. J., Methot, R., Kaplan, I. C., Eveson, J. P., et al. (2017). Managing living marine resources in a dynamic environment: the role of seasonal to decadal climate forecasts. *Progr. Oceanogr.* 152, 15–49.

Uppström, L. R. (1974). The boron/chlorinity ratio of deep-sea water from the Pacific Ocean. *Deep Res. Oceanogr. Abstr.* 21, 161–162. doi: 10.1016/0011-7471(74)90074-6

Venables, W. N., and Dichmont, C. M. (2004). GLMs, GAMs and GLMMs: an overview of theory for applications in fisheries research. *Fish. Res.* 70, 319–337. doi: 10.1016/j.fishres.2004.08.011

Waldbusser, G. G., Hales, B., Langdon, C. J., Haley, B. A., Schrader, P., Brunner, E. L., et al. (2015). Saturation-state sensitivity of marine bivalve larvae to ocean acidification. *Nat. Clim. Chang.* 5, 273–280. doi: 10.1038/NCLIMATE2479

Wild, P. W. (1980). Effects of seawater temperature on spawning, egg development, hatching success, and population fluctuations of the Dungeness crab, *Cancer magister*. *Calif. Coop. Ocean. Fish. Investig. Rep.* 21, 115–120.

Wilks, D. S. (1995). *Statistical Methods in the Atmospheric Sciences: An Introduction*. San Diego, CA: Academic Press.

Conflict of Interest: The authors declare that the research was conducted in the absence of any commercial or financial relationships that could be construed as a potential conflict of interest.

frontiers in Marine Science

ORIGINAL RESEARCH
published: 16 April 2020
doi: 10.3389/fmars.2020.00232

Projected Economic Impact of Climate Change on Marine Capture Fisheries in the Philippines

David Suh[1] *and Robert Pomeroy*[2*]

[1] *Department of Agricultural and Resource Economics, University of Connecticut, Storrs, CT, United States,* [2] *Department of Agricultural and Resource Economics, Connecticut Sea Grant, University of Connecticut at Avery Point, Groton, CT, United States*

Climate change and its impact on fisheries is a key issue for fishing nations, particularly the Philippines. The Philippines is highly vulnerable to the impacts of climate change on fisheries and it can lead to economic shock on the nation's economy. This paper examines the impact of climate change on marine capture fisheries in the Philippines using a computable general equilibrium (CGE) model to elaborate and project impacts on the national economy. In the simulation, one baseline scenario and two climate change scenarios based on greenhouse gas concentration—RCP 2.6 and RCP 8.5—were considered. The model focuses on Gross Domestic Product (GDP) and income distribution by region, which can represent economic conditions in terms of economic growth and distribution. Results show that there will be a negative change on both the fisheries and economic variables where more extreme changes in climate occur.

Keywords: climate change, marine capture, fisheries economics, economic growth, income distribution

Edited by:
Darren Pilcher,
University of Washington and NOAA/PMEL, United States

Reviewed by:
Jonathan A. Anticamara,
University of the Philippines Diliman, Philippines
Edison D. Macusi,
Wageningen University of Life, Netherlands

***Correspondence:**
Robert Pomeroy
robert.pomeroy@uconn.edu

Specialty section:
This article was submitted to Global Change and the Future Ocean, a section of the journal Frontiers in Marine Science

Received: *28 August 2019*
Accepted: *25 March 2020*
Published: *16 April 2020*

Citation:
Suh D and Pomeroy R (2020) Projected Economic Impact of Climate Change on Marine Capture Fisheries in the Philippines. Front. Mar. Sci. 7:232. doi: 10.3389/fmars.2020.00232

INTRODUCTION

The Philippines, a maritime nation that is a complex of islands, comprises 7,641 islands and has the territorial sea that covers 679,800 km^2 and Exclusive Economic Zone (EEZ) of 2,263,816 km^2. Most parts of the Philippines are coastal areas, and about 70% of Filipinos are estimated to live in coastal areas (Palomares and Pauly, 2014). Fisheries have a great significance in terms of food security and economy in the Philippine (Santos et al., 2011). There is a need to secure the food supply to keep feeding people as poverty has remained continuously high and the population has grown in the Philippines. Fisheries are a strategically important factor because it has a positive nutritional effect as a source of necessary protein and essential nutrients (Prein and Ahmed, 2000; Irz et al., 2007)[1]. Total fish consumption has been rising steadily with increases in production (Cuvin-Aralar et al., 2016).

The fisheries in the Philippines makes a significant contribution to the national economy in terms of income and employment. Total fish production was estimated at 4.65 million metric tons, and the fisheries sector contributed almost 4.33 billion dollars to the country's economy in 2015 (BFAR, 2016). The fisheries sector employed an estimated 1.6 million people national wide, contributing 1.5% to the gross domestic product (GDP) in 2015 (BFAR, 2016; PSA, 2017a). According to an FAO report, the Philippines places eighth globally in fish production, as of 2014, and is a key economic sector for the country (BFAR, 2016).

---

[1] According to the prevalence of undernourishment data, in 2017, about 13.5% of the population was malnourished in the Philippines [World Bank (n.d.), "Prevalence of undernourishment"], and fish provides Filipino people with approximately one-third of their average per capita intake of animal protein (Bennett et al., 2018).

Climate change has been considered particularly important for fishing nations (Kelleher et al., 2009; Barange et al., 2014), but discussion of climate change and impact on fisheries is also a key issue for the Philippines (Santos et al., 2011; Geronimo, 2018). These changes may cause not only loss of productivity, but also economic shock on the nation's economy. Since climate change is expected to have different consequences, impacts can be related to vulnerability in countries heavily dependent on fishery, in view of the important contribution of these sectors to employment, supply, income and nutrition (Vannuccini et al., 2018). The Philippines is actually vulnerable to the impacts of climate change on fisheries and it can lead to economic shock on the nation's economy. Among fishing nations, Philippines is one of the most vulnerable countries to climate change (Badjeck et al., 2010; FAO, 2016). The Philippines is third in the ranking of vulnerability to climate change risks among 67 developed, emerging and frontier market countries, and is particularly very sensitive to extreme weather events in terms of people affected and economic costs (Paun et al., 2018).

Since fisheries is intimately related to various economic sectors, such as transportation, storage, processing, it is necessary to elaborate a systematic model to understand the economic impact of climate change on fisheries throughout an economy. In this paper, a computable general equilibrium (CGE) model, which is useful to explain economic impacts of events in a quantitative manner (Dwyer et al., 2005), is developed to examine how climate change may affect the marine capture fishing sector in the Philippines and consequently how the economy may react to the change. The paper will contribute to the current discussion of climate impacts in the ocean of the Philippines, adding dimensions to macroeconomic interpretations of impact on fisheries focusing on marine capture fish[2] which can be relatively more affected by climate change.

CLIMATE CHANGE AND OCEAN IN THE PHILIPPINES

Climate change is an important thread in the tapestry of earth's history along with the evolution of life and the physical transformations of this planet (Ruddiman, 2001). The study of climate in fisheries also matters for a practical reason: climate is a primary determinant of fish population (Lehodey et al., 2006). Changes in climate condition and shifts in the distribution of species are closely related to the productivity of fish stocks (Perry et al., 2005; Munday et al., 2008; Nilsson et al., 2009; Pankhurst and Munday, 2011; Pratchett et al., 2014). Climate change causes the change of oceanic currents[3] and consequently affects the environment for fish: areas that have favorable conditions increase resulting in expansion in species' range and the growth in population; areas where favorable conditions exist may move, causing a population's numbers to decline in certain areas and increase in others, effectively shifting the population's range; and favorable conditions for a species may disappear, leading to a population crash and possible extinction (Roessig et al., 2004; Ganachaud et al., 2011; Stock et al., 2011; Dunne et al., 2012, 2013). Mora and Ospina (2001) examined the critical thermal maximum of 15 fishes. The critical thermal maximum ranges from 34.7 to 40.8°C while sea temperature reached 32°C in a broad range of latitudes in the tropical eastern Pacific Ocean during El Niño. They argue the studied fish are tolerant to temperatures occurring during the particular warm event such as El Niño. Eme and Bennett (2009) examined thermal limits of fishes around Banda Sea of Indonesia which is connected to the Pacific Ocean using the critical thermal methodology and chronic lethal methodology. Thermal limits show different figures by species, for example, such Squaretail mullet did not survive temperatures higher than 38.9 ± 0.7°C while such common goby did not survive temperatures below 10.9 ± 0.2°C.

Increase in temperature on the Philippines seas has been reported by several studies (Peñaflor et al., 2009; Pörtner et al., 2014; Khalil et al., 2016; Hoegh-Guldberg et al., 2017; Geronimo, 2018). Sea surface temperature in the sea near the Philippines shows upward trend with the warming rate of 0.2°C per decade over the period 1985–2017, based on 0.05° resolution satellite-based sea surface temperature data (Peñaflor et al., 2009; Khalil et al., 2016). The warming trend is not spatially identical for the Philippines and the warming rate varies by region. The warming rate in the West Philippine Sea bordering the west-central part of the Province of Ilocos Norte shows a faster rate while the rate in the sea surrounding Palawan Island and the sea between Catanduanes Island and Samar Island shows slower compared to other sea areas in the Philippines (Khalil et al., 2016). The forecasting model of warming with a scenario of greenhouse gas (GHG) concentration mitigation under the phase 5 of Coupled Model Intercomparison Project (CMIP), which is collaboration between climate modeling groups for the purpose of advance in knowledge of climate change, indicates that sea surface temperature in the Philippine will increase around 0.36°C by 2100 based on the RCP 2.6 emissions scenario, noting that the majority of this warming will happen over the next 30 years (Khalil et al., 2016).

The use of linear regression from CMIP5 provides projected changes in SST around the Philippines including the Coral Triangle in the next 90 years. Increase in SST ranges from 0.42 to 0.76°C for near-term, and 0.58 to 2.95°C for a long-term, depending on level of GHG concentrations and mitigation (Hoegh-Guldberg et al., 2017). Climate model simulations driven with historical changes in anthropogenic and natural drivers, and GHG concentration scenarios (the RCP 4.5 and the RCP 8.5), based on the average of Hadley Centre Interpolated SST 1.1 data, also indicate that SST around the Philippines will increase (Pörtner et al., 2014; Hoegh-Guldberg et al., 2017).

---

[2] Capture fisheries includes not only marine capture fisheries but also inland capture fisheries. This paper focuses on marine capture fisheries which is dominant in capture fisheries – according to fisheries situation report (PSA, 2014), it shows 95% of capture fisheries.

[3] El Niño is associated with warming in the tropical Pacific Ocean, and has global climatic teleconnections, affecting the global climate change (Yeh et al., 2009). Sea Surface Temperature (SST) in Southeast Asia has shown an extreme trend due to El Niño (Thirumalai et al., 2017).

ECONOMIC REVIEW ON IMPACTS OF CLIMATE CHANGE ON FISHERIES

Many empirical studies in oceanography, physiology and ecology began to deal with the relationship between fisheries and climate due to the growing need for extension of the discussion about continued climate change (Brander, 2007; Barange and Perry, 2009), but few studies cover the economic impact on fisheries. Several studies have argued that climate change affects the amount of catch in business terms. Cheung et al. (2010) present maximum exploitable catch of a species under climate change using a dynamic bioclimate envelope model. They demonstrate climate change considerably affects the distribution of catch potential leading to potential fisheries productivity. Their estimation shows that catch potentials will fall in many coastal regions, particularly in the tropics and the southern margin of semi-enclosed seas, since species are expected to move away from the regions due to rising temperature in the ocean. Lam et al. (2016) demonstrate the impacts of climate change on global fisheries revenues. They argue climate change will have a negative impact on the maximum revenue potential of most fishing countries. It was found that coastal low-income food deficit countries (LIFDC) are heavily dependent on fish catches as a way of meeting their nutritional needs but almost every coastal LIFDC is in danger of decrease in fisheries maximum revenue potential. Merino et al. (2011) examined the synergistic effect of climate variability and production of fish with estimation of maximum sustainable yield. They put emphasis on global management measures to achieve optimized global supply of marine products, suggesting interaction between global markets and regional climate may be acting as a factor causing sequential overexploitations and resource depletion.

Few studies have analyzed the economic impacts of climate change on fisheries dealing with the national economy. Arnason (2007) estimated the impact of global warming on fish stocks in Iceland and Greenland using Monte Carlo simulations. The result shows positive impact on GDP in Iceland and Greenland. Ibarra et al. (2013) examined economic impacts of climate change in Mexican coastal fisheries in terms of shrimp and sardine fisheries. They found climate change causes a decrease in shrimp production and a high degree of variability and uncertainty of sardine fisheries stocks.

This paper will make several contributions to this literature. First, this study analyzes the impact of climate change in fisheries from the perspective of the economic modeling. It estimates the impact of climate change adding dimensions to macroeconomic interpretations of impact on marine capture fisheries. Few studies deal with the economic impact of climate change on fisheries, but even these studies focus on changes of catch in terms of productivity with simplistic calculations. Thus, the evidence for projection is limited. This study covers the potential causes of economic impact other than production associated with climate change. This paper also presents an economic impact which includes notable indicators, such as GDP and income distribution with estimation using major national economic variables, so it can be useful in establishing economic mechanism related to fisheries.

Second, the study examines the economic impact of climate change on fisheries for a specific country rather than at a global level. Climate change impacts will differ from region to region and country to country. Some regions will get warmer well above the average, in contrast, others may not get warmer or may even get colder (Arnason, 2006). In addition, the economy of each country has different characteristics. This study carries out modeling specific to the Philippines so that the results obtained will prove helpful in decision-making related to adaptation options.

METHODS

Construction of Model

In this paper, the model estimates the impacts of climate change constructing future scenarios including one baseline scenario and two climate scenarios for the Philippines. The baseline scenario depicts how the economy of the Philippines might be expected to change if the condition related to climate were not changed. Climate scenarios are based on the Representative Concentration Pathways (RCP) which describes trajectories of greenhouse gas concentration, provided by the fifth assessment report (AR5) of the Intergovernmental Panel on Climate Change (IPCC, 2013). One of climate scenarios assumes RCP 2.6 which is a scenario of strong mitigation (Scenario A) and the other one assumes RCP 8.5 which is a scenario of comparatively high greenhouse gas emissions (Scenario B).

The model employs the method of the projected change in maximum revenue potential (MRP) which is explained by Lam et al. (2016). MRP in the study implies the potential change in revenue, which can be expected under climate change scenarios, resulted from the change in the amount of fish catches due to climate change. The combined outputs of coupled atmospheric-ocean physical and biogeochemical Earth System Models (ESM) with Dynamic Bioclimate Envelope Models (DBEM) and outputs from three ESMs that are available for the Coupled Models Intercomparison Project Phase 5 (CMIP5): the Geophysical Fluid Dynamics Laboratory Earth System Model 2 M (GFDLESM2M,) the Institute Pierre Simon Laplace (IPSL) (IPSL-CM5-MR) and Max Planck Institute for Meteorology Earth System Model (MPI-ESM MR) (Method) were used, employing the model described in Sarmiento et al. (2004), and Cheung et al. (2010). In the model, projected revenue is calculated by the product of ex-vessel price and maximum catch potential. The model assumes that real ex-vessel price is constant for the study period with the fact that the real ex-vessel prices have remained relatively stable since 1970. Maximum catch potential is derived from the product of projected fishing mortality required to achieve the maximum sustainable yield and projected biomass. Since projected fishing mortality is required to achieve the maximum sustainable yield approximates natural mortality rate of the stock, change in revenue is determined by change in biomass. So, in this paper the trend of production is subject to the trend of MRP, assuming production is proportional to biomass *ceteris paribus*.

Linearly calculated trends based on the projected change in MRP are put into the production in the capture fisheries sector data assuming functions in the models are the same. To calculate change in production of fisheries, it is necessary to determine the latitude of the Philippine in the Pacific Ocean. The Philippines extends 1,150 miles from north to south and has a comparatively wide range of latitude with reference to Manila (about 14.5°). Initial general equilibrium is constructed from production of capture fisheries in initial data, and the new states are applied by reflecting changes in production repeatedly. As the capture sector is a subsector of primary industry and products in the capture sector are not an intermediate product which are value added, the effects of marine capture are estimated by calculation of the share of marine capture in the total effects of capture, with the assumption that the marine capture sector and other capture sectors such as freshwater capture do not affect each other's sector.

Climate change involves large changes that are well outside of historical experiences. This suggests the need to use simulation techniques of some kind. The simulation is based on the CGE model which is a system of equations that describes an economy as a whole and the interactions among its parts. The CGE model is primarily used to simulate and assess the structural adjustments, undertaken by economic systems, as a consequence of shocks, like changes in technology, preferences, or economic policy (Berrittella et al., 2006). In the context of the study, climate change works as the shock which affects the economy since increases or decreases in catch is directly connected to supply level and production in the fishing industry and fisheries sector.

CGE has the advantage of analyzing direct and indirect impacts on the nation's economy and estimating how an economy might react to changes because it provides a before and after comparison of an economy when a shock, such as a tax, causes it to reallocate its productive resources in more or less efficient ways (Burfisher, 2017). Static models can tell a powerful story about the ultimate winners and losers from economic shocks, but it cannot represent the object interactions over time, so dynamic CGE model is considered an appropriate model since climate change is not just a one-off shock.

Dynamic CGE has the advantage of reflecting adjustment process in a recursive dynamic framework. The earliest forms of dynamic CGE were carried out by Hudson and Jorgenson (1974) and Adelman and Robinson (1978). Dynamic CGE has become common in forward-looking expectation since Ballard et al. (1985) performed dynamic CGE model for the analysis on tax policy. Recently, the model is often used to figure out the economic effect related to environment such as pollution abatement (Dessus and Bussolo, 1998; Dellink et al., 2004), environment tax (Wendner, 2001; Kumbaroglu, 2003; Siriwardana et al., 2011), and climate change (Eboli et al., 2010; Robinson et al., 2012). In this paper, the iterative method is used and the updated dataset provided by the simulation of the current period is used for the simulation of the next period, so that each solution is solved in a recursive year-on-year framework (**Figure 1**). Through the analysis, it can derive intuitive economic indicators such as change in GDP and income distribution, according to climate change.

Supply

The model covers economic features that reflect the characteristics of the Philippines and the structure follows the approach of Dervis et al. (1982), Robinson (1989), Shoven and Whalley (1992), Ginsburgh and Keyzer (1997), and Lofgren et al. (2002) based on neoclassical perspective. On the side of supply, the model is established under the assumption of profit maximization. Production involves information of input-output based on factors of production and has flexibility for substitution between the labor and capital. The model assumes a Cobb-Douglas production function for the technology in the production process, so the function is homogeneous of degree one and it has constant returns to scale. The formula for production function can be represented as follows:

$$\boldsymbol{QA_a = ad_a \cdot \prod_{f} QF_{fa}^{\alpha va_{fa}}}$$

where ad_a is production function efficiency, αva_{fa} is value-added share for factor f in activity a, QA_a is production activity level, and QF_{fa} is quantity demanded of factor f by production activity a.

In the model, domestic and export commodity have a constant elasticity of transformation (CET). In other word, the distribution of theses commodities is modeled in the form of CET function, so output transformation can be represented by the function of the quantity of exports and the quantity of domestic output as follows:

$$\boldsymbol{QX_c = at_c \cdot \left(\alpha tr_c^t \cdot EX_c^{\rho_c^t} + (1 - \alpha tr_c^t) \cdot QD_c^{\rho_c^t}\right)^{1/\rho_c^t}}$$

where at_c is shift for output transformation, αtr_c^t is share for output transformation, ρ_c^t is exponent for output transformation, QX_c is the quantity of domestic output, QD_c is the quantity of domestic output sold domestically, and EX_c is the quantity of exports.

Market is represented by perfect competition. Consequently, incidental assumptions are required to develop the model. If price of an input changes then the quantity of the output sold alters, and that affects demand for the input (Hoffmann, 2003). The model assumes the impact of input price is insignificant and firms do not make economic profit, not measuring elasticity of demand which reflects the market power that firms have.

Demand

On the side of demand, the model consists of household, government and the foreign sector reflecting the consumption of domestic good and imported good. Households are classified depending on region. They are divided into two groups: urban and rural household. The government of the model has similar expenditure to the household and gets money through taxation and consumes commodity quantities paying market prices and transfers to households according to the expenditure function. Foreign sector in the model also purchases domestically produced commodity.

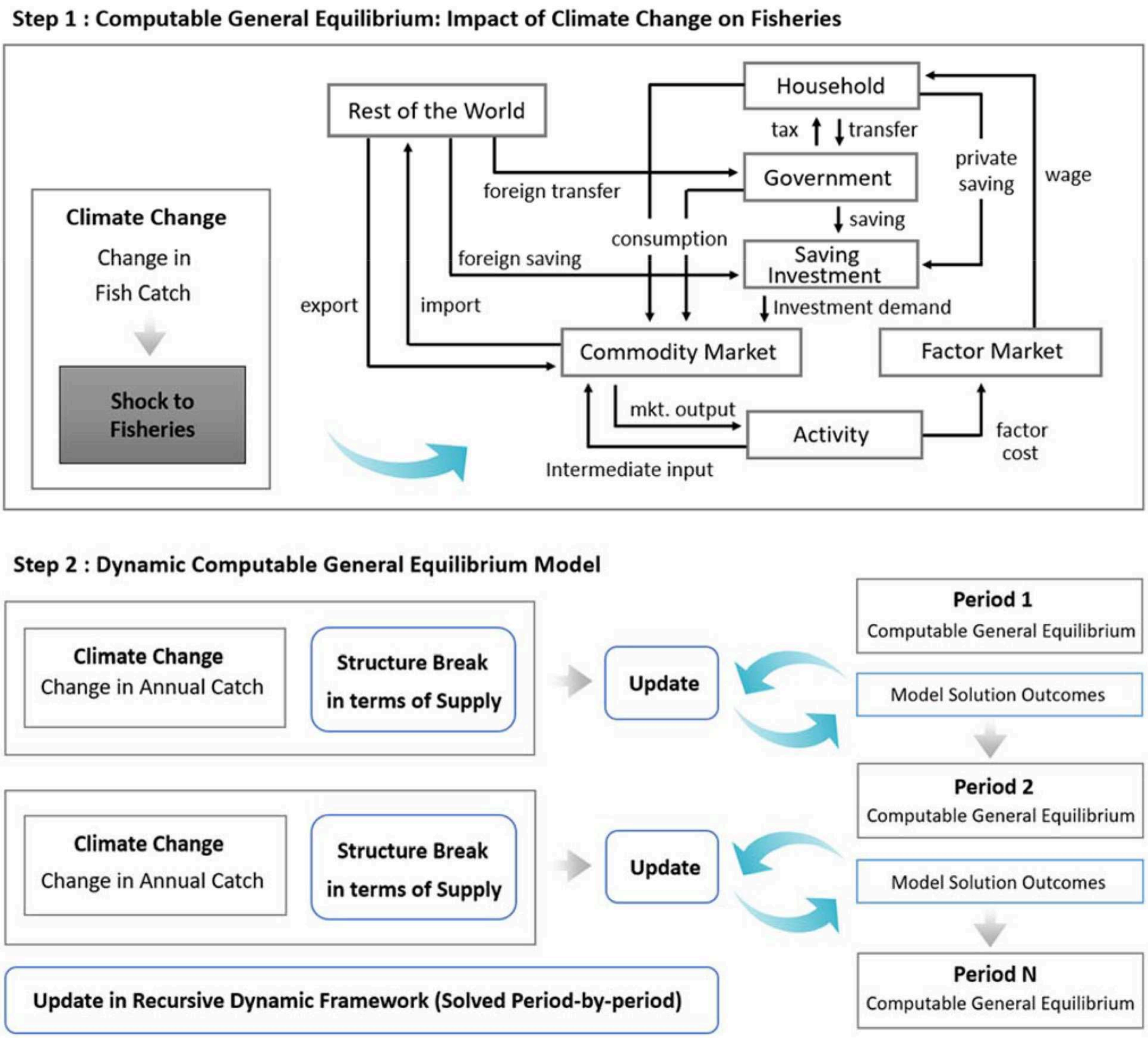

FIGURE 1 | Conceptual framework of CGE for impact of change on fisheries.

The demand side can be represented by the combination of domestic commodity use as follows:

$$QD_c = \sum_a IC_{ca} + \sum_h QH_{ch} + gdo_c + QI_c$$

where QD_c is domestic sales of domestic output, IC_{ca} is intermediate use of commodity c by activity a, QH_{ch} is quantity of consumption of commodity c by household h, gdo_c is government demand for commodity, and QI_c is investment demand.

Armington assumption is used for determination of the combination of domestically produced commodity and imported commodity reflecting responses of trade to price changes. Composite supply takes the form of Armington function as follows:

$$QQ_c = aq_c \cdot \left(\alpha co_c^q \cdot IM_c^{-\rho_c^q} + (1 - \alpha co_c^q) \cdot QD_c^{-\rho_c^q}\right)^{-1/\rho_c^q}$$

where QQ_c is quantity supplied to domestic commodity demanders, aq_c is shift parameter for composite supply, αco_c^q is share parameter for composite supply, ρ_c^q is exponent $(-1 < \rho < \infty)$ for composite supply, and IM_c is quantity of imports, and QD_c is domestic use of domestic output. Due to the equilibrium of demand and supply (i.e., $QD_c = QQ_c$), the demand side is connected with Armington assumption.

Government

Government also plays a role as an economic agent in general equilibrium. Government consumes commodities while it obtains revenue by collecting tax and transfer. Government revenue and expenditure are represented as follows:

$$\boldsymbol{YG = \sum_{h} tdh_{h} \cdot YH_{h} + CR \cdot tr_{g,r} + \sum_{c} tco_{c} \cdot (PD_{c} \cdot QD_{c} + (PM_{c} \cdot IM_{c})_{|c \in CM}) + \sum_{c} tim_{c} \cdot CR \cdot pm_{c} \cdot IM_{c} + \sum_{c} tix_{c} \cdot CR \cdot pe_{c} \cdot EX_{c}}$$

where YG *is* government revenue, tdh_h is the income tax rate of household, $tr_{g,r}$ is transfer from government to rest of world, tco_c is the rate of consumption tax, tim_c is the tariff rate on import, pm_c is import price, tix_c is the rate of tax on exports, pe_c is price of exports, CR is the exchange rate, PD_c is the price of domestic output, QD_c is the quantity of domestic output sold domestically, PM_c is the price of imports in domestic currency, IM_c is the quantity of imports, and EX_c is the quantity of exports.

$$\boldsymbol{GX = \sum_{h} \mathrm{tr}_{h,g} + \sum_{c} \mathrm{gdo}_{c} \bullet \mathrm{PC}_{c}}$$

where GX *is* government expenditure $tr_{h,g}$ is transfer from household to government, gdo_c is government demand for commodity, and PC_c is price of composite commodity c.

Market Clearing

In the CGE model, some constraints are considered for the equilibrium. One of important constraints is the market clearing, so the model assumes market clearing in the factor market and the commodity market. The condition of the factor market clearing can be represented by the equality of supply and demand of factor as follows:

$$\boldsymbol{FS_{f} = \sum_{a} QF_{fa}}$$

where FS_f is supply of factor f and QF_{fa} is quantity demanded of factor f by activity a.

The condition of the commodity market clearing comes from relationship between two equations in demand, and it can be represented as follows:

$$\boldsymbol{QQ_{c} = \sum_{a} IC_{ca} + \sum_{h} QH_{ch} + gdo_{c} + QI_{c}}$$

where QQ_c is quantity supplied to domestic commodity demanders, IC_{ca} is intermediate use of commodity c by activity a, QH_{ch} is quantity of consumption of commodity c by household h, gdo_c is government demand for commodity, and QI_c is investment demand.

Data

In the study, the one country, multi-sector and recursive CGE model is constructed. For the analysis, information of the value of all transactions in an economy is required. Thus, it is necessary to utilize a social accounting matrix (SAM) which indicates a logical framework of rows and columns providing a visual display of the transactions as a circular flow of national income and spending in an economy (Burfisher, 2017). In this study, the model uses SAM by modification of the 2013 Social Accounting Matrix from the compilation of the Agricultural Model for Policy Evaluation which is constructed by Briones (2016). It provides a set of transactions between fisheries, industry and service sub-sectors in the Philippines. The SAM includes the primary sector, the manufacturing and industry sector, the service sector, and the public sector. The primary sector encompasses the capture fisheries and aquaculture fisheries and other primary sector such as the agriculture. Parameters are drawn from SAM with econometric analysis, and the effect of marine capture fisheries is calculated by interpolation because values of capture fisheries sector are aggregated in the SAM. The modeling[4] is based on standard hypotheses of CGE and the model is solved in Generalized Algebraic Modeling System (GAMS).

After the construction of the general equilibrium, GDP is calculated by sum of the value of final demands and net exports as follows:

$$\begin{aligned} GDP = & \sum_{h}\sum_{c} PC_{c}QH_{c,h} + \sum_{a}\sum_{c}\sum_{h} CA_{ac}QHA_{ach} \\ & + \sum_{c} PC_{c}QG_{c} + \sum_{c} PC_{c}QI_{c} + \sum_{c} PC_{c}qst_{c} \\ & + \sum_{h}\sum_{c} PC_{c}QH_{c,h} + \sum_{c} PM_{c}IM_{c} + \sum_{c} PE_{c}EX_{c} \end{aligned}$$

where PC_c *is* composite commodity price, QH_{ch} is quantity of commodity consumption by household, CA_{ac} is marginal cost of commodity from activity, QHA_{ach} is quantity of household consumption of commodity from activity for household, QG_c is government consumption demand for commodity, QI_c is quantity of investment demand, PM_c is price of imports in domestic currency, IM_c is quantity of imports, PE_c is price of exports in domestic currency, EX_c is quantity of exports, and qst_c is quantity of stock change.

RESULTS

Philippines Economy

In the simulations, results show more negative change in economic variables where more extreme changes in climate occur. Since three scenarios are applied in this study, the model focuses on the results on differences in GDP. The result of simulation is shown in **Figure 2**. *Ceteris paribus* except change in production of fisheries resulted from climate change, baseline

---

[4] The model includes 27 equations to form the system. Most parameters, variables and equations and the code for the model are developed based on Lofgren et al. (2002) and Lofgren (2003) following the neoclassical structure which is well-developed by Dervis et al. (1982).

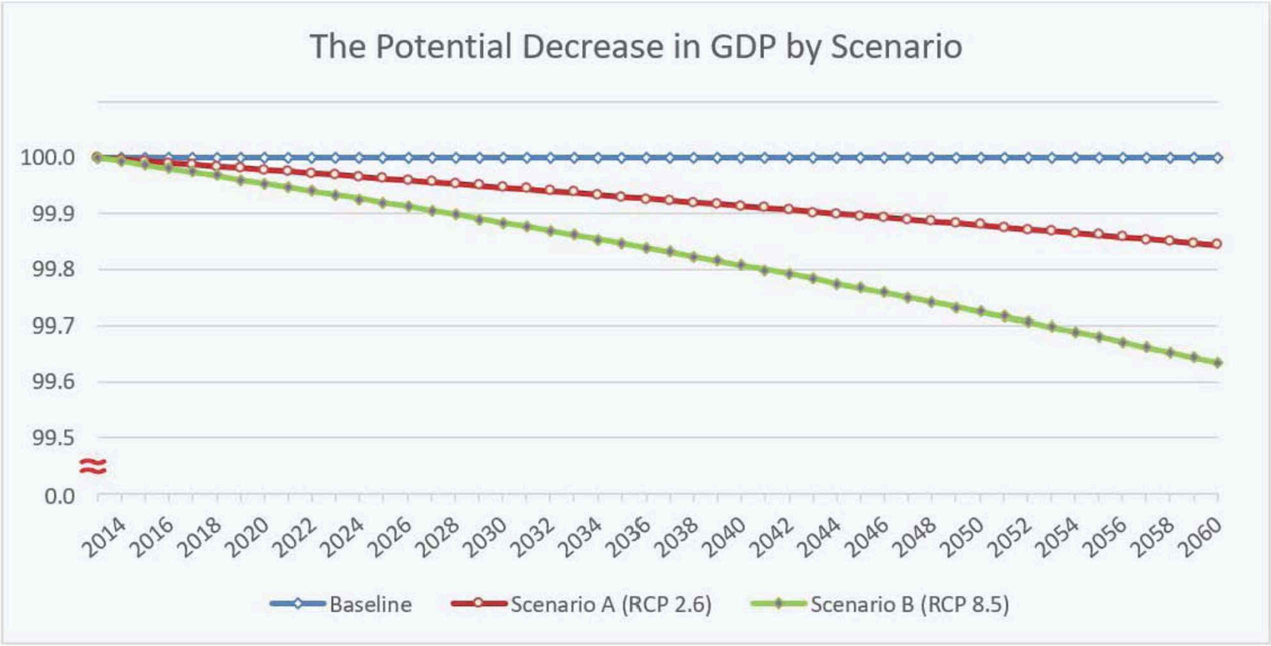

FIGURE 2 | Projection of decrease in GDP by scenario.

scenario is normalized in the analysis. Index score of 100 is set based on GDP of baseline specifying 100 as a reference point. So, the score of 100 means the level of GDP in baseline for each year, and scores <100 indicate the levels in scenarios are underperforming the comparison in the year. As it shows, higher radiative forcing value causes lower level of GDP compared to baseline scenario assuming no changes in the status quo.

As a result of simulation, GDP is expected to decrease by 0.16% with scenario A (RCP 2.6) and 0.37% with scenario B (RCP 8.5) up to 2060. This state came from direct effect, i.e., reduction in catch in exclusive economic zone and seas in the Philippines leading to dwindling supplies, and indirect effect i.e., effects that came about as other product and factor markets in the Philippines respond to the change in productivity.

For the examination of distributional aspects between urban and rural area, households are grouped by residence. Looking at consumption patterns, the nation's service sector seems most active, and that is especially predominant in urban areas. It is shown that rural households spend more on the primary sector and manufacturing and industry sector compared to urban households. On the other hand, urban households appear to spend more on the service sector. To review the fisheries sector, urban households and rural households are on nearly the same share of household consumption spending on fishery commodities. The share of household expenditure allocated to fisheries indicates about 1.4% (**Table 1**). Urban households spend more on aquaculture products (0.83%) compared to rural households (0.80%), while rural households relatively spend more on marine capture products (0.67%) compared to urban household (0.54%), but there is no significant difference between patterns on the whole.

TABLE 1 | Share of household consumption spending on commodity.

	Primary sector		Mfg. and industry	Service sector	Public sector
	Fisheries	**Other**			
U-HH	0.014	0.056	0.323	0.601	0.006
R-HH	0.015	0.108	0.389	0.482	0.005

TABLE 2 | Distribution of household income in the fisheries by scenario.

	Baseline	Scenario A	Scenario B
U-HH	100.000	99.840	99.640
R-HH	100.000	99.837	99.628

Table 2 presents the household income related with the fisheries sector normalized to 100 for the baseline scenario. Ceteris paribus, the result implies that the more global warming, the greater loss of income that will occur. That is to say, climate change has an effect of income reduction. The rate of decrease in income of rural household is 0.163 and 0.372, for scenario A (RCP 2.6) and scenario B (RCP 8.5), respectively; while for the rate of decrease in income of urban household, is 0.160 and 0.360, for scenario A and B, respectively.

Marine Capture Fisheries Sector

Marine capture fisheries in the simulation represents fisheries excluding inland capture and aquaculture. This follows a classification of the fisheries subsector used in the fisheries

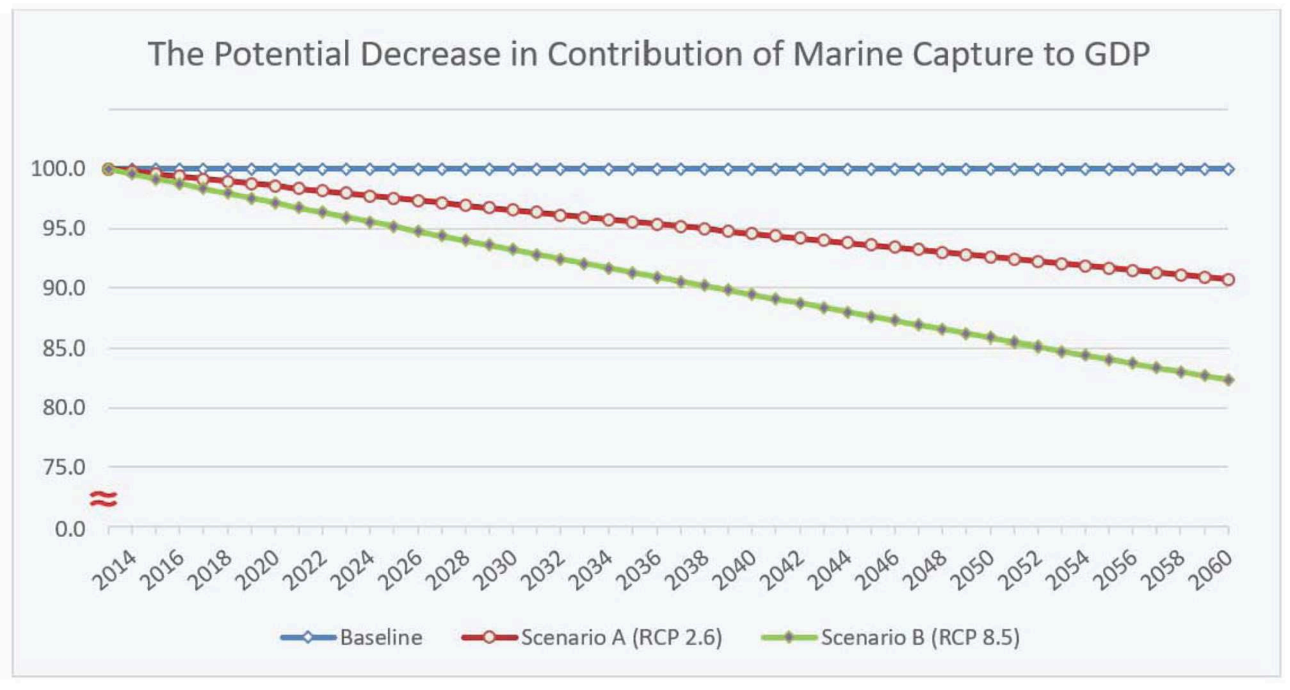

FIGURE 3 | Projection of decrease in contribution of marine capture to GDP by scenario.

situation report issued by the Philippine statistics authority (PSA, 2014). According to the volume of fisheries production data in the Philippines (1980–2010), capture fisheries have made up a high percentage (82%) of the total fisheries production for three decades, and the percentage of marine capture fisheries is 89% and that of inland fisheries is 11% among capture fisheries. The percentage of capture fisheries is decreasing recently, while that of aquaculture is growing. In 2013, capture fisheries accounts for 59% of the total fisheries production in terms of the value of production at constant prices, but based on capture fisheries, marine capture fisheries became more dominant showing 95% of total capture fisheries (PSA, 2014).

Climate change is one of the underlying causes of decrease in production in the marine capture fisheries sector, and the impact of climate change on marine capture fisheries sector is substantial since production is a big part of the economy. In the Philippines, marine capture is currently dominated by roundscad, big-eyed scad, anchovy, Indian oil sardines, Indian mackerel, threadfin bream and tuna species (PSA, 2017a). Production of anchovy is greatly affected by climate change compared to big-eyed scad, Indian mackerel and threadfin bream. Sardine is relatively less vulnerable compared to anchovy but weak upwelling conditions can affect its population. With warmer water and less oxygen available, tuna species in the Philippines (frigate tuna, eastern little tuna, yellowfin tuna, skipjack, bigeye tuna), making 28% of the catch (PSA, 2017a), are expected to decrease due to the shortage of microscopic plants and animals which are an integral part of the tuna food webs (Vousden, 2018).

The marine capture fisheries sector is affected directly by decrease in production while other sectors of the Philippines economy are influenced by only indirect effect. Thus, looking over the marine capture sector, the economic impact of climate change is significant in terms of the ratio. As a result of the simulation, the contribution of marine capture to GDP is expected to decrease by 9.41% with scenario A and 17.95% with scenario B up to 2060 (**Figure 3**).

The decrease in contribution of marine capture to GDP leads to the decrease in income of fishermen. Fishermen in the Philippines, one of the poorest groups in the nine basic sectors, belong to households with income below the official poverty threshold, representing a poverty incidence of 34% (PSA, 2017b). Thus, a decrease in contribution of marine capture to GDP has a negative impact on the mitigation of poverty incidence, and that means climate change adds to the social welfare in the Philippines.

Climate change brings negative consequences in terms of rural household income (**Figure 4**). Decreases in productivity leads to income reduction of households engaged in fisheries, dampening profitability of fishing industries. Considering fishermen reside more in rural areas rather than urban areas, it is expected that climate change affects income of rural households more than urban households. Income of rural households is liable to decrease as climate change continues, and it is expected to deepen as climate change becomes extreme.

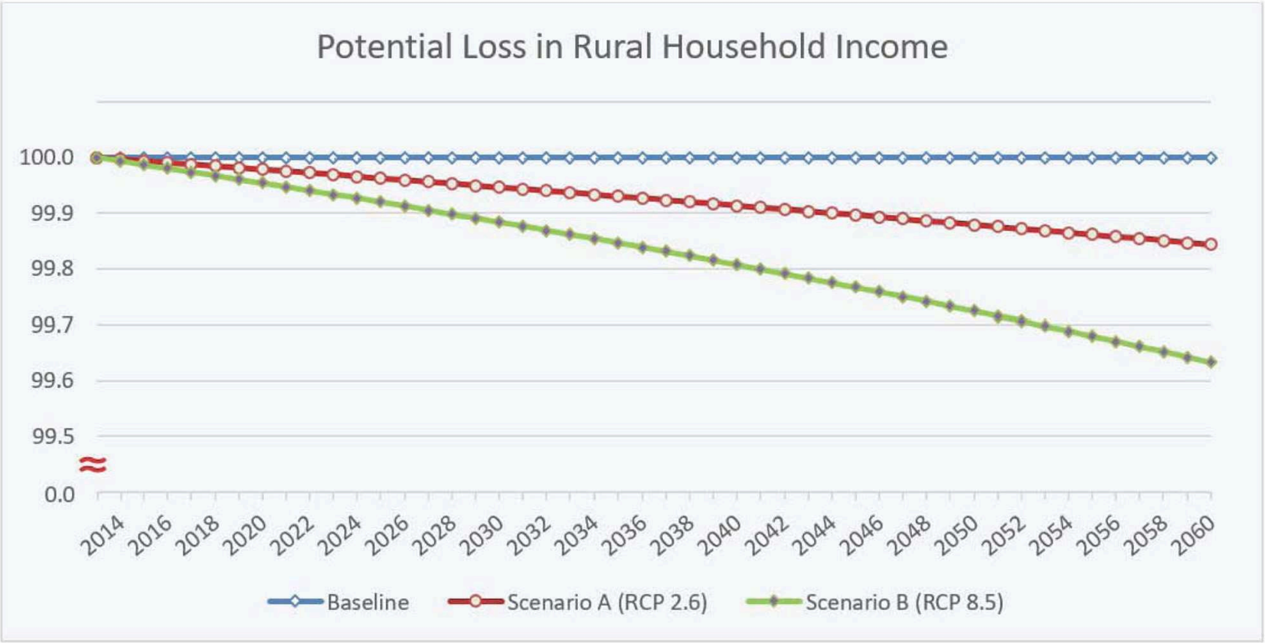

FIGURE 4 | Projection of loss in rural household income by scenario. Income level in base year is normalized to 100.

Capture-Aquaculture Combined Fisheries Sector

In order to examine the impact of climate change on the production of marine capture fisheries, a simulation about capture-aquaculture combined fisheries is carried out. Capture-aquaculture combined fisheries in this section refers to all kinds of fisheries traded in the Philippine market and Filipino fisheries exported to the world market. As shown by the simulation of the economic sector, GDP of the Philippines is expected to decrease from 0.16 to 0.37% compared to the baseline scenario. In light of the proportion of the fisheries sector (which is about 1.8%) to the national economy, there is a huge amount of influence on the economy. Fisheries GDP is expected to decrease by about 9.27% with scenario A and bout 17.65% with scenario B up to 2060 compared to the baseline (**Figure 5**).

Economic growth is an increase in the production of goods and services due to an improvement in production capacity, and is represented by an increase in GDP. The current Philippines economic data suggests that the fisheries sector will continue to grow due to a rise in demand, an increase in productive capacity, and the development of new technology. Economic growth in fisheries is expected to slow compared to the baseline scenario since climate change brings negative effects. **Figure 6** shows economic growth in the fishing sector based on capture indicating inflation-adjusted measures in a corresponding year, i.e., the increase in real GDP. As shown in **Figure 6**, the model notes that economic growth in the fisheries slopes upward in all scenarios, but the curves in the scenario A and B show relatively slower economic growth.

Like the marine capture fisheries sector, loss of income affects rural households slightly more than urban households as climate change continues. It implies that climate change can cause urban-rural income disparity. This is because there are more people who work in fisheries in rural areas than urban areas and a decrease in fish catch affects rural household income. Thus, climate change has more negative effect on rural households in terms of fisheries. **Figure 7** represents loss in rural household income by scenarios A and B. As shown in the figure, climate change has negative effect of income.

DISCUSSION

Vicious Circle in Fisheries Sector

The economy of the Philippines has grown for the last decade, but more than 20% of the Philippines population remains poor and the Philippines does not show big dynamism in improvement of economic security, rise in the middle class and even elimination of poverty, compared to other East Asian countries (World Bank, 2016, 2018). The problem is that the poor in the Philippines (30.8% of the population was economically vulnerable, 18.7% was moderately poor, and 6.6% of the population was extremely poor) are more vulnerable to negative shocks being exposed to more risks for shortage of resources without ability to cope and capacities necessary to adapt to potential risks (World Bank, 2018). In other words, climate change leads to problems for the collective economy

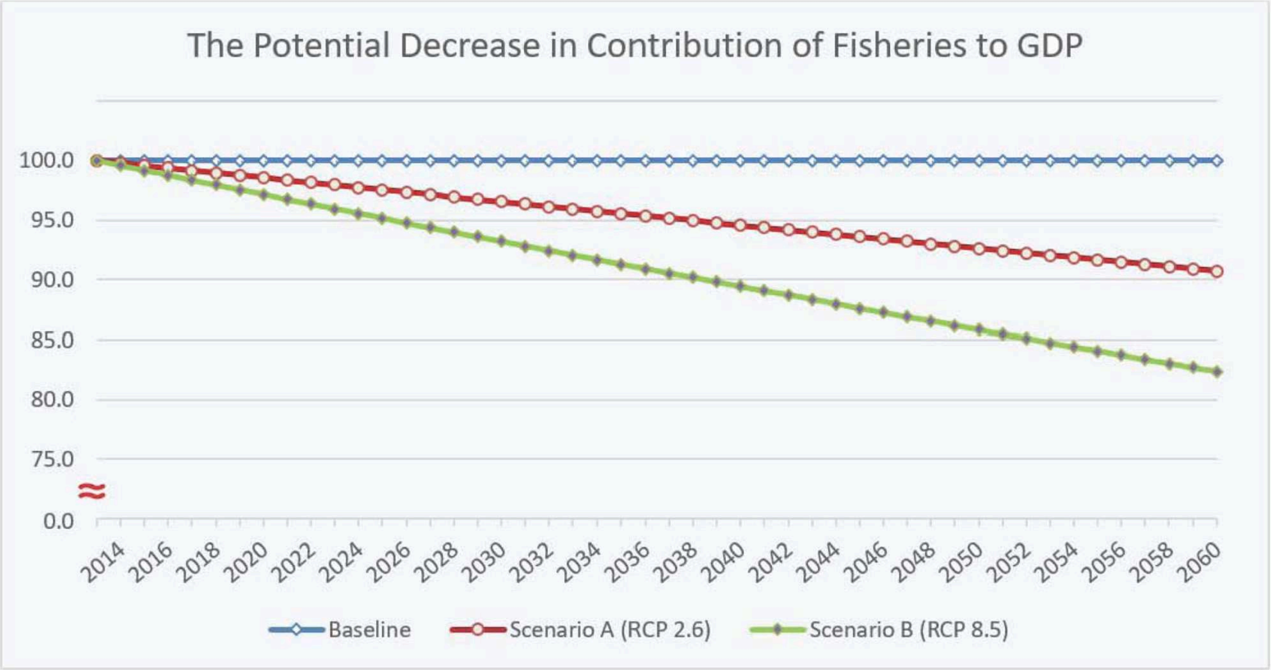

FIGURE 5 | Projection of decrease in contribution of capture-aquaculture combined fisheries to GDP by scenario.

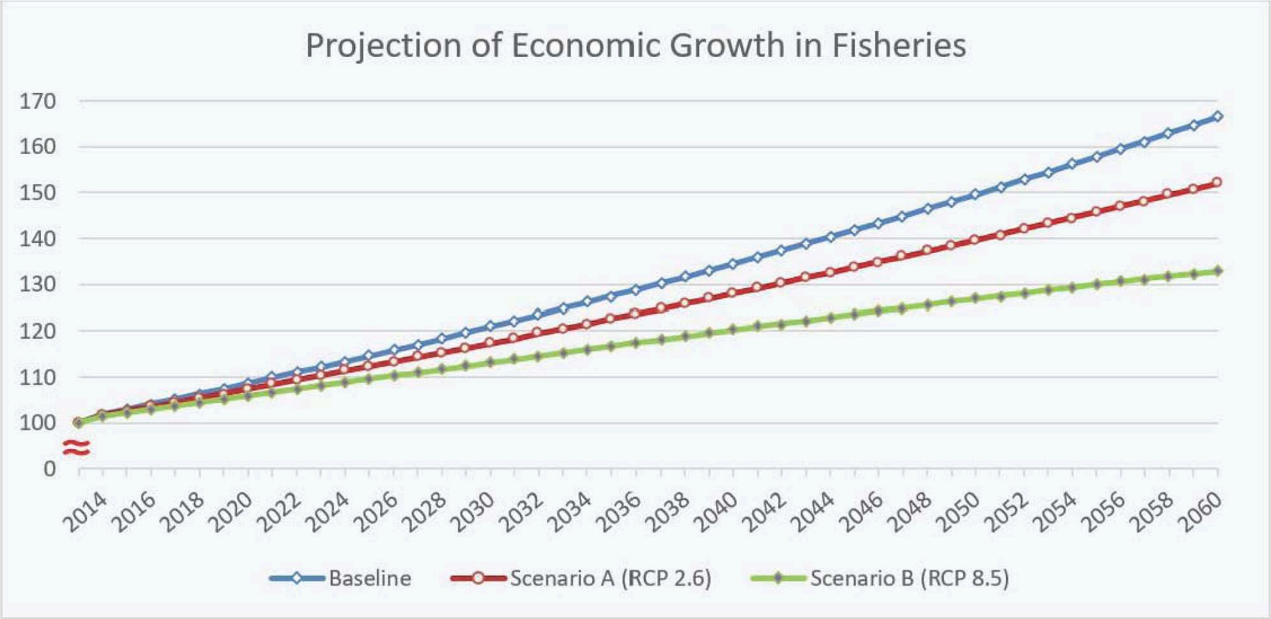

FIGURE 6 | Projection of economic growth in the fisheries by scenario. The GDP in base year is normalized to 100.

of the Philippines represented by slow economic growth and deterioration of income distribution. In addition, climate change contributes to accelerating the plight of the poor in the Philippines.

The issue related with climate change and fisheries resulting from this study is the slowdown in economic growth in the fisheries sector. The problem is that for poor households in rural regions, a large share of income comes from activities associated

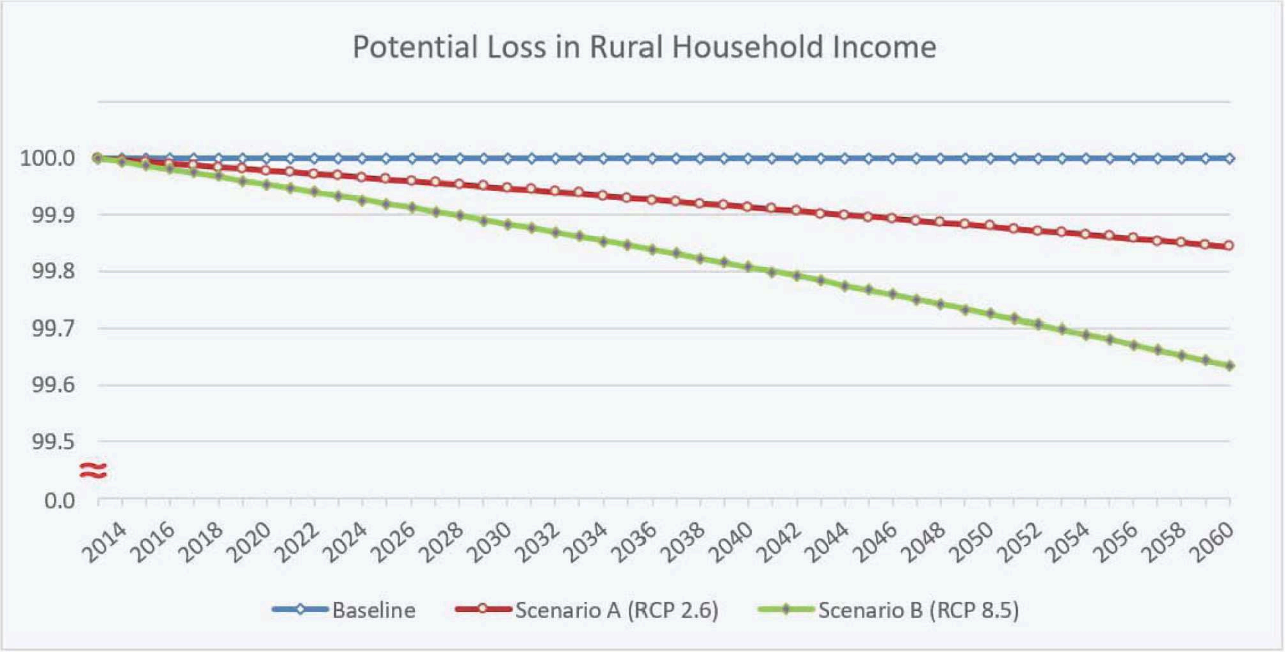

FIGURE 7 | Projection of loss in rural household income by scenario. Income level in base year is normalized to 100.

with the primary sector (World Bank, 2018). Therefore, it is expected that factors such as climate change will contribute to the plight of the poor in the Philippine due to slow growth of fisheries and the poor's dependency on fisheries sector. The second problem is the fact that negative economic impacts on the fisheries sector may affect fishery resources in Philippines making a vicious cycle since changes in fish abundance and location will cause more completion and conflict for the remaining resources. It would result in a decline in food resources and food security. Decrease in fish products, which are the means of inexpensive and nutritious food supply, causes significant strain on the cost of living of low-Income people in the Philippine due to limited options in terms of food consumption. Thus, poor fisheries productivity caused by climate change is expected to affect the nation's economy but particularly bring hardships to the poor.

Limitations on the Model

Several points are worth noting to contemplate what are the limitations and how they could be extended in future work. The paper assumed perfect competition in the market of the Philippines. In reality, it may be natural to face different types of market structure that do not meet rigorous criteria of perfect competition. It is necessary to incorporate cases of imperfect markets such as price controls, if applicable. It is also necessary to consider the more flexible and complex functional form of analysis, as well as Cobb-Douglas functions, to better reflect the structure of the Philippine economy.

Second, the paper assumed productivity of all sectors except fisheries, which remains constant, i.e., supply of other fields might be altered under the model mechanism, but it does not mean they are directly affected by climate change. The assumption is advantageous for identifying the influence on fisheries, but leaves something to be desired if someone wants to completely examine the state of the economy itself. To improve predictive power of the model and better represent comprehensive economic condition, it is necessary to consider all products being influenced by climate change, such as agricultural products, simultaneously. Also, the paper assumed paradigm of general equilibrium depending on aggregated data. It is necessary to note that a possibility of spatial variation in fisheries productivity and decline in fisheries is inherent in reality.

Third, the adaption needs to be discussed in depth. This study focuses on assessment of the economic impact by means of the CGE model by reflecting changes in fish catch due to climate change. The model used in this study is reflective of dynamic reaction to change in factors like labor, capital and inputs. However, the adjustment is limited to the changes within the system built to reproduce the economy. Consequently, the adjustments that can progress beyond the current structure is not mechanically reflected in the model as when dealing with non-monetary objectives such as adaptation to climate change. Different adaptabilities could result in change in market structure according to learning effect, change in preference, and new policies. Simulations are performed under the assumption that the current condition persists, but it would be desired to include many situations. It is necessary to reflect various situations with collecting information for any future study.

CONCLUSION AND RECOMMENDATION

This paper examined economic impacts of climate change on fisheries in the Philippines applying the dynamic computable general equilibrium (CGE) model. In the analysis, one baseline scenario and two climate change scenarios based on greenhouse gas concentration were considered. The study focused on GDP and income distribution by sector, which can represent economic conditions in terms of economic growth and distribution.

The climate change impacts on marine capture fisheries in the Philippines is projected to cause a decrease by about 9% of fisheries GDP with the mitigation scenario and about 18% of GDP with the extreme scenario up to 2060, compared to the baseline scenario. This impact results in income reduction by as much as 0.36% for urban households and 0.38% for rural households in the Philippine economy. In addition, urban-rural income disparity increases because loss for rural households is slightly higher than that of urban households.

Climate change will affect the fisheries over a long period of time. Accordingly, it means that the Philippines must prepare itself to get ready for the impact and endeavor to mitigate climate change. To prepare for climate change, the Philippine needs to: (i) conduct an assessment of vulnerability to climate change for fisheries at the national level in order to respond to changing economic conditions expected to worsen over time and that the assessment is continuously and periodically carried out; (ii) carry out a gap analysis on the capability to cope with the impact of climate change on fisheries for the national economy; the gap analysis enables organizations to take the selective and premeditated actions providing the information about whether a sector or area can potentially be associated with the issue or which community is more vulnerable to climate change; (iii) make effective management plans for fisheries to develop adaptation to climate change with the accumulated information in the process—for an effective plan, it is necessary to establish reliable research materials by collecting climate data and fisheries-related information, and these sources should be open to both organizations and the public to help make more informed fisheries management decision; (iv) incorporate climate change impacts into national economic development plans and fisheries development plans; and (v) incorporate climate adaptation into the fisheries management plan—it should be accompanied by education on climate change that can increase awareness of impacts of climate change and promotion of adaptation strategies that can reduce the effect of climate change on fisheries.

DATA AVAILABILITY STATEMENT

The datasets generated for this study are available on request to the corresponding author.

AUTHOR CONTRIBUTIONS

DS and RP have made a substantial contribution to the research work and they were both involved in drafting and editing of the manuscript.

ACKNOWLEDGMENTS

We sincerely thank Dr. F. Shah (University of Connecticut) for his advice on general equilibrium analysis in the theory.

REFERENCES

Adelman, I., and Robinson, S. (1978). *Income Distribution Policy in Developing Countries: A Case Study of Korea*. Stanford, CA: Stanford University Press.

Arnason, R. (2006). "Global warming, small pelagic fisheries and risk," in *Climate Change and the Economics of the World's Fisheri'es: Examples of Small Pelagic Stocks*, eds R. Hannesson, M. Barange, and S. Herrick (Northampton, MA: Edward Elgar), 1–32.

Arnason, R. (2007). Climate change and fisheries: assessing the economic impact in Iceland and Greenland. *Nat. Resour. Model.* 20, 163–197. doi: 10.1111/j.1939-7445.2007.tb00205.x

Badjeck, M. C., Allison, E. H., Halls, A. S., and Dulvy, N. K. (2010). Impacts of climate variability and change on fishery-based livelihoods. *Mar. Policy* 34, 375–383. doi: 10.1016/j.marpol.2009.08.007

Ballard, C. L., Fullerton, D., Shoven, J. B., and Whalley, J. (1985). "Data on household income and expenditure, investment, the government, and foreign trade," in *A General Equilibrium Model for Tax Policy Evaluation* (Chicago, IL: University of Chicago Press), 90–112. doi: 10.7208/chicago/9780226036335.001.0001

Barange, M., Merino, G., Blanchard, J. L., Scholtens, J., Harle, J., Allison, E. H., et al. (2014). Impacts of climate change on marine ecosystem production in societies dependent on fisheries. *Nat. Clim. Change* 4, 211–216. doi: 10.1038/nclimate2119

Barange, M., and Perry, R. I. (2009). Physical and ecological impacts of climate change relevant to marine and inland capture fisheries and aquaculture. *Clim. Change Implic. Fish. Aquacul.* 503, 7–106. Retrieved from: http://www.lis.edu.es/uploads/07483fb7_72a2_45ca_b8e7_48bf74072fd3.pdf#page=15

Bennett, A., Patil, P., Kleisner, K., Rader, D., Virdin, J., and Basurto, X. (2018). *Contribution of Fisheries to Food and Nutrition Security: Current Knowledge, Policy, and Research*. Nicholas Institute Report 18-02. Durham, NC: Duke University.

Berrittella, M., Bigano, A., Roson, R., and Tol, R. S. (2006). A general equilibrium analysis of climate change impacts on tourism. *Tourism Manage.* 27, 913–924. doi: 10.1016/j.tourman.2005.05.002

BFAR (2016). *Philippine Fisheries Profile 2015*. Quezon: Bureau of fisheries and aquatic resources.

Brander, K. M. (2007). Global fish production and climate change. *Proc. Natl. Acad. Sci. U.S.A.* 104, 19709–19714. doi: 10.1073/pnas.0702059104

Briones, R. M. (2016). *Embedding the AMPLE in a CGE Model to Analyze Intersectoral and Economy-Wide Policy Issues*. PIDS Discussion Paper Series, No. 2016-38. Makati: Philippine Institute for Development Studies.

Burfisher, M. E. (2017). *Introduction to Computable General Equilibrium Models*. New York, NY: Cambridge University Press.

Cheung, W. W., Lam, V. W., Sarmiento, J. L., Kearney, K., Watson, R. E. G., Zeller, D., et al. (2010). Large-scale redistribution of maximum fisheries catch potential in the global ocean under climate change. *Glob. Change Biol.* 16, 24–35. doi: 10.1111/j.1365-2486.2009.01995.x

Cuvin-Aralar, M. L. A., Ricafort, C. H., and Salvacion, A. (2016). *An Overview of Agricultural Pollution in the Philippines: The Fisheries Sector*. Washington, DC: World Bank.

Dellink, R., Hofkes, M., van Ierland, E., and Verbruggen, H. (2004). Dynamic modelling of pollution abatement in a CGE framework. *Econ. Model.* 21, 965–989. doi: 10.1016/j.econmod.2003.10.009

Dervis, K., De Melo, J., and Robinson, S. (1982). *General Equilibrium Models for Development Policy.* New York, NY: Cambridge University Press.

Dessus, S., and Bussolo, M. (1998). Is there a trade-off between trade liberalization and pollution abatement?: a computable general equilibrium assessment applied to Costa Rica. *J. Policy Model.* 20, 11–31. doi: 10.1016/S0161-8938(96)00092-0

Dunne, J. P., John, J. G., Adcroft, A. J., Griffies, S. M., Hallberg, R. W., Shevliakova, E., et al. (2012). GFDL's ESM2 global coupled climate–carbon earth system models. Part I: Physical formulation and baseline simulation characteristics. *J. Clim.* 25, 6646–6665. doi: 10.1175/JCLI-D-11-00560.1

Dunne, J. P., John, J. G., Shevliakova, E., Stouffer, R. J., Krasting, J. P., Malyshev, S. L., et al. (2013). GFDL's ESM2 global coupled climate–carbon earth system models. Part II: carbon system formulation and baseline simulation characteristics. *J. Clim.* 26, 2247–2267. doi: 10.1175/JCLI-D-12-00150.1

Dwyer, L., Forsyth, P., and Spurr, R. (2005). Estimating the impacts of special events on an economy. *J. Travel Res.* 43, 351–359. doi: 10.1177/0047287505274648

Eboli, F., Parrado, R., and Roson, R. (2010). Climate-change feedback on economic growth: explorations with a dynamic general equilibrium model. *Environ. Dev. Econ.* 15, 515–533. doi: 10.1017/S1355770X10000252

Eme, J., and Bennett, W. A. (2009). Critical thermal tolerance polygons of tropical marine fishes from Sulawesi, Indonesia. *J. Thermal Biol.* 34, 220–225. doi: 10.1016/j.jtherbio.2009.02.005

FAO (2016). *The State of World Fisheries and Aquaculture 2016. Contributing to Food Security and Nutrition for All.* Rome: FAO.

Ganachaud, A. S., Sen Gupta, A., Orr, J. C., Wijffels, S. E., Ridgway, K. R., Hemer, M. A. et al. (2011). "Observed and expected changes to the tropical Pacific Ocean," in *Vulnerability of Tropical Pacific Fisheries and Aquaculture to Climate Change*, ed J. D. Bell, J. E. Johnson, A. S. Ganachaud, P. C. Gehrke, A. J., Hobday, O. Hoegh-Guldberg, et al. (Noumea: Secretariat of the Pacific Community), 101–187.

Geronimo, R. C. (2018). *Projected Climate Change Impacts on Philippine Marine Fish Distributions*. Quezon: Department of Agriculture – Bureau of Fisheries and Aquatic Resources.

Ginsburgh, V., and Keyzer, M. (1997). *The Structure of Applied General Equilibrium*. Cambridge: Massachusetts Institute of Technology.

Hoegh-Guldberg, O., Poloczanska, E. S., Skirving, W., and Dove, S. (2017). Coral reef ecosystems under climate change and ocean acidification. *Front. Mar. Sci.* 4:158. doi: 10.3389/fmars.2017.00158

Hoffmann, A. N. (2003). Imperfect competition in computable general equilibrium models—a primer. *Econ. Model.* 20, 119–139. doi: 10.1016/S0264-9993(01)00088-8

Hudson, E. A., and Jorgenson, D. W. (1974). US energy policy and economic growth, 1975-2000. *Bell J. Econ.* 5, 461–514. doi: 10.2307/3003118

Ibarra, A. A., Vargas, A. S., and Lopez, B. M. (2013). Economic impacts of climate change on two Mexican coastal fisheries: implications for food security. *Economics* 7, 1–38. doi: 10.5018/economics-ejournal.ja.2013-36

IPCC (2013). *Climate Change 2013: The Physical Science Basis.* Contribution of Working Group I to the Fifth Assessment Report of the Intergovernmental Panel on Climate Change (New York, NY: Cambridge University Press).

Irz, X., Stevenson, J. R., Tanoy, A., Villarante, P., and Morissens, P. (2007). The equity and poverty impacts of aquaculture: insights from the Philippines. *Dev. Policy Rev.* 25, 495–516. doi: 10.1111/j.1467-7679.2007.00382.x

Kelleher, K., Willmann, R., and Arnason, R. (2009). *The Sunken Billions: The Economic Justification for Fisheries Reform*. Washington, DC: World Bank.

Khalil, I., Atkinson, P. M., and Challenor, P. (2016). Looking back and looking forwards: Historical and future trends in sea surface temperature (SST) in the Indo-Pacific region from 1982 to 2100. *Int. J. Appl. Earth Observ. Geoinform.* 45, 14–26. doi: 10.1016/j.jag.2015.10.005

Kumbaroglu, G. S. (2003). Environmental taxation and economic effects: a computable general equilibrium analysis for Turkey. *J. Policy Model.* 25, 795–810. doi: 10.1016/S0161-8938(03)00076-0

Lam, V. W., Cheung, W. W., Reygondeau, G., and Sumaila, U. R. (2016). Projected change in global fisheries revenues under climate change. *Sci. Rep.* 6:32607. doi: 10.1038/srep32607

Lehodey, P., Alheit, J., Barange, M., Baumgartner, T., Beaugrand, G., Drinkwater, K., et al. (2006). Climate variability, fish, and fisheries. *J. Clim.* 19, 5009–5030. doi: 10.1175/JCLI3898.1

Lofgren, H. (2003). *Exercises in CGE Modeling Using GAMS*. Washington, DC: Intl Food Policy Res Inst.

Lofgren, H., Harris, R. L., and Robinson, S. (2002). *A Standard Computable General Equilibrium (CGE) Model in GAMS*. Washington, DC: Intl Food Policy Res Inst.

Merino, G., Barange, M., Rodwell, L., and Mullon, C. (2011). Modelling the sequential geographical exploitation and potential collapse of marine fisheries through economic globalization, climate change and management alternatives. *Sci. Mar.* 75, 779–790. doi: 10.3989/scimar.2011.75n4779

Mora, C., and Ospina, A. (2001). Tolerance to high temperatures and potential impact of sea warming on reef fishes of Gorgona Island (tropical eastern Pacific). *Mar. Biol.* 139, 765–769. doi: 10.1007/s002270100626

Munday, P. L., Jones, G. P., Pratchett, M. S., and Williams, A. J. (2008). Climate change and the future for coral reef fishes. *Fish Fish.* 9, 261–285. doi: 10.1111/j.1467-2979.2008.00281.x

Nilsson, G. E., Crawley, N., Lunde, I. G., and Munday, P. L. (2009). Elevated temperature reduces the respiratory scope of coral reef fishes. *Glob. Change Biol.* 15, 1405–1412. doi: 10.1111/j.1365-2486.2008.01767.x

Palomares, M. L. D., and Pauly, D. (2014). *Philippine Marine Fisheries Catches: A Bottom-Up Reconstruction, 1950 to 2010.* Vancouver, BC: University of British Columbia.

Pankhurst, N. W., and Munday, P. L. (2011). Effects of climate change on fish reproduction and early life history stages. *Mar. Freshw. Res.* 62, 1015–1026. doi: 10.1071/MF10269

Paun, A., Acton, L., and Chan, W. S. (2018). *Fragile Planet: Scoring Climate Risks Around the World*. London: HSBC Bank Plc.

Peñaflor, E. L., Skirving, W. J., Strong, A. E., Heron, S. F., and David, L. T. (2009). Sea-surface temperature and thermal stress in the Coral Triangle over the past two decades. *Coral Reefs* 28:841. doi: 10.1007/s00338-009-0522-8

Perry, A. L., Low, P. J., Ellis, J. R., and Reynolds, J. D. (2005). Climate change and distribution shifts in marine fishes. *Science* 308, 1912–1915. doi: 10.1126/science.1111322

Pörtner, H. O., Karl, D. M., Boyd, P. W., Cheung, W., Lluch-Cota, S. E., Nojiri, Y., et al. (2014). "Ocean systems," in *Climate Change 2014: Impacts, Adaptation, and Vulnerability. Part A: Global and Sectoral Aspects*, eds C. B. Field, V. R. Barros, D. J. Dokken, K. J. Mach, M. D. Mastrandrea, T. E. Bilir, M. Chatterjee, K. L. Ebi, Y. O. Estrada, R. C. Genova, B. Girma, E. S. Kissel, A. N. Levy, S. MacCracken, P. R. Mastrandrea, and L. L. White (New York, NY: Cambridge University Press), 411–484.

Pratchett, M. S., Hoey, A. S., and Wilson, S. K. (2014). Reef degradation and the loss of critical ecosystem goods and services provided by coral reef fishes. *Curr. Opin. Environ. Sustain.* 7, 37–43. doi: 10.1016/j.cosust.2013.11.022

Prein, M., and Ahmed, M. (2000). Integration of aquaculture into smallholder farming systems for improved food security and household nutrition. *Food Nutr. Bull.* 21, 466–471. doi: 10.1177/156482650002100424

PSA (2014). Fisheries Situationer, January - December 2014. Quezon: PSA.

PSA (2017a). *Fisheries Situation Report, 2017 January-December*. Quezon: PSA.

PSA (2017b). *2017 Annual Report*. Quezon: PSA.

Robinson, S. (1989). Multisectoral models. *Handb. Dev. Econ.* 2, 885–947. doi: 10.1016/S1573-4471(89)02005-X

Robinson, S., Willenbockel, D., and Strzepek, K. (2012). A dynamic general equilibrium analysis of adaptation to climate change in Ethiopia. *Rev. Dev. Econ.* 16, 489–502. doi: 10.1111/j.1467-9361.2012.00676.x

Roessig, J. M., Woodley, C. M., Cech, J. J., and Hansen, L. J. (2004). Effects of global climate change on marine and estuarine fishes and fisheries. *Rev. Fish Biol. Fish.* 14, 251–275. doi: 10.1007/s11160-004-6749-0

Ruddiman, W. F. (2001). *Earth's Climate: Past and Future*. New York, NY: W. H. Freeman.

Santos, M. D., Dickson, J. O., and Velasco, P. L. (2011). "Mitigating the impacts of climate change: Philippine fisheries in focus," in *Fish for the People*, ed. C. Pongsri (Bangkok: Southeast Asian Fisheries Development Center), 101–110.

Sarmiento, J. L., Slater, R., Barber, R., Bopp, L., Doney, S. C., Hirst, A. C., et al. (2004). Response of ocean ecosystems to climate warming. *Glob. Biogeochem. Cycles* 18. doi: 10.1029/2003GB002134

Shoven, J. B., and Whalley, J. (1992). *Applying General Equilibrium*. New York, NY: Cambridge University Press.

Siriwardana, M., Meng, S., and McNeill, J. (2011). *The Impact of a Carbon Tax on the Australian Economy: Results From a CGE Model.* Business, Economics and Public Policy Working Papers. Armidale, NSW: University of New England.

Stock, C. A., Alexander, M. A., Bond, N. A., Brander, K. M., Cheung, W. W., Curchitser, E. N., et al. (2011). On the use of IPCC-class models to assess the impact of climate on living marine resources. *Prog. Oceanog.* 88, 1–27. doi: 10.1016/j.pocean.2010.09.001

Thirumalai, K., DiNezio, P. N., Okumura, Y., and Deser, C. (2017). Extreme temperatures in Southeast Asia caused by El Niño and worsened by global warming. *Nat. Commun.* 8, 1–8. doi: 10.1038/ncomms15531

Vannuccini, S., Kavallari, A., Bellù, L. G., Müller, M., and Wisser, D. (2018). "Understanding the impacts of climate change for fisheries and aquaculture: global and regional supply and demand trends and prospects," in *Impacts of Climate Change on Fisheries and Aquaculture*, ed M. Barange (Rome: FAO), 41–62.

Vousden, D. (2018). *Western and Central Pacific Ocean.* Transboundary Diagnostic Analysis. Honiara: Pacific Islands Oceanic Fisheries Management.

Wendner, R. (2001). An applied dynamic general equilibrium model of environmental tax reforms and pension policy. *J. Policy Model.* 23, 25–50. doi: 10.1016/S0161-8938(00)00025-9

World Bank (2016). *Philippines Economic Update: Outperforming the Region and Managing the Transition*. Washington, DC: World Bank.

World Bank (2018). *Making Growth Work for the Poor: A Poverty Assessment for the Philippines*. Washington, DC: World Bank. doi: 10.1596/29960

World Bank (n.d.). "Prevalence of undernourishment," in *World Development Indicators*, The World Bank Group. Retrieved from: https://data.worldbank.org/indicator/SN.ITK.DEFC.ZS

Yeh, S. W., Kug, J. S., Dewitte, B., Kwon, M. H., Kirtman, B. P., and Jin, F. F. (2009). El Niño in a changing climate. *Nature* 461, 511–514. doi: 10.1038/nature08316

Conflict of Interest: The authors declare that the research was conducted in the absence of any commercial or financial relationships that could be construed as a potential conflict of interest.

frontiers
in Marine Science

ORIGINAL RESEARCH
published: 10 July 2020
doi: 10.3389/fmars.2020.00580

Chemical Exposure Due to Anthropogenic Ocean Acidification Increases Risks for Estuarine Calcifiers in the Salish Sea: Biogeochemical Model Scenarios

Nina Bednaršek[1]*, *Greg Pelletier*[1], *Anise Ahmed*[2] *and Richard A. Feely*[3]

[1] Southern California Coastal Water Research Project, Costa Mesa, CA, United States, [2] Washington State Department of Ecology, Olympia, WA, United States, [3] NOAA Pacific Marine Environmental Laboratory, Seattle, WA, United States

Edited by:
Sara Rivero-Calle,
University of North Carolina
Wilmington, United States

Reviewed by:
Kristen Marie Krumhardt,
National Center for Atmospheric
Research (NCAR), United States
Xiao Liu,
NCEP Environmental Modeling Center
(EMC), United States

***Correspondence:**
Nina Bednaršek
ninab@sccwrp.org;
nina.bednarsek@gmail.com

Specialty section:
This article was submitted to
Global Change and the Future Ocean,
a section of the journal
Frontiers in Marine Science

Received: *06 April 2020*
Accepted: *23 June 2020*
Published: *10 July 2020*

Citation:
Bednaršek N, Pelletier G,
Ahmed A and Feely RA (2020)
Chemical Exposure Due
to Anthropogenic Ocean Acidification
Increases Risks for Estuarine
Calcifiers in the Salish Sea:
Biogeochemical Model Scenarios.
Front. Mar. Sci. 7:580.
doi: 10.3389/fmars.2020.00580

Ocean acidification (OA) is projected to have profound impacts on marine ecosystems and resources, especially in estuarine habitats. Here, we describe biological risks under current levels of exposure to anthropogenic OA in the Salish Sea, an estuarine system that already experiences inherently low pH and aragonite saturation state (Ω_{ar}) conditions. We used the Pacific Northwest National Laboratory and Washington State Department of Ecology Salish Sea biogeochemical model (SSM) informed by a selection of OA-related biological thresholds of ecologically and economically important calcifiers, pteropods, and Dungeness crabs. The SSM was implemented to assess current exposure and associated risk due to reduced Ω_{ar} and pH conditions with respect to the magnitude, duration, and severity of exposure below the biological thresholds in the Salish Sea in comparison to the pre-industrial era. We further investigated the individual effects of atmospheric CO_2 uptake and nutrient-driven eutrophication on changes in chemical exposure since pre-industrial times. Our model predicts average decreases in Ω_{ar} and pH since pre-industrial times of about 0.11 and 0.06, respectively, in the top 100 m of the water column of the Salish Sea. These decreases predispose pelagic calcifiers to increased duration, intensity, and severity of exposure. For pteropods, present-day exposure is below the thresholds related to sublethal effects across the entire Salish Sea basin, while mortality threshold exposure occurs on a spatially limited basis. The greatest risk for larval Dungeness crabs is associated with spatially limited exposures to low calcite saturation state in the South Sound in the springtime, triggering an increase in internal dissolution. The main anthropogenic driver behind the predicted impacts is atmospheric CO_2 uptake, while nutrient-driven eutrophication plays only a marginal role over spatially and temporally limited scales. Reduction of CO_2 emissions can help sustain biological species vital for ecosystem functions and society.

Keywords: ocean acidification, threshold, attribution analyses, anthropogenic stressors, nutrient remineralization, Dungeness crab, pteropods, biogeochemical projections

INTRODUCTION

Anthropogenically enhanced ocean acidification (OA) represents one of the most significant risks to coastal marine ecosystems (Feely et al., 2010, 2016, 2018; Bednaršek et al., 2016, 2014, 2017a, 2018, 2019, 2020; Wallace et al., 2014; O'Neill et al., 2017; Evans et al., 2019). These concerns are especially relevant in highly productive eastern boundary upwelling systems, as well as the coastal and estuarine systems where OA impacts on key marine organisms are already detectable. These organisms face a high risk of impacts well before 2100, even under the low-emissions scenario (RCP2.6; Gattuso et al., 2015), that will negatively affect human benefits and services. The identification of major drivers and trends of OA variability is critical for understanding the biological changes related to OA.

The upwelling regime along the United States West Coast has experienced a pH decline of at least 0.1 pH unit since pre-industrial times (Chavez et al., 2017; Laruelle et al., 2018; Osborne et al., 2020). The results of intensifying OA have resulted in increased magnitude, duration, and frequency of OA exposure (Feely et al., 2008, 2016, 2018; Gruber et al., 2012; Hauri et al., 2013; Turi et al., 2016; Chan et al., 2017; Sutton et al., 2019). Experimental simulations of OA exposure demonstrate copious evidence of the detrimental effects of OA on a variety of ecologically and economically important calcifiers along the United States West Coast (Gaylord et al., 2011; Baumann et al., 2012; Lischka and Riebesell, 2012; Waldbusser et al., 2015; McLaskey et al., 2016; Miller et al., 2016; Osborne et al., 2016; Giltz and Taylor, 2017; Hales et al., 2017; Kapsenberg et al., 2018; Williams et al., 2019). Furthermore, synthesis and meta-analyses work indicate a much broader vulnerability with the ultimate impact on marine ecosystems (Kroeker et al., 2013; Busch and McElhany, 2016). Moreover, the impact is noticeable under present-day conditions, with field studies delineating effects in some of the most vulnerable marine species, such as oysters (Barton et al., 2012, 2015), copepods (Engström-Öst et al., 2019), foraminifera (Osborne et al., 2016, 2020), pteropods (Bednaršek et al., 2014, 2016, 2017a, 2018, 2019; Feely et al., 2016) and Dungeness crab larvae (Bednaršek et al., 2020). For the last three species in particular, robust attribution analyses have unequivocally demonstrated the impact of anthropogenic OA as a driver behind observed negative responses (Bednaršek et al., 2014, 2020; Osborne et al., 2020). Due to the shortness of time series, population-specific measurements linked to *in situ* anthropogenic CO_2 are still lacking.

It is particularly important to address the risks related to anthropogenic drivers on regional scales because of their connection to local economies based on marine resources, fisheries, and recreation (Barange et al., 2014; Gattuso et al., 2015). Fingerprinting of the anthropogenic OA signal is particularly essential in estuarine systems that support structural and functional biodiversity and productivity in order to evaluate, manage, and limit the risks to habitats. However, these systems are characterized by extensive spatial and seasonal variability and prolonged time of emergence (Cai et al., 2011; Sunda and Cai, 2012; Feely et al., 2018; Sutton et al., 2019), and conclusively linking anthropogenic attribution to baseline shifts is difficult. Despite this, recent studies have identified remarkably consistent bounds for anthropogenic CO_2 concentrations for the coastal waters of the California Current Ecosystem and the Salish Sea (Feely et al., 2016; Evans et al., 2019).

The Salish Sea in the Pacific Northwest is one of the most productive estuarine systems in the United States with many ecologically, economically, and culturally significant species. Yet, the Salish Sea is rapidly changing because of its poor buffering capacity (Feely et al., 2010, 2012, 2018; Fassbender et al., 2018; Evans et al., 2019) and multiple anthropogenic and natural drivers that can simultaneously exacerbate OA, including freshwater (riverine) inputs, respiration processes, and other redox reactions (e.g., Feely et al., 2010, 2016, 2018; Alin et al., 2018; Evans et al., 2019, and references therein). Anthropogenic CO_2 uptake and local eutrophication enhancing respiration have been recognized as the most important contributions to changing OA baseline conditions (Feely et al., 2010, 2012, 2018; Pelletier et al., 2017, 2018; Bianucci et al., 2018; Evans et al., 2019). Anthropogenic CO_2 concentrations are changing surface ocean habitats following the exchange of CO_2 across the air/water interface, with increased concentration of dissolved inorganic carbon (DIC) from the atmosphere.

While these processes are subjecting ecologically and economically important calcifying species to enhanced anthropogenic OA exposure (Feely et al., 2016, 2018), the understanding of OA's impacts on important species to the Salish Sea ecosystem is currently restricted to experimental results and food web model outputs of projected OA changes. Several studies demonstrate the most damaging OA impacts on various pelagic calcifiers, including pteropods, benthic grazers, and Dungeness crabs (Busch et al., 2013, 2014; Miller et al., 2016). However, because of the uncertainties associated with extrapolating from experimental results to highly variable estuarine conditions, OA risk assessment across spatial and temporal windows of exposures is limited.

Pteropods are ecologically important as a food resource for various fish (Aydin et al., 2005), and are regarded as sensitive OA indicators of ecological health (Bednaršek et al., 2017b). Their OA sensitivity is related to multiple pathways ranging from shell dissolution, physiological and behavioral responses, and mortality (Lischka et al., 2011; Busch et al., 2014; Bednaršek et al., 2017a,b). As described by Wang et al. (2018) and Bednaršek et al. (unpublished), pteropod life history in the Salish Sea consists of are two major spawning events in the Salish Sea: a primary event occurs during the springtime (March–May) and a secondary event occurs in the fall (September–October), generating most sensitive early life stages that inhabit upper 100 m of their vertical habitat (Wang et al., 2018; Bednaršek et al., unpublished). A single field study so far in the Salish Sea shows evidence of negative biological effects, shell dissolution, under present OA gradients for pteropods (Bednaršek et al., unpublished); these findings are indicative of high pteropod sensitivity yet insufficient to accurately ascribe the risks for the pteropod community in the Salish Sea.

Dungeness crabs are the most important fishery in Washington State, with an estimated total value between $90 and $110 million annually (Childers, R., Washington Fish and

Wildlife, personal communication). Exposure to OA conditions is pre-determined by the life history of larval Dungeness crabs occurring during the springtime (May–June), with early life stages inhabiting upper 160 m of water column considered to be their diel vertical habitat in the Salish Sea (Jamieson and Phillips, 1993). Experimental analyses of the Dungeness crab demonstrate delayed development and increased mortality in the zoea stages (Miller et al., 2016), while megalopae show evidence of increased exoskeleton dissolution (Bednaršek et al., 2020). There is consistent evidence of a regionally limited population collapse of Dungeness crabs (Childers, R., Washington Fish and Wildlife, personal communication) but causality behind the observed phenomenon has not yet been determined because the pathways of sensitivity or attribution analyses to specific drivers are lacking.

To evaluate OA-related risks and uncertainties on biological populations, an understanding of two factors, i.e., species sensitivity and associated exposure to unfavorable OA conditions, is needed. Standardizing sensitivity across species, life stages, studies, and different approaches is difficult and potentially biased. In the absence of a comprehensive understanding of species sensitivity, needed to predict future OA effects, the United Nations Intergovernmental Panel on Climate Change (IPCC) uses thresholds with associated confidence levels to communicate the risks (Mastrandrea et al., 2010). Biological thresholds are recommended tools for evaluating species sensitivity, especially when derived through the expert consensus process (Mastrandrea et al., 2010; Bednaršek et al., 2019). As such, they can be used to assess biological vulnerability when there are gaps in the empirical evidence. Although there is a significant gap of known OA thresholds for most marine organisms, such thresholds are currently available for different life stages of pteropods (Bednaršek et al., 2019). The biological thresholds cover a range of conditions specifically related to aragonite saturation state (Ω_{ar}) that can induce either sublethal (increased dissolution, reduced growth) or lethal (mortality) effects. Species life histories provide a context for interpreting sensitivity during their most sensitive biological stages (Bednaršek et al., 2019).

In regard to OA exposure in regionally specific coastal-estuarine ecosystems, downscaled biogeochemical models are among the best tools for evaluating current conditions and predicting changes against a background of ocean variability. More importantly, they can help delineate the location and potential impact of specific anthropogenic stressors, such as atmospheric CO_2 addition or eutrophication, as well as quantitatively assess the changes to either of these two stressors. Biological thresholds can be incorporated easily into biogeochemical models as an application tool to identify spatially explicit OA hotspots and refugia, as well as temporal windows in which the biological risks will be most significant. Furthermore, applying thresholds to biogeochemical models with distinct "scenarios" can help delineate the extent of currently observed biological impacts due to a specific anthropogenic OA driver, e.g., CO_2 emissions vs. nutrient loading.

The application of biological thresholds into the Salish Sea Model (SSM) to identify spatial and temporal windows of conditions that induce sublethal and/or lethal biological effects is a novel approach in assessing risk associated with OA. Here, we apply a highly resolved biogeochemical SSM to assess the changes in chemical exposure since the pre-industrial era using an attribution analysis of atmospheric CO_2 emissions and nutrient-driven eutrophication in the Salish Sea. Metrics of exposure (duration, intensity, severity) were modeled to delineate predominant anthropogenic drivers, atmospheric CO_2 and nutrient-related eutrophication, and discern their effects across spatial and temporal scales since the pre-industrial era. We conducted OA risk analyses using two pelagic calcifiers with the greatest predisposition to exposure and demonstrated vulnerability to OA conditions in the Salish Sea: pteropods (*Limacina helicina*) and larval stages of Dungeness crab (*Metacarcinus magister*). The interpretation of their biological risks was based either on the biological thresholds (pteropods, Bednaršek et al., 2019) or sensitivity equation related to the OA conditions (larval Dungeness crabs, Bednaršek et al., 2020). In doing so, we were able to determine current risks facing ecologically and economically important species in the Salish Sea, as well as delineate the anthropogenic drivers associated with the greatest risk for species sustainability.

MATERIALS AND METHODS

Description of the Salish Sea Model

This project utilizes a recently completed physical-biogeochemical model for the Salish Sea coastal waters developed by the Pacific Northwest National Laboratory (PNNL) and the Washington State Department of Ecology (DOE) (Pelletier et al., 2017; Bianucci et al., 2018). Our project focus is on the Salish Sea; therefore, we call it the SSM, but the model domain also extends into the Strait of Juan de Fuca and Strait of Georgia. The hydrodynamic module of the SSM is an application of the Finite-Volume Community Ocean Model (FVCOM; Chen et al., 2003).

The SSM uses an unstructured grid that represents the complex shoreline, islands, bathymetry, and waterways of the Salish Sea. The unstructured SSM grid consists of 9,013 nodes and 13,941 elements. The vertical resolution of the model employs a sigma coordinate system with 10 layers. Layer thicknesses are distributed with highest density near the surface. The thickness of the surface layer ranges from about 0.16 m in the shallow nearshore areas to 7.6 m in the deepest areas, with an average thickness of about 1.9 m across the model domain. The thickness of the bottom layer ranges from about 0.75 m in the shallow nearshore areas to 35 m in the deepest areas, with an average thickness of about 8.6 m across the model domain. The number of model grid layers within the euphotic zone depth of approximately 20 m varies from all 10 layers in the nearshore regions to the top two layers in the deepest areas.

The biogeochemical module of the SSM is adapted from the Integrated Compartment Model (CE-QUAL-ICM; Cerco and Cole, 1993, 1994). Bianucci et al. (2018) extended the SSM to include carbonate system variables, i.e., total alkalinity (TA) and DIC in the water column and a two-layer sediment diagenesis module (Di Toro, 2001). The SSM is driven by boundary conditions at two open boundaries (Strait of Juan de Fuca and Strait of Georgia), nearly 100 freshwater sources, including rivers, other watershed sources, and wastewater treatment plants, and meteorological forcing at the water surface. The SSM tracks the following state variables: phytoplankton (two groups), nutrients (nitrate, ammonium, and phosphate), dissolved oxygen, dissolved and particulate organic carbon and nitrogen (labile and refractory), alkalinity, and DIC. The SSM is an offline model that uses input from a previously computed hydrodynamic solution. A detailed description of the SSM is provided by Yang et al. (2010), Khangaonkar et al. (2011), Khangaonkar et al. (2012), and Kim and Khangaonkar (2012).

The model setup for realistic historical conditions in 2008 is exactly the same as described by Bianucci et al. (2018), except for the following changes to better represent model boundary conditions:

- Monthly averages were used to represent alkalinity in rivers instead of using a constant value for each river for the entire year, using the same data sources described by Bianucci et al. (2018);
- Atmospheric $x\mathrm{CO}_2$ of 390 ppm was used instead of 400 ppm to better match the observed data off the coast of Washington during 2008 (PSEMP Marine Waters Workgroup, 2016).

Model Scenarios

Several model runs were used in this project to represent the following scenarios:

(1) Existing conditions in 2008. These are the realistic historical conditions observed in 2008 (referred as S1Ex);
(2) Hypothetical reference conditions in 2008 without regional human nutrients. This is the same as Scenario 1, except with regional anthropogenic sources of nutrients removed (e.g., wastewater treatment plant loads and freshwater anthropogenic nonpoint sources). The regional anthropogenic nutrient loads that were excluded from the reference condition scenario include anthropogenic inorganic N (nitrate and ammonium), dissolved and particulate organic N, and dissolved and particulate organic carbon (referred as S2Ex-nut);
(3) Hypothetical reference conditions without global anthropogenic CO_2. This is the same as Scenario 1 except with atmospheric and ocean boundary partial pressure of CO_2 ($p\mathrm{CO}_2$) and DIC reduced to pre-industrial conditions (referred as S3Ex-atm);
(4) Hypothetical pre-industrial conditions without global anthropogenic CO_2 or local human nutrients. This is the same as Scenario 1, except with atmospheric and ocean boundary $p\mathrm{CO}_2$ and DIC reduced to pre-industrial conditions and regional anthropogenic nutrient sources excluded (referred as S4Ex-nut-atm);
(5) Hypothetical conditions from the years 1780 to 2100 in response to changing global CO_2 under RCP 8.5. This is a set of 17 separate scenarios that are same as Scenario 1, except with atmospheric and ocean boundary $p\mathrm{CO}_2$ and DIC changed to reflect projected conditions between the years 1780 and 2100 with atmospheric increase from 280 to 910 ppm (Scenario 5, S5-Future).

The effects of regional anthropogenic nutrient sources on water quality were evaluated by analyzing the difference in results between the historical conditions in 2008 and the reference conditions with human nutrients excluded [difference between Scenario 1 (S1Ex) and 2 (S2Ex-nut)]. Regional anthropogenic nutrient sources that were removed in the reference conditions include the anthropogenic component of loading in the wastewater treatment plants and all freshwater sources within Washington State. The effects of global anthropogenic sources of CO_2 were evaluated by analyzing the difference in results between the historical conditions in 2008 and the reference conditions with global anthropogenic CO_2 excluded [difference between Scenario 1 (S1Ex) and 3(S2Ex-atm)]. The combined effect of global anthropogenic CO_2 and human nutrient sources was based on the difference between Scenarios 1 (S1Ex) and 4 (S4Ex-nut-atm).

The method used to calculate DIC at the ocean boundary under pre-industrial conditions assumes that $p\mathrm{CO}_2$ in the water is increased at the same rate as in the atmosphere (Takahashi et al., 2009). Atmospheric CO_2 was 390 ppm in 2008 and 280 ppm under pre-industrial conditions; therefore, the difference of 110 ppm was subtracted from the 2008 ocean boundary $p\mathrm{CO}_2$ in the water to estimate ocean boundary $p\mathrm{CO}_2$ under pre-industrial conditions, and pre-industrial DIC was calculated with CO2SYS (Lewis and Wallace, 1998; Evans et al., 2019).

The methods used to estimate the nutrient loading from all existing sources and reference conditions (with estimated regional anthropogenic sources excluded) are presented in Mohamedali et al. (2011) and Pelletier et al. (2017). Regional anthropogenic sources of nutrients that were removed from the reference conditions include wastewater treatment plant loads and freshwater anthropogenic nonpoint sources of nutrients, including anthropogenic inorganic N (nitrate and ammonium), organic N (dissolved and particulate), and organic carbon (dissolved and particulate). Natural reference conditions were established from the results of a meta-analysis considering concentration data from various sources (Mohamedali et al., 2011): ambient monitoring data, rainfall data, and data from other studies. Monthly 10th percentiles of ambient data were used to represent natural nutrient concentrations for different regions in Puget Sound and the Strait of Georgia. Monthly 50th percentiles were used for the Olympic Peninsula watersheds draining to the Strait of Juan de Fuca and Hood Canal.

We demonstrate the effects of the changes in carbonate chemistry conditions over the entire Salish Sea region through the model outputs, and additionally focus on the stations in Puget Sound, which represent the southern part of the Salish Sea where current OA monitoring is taking place (**Figure 1**). All of the model scenarios used in this study use the same hydrodynamic and physical conditions as the year 2008. Therefore, the differences between scenarios isolate the effects of only regional human nutrients and global anthropogenic CO_2.

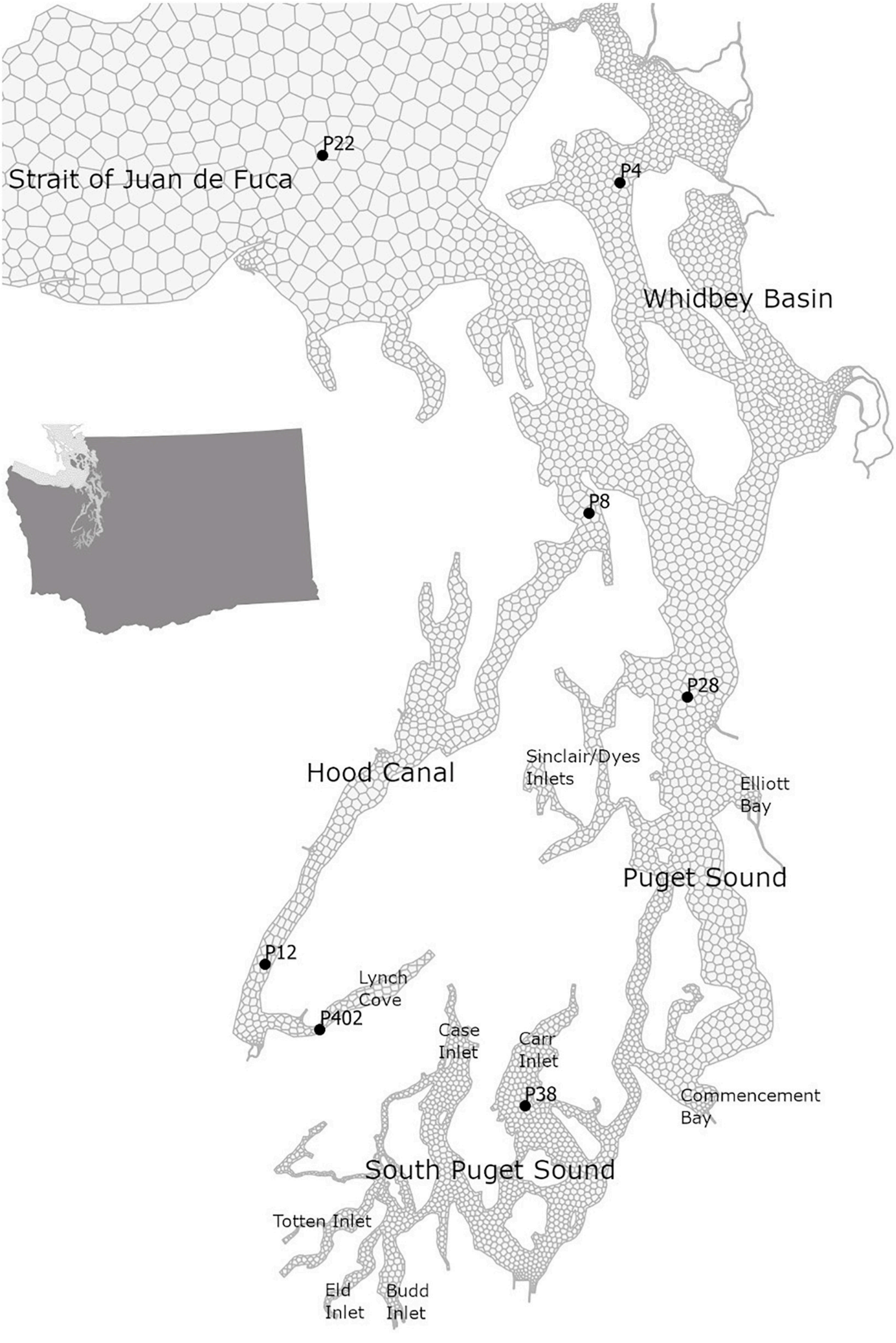

FIGURE 1 | Map of the Salish Sea with selected stations in its southern part of Puget Sound with Main Basin (P28) that are part of the OA monitoring efforts in Washington state.

Determining the Exposure and Sensitivity for Two Groups of Marine Calcifiers

The availability of tools that allow interpretation of *biological sensitivity*, as well as model outputs that allow assessment of *chemical exposure*, made it possible to evaluate the risks for two pelagic calcifiers, i.e., pteropods and larval stages of Dungeness crabs.

Depending on the application of the tools in the biogeochemical model, the exposure can be assessed temporally and spatially. In assessing temporal exposure, we applied the sensitivity tools across different seasonal scales that align with the species life history, i.e., when the magnitude of seasonal exposure co-occurs with the most sensitive biological processes. Spatial sensitivity was assessed over the entire Salish Sea, which is the spatial domain of the SSM biogeochemical model.

Pteropods in the Salish Sea inhabit the upper 100 m water column and undergo two spawning events. One event occurs in the springtime (March–May) and the other occurs in the fall (September–October). For pteropods, biological sensitivity is based on thresholds describing the sublethal and acute biological responses that were derived through expert consensus (Bednaršek et al., 2019). Each of the six thresholds in the study was assigned a specific confidence score, which was based on the combination of evidence and agreement (Mastrandrea et al., 2010).

Life history context was used for assessing the OA risks to larval Dungeness crabs considering their diel vertical migration pattern within the upper 160 m during the spring (May–June). Biological thresholds, however, were not available for the larval Dungeness crabs. Consequently, we used the equation that best describes their sensitivity against regionally specific OA gradients (Bednaršek et al., 2020). Larval stages of the Dungeness crab are susceptible to OA exposure, which can induce internal and external exoskeleton carapace dissolution (Bednaršek et al., 2020). Internal dissolution was correlated against calcite saturation state (Ω_{cal}; Eq. 1; $p = 0.003$), derived from *in situ* vertical coastal gradients at the stations along Washington's coast that are interconnected with the waters of the Salish Sea. Because of the regional similarity, we extrapolated this equation to the waters of the Salish Sea. The extent of internal dissolution is associated with extracellular acid-base control, which is linked to increased energetic demands and thus related to physiological impairments (Michaelidis et al., 2005; Hans et al., 2014; Bednaršek et al., 2020).

While evaluating the risks of sublethal exposure is simple, interpreting the risks at the population level is more complex and multifaceted. Here, we consider population-level effects to be most significant if anthropogenically induced OA conditions result in exposure inducive to the mortality threshold, particularly during the most vulnerable early-life stages. Alternatively, if the magnitude of exposure inducive to sublethal effects prevails for a prolonged time, it can contribute to compromised organismal performance and thus indirectly induce mortality. As such, we delineate the exposure related to sublethal effects on either seasonal (September–October or January-February) or annual bases to provide us with different temporal windows of OA-associated risks.

Applied Thresholds or Sensitivity Equations for Pteropods and Dungeness Crabs

Pteropod thresholds describe biological condition gradients ranging from sublethal biological effects (mild to severe dissolution, growth impairment) to lethal effects (survival). Each pteropod threshold is associated with the magnitude (T_{mag} in units of Ω_{ar}) and duration (T_{dur} in units of days) of exposure at which significantly negative impacts occur. Each threshold is additionally characterized by a confidence score determined by using a combination of the evidence and agreement, as based on the IPCC approach (Mastrandrea et al., 2010; Bednaršek et al., 2019).

Pteropod thresholds were applied over the upper 100 m integrated water column, which delineates the vertical habitat of pteropods in the Salish Sea. We conducted the application for three thresholds:

1. Mild dissolution (sublethal response; $\Omega_{ar} = 1.5$ for 5 days; high confidence score)
2. Growth impairment (sublethal response; $\Omega_{ar} = 1.0$ for 7 days; medium confidence score)
3. Mortality (lethal response; $\Omega_{ar} = 0.95$ for 14 days; low confidence score).

For larval Dungeness crab, we used the equation (Eq. 1) for Ω_{cal} over the upper 160 m water column to delineate the sublethal effects in the Salish Sea. Since the megalopae build their exoskeleton of calcite, the model outputs are in calcite saturation state (Ω_{cal}), which is linearly correlated to Ω_{ar}. Internal dissolution describes a relative extent of dissolution per each individual (Bednaršek et al., 2020).

$$\text{Internal dissolution} = -0.448\,\Omega_{cal} + 1.147 \tag{1}$$

Evaluation of Biological Thresholds Using Model Outputs

Conditions of adverse Ω_{ar} below biological thresholds for pteropods are defined as the cumulative length of time with duration (D, days) of Ω_{ar} less than the defined threshold magnitude value (T_{mag}) for all events that each have time periods greater than the defined threshold for duration of each event (T_{dur}). We adopt the approach of Hauri et al. (2013) to define the intensity (I, unitless) of adverse events as:

$$I = T_{mag} - \Omega_{ar,mean} \tag{2}$$

where $\Omega_{ar,mean}$ is the mean Ω_{ar} averaged over the time of the event. The intensity represents the average magnitude of decrease in Ω_{ar} below the threshold during events. Both duration and intensity have an impact on health of organisms (e.g., Beesley et al., 2008), therefore the combined effect of duration and intensity is represented by a metric called severity (S, omega-days):

$$S = I \times D \tag{3}$$

The following steps are involved in processing the model outputs:

(1) Extract the time series of predicted Ω_{ar} values and adjust for average model bias of −0.08 units. Model outputs are a continuous time series of predicted Ω_{ar} values at intervals of every 6 h;
(2) Step through the time series of bias-adjusted omega values to identify all events that have magnitudes less than T_{mag} for event durations greater than T_{dur};
(3) Calculate the cumulative duration integrated across all events for the time period being evaluated (e.g., annual or seasonal);
(4) Calculate the cumulative intensity during events integrated across all events using Eq. 2;
(5) Calculate the integrated severity across all events from the cumulative duration and intensity using Eq. 3.

RESULTS

Carbonate Chemistry Changes Due to Anthropogenic Contributions

Under the current conditions (Scenario 1; S1Ex) in the upper 100 m, about 94% of surface area of the Salish Sea has an average $\Omega_{ar} < 1$ annually, with the remaining 6% ranges of $1 < \Omega_{ar} < 1.2$ (**Figure 2** and **Table 1**). The worst conditions, in terms of the intensity, are located in the stratified bays of Hood Canal (stations P12 and P402), Whidbey Basin (station P4), and the northern part of the Salish Sea (station P28; **Figure 2** and **Table 1**). Since pre-industrial times, Ω_{ar} conditions have been significantly affected by anthropogenic inputs, particularly atmospheric CO_2. The annual mean Ω_{ar} over the 0–100 m depth range was 0.91 in the pre-industrial period compared to the current value of 0.8. The difference between current and pre-industrial water-column averages is nearly the same regardless of depth, while the average Ω_{ar} is higher toward the shallower depths (**Table 1**). In comparison, the mean pH for 0–100 m across the entire system is currently 7.69, while in the pre-industrial it was 7.76. The carbonate chemistry in the Main Basin (station P28) and various sub-basins have been mostly affected by atmospheric CO_2 uptake (**Table 1** and **Figures 2**, **3**). These changes indicate that anthropogenically induced OA significantly increases the exposure below biological thresholds of pelagic calcifiers, i.e., pteropods and larval crabs. Spatially, the most affected habitats are the stratified bays of Hood Canal (station P12, P402), South Sound (station P38), and Whidbey Basin (station P4). With respect to the nutrient impacts, the calculated annual mean change in pH and Ω_{ar} is everywhere close to or below the root mean squared error (RMSE) of the SSM.

Anthropogenic inputs play a major role in lowering Ω_{ar} on a seasonal basis, with unequal contributions to the baseline Ω_{ar} shifts during different seasons and locations. In terms of the latter, the underlying variability in carbonate chemistry dictates the changes due to anthropogenic inputs with a lower mean and amplitude of change, but the same frequency (**Figure 3**). In this manner, different regions exhibit different patterns. For example, the greatest difference in total change since the pre-industrial period appears to be at the deeper, well-mixed stations (e.g., P8, P28), while anthropogenic impacts are the smallest in the Hood Canal (P4 and P12; **Figure 4**).

When assessing estuarine habitat conditions, we separated habitats into two categories: first, the habitats with a low Ω_{ar} baseline level in which exposure can induce biological risk, while the anthropogenic component only adds to a minor extent of the overall change (0.06–0.08 Ω_{ar}). Such is the case at stations P12 and P402 (**Figure 4**). Second, the habitats with higher Ω_{ar} levels where the anthropogenic component contributes to more significant changes, with Ω_{ar} change up to 0.15 at stations P8, P4, P28, and P38 (**Figure 4**).

Impacts of Nutrient-Driven Eutrophication

The observed trends show that nutrient-driven eutrophication impacts on Ω_{ar} changes are largely dependent on primary production and respiration processes, and can have positive or negative effects, respectively, depending on spatial location and season. Based on the seasonally specific distributions, the greatest magnitude in Ω_{ar} change over the upper 100 m occurs during the early spring and late autumn period at stations

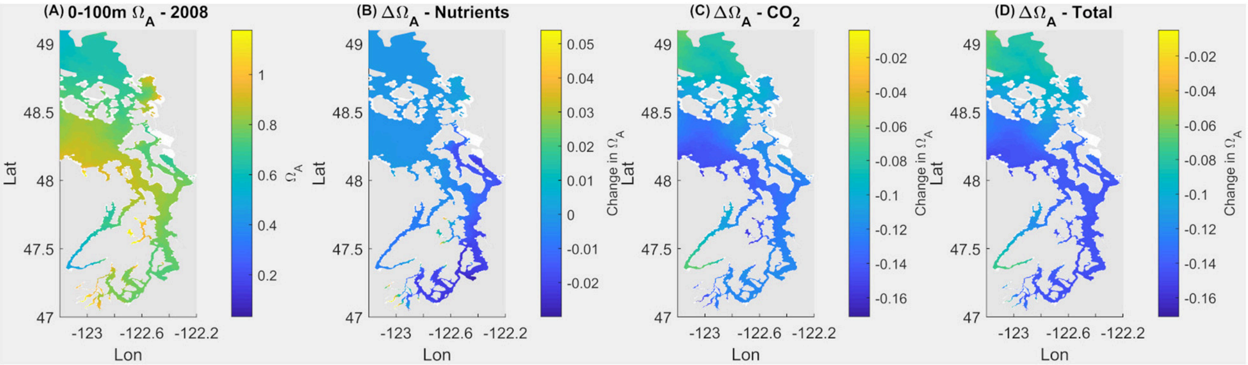

FIGURE 2 | Current omega saturation state (Ω_{ar}) averaged over 100 m in the Salish Sea **(A)**, with the changes in Ω_{ar} due to nutrients **(B)**, atmospheric CO_2 **(C)**, and a combination of both **(D)**.

TABLE 1 | Quantitative changes in omega saturation state due to nutrients, atmospheric CO_2, and the combination of both at 100 m depth.

Parameter	Scenario 1: Existing conditions in 2008 (S1Ex)	Scenario 2: Hypothetical reference conditions in 2008 without human nutrients (S2Ex-nut)	Scenario 3: Hypothetical reference conditions in 2008 without global anthropogenic CO_2 (S3Ex-atm)	Scenario 4: Hypothetical pre-industrial conditions without global anthro CO_2 or human nutrients (S4Ex-nut-atm)	Change due to human nutrients and CO_2 combined (Scenario 1–4)	Change due to global anthropogenic CO_2 (Scenario 1–3)	Change due to human nutrients (Scenario 1–2)
Mean_pHtot_KT100	7.69	7.70	7.75	7.76	−0.067	−0.060	−0.007
Mean_OmegaAr_KT100	0.80	0.80	0.90	0.91	−0.111	−0.104	−0.006
P12_pHtot_KT100	7.51	7.52	7.57	7.58	−0.069	−0.062	−0.007
P12_OmegaAr_KT100	0.58	0.59	0.66	0.66	−0.080	−0.072	−0.007
P22_pHtot_KT100	7.78	7.78	7.85	7.85	−0.071	−0.070	−0.001
P22_OmegaAr_KT100	0.95	0.96	1.10	1.10	−0.142	−0.141	−0.001
P28_pHtot_KT100	7.73	7.74	7.80	7.81	−0.079	−0.069	−0.009
P28_OmegaAr_KT100	0.87	0.89	1.00	1.02	−0.143	−0.126	−0.015
P38_pHtot_KT100	7.71	7.73	7.78	7.80	−0.082	−0.067	−0.015
P38_OmegaAr_KT100	0.86	0.88	0.98	1.01	−0.143	−0.118	−0.021
P4_pHtot_KT100	7.71	7.72	7.78	7.79	−0.082	−0.070	−0.012
P4_OmegaAr_KT100	0.82	0.83	0.94	0.95	−0.136	−0.117	−0.016
P402_pHtot_KT100	7.48	7.48	7.53	7.54	−0.064	−0.057	−0.006
P402_OmegaAr_KT100	0.57	0.57	0.63	0.64	−0.069	−0.064	−0.004
P8_pHtot_KT100	7.77	7.77	7.84	7.84	−0.071	−0.068	−0.002
P8_OmegaAr_KT100	0.95	0.95	1.08	1.09	−0.138	−0.135	−0.003

P28 and P38 (**Figures 3**, **4**). When Ω_{ar} is above 1–1.2 in the upper water column, the effect of added nutrients increases Ω_{ar} because the addition of eutrophication fuels primary production, which increases $\Omega_{ar} > 1$ in near-surface waters. In this region, increased nutrient loading induces greater organic production and uptake of CO_2 from the water by phytoplankton. When the additional phytoplankton settles to deeper depths, the decomposition of organic matter via respiration processes releases CO_2. Consequently, the added nutrients contribute to greater decomposition of organic carbon, decreased pH, and lower Ω_{ar} values in deeper waters. This is reflected in the shape of the curve describing baseline vs. change in Ω_{ar} due to anthropogenic nutrients (at different regions throughout the year; **Figures 3–5**), the negative values of change in Ω_{ar} (indicating decrease in Ω_{ar} due to added nutrients), and the decreasing slope of the curve with decreasing $\Omega_{ar} < 1$ values at most stations (**Figure 5**).

Model Skill

Root mean squared error and bias are appropriate measures of model skill for numerical biogeochemical models (Stow et al., 2009). Average model RMSE and bias for Ω_{ar} is ±0.29 and −0.08, respectively. Average RMSE and bias for pH is ±0.12 and −0.05, respectively. The model predictions of Ω_{ar} and pH were adjusted by the average model bias before reporting summary statistics or comparing with thresholds. In this report we use the model to calculate differences in carbonate system variables between realistic historical conditions in 2008 (Scenario 1: S1Ex, also referred to as "existing conditions") and the other model scenarios to estimate the changes caused by anthropogenic CO_2 and nutrients. Because the results of the different model scenarios are highly correlated with the existing conditions, the RMSE of the differences between scenarios is much less than the RMSE of the existing conditions. Pelletier et al. (2017) estimate the RMSE of predicted anthropogenic changes in pH and Ω_{ar} to be ±0.006 and ±0.03, respectively, using the SSM.

Threshold Application

Chemical Exposure Related to Pteropod Sublethal Thresholds

Sublethal and lethal pteropod thresholds were examined separately to ascribe the range of biological responses, from the subacute (dissolution and growth impairment) to the acute (mortality).

The most sensitive of the sublethal thresholds is mild shell dissolution (Ω_{ar} = 1.5 for 5 days), which describes the early warning stage of pteropod sensitivity (**Figure 6**). Under the current conditions, the duration of exposure for these thresholds occurs throughout the year (**Figure 6A**), with the intensity of exposure at 0.4–0.6 Ω_{ar} unit below the thresholds (**Figure 6G**), which is almost uniformly distributed within the Salish Sea basin. While the duration of exposure has not changed since pre-industrial times (**Figure 6D**), the intensity of exposure has increased from 0.06 in the smallest bays and inlets of the Hood Canal and the South Sound to 0.16 Ω_{ar} unit in

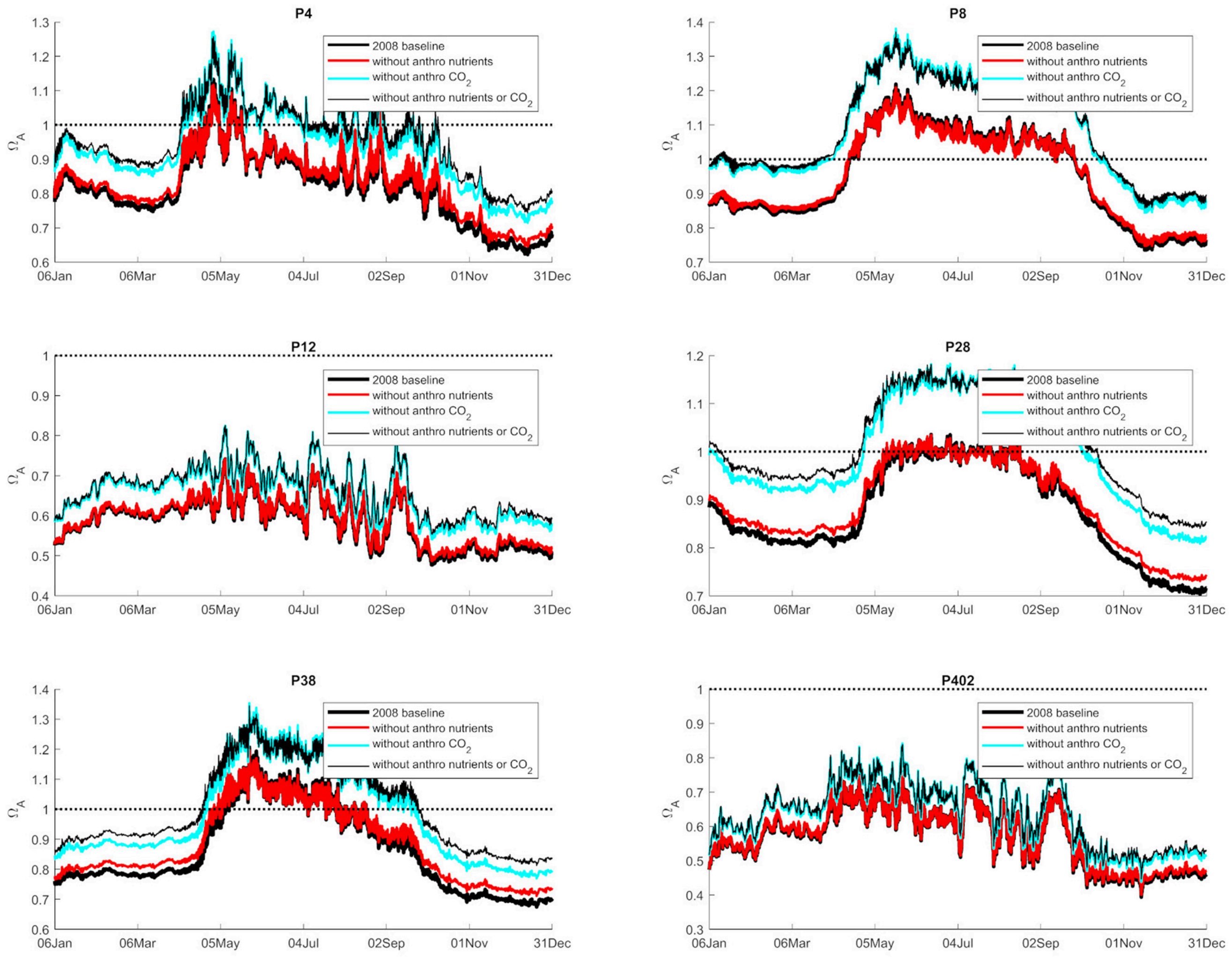

FIGURE 3 | Graphical representation of the average annual 0–100 m values of Ω_{ar} (2008 baseline), and separated as a contribution to nutrients, atmospheric CO_2, and both at six selected stations in Puget Sound (P4, P8, P12, P28, P38, P402 with locations shown in **Figure 1**).

the Main Basin (station P28) and most of the South Sound (station P38; **Figure 6J**), mostly due to the atmospheric CO_2 uptake (60–90%; **Figures 6I,L**). Moreover, the nutrient-driven eutrophication contributes, on average, a 10% increase in the intensity of exposure across the wider Salish Sea, while up to 20–40% increase (up to 0.05 Ω_{ar} unit) occurs in the smaller inlets of the South Sound (**Figure 6K**). The increase in severity of exposure resembles the intensity (**Figures 6M–R**). Our results suggest that nutrient-driven eutrophication might increase pteropod exposure inducive of mild dissolution during the late fall to early spring period in the smaller inlets of the South Sound, an increase that is greater than the model RMSE of 0.03 Ω_{ar} unit (**Figure 4**).

The sublethal threshold of growth impairment (Ω_{ar} = 1.2 for 14 days; **Figure 7**) was applied in the SSM during the fall (September–October), co-occurring with the sensitive time period of growth of the secondary spawning pteropod cohort. During this period, the duration of exposure below the threshold is 40–60 days (**Figure 7A**). Since the pre-industrial period, this duration has increased from 10 to up to 50 days in the small inlets of the South Sound (station P38) and the Main Basin (station P28), respectively (**Figure 7D**). The model output of present-day Ω_{ar} exposure related to the intensity shows the conditions to be 0.1–0.4 Ω_{ar} unit below the growth impairment threshold (**Figure 7G**). The intensity-related conditions have changed considerably since pre-industrial times, with up to a 70–100% increase in the South Sound and the Main Basin due to atmospheric CO_2 emissions (**Figures 7J–L**). A change of up to 30% (with more than 0.03 Ω_{ar} unit change) can be attributable to nutrient-driven eutrophication in the long, stratified embayments of the South Sound during the fall to spring period (**Figure 7K**), possibly triggering growth impairment. Moreover, when applying growth thresholds to the fall-winter period (November–February), the conditions can induce the same extent of sublethal responses as in the fall, indicating that pteropod sublethal processes are affected for

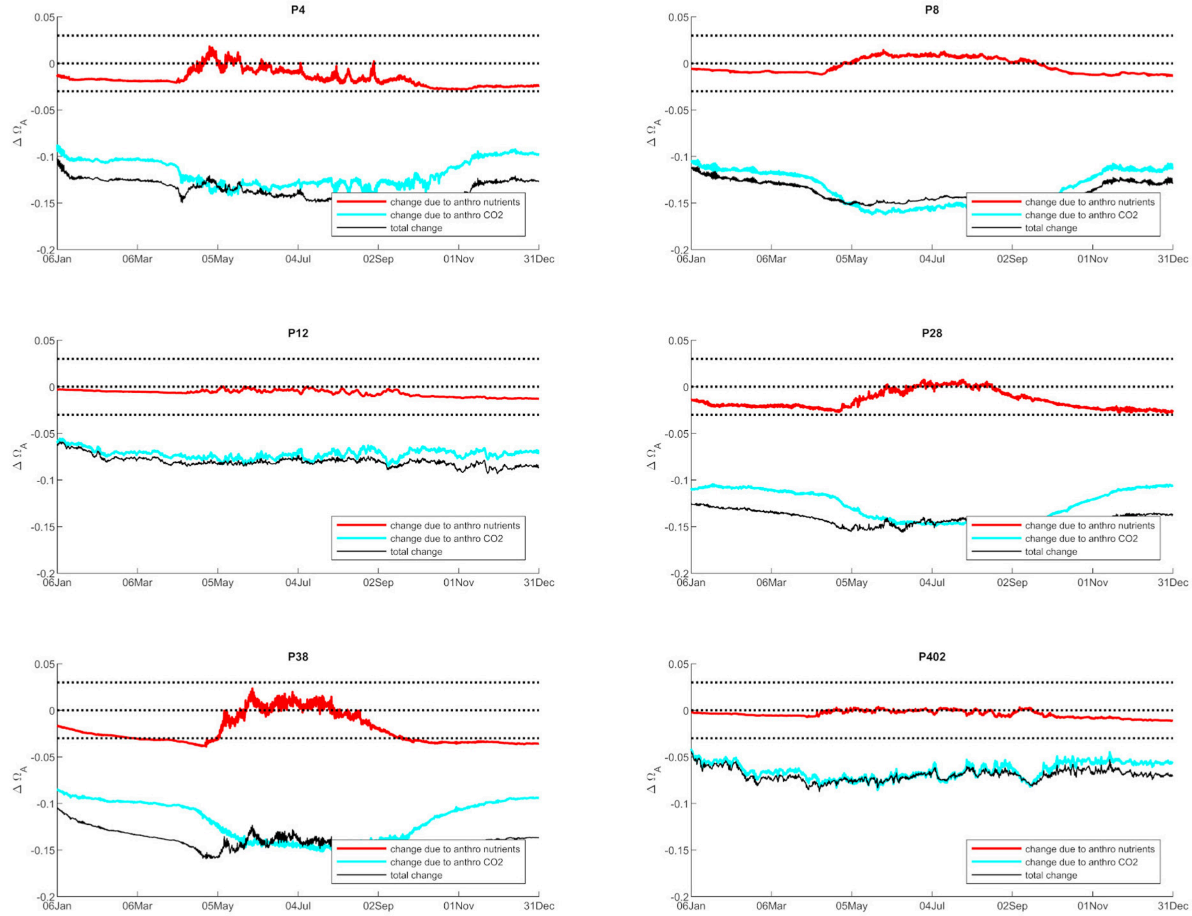

FIGURE 4 | The changes in Ω_{ar} due to anthropogenic nutrients (red line) and atmospheric CO_2 (blue line), while the black line represents the total change from both nutrients and atmospheric CO_2 at six selected stations in Puget Sound (P4, P8, P12, P28, P38, P402 with locations shown in **Figure 1**).

a prolonged period, resulting in more severe exposure than predicted if only a limited time period is considered.

Chemical Exposure Related to Pteropod Lethal Thresholds

Model outputs with applied mortality thresholds (Ω_{ar} = 0.95 for 14 days) demonstrate that various regions under present-day conditions are differentially affected in their duration of exposure on an annual basis. The largest duration and intensity of exposure is in the northern part of the Salish Sea (station P22), Whidbey Basin (station P4), and Hood Canal (**Figure 8**). The exposure is below the survival threshold for a considerable amount of time and magnitude, ranging from 70 to 300 days in the Main Basin (station P28) and Hood Canal (stations P402 and P12), respectively (**Figure 8A**), and intensity in the range of 0.1–0.4 Ω_{ar} (**Figure 8B**). When exposure was considered across the seasonal time scale, we observed conditions below the survival threshold to be prevalent during the late summer to early spring period. This indicates that vital population processes are affected for a prolonged duration and could subsequently result in changes on the population level.

Since pre-industrial times, the overall change of 0.11 Ω_{ar} (**Figure 8J**), with 70–90% of the change attributable to atmospheric CO_2 uptake, occurred within the Main Basin, the northern part of the Salish Sea, and Hood Canal (**Figures 8I,J**). Comparatively, the impact of nutrient-driven eutrophication since pre-industrial times was not significant (**Figures 8H,K**).

Impact of Anthropogenic OA on the Larval Stages of Dungeness Crab

Exposure to current Ω_{cal} during the springtime (May–June) induces a spatially differential extent of internal dissolution of the larval stages of the Dungeness crab (**Figure 9**). The most severe extent of internal dissolution occurs in the Hood Canal, Whidbey Basin, and partially in the South Sound (**Figure 9A**). The lowest baseline Ω_{cal}, which occurs in the early spring and fall–winter periods (**Figure 4**), coincides with the increases in internal dissolution over the same seasonal scales. The magnitude of exposure since pre-industrial times has resulted in increased internal dissolution of 20–30% across the Salish Sea. A few spatially limited bays of the South Sound have experienced more than a 60% increase (**Figure 9D**). In terms of attribution, CO_2

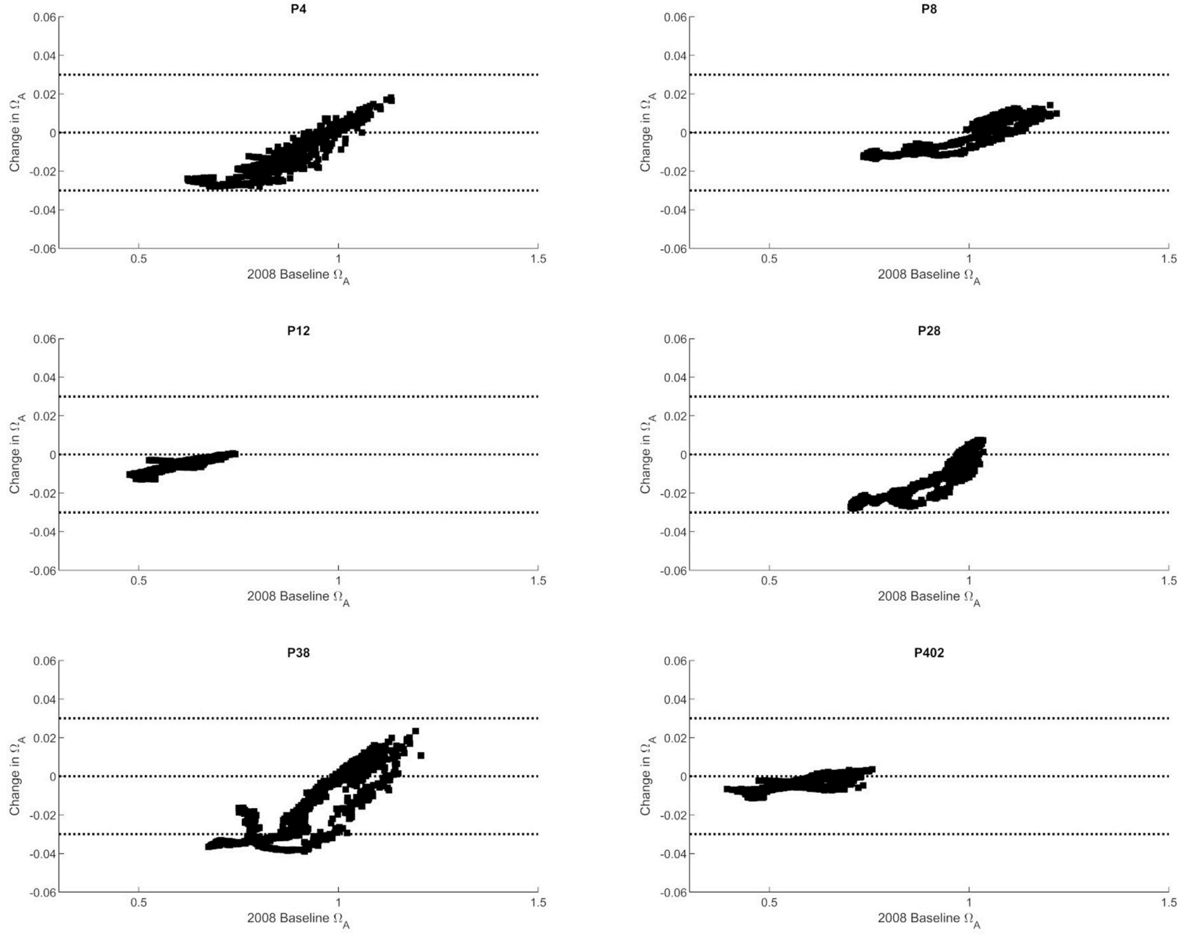

FIGURE 5 | The correlation between baseline Ω_{ar} (as modeled for 2008) and changes in Ω_{ar} at six selected stations in the Puget Sound (P4, P8, P12, P28, P38, P402 with locations shown in **Figure 1**).

emissions uptake results in the greatest increase in internal dissolution (**Figure 9C**), while nutrient-related eutrophication caused an insignificant increase (**Figure 9B**). Areas currently exhibiting the most extensive dissolution are not always the same as the areas with the most rapid change. This is evident where changes related to the combination of both anthropogenic stressors are larger than the current state of internal dissolution (**Figures 9A** vs. **9C**) regionally in the South Sound, Sinclair, and Dyes Inlets.

Temporal and Spatial Scale of Anthropogenic Drivers Inducing Negative Biological Responses

In evaluating the impact of the anthropogenic drivers since pre-industrial times, there are differences in the spatial and temporal extent of impact between two anthropogenic drivers, i.e., atmospheric CO_2 emissions and nutrient-related eutrophication. As such, the contributions of each to driving the conditions below the biological thresholds are different. The results of the attribution analyses show a predominant impact of anthropogenic CO_2 from atmospheric CO_2 emissions that increase the influx of DIC from the open ocean boundary, as well as the exchange of CO_2 across the air/water interface, driving $\Omega_{ar,cal}$ conditions below the sublethal and lethal thresholds. Such impacts have been observed over most spatial scales in the Salish Sea from the deeper basins to the inlets, although not to the same extent, with $\Omega_{ar,cal}$ conditions in the deep basins being significantly more susceptible to the changes compared to the smaller bays and inlets. The Main Basin is consistently more affected by atmospheric CO_2 than the inlets of the South Sound (**Figures 2–4**). The temporal attribution of atmospheric CO_2 impacts is equally noted across all the seasons, although at one station in the South Sound (station P38 in Carr Inlet), the greatest impact is during the fall to spring months (**Figure 4**). As such, atmospheric CO_2 emissions directly contribute to the change in $\Omega_{ar,cal}$, and thus related duration, magnitude, and severity of exposure for major sublethal (shell dissolution and growth) and, possibly, lethal (mortality) biological effects (**Figures 6**, **7** vs. **Figure 8**), and thus increase in risk for both pteropods and larval Dungeness crabs.

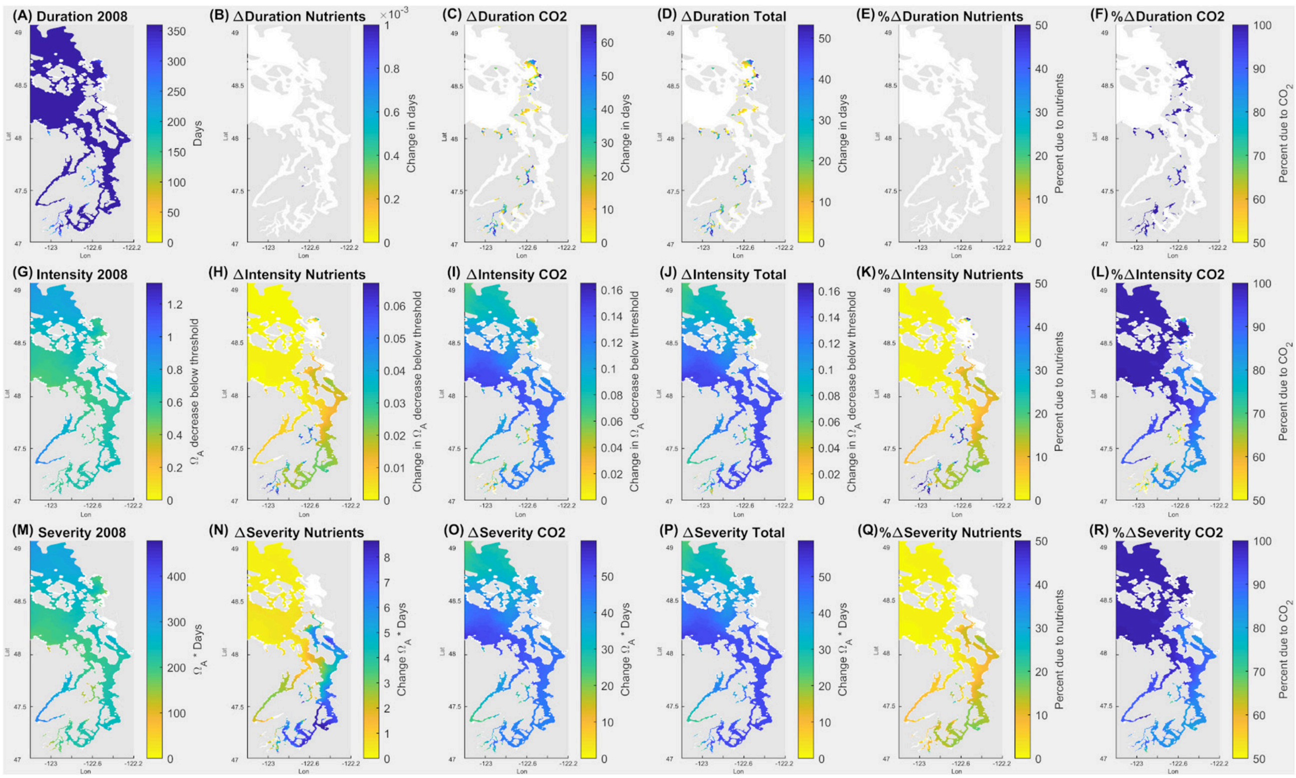

FIGURE 6 | Application of pteropod threshold for mild dissolution (5 days at Ω_{ar} = 1.5) over the annual scale in the upper 100 m in the Salish Sea. Model outputs demonstrate current (2008) duration, intensity, and severity of the conditions **(A,G,M)**. The second column indicates all the changes due to nutrients **(B,H,N)**; the third column is related to the changes due to atmospheric CO_2 **(C,I,O)**; and the fourth column **(D,J,P)** shows total changes due to both nutrients and atmospheric CO_2. The fifth column **(E,K,Q)** depicts % changes in Ω_{ar} due to nutrients, and the sixth column **(F,L,R)** is the % change in Ω_{ar} due to atmospheric CO_2. Values of zero are masked in white.

Eutrophication contributes to the change in $\Omega_{ar,cal}$ conditions below the thresholds to a much smaller extent than atmospheric CO_2. Since the change in Ω_{ar} due to eutrophication is less than the model uncertainty, eutrophication plays an insignificant role across spatial and temporal scales for the annual mean (**Figure 2**). The change is the greatest when baseline $\Omega_{ar,cal}$ conditions are already low, which occurs during the late summer to early spring period. Spatially, the attribution of nutrient-driven eutrophication on conditions above the 0.03 Ω_{ar} threshold was mainly observed in smaller, less vertically mixed bays and inlets of the South Sound, representative of the conditions at station P38 in Carr Inlet (**Figure 4**).

From a biological standpoint, added nutrients may have more adverse impacts on the lower thresholds when Ω_{ar} is closer to or lower than 1.0 and can indirectly exacerbate biological status of organisms when they are already severely impacted (**Figures 4**, **5**). This could happen by small-scale reductions of the initially low baseline conditions that result in the threshold crossing during some months that can affect the most critical life stages, in the early spring and the late summer-early fall period. Namely, around $\Omega_{ar} < 1.0$, a very small reduction in Ω_{ar} can shift the conditions inducive to sublethal processes toward lethal processes. On the other hand, the addition of nutrients in the spring and summer periods can increase $\Omega_{ar} > 1$, with nutrients having a less detrimental effect, or in fact, partially alleviating OA stress. Overall, however, because of spatially and temporally limited impacts, we conclude that eutrophication contributes minimally to the change in chemical exposure and, thus, associated biological risks.

Future Projections

Here, we demonstrate future projected changes related to the seasonal Ω_{ar} distribution under RCP 8.5 for the year 2100 integrated for 0–100 m. We chose station P28 to represent a centrally located region of the Main Basin, of Puget Sound (**Figure 10A**), with the future projection scenario as described in Scenario 5 (S5-Future; see section "Model Scenarios"). The projections show a dramatic decrease in Ω_{ar}. Pre-industrial summer conditions were mostly supersaturated ($\Omega_{ar} > 1$). The increase in seasonal exposure is reflected in a reduced amount of time above the sublethal and lethal thresholds (**Figure 9B**). The conditions above the sublethal thresholds (Ω_{ar} of 1.5, 1.2, and 1.0) start to rapidly decline in the past few decades and disappear before the year 2050. In contrast, the conditions above the lethal threshold (Ω_{ar} = 0.9) since pre-industrial times at first decline gradually, then exponentially over the last few decades, and completely disappear by the year 2050. Such exposure below

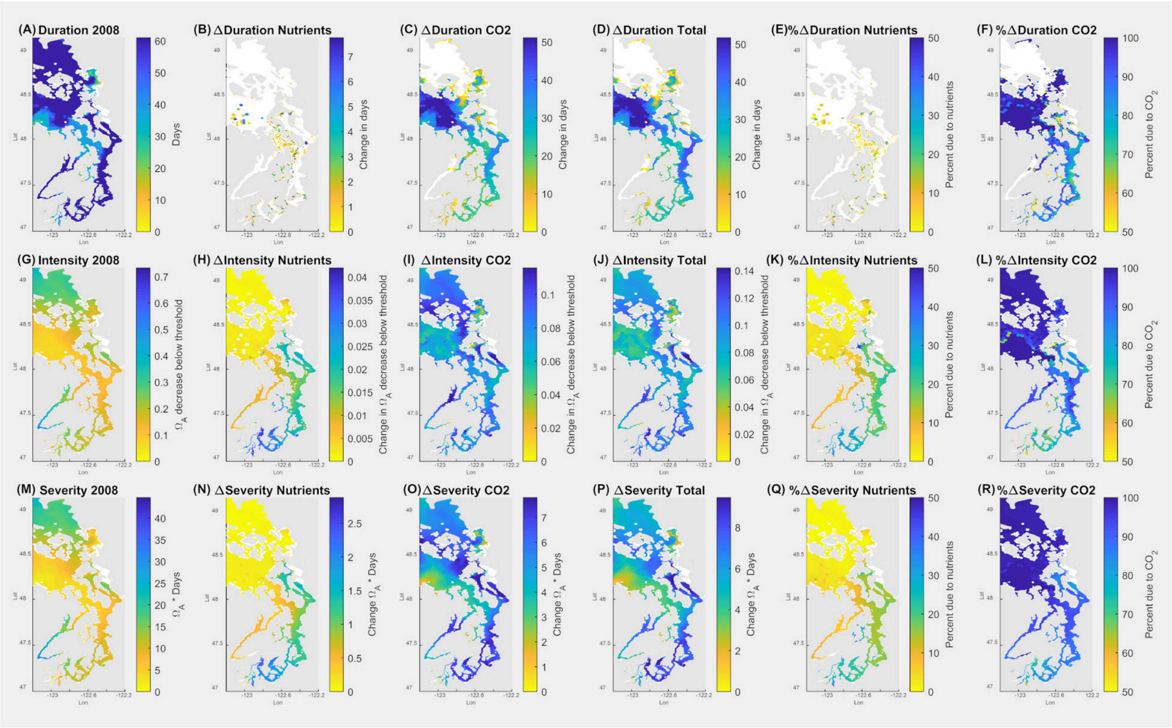

FIGURE 7 | Application of pteropod threshold for growth impairment (7 days at Ω_{ar} = 1.0) over the seasonal scale in the upper 100 m of the Salish Sea during September–October. Model outputs demonstrate current (2008) duration, intensity, and severity of the conditions **(A,G,M)**. The second column indicates the changes due to nutrients **(B,H,N)**; the third column depicts the changes due to atmospheric CO_2 **(C,I,O)**; the fourth column **(D,J,P)** shows total changes due to both nutrients and atmospheric CO_2. The fifth column **(E,K,Q)** depicts % changes in Ω_{ar} due to nutrients, and the sixth column **(F,L,R)** is % change in Ω_{ar} due to atmospheric CO_2. Values of zero are masked in white.

the thresholds can impose detrimental impacts on marine calcifiers' sustainability.

DISCUSSION

Current and Future Exposures

This is the first study along the United States West Coast that has considered the changes in OA exposure and risk to estuarine habitats using a combination of sensitivity tools and a highly resolved biogeochemical model. Our results demonstrate that the most biologically relevant changes in carbonate chemistry in the Salish Sea since pre-industrial times are driven on seasonal time scales. Since the seasonal conditions are spatially dependent on the Ω_{ar} status, the interpretation of seasonal Ω_{ar} projections suggest that time-sensitive biological processes (spring and autumn spawning, spring growth) will be most affected. Habitats currently with the lowest OA baseline conditions (the greatest exposure) and those that are rapidly changing due to anthropogenic drivers will likely be the most affected. Based on seasonal exposure outputs, all of the species are exposed to unfavorable conditions below the thresholds for a considerable amount of time and, as such, important processes during various life stages can be impacted. However, while organisms in the regions currently characterized by low OA exposure could potentially have some time to adapt, that is not the case in the rapidly changing habitats (especially in the small inlets of the South Sound; **Figure 9D**), where the lack of available time for adaptation could impose the most detrimental ecological changes. This is an important distinction to consider when evaluating future habitat suitability.

Intense anthropogenic acidification is rapidly changing urban estuaries such as the Salish Sea, driving increased risk for pelagic calcifiers. Evans et al. (2019) quantitatively characterized future seasonal projections for the Salish Sea, finding that the process of acidification is predicted to non-linearly intensify in the future. In comparison, our study of future 2050 seasonal Ω_{ar} projections of habitat suitability in the Puget Sound shows that future suitable conditions are predominantly dependent on the vertical extent of habitat considered. The vertical averaging of 0–100 m renders substantially faster exponential declines with no suitable habitat available (**Figure 10B**) compared to only surface waters with some extent of suitable conditions (Evans et al., 2019).

Caveats and Strengths of Using Biological Thresholds

The application of thresholds in the biogeochemical model to deduce the attribution of anthropogenic stressors in the estuarine system is a simplified approach for predicting changes in OA exposure related to potential habitat of marine calcifiers.

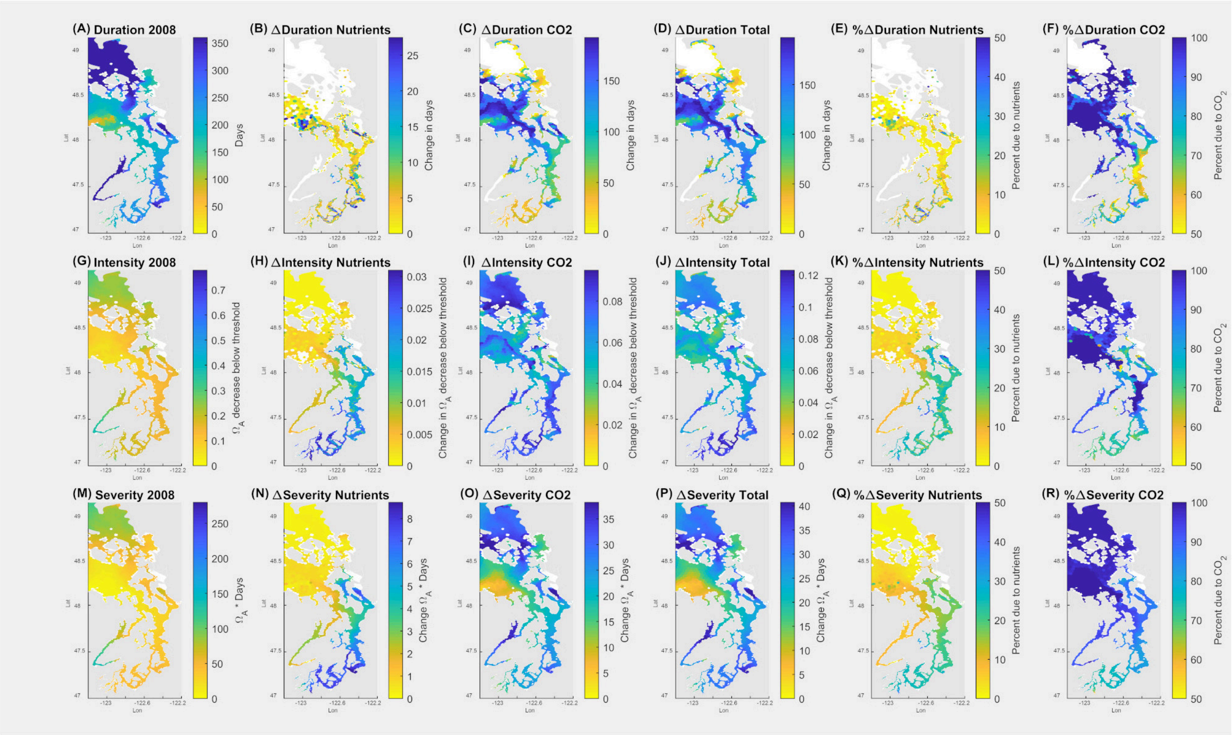

FIGURE 8 | Application of pteropod threshold for survival in the upper 100 m (14 days at Ω_{ar} = 0.95) over the annual scale in the Salish Sea. Model outputs demonstrate current duration, intensity, and severity of the conditions **(A,G,M)**. The second column indicates all the changes due to nutrients **(B,H,N)**; the third column depicts the changes due to atmospheric CO_2 **(C,I,O)**, the fourth column **(D,J,P)** shows total changes due to both nutrients and atmospheric CO_2. The fifth column **(E,K,Q)** depicts % changes in Ω_{ar} due to nutrients, and the sixth column **(F,L,R)** is % change in Ω_{ar} due to atmospheric CO_2. Values of zero are masked in white.

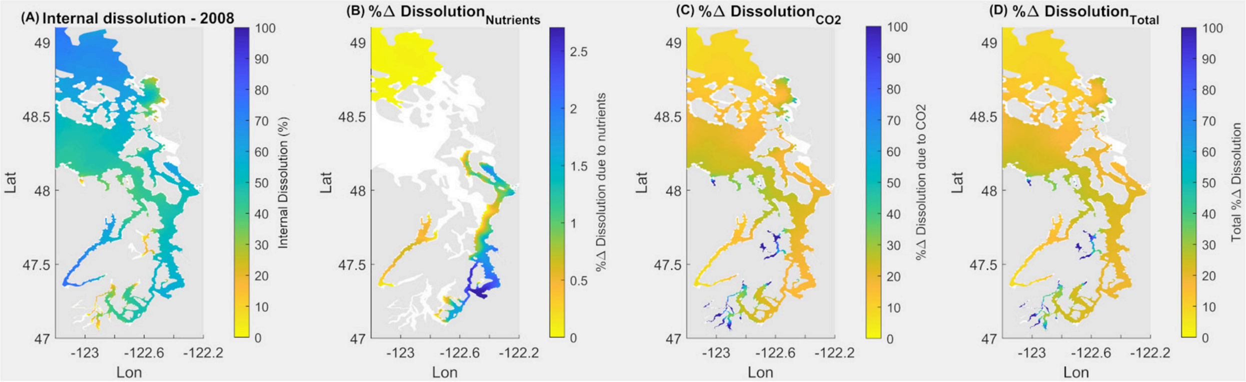

FIGURE 9 | Application of equation for larval Dungeness crab dissolution over upper 160 m integrated water depth for May–June in the Salish Sea to demonstrate current (2008) state of internal dissolution in % **(A)**; % change of dissolution due to nutrients **(B)**; due to atmospheric CO_2 **(C)**; and combined % change due to both nutrients and atmospheric CO_2 **(D)**.

While it does not take complex variability in exposure regime or co-occurring multiple stressors into account, here we have used it to identify spatial and temporal anthropogenic OA hotspots in the ecosystem. Biological thresholds are further characterized by different levels of confidence scores, with the lowest confidence implying greater uncertainty in interpretations of the biological responses. Applying thresholds only over time periods when biological processes occur, however, ensures that temporal exposure below the threshold are correctly interpreted within the context of species life history. Furthermore, comparing the sensitivity of thresholds that were derived either from experimental or synthesis studies can yield different results and, thus, interpretation of different species risks and sensitivities.

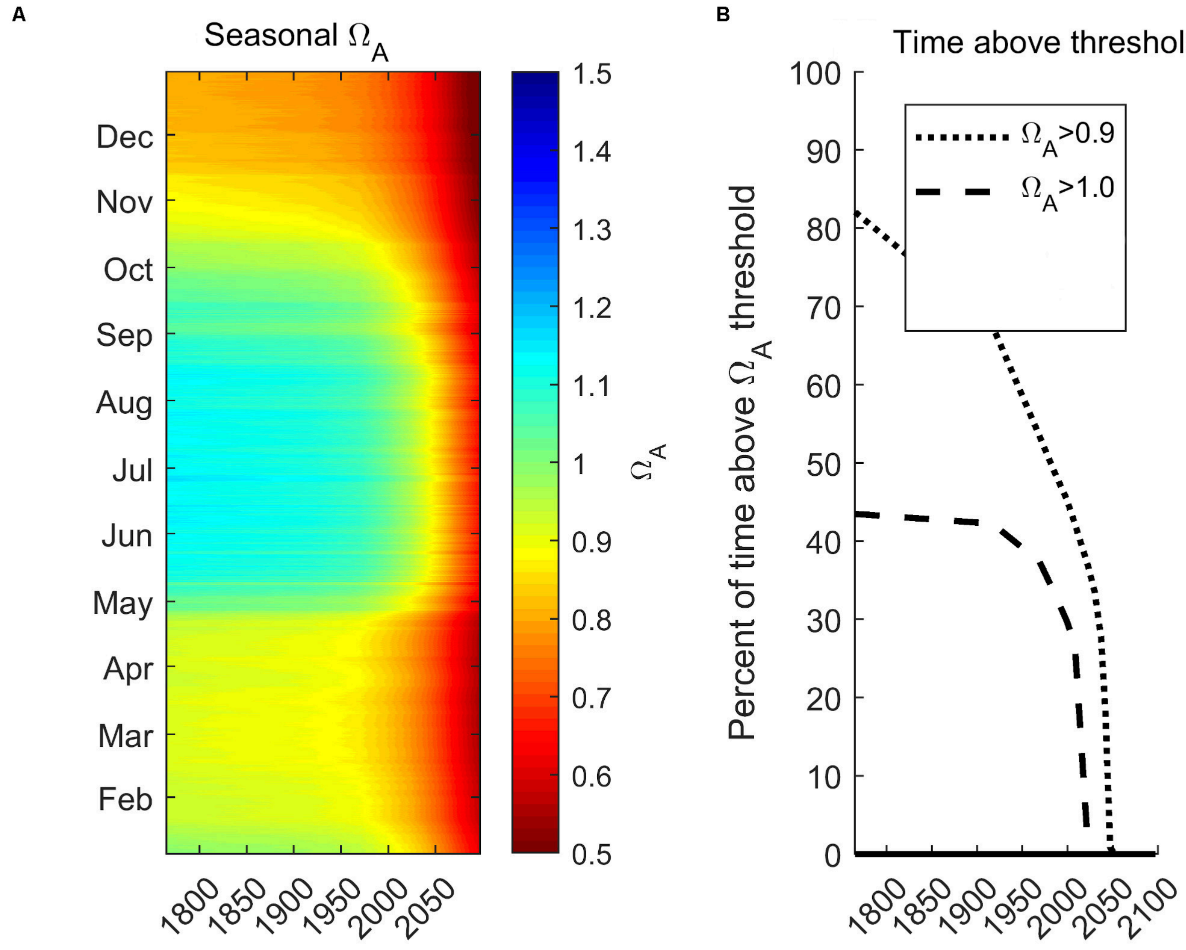

FIGURE 10 | Future seasonal projections of vertically integrated (0–100 m) Ω_{ar} at the station P28 in the Main Basin under RCP 8.5 scenario for the year 2100 **(A)** and projected time above pteropod thresholds for sublethal (Ω_{ar} of 1.0) and lethal (Ω_{ar} of 0.9; **B**).

The impact of anthropogenic stressors in the Salish Sea currently results in exposures that induce a variety of negative sublethal responses, such as mild dissolution and growth impairments, but those risks vary spatially and temporally. The greatest magnitude change in Ω_{ar} during the spring transition is associated with the time of spawning and most intense growth, implying a potential temporal mismatch between the early life stages and less favorable habitats. Furthermore, there are other sublethal thresholds that have been identified for pteropods, such as severe dissolution, and reduced calcification and reproductive efforts (Bednaršek et al., 2019). Given the similarity in the magnitude and duration of these thresholds, the current OA exposure regime, either seasonally or on annual basis, is below multiple thresholds. This means that current exposure can affect multiple pathways of physiological sensitivity and can cumulatively contribute to a greater impact than only predicted based on one pathway. It is difficult to extrapolate exposure to mortality thresholds on the population dynamics in the Salish Sea. Since the intensity of exposure associated with mortality thresholds is currently still very limited spatially, we can only infer that any potential population-level decline would be a result of prolonged impairments on the organismal level, with the trends outside the variability envelope taking significantly longer to be demonstrated.

Comparisons of different thresholds for various marine calcifiers and their life stages confirm similar magnitude of sublethal thresholds for various oysters and mussels, ranging from 1.4 to 1.8 (Gaylord et al., 2011; Barton et al., 2012). With respect to the larval lethal threshold at Ω_{ar} = 1.2 (Waldbusser et al., 2015), pteropod mortality threshold is less sensitive, thus providing a more conservative estimate of Ω_{ar} impacts. Nevertheless, since none of these studies provide a threshold duration, the risk estimates for these species cannot be assessed in a manner similar to this study, urging future experimental studies to derive all elements (magnitude and duration) needed for risk assessment.

Uncertainty of the Projections

Model projections of OA exposure below biologically relevant thresholds include uncertainty from several sources: model uncertainty (including parameter and structural uncertainty), scenario uncertainty, potential changes in hydrodynamics, and threshold uncertainty (Bednaršek et al., 2019). Scenario uncertainty is likely to be the most important factor for long-term projections (Hawkins and Sutton, 2009) beyond the 2060s. In addition, OA co-occurs with warming and deoxygenation in the Salish Sea (Reum et al., 2014), and these interactions are not captured in these predictions, but the fast warming rates predicted in the Salish Sea (Hamel et al., 2015) may additionally exacerbate already compromised biological responses imposed by OA exposure. The uncertainty of the predicted $\Omega_{ar,\,cal}$, and pH from the Salish Sea model has been described using a variety of model skill metrics (Bianucci et al., 2018). Model skill estimates are based on the differences between predicted and observed conditions. By keeping hydrodynamics the same for all scenarios, we include the caveat that the differences between scenarios isolate the effects of only regional human nutrients and global anthropogenic CO_2 while not taking future physical and hydrodynamics changes into account.

The sum of separately evaluated relative effects of anthropogenic CO_2 and regional anthropogenic nutrient inputs as a percentage of the combined effects of CO_2 and nutrients together does not necessarily equal 100%. This is partly because the effects were evaluated individually, and partly because these processes are not necessarily linear. In other words, the effect of added nutrient loading may differ depending on whether the effect of added CO_2 is considered or not. The separate effects of nutrients and CO_2 also may occur at different times. The effect of nutrients in some locations and seasons decreases the severity of adverse conditions, especially in the euphotic zone during the growing season, when added nutrients increase photosynthesis. In other locations and seasons, the effect of added nutrients increases the severity of adverse conditions, especially below the euphotic zone.

Validation Between the Observation and Synthesis Studies

Since this is the first study that evaluates the risks related to anthropogenic OA using biogeochemical scenarios, it is difficult to ascribe the significance of the study's model outputs or compare it to any previous work. Evaluations should always be considered in comparative terms. In an effort to interpret observed increases related to the sublethal and lethal effects in the model, it is clear that we cannot evaluate the absolute numbers and conclude what this means for the organisms or populations, although the magnitude change of 0.16 to 0.12 Ω_{ar} unit appears large. The available experimental and field data can, however, be used to reflect and possibly validate the magnitude increases observed in the model outputs.

Comparisons with the food web model outputs and food web modeling conducted in the Salish Sea and the West Coast, respectively (Busch et al., 2013; Busch and McElhany, 2016; Marshall et al., 2017), delineate the most sensitive species, i.e., pteropods and Dungeness crabs. Furthermore, the experimental work by Busch et al. (2014) confirmed pteropod sensitivity to OA through increased shell dissolution and mortality. This finding has been recently confirmed in a field study by Bednaršek et al. (unpublished) that delineates spatial distribution of pteropod shell dissolution in the Salish Sea. The latter work locates the most severe exposure to be in the Hood Canal and Whidbey Island in the late summer, and to a minor extent in the inlets of the South Sound. Such spatial designation of OA hotspots aligns explicitly with the findings of this study despite using a completely different approach, i.e., applying shell dissolution thresholds in the biogeochemical model. Given that the sublethal threshold of mild dissolution is characterized by a high confidence score, the biological interpretation of the induced sublethal effects is more certain. The agreement between the field and biogeochemical approaches of spatial and temporal exposure inducing risk offers some validity to the SSM modeling.

Furthermore, the survival threshold derived from experimental studies on pteropods from the Salish Sea is below Ω_{ar} = 0.56 (Busch et al., 2014). Despite a difference between the experimentally derived threshold (Ω_{ar} = 0.56) and the one based on expert-based consensus (Ω_{ar} = 0.95) used in this study, our model outputs demonstrate that there are areas in the Salish Sea with the exposure to the lower, experimentally derived thresholds. As such, expert-based thresholds are much more sensitive in their value compared to experimental ones, with this approach being more precautionary than the experimentally derived thresholds when used to delineate areas of increased pteropod mortality. However, since the confidence score related to interpretation of the mortality threshold is low (Bednaršek et al., 2019), a more scrutinized and careful interpretation is warranted.

The sensitivity of larval Dungeness crabs relies on the estimates of internal dissolution, the extent of which is associated with increased energetic demand (Hans et al., 2014; Bednaršek et al., 2020). We identified the exposure inducive to increased internal dissolution to be spatially limited to the inlets and bays of the South Sound, where the risks are the greatest. Based on the data from Washington Department of Fish and Wildlife (Bosley, Katelyn; Washington Department of Fish and Wildlife, personal communication), the largest megalopae abundances correspond to stations P8, P28, and P4, where the carbonate chemistry conditions are most favorable, while some of the stations with the lowest recorded data are at the Hood Canal (station P402) and South Sound (P38), characterized by the lowest carbonate chemistry conditions. Importantly, time series from the same area identify Dungeness crab population declines over the last years, illustrating some parallels between the model outputs and field observations. Although the drivers behind the population decline in the South Sound have not been identified yet, we emphasize anthropogenic OA must be taken into account. Field data for Dungeness crab internal dissolution are limited to the Pacific Northwest coast (Bednaršek et al., 2020) and are not specific to the Salish Sea. As such, direct comparison of the results related to the spatial or temporal exposure is not feasible. Nevertheless, the greatest extent of internal dissolution is found at the lowest Ω_{cal} (Bednaršek et al., 2020), which is also observed in the biogeochemical model outputs. Despite the absence of additional sensitivity tools (e.g., thresholds) in the model, our approach still validates the use of the sensitivity equation in the SSM to identify the spatially relevant exposures associated with increased risks for larval Dungeness crab.

In conclusion, these observations, experimental results, and model output largely confirm the validity of the use of thresholds to detect risks of anthropogenic OA exposures inducive of sublethal and lethal responses. As a result, we propose that thresholds be used to detect changes in exposure in comparison with pre-industrial times, which is something that cannot be achieved using the results of the meta-analyses, experimental, or synthesis work that are based on future conditions. In addition, thresholds' applicability can resolve the changes in the magnitude and duration of exposure attributable to specific anthropogenic stressors. This can ultimately provide new research venues to translate threshold species-specific model outputs to habitat suitability modeling efforts.

Implications for Management

Overall, our results provide a set of scenarios that set the stage to evaluate current biological risks related to anthropogenic OA in the estuarine habitats of the Salish Sea for ecologically and economically important species. We demonstrate that atmospheric CO_2 emissions are a major driver behind the modeled changes and responses, the reduction of which can help sustain biological species vital for ecosystem functions and society. In contrast, nutrient-driven eutrophication plays only a marginal role over spatially and temporally limited scales. Our results provide an initial step toward the development of management actions related to OA in the Salish Sea that focus on mitigation strategies to reduce atmospheric CO_2 emissions. However, in the absence of regional and locally supported actions for lowering CO_2, other resilient strategies that buffer against OA, such as kelp and seaweed farming, may be effective on a local or regional scale.

DATA AVAILABILITY STATEMENT

The the NetCDF model outputs supporting the conclusions of this article will be made available by the authors, without undue reservation, to any qualified researcher.

AUTHOR CONTRIBUTIONS

NB, GP, and RF conceptualized the research and design of the study. NB wrote the proposal and obtained the funding for this work through the SeaDoc Society, provided biological interpretation, and wrote the first draft of the manuscript. GP and AA conducted the modeling work. GP performed the statistical analyses. RF contributed with the observation-model comparisons. All authors contributed to manuscript revisions, read and approved the submitted version.

FUNDING

This project (#201702053-02) was supported by the SeaDoc Society through the Wildlife Health Center, School of Veterinary Medicine, University of California, Davis. RF was supported by the Pacific Marine Environmental Laboratory and the NOAA Ocean Acidification Program Contribution number 5095 from the NOAA Pacific Marine Environmental Laboratory. The Salish Sea Model used in this project is supported by the modeling teams at the Pacific Northwest National Laboratory (PNNL) and the Washington State Department of Ecology (DOE), including Tarang Khangaonkar (PNNL), Cristiana Figueroa-Kaminsky (DOE), Teizeen Mohamedali (DOE), Sheelagh McCarthy (DOE), and John Gala (DOE), and funding from the United States Environmental Protection Agency.

ACKNOWLEDGMENTS

The Salish Sea Model used in this project is supported by the modeling teams at the Pacific Northwest National Laboratory (PNNL) and the Washington State Department of Ecology (DOE), including Tarang Khangaonkar (PNNL), Cristiana Figueroa-Kaminsky (DOE), Teizeen Mohamedali (DOE), Sheelagh McCarthy (DOE), and John Gala (DOE). In memoriam T. Bednaršek.

REFERENCES

Alin, S., Newton, J. A., Curry, B., Greeley, D. J., and Lebrec, M. (2018). "A decade-long biogeochemical cruise time-series from the Salish Sea and Washington coast: regional connections to large-scale ocean climate drivers of ocean acidification and hypoxia," in *Proceedings of the Presentation, Salish Sea Ecosystem Conference, Washington, May 4, 2018* Washington, DC.

Aydin, K. Y., McFarlane, G. A., King, J. R., Megrey, B. A., and Myers, K. W. (2005). Linking oceanic food webs to coastal production and growth rates of Pacific salmon (*Oncorhynchus* spp.), using models on three scales. *Deep Sea Res. Part II* 52, 757–780. doi: 10.1016/j.dsr2.2004.12.017

Barange, M., Merino, G., Blanchard, J. L., Scholtens, J., Harle, J., Allison, E. H., et al. (2014). Impacts of climate change on marine ecosystem production in societies dependent on fisheries. *Nat. Clim. Change* 4, 211–216. doi: 10.1038/nclimate2119

Barton, A., Hales, B., Waldbusser, G. G., Langdon, C., and Feely, R. A. (2012). The Pacific oyster, *Crassostrea gigas*, shows negative correlation to naturally elevated carbon dioxide levels: implications for near-term ocean acidification effects. *Limnol. Oceanogr.* 57, 698–710. doi: 10.4319/lo.2012.57.3.0698

Barton, A., Waldbusser, G. G., Feely, R. A., Weisberg, S. B., Newton, J. A., Hales, B., et al. (2015). Impacts of coastal acidification on the Pacific Northwest shellfish industry and adaptation strategies implemented in response. *Oceanography* 28, 146–159. doi: 10.5670/oceanog.2015.38

Baumann, H., Talmage, S. C., and Gobler, C. J. (2012). Reduced early life growth and survival in a fish in direct response to increased carbon dioxide. *Nat. Clim. Change* 2, 38–41. doi: 10.1038/nclimate1291

Bednaršek, N., Feely, R. A., Beck, M. W., Alin, S. R., Siedlecki, S. A., Calosi, P., et al. (2020). Exoskeleton dissolution with mechanoreceptor damage in larval Dungeness crab related to severity of present-day ocean acidification vertical gradients. *Sci. Total Environ.* 716:136610. doi: 10.1016/j.scitotenv.2020.136610

Bednaršek, N., Feely, R. A., Beck, M. W., Glippa, O., Kanerva, M., and Engström-Öst, J. (2018). El Niño-related thermal stress coupled with upwelling-related ocean acidification negatively impacts cellular to population-level responses in pteropods along the California Current System with implications for increased bioenergetic costs. *Front. Mar. Sci.* 4:486. doi: 10.3389/fmars.2018.00486

Bednaršek, N., Feely, R. A., Howes, E. L., Hunt, B., Kessouri, F., León, P., et al. (2019). Systematic review and meta-analysis towards synthesis of thresholds of ocean acidification impacts on calcifying pteropods and interactions with warming. *Front. Mar. Sci.* 6:227. doi: 10.3389/fmars.2019.00227

Bednaršek, N., Feely, R. A., Reum, J. C. P., Peterson, B., Menkel, J., Alin, S. R., et al. (2014). *Limacina helicina* shell dissolution as an indicator of declining habitat suitability owing to ocean acidification in the California Current Ecosystem. *Proc. Biol. Sci.* 281:20140123. doi: 10.1098/rspb.2014.0123

Bednaršek, N., Feely, R. A., Tolimieri, N., Hermann, A. J., Siedlecki, S. A., Waldbusser, G. G., et al. (2017a). Exposure history determines pteropod vulnerability to ocean acidification along the US West Coast. *Sci. Rep.* 7:4526. doi: 10.1038/s41598-017-03934-z

Bednaršek, N., Harvey, C. J., Kaplan, I. C., Feely, R. A., and Možina, J. (2016). Pteropods on the edge: cumulative effects of ocean acidification, warming, and deoxygenation. *Prog. Oceanogr.* 145, 1–24. doi: 10.1016/j.pocean.2016.04.002

Bednaršek, N., Klinger, T., Harvey, C. J., Weisberg, S., McCabe, R. M., Feely, R. A., et al. (2017b). New ocean, new needs: application of pteropod shell dissolution as a biological indicator for marine resource management. *Ecol. Indic.* 76, 240–244. doi: 10.1016/j.ecolind.2017.01.025

Beesley, A., Lowe, D. M., Pascoe, C. K., and Widdicombe, S. (2008). Effects of CO_2-induced seawater acidification on the health of *Mytilus edulis*. *Clim. Res.* 37, 215–225. doi: 10.3354/cr00765

Bianucci, L., Long, W., Khangaonkar, T., Pelletier, G., Ahmed, A., Mohamedali, T., et al. (2018). Sensitivity of the regional ocean acidification and the carbonate system in Salish Sea to ocean and freshwater inputs. *Ele. Sci. Anth.* 6:22. doi: 10.1525/elementa.151

Busch, D. S., Harvey, C. J., and McElhany, P. (2013). Potential impacts of ocean acidifcation on the Puget Sound food web. *ICES J. Mar. Sci.* 70, 823–833. doi: 10.1093/icesjms/fst061

Busch, D. S., Maher, M., Thibodeau, P., and McElhany, P. (2014). Shell condition and survival of Puget Sound pteropods are impaired by ocean acidification conditions. *PLoS One* 9:e105884. doi: 10.1371/journal.pone.0105884

Busch, D. S., and McElhany, P. (2016). Estimates of the direct effect of seawater pH on the survival rate of species groups in the California current ecosystem. *PLoS One* 11:e0160669. doi: 10.1371/journal.pone.0160669

Cai, W.-J., Hu, X., Huang, W.-J., Murrell, M. C., Lehrter, J. C., Lohrenz, S. E., et al. (2011). Acidification of subsurface coastal waters enhanced by eutrophication. *Nat. Geosci.* 4, 766–770. doi: 10.1038/ngeo1297

Cerco, C. F., and Cole, T. (1993). Three-dimensional eutrophication model of Chesapeake Bay. *J. Environ. Eng.* 119, 1006–1025. doi: 10.1061/(ASCE)0733-93721993119:61006

Cerco, C. F., and Cole, T. M. (1994). *Three-Dimensional Eutrophication Model of Chesapeake Bay*. Vicksburg, MS: U.S. Army Corps of Engineers.

Chan, F., Barth, J. A., Blanchette, C. A., Byrne, R. H., Chavez, F. P., Cheriton, O., et al. (2017). Persistent spatial structuring of coastal ocean acidification in the California current system. *Sci. Rep.* 7:2526. doi: 10.1038/s41598-41017-02777-y

Chavez, F. P., Pennington, J. T., Michisaki, R. P., Blum, M., Chavez, G. M., Friederich, J., et al. (2017). Climate variability and change: response of a coastal ocean ecosystem. *Oceanography* 30, 128–145. doi: 10.5670/oceanog.2017.429

Chen, C., Liu, H., and Beardsley, R. C. (2003). An unstructured grid, finite-volume, three-dimensional, primitive equations ocean model: application to coastal ocean and estuaries. *J. Atmos. Ocean Technol.* 20, 159–186.

Di Toro, D. M. (2001). *Sediment Flux Modeling*. New York, NY: Wiley-Interscience.

Engström-Öst, J., Glippa, O., Feely, R. A., Kanerva, M., Keister, J. E., Alin, S. R., et al. (2019). Eco-physiological responses of copepods and pteropods to ocean warming and acidification. *Sci. Rep.* 9:4748. doi: 10.1038/s41598-019-41213-1

Evans, W., Pocock, K., Hare, A., Weekes, C., Hales, B., Jackson, J., et al. (2019). Marine CO_2 patterns in the Northern Salish Sea. *Front. Mar. Sci.* 5:536. doi: 10.3389/fmars.2018.00536

Fassbender, A. J., Alin, S. R., Feely, R. A., Sutton, A. J., Newton, J. A., Krembs, C., et al. (2018). Seasonal carbonate chemistry variability in marine surface waters of the Pacific Northwest. *Earth Syst. Sci. Data* 10, 1367–1401. doi: 10.5194/essd-10-1367-2018

Feely, R. A., Alin, S. R., Carter, B., Bednaršek, N., Hales, B., Chan, F., et al. (2016). Chemical and biological impacts of ocean acidification along the west coast of North America. *Estuar. Coast. Shelf Sci.* 183, 260–270. doi: 10.1016/j.ecss.2016.08.043

Feely, R. A., Alin, S. R., Newton, J., Sabine, C. L., Warner, M., Devol, A., et al. (2010). The combined effects of ocean acidification, mixing, and respiration on pH and carbonate saturation in an urbanized estuary. *Estuar. Coast Shelf Sci.* 88, 442–449. doi: 10.1016/j.ecss.2010.05.004

Feely, R. A., Klinger, T., Newton, J., and Chadsey, M. (2012). *Scientific Summary of Ocean Acidification in Washington State Marine Waters.* NOAA ORR Special Report. Lacey, WA: Washington State Department of Ecology.

Feely, R. A., Okazaki, R. R., Cai, W. J., Bednaršek, N., Alin, S. R., Byrne, R. H., et al. (2018). The combined effects of acidification and hypoxia on pH and aragonite saturation in the coastal waters of the California current ecosystem and the northern Gulf of Mexico. *Cont. Shelf Res.* 152, 50–60. doi: 10.1016/j.csr.2017.11.002

Feely, R. A., Sabine, C. L., Hernandez-Ayon, J. M., Ianson, D., and Hales, B. (2008). Evidence for upwelling of corrosive "acidified" water onto the Continental Shelf. *Science* 320, 1490–1492. doi: 10.1126/science.1155676

Gattuso, J. P., Magnan, A., Billé, R., Cheung, W. W. L., Howes, E. L., Joos, F., et al. (2015). Contrasting futures for ocean and society from different anthropogenic CO2 emissions scenarios. *Science* 349:aac4722. doi: 10.1126/science.aac4722

Gaylord, B., Hill, T. M., Sanford, E., Lenz, E. A., Jacobs, L. A., Sato, K. N., et al. (2011). Functional impacts of ocean acidification in an ecologically critical foundation species. *J. Exp. Bio.* 214, 2586–2594. doi: 10.1242/jeb.055939

Giltz, S. M., and Taylor, C. M. (2017). Reduced growth and survival in the larval blue crab callinectes sapidus under predicted ocean acidification. *J. Shellfish Res.* 36, 481–485. doi: 10.2983/035.036.0219

Gruber, N., Hauri, C., Lachkar, Z., Loher, D., Frölicher, T. L., and Plattner, G. K. (2012). Rapid progression of ocean acidification in the California current system. *Science* 337, 220–223. doi: 10.1126/science.1216773

Hales, B., Suhrbier, A., Waldbusser, G. G., Feely, R. A., and Newton, J. A. (2017). The carbonate chemistry of the "fattening line," Willapa Bay, 2011–2014. *Estuaries Coasts* 40, 173–186. doi: 10.1007/s12237-016-0136-7

Hamel, N. J., Joyce, J., Fohn, M., James, A., Toft, J., Lawver, A., et al. (2015). *State of the Sound: Report on the Puget Sound Vital Signs. November 2015*. Available online at: www.psp.wa.gov/sos (accessed August 20, 2019).

Hans, S., Fehsenfeld, S., Treberg, J. R., and Weihrauch, D. (2014). Acid–base regulation in the Dungeness crab (*Metacarcinus magister*). *Mar. Biol.* 161, 1179–1193. doi: 10.1007/s00227-014-2409-7

Hauri, C., Gruber, N., McDonnell, A. M. P., and Vogt, M. (2013). The intensity, duration, and severity of low aragonite saturation state events on the California continental shelf. *Geophys. Res. Lett.* 40, 3424–3428. doi: 10.1002/grl.50618

Hawkins, E., and Sutton, R. (2009). The potential to narrow uncertainty in regional climate predictions. *B. Am. Meteorol. Soc.* 90, 1095–1108. doi: 10.1175/2009BAMS2607.1

Jamieson, G. S., and Phillips, A. (1993). Megalopal spatial distribution and stock separation in Dungeness crab (*Cancer magister*). *Can. J. Fish Aquat. Sci.* 50, 416–429. doi: 10.1139/f93-047

Kapsenberg, L., Miglioli, A., Bitter, M. C., Tambutté, E., Dumollard, R., and Gattuso, J.-T. (2018). Ocean pH fluctuations affect mussel larvae at key developmental transitions. *Proc. R. Soc. B.* 285:20182381. doi: 10.1098/rspb.2018.2381

Khangaonkar, T., Sackmann, B., Long, W., Mohamedali, T., and Roberts, M. (2012). Simulation of annual biogeochemical cycles of nutrient balance, phytoplankton bloom(s), and DO in Salish Sea using an unstructured grid model. *Ocean Dyn.* 62, 1353–1379. doi: 10.1007/s10236-012-0562-4

Khangaonkar, T., Yang, Z., Kim, T., and Roberts, M. (2011). Tidally averaged circulation in Salish Sea sub-basins: comparison of historical data, analytical model, and numerical model. *Estuar. Coast Shelf Sci.* 93, 305–319. doi: 10.1016/j.ecss.2011.04.016

Kim, T., and Khangaonkar, T. (2012). An offline unstructured biogeochemical model (UBM) for complex estuarine and coastal environments. *Environ. Modell. Softw.* 31, 47–63. doi: 10.1016/j.envsoft.2011.11.010

Kroeker, K. J., Kordas, R. L., Crim, R., Hendriks, I. E., Ramajo, L., Singh, G. S., et al. (2013). Impacts of ocean acidification on marine organisms: quantifying sensitivities and interaction with warming. *Glob. Change Biol.* 19, 1884–1896. doi: 10.1111/gcb.12179

Laruelle, G. G., Cai, W.-J., Hu, X., Gruber, N., Mackenzie, F. T., and Regnier, P. (2018). Continental shelves as a variable but increasing global sink for atmospheric carbon dioxide. *Nat. Commun.* 9:454. doi: 10.1038/s41467-017-02738-z

Lewis, E., and Wallace, D. (1998). *Program Developed for CO2 System Calculations. ORNL/CIAC-105*. Oak Ridge, TN: Oak Ridge National Laboratory, US Department of Energy.

Lischka, S., Büdenbender, J., Boxhammer, T., and Riebesell, U. (2011). Impact of ocean acidification and elevated temperatures on early juveniles of the polar shelled pteropod *Limacina helicina*: mortality, shell degradation, and shell growth. *Biogeosciences* 8, 919–932. doi: 10.5194/bg-8-919-2011

Lischka, S., and Riebesell, U. (2012). Synergistic effects of ocean acidification and warming on overwintering pteropods in the Arctic. *Glob. Change Biol.* 18, 3517–3528. doi: 10.1111/gcb.12020

Marshall, K. N., Kaplan, I. C., Hodgson, E. E., Hermann, A., Busch, D. S., McElhany, P., et al. (2017). Risks of ocean acidification in the California current food web and fisheries: ecosystem model projections. *Glob. Chang. Biol.* 23, 1525–1539. doi: 10.1111/gcb.13594

Mastrandrea, M. D., Field, C. B., Stocker, T. F., Edenhofer, O., Ebi, K. L., Frame, D. J., et al. (2010). *Guidance Note for Lead Authors of the IPCC Fifth Assessment Report on Consistent Treatment of Uncertainties. Intergovernment Panel Climate Change*. Available online at: http://www.ipcc.ch (accessed May, 2018).

McLaskey, A. K., Keister, J. E., McElhany, P., Brady Olson, M., Shallin Busch, D., Maher, M., et al. (2016). Development of *Euphausia pacifica* (krill) larvae is impaired under pCO_2 levels currently observed in the Northeast Pacific. *Mar. Ecol. Prog. Ser.* 555, 65–78. doi: 10.3354/meps11839

Michaelidis, B., Ouzounis, C., Paleras, A., and Pörtner, H. O. (2005). Effects of long-term moderate hypercapnia on acid–base balance and growth rate in marine mussels *Mytilus galloprovincialis*. *Mar. Ecol. Prog. Ser.* 293, 109–118. doi: 10.3354/meps293109

Miller, J. J., Maher, M., Bohaboy, E., Friedman, C. S., and McElhany, P. (2016). Exposure to low pH reduces survival and delays development in early life stages of Dungeness crab (*Cancer magister*). *Mar. Biol.* 163:118. doi: 10.1007/s00227-016-2883-1

Mohamedali, T., Roberts, M., Sackmann, B., and Kolosseus, A. (2011). *Puget Sound Dissolved Oxygen Model Nutrient Load Summary for 1999-2008*. Olympia, WA: Washington Department of Ecology.

O'Neill, B. B., Oppenheimer, M., Warren, R., Hallegatte, S., Kopp, R. E., Pörtner, H. O., et al. (2017). IPCC reasons fro concern regarding climate change risks. *Nat. Clim. Change* 7, 28–37. doi: 10.1038/nclimate3179

Osborne, E. B., Thunell, R. C., Gruber, N., Feely, R. A., and Benitez-Nelson, C. R. (2020). Decadal variability in twentieth-century ocean acidification in the California current ecosystem. *Nat. Geosci.* 13, 43–49. doi: 10.1038/s41561-019-0499-z

Osborne, E. B., Thunell, R. C., Marshall, B. J., Holm, J. A., Tappa, E. J., Benitez-Nelson, C., et al. (2016). Calcification of the planktonic foraminifera *Globigerina bulloides* and carbonate ion concentration: results from the Santa Barbara basin. *Paleoceanography* 31, 1083–1102. doi: 10.1002/2016pa002933

Pelletier, G., Bianucci, L., Long, W., Khangaonkar, T., Mohamedali, T., Ahmed, A., et al. (2017). *Salish Sea Model Ocean Acidification Module and the Response to Regional Anthropogenic Nutrient Sources. Salish Sea Model Sediment Diagenesis Module*. Olympia, WA: Washington State Department of Ecology.

Pelletier, G., Roberts, M., Keyzers, M., and Alin, S. R. (2018). Seasonal variation in aragonite saturation in surface waters of Puget sound — a pilot study. *Elementa Sci. Anthrop.* 6:5. doi: 10.1525/elementa.270

PSEMP Marine Waters Workgroup (2016). *Puget Sound Marine Waters: 2015 Overview*, eds S. K. Moore, R. Wold, K. Stark, J. Bos, P. Williams, K. Dzinbal, et al. Available online at: www.psp.wa.gov/PSEMP/PSmarinewatersoverview.php (accessed April, 2019).

Reum, J. C., Alin, S. R., Feely, R. A., Newton, J., Warner, M., and McElhany, P. (2014). Seasonal carbonate chemistry covariation with temperature, oxygen, and salinity in a fjord estuary: implications for the design of ocean acidification experiments. *PLoS One* 9:e89619. doi: 10.1371/journal.pone.0089619

Stow, C. A., Jolliff, J., McGillicuddy, D. J., Doney, S. C., Allen, J. I., Friedrichs, M. A., et al. (2009). Skill assessment for coupled biological/physical models of marine systems. *J. Mar. Syst.* 76, 4–15. doi: 10.1016/j.jmarsys.2008.03.011

Sunda, W. G., and Cai, W. J. (2012). Eutrophication induced CO_2-acidification of subsurface coastal waters: interactive effects of temperature, salinity, and atmospheric pCO_2. *Environ. Sci. Technol.* 46, 10651–10659. doi: 10.1021/es300626f

Sutton, A. J., Feely, R. A., Maenner-Jones, S., Musielewicz, S., Osborne, J., Dietrich, C., et al. (2019). Autonomous seawater pCO_2 and pH time series from 40 surface buoys and the emergence of anthropogenic trends. *Earth Syst. Sci. Data* 11, 421–439. doi: 10.5194/essd-11-421-2019

Takahashi, T., Sutherland, S. C., Wanninkhof, R., Sweeney, C., Feely, R. A., Chipman, D. W., et al. (2009). Climatological mean and decadal change in surface ocean pCO_2, and net sea-air CO_2 flux over the global oceans. *Deep Sea Res. Part II Top. Stud. Oceanogr.* 56, 554–577. doi: 10.1016/j.dsr2.2008.12.009

Turi, G., Lachkar, Z., Gruber, N., and Münnich, M. (2016). Climate modulation of recent trends in ocean acidification in the California current system. *Environ. Res. Lett.* 11:014007. doi: 10.1088/1748-9326/11/1/014007

Waldbusser, G. G., Hales, B., Langdon, C. J., Haley, B. A., Schrader, P., Brunner, E. L., et al. (2015). Saturation-state sensitivity of marine bivalve larvae to ocean acidification. *Nat. Clim. Chang.* 5, 273–280. doi: 10.1038/nclimate2479

Wallace, R. B., Baumann, H., Grear, J. S., Aller, R. C., and Gobler, C. J. (2014). Coastal ocean acidification: the other eutrophication problem. *Estuar. Coast. Shelf Sci.* 148, 1–13. doi: 10.1016/j.ecss.2014.05.027

Wang, Y., Hu, M., Wu, F., Storch, D., and Pörtner, H. O. (2018). Elevated pCO_2 affects feeding behavior and acute physiological response of the Brown Crab *Cancer pagurus*. *Front. Physiol.* 9:1164. doi: 10.3389/fphys.2018.01164

Williams, C. R., Dittman, A. H., McElhany, P., Busch, D. S., Maher, M. T., Bammler, T. K., et al. (2019). Elevated CO_2 impairs olfactory-mediated neural and behavioral responses and gene expression in ocean-phase coho salmon (*Oncorhynchus kisutch*). *Glob. Change Biol.* 25, 963–977. doi: 10.1111/gcb.14532

Yang, Z., Khangaonkar, T., Labiosa, R., and Kim, T. (2010). *Salish Sea Dissolved Oxygen Modeling Study: Development of an Intermediate-Scale Hydrodynamic Model*. Richland, WA: Pacific Northwest National Laboratory.

Conflict of Interest: The authors declare that the research was conducted in the absence of any commercial or financial relationships that could be construed as a potential conflict of interest.

frontiers in Marine Science

ORIGINAL RESEARCH
published: 14 July 2020
doi: 10.3389/fmars.2020.00570

Future Distribution of Suitable Habitat for Pelagic Sharks in Australia Under Climate Change Models

Charlotte A. Birkmanis[1,2]*, *Jennifer J. Freer*[3], *Leigh W. Simmons*[4], *Julian C. Partridge*[2] *and Ana M. M. Sequeira*[1,2]

[1] School of Biological Sciences, The University of Western Australia, Perth, WA, Australia, [2] The UWA Oceans Institute, The University of Western Australia, Perth, WA, Australia, [3] British Antarctic Survey, Cambridge, United Kingdom, [4] Centre for Evolutionary Biology, School of Biological Sciences, The University of Western Australia, Perth, WA, Australia

OPEN ACCESS

Edited by:
Darren Pilcher,
University of Washington
and NOAA/PMEL, United States

Reviewed by:
Stephanie Brodie,
University of California, Santa Cruz,
United States
Brad Wetherbee,
The University of Rhode Island,
United States

***Correspondence:**
Charlotte A. Birkmanis
charlotte.birkmanis@
research.uwa.edu.au

Specialty section:
This article was submitted to
Global Change and the Future Ocean,
a section of the journal
Frontiers in Marine Science

Received: 07 February 2020
Accepted: 22 June 2020
Published: 14 July 2020

Citation:
Birkmanis CA, Freer JJ,
Simmons LW, Partridge JC and
Sequeira AMM (2020) Future
Distribution of Suitable Habitat
for Pelagic Sharks in Australia Under
Climate Change Models.
Front. Mar. Sci. 7:570.
doi: 10.3389/fmars.2020.00570

Global oceans are absorbing over 90% of the heat trapped in our atmosphere due to accumulated anthropogenic greenhouse gases, resulting in increasing ocean temperatures. Such changes may influence marine ectotherms, such as sharks, as their body temperature concurrently increases toward their upper thermal limits. Sharks are high trophic level predators that play a key role in the regulation of ecosystem structure and health. Because many sharks are already threatened, it is especially important to understand the impact of climate change on these species. We used shark occurrence records collected by commercial fisheries within the Australian continental Exclusive Economic Zone (EEZ) to predict changes in future (2050–2099) relative to current (1956–2005) habitat suitability for pelagic sharks based on an ensemble of climate models and emission scenarios. Our predictive models indicate that future sea temperatures are likely to shift the location of suitable shark habitat within the Australian EEZ. On average, suitable habitat is predicted to decrease within the EEZ for requiem and increase for mackerel sharks, however, the direction and severity of change was highly influenced by the choice of climate model. Our results indicate the need to consider climate change scenarios as part of future shark management and suggest that more broad-scale studies are needed for these pelagic species.

Keywords: sea surface temperature, climate change, marine ecosystems, species distribution models, global warming, Lamnidae, Carcharhinidae

INTRODUCTION

Climate change is predicted to have unprecedented effects on the marine environment, with changes in ocean temperature increasing extinction risk for many species (Dulvy et al., 2003; Barnosky et al., 2011; Bruno et al., 2018; Pinsky et al., 2019) and altering the global distribution of marine life (Tittensor et al., 2010; Garciá Molinos et al., 2016). Changes in species distribution (Perry et al., 2005; Poloczanska et al., 2013) and community structure (Doney et al., 2012) are already being observed in marine ecosystems due to temperature shifts associated with rising emissions and accumulation of atmospheric carbon dioxide (Hoegh-Guldberg and Bruno, 2010;

Doney et al., 2012; Gattuso et al., 2015). Recent modeling of biodiversity under different future climate change scenarios, across a wide range of marine and terrestrial ecosystems, predicts abrupt and irreversible ecosystem disruption during the late 21st century (Trisos et al., 2020). With predicted increases of up to ∼5°C in worldwide sea-surface temperature (SST) by the end of the 21st century (IPCC, 2015), there is a critical need to investigate how marine species will be affected, especially ectotherms which are dependent on external sources for body heat. As ectotherms, sharks may be influenced by climate change (Bernal et al., 2012; Rosa et al., 2014, 2017; Syndeman et al., 2015; Pinsky et al., 2019), with higher temperatures increasing their metabolism and oxygen demand (Pistevos et al., 2015; Lawson et al., 2019). The exception to this may be Lamnid mackerel sharks, which have some endothermic capability (Watanabe et al., 2015).

Many shark species are already globally threatened due to fisheries overexploitation (Queiroz et al., 2019) coupled with their low fecundity, late age at maturity, and slow growth (Cortés, 2000; Garcia et al., 2008; Yokoi et al., 2017). In fact, 16.6% of shark species are estimated to be threatened with extinction, and another 37.9% of shark species are categorized as "Data Deficient" by the International Union for Conservation of Nature (IUCN, 2020). Nevertheless, sharks are known to have direct economic value in fisheries (Dulvy et al., 2017) and ecotourism (Cisneros-Montemayor et al., 2013; Huveneers et al., 2017). They also play a key role in ecosystem functioning and stability, connecting distant ecosystems via their long-distance migrations (Rogers et al., 2015), and altering prey behavior, distribution and energy use (Heupel et al., 2015; Roff et al., 2016; Dulvy et al., 2017). Climate change may exacerbate existing threats for sharks, for example, suitable pelagic shark habitat in the north Pacific Ocean is projected to decline by the year 2100 (Hazen et al., 2013).

Future projections based on existing observations and modeling techniques can be used to investigate the effects of climate change on pelagic sharks (Barange et al., 2016). Using Earth System Models from the Coupled Model Intercomparison Project Phase 5 (CMIP5; hereafter called "climate models"), complex relationships between ecosystem health, human activities and global climate can be included to evaluate alternative future scenarios with varying severity of emissions (Moss et al., 2010; Freer et al., 2017). There are four emission scenarios commonly referred to as Representative Concentration Pathways (RCP 2.6, RCP 4.5, RCP 6, and RCP 8.5) (IPCC, 2013). These RCP scenarios are used to predict radiative forcing values, a measure of absorbed and retained energy in the lower atmosphere, for the year 2100 (Moss et al., 2010; Vuuren et al., 2011). RCP 4.5, also referred to as "stabilization scenario," is an optimistic scenario assuming a decline in overall energy usage from fossil fuel sources that limits emissions and radiative forcing (Thomson et al., 2011). Conversely, RCP 8.5, also referred to as "business-as-usual," is the most pessimistic scenario assuming minimal stabilization of greenhouse gas emissions alongside a large human population with high energy demands (Riahi et al., 2011).

The Australian Exclusive Economic Zone (EEZ) is already being impacted by climate change with waters off south-east Australia warming at almost four times the global average (Oliver et al., 2017) and range extensions already documented in several fish species (Last et al., 2011). Australia has one of the world's most diverse communities of sharks, with 182 recognized species (Simpfendorfer et al., 2019), and SST has been shown consistently to be a strong predictor of pelagic shark occurrence in Australian waters (Rogers et al., 2009, 2015; Stevens et al., 2010; Heard et al., 2017; Birkmanis et al., 2020). It is therefore important to investigate the likely impact of temperature changes on pelagic shark distribution and the location of suitable habitat on a continental scale if these species are to be appropriately managed into the future – especially if such changes may require a reassessment of interactions with fisheries in the future. Sharks comprise approximately 27% of the total catch (by number) of Australian pelagic longline fisheries (Gilman et al., 2008), with Australian stocks of the IUCN classified "Critically Endangered" oceanic whitetip (*Carcharhinus longimanus*), "Endangered" shortfin mako (*Isurus oxyrinchus*), and "Endangered" longfin mako (*Isurus paucus*) sharks listed respectively as "overfished," "depleting," and "undefined" due to a lack of data (Simpfendorfer et al., 2019; IUCN, 2020).

This study follows on from Birkmanis et al. (2020) in which occurrence records of pelagic sharks belonging to the Carcharhinidae and Lamnidae families (hereafter "requiem" and "mackerel," respectively) were obtained from commercial fisheries and used to develop generalized linear models with which to predict suitable habitat for these species within the Australian continental EEZ. After accounting for fishing effort bias, these models showed that SST was an important predictor of shark distributions, with the highest ranked model also including turbidity. Here, we extend our modeling to assess the impact of climate change on pelagic shark habitat across the entire continental Australian EEZ.

MATERIALS AND METHODS

Shark Occurrence

Catch records of 3,973 individual sharks from two families; requiem (silky *Carcharhinus falciformis*, oceanic whitetip *Carcharhinus longimanus*, dusky *Carcharhinus obscurus* and blue *Prionace glauca*) and mackerel (shortfin mako *Isurus oxyrinchus*, longfin mako *Isurus paucus* and porbeagle *Lamna nasus*) were obtained through the Global Biodiversity Information Facility online database (GBIF.org, 2017), as per details included in Birkmanis et al. (2020). These oceanic sharks were caught predominantly using commercial longlines in Commonwealth managed fisheries (more detailed data unavailable), with catch locations depicted in **Supplementary Figure S1**.

Predictors for Modeling Baseline and Future Climate Environmental Data

A climatological baseline was used as a reference point for projected future climate changes. According to Birkmanis et al. (2020), SST and turbidity were the most suitable predictors of requiem and mackerel shark occurrence within the Australian EEZ. We therefore focused on these two predictors to develop a climatological baseline to use as a reference for projected future climate changes. To calculate the SST baseline data, we downloaded monthly SST values for the years 1956–2005, covering the time period of our observed shark occurrence data, from the Integrated Marine Observing System (IMOS, 2016). We then averaged the SST values for each 0.1° grid-cell in the study area using ArcGIS 10.5 from Environmental Systems Research Institute (ESRI, 2017). We incorporated the observed turbidity values (measured as mean diffuse attenuation coefficient at wavelength 490 nm, downloaded using the Marine Geospatial Ecology Tool; Roberts et al., 2010) from 2000 to 2002 into our models with the assumption that turbidity will remain unchanged in the future.

Future SST data were taken from 24 CMIP5 climate models, using only one realization per climate model, under two emission scenarios, RCP 4.5 and RCP 8.5, amounting to 48 total simulations (**Table 1**). We downloaded the SST field and the anomaly statistic for each climate model (**Table 1**) under both RCP 4.5 and RCP 8.5 from the Climate Change Web Portal (Earth Systems Research Laboratory, 2014), developed by the National Oceanic and Atmospheric Administration's Earth System Research Laboratory to collate climate data and climate model outputs from the CMIP5 (see Scott et al., 2016 for details). We used the portal to calculate the difference in the mean SST between the future climate (2050–2099) and the model baseline reference period (1956–2005), hereafter called "anomaly" data. We then added these anomaly data to our baseline data across the extent of the Australian EEZ using ArcGIS and included this as the SST predictor for the future values.

Modeling Habitat Suitability for Baseline and Future Climate Data

We developed binomial generalized linear models with a logit link function for each of the two pelagic shark families, following

TABLE 1 | Mean and maximum projected sea surface temperature (SST) anomalies for the end of the 21st century (2050–2099) in Australian waters for each climate model under both emission scenarios (RCP 4.5 and RCP 8.5; standard deviation shown in parentheses).

Climate model name	Founding institute	Projected SST anomaly from baseline at year 2100 (°C)			
		Mean (SD)		Maximum	
		4.5	8.5	4.5	8.5
ACCESS-1.0	CSIRO and BOM, Australia	1.56 (0.39)	2.44 (0.65)	3.01	4.61
ACCESS-1.3	CSIRO and BOM, Australia	1.42 (0.36)	2.4 (0.56)	2.40	3.98
CAN-ESM2	CCCMA, Canada	1.78 (0.42)	2.86 (0.62)	3.73	5.46
CCSM4	NCAR, United States	1.35 (0.11)	2.4 (0.21)	1.65	2.96
CESM1-BGC	NSF, NCAR, United States	1.35 (0.1)	2.39 (0.22)	1.65	2.99
CESM1-CAM5	NSF, NCAR, United States	1.61 (0.25)	2.52 (0.37)	2.33	3.66
CMCC_CM	CMCC, Italy	1.43 (0.34)	2.47 (0.57)	2.52	4.33
GFDL_CM3	NOAA GFDL, United States	1.66 (0.48)	1.43 (0.34)	2.62	2.52
GFDL-ESM2G	NOAA GFDL, United States	0.98 (0.24)	1.83 (0.37)	1.52	2.56
GFDL-ESM2M	NOAA GFDL, United States	1.12 (0.3)	1.89 (0.47)	2.04	3.18
GISS-E2-H	NASA GISS, United States	1.18 (0.31)	1.91 (0.5)	2.47	4.08
GISS-E2-R	NASA GISS, United States	0.93 (0.23)	1.8 (0.45)	1.82	3.80
HADGEM2-AO	MOHC, United Kingdom	1.63 (0.35)	0.69 (0.23)	2.87	1.36
HADGEM2-CC	MOHC, United Kingdom	1.64 (0.54)	2.8 (0.79)	3.62	5.58
HADGEM2-ES	MOHC, United Kingdom (additional realizations from Instituto Nacional de Pesquisas Espaciais, Brazil)	1.69 (0.45)	2.69 (0.61)	3.33	4.57
INMCM4	INM, Russia	0.93 (0.3)	1.64 (0.43)	2.04	3.35
IPSL-CM5A-LR	IPSL, France	1.73 (0.4)	3 (0.6)	3.44	5.67
IPSL-CM5A-MR	IPSL, France	1.83 (0.35)	3.13 (0.56)	3.48	5.69
IPSL-CM5B-LR	IPSL, France	1.08 (0.18)	1.79 (0.43)	1.71	2.99
MIROC-ESM	JAMSTEC and NIES, Japan	1.67 (0.35)	2.82 (0.61)	3.40	5.92
MPI-ESM-LR	MPI-M, Germany	1.3 (0.47)	2.21 (0.76)	3.76	5.71
NORESM1-M	NCC, Norway	1.08 (0.2)	2 (0.28)	1.73	4.11
NORESM1-ME	NCC, Norway	1.26 (0.14)	2.15 (0.23)	1.72	3.04
NORESM1-MR	NCC, Norway	1.2 (0.29)	2.13 (0.51)	2.34	2.99

BOM, Bureau of Meteorology; CCCMA, Canadian Centre for Climate Modeling and Analysis; CMCC, Euro-Mediterranean Centre on Climate Change; CSIRO, Commonwealth Scientific and Industrial Research Organization; INM, Institute of Numerical Mathematics; IPSL, Institut Pierre-Simon Laplace; JAMSTEC, Japan Agency for Marine-Earth Science and Technology; MOHC, Met Office Hadley Centre; NASA GISS, National Aeronautics and Space Administration Goddard Institute for Space Studies; NCAR, National Centre for Atmospheric Research; NIES, Japanese National Institute for Environmental Studies; NOAA GFDL, National Oceanic and Atmospheric Administration Geophysical Fluid Dynamics Laboratory; NSF, National Science Foundation; MPI-M, Max Planck Institute for Meteorology; NCC, Norwegian Climate Centre.

Birkmanis et al. (2020). In brief, the probability of shark occurrence (calculated as the number of sharks caught divided by the number of fishing boats occurring in the same grid-cell) was used as the response variable, with turbidity and SST values for either the climatological baseline or the future used as predictors. We included effort, defined as the number of boats recorded in each grid-cell from the same time period as the occurrence data (2000–2002), as a model weight to account for differing amounts of catch per unit effort (CPUE) within the entire EEZ. As in, we weighted our models by fishing effort to estimate the probability of finding a shark in each grid-cell within the Australian EEZ which minimized the effect of fisheries effort on the data (Birkmanis et al., 2020). To stabilize parameter estimation, we standardized both predictors to z-scores using the scale function in R statistical software (R Core Team, 2017) before inclusion in our models (James et al., 2015). We also included a quadratic term for SST using the poly function from the stats package (R Core Team, 2017) in R statistical software to account for likely preferential SST ranges. We then quantified the goodness-of-fit for each model using the percentage of deviance explained, and used the predict function from the *stats* package in R statistical software to predict shark habitat suitability for the baseline data and also for the end of the century using the future climate data. To calculate the amount of change in suitable habitat under each climate model and emission scenario, we subtracted the number of grid-cells with resulting suitable habitat ≥0.5 in the future climate scenarios from those obtained in the baseline scenario. Differences between baseline and future scenarios show the change in suitable habitat area predicted for each family under possible future conditions.

RESULTS

Anomalies in SST in the Australian EEZ varied according to the climate model and emission scenario used (**Figure 1** and **Table 1**). The mean SST anomaly for all climate models was 2.27°C (SD: 0–1.2) for RCP 4.5 and 3.78°C (SD: 0–1.21) for RCP 8.5. Our results show that the predicted mean SST anomaly ranged from minima of 0.93°C (for climate model GISS-E2-R, RCP 4.5) and 0.69°C (for climate model HADGEM2-AO, RCP 8.5), to mean maxima of 1.83°C (for climate model IPSL-CM5A-MR for both emission scenarios) at the end of the century (**Figure 1** and **Table 1**). The climate model MPI-ESM_LR resulted in the maximum SST anomaly projected by all climate models (3.76°C for RCP 4.5 and 5.71°C for RCP 8.5, respectively). Despite model-to-model variation in the magnitude of anomalies, all climate models predicted south-eastern Australia would experience the greatest SST increases by the end of the century (**Figure 1**).

Both the baseline and future habitat suitability models explained slightly higher deviance for requiem than mackerel sharks but all values were around 30% (**Supplementary Table S1**). The baseline models explained 31.13 and 27.33% for requiem and mackerel sharks, respectively. The future models explained 29.91 and 31.76% for RCP 4.5 and RCP 8.5, respectively for requiem, and 26.47 and 26.22% for RCP 4.5 and RCP 8.5, respectively for mackerel sharks. The resulting predicted habitat suitability maps are presented as the mean across all climate models for requiem (**Figure 2**) and mackerel sharks (**Figure 3**), with the predicted change per climate model presented in **Figures 4, 5**. Predicted habitat suitability was highly dependent on the climate model used, with similar baseline values for

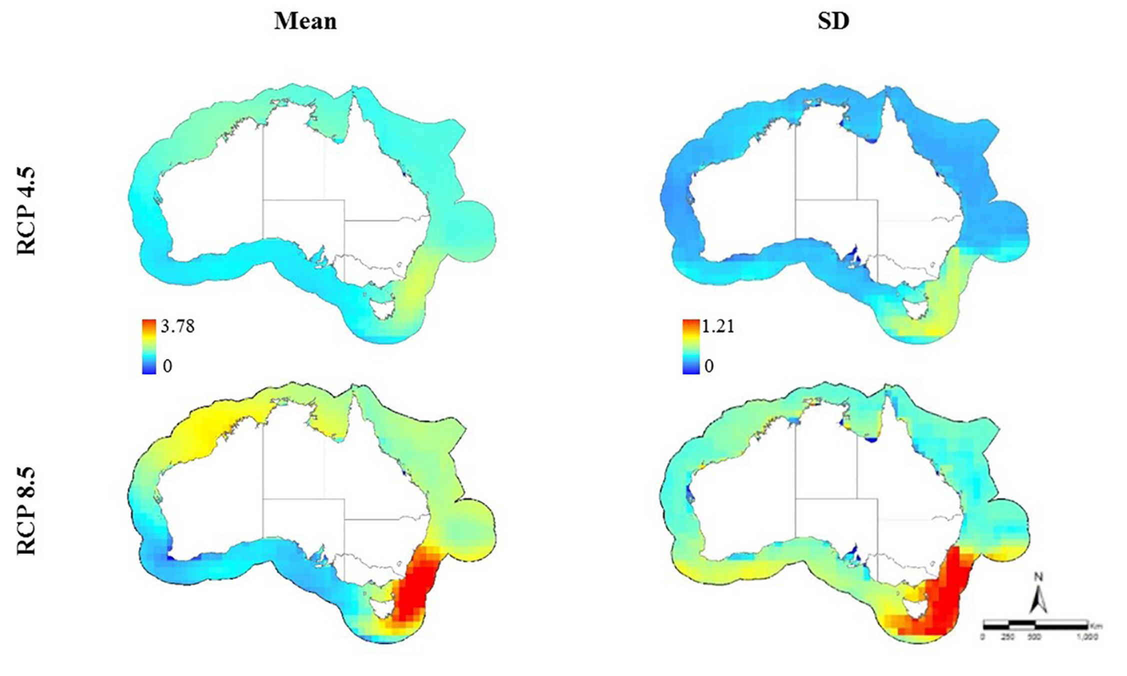

FIGURE 1 | Anomalies in sea surface temperatures throughout the Australian EEZ for the end of the twenty-first century (2050–2099) relative to the baseline period (1956–2005) under two emission scenarios (RCP 4.5 mean anomaly: 0–2.27, SD: 0–1.2; RCP 8.5 mean anomaly: 0–3.78, SD: 0–1.21).

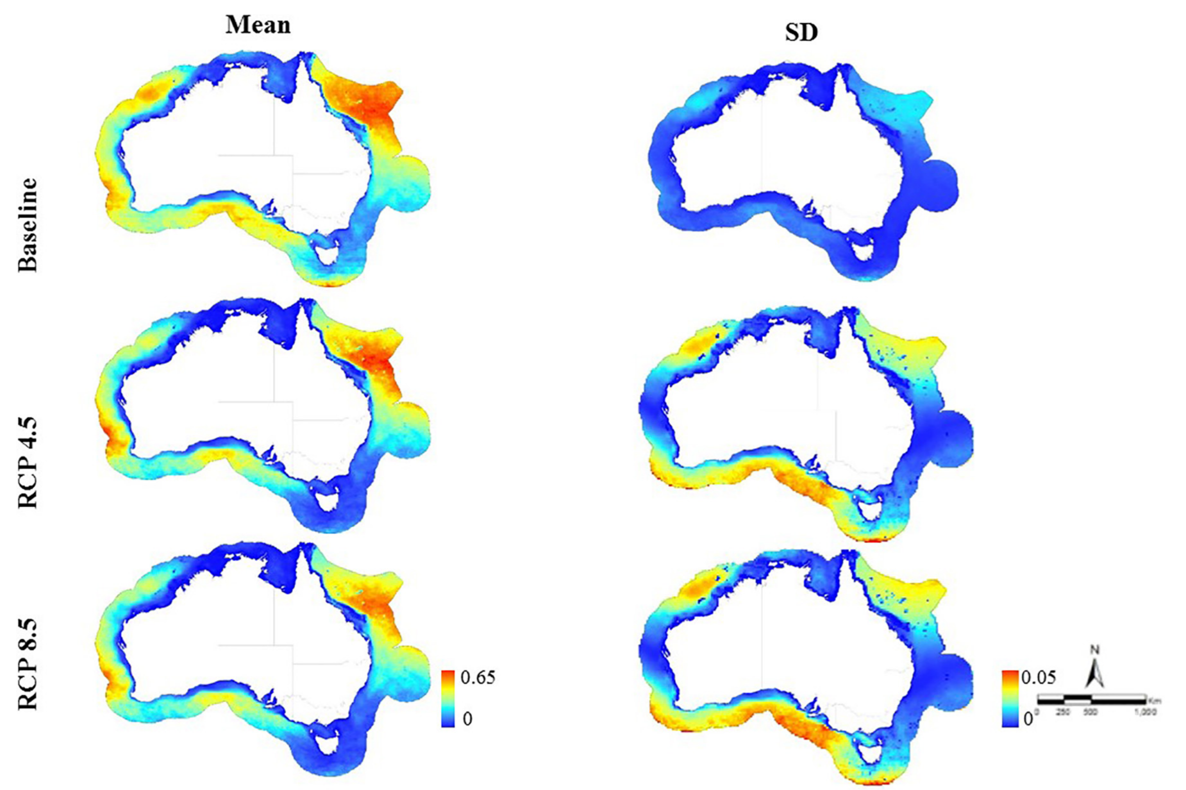

FIGURE 2 | Predicted habitat suitability for requiem sharks across the Australian EEZ for baseline time period (1956–2005; mean habitat suitability: 0–0.65, SD: 0–0.02) and at the end of the twenty-first century (2050–2099) under two emission scenarios (RCP 4.5 mean habitat suitability: 0–0.62, SD: 0–0.04; RCP 8.5 mean habitat suitability: 0–0.6, SD: 0–0.05).

requiem and mackerel sharks (0.65 and 0.63, respectively). For both requiem and mackerel sharks, the maximum habitat suitability (∼0.8) was predicted by climate model NORESM1-ME under both emission scenarios (**Figure 4**). Regions where habitat was predicted to be suitable (i.e., ≥0.5) at the end of the century varied by family, with southern Australia suitable for mackerel sharks, and north-eastern Australia for requiem sharks (**Figures 2**, **3**).

Based on 48 climate simulations, our results suggest a shift in suitable habitat for both requiem and mackerel sharks within the Australian EEZ in the last half of the twenty-first century (2050–2099). The severity and direction of this shift varied, with suitable habitat for requiem sharks predicted to decrease under most climate models, while habitat suitability for mackerel sharks varied to a greater degree depending on the climate model and emission scenario. On average, predicted suitable habitat for requiem sharks under RCP 4.5 extended south on the north-eastern (∼600 km) and south-western coast (∼200 km), but decreased in the north-west (∼400 km). For RCP 8.5, suitable habitat was projected to extend south on the north-eastern coast (∼650 km) and decrease across the north-west (∼500 km) with similar increases on the south-western coast (**Figure 2**). For mackerel sharks, the average of all climate models predicted an increase in suitable habitat across on the southern coast (∼900 km) and off the southern extent of the EEZ south of Tasmania (∼400 km) for RCP 4.5, with increases also projected to occur under RCP 8.5 (∼700 km across and ∼200 km south along the southern coast and ∼150 km south off the southern extent of the EEZ south of Tasmania) (**Figures 3**, **4**).

DISCUSSION

Significant shifts in the distributions of marine organisms are being observed in the global ocean due to anthropogenic climate change (Poloczanska et al., 2013). Our results highlight that shifts in the location of suitable habitat for requiem and mackerel sharks by the end of the century are to be expected, with a decrease in predicted suitable habitat for requiem sharks off the south-western coast under both emission scenarios. This agrees with predicted habitat shifts for silky, blue (both requiem family; Cheung et al., 2015; Lezama-Ochoa et al., 2016), and mako sharks (mackerel family; Hazen et al., 2013) in other areas. The waters of south-western and south-eastern Australia are warming at an increased rate, almost three and four times higher than the global average, respectively (Hartmann et al., 2013; Robinson et al., 2015a) as indicated in **Figure 1**. Our models predict that this area will become unsuitable for both requiem and mackerel sharks, likely due to the water temperatures at the end of the

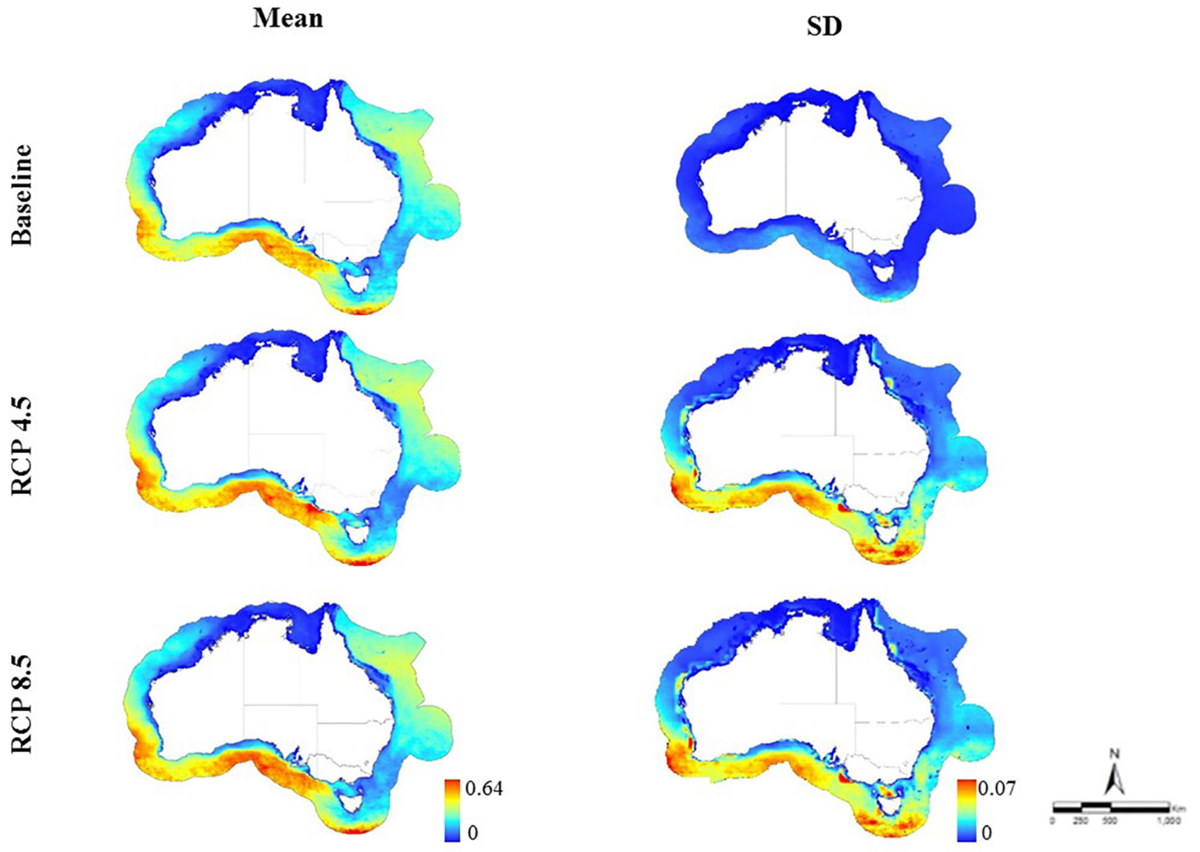

FIGURE 3 | Predicted habitat suitability for mackerel sharks in the Australian EEZ for baseline time period (1956–2005; mean habitat suitability: 0–0.63, SD: 0–0.02) and at the end of the twenty-first century (2050–2099) under two emission scenarios (RCP 4.5 mean habitat suitability: 0–0.64, SD: 0–0.05; RCP 8.5 mean: 0–0.62, SD: 0–0.07).

century exceeding the thermal tolerance of these pelagic sharks. In our analysis, and those of Robinson et al. (2015b) and Hobday (2010), southward shifts in suitable habitat for blue and mako sharks on the eastern coast of Australia are predicted. This is in line with ocean climate zones (areas with distinct climate, based on annual SST values) shifting southwards by 200 km along the north-eastern coast and approximately 100 km along the north-western coast in tropical Australian waters (Lough, 2008). In the north Pacific Ocean suitable habitat loss was predicted for both blue and mako sharks by the end of the century (Hazen et al., 2013). Such differences in predictions may be due to currents and northern latitude prey species being able to migrate poleward along the coastline (Perry et al., 2005). Due to the east-west orientation of the temperate Australian coastline and limited continental shelf area to the south of the continent (Urban, 2015), there are few opportunities for continental shelf marine organisms, including fish that are shark prey species, to move to higher latitudes and avoid increased water temperatures. Even with suitable habitat available for pelagic sharks within Australian waters these predators will follow prey species, such as tuna (Hobday and Poloczanska, 2010), which are expected to decline in the tropics and shift poleward in response to a warming ocean (Erauskin-Extramiana et al., 2019).

Although relatively little is known about how elevated temperatures will affect sharks (Pistevos et al., 2015), pelagic sharks are vulnerable to climate change impacts (Jones and Cheung, 2018) and life history strategies may play a part in determining ultimate patterns of species distribution. For relatively sedentary, benthic shark species, exposure to projected end-of-century temperatures has been shown to result in both positive and negative impacts. Port Jackson sharks (*Heterodontus portusjacksoni*) exposed to elevated temperatures exhibited an increase in mortality, altered behavior, increased learning performance and feeding, but reduced growth and embryonic development time (Pistevos et al., 2015; Vila et al., 2018, 2019). Conversely, brownbanded bamboo sharks (*Chiloscyllium punctatum*) showed decreased survival alongside significantly increased embryonic growth and ventilation rates (Rosa et al., 2014), while juvenile epaulet sharks (*Hemiscyllium ocellatum*) showed significantly decreased growth rates and 100% mortality (Gervais et al., 2018). It is likely that the physiological impacts of increasing ocean temperature will be greater for more active pelagic sharks than for benthic species (Rosa et al., 2014), given their reliance on ram ventilation and continuous movement (Lawson et al., 2019). Sharks already at their provisioning limit may be faced with starvation if temperature-driven

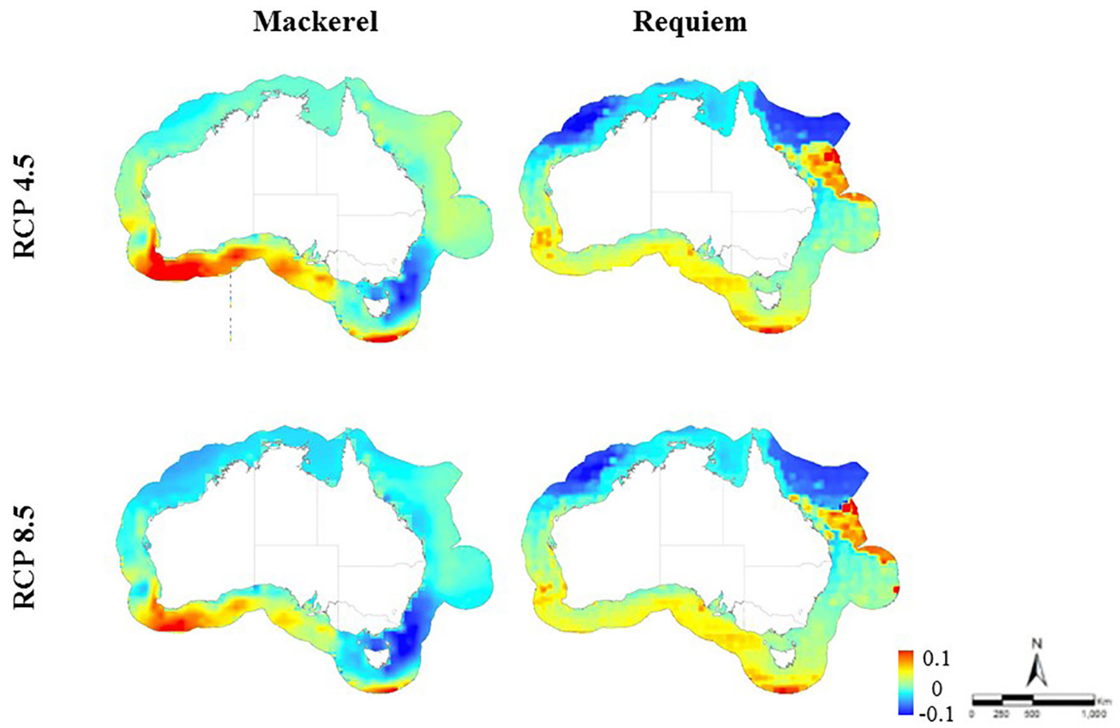

FIGURE 4 | Change in predicted habitat suitability for requiem and mackerel sharks in the Australian EEZ between the baseline time period (1956–2005) and at the end of the twenty-first century (2050–2099) under two emission scenarios (RCP 4.5 and 8.5).

increases in metabolic rates are not met with higher food intake (Pistevos et al., 2015), and this risk will be heightened should environmental perturbations concurrently influence prey availability and abundance. However, the thermal tolerance of requiem and mackerel sharks (Francis and Stevens, 2002; Last and Stevens, 2009; Corrigan et al., 2018; Hueter et al., 2018; Young and Carlson, 2020) may enable them to cope with changing temperatures.

Even though we predicted an overall increase in the amount of suitable habitat for mackerel sharks at the end of the 21st century, temperature acclimatization comes with an energetic cost that impacts other functions such as reproduction, growth, foraging and swimming. Changes in the marine environment may result in novel ecosystems requiring predators to alter foraging behaviors and adapt to new prey species (Nagelkerken and Munday, 2016; Rivest et al., 2019). Under such stresses, individuals become less competitive with decreases in reproduction and population density (Beaugrand and Kirby, 2018) and may exploit habitat heterogeneity by undertaking vertical migrations to suitable temperatures to maximize biological efficiency and minimize physiological adjustment costs (Chin et al., 2010; Beaugrand and Kirby, 2018). The endothermic ability to swim faster and farther (Watanabe et al., 2015) may allow mackerel sharks to migrate longer distances and forage over wider areas with greater access to prey and seasonal resources, although at higher energetic costs than ectothermic species. However, the ability of pelagic sharks to move and follow the shifting suitable habitat outside their current ranges, may potentially alter their interactions with fisheries. It is worth noting that latitudinal species shifts in response to warming can be misleading with some pelagic species migrating vertically not latitudinally (Perry et al., 2005; Beaugrand and Kirby, 2018) and this may be the case with some pelagic shark species. In Australian waters, pelagic sharks have been recorded regulating their depth to occupy regions of favorable temperatures, although this behavior could also be related to prey movements (Rogers et al., 2009; Stevens et al., 2010; Heard et al., 2017) as well as habitat suitability.

Our study predicts changes in habitat suitability for pelagic sharks in the Australian EEZ, but predictions at the end of the century are highly dependent on the climate model and emission scenario chosen to represent future conditions. This has been the case for similar studies on other species, for example, freshwater fish assemblages (Buisson et al., 2010) and mesopelagic lanternfish in the Southern Ocean (Freer et al., 2019) highlighting the benefit of using an ensemble approach to capture high climate uncertainty. Moreover, the SST anomalies across the Australian EEZ also vary according to the climate model and emission scenario used in the analysis. Our analysis was done at the family level due to the sample size available. Analysis at family level, whilst valuable for relatively homogenous species groups, inevitably results in loss of information at lower taxonomic levels. Further research is needed in more localized areas, including telemetry studies on single species, to add greater certainty to species distribution model predictions. There is

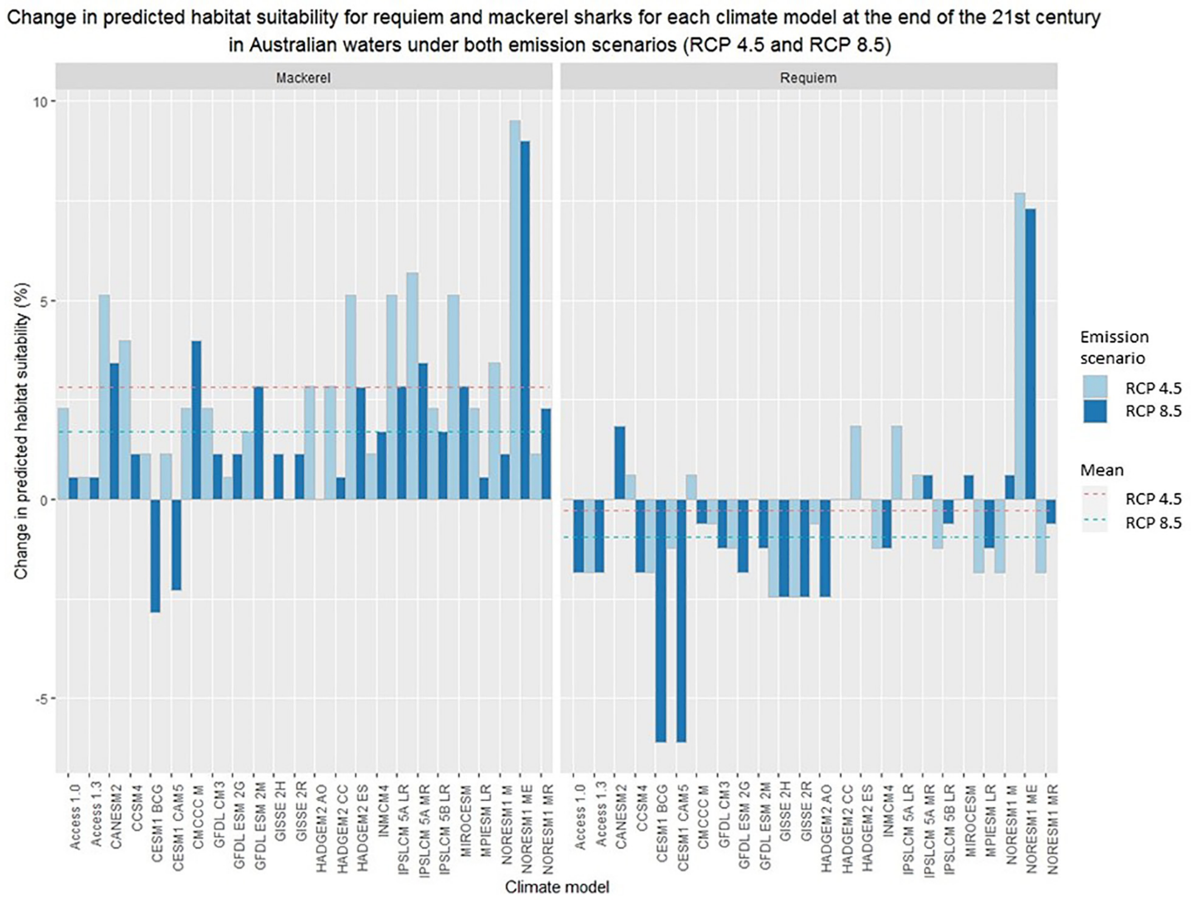

FIGURE 5 | Change in predicted habitat suitability averaged across all cells for requiem and mackerel sharks for each climate model for the end of the 21st century (2050–2099) in continental Australian waters under two emission scenarios (RCP 4.5 and 8.5). Refer to **Table 1** for model name abbreviations.

no consensus about how turbidity may vary under a changing climate, and in our models we assumed that turbidity levels would remain stable at the end of the century. However, a predicted increase in extreme rainfall influenced by changes in atmospheric circulation may increase coastal turbidity due to terrestrial-derived nutrients and pollutant input (Harley et al., 2006). Additionally, turbidity is correlated with chlorophyll-*a* in pelagic systems, and warmer water temperatures drive phytoplankton blooms, with elevated temperatures increasing both cyanobacterial and algal chlorophyll-*a* concentrations (Lürling et al., 2018; Trombetta et al., 2019). As aquatic nutrients have a greater impact on chlorophyll-*a* concentrations than temperature, and salinity and wind are also correlated with plankton blooms (Lürling et al., 2018; Trombetta et al., 2019), the impact this may have on pelagic systems in Australian waters is still unclear. Despite the uncertainties associated with predicting future conditions, studies such as ours using remotely sensed environmental information and occurrence data from fisheries over a large spatial scale, are important to understand how pelagic species with broad geographic ranges might fare in the future. Such studies are a first component of broader research in which the distribution of multiple species are predicted in a likely altered future marine environment.

DATA AVAILABILITY STATEMENT

All datasets generated for this study are included in the article/**Supplementary Material**.

AUTHOR CONTRIBUTIONS

CB, AS, and JP conceived the study. CB, JP, AS, and LS designed the methodology with assistance from JF. CB collated and analyzed the data and led the writing of the manuscript with significant contributions from AS. All authors contributed critically to the drafts and gave final approval for publication.

FUNDING

CB was supported by a Research Training Scheme scholarship and a Robson and Robertson Award from the Jock Clough

Marine Foundation. AS was supported by an ARC grant DE170100841 and research funds from Australian Institute of Marine Science (AIMS).

ACKNOWLEDGMENTS

We thank R. Summerson for assistance with accessing the fisheries data and acknowledge Australian Bureau of Agricultural and Resource Economics and Sciences (ABARES) as the source of the fisheries data, originally supplied by Australian Fisheries Management Authority (AFMA) and state fisheries management agencies.

SUPPLEMENTARY MATERIAL

The Supplementary Material for this article can be found online at: https://www.frontiersin.org/articles/10.3389/fmars.2020.00570/full#supplementary-material

REFERENCES

Barange, M., King, J., Valdes, L., and Turra, A. (2016). The evolving and increasing need for climate change research on the oceans. *ICES J. Mar. Sci.* 73, 1267–1271. doi: 10.1093/icesjms/fsw052

Barnosky, A. D., Matzke, N., Tomiya, S., Wogan, G. O. U., Swartz, B., Quental, T. B., et al. (2011). Has the Earth's sixth mass extinction already arrived? *Nature* 471, 51–57. doi: 10.1038/nature09678

Beaugrand, G., and Kirby, R. R. (2018). How do marine pelagic species respond to climate change? Theories and observations. *Ann. Rev. Mar. Sci.* 10, 169–197. doi: 10.1146/annurev-marine-121916-063304

Bernal, D., Carlson, J. K., Goldman, K. J., and Lowe, C. G. (2012). "Energetics, metabolism, and endothermy in sharks and rays," in *Biology of Sharks and Their Relatives*, eds J. C. Carrier, J. A. Musick, and M. R. Heithaus (Boca Raton, FL: CRC Press), 211–237.

Birkmanis, C. A., Partridge, J. C., Simmons, L. W., Heupel, M. R., and Sequeira, A. M. M. (2020). Shark conservation hindered by lack of habitat protection. *Glob. Ecol. Conserv.* 21:e00862. doi: 10.1016/j.gecco.2019.e00862

Bruno, J. F., Bates, A. E., Cacciapaglia, C., Pike, E. P., Amstrup, S. C., Van Hooidonk, R., et al. (2018). Climate change threatens the world's marine protected areas. *Nat. Clim. Chang.* 8, 499–503. doi: 10.1038/s41558-018-0149-2

Buisson, L., Grenouillet, G., Casajus, N., and Lek, S. (2010). Predicting the potential impacts of climate change on stream fish assemblages. *Am. Fish. Soc. Symp.* 73, 327–346.

Cheung, W. W. L., Brodeur, R. D., Okey, T. A., and Pauly, D. (2015). Projecting future changes in distributions of pelagic fish species of Northeast Pacific shelf seas. *Prog. Oceanogr.* 130, 19–31. doi: 10.1016/j.pocean.2014.09.003

Chin, A., Kyne, P. M., Walker, T. I., and McAuley, R. B. (2010). An integrated risk assessment for climate change: analysing the vulnerability of sharks and rays on Australia's Great Barrier Reef. *Glob. Chang. Biol.* 16, 1936–1953. doi: 10.1111/j.1365-2486.2009.02128.x

Cisneros-Montemayor, A. M., Barnes-Mauthe, M., Al-Abdulrazzak, D., Navarro-Holm, E., and Sumaila, U. R. (2013). Global economic value of shark ecotourism: Implications for conservation. *Oryx* 47, 381–388. doi: 10.1017/S0030605312001718

Corrigan, S., Lowther, A. D., Beheregaray, L. B., Bruce, B. D., Cliff, G., Duffy, C. A., et al. (2018). Population connectivity of the highly migratory shortfin mako (*Isurus oxyrinchus* Rafinesque 1810) and implications for management in the Southern Hemisphere. *Front. Ecol. Evol.* 6:187. doi: 10.3389/fevo.2018.00187

Cortés, E. (2000). Life history patterns and correlations in sharks. *Rev. Fish. Sci.* 8, 299–344. doi: 10.1080/10641260008951115

Doney, S. C., Ruckelshaus, M., Duffy, J. E., Barry, J. P., Chan, F., English, C. A., et al. (2012). Climate change impacts on marine ecosystems. *Ann. Rev. Mar. Sci.* 4, 11–37. doi: 10.1146/annurev-marine-041911-111611

Dulvy, N. K. N., Sadovy, Y., and Reynolds, J. D. (2003). Extinction vulnerability in marine populations. *Fish Fish.* 4, 25–64. doi: 10.1046/j.1467-2979.2003.00105.x

Dulvy, N. K. N., Simpfendorfer, C. A., Davidson, L. N. K., Fordham, S. V., Bräutigam, A., Sant, G., et al. (2017). Challenges and priorities in shark and ray conservation. *Curr. Biol.* 27, 565–572. doi: 10.1016/j.cub.2017.04.038

Earth Systems Research Laboratory (2014). *Climate Change Web Portal. NOAA's Ocean Clim. Chang. Web Portal.* Available online at: www.esrl.noaa.gov/psd/ipcc/ (accessed January 10, 2018).

ESRI (2017). *ArcGIS Desktop Release 10.5*. New York, NY: Environmental Systems Research Institute.

Erauskin-Extramiana, M., Arrizabalaga, H., Hobday, A. J., Cabré, A., Ibaibarriaga, L., Arregui, I., et al. (2019). Large-scale distribution of tuna species in a warming ocean. *Glob. Chang. Biol.* 19:gcb.14630. doi: 10.1111/gcb.14630

Francis, M. P., and Stevens, J. D. (2002). Reproduction, embryonic development, and growth of the porbeagle shark, *Lamna nasus*, in the southwest Pacific Ocean. *Fish. Bull.* 98, 1–120. doi: 10.1007/b136546

Freer, J. J., Partridge, J. C., Tarling, G. A., Collins, M. A., and Genner, M. J. (2017). Predicting ecological responses in a changing ocean: the effects of future climate uncertainty. *Mar. Biol.* 165:7. doi: 10.1007/s00227-017-3239-1

Freer, J. J., Tarling, G. A., Collins, M. A., Partridge, J. C., and Genner, M. J. (2019). Predicting future distributions of lanternfish, a significant ecological resource within the Southern Ocean. *Divers. Distrib.* 25, 1259–1272. doi: 10.1111/ddi.12934

Garcia, V. B., Lucifora, L. O., and Myers, R. A. (2008). The importance of habitat and life history to extinction risk in sharks, skates, rays and chimaeras. *Proc. R. Soc. B Biol. Sci.* 275, 83–89. doi: 10.1098/rspb.2007.1295

Garciá Molinos, J., Halpern, B. S., Schoeman, D. S., Brown, C. J., Kiessling, W., Moore, P. J., et al. (2016). Climate velocity and the future global redistribution of marine biodiversity. *Nat. Clim. Chang.* 6, 83–88. doi: 10.1038/nclimate2769

Gattuso, J. P., Magnan, A., Billé, R., Cheung, W. W. L., Howes, E. L., Joos, F., et al. (2015). Contrasting futures for ocean and society from different anthropogenic CO_2 emissions scenarios. *Science* 349:4722. doi: 10.1126/science.aac4722

GBIF.org (2017). *GBIF Occurrence Download. GBIF Occur. Download*. Available online at: https://doi.org/10.15468/dl.1ij1w6 (accessed November 15, 2017).

Gervais, C. R., Nay, T. J., Renshaw, G., Johansen, J. L., Steffensen, J. F., and Rummer, J. L. (2018). Too hot to handle? Using movement to alleviate effects of elevated temperatures in a benthic elasmobranch, *Hemiscyllium ocellatum*. *Mar. Biol.* 165, 1–12. doi: 10.1007/s00227-018-3427-7

Gilman, E., Clarke, S. C., Brothers, N., Alfaro-Shigueto, J., Mandelman, J., Mangel, J., et al. (2008). Shark interactions in pelagic longline fisheries. *Mar. Policy* 32, 1–18. doi: 10.1016/j.marpol.2007.05.001

Harley, C. D. G., Hughes, A. R., Hultgren, K. M., Miner, B. G., Sorte, C. J. B., Thornber, C. S., et al. (2006). The impacts of climate change in coastal marine systems. *Ecol. Lett.* 9, 228–241. doi: 10.1111/j.1461-0248.2005.00871.x

Hartmann, D., Klein, T. A., Rusticucci, M., Alexander, L., Brönnimann, S., Charabi, Y., et al. (2013). in *Climate Change 2013 the Physical Science Basis: Working Group I Contribution to the Fifth Assessment Report of the Intergovernmental Panel on Climate Change*, eds T. Stocker, D. Qin, G.-K. Plattner, M. Tignor, S. Allen, J. Boschung, et al. (Cambridge: Cambridge University Press), doi: 10.1017/CBO9781107415324.008

Hazen, E. L., Jorgensen, S., Rykaczewski, R. R., Bograd, S. J., Foley, D. G., Jonsen, I. D., et al. (2013). Predicted habitat shifts of Pacific top predators in a changing climate. *Nat. Clim. Chang.* 3, 234–238. doi: 10.1038/nclimate1686

Heard, M., Rogers, P. J., Bruce, B. D., Humphries, N. E., and Huveneers, C. (2017). Plasticity in the diel vertical movement of two pelagic predators (*Prionace glauca* and *Alopias vulpinus*) in the southeastern Indian Ocean. *Fish. Oceanogr.* 27, 199–211. doi: 10.1111/fog.12245

Heupel, M. R., Simpfendorfer, C. A., Espinoza, M., Smoothey, A. F., Tobin, A., and Peddemors, V. (2015). Conservation challenges of sharks with continental scale migrations. *Front. Mar. Sci.* 2:12. doi: 10.3389/fmars.2015.00012

Hobday, A. J. (2010). Ensemble analysis of the future distribution of large pelagic fishes off Australia. *Prog. Oceanogr.* 86, 291–301. doi: 10.1016/j.pocean.2010.04.023

Hobday, A. J., and Poloczanska, E. S. (2010). *Adapting Agriculture to Climate Change: Preparing Australian Agriculture, Forestry and Fisheries for the Future*, eds C. Stokes, and M. Howden (Collingwood, VIC: CSIRO Publishing).

Hoegh-Guldberg, O., and Bruno, J. F. (2010). The impact of climate change on the world's marine ecosystems. *Science* 328, 1523–1528. doi: 10.1126/science.1189930

Hueter, R. E., Tyminski, J. P., Pina-Amargós, F., Morris, J. J., Abierno, A. R., Valdés, J. A. A., et al. (2018). Movements of three female silky sharks (*Carcharhinus falciformis*) as tracked by satellite-linked tags off the Caribbean coast of Cuba. *Bull. Mar. Sci.* 94, 345–358. doi: 10.5343/bms.2017.1162

Huveneers, C., Meekan, M. G., Apps, K., Ferreira, L. C., Pannell, D., and Vianna, G. M. S. (2017). The economic value of shark-diving tourism in Australia. *Rev. Fish Biol. Fish.* 27, 665–680. doi: 10.1007/s11160-017-9486-x

IMOS (2016). *Ocean Acidification Historical Reconstruction–Temperature*. Available online at: https://portal.aodn.org.au/ (accessed October 15, 2018).

IPCC (2013). "2013: Technical Summary," in *Climate Change 2013: The Physical Science Basis. Contribution of Working Group I to the Fifth Assessment Report of the Intergovernmental Panel on Climate Change*, eds T. F. Stocker, Q. Dahe, G.-K. Plattner, L. V. Alexander, S. K. Allen, N. L. Bindoff, et al. (Cambridge: Cambridge University Press), 33–115. doi: 10.1017/ CBO9781107415324.005

IPCC (2015). *IPCC, 2014: Climate Change 2014: Synthesis Report*. Geneva: IPCC.

IUCN (2020). *The IUCN Red List of Threatened Species*. Available online at: www.iucnredlist.org (accessed January 6, 2020).

James, G., Witten, D., Hastie, T., and Tibshirani, R. (2015). *An Introduction to Statistical Learning With Applications in R*. Berlin: Springer, 618. doi: 10.1016/j.peva.2007.06.006

Jones, M. C., and Cheung, W. W. L. (2018). Using fuzzy logic to determine the vulnerability of marine species to climate change. *Glob. Chang. Biol.* 24, e719–e731. doi: 10.1111/gcb.13869

Last, P. R., and Stevens, J. D. (2009). *Sharks and Rays of Australia*, 2nd Edn. Collingwood, VIC: CSIRO Publishing.

Last, P. R., White, W. T., Gledhill, D. C., Hobday, A. J., Brown, R., Edgar, G. J., et al. (2011). Long-term shifts in abundance and distribution of a temperate fish fauna: a response to climate change and fishing practices. *Glob. Ecol. Biogeogr.* 20, 58–72. doi: 10.1111/j.1466-8238.2010.00575.x

Lawson, C. L., Halsey, L. G., Hays, G. C., Dudgeon, C. L., Payne, N. L., Bennett, M. B., et al. (2019). Powering ocean giants: The energetics of shark and ray megafauna. *Trends Ecol. Evol.* 19, 1–13. doi: 10.1016/j.tree.2019.07.001

Lezama-Ochoa, N., Murua, H., Chust, G., Van Loon, E., Ruiz, J., Hall, M., et al. (2016). Present and future potential habitat distribution of *Carcharhinus falciformis* and *Canthidermis maculata* by-catch species in the tropical tuna purse-seine fishery under climate change. *Front. Mar. Sci.* 3:34. doi: 10.3389/fmars.2016.00034

Lough, J. M. (2008). Shifting climate zones for Australia's tropical marine ecosystems. *Geophys. Res. Lett.* 35, 1–5. doi: 10.1029/2008GL034634

Lürling, M., Mello, M. M., van Oosterhout, F., Domis, L., de, S., and Marinho, M. M. (2018). Response of natural cyanobacteria and algae assemblages to a nutrient pulse and elevated temperature. *Front. Microbiol.* 9:1851. doi: 10.3389/fmicb.2018.01851

Moss, R. H., Edmonds, J. A., Hibbard, K. A., Manning, M. R., Rose, S. K., Van Vuuren, D. P., et al. (2010). The next generation of scenarios for climate change research and assessment. *Nature* 463, 747–756. doi: 10.1038/nature08823

Nagelkerken, I., and Munday, P. L. (2016). Animal behaviour shapes the ecological effects of ocean acidification and warming: Moving from individual to community-level responses. *Glob. Chang. Biol.* 22, 974–989. doi: 10.1111/gcb.13167

Oliver, E. C. J., Benthuysen, J. A., Bindoff, N. L., Hobday, A. J., Holbrook, N. J., Mundy, C. N., et al. (2017). The unprecedented 2015/16 Tasman Sea marine heatwave. *Nat. Commun.* 8, 1–12. doi: 10.1038/ncomms16101

Perry, A. L., Low, P. J., Ellis, J. R., and Reynolds, J. D. (2005). Climate change and distribution shifts in marine fishes. *Science* 308, 1912–1915. doi: 10.1126/science.1111322

Pinsky, M. L., Eikeset, A. M., McCauley, D. J., Payne, J. L., and Sunday, J. M. (2019). Greater vulnerability to warming of marine versus terrestrial ectotherms. *Nature* 569, 108–111. doi: 10.1038/s41586-019-1132-4

Pistevos, J. C. A., Nagelkerken, I., Rossi, T., Olmos, M., and Connell, S. D. (2015). Ocean acidification and global warming impair shark hunting behaviour and growth. *Sci. Rep.* 5:16293. doi: 10.1038/srep16293

Poloczanska, E. S., Brown, C. J., Sydeman, W. J., Kiessling, W., Schoeman, D. S., Moore, P. J., et al. (2013). Global imprint of climate change on marine life. *Nat. Clim. Chang.* 3, 919–925. doi: 10.1038/nclimate1958

Queiroz, N., Humphries, N. E., Couto, A., Vedor, M., da Costa, I., Sequeira, A. M. M., et al. (2019). Global spatial risk assessment of sharks under the footprint of fisheries. *Nature* 461–466. doi: 10.1038/s41586-019-1444-4

R Core Team (2017). *R: A Language and Environment for Statistical Computing*. Available at: https://www.r-project.org/ (accessed January 15, 2017).

Riahi, K., Rao, S., Krey, V., Cho, C., Chirkov, V., Fischer, G., et al. (2011). RCP 8.5–A scenario of comparatively high greenhouse gas emissions. *Clim. Change* 109, 33–57. doi: 10.1007/s10584-011-0149-y

Rivest, E. B., Jellison, B., Ng, G., Satterthwaite, E. V., Bradley, H. L., Williams, S. L., et al. (2019). Mechanisms involving sensory pathway steps inform impacts of global climate change on ecological processes. *Front. Mar. Sci.* 6:346. doi: 10.3389/fmars.2019.00346

Roberts, J. J., Best, B. D., Dunn, D. C., Treml, E. A., and Halpin, P. N. (2010). Marine geospatial ecology tools: an integrated framework for ecological geoprocessing with ArcGIS. Python, R, MATLAB, and C++. Environ. *Model. Softw.* 25, 1197–1207. doi: 10.1016/j.envsoft.2010.03.029

Robinson, L. M., Gledhill, D. C., Moltschaniwskyj, N. A., Hobday, A. J., Frusher, S., Barrett, N., et al. (2015a). Rapid assessment of an ocean warming hotspot reveals "high" confidence in potential species' range extensions. *Glob. Environ. Chang.* 31, 28–37. doi: 10.1016/j.gloenvcha.2014.12.003

Robinson, L. M., Hobday, A. J., Possingham, H. P., and Richardson, A. J. (2015b). Trailing edges projected to move faster than leading edges for large pelagic fish habitats under climate change. *Deep. Res. Part II Top. Stud. Oceanogr.* 113, 225–234. doi: 10.1016/j.dsr2.2014.04.007

Roff, G., Doropoulos, C., Rogers, A., Bozec, Y.-M., Krueck, N. C., Aurellado, E., et al. (2016). The ecological role of sharks on coral reefs. *Trends Ecol. Evol.* 31, 395–407. doi: 10.1016/j.tree.2016.02.014

Rogers, P. J., Huveneers, C., Page, B., and Goldsworthy, S. (2009). *Movement Patterns of Pelagic Sharks in the Southern and Indian Oceans: Determining Critical Habitats and Migration Paths. : SARDI Publication Number F2009/000167-1*. Adelaide, SA: South Australian Research and Development Institute.

Rogers, P. J., Huveneers, C., Page, B., Goldsworthy, S. D., Coyne, M., Lowther, A. D., et al. (2015). Living on the continental shelf edge: habitat use of juvenile shortfin makos *Isurus oxyrinchus* in the Great Australian Bight, southern Australia. *Fish. Oceanogr.* 24, 205–218. doi: 10.1111/fog.12103

Rosa, R., Baptista, M., Lopes, V., Pegado, M., Ricardo, P. J., Trubenbach, K., et al. (2014). Early-life exposure to climate change impairs tropical shark survival. *Proc. R. Soc. B* 281:20141738. doi: 10.1098/rspb.2014.1738

Rosa, R., Rummer, J. L., and Munday, P. L. (2017). Biological responses of sharks to ocean acidification. *Biol. Lett.* 13:20160796. doi: 10.1098/rsbl.2016.0796

Scott, J. D., Alexander, M. A., Murray, D. R., Swales, D., and Eischeid, J. (2016). The climate change web portal: A system to access and display climate and earth system model output from the CMIP5 archive. *Bull. Am. Meteorol. Soc.* 97, 523–530. doi: 10.1175/BAMS-D-15-00035.1

Simpfendorfer, C., Chin, A., Kyne, P., Rigby, C., Sherman, S., and White, W. (2019). *A Report Card for Australia's Sharks*. Townsville, QL: Centre for Sustainable Tropical Fisheries and Aquaculture, James Cook University.

Stevens, J. D., Bradford, R. W., and West, G. J. (2010). Satellite tagging of blue sharks (*Prionace glauca*) and other pelagic sharks off eastern Australia: depth behaviour, temperature experience and movements. *Mar. Biol.* 157, 575–591. doi: 10.1007/s00227-009-1343-6

Syndeman, W. J., Poloczanska, E., Reed, T. E., and Thompson, S. A. (2015). Climate change and marine vertebrates. *Science* 350, 772–777. doi: 10.1126/science.aac9874

Thomson, A. M., Calvin, K. V., Smith, S. J., Kyle, G. P., Volke, A., Patel, P., et al. (2011). RCP4.5: A pathway for stabilization of radiative forcing by 2100. *Clim. Change* 109, 77–94. doi: 10.1007/s10584-011-0151-4

Tittensor, D. P., Mora, C., Jetz, W., Lotze, H. K., Ricard, D., Berghe, E., et al. (2010). Global patterns and predictors of marine biodiversity across taxa. *Nature* 466, 1098–1101. doi: 10.1038/nature09329

Trisos, C. H., Merow, C., and Pigot, A. L. (2020). The timing and abruptness of potential ecological disruption from climate change. *Nature* 20, 1–39. doi: 10.1038/s41586-020-2189-9

Trombetta, T., Vidussi, F., Mas, S., Parin, D., Simier, M., and Mostajir, B. (2019). Water temperature drives phytoplankton blooms in coastal waters. *PLoS One* 14:214933. doi: 10.1371/journal.pone.0214933

Urban, M. C. (2015). Accelerating extinction risk from climate change. *Science* 348, 571–573. doi: 10.1126/science.aaa4984

Vila, P. C., Gervais, C., Reed, J., and Brown, C. (2018). Incubation under climate warming affects behavioral lateralisation in Port Jackson sharks. *Symmetry (Basel).* 10, 1–9. doi: 10.3390/sym10060184

Vila, P. C., Gervais, C., Reed, J., Michard, J., and Brown, C. (2019). Quantity discrimination in Port Jackson sharks incubated under elevated temperatures. *Behav. Ecol. Sociobiol.* 73:93. doi: 10.1007/s00265-019-2706-8

Vuuren, D. P., van, Edmonds, J., Kainuma, M., Riahi, K., Thomson, A., et al. (2011). The representative concentration pathways: an overview. *Clim. Chang.* 109, 5–31. doi: 10.1007/s10584-011-0148-z

Watanabe, Y. Y., Goldman, K. J., Caselle, J. E., Chapman, D. D., and Papastamatiou, Y. P. (2015). Comparative analyses of animal-tracking data reveal ecological significance of endothermy in fishes. *Proc. Natl. Acad. Sci. U.S.A.* 112, 6104–6109. doi: 10.1073/pnas.1500316112

Yokoi, H., Ijima, H., Ohshimo, S., and Yokawa, K. (2017). Impact of biology knowledge on the conservation and management of large pelagic sharks. *Sci. Rep.* 7:10619. doi: 10.1038/s41598-017-09427-3

Young, C. N., and Carlson, J. K. (2020). The biology and conservation status of the oceanic whitetip shark (*Carcharhinus longimanus*) and future directions for recovery. *Rev. Fish Biol. Fish.* 3, 293–312. doi: 10.1007/s11160-020-09601-3

Conflict of Interest: The authors declare that the research was conducted in the absence of any commercial or financial relationships that could be construed as a potential conflict of interest.

frontiers in Marine Science

ORIGINAL RESEARCH
published: 05 August 2020
doi: 10.3389/fmars.2020.00639

Potential Consequences of Climate and Management Scenarios for the Northeast Atlantic Mackerel Fishery

Robin Boyd[1]*, Robert Thorpe[2], Kieran Hyder[2,3], Shovonlal Roy[4], Nicola Walker[2] and Richard Sibly[5]

[1] Centre for Ecology and Hydrology, Wallingford, United Kingdom, [2] Centre for Environment, Fisheries and Aquaculture Science, Lowestoft, United Kingdom, [3] School of Environmental Sciences, University of East Anglia, Norfolk, United Kingdom, [4] Department of Geography and Environmental Science, University of Reading, Reading, United Kingdom, [5] School of Biological Sciences, University of Reading, Reading, United Kingdom

Climate change and fishing represent two of the most important stressors facing fish stocks. Forecasting the consequences of fishing scenarios has long been a central part of fisheries management. More recently, the effects of changing climate have been simulated alongside the effects of fishing to project their combined consequences for fish stocks. Here, we use an ecological individual-based model (IBM) to make predictions about how the Northeast Atlantic mackerel (NEAM) stock may respond to various fishing and climate scenarios out to 2050. Inputs to the IBM include Sea Surface Temperature (SST), chlorophyll concentration (as a proxy for prey availability) and rates of fishing mortality F at age. The climate scenarios comprise projections of SST and chlorophyll from an earth system model GFDL-ESM-2M under assumptions of high (RCP 2.6) and low (RCP 8.5) climate change mitigation action. Management scenarios comprise different levels of F, ranging from no fishing to rate F_{lim} which represents an undesirable situation for management. In addition to these simple management scenarios, we also implement a hypothetical area closure in the North Sea, with different assumptions about how much fishing mortality is relocated elsewhere when it is closed. Our results suggest that, over the range of scenarios considered, fishing mortality has a larger effect than climate out to 2050. This result is evident in terms of stock size and spatial distribution in the summer months. We then show that the effects of area closures are highly sensitive to assumptions about how fishing mortality is relocated elsewhere after area closures. Going forward it would be useful to incorporate: (1) fishing fleet dynamics so that the behavioral response of fishers to area closures, and to the stock's spatial distribution, can be better accounted for; and (2) additional climate-related stressors such as ocean acidification, deoxygenation and changes in prey composition.

Keywords: Atlantic mackerel, climate change, fisheries management, earth system models, individual-based model, approximate Bayesian computation

OPEN ACCESS

Edited by:
Rebecca G. Asch,
East Carolina University, United States

Reviewed by:
Brian R. MacKenzie,
Technical University of Denmark, Denmark
Ryan Heneghan,
The University of Queensland, Australia

****Correspondence:***
Robin Boyd
Robboy@ceh.ac.uk

Specialty section:
This article was submitted to Global Change and the Future Ocean, a section of the journal Frontiers in Marine Science

Received: *04 November 2019*
Accepted: *13 July 2020*
Published: *05 August 2020*

Citation:
Boyd R, Thorpe R, Hyder K, Roy S, Walker N and Sibly R (2020) Potential Consequences of Climate and Management Scenarios for the Northeast Atlantic Mackerel Fishery. Front. Mar. Sci. 7:639. doi: 10.3389/fmars.2020.00639

INTRODUCTION

Mackerel (*S. scombrus*, NEAM) is among the most widely-distributed and economically valuable fish stocks in the Northeast Atlantic (Trenkel et al., 2014; Jansen et al., 2016). An increase in stock size over recent years has supported large catches, which reached a peak in 2014 at around 1.4 million tons (ICES, 2019c). As a result, the NEAM fishery is now a major contributor to the economies of several coastal states in the Northeast Atlantic (Jansen et al., 2016). Although current stock size is high, it is estimated that recent levels of exploitation will lead to sub-optimal yield in the long-term due to overfishing (ICES, 2019c). This in part because, despite agreeing on a management strategy in 2015, the European Union, Norway and the Faroe Islands have since all declared quotas above those advised by the International Council for the Exploration of the Seas (ICES) (ICES, 2019a). Management of NEAM is further complicated by the fact that the spatial distribution of the stock in the summer months has recently expanded (Berge et al., 2015; Ólafsdóttir et al., 2018). It is now found in substantial numbers in the jurisdictions of Iceland and Greenland which previously had no share of the catch (Kooij et al., 2015; Olafsdottir et al., 2016). Both countries have since set unilateral quotas without international agreement (ICES, 2019a). Given the commercial value of the NEAM stock it is crucial that the fishery is managed appropriately in order to preserve the economic benefits it currently provides.

Management of NEAM depends on scientific advice regarding acceptable levels of exploitation. This advice is provided by ICES, who assess the state of the stock using an age-structured state-space assessment model (SAM) (Nielsen and Berg, 2014). The first step in the stock assessment is to estimate current levels of spawning stock biomass (SSB) and the rate of fishing mortality (F). These outputs are then used as starting points for forecasts of future stock status under various catch scenarios, which inform the advisory total allowable catch (TAC) for the following year [see ICES (2019a) and earlier advice reports]. SAM is used in stock assessment because it is able to assimilate the large amounts of data required (e.g., catch, tag-recapture, survey indices), and can tractably estimate many parameters. However, like most models used for stock assessment (MacKenzie et al., 2008; Goethel et al., 2011; Kuparinen et al., 2012), SAM does not incorporate the spatial structure of a stock or any environmental influence on its population dynamics. For this reason, it is limited in its ability to make predictions about: (1) longer-term fluctuations in the stock which may be affected by changing climate; and (2) the effects of spatial management measures which depend on a stock's distribution.

Spatial management in fisheries is becoming increasingly prevalent (Halpern et al., 2012), often in the form of seasonal or permanent area closures in which certain stocks may not be targeted (Hall, 2001; STECF, 2007). With respect to the NEAM fishery, sectors of the North Sea are subject to closures for different portions of the year. Mackerel fishing is not permitted in the southern and central regions of the North Sea at any time (ICES, 2019c). This measure was implemented to protect the North Sea spawning component of the NEAM stock, which has not recovered since being heavily depleted in the 1970s (Jansen, 2014). The Northern region of the North Sea is subject to a seasonal closure from February 15th to July 31st each year. The reason that mackerel fishing is permitted in the Northern North Sea outside of this period (August 1st to February 14th) is that the much larger western spawning component of the stock migrates into the area in large numbers during this time. ICES recommends that existing area closures remain in place to protect the North Sea spawning component (ICES, 2019c), but understanding the effects of closures is difficult. One approach that has been used to study the effects of spatial fishery management options is to implement them in spatially explicit models and test how the populations respond. For example, spatially explicit individual-based models (IBMs) have been used predict how fish communities may respond to the implementation of marine protected areas (Yemane et al., 2009; Brochier et al., 2013).

In addition to exploitation, climate is likely to affect the NEAM stock in the future. Projections using Earth System Models (ESMs) indicate that there will be changes in temperature and primary productivity in the North Atlantic over the twenty-first century (Gregg et al., 2003; Henson et al., 2013; Alexander et al., 2018). As mackerel population dynamics, such as spatial distribution and recruitment, are highly sensitive to these drivers (Runge et al., 1999; Borja et al., 2002; Overholtz et al., 2011; Plourde et al., 2014; Pacariz et al., 2016; Nikolioudakis et al., 2018; Ólafsdóttir et al., 2018), it is important to include their effects when making predictions about the future state of the stock. Recent years have seen the development of a first wave of marine ecological forecast products (Payne et al., 2017)[1]. These products exploit empirical relationships between biological response variables (e.g., fish spatial distribution and recruitment) and environmental covariates which can typically be predicted with greater skill (Payne et al., 2017). Some ecological forecasts have sufficient skill to be useful in a decision-making context, but only on a seasonal basis (e.g., <6 months out) (Kaplan et al., 2016; Payne et al., 2017). It is also possible to make longer-term ecological projections, albeit with considerably more uncertainty. For example, Bruge et al. (2016) projected possible changes in the spawning distribution of NEAM out to 2100 under various climate scenarios. Long-term projections of fish stock dynamics are likely of little direct use to decision makers (i.e., tactical management), but can provide important, broad-scale insight into possible directions of change under varying climate scenarios.

Long-term (out to 2100) projections of future temperature and primary productivity can be obtained from a number of ESMs participating in the Coupled Model Intercomparsion Project (CMIP) (Taylor et al., 2012). These projections are typically available under a range of standardized greenhouse gas emissions scenarios, such as the Representative Concentration Pathways (RCP), which contain different assumptions about economic activity, population growth and other socio-economic factors (van Vuuren et al., 2011). Recently, a fisheries and marine ecosystem model intercomparison project (FISH-MIP) was established (Tittensor et al., 2018). In FISH-MIP physical

---

[1] www.fishforecasts.dtu.dk/forecasts

and biogeochemical fields from CMIP projections under various RCP scenarios are used as input to marine ecosystem models. In this way predictions can be made about how the marine ecosystem may respond to climate change. Thus far FISH-MIP simulations have made simple assumptions about future levels of fishing activity (i.e., fished or unfished) (Lotze et al., 2018), likely because of the difficulty in specifying harvesting regimes for numerous stocks at the global scale. By focusing on a target stock (or subset of stocks), however, it should be possible to predict the effects of more detailed management scenarios alongside the effects of climate (e.g., Reum et al., 2020).

Here, we use an existing spatially explicit IBM (Boyd et al., 2018, 2020) to simulate NEAM population dynamics and yield from the fishery out to 2050 under a range of management and climate scenarios. It should be noted from the outset that our IBM is designed to represent the biological component of the system, as opposed to the human dimension, and as such the spatial distribution of fishing effort is represented in a simple manner. Inputs to the IBM include Sea Surface Temperature (SST), chlorophyll concentration (used as a proxy for prey availability), and rates of fishing mortality (F). Predictions of future SST and chlorophyll were obtained from the ESM GFDL-ESM-2M under the highest and lowest climate mitigation action (or RCP) scenarios. Future management scenarios comprise one of three annual rates of F, ranging from no fishing to rate F_{lim}. By combining the different climate and management scenarios, we generate six multi-stressor scenarios that span a range of possible future conditions. In addition to these scenarios, we also implement simple spatial management measures. These measures comprise a hypothetical area closure in the Northern North Sea, with different assumptions about how much fishing mortality is relocated elsewhere when it is closed. We quantify changes to the stock under each scenario in terms of three outputs: (1) SSB, which is a key output in the stock assessment because it represents the stock's reproductive potential; (2) the summer distribution, which is relevant to the division of the NEAM catch allocation among national fisheries; and (3) yield from the fishery. The results are discussed in the context of the utility of long-term projections for scientific and management purposes.

MATERIALS AND METHODS

IBM Description

In this section we give a brief overview of the IBM (Boyd et al., 2018, 2020) and details of its key features. For a full technical specification see the "TRAnsparent and Comprehensive model Evaluation" (TRACE) document in **Supplementary Material**. In section "Materials and Methods" of the TRACE we provide a full model description in the standard Overview Design concepts and Details (ODD) format (Grimm et al., 2006). The IBM was built in the open-source software NetLogo (Wilensky, 1999), where it comes with an easy-to-use GUI, but can be run from the R statistical environment (R Core Team, 2019) using the RNetLogo package (Thiele, 2017). The R and NetLogo code can be found at https://github.com/robboyd/SEASIM-NEAM/tree/master.

Overview

The model environment consists of dynamic maps of SST and phytoplankton density, which we use to represent baseline food availability (**Figure 1**). The fish population represents the largest sub-unit of the NEAM stock, the western spawning component, which has comprised a reasonably stable proportion of the stock's total biomass through time (∼80%) (ICES, 2014a,b, 2017). It should be noted, however, that there is evidence of straying between the western and the much smaller North Sea spawning component of NEAM (Jansen and Gislason, 2013), which is not represented in the IBM. Fish are grouped into super-individuals (SIs), which comprise a *number of individuals* with identical variables (Scheffer et al., 1995). SIs are sometimes considered to represent schools of identical individuals in varying abundances (Shin and Cury, 2001), but the approach is mainly used for computational tractability. SIs move around the seascape according to their life cycles (e.g., to spawn, feed and overwinter, **Figure 1**). Each has an energy budget which determines how its characteristics (e.g., body size, life stage, energy reserves) change in response to local food availability and SST. Time- and age-varying fishing determines the rate of mortality from exploitation. A constant number of new SIs enter the model as juveniles each year, but the abundance that they represent on entry (recruitment) is given as a function of SSB and temperature on the spawning grounds. Abundance reduces as fishing and natural mortalities are applied throughout life. Population measures such as SSB and spatial distribution are obtained by summarizing the characteristics of all the individuals including their abundances.

State Variables and Scales

The model landscape comprises a two-dimensional grid of patches of sea surface (**Figure 1**). The spatial extent spans from 47–77°N, and from −45° to 20°E. Each patch represents 60 × 60 km (Lambert Azimuthal equal area projection) and is characterized by prey density, sea surface temperature (SST), mackerel density, photoperiod and horizontal current velocities. The mackerel population is represented by a constant 4000 SIs; as n_{cohort} new SIs enter the model as juveniles each year, an equal number reach terminal age ($>$ 15 years) and are removed from the model. While the number of SIs remains constant, the abundance that they represent differs; a SI's abundance is determined by the level of recruitment in the year that it entered the model, and all subsequent mortality. Each SI is characterized by age, gender, life stage (egg, yolk-sac larvae, larvae, juvenile or adult), length, mass (structural, lipid and gonad), abundance and location. The temporal extent of the historical period spans from January 1st 2005 to December 31st 2018, and is extended to December 31st 2050 for projections. The model proceeds in discrete five-day time-steps.

Sub-models

In the following we give details of the IBM's movement, bioenergetics and recruitment sub-models.

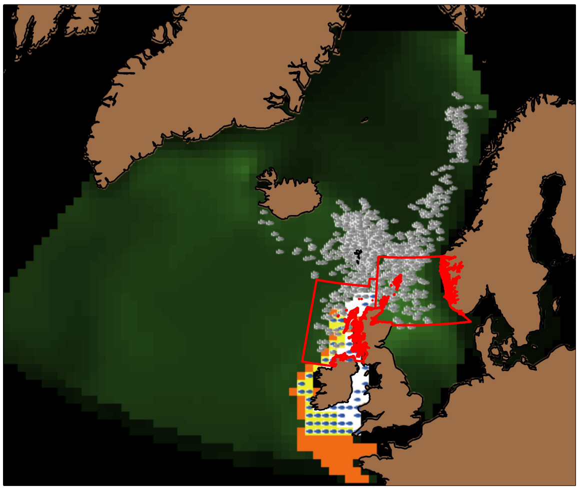

FIGURE 1 | Snapshot of the IBM interface on August 1st 2009. Gray SIs in the Nordic and North Seas are adults, and blue SIs to the west of the British Isles are juveniles. The color of the landscape indicates phytoplankton density: darkest green equals 0 g m^{-2} through light green which equals 3 g m^{-2}. Orange cells indicate potential spawning areas, white cells potential nursery areas, and yellow cells indicate areas that are both potential spawning *and* nursery areas. The nursery area is delimited by the 200 m isobath to the west of the British Isles, and the potential spawning area corresponds to the European shelf edge (−500 m < depth < −50 m). The red boxes (ICES divisions 6a and 4a) delimit the potential overwintering areas. The easternmost box (division 4a) is that which we close in our spatial management scenarios (see **Table 2**).

Movement

In broad terms, juveniles move randomly in nursery areas, and adults cycle between spawning, feeding and overwintering areas (see TRACE section 2 and **Figure 1**). For the purposes of this paper, we focus on the summer feeding period (July through September). We focus on this period because: (1) the summer distribution has recently expanded into the jurisdictions of Iceland and Greenland, which has complicated division of the catch allocation among states; and (2) we have recently validated an optimal-foraging model for this period (Boyd et al., 2020), outlined below.

In summer adults actively move in search of the most profitable patches on which to feed. Each patch is characterized by a profitability cue c_{dd} which is proportional to potential ingestion rate in that location. c_{dd} represents the bottom-up effect of phytoplankton density as a proxy for prey availability, a density-dependent effect of intraspecific competition, an effect of photoperiod (as NEAM are primarily visual feeders), and an effect of SST (Kelvins), in the form of a modified Beddington-DeAngelis (Beddington, 1975; DeAngelis et al., 1975) functional response:

$$c_{dd} = A\,(SST)\;\; p_{photo}\,\frac{X}{X + h + c\,D} \tag{1}$$

where X is phytoplankton density (g m^{-2}), h is a half saturation constant, p_{photo} is photoperiod (as a proportion of 24 h) at the SI's location, D is local mackerel density (g $patch^{-1}$), c determines the strength of the density dependence, and A(SST) is an Arrhenius function giving the effect of SST (see Eq. 2). h was estimated by fitting the IBM to data on NEAM SSB and weight-at-age using rejection approximate Bayesian computation (see section "IBM Calibration"). c was estimated using the same approach but in a previous application of the IBM (Boyd et al. submitted). A(SST) is given as:

$$A\,(SST) = e^{\frac{-E_a}{K}\left(\left(\frac{1}{SST}\right) - \left(\frac{1}{T_{ref}}\right)\right)} \tag{2}$$

where E_a is an activation energy, K is Boltzmann's constant and T_{ref} is an arbitrary reference temperature.

SIs move in search of the most profitable locations (Eq. 1) at which to feed following a gradient area search (GAS). The GAS algorithm is similar to that presented by Tu et al. (2012); Politikos et al. (2015), and Boyd et al. (2020). It should be noted that this model is a slight update to that presented in Boyd et al. (2020) as it now includes explicit effects of photoperiod and horizontal current velocities. See TRACE section 9 for a comparison of predicted and observed NEAM occurrence over summer. SIs can detect the profitability of the four neighboring patches in x and y dimensions. Positions are updated five times per time step (i.e., once per day) to ensure that SIs cannot overshoot the neighboring patch. Positions in x and y dimensions are updated in continuous space, as:

$$\begin{aligned} x_{t+1} &= x_t + (D_x + R_x + C_x) \\ y_{t+1} &= y_t + \left(D_y + R_y + C_y\right) \end{aligned} \tag{3}$$

where D_x and D_y denote directed movements toward the most profitable patches, R_x and R_y denote random movements, and C_x and C_y are displacements caused by zonal and meridional horizontal currents, respectively.

In the orientated component of Eq. (3) D_x and D_y, SIs compare the profitability at their current location with that of the day before. If it has become more profitable, they will continue to swim in the same direction as the directed component of their movement the day before. If a SI's current environment is less profitable than the day before, it follows a gradient search toward what is perceived to be the most profitable patch based on information in x and y dimensions, at realized velocity V_r, given by:

$$\begin{aligned} D_x &= V_r\;\frac{g_x}{\sqrt{g_x^2 + g_y^2}} \\[1em] D_y &= V_r\;\frac{g_y}{\sqrt{g_x^2 + g_y^2}} \end{aligned} \tag{4}$$

where g_x and g_y are the gradients of the profitability cues (Eq. 3) in x and y dimensions. V_r is given as minimum swimming velocity (V_{min}) plus random noise. V_{min} is as a function of body length L, as $V_{min} = a_v\,L^{b_v} A_r^{c_v}$, where a_v is a normalizing constant, b_v and c_v are scaling exponents, and A_r is the caudal fin aspect ratio (Sambilay, 1990). V_r is given by $V_r = V_{min} + (V_{min}\,\varepsilon)$, where ε is drawn randomly from a uniform distribution ranging from zero to one. The directed component of the GAS algorithm amounts to what is called a state-location orientation mechanism (basing new orientation on a comparison of the current and previous environment), and there is some indication that herring follow a similar strategy in the Norwegian sea (Fernö et al., 1998).

Following Politikos et al. (2015) we assume that movement is directed (D_x, D_y) for 12 h day^{-1}, and movement in the other 12 h follows the random component of Eq. (3), R_x, R_y, given as moving at velocity V_{min} in a random direction that is not southward. Random southward movement is not permitted because acoustic studies have shown that NEAM infrequently swim southwards over summer (Nøttestad et al., 2016). However, SIs may still move southward during the oriented component of the GAS algorithm (i.e., if feeding conditions are best on a more southerly patch), or due to currents. R_x and R_y introduce stochasticity into the GAS models and combine with the competition term in Eq. (1), cD, to prevent unrealistic overcrowding on optimal patches.

The effects of horizontal currents on SIs' locations, C_x, C_y, are given as zonal (u) and meridional (v) current velocities (km h^{-1}), respectively, multiplied by the time step (here 24 h as the GAS model operates five times per 5 day time-step).

In addition to its effect on the perceived profitability of a patch (Eqs. 1, 2), SST delimits the possible modeled NEAM distribution. NEAM avoid areas in which temperature is below 7°C (Ólafsdóttir et al., 2018). To reflect this, SIs are deterred from moving to patches on which SST is below this threshold. In the directed component of Eq. (3), SIs are repelled from patches with SST $< 7°C$ by setting profitability cues in those areas to 0. For the random component of Eq. (3), if a SI's orientation would direct it on to a patch with SST $< 7°C$, its heading is reversed. If currents displace individuals on to an intolerably cold patch (or land) then this movement is abandoned and the SI instead moves to the centroid of the nearest suitable patch.

Bioenergetics

Individuals obtain energy from food X in the form of either phytoplankton (a proxy for baseline food availability) or smaller mackerel located on the same patch (see TRACE section 2 for size-based criteria that a SI must meet to be classed as potential prey). Over summer adults do not overlap with sufficient small mackerel, so in Eq. (1) X refers only to phytoplankton density. Energy uptake is proportional to Eq. (1). A proportion of the energy ingested from food is assimilated and made available to the vital processes maintenance (metabolic rate), growth, reproduction and energy storage. The rates at which energy is allocated to these processes depend on temperature and body size. The effect of temperature is generally given by the Arrhenius function (Eq. 2). The partitioning of energy to vital processes depends on an individual's life stage and time of year. See Sibly et al. (2013) for an overview, and TRACE section 2 for full details. Note that, while adults allocate energy to reproduction, recruitment is modeled separately using a Ricker-style stock-recruitment model (see section "Recruitment").

Movement-bioenergetics coupling

The energy cost of searching for food is subsumed into an individual's active metabolic rate AMR. AMR is given as a function of SST, body mass M and swimming velocity V as:

$$AMR = a_{AMR}\ M^{b_{AMR}}\ V^{c_{AMR}}\ A(SST) \tag{5}$$

where a_{AMR} is a normalizing constant, b_{AMR} and c_{AMR} are scaling exponents, and V is given by $V = (V_r + V_{min})/2$, i.e., assuming that half of each day is spent at V_{min}, and half at V_r.

Recruitment

In this paper, recruitment is modeled differently than in previous applications of our IBM (Boyd et al., 2018, 2020). Here, we use a modified Ricker stock-recruitment function because it provides better fits to the latest recruitment estimates from the NEAM stock assessment. The Ricker model gives recruitment R as a function of SSB and average SST on the spawning grounds over the months March and April, as:

$$R = a_R\ SSB\ e^{-a_R\ SSB\ +\ b_R\ SST} \tag{6}$$

where a_R and b_R were estimated by fitting Eq. (6) (in log-linear regression form, $R^2 = 0.45$) to data from the stock assessment. See TRACE section 3 for details of the Ricker model fitting process, variable importance and model diagnostics.

On December 31st each year, n_{cohort} new SIs (recruits) enter the model as juveniles at a random location in the nursery area, with abundance equal to R/n_{cohort}. Recruits' body lengths set at the maximum length at the end of the first growth phase (20 cm, Villamor et al., 2004) minus ε 3 (cm), where ε is drawn randomly from a uniform distribution ranging from 0 to 1.

Emergent Properties

The movement and bioenergetics models describe the ways in which individuals' characteristics (e.g., body mass, energy reserves, location) respond to their local food availability and SST. By summarizing the characteristics of all the individuals, we can obtain population measures. For example, SSB can be obtained by summing the individual body masses of all adults, and spatial distribution by summarizing the locations of the SIs.

Initialization

The IBM is initialized on 1 January 1995 using estimates of numbers-at-age from the stock assessment. This population is then apportioned into 4000 super-individuals such that there is an equal number of SIs in each year class. Body lengths are calculated from age using the standard von Bertalanffy equation, and energy reserves are set at half maximum. From these all other state variables are calculated when the simulation begins. Adults and juveniles are distributed randomly in the overwintering and nursery areas, respectively (see **Figure 1**). After initialization we allow the model to spin up from 1995–2005, after which point we begin to record outputs for model calibration. See TRACE section 2 for full details of initialization.

Model Forcing

In this section we describe the data used to force the IBM during the historical period 1 January 2005–31 December 2018.

Environmental Inputs

Environmental inputs to the model include maps of surface chlorophyll concentration, SST, horizontal current velocities and photoperiod. Chlorophyll and SST are derived from the global ESM GFDL-ESM-2M (Dunne et al., 2013; Geophysical Fluid Dynamics Laboratory, 2017). GFDL-ESM-2M has been identified as a suitable candidate for forcing fisheries and marine ecosystem models because: (1) it contains a relatively highly resolved representation of ocean biochemistry and its predictions correlate well with net primary productivity data; and (2) because model drift is negligible (Lotze et al., 2018; Tittensor et al., 2018). Environmental inputs are updated monthly. A slight complication arises in that the historical period as defined for CMIP (phase 5 as used here) ends in December 2005, after which RCP scenario-driven estimates are produced from the ESMs. This does not match the historical period as defined in this study (everything up to 2019). For this reason, from 2006 we had multiple environmental trajectories (one from each RCP) from which to choose as input to our IBM. Inspection of the environmental inputs revealed negligible divergence between fields of chlorophyll and SST out to 2019 from RCPs 2.6 and 8.5 (RMSEs of 0.31°C and 0.024 mg m^{-2}, respectively; see TRACE section 3). For this reason we simply took the mean of the environmental inputs from RCPs 2.6 and 8.5 as forcing to the IBM from 2006–2019.

Near surface (average over 0 to -30 m) horizontal current velocities were taken from the 1/3° OSCAR dataset (ESR 2009). Currents influence the movements of adults over summer (Eq. 4), so we obtained data for the months May through September. Outside of this period current velocities have no effect in the IBM. It would not be appropriate to include the effects of near surface current velocities on individuals outside of the summer period, when mackerel may inhabit deeper waters (e.g., -50 to -220 m over winter) (Jansen et al., 2012). Over summer NEAM are found in the upper water layer (average of ~ -20 m) (Nøttestad et al., 2016). As data are not available for the selected months prior to 2012, we generated mean climatologies for each month over 2012–2018. As such we do not account for inter-annual variability in current velocities.

Data on photoperiod (as a proportion of 24 h) at all latitudes in the IBM grid was extracted for each month using the daylength() function in the R package geosphere (Hijmans, 2019). Values correspond to the 15th day of each month, and are updated at the start of each month. All environmental data required processing for use in the IBM (e.g., re-gridding), the details of which can be found in TRACE section 3.

Fishing Mortality

As our IBM does not explicitly represent fleet dynamics, fishing mortality F is applied to the stock in a simple manner. Annual rates of F at age each year were taken from the 2019 NEAM stock assessment [ICES (2019b), extracted from stockassessment.org]. We incorporate monthly variation in F by setting the fraction of annual F in each month proportional to the mean historical fraction of annual NEAM catch taken in each month (see **Table 1**). Unless stated otherwise (see section "Spatial Management Scenarios"), F is applied uniformly to all individuals within an age group regardless of their location.

TABLE 1 | Mean proportion of total annual catch taken in each month and whether or not division 4a is closed to fishing.

Month	Proportion of annual catch	4a status
Jan	0.22	Open
Feb	0.07	Open until 15th
Mar	0.14	Closed
Apr	0.12	Closed
May	0.004	Closed
Jun	0.02	Closed
Jul	0.08	Closed
Aug	0.08	Open
Sep	0.09	Open
Oct	0.11	Open
Nov	0.05	Open
Dec	0.02	Open

Mean values are calculated over the period 1998–2018.

Future Scenarios

From 1 January 2019–31 December 2050 the IBM simulates the NEAM population under various scenarios, each with different assumptions about future climate and fishing pressure.

Climate Scenarios

We include two environmental scenarios representing the low and high levels of climate change mitigation action. Both scenarios comprise projections of chlorophyll and SST from GFDL-ESM-2M, with forcing from RCPs 2.6 and 8.5, i.e., low and high greenhouse gas emissions, respectively (see van Vuuren et al. (2011) for details). Current velocities remain as described in section "Environmental Inputs" in the future period for lack of available projections. It is important to note that we do not account for other climate-related stressors (e.g., ocean acidification).

Fishing Scenarios

For future fishing pressure we take mean F-at-age over the historical period 2001–2018 (**Figure 2**) and adjust it using one of three multipliers. The multipliers are used to set mean F over the most important age groups to the fishery (for NEAM 4–8 years) at one of three rates: F = 0; F_{MSY} (0.23 $year^{-1}$), i.e., the level of harvesting that is likely to result in maximum sustainable yield in the long-term; and F_{lim} (0.46 $year^{-1}$), i.e., high mortality used as an upper reference point (ICES, 2012, 2019c). F_{lim} is slightly larger than the highest F on record (ICES, 2019c). Monthly variation in F is implemented as in the historical period.

Spatial Management Scenarios

In addition to changes in annual F, we also simulate the consequences of two simple spatial management scenarios. Currently, no mackerel fishing is permitted the Northern North Sea (ICES division 4a, **Figure 1**) over the period 15 February to 31 July (ICES, 2019c). We simulate the possible consequences of a hypothetical measure in which this seasonal closure is extended to span the whole year. To do this we split fishing mortality into that which is applied inside 4a, and that which is applied outside.

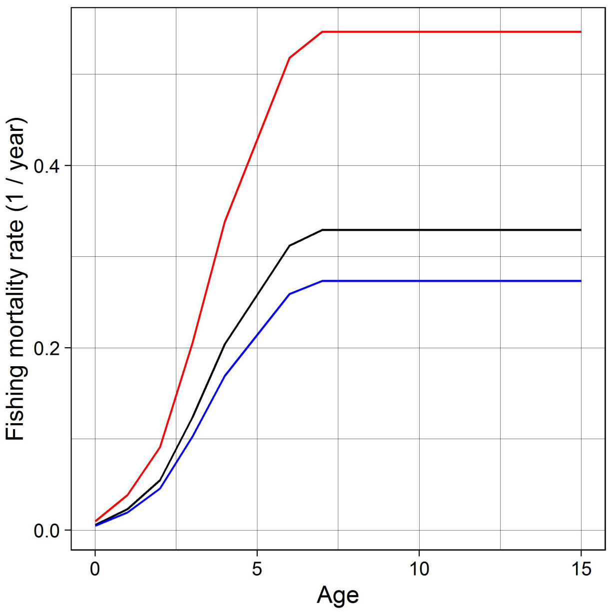

FIGURE 2 | Mean F at age over 2001–2018 **(black line)**, from which F_{MSY} **(blue line)** is calculated with a multiplier of 0.83, and F_{lim} **(red line)** with a multiplier of 1.66.

We then make assumptions about the amount of fishing mortality that will be redistributed from inside to outside of division 4a if it is closed. The first assumption is that none of the fishing mortality that would have taken place in division 4a is relocated, i.e., fishing mortality at age t F_t is set to zero inside division 4a when it is closed, but remains unchanged elsewhere. Under this assumption total F is reduced. The second assumption is that all of the fishing mortality that would have been inflicted in division 4a will be uniformly redistributed elsewhere. Under the second assumption F_t is raised outside of 4a to give redistributed fishing mortality at age t, F'_t, as:

$$F'_t = F_t \left(1 - p_{in,\,t}\right)^{-1} \tag{7}$$

where $p_{in,t}$ is the proportion of SIs in age group t that are inside division 4a in that time-step (see Yemane et al., 2009, for a similar approach). Under this assumption the spatial distribution of F changes, but the overall rate is unchanged. These scenarios are simplistic, but represent the extremes of possible fishery responses to area closures: relocating none or all of the fishing mortality. As such they give the bounds of possible outcomes.

Multi-Stressor Scenarios

To generate a range of future conditions for the NEAM stock, we combine the different assumptions about future climate and management decisions to generate nine multi-stressor scenarios. The first six scenarios represent each combination of RCP (2.6 and 8.5) and annual fishing mortality rate (unfished, F_{MSY} and F_{lim}). In these scenarios F is applied uniformly to all individuals within an age group. The final three scenarios represent the different assumptions about when ICES division 4a is closed to mackerel fishing, and if it is, how much of the fishing pressure that would have taken place inside is relocated elsewhere. For these latter scenarios we assume $RCP = 8.5$ and $F = F_{MSY}$. See **Table 2** for a summary of the multi-stressor scenarios.

IBM Calibration

We calibrated the half saturation constant (h in Eq. 1), i.e., the prey density at which ingestion rate reaches half maximum at a given temperature. h was estimated by fitting the IBM to data on SSB and weight-at-age using rejection approximate Bayesian computation (ABC) (van der Vaart et al., 2015) (see TRACE section 5 for model fits). In broad terms, we ran 2000 simulations while randomly sampling values of h from a uniform prior distribution. We then "accepted" the values of h that resulted in the best-fitting 30 simulations (1.5% tolerance), giving an approximation of its posterior distribution (see TRACE section 3 for full details of the ABC). To account for uncertainty in h, we simulated all future scenarios (**Table 2**) once for each of the 30 accepted parameter values.

IBM Simulations and Outputs

The IBM simulates the full life cycle of the NEAM population from 1 January 2005–31 December 2050. Simulations are forced by fishing mortality F at age, phytoplankton density X and SST. F is updated annually in the historical period, but remains constant in the future period. SST and phytoplankton density are updated monthly. From 2019 management and climate scenarios take effect (**Table 2**).

For the purposes of this paper, key outputs from the IBM are SSB (tonnes), annual catch (tonnes) from the fishery and mackerel density (tonnes km^{-2}) over the summer period (1 July to 30 September). SSB is calculated as the sum of the body masses of all mature individuals at spawning time (extracted 1 May). Catch is calculated is calculated cumulatively throughout each year from rates of fishing and natural mortality (see TRACE section 2), and mackerel biomass-at-age, using the standard Baranov equation (see TRACE section 2).

TABLE 2 | Summary of the multi-stressor future scenarios.

Scenario	RCP	Annual F	4a status	F redistributed when 4a is closed?
1	2.6	0	Open	No
2	8.5	0	Open	No
3	2.6	F_{MSY}	Open	No
4	8.5	F_{MSY}	Open	No
5	2.6	F_{lim}	Open	No
6	8.5	F_{lim}	Open	No
7	8.5	F_{MSY}	Closed 15 Feb–31 Jul	Yes
8	8.5	F_{MSY}	Closed all year	Yes
9	8.5	F_{MSY}	Closed all year	No

RESULTS

Effect of Future Scenarios on SSB and Yield

To test how the NEAM stock size and associated yield from the fishery may respond to future climate change and management options, we compared future SSB and annual catch from multi-stressor scenarios 1–6 (**Table 2** and **Figure 3**). For both SSB and catch we present means over the period 2021–2050. Our results show that, for both SSB and catch, the choice of fishing mortality has a significant effect (ANOVA, $p < 0.01$). As expected SSB increases as rates of fishing mortality are lowered. The effect of management decision on catch is more subtle. There is a significantly higher catch under F_{lim} than under F_{MSY} where $RCP = 8.5$ (paired t-test, $p < 0.05$, mean difference of 0.03 million tons), but the mean difference is not statistically significant in the RCP 2.6 scenario (0.009 million tons, $p > 0.05$). Within the F_{lim} and F_{MSY} scenarios, SSB is greater in the RCP 8.5 scenarios (paired t tests, $p < 0.05$, mean differences of 0.48 and 0.33 million tons, respectively). Within the F_{lim} and F_{MSY} scenarios catch was also higher in the RCP 8.5 scenario (mean differences of 0.10 and 0.08 million tons, respectively). Overall, the effect of fishing mortality appears much greater than that of climate over the range of scenarios considered (discussed in section “Discussion”).

Effect of Future Scenarios on the Summer Feeding Distribution

To test how the summer feeding distribution of NEAM may change in future, we compare mean mackerel density in July-September over 2005–2010, with that over 2045–2050, for each of scenarios 1–6 (**Figure 4**). There are positive anomalies in the North East region south of Svalbard in all scenarios, with the most pronounced increases of $\sim$ 400 tons km^{-2} in the unfished scenarios. Increased density in these regions is expected because warming opens up new habitat in the North. Another expected finding is that, in the unfished and F_{MSY} scenarios, there are positive anomalies in the western region south and East of Iceland. Again, these anomalies are most pronounced in the unfished scenario (up to $\sim$ 200 tons km^{-2}). This can be explained by an increase in stock size in these scenarios, most notably in the unfished scenario (**Figure 3**). Increasing stock size provides an incentive to move further from the traditional feeding area (Norwegian Sea) in search of areas in which competition for food is less intense (due to the density term, cD, in Eq. 1). Aside from these expected results, the distribution changes are not intuitive. Reasons for this are discussed in section “Discussion.”

Effect of Spatial Management Scenarios

To show how it may be possible to simulate the effects of spatial management options, in **Figure 5** we compare predictions of mean SSB and catch over the period 2021–2050 from a baseline scenario that represents the current situation (2019), to those from two alternative scenarios. The hypothetical scenarios both represent an extension from a seasonal to permanent closure in ICES division 4a, with different assumptions about how much fishing pressure is relocated elsewhere when it is closed (details in **Figure 5** caption). As expected, we found that if fishing mortality is relocated outside division 4a when it is closed, then future SSB does not differ from the baseline scenario (paired t-test, $p > 0.05$, mean difference of 0.10 million tons). However, if fishing mortality is not redistributed when division 4a is closed, then future SSB is significantly higher than the baseline scenario (paired t-test, $p < 0.05$, mean difference of 1.04 million tons). To gauge the consequences of each scenario for the fishery we also present future catch in **Figure 5**. It can be seen that closing division 4a for the entire year without redistributing fishing mortality would result in a significantly lower yield for the fishery (paired t-test $p < 0.05$, mean difference of 0.11 million tons). In summary, these results show that closing division 4a could increase NEAM SSB, but that this will depend on the response of the fishers in terms of how much F is redistributed.

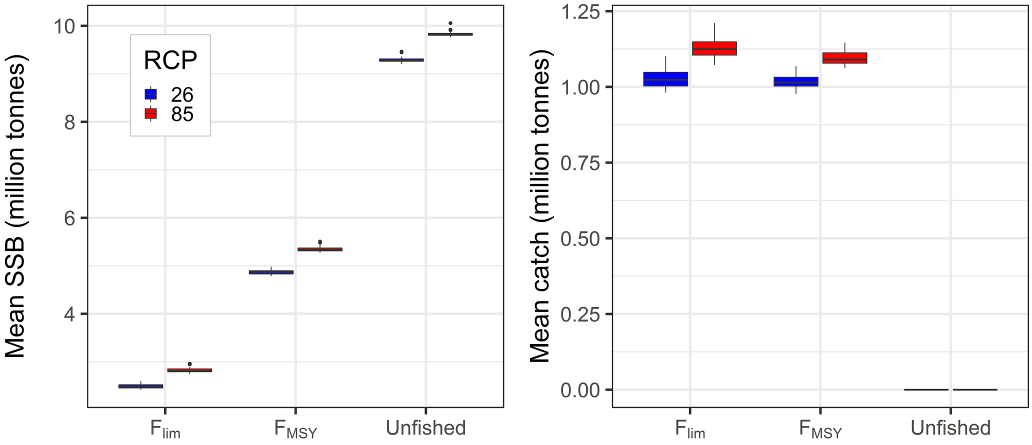

FIGURE 3 | Left: Mean SSB at spawning time over the period 2021–2050; and right: mean annual catch from the fishery over the same period. From left to right within each panel, boxes represent scenarios 1–6 (**Table 2**). Within management scenarios the left-hand boxes correspond to RCP 2.6 and the right-hand boxes to RCP 8.5. Boxplots show medians and interquartile ranges, with the spread representing uncertainty in the parameter h and stochasticity in the IBM.

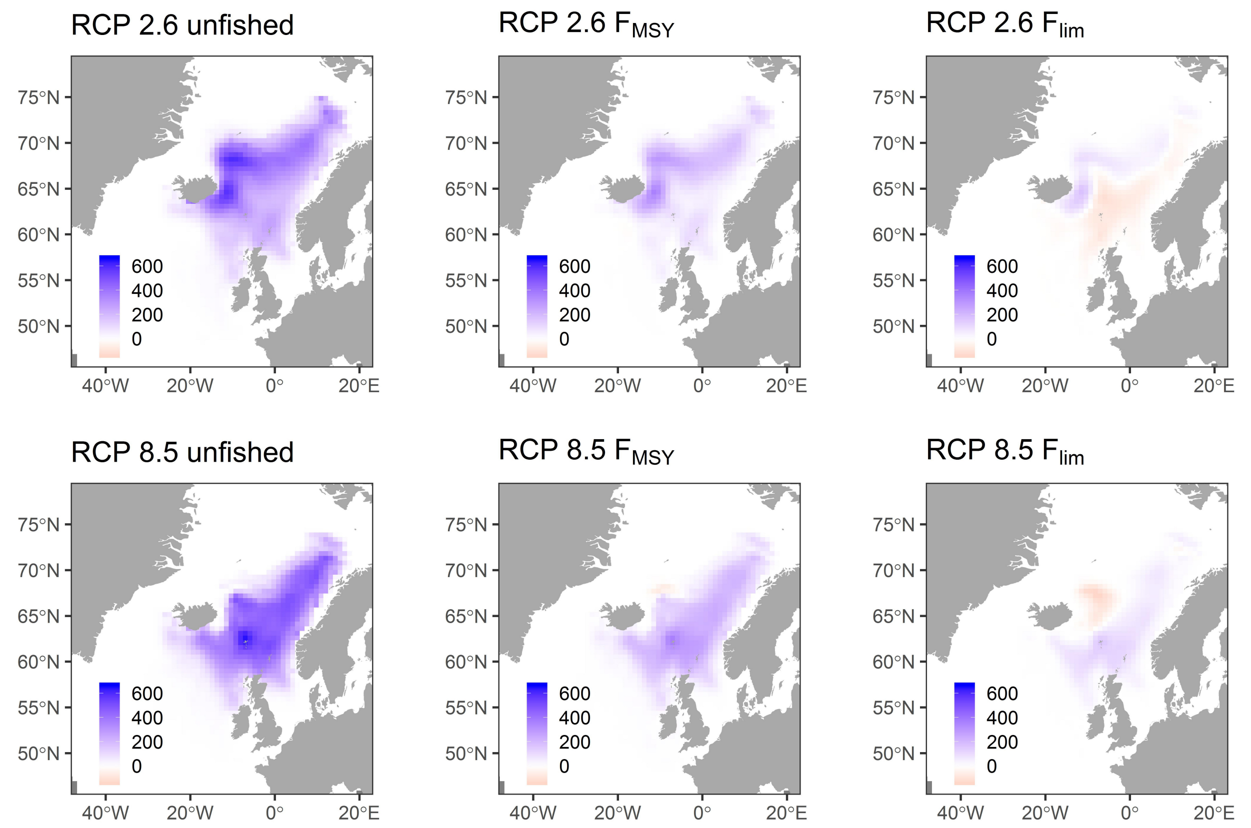

FIGURE 4 | Change in mean mackerel density (tonnes km^{-2}) between the start and end of a simulation for scenarios 1–6 (**Table 2**). Start is taken as the mean over 2005–2010, and end as the mean over 2045–2050.

A reduction in catch when F is not redistributed suggests that fishers would be likely to redistribute their effort elsewhere should legislation allow it.

DISCUSSION

Using an existing spatially explicit IBM, we have simulated NEAM population dynamics and yield from the fishery out to 2050 under a range of climate and fishing scenarios. Environmental inputs to the IBM were obtained from the ESM GFDL-ESM-2M assuming high and low levels of climate change mitigation action. Management scenarios comprised a range of levels of fishing mortality F. After testing the effects of these simple management scenarios, we then implemented an extension to an existing seasonal fishery closure in the Northern North Sea, assuming a moderate level of F and low climate mitigation action. We further divided this spatial scenario by making assumptions about how much of the fishing mortality that would have been inflicted in the Northern North Sea is relocated elsewhere when it is closed. Our results suggest that, over the range of scenarios considered, the effects of fishing mortality are greater than those of climate. These results hold in terms of future SSB, yield from the fishery and the extent to which the summer distribution changes. We then showed that closing an area to fishing may have positive effects for a stock, but that this is highly dependent on how the fishery responds in terms of whether or not fishing is relocated elsewhere.

In this paper we have taken a single-species approach primarily because it allowed us to incorporate sensible assumptions about future fishing mortality. We were able to force the IBM with plausible rates of fishing mortality, including a crude representation of its spatial distribution (e.g., inside or outside of division 4a) and intra-annual variation, as well as the relative catchability of different age groups. This would be difficult to achieve for numerous species or functional groups represented in, for example, ecosystem models. Second, we have extensively validated our IBM using data on population dynamics, structure and spatial distribution (Boyd et al., 2018, 2020). Again, because more holistic models represent numerous species or functional groups, it would be difficult to achieve the same level of validation for a single species. There are, however, processes that single-species models cannot include, notably interspecific competition and predation (Hollowed et al., 2000). NEAM cohabit the Nordic Seas with herring and blue whiting in the summer months. There are contrasting reports over the degree to which the species' diets overlap (Langøy et al., 2012; Bachiller et al., 2016), but recent work has shown that herring larvae are an important prey for NEAM (Skaret et al., 2015). Moreover, herring stock size may affect the distribution of NEAM

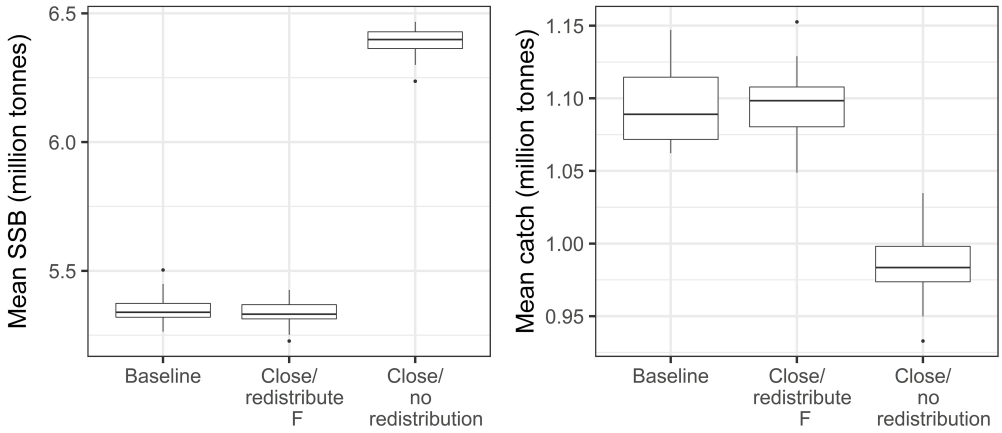

FIGURE 5 | Mean SSB **(left panel)** and annual catch **(right panel)** over the period 2021–2050 under three scenarios: (1) baseline, i.e., ICES division 4a is closed from February 15th to July 31st as at present (2019) and F is raised elsewhere to account for this; (2) division 4a is closed for the entire year and F is raised elsewhere to account for this; and (3) division 4a is closed all year and F is not redistributed, i.e., there is an overall reduction in F. Boxplots show medians and interquartile ranges, representing variability arising from stochasticity the IBM and uncertainty in the parameter h.

over summer (Nikolioudakis et al., 2018). When interpreting our results, it is important to keep in mind that our IBM does not account for interspecific interactions.

Our results suggest that, while climate is important, fishing intensity is likely to have a much larger effect on the NEAM stock out to 2050. This result is evident both in terms of SSB (**Figure 3**), and the degree to which the summer distribution changes (**Figure 4**). There are four possible explanations for this finding. First, the relative impacts of climate and fishing depend on the choice of scenarios. Inclusion of an "unfished" scenario is extreme and would be expected to result in a dramatic increase in SSB (note there is no equivalent zero emissions scenario). However, between the more plausible F_{MSY} and F_{lim} scenarios, the effect of fishing remains much greater than that of climate. Second, the western spawning component of NEAM may less susceptible to the effects of climate due to its latitudinal position within the species' thermal niche. It has been shown that populations inhabiting the cooler parts of their species' distribution are less negatively or more positively affected by increasing temperature than those in the warmer regions (Free et al., 2019). Atlantic mackerel are found as far south as Morocco (Trenkel et al., 2014), meaning that the western spawning component of NEAM represents one of the northernmost sub-units of the stock. Another possibility is that the effect of climate is smaller than fishing due to the oceanographic regime in the North Atlantic. The ensemble of ESMs participating in CMIP indicate that the region to the east of Greenland and south of Iceland will not exhibit a significant increase in SST out to 2100 (Alexander et al., 2018). This could be explained by a weakening of the Atlantic meridional overturning circulation (AMOC) which results in reduced poleward transport of warm water in the Atlantic (Alexander et al., 2018). Indeed, simulations using an ensemble of 10 ESMs predict a weakening of AMOC out to 2100, with the most marked weakening (15–60%) under RCP 8.5 (Cheng et al., 2013). Finally, the relatively small change in the NEAM stock between climate scenarios may reflect the time period chosen in our study. Projections of SST from the CMIP ensemble begin to diverge around the mid-twenty-first century (Hutchings et al., 2012, **Supplementary Figure S22**), and the same is true for the projections used here (see TRACE section 3). It is possible that the effect of climate on the NEAM would increase if simulations were conducted further into the future.

Within fishing scenarios the IBM predicts highest SSB, and hence catch, under RCP 8.5. This is largely down to the positive relationship between SST and recruitment included in the stock-recruitment model. Recruitment is almost always positively correlated with temperature for species inhabiting the cooler regions of their thermal niche (Myers, 1998). So, while the western component of the NEAM stock continues to spawn in cooler regions than e.g., the southern component, the sign of this relationship is likely to hold. This could have important implications for the NEAM fishery if warming waters make sustainable management easier. However, such inferences should be made with extreme caution because we do not know if this positive relationship will break down as waters warm. At some temperature the relationship will shift from positive to negative and this is not accounted for in our IBM (because we are not able to establish the limit from historical data). If the positive effect of temperature on recruitment ceases due to warming in the North East Atlantic over the time period considered, then our projections may be optimistic.

The main caveat of our approach is that we use a single ESM to provide inputs to a single ecological model. As a result, our predictions do not account for structural uncertainty—arising from what processes are represented and by what functional forms-in either of the models (Spence et al., 2018). We chose to use the ESM GFDL-ESM-2M (Dunne et al., 2013) to provide environmental forcing to our IBM because it has previously been identified as suitable for this purpose as part of FISH-MIP (Tittensor et al., 2018). Of particular relevance to our study is that the GFDL ESM has a relatively well-developed biogeochemical formulation and correlates well with primary productivity data

(Tittensor et al., 2018). In addition to GFDL-ESM-2M another ESM, IPSL-CM5A-LR, was identified by FISH-MIP as a suitable candidate for forcing marine ecosystem models. We attempted to include inputs from the IPSL ESM but found that an under-prediction of SST on the NEAM spawning grounds led to frequent recruitment failures in our IBM. With respect to the fish population model, we are aware of other IBMs representing NEAM (Utne et al., 2012; Heinänen et al., 2018). However, to our knowledge these IBMs were designed primarily to represent the stock's spatial distribution and do not make multi-generational predictions of stock size. For this reason, they cannot make predictions about how the stock may develop in future. While we do not account for variation in model structures, we have included a wide range of possible future conditions in terms of climate and harvesting regimes.

While our IBM captures some of the key individual level processes that relate fish population dynamics to prey availability and temperature, there are other climate-related stressors that it does not account for. First, the ocean is projected to become more acidic over the twenty-first century (Holsman et al., 2018). It is thought that ocean acidification will have deleterious effects on fish stocks, such as increased larval mortality and reduced recruitment (Stiasny et al., 2016). Second, ocean oxygen concentration is declining (deoxygenation) in response to increasing temperature (Breitburg et al., 2018). Oxygen concentration affects rates of energy expenditure, such as growth and metabolism (e.g., Del Toro-Silva et al., 2008), which is not accounted for in our bioenergetics model. Third, our IBM uses fields of chlorophyll concentration as a proxy for prey availability. Use of chlorophyll concentration does not account for potential changes to the composition of prey which may occur under novel environmental conditions (Holsman et al., 2018). This may reduce the predictive power of our IBM if NEAM vital rates depend on the composition of available prey. Indeed, *S. scombrus* recruitment appears to be related to the prevalence of large copepods such as *Calanus* species (Ringuette et al., 2002; Jansen, 2016). This is also a problem in that zooplankton is expected to decline at a greater rate than phytoplankton (negative amplification) (Chust et al., 2014), and the pathways of energy transfer from primary producers to e.g., pelagic or benthic food-webs may change, partly in response to the composition of the primary producers themselves (Van Denderen et al., 2018). For these reasons our assumption that chlorophyll concentration is near proportional to prey availability may not hold. Finally, while our IBM captures broad scale effects of prey availability and temperature on the NEAM stock, use of environmental fields derived from a global ESM limited our study to a relatively coarse (60 km^2) spatial resolution (even working at this resolution required some downscaling of the ESM outputs, see TRACE section 3). For this reason our IBM is unable to capture mesoscale processes, such as fronts, that could affect the distribution and productivity of the NEAM stock (Sato et al., 2018). In all, our IBM accounts only for broad scale effects of temperature and a proxy for prey availability on NEAM physiology and behavior, and the results should be interpreted with this in mind.

In addition to stock size, the future distribution of NEAM over summer is an important output from our IBM. Over recent years the summer feeding distribution of NEAM has expanded from its traditional core in the Norwegian Sea, north and westward into the jurisdictions of Iceland and Greenland (Berge et al., 2015; Pacariz et al., 2016; Nikolioudakis et al., 2018; Ólafsdóttir et al., 2018). This has caused political disputes over how the catch should be allocated among coastal states in the region (Hannesson, 2018). Our IBM predicts a north-and westward expansion of the NEAM summer distribution under the F_{MSY} and unfished scenarios (**Figure 4** and see **Supplementary Figure S22**). This finding is expected because under these scenarios SSB increases which forces SIs to the northern and western fringes of the distribution where competition for food is less intense. However, the IBM does not predict an increase in density in Greenlandic waters out to 2050, where NEAM have been present in large densities since ca. 2012 (Ólafsdóttir et al., 2018). This discrepancy cannot be explained by e.g., temperature, which remains suitable for NEAM in this region in all scenarios, but rather reflects the assumptions made in our IBM. First, our foraging model assumes that SIs move in response to local gradients in feeding opportunities (reactive orientation). Under this assumption SIs do not reach Greenlandic waters in appreciable numbers. It may be the case that NEAM use a combination of reactive and predictive orientation, i.e., where individuals move toward areas that are *predicted* to be best, when foraging. Indeed, Nøttestad et al. (2016) suggest that NEAM may use current direction as a cue on which to base predictive orientation. Another possibility is that changes in the spawning distribution, which occurs in spring directly before feeding, could influence the summer distribution. The spawning distribution of NEAM has changed in the past (Hughes et al., 2014) and will likely change in future (Bruge et al., 2016), which is not captured fully by our IBM (spawning is constrained by temperature but only occurs on the European shelf edge). An individuals' location once spent after spawning is equivalent to its starting point for the feeding migration so could influence the subsequent distribution over summer. Our IBM can reproduce the summer distribution from Norway in the East to Iceland in the west with high skill (Boyd et al., 2020), but its predictions of NEAM density west of Iceland should be viewed with caution.

Generally speaking species' distributions are expected to shift poleward as temperature increases (Hughes et al., 2014; Bruge et al., 2016; Pacariz et al., 2016). However, our IBM predicts more nuanced effects of climate on the NEAM summer distribution. For example, density anomalies are more positive in the northern regions under RCP 2.6, which is usually associated with cooler conditions, than under RCP 8.5. Moreover, there are negative anomalies in the northern Norwegian Sea under the RCP 8.5 F_{lim} scenario, but not in the equivalent RCP 2.6 scenario. These results can be explained by a slight cooling of surface waters in these regions under RCP 8.5, which may reflect the enhanced weakening of AMOC under RCP 8.5 (Cheng et al., 2013). In summary, there are some intuitive changes to the NEAM summer distribution (e.g., expansion when stock size is high) out to 2050, but a weakening of AMOC could result in more unexpected distribution patterns.

In addition to changes in rates of total fishing mortality, we also simulated the effects of a hypothetical extension to a fishery closure in the Northern North Sea. To do this we made two simple assumptions about the redistribution of fishing mortality from inside to outside of the area when it is closed. Our results show that predicted stock size and yield from the fishery are highly sensitive to these assumptions (**Figure 5**). This result is intuitive, and as much as our model in its current form can say, but does highlight the potential value of modeling fishing pressure explicitly. Strides are being made toward development of socio-economic IBMs [or, as they are known in this field, agent-based models (ABMs)] in which fishing pressure emerges from the decisions of individual fishers (Lindkvist et al., 2020). To date, these socio-economic ABMs have been coupled to simple models of fish population dynamics, such as a simple logistic growth models (e.g., Bailey et al., 2019). In future socio-economic ABMs could be coupled to biological IBMs such as ours, providing a detailed description of the human-environment system. Then, variables such as the amount of fishing pressure that is redistributed from inside to outside an area if it is closed to fishing (as in our simple scenario), or how the spatial distribution of fishing effort may change in response to changes in a stock's distribution, would emerge. Indeed, the NEAM fishery, with its associated geopolitical issues, may provide an interesting candidate for studying the coupling of fisher behavior and fish stock dynamics.

In summary, we feel that our results give valuable, broad-scale insight into the ways in which the NEAM stock may respond to climate and management scenarios. By simulating the stock under a range of scenarios spanning the extremes of climate mitigation action and fishing pressure, we hope to have given some indication of the bounds of possible future responses. We would like to stress, however, that our results are not intended to be used in a decision-making context; such long-term projections come with too much uncertainty for use in tactical management. It is possible that our projections are optimistic as we do not account for e.g., ocean acidification, deoxygenation and changes in the composition of prey, all of which could have deleterious effects on the NEAM stock. Going forward it would be useful to extend our approach and incorporate: (1) additional species in the IBM, such as herring and blue whiting (though this will be time-consuming); (2) some representation of fleet dynamics and fisher behavior in order to make more realistic predictions about the effects of spatial management options; and (3) additional climate-related stressors such as ocean acidification, deoxygenation and changes in prey composition.

DATA AVAILABILITY STATEMENT

All datasets generated for this study are included in the article/**Supplementary Material**.

AUTHOR CONTRIBUTIONS

RB led the model development and writing of the manuscript. All authors contributed conceptually to the study design and gave critical comments on the manuscript.

FUNDING

This work was supported by the NERC Ph.D. studentship (Grant No. NE/L002566/1) with CASE sponsorship from CEFAS.

ACKNOWLEDGMENTS

We would like to thank Andrew Campbell for providing us with NEAM catch data and Richard Nash for his helpful comments on this manuscript.

SUPPLEMENTARY MATERIAL

The Supplementary Material for this article can be found online at: https://www.frontiersin.org/articles/10.3389/fmars.2020.00639/full#supplementary-material

DATA SHEET S1 | TRACE.

DATA SHEET S2 | Scenarios 1 to 6.

DATA SHEET S3 | Scenarios 7 to 9.

REFERENCES

Alexander, M. A., Scott, J. D., Friedland, K. D., Mills, K. E., Nye, J. A., Pershing, A. J., et al. (2018). Projected sea surface temperatures over the 21st century: changes in the mean, variability and extremes for large marine ecosystem regions of Northern Oceans. *Elem. Sci. Anth.* 6:9. doi: 10.1525/elementa.191

Bachiller, E., Skaret, G., Nøttestad, L., and Slotte, A. (2016). Feeding ecology of Northeast Atlantic mackerel, Norwegian spring-spawning herring and blue whiting in the Norwegian Sea. *PLoS One* 11:e0149238. doi: 10.1371/journal.pone.0149238

Bailey, R. M., Carrella, E., Axtell, R., Burgess, M. G., Cabral, R. B., Drexler, M., et al. (2019). A computational approach to managing coupled human–environmental systems: the POSEIDON model of ocean fisheries. *Sustain. Sci.* 14, 259–275. doi: 10.1007/s11625-018-0579-9

Beddington, J. R. (1975). Mutual interference between parasites or predators and its effect on searching efficiency. *J. Anim. Ecol.* 44, 331–340. doi: 10.2307/3866

Berge, J., Heggland, K., Lønne, O. J., Cottier, F., Hop, H., Gabrielsen, G. W., et al. (2015). First records of Atlantic mackerel (*Scomber scombrus*) from the Svalvard Archipelago, Norway, with possible explanations for the extension of its distribution. *Arctic* 68, 54–61. doi: 10.14430/arctic4455

Borja, A., Uriarte, A., and Egana, J. (2002). Environmental factors and recruitment of mackerel, *Scomber scombrus* L. 1758, along the north-east Atlantic coasts of Europe. *Fish. Oceanogr.* 11, 116–127. doi: 10.1046/j.1365-2419.2002.00190.x

Boyd, R., Roy, S., Sibly, R., Thorpe, R., and Hyder, K. (2018). A general approach to incorporating spatial and temporal variation in individual-based models of fish populations with application to Atlantic mackerel. *Ecol. Modell.* 382, 9–17. doi: 10.1016/j.ecolmodel.2018.04.015

Boyd, R., Sibly, R. M., Hyder, K., Thorpe, R. B., Walker, N. D., and Roy, S. (2020). Simulating the summer feeding distribution of Northeast Atlantic mackerel with a mechanistic individual-based model. *Prog. Oceanogr.* 183:102299. doi: 10.1016/j.pocean.2020.102299

Breitburg, D., Levin, L. A., Oschlies, A., Grégoire, M., Chavez, F. P., Conley, D. J., et al. (2018). Declining oxygen in the global ocean and coastal waters. *Science* 359:eaam7240. doi: 10.1126/science.aam7240

Brochier, T., Ecoutin, J. M., de Morais, L. T., Kaplan, D. M., and Lae, R. (2013). A multi-agent ecosystem model for studying changes in a tropical estuarine fish assemblage within a marine protected area. *Aquat. Living Resour.* 26, 147–158. doi: 10.1051/alr/2012028

Bruge, A., Alvarez, P., Fontán, A., Cotano, U., and Chust, G. (2016). Thermal niche tracking and future distribution of atlantic mackerel spawning in response to ocean warming. *Front. Mar. Sci.* 3:86. doi: 10.3389/fmars.2016.00086

Cheng, W., Chiang, J. C. H., and Zhang, D. (2013). Atlantic meridional overturning circulation (AMOC) in CMIP5 Models: RCP and historical simulations. *J. Clim.* 26, 7187–7197. doi: 10.1175/JCLI-D-12-00496.1

Chust, G., Allen, J. I., Bopp, L., Schrum, C., Holt, J., Tsiaras, K., et al. (2014). Biomass changes and trophic amplification of plankton in a warmer ocean. *Glob. Chang. Biol.* 20, 2124–2139. doi: 10.1111/gcb.12562

DeAngelis, D. L., Goldstein, R. A., and O'Neill, R. V. (1975). A model for tropic interaction. *Ecology* 56, 881–892. doi: 10.2307/1936298

Del Toro-Silva, F. M., Miller, J. M., Taylor, J. C., and Ellis, T. A. (2008). Influence of oxygen and temperature on growth and metabolic performance of *Paralichthys lethostigma* (Pleuronectiformes: Paralichthyidae). *J. Exp. Mar. Bio. Ecol.* 358, 113–123. doi: 10.1016/j.jembe.2008.01.019

Dunne, J. P., John, J. G., Shevliakova, S., Stouffer, R. J., Krasting, J. P., Malyshev, S. L., et al. (2013). GFDL's ESM2 global coupled climate-carbon earth system models. Part II: Carbon system formulation and baseline simulation characteristics. *J. Clim.* 26, 2247–2267. doi: 10.1175/JCLI-D-12-00150.1

Fernö, A., Pitcher, T. J., Melle, W., and Nøttestad, L. (1998). The challenge of the herring in the Norwegian Sea: making optimal collective spatial decisions. *Sarsia* 83, 149–167. doi: 10.1080/00364827.1998.10413679

Free, C. M., Thorson, J. T., Pinsky, M. L., Oken, K. L., Wiedenmann, J., and Jensen, O. P. (2019). Impacts of historical warming on marine fisheries production. *Science* 363, 979–983. doi: 10.1126/science.aau1758

Geophysical Fluid Dynamics Laboratory (2017). *WCRP CMIP5: Geophysical Fluid Dynamics Laboratory (GFDL) GFDL-ESM2M Model Output Collection*. Princeton, NJ: Geophysical Fluid Dynamics Laboratory.

Goethel, D. R., Quinn, T. J., and Cadrin, S. X. (2011). Incorporating spatial structure in stock assessment: movement modeling in marine fish population dynamics. *Rev. Fish. Sci.* 19, 119–136. doi: 10.1080/10641262.2011.557451

Gregg, W. W., Conkright, M. E., Ginoux, P., O'Reilly, J. E., and Casey, N. W. (2003). Ocean primary production and climate: global decadal changes. *Geophys. Res. Lett.* 30:1809. doi: 10.1029/2003GL016889

Grimm, V., Berger, U., Bastiansen, F., Eliassen, S., Ginot, V., Giske, J., et al. (2006). A standard protocol for describing individual-based and agent-based models. *Ecol. Modell.* 198, 115–126. doi: 10.1016/j.ecolmodel.2006.04.023

Hall, S. J. (2001). "The use of technical measures in responsible fisheries: area and time restrictions," in *A Fishery Manager's Guidebook*, eds K. L. Cochrane and S. M. Garcia (Hoboken, NJ: Wiley).

Halpern, B. S., Diamond, J., Gaines, S., Gelcich, S., Gleason, M., Jennings, S., et al. (2012). Near-term priorities for the science, policy and practice of Coastal and Marine Spatial Planning (CMSP). *Mar. Policy* 36, 198–205. doi: 10.1016/j.marpol.2011.05.004

Hannesson, R. (2018). Shared stocks, game theory and the zonal attachment principle. *Fish. Res.* 203, 6–11. doi: 10.1016/j.fishres.2017.07.026

Heinänen, S., Chudzinska, M. E., Brandi Mortensen, J., Teo, T. Z. E., Rong Utne, K., Doksæter Sivle, L., et al. (2018). Integrated modelling of Atlantic mackerel distribution patterns and movements: a template for dynamic impact assessments. *Ecol. Modell.* 387, 118–133. doi: 10.1016/j.ecolmodel.2018.08.010

Henson, S., Cole, H., Beaulieu, C., and Yool, A. (2013). The impact of global warming on seasonality of ocean primary production. *Biogeosciences* 10, 4357–4369. doi: 10.5194/bg-10-4357-2013

Hijmans, R. J. (2019). *geosphere: Spherical Trigonometry*. R package version 1.5–10. Available online at: https://CRAN.R-project.org/package=geosphere

Hollowed, A. B., Bax, N., Beamish, R., Collie, J., Fogarty, M., Livingston, P., et al. (2000). Are multispecies models an improvement on single-species models for measuring fishing impacts on marine ecosystems? *ICES J. Mar. Sci.* 57, 707–719. doi: 10.1006/jmsc.2000.0734

Holsman, K., Hollowed, A., Ito, S., Bograd, S., Hazen, E., King, J., et al. (2018). "Climate change impacts, vulnerabilities and adaptations: North Pacific and Pacific Arctic marine fisheries," in *Impacts of Climate Change on Fisheries and Aquaculture: Synthesis of Current Knowledge, Adaptation and Mitigation Options*, eds M. Barange, T. Bahri, M. Beveridge, K. Cochrane, S. Funge-Smith, and F. Poulain (Rome: FAO), 113–138.

Hughes, K. M., Dransfeld, L., and Johnson, M. P. (2014). Changes in the spatial distribution of spawning activity by north-east Atlantic mackerel in warming seas: 1977–2010. *Mar. Biol.* 161, 2563–2576. doi: 10.1007/s00227-014-2528-1

Hutchings, J. A., Cote, I., Dodson, J., Fleming, I., Jennings, S., Mantua, N., et al. (2012). Canada's international and national commitments to sustain marine biodiversity. *Environ. Rev.* 20, 312–352. doi: 10.1139/a2012-013

ICES (2012). *1.7 Acronyms and Terminology*. Copenhagen: ICES.

ICES (2014a). *Report of the Benchmark Workshop on Pelagic Stocks (WKPELA)*. Copenhagen: ICES.

ICES (2014b). *Report of the Report of the Working Group on Widely Distributed Stocks (WGWIDE) report 2014*. Copenhagen: ICES, 37–192.

ICES (2017). *Ices Wgwide Report*. Copenhagen: ICES, 356–503.

ICES (2019a). *ICES Wgwide Report*. Copenhagen: ICES, 21–27.

ICES (2019b). *Mackerel (Scomber scombrus) in subareas 1–8 and 14, and in Division 9.a (the Northeast Atlantic and adjacent waters). ICES Advice Fish. Oppor. Catch, Effort*. Copenhagen: ICES.

ICES (2019c). *Norway Special Request For Revised 2019 Advice on Mackerel (Scomber scombrus) in Subareas 1 – 8 and 14, and in Division 9 . a (the Northeast Atlantic and Adjacent Waters)*. Copenhagen: ICES, 1–17.

Jansen, T. (2014). Pseudocollapse and rebuilding of North Sea mackerel (*Scomber scombrus*). *ICES J. Mar. Sci.* 71, 299–307. doi: 10.1093/icesjms/fst148

Jansen, T. (2016). First-year survival of North East Atlantic mackerel (*Scomber scombrus*) from 1998 to 2012 appears to be driven by availability of Calanus, a preferred copepod prey. *Fish. Oceanogr.* 25, 457–469. doi: 10.1111/fog.12165

Jansen, T., and Gislason, H. (2013). Population structure of atlantic mackerel (*Scomber scombrus*). *PLoS One* 8:e0064744. doi: 10.1371/journal.pone.0064744

Jansen, T., Post, S., Kristiansen, T., Skarsson, G. J., Boje, J., MacKenzie, B. R., et al. (2016). Ocean warming expands habitat of a rich natural resource and benefits a national economy. *Ecol. Appl.* 26, 2021–2032. doi: 10.1002/eap.1384

Jansen, T., Campbell, A., Kelly, C., Hátún, H., and Payne, M. R. (2012). Migration and fisheries of north east atlantic mackerel (*Scomber scombrus*) in autumn and winter. *PLoS One* 7. doi: 10.1371/journal.pone.0051541

Kaplan, I. C., Williams, G. D., Bond, N. A., Hermann, A. J., and Siedlecki, S. A. (2016). Cloudy with a chance of sardines: forecasting sardine distributions using regional climate models. *Fish. Oceanogr.* 25, 15–27. doi: 10.1111/fog.12131

Kooij, J., Van Der Fa, S. M. M., Stephens, D., Readdy, L., Scott, B. E., and Roel, B. A. (2015). Opportunistically recorded acoustic data support Northeast Atlantic mackerel expansion theory. *ICES J. Mar. Sci.* 73, 1115–1126. doi: 10.1093/icesjms/fsv243

Kuparinen, A., Mantyniemi, S., Hutchings, J. A., and Kuikka, S. (2012). Increasing biological realism of fisheries stock assessment: towards hierarchical Bayesian methods. *Environ. Rev.* 20, 135–151. doi: 10.1139/a2012-006

Langøy, H., Nøttestad, L., Skaret, G., Broms, C., and Fernö, A. (2012). Overlap in distribution and diets of Atlantic mackerel (*Scomber scombrus*), Norwegian spring-spawning herring (*Clupea harengus*) and blue whiting (*Micromesistius poutassou*) in the Norwegian Sea during late summer. *Mar. Biol. Res.* 8, 442–460. doi: 10.1080/17451000.2011.642803

Lindkvist, E., Wijermans, N., Daw, T. M., Gonzalez-mon, B., Giron-nava, A., Johnson, A. F., et al. (2020). Navigating complexities: agent-based modeling to support management in small-scale fisheries. *Front. Mar. Sci.* 6:733. doi: 10.3389/fmars.2019.00733

Lotze, H. K., Tittensor, D. P., Bryndum-Buchholz, A., Eddy, T. D., Cheung, W. W., Galbraith, E. D., et al. (2018). Ensemble projections of global ocean animal biomass with climate change. *bioRxiv* [Preprint]. doi: 10.1101/467175

MacKenzie, B. R., Horbowy, J., and Köster, F. W. (2008). Incorporating environmental variability in stock assessment: predicting recruitment, spawner biomass, and landings of sprat (*Sprattus sprattus*) in the Baltic Sea. *Can. J. Fish. Aquat. Sci.* 65, 1334–1341. doi: 10.1139/F08-051

Myers, R. A. (1998). When do environment-recruitment correlations work? *Rev. Fish Biol. Fish.* 8, 285–305.

Nielsen, A., and Berg, C. W. (2014). Estimation of time-varying selectivity in stock assessments using state-space models. *Fish. Res.* 158, 96–101. doi: 10.1016/j.fishres.2014.01.014

Nikolioudakis, N., Skaug, H. J., Olafsdottir, A. H., Jansen, T., Jacobsen, J. A., and Enberg, K. (2018). Drivers of the summer-distribution of Northeast Atlantic mackerel (*Scomber scombrus*) in the Nordic Seas from 2011 to 2017; a Bayesian hierarchical modelling approach. *ICES J. Mar. Sci.* 76, 530–548. doi: 10.1093/icesjms/fsy085

Nøttestad, L., Diaz, J., Peña, H., Søiland, H., Huse, G., and Fernö, A. (2016). Feeding strategy of mackerel in the Norwegian Sea relative to currents, temperature, and prey. *ICES J. Mar. Sci.* 73, 1127–1137. doi: 10.1093/icesjms/fsv239

Olafsdottir, A., Slotte, A., Arge Jacobsen, J., Gudmundur, J., Oskarssn, G., Utne, K., et al. (2016). Changes in weight-at-length and size-at-age of mature Northeast Atlantic mackerel from 1984:2013: effects of mackerel stock size and herring stock size. *ICES J. Mar. Sci.* 69, 682–693. doi: 10.1093/icesjms/fsv142

Ólafsdóttir, A. H., Utne, K. R., Jacobsen, J. A., Jansen, T., Óskarsson, G. J., Nøttestad, L., et al. (2018). Geographical expansion of Northeast Atlantic mackerel (*Scomber scombrus*) in Nordic Seas from 2007 - 2016 was primarily driven by stock size and constrained by low temperatures. *Deep. Res. II Top. Stud. Oceanogr.* 159, 152–168. doi: 10.1016/j.dsr2.2018.05.023

Overholtz, W. J., Hare, J. A., and Keith, C. M. (2011). Impacts of interannual environmental forcing and climate change on the distribution of atlantic mackerel on the U.S northeast continental shelf. *Mar. Coast. Fish.* 3, 219–232. doi: 10.1080/19425120.2011.578485

Pacariz, S. V., Hátún, H., Jacobsen, J. A., Johnson, C., Eliasen, S., and Rey, F. (2016). Nutrient-driven poleward expansion of the Northeast Atlantic mackerel (*Scomber scombrus*) stock: a new hypothesis. *Elem. Sci. Anthr.* 4:105. doi: 10.12952/journal.elementa.000105

Payne, M. R., Hobday, A. J., MacKenzie, B. R., Tommasi, D., Dempsey, D. P., Fässler, S. M. M., et al. (2017). Lessons from the first generation of marine ecological forecast products. *Front. Mar. Sci.* 4:289. doi: 10.3389/fmars.2017.00289

Plourde, S., Grégoire, F., Lehoux, C., Galbraith, P. S., Castonguay, M., and Ringuette, M. (2014). Effect of environmental variability on body condition and recruitment success of atlantic mackerel (*Scomber scombrus* L.) in the Gulf of St. Lawrence. *Fish. Oceanograph.* 24, 347–363. doi: 10.1111/fog.12113

Politikos, D., Huret, M., and Petitgas, P. (2015). A coupled movement and bioenergetics model to explore the spawning migration of anchovy in the Bay of Biscay. *Ecol. Modell.* 313, 212–222. doi: 10.1016/j.ecolmodel.2015.06.036

R Core Team (2019). *R: A Language and Environment for Statistical Computing*. Vienna: R Foundation for Statistical Computing.

Reum, J. C. P., Blanchard, J. L., Holsman, K. K., Aydin, K., Hollowed, A. B., Hermann, A. J., et al. (2020). Ensemble projections of future climate change impacts on the eastern bering sea food web using a multispecies size spectrum model. *Front. Mar. Sci.* 7:124. doi: 10.3389/fmars.2020.00124

Ringuette, M., Castonguay, M., Runge, J. A., and Gregoire, F. (2002). Atlantic mackerel (*Scomber scombrus*) recruitment fluctuations in relation to copepod production and juvenile growth. *Can. J. Fish Aquat. Sci.* 656, 646–656. doi: 10.1139/F02-039

Runge, J. A., Castonguay, M., De Lafontaine, Y., Ringuette, M., and Beaulieu, J. L. (1999). Covariation in climate, zooplankton biomass and mackerel recruitment in the southern Gulf of St Lawrence. *Fish. Oceanogr.* 8, 139–149. doi: 10.1046/j.1365-2419.1999.00095.x

Sambilay, V. Jr. (1990). Interrelationships between swimming speed, caudal fin aspect ratio and body length of fishes. *Fishbyte* 8, 16–20.

Sato, M., Barth, J. A., Benoit-Bird, K. J., Pierce, S. D., Cowles, T. J., Brodeur, R. D., et al. (2018). Coastal upwelling fronts as a boundary for planktivorous fish distributions. *Mar. Ecol. Prog. Ser.* 595, 171–186. doi: 10.3354/meps12553

Scheffer, M., Baveco, J. M., Deangelis, D. L., Rose, K. A., and Vannes, E. H. (1995). Super-individuals a simple solution for modeling large populations on an individual basis. *Ecol. Modell.* 80, 161–170. doi: 10.1016/0304-3800(94)00055-M

Shin, Y. J., and Cury, P. (2001). Exploring fish community dynamics through size-dependent trophic interactions using a spatialized individual-based model. *Aquat. Living Resour.* 14, 65–80. doi: 10.1016/S0990-7440(01)01106-8

Sibly, R. M., Grimm, V., Martin, B. T., Johnston, A. S. A., Kulakowska, K., Topping, C. J., et al. (2013). Representing the acquisition and use of energy by individuals in agent-based models of animal populations. *Methods Ecol. Evol.* 4, 151–161. doi: 10.1111/2041-210x.12002

Skaret, G., Bachiller, E., Langøy, H., and Stenevik, E. K. (2015). Mackerel predation on herring larvae during summer feeding in the Norwegian Sea. *ICES J.* 158, 950–950. doi: 10.1126/science.158.3803.950

Spence, M. A., Blanchard, J. L., Rossberg, A. G., Heath, M. R., Heymans, J. J., Mackinson, S., et al. (2018). A general framework for combining ecosystem models. *Fish Fish.* 19, 1031–1042. doi: 10.1111/faf.12310

STECF (2007). *Commission Staff Working Document: Evaluation of Closed Area Schemes*. Lucknow: STECF.

Stiasny, M. H., Mittermayer, F. H., Sswat, M., Voss, R., Jutfelt, F., Chierici, M., et al. (2016). Ocean acidification effects on Atlantic cod larval survival and recruitment to the fished population. *PLoS One* 11:e0155448. doi: 10.1371/journal.pone.0155448

Taylor, K. E., Stouffer, R. J., and Meehl, G. A. (2012). An overview of CMIP5 and the experiment design. *Bull. Am. Meteorol. Soc.* 93, 485–498. doi: 10.1175/BAMS-D-11-00094.1

Thiele, M. J. C. (2017). *Package 'RNetLogo'*. Available online at: https://cran.r-project.org/web/packages/RNetLogo/RNetLogo.pdf

Tittensor, D. P., Eddy, T. D., Lotze, H. K., Galbraith, E. D., Cheung, W., Barange, M., et al. (2018). A protocol for the intercomparison of marine fishery and ecosystem models: fish-MIP v1.0. *Geosci. Model Dev.* 11, 1421–1442. doi: 10.5194/gmd-11-1421-2018

Trenkel, V. M., Huse, G., MacKenzie, B. R., Alvarez, P., Arrizabalaga, H., Castonguay, M., et al. (2014). Comparative ecology of widely distributed pelagic fish species in the North Atlantic: implications for modelling climate and fisheries impacts. *Prog. Oceanogr.* 129, 219–243. doi: 10.1016/j.pocean.2014.04.030

Tu, C. Y., Tseng, Y. H., Chiu, T. S., Shen, M. L., and Hsieh, C. H. (2012). Using coupled fish behavior-hydrodynamic model to investigate spawning migration of *Japanese anchovy*, *Engraulis japonicus*, from the East China Sea to Taiwan. *Fish. Oceanogr.* 21, 255–268. doi: 10.1111/j.1365-2419.2012.00619.x

Utne, K. R., Hjøllo, S. S., Huse, G., and Skogen, M. (2012). Estimating the consumption of *Calanus finmarchicus* by planktivorous fish in the Norwegian Sea using a fully coupled 3D model system. *Mar. Biol. Res.* 8, 527–547. doi: 10.1080/17451000.2011.642804

Van Denderen, P. D., Lindegren, M., MacKenzie, B. R., Watson, R. A., and Andersen, K. H. (2018). Global patterns in marine predatory fish. *Nat. Ecol. Evol.* 2, 65–70. doi: 10.1038/s41559-017-0388-z

van der Vaart, E., Beaumont, M. A., Johnston, A. S. A., and Sibly, R. M. (2015). Calibration and evaluation of individual-based models using approximate Bayesian Computation. *Ecol. Modell.* 312, 182–190. doi: 10.1016/j.ecolmodel.2015.05.020

van Vuuren, D. P., Edmonds, J., Kainuma, M., Riahi, K., Thomson, A., Hibbard, K., et al. (2011). The representative concentration pathways: an overview. *Clim. Change* 109, 5–31. doi: 10.1007/s10584-011-0148-z

Villamor, B., Bernal, M., and Hernandez, C. (2004). Models describing mackerel (*Scomber scombrus*) early life growth in the North and Northwest of the Iberian Peninsula in 2000. *Sci. Mar.* 68, 571–583. doi: 10.3989/scimar.2004.68n4571

Wilensky, U. (1999). *NetLogo. Cent. Connect. Learn. Comput. Model*. Evanston: Northwest. Univ. Evanston.

Yemane, D., Shin, Y., and Field, J. G. (2009). Exploring the effect of Marine Protected Areas on the dynamics of fish communities in the southern Benguela: an individual-based modelling approach. *ICES J. Mar. Sci.* 66, 378–387. doi: 10.1093/icesjms/fsn171

Conflict of Interest: The authors declare that the research was conducted in the absence of any commercial or financial relationships that could be construed as a potential conflict of interest.

frontiers
in Marine Science

ORIGINAL RESEARCH
published: 19 August 2020
doi: 10.3389/fmars.2020.00662

Less Nutrients but More Phytoplankton: Long-Term Ecosystem Dynamics of the Southern North Sea

Xu Xu, Carsten Lemmen and Kai W. Wirtz*

Institute of Coastal Research, Helmholtz-Zentrum Geesthacht Zentrum für Material- und Küstenforschung, Geesthacht, Germany

We here assess long-term trends in marine primary producers in the southern North Sea (SNS) with respect to ongoing regional Earth system changes. We applied a coupled high-resolution (1.5–4.5 km) 3d-physical-biogeochemical regional Earth System model that includes an advanced phytoplankton growth model and benthic biogeochemistry to hindcast ecosystem dynamics in the period 1961–2012. We analyzed the simulation together with *in situ* observations. Coinciding with the decreasing nutrient level at the beginning of the 1990s, we find a surprising increase in phytoplankton in the German Bight, but not in the more offshore parts of the SNS. We explain these complex patterns by a series of factors which are lacking in many state-of-the-art coupled ecosystem models such as changed light availability and physiological acclimation in phytoplankton. We also show that many coastal time-series stations in the SNS are located in small patches where our model predicts an opposite trend than found for the surrounding waters. Together, these findings call for a reconsideration of current modeling and monitoring schemes.

Keywords: ecosystem, modeling, North Sea, biomass, chlorophyll, regime shift

OPEN ACCESS

Edited by:
Johnna M. Holding,
Arctic Research Centre, Aarhus University, Denmark

Reviewed by:
Eva Ehrnsten,
Stockholm University, Sweden
Juris Aigars,
Latvian Institute of Aquatic Ecology, Latvia

Correspondence:
Xu Xu
xu.xu@hzg.de

Specialty section:
This article was submitted to Global Change and the Future Ocean, a section of the journal Frontiers in Marine Science

Received: *01 March 2020*
Accepted: *21 July 2020*
Published: *19 August 2020*

Citation:
Xu X, Lemmen C and Wirtz KW (2020) Less Nutrients but More Phytoplankton: Long-Term Ecosystem Dynamics of the Southern North Sea. Front. Mar. Sci. 7:662. doi: 10.3389/fmars.2020.00662

INTRODUCTION

Marine phytoplankton constitute the fundamental basis of the marine food web and biogeochemical cycles. Phytoplankton mediates around half of net primary production (NPP) on Earth (Field et al., 1998; Falkowski and Raven, 2007). Changes in primary production impact higher trophic levels, from zooplankton to fish, marine mammals, and seabirds (Chassot et al., 2010; Capuzzo et al., 2018).

Coasts and shelf seas generally reveal higher NPP due to shallower water depth and high nutrient influx by upwelling or river inflow. The North Sea, a shallow shelf sea to the eastern North Atlantic is one of the most utilized and highly productive sea areas in the world (Ducrotoy et al., 2000; Emeis et al., 2015). The southern North Sea (SNS) features low water depth, strong tidal mixing, diminished ocean influence, and high riverine nutrient inflow. Nutrient loads were elevated from the 1950s to the 1980s due to increased wastewater discharge and use of fertilizers (eutrophication) but declined in the recent decades (Painting et al., 2013; Burson et al., 2016) due to regulations and better wastewater treatment.

Nutrient levels, together with light availability, are primordial factors controlling phytoplankton growth. Phytoplankton in coastal areas such as the SNS are thus directly perturbed by human action, but in addition often seem to track climatic changes (Reid et al., 1998; Taylor et al., 2000; Schlüter et al., 2008). A sustainable management of this sea as requested by a number of national and international directives thus needs to disentangle and to attribute observed changes to natural, proximate, and to direct anthropogenic pressures.

Long-term *in situ* observations of phytoplankton and nutrient concentration are available for a number of sites (Cadee and Hegeman, 2002; Smaal et al., 2013; Desmit et al., 2019), but prior model studies of long-term biomass dynamics (Daewel and Schrum, 2013; Lynam et al., 2017; Capuzzo et al., 2018) have been validated only against sparse data sets, which lack regional details and long-term variability. Moreover, state-of-the-art coupled biogeochemical models often come with a relatively coarse spatial resolution and rarely resolve strong gradients in phytoplankton community composition and ecophysiology. These models thus face difficulties to represent strong coast-to-shelf variability in phytoplankton (Daewel et al., 2015; Ford et al., 2017). As a consequence, the reliability of hindcasted as well as projected trends in coastal ecosystem states is not clear.

In this study, we employ a novel trait-based phytoplankton model embedded into a high-resolution coastal Earth System set-up to simulate long-term (1961–2012) variations of ecosystem states and primary production in the SNS. The trait-based physiological phytoplankton model has been shown to represent major acclimation patterns over time and within the SNS (Kerimoglu et al., 2017; Wirtz, 2019). It is modularly coupled within a coastal Earth system model context also tested in a number of applications. We aim to further investigate the validity of the set-up using a large amount of *in situ* data for then unraveling the response of phytoplankton biomass to changes in nutrient levels and climate.

MATERIALS AND METHODS

Numerical Model System

Biogeochemical (BGC) cycling in the SNS is strongly influenced by riverine and open ocean fluxes and mediated by benthic–pelagic exchange. For the numerical description of the SNS biogeochemistry, we employ an application of the Modular System for Shelves and Coasts (MOSSCO, Lemmen et al., 2018), an Earth System Modeling Framework (ESMF, Theurich et al., 2016) software layer that here interlinks the General Estuarine Turbulence Model (GETM, Burchard and Bolding, 2002) with adjacent compartments as described in more detail below: atmospheric physical and chemical forcing, riverine discharges, and two BGC models in the pelagic and in the benthic domain. The latter are represented within the Framework for Aquatic Biogeochemical Modeling (FABM, Bruggeman and Bolding, 2014). This coupled system of hydrodynamics and benthic and pelagic BGC is the core of several published MOSSCO applications for the SNS that describe spatial–temporal patterns in nutrient concentration (Kerimoglu et al., 2017, 2018; Wirtz, 2019), filter-feeder effects on primary productivity (Lemmen, 2018; Slavik et al., 2019), or benthic sediment and biota interaction (Nasermoaddeli et al., 2018).

Hydrodnamics

The General Estuarine Transport Model (GETM, Burchard and Bolding, 2002) is a structured grid three-dimensional coastal ocean model that has been frequently applied in the North Sea (e.g., Stips et al., 2004; Gräwe et al., 2015). It features vertically adaptive layers (Hofmeister et al., 2010) and vertical density and momentum mixing provided by the General Ocean Turbulence Model (GOTM, Burchard et al., 2006). GETM prognostically calculates local sea surface elevation, tidal dry-falling, currents, temperature, salinity, and transports tracers from other components of the coupled system, i.e., the BGC state variables from the pelagic FABM component.

Pelagic Biogeochemistry

For the representation of pelagic BGC and phytoplankton physiology, the Model for Adaptive Ecosystems in Coastal Seas (MAECS, Wirtz and Kerimoglu, 2016; Kerimoglu et al., 2017) was operated as the single module of a FABM pelagic component in the MOSSCO coupled system. MAECS employs a trait-based approach for the optimal allocation between different intracellular machineries (i.e., photo harvesting, electron chain, high number of nutrient uptake systems; major element flows described by MACES are depicted in **Supplementary Figure S1**). Simulated changes in physiological characteristic such as light affinity or growth rate only partially reflect changes in phytoplankton community structure. Variations in physiology in a single species can be much greater than differences between species (Wirtz and Kerimoglu, 2016), which makes it difficult to reconstruct underlying changes in community structure as often observed through, e.g., shifting diatom-to-flagellate ratios. MAECS realistically simulates observed photo-acclimation patterns and the co-limitation by, e.g., P and N (Wirtz and Kerimoglu, 2016). It includes viral infection as a relevant post-bloom phytoplankton mortality factor and a dependence of carnivory (zooplankton mortality) on light conditions, shallowness as a requirement for visual predation, and the presence of suspension feeders (Wirtz, 2019). MAECS prognostically calculates the states and variable stoichiometry of phytoplankton chlorophyll, P and N in relation to C, and can reproduce meso-scale patterns in chlorophyll and nutrients at several temporal scales (Kerimoglu et al., 2017; Wirtz, 2019). The model has, amongst others, been applied for scenario analyses of nutrient loading for water quality in the SNS (Kerimoglu et al., 2017, 2018) and for investigating the coastal chlorophyll gradient (Lemmen, 2018; Wirtz, 2019).

Benthic Biogeochemistry

Nitrogen, oxygen and carbon cycling in the sea floor are represented by the one-dimensional Ocean Margin Experiment exchange early Diagenesis model (OMExDia, Soetaert et al., 1996), extended for phosphorous by Hofmeister et al. (2014) and Wirtz (2019). Two-way exchange and conversion between the pelagic MAECS and benthic OMExDia models are mediated by a specialized MOSSCO component for benthic–pelagic exchange (Hofmeister et al., 2014; Lemmen et al., 2018). Particulate carbon is fractionated in labile and semilabile components with different mineralization rate and N:C ratio; dissolved nitrogen is represented by ammonium and nitrate. OMExDia resolves both aerobic as well as anaerobic processes in the pore water. Particulate material is bioperturbed, dissolved species are diffused in the vertical dimension, which is discretized with linearly increasing depth layers.

Setup and Boundary Conditions

Our SNS set-up is delineated by the Dutch and German coastline to the South and East, and it has open boundaries to the West (English Channel) and North (open North Sea). It is spatially represented as a 139 × 98 grid with curvilinear projection, with 1.5 km horizontal resolution in the coastal German Bight and up to 4.5 km resolution at the open ocean boundaries (**Supplementary Figure S2**). Bottom roughness is constant throughout the domain (10^{-3} m) as proposed by Gräwe et al. (2015). Average water depth is 20 m, and maximum 50 m, which is resolved by 20 terrain-following model layers. Ten river sources, including the German Bight tributaries Elbe and Weser, provide freshwater, total nitrogen, and total phosphorous. The river nutrient data have been compiled from regional government, research institutions, universities and protection organizations and are in detail described by Eisele and Kerimoglu (2015). Sea surface height, climatological temperature, salinity, and hourly meteorological boundary conditions were obtained from the CoastDat II regional climate hindcast based on the models COSMO-CLM, TRIM-NP and HAMSOM (Geyer, 2014)[1] . A monthly climatology of depth-dependent open ocean boundary conditions for dissolved inorganic N and P was prescribed. This climatology was obtained from Grosse et al., 2016's ECOHAM (Ecosystem Hamburg) 2000–2010 simulation, which in turn derives from the POLCOMS-ERSEM (Proudman Oceanographic Laboratory Coastal Ocean Modeling System European Regional Seas Ecosystem Model) common boundary condition used in the North Sea ecosystem model comparison by Lenhart et al., 2010. This physical and BGC setup was validated by Kerimoglu et al. (2017). The sediment was constrained by sea bottom temperature from GETM, constant saturated oxygen and porosity ranging from 0.9 to 0.7 in the 15 layers down to 16 cm depth.

Simulations were performed for 1960 through 2012 and evaluated between 1961 and 2012 (52 years). Physical fields were initialized from CoastDat climatological values; pelagic BGC variables were initialized with constant fields from Wirtz and Kerimoglu (2016), and spun up for 1 year (1960, discarded from the analysis), benthic BGC was initialized with an equilibrium steady state derived from a 30-year spin-up; all data were saved at 36-h interval for further analysis. BGC–hydrodynamics coupling timestep was 30 min, internal integration for hydrodynamics 60 s with 4th order Runge-Kutta scheme, for pelagic BGC 480 s with adaptive Euler refinement and 720 s with 4th order Runge-Kutta integration for OMExDia.

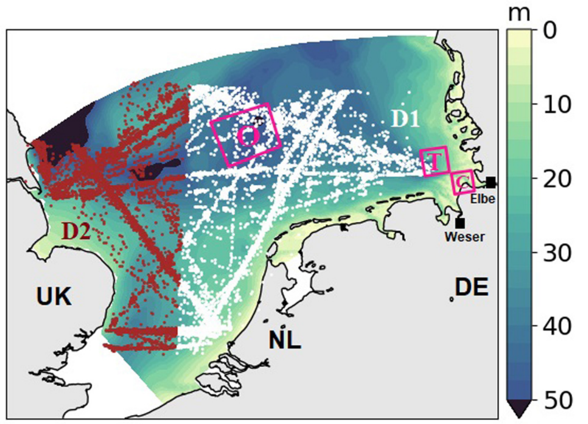

FIGURE 1 | Bathymetry of the model domain, the southern North Sea. Locations of the CPR measurements from the standard CPR area D1 (white dots) and D2 (red dots). Three pink rectangular show the selected analyzed areas, referred to as coast ("C"), transitional ("T") and offshore ("O"). Black squares indicate the rivers Elbe and Weser.

All simulations presented here were produced with MOSSCO v1.0.0 (archived at https://doi.org/10.5281/zenodo.438922). All parameter files for the configuration of the coupled system, GETM, MAECS, and OMExDia are archived at https://doi.org/10.5281/zenodo.3688216).

Data Integration

The Continuous Plankton Recorder (CPR) survey, managed by the Sir Alister Hardy Foundation for Ocean Science in the United Kingdom, using self-contained automatic plankton recorders, collects plankton continuously from a standard depth of ∼7 m (Hays and Warner, 1993) along the towed routes (Richardson et al., 2006). It provides a long-term (∼70 years) plankton abundance at fine taxonomic resolution and a comprehensive proxy of epipelagic biomass, which is represented by CPR's Phytoplankton Colour Index (PCI), often referred to as greenness, at the regional scale (Richardson et al., 2006; McQuatters-Gollop et al., 2015). The PCI is assigned a numerical value to represent the amount of phytoplankton pigment on the sample silk (Colebrook and Robinson, 1965), and it is also considered as the best estimate of total phytoplankton chlorophyll concentration from CPR data as it strongly agrees with chlorophyll measurements from CPR samples (Hays and Lindley, 1994) and with satellite estimates of chlorophyll (Batten et al., 2003; Raitsos et al., 2005).

In this work, we used CPR observations in the standard area D1 and most data in area D2 (Richardson et al., 2006) from 1961 to 2012 (**Figure 1**, database includes 15,986 samples, Helaouet, 2020)[2]. We interpolated the PCI to the nearest model grid and compared the annual average of simulated chlorophyll with the corresponding greenness.

No CPR data exist for coastal areas shallower than the sampling depth (∼7 m, see **Figure 1**). To compensate for the

---

[1] www.coastdat.de

[2] https://doi.org/10.17031/1650

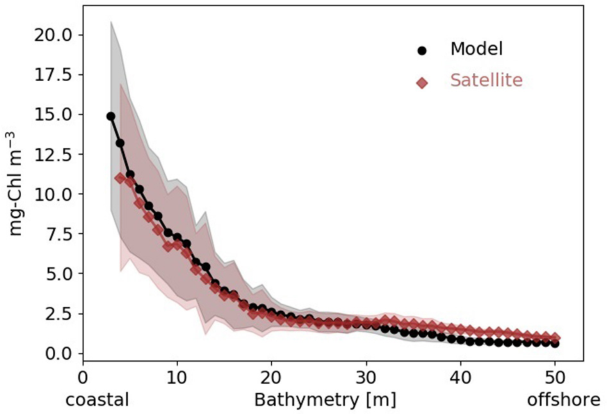

FIGURE 2 | Mean surface Chl concentration (black circles: model simulation, red diamonds: satellite data) 1997–2012 averaged along depth bands from coast to offshore in the SNS. Shading indicates standard deviation within depth band.

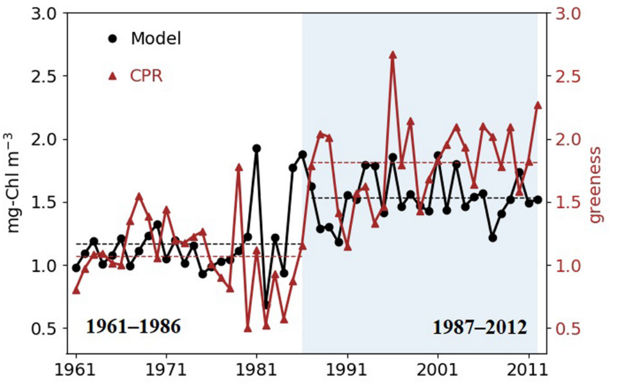

FIGURE 3 | Simulated surface annual mean Chl (black circles) and annual mean CPR greenness (red triangles) in the SNS. Shaded area shows the years after the change point detected by binary segmentation in both simulation and CPR data (1987–2012). Dashed lines are mean values of the two time periods.

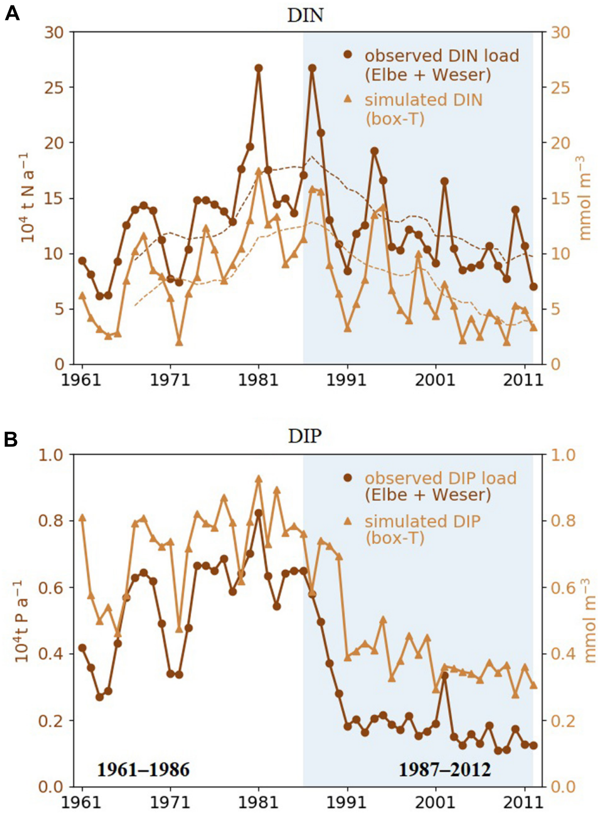

FIGURE 4 | (A) Simulated annual mean DIN concentration averaged over area "T" shown in **Figure 1** (yellow triangles) and measured annual total DIN loads of rivers Elbe and Weser (brown circles). Dashed lines are 7-year running means. **(B)** Same as panel **(A)**, but for DIP. The recent period (1987–2012) are highlighted by shaded areas.

spatial blank in CPR data, we applied satellite data in our model–data spatial comparison. The derived chlorophyll of ocean color CCI (Climate Change Initiative) between 1997 and 2012 from the European Space Agency (ESA, available from http://cci.esa.int) were averaged over time to compare with mean simulated Chl. For analyzing the nutrient variations in the transitional area ("T," section "Variations of Nutrients and Chlorophyll"), regional variations in biomass, and seasonality of nutrients (section "Seasonal Variations of Nutrients and Phytoplankton Biomass"), we used the averages over three typical domains in the SNS that represent the coast–offshore transect from the outer Elbe estuary (denoted "coast" C) to the waters around the island Helgoland (denoted "transitional," T) in the core of the German Bight to an offshore location in the central SNS (denoted "offshore," O, **Figure 1**).

RESULTS

Variations of Nutrients and Chlorophyll

Chlorophyll concentration (Chl) sharply decreases by 70–80% from the coast to the transitional area, both in the simulation and satellite data (**Figure 2**). The decline is slightly steeper in the simulation, but the relative error between the climatological coastal gradients in observed and simulated Chl distributions rarely exceeds 20%, which for Chl can be regarded as exceptional skill.

The long-term dynamics of simulated Chl tracks the observed dynamics, and the Pearson correlation coefficient between yearly (1961–2012) CPR greenness and model Chl is 0.5 ($p < 0.001$, $n = 15986$). The binary segmentation search method reviewed by Truong et al. (2020) indicates a change point in 1986 in both simulated and observed data with higher chlorophyll since 1987 (**Figure 3**); Mean Chl in the SNS increases from 1.12 mg m^{-3} (1.07 in greenness) before 1987 to 1.54 mg m^{-3} (1.82 in greenness) in the recent decades. We therefore partition the data in the two time slices 1961–1986 and 1987–2012 and denote the latter as a high production period.

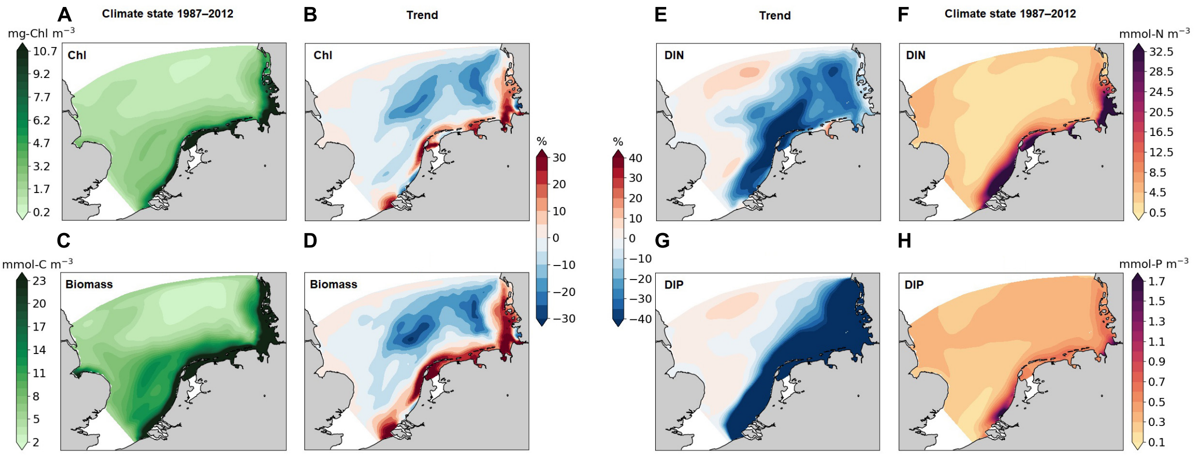

FIGURE 5 | Simulated mean Chl **(A)**, phytoplankton biomass **(C)**, DIN **(F)**, DIP **(H)** in the time period 1987–2012 averaged over the water column. The trends of Chl **(B)**, phytoplankton biomass **(D)**, DIN **(E)**, DIP **(G)** denote the difference from the 2nd period (after 1987) to the first one (before 1987).

Our simulation shows a reduction of mean dissolved inorganic nitrogen (DIN) and dissolved inorganic phosphate (DIP) in the area "T" since the end of 1980s (**Figures 4A,B**). Interannual variations in simulated DIN and DIP in area "T" track the changes in the observed yearly nutrient load of the rivers Elbe and Weser, which indicate a strong control of nutrient levels by riverine influx. Both DIN and DIP decrease over time, but very differently. Simulated DIN decreases slowly after 1987 and exhibits a ~7-year oscillation, which may be connected to the NAO pattern in atmospheric precipitation (Visser et al., 1996; Fock, 2003; Radach and Pätsch, 2007). DIP displays a segmented trend with a sharp transition from high values before 1987 to lower ones after 1990. The riverine input strongly decreases (~50%) from 1987 to 1989, while the negative DIP trend in "T" seems to combine a relatively gentle decrease before 1990 and a sharp drop from 1990 to 1991.

Climatological Changes in Spatial Physical and Biological Distributions

In agreement with the mean cross-sectional distribution for the SNS (**Figure 2**), Chl along the German, Dutch, and Belgian coasts is much higher (>10 mg m^{-3}) than in most offshore areas (<1 mg m^{-3}, **Figure 5A**). These high levels of coastal Chl further increase from the 1960–1980s to the 1990–2000s in most southern coastal areas by up to 20% (**Figure 5B**). In the offshore areas, small decreases in Chl produce high relative changes due to the low concentration there. In most of the western SNS, Chl drops by at most 5%, compared to up to 20% in the eastern SNS.

The phytoplankton biomass distribution (in terms of carbon) exhibits a similar pattern as Chl (**Figure 5C**). Areas with high biomass (>23 mmol C m^{-3}) are located in a narrow coastal band and overlap with the band of accumulated chlorophyll. The northern water body with low biomass (<5 mmol C m^{-3}) penetrates into the transition zone following the old Elbe river valley. The interdecadal trend of biomass is consistent with the respective chlorophyll trend, but stronger and less confined to the narrow band. There is a strong increase in phytoplankton production in most high biomass areas (more than 30%). A decoupling of the biomass–chlorophyll trend is found in the West-Frisian Wadden Sea, where biomass increases and Chl decreases. At parts of the coast of the southern Netherlands, the northern Elbe estuary, and the Danish coast, chlorophyll decreases much stronger than biomass (**Figures 5B,D**).

The spatial distributions of dissolved macro-nutrients (DIN and DIP) match the biomass distributions (**Figures 5F,H**), which decreases from coasts to offshore. Nutrients declined in the recent decades (**Figures 5E,G**) within the entire southeastern SNS (as exemplified by **Figure 4**, "T"), in particular, DIP drastically decreases in the whole southern coastal and transitional areas, whereas relative changes in other areas are small. The trends in DIN and DIP are decoupled from phytoplankton biomass in areas "C" and "T" during de-eutrophication. However, for the less productive offshore parts in the eastern SNS, our results display a ~20% decrease in both biomass and nutrients.

Lateral gradients in annual mean sea surface temperature (SST) in the range from 9 to 11°C are largely determined by the warm tongue of the Atlantic water entering through the English Channel (**Figure 6**). Winds at 10 m height dominantly come from west (average speed 1.65 m s^{-1}). After 1986, wind speeds increase over the whole model domain (by 0.4 m s^{-1} on average) while wind direction slightly changes to the north (on average by 4°). In parallel, the Atlantic warm tongue strengthens such that surface waters of the SNS are warmed by around 0.5°C, and the southeastern cold-water body retreats to the shallower areas along the Frisian archipelago and the North Frisian near-shore waters.

Seasonal Variations of Nutrients and Phytoplankton Biomass

The seasonality in phytoplankton biomass markedly differs between the "C," "T," and the "O" areas in both climate states analyzed (**Figure 7**). In the coast area, simulated phytoplankton

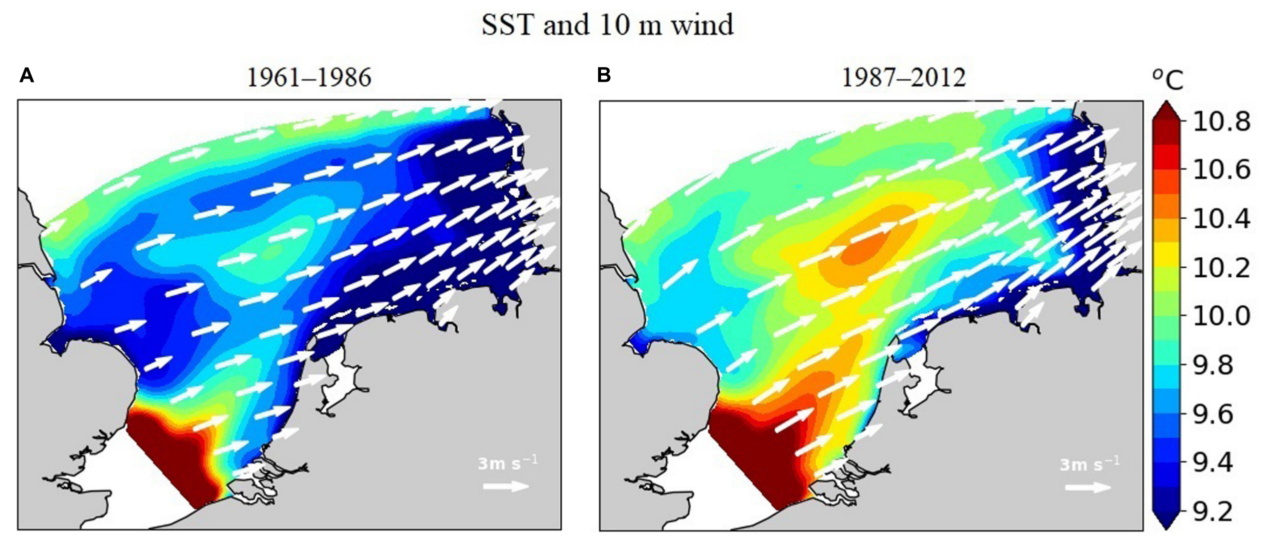

FIGURE 6 | Simulated mean sea surface temperature and 10-m wind speed in **(A)** 1961–1986 and **(B)** 1987–2012.

growth starts at the end of February, followed by the bloom peak at late March (1961–1986) to late April (1987–2012). From mid-spring to the end of summer, biomass remains high. Bloom timing in transitional waters is similar to the one at the coasts, but biomass drops after the spring bloom and is not sustained throughout the summer. Bloom timing in the offshore domain is delayed by a few days in comparison to the coastal and transitional areas. After a strong post-bloom decline biomass attains even lower values in summer compared to winter concentration due to combined nutrient limitation and zooplankton grazing.

Our reconstructed seasonal cycle of phytoplankton reveals long-term changes in terms of both timing and intensity. Despite a very similar timing of the coastal bloom start in 1961–1986 and 1987–2012, the late spring and summer dynamics are different. In the recent decades, the spring peak bloom is much more pronounced (peaking at twice the early period biomass) and has a pronounced maximum in late spring, which slowly declines toward winter. In contrast, the earlier period features a sustained (and lower) maximum biomass until late summer. In the transitional area, the bloom peak is pronounced in 1961–1986 and sustained in the later period, but at the high level of the early period peak. For both the coastal and transitional areas, the spring and summer phytoplankton biomass is much higher in the recent than in the early period. These differences vanish in the offshore area, except for a ∼30% long-term decrease in biomass.

The Chl:C ratio is lower in the period 1987–2012 compared to the earlier period. The decrease reaches up to 25% at the coast in fall, and up to 10% in transitional waters throughout summer and fall (**Figure 8A**). For DIP, the maximum interdecadal difference occurs in summer, with up to 90% reduction at the coast and 50% reduction in "T" (**Figures 8B,C**). Similar decreasing trends are found in "C" and "T" DIP concentrations throughout the year in 1987–2012, with greater magnitude in the coastal region, while DIN exhibits richer variability. Coastal DIN concentration does not change between the two analysis periods through the winter and early spring but decreases in summer and fall in the period 1987–2012. The DIN variation in the "T" area reveals a negative long-term trend.

DISCUSSION

The comparison between the satellite-observed Chl, CPR greenness, and the model Chl reconstruction testify the ability of the model system to reproduce spatial, multi-scale patterns and temporal interdecadal dynamics of the SNS very well. The ecosystem model MAECS in particular features a realistic simulation of the coastal Chl gradient, i.e., the increase of Chl from continental shelves toward the coast, which is observed by satellite (Ribalet et al., 2010; Nezlin et al., 2012; Müller et al., 2015), and has already been discussed in terms of phytoplankton growth and mortality factors by Wirtz (2019) for the period 2000–2014. Low light availability in shallow areas is more than compensated by lower grazing losses since zooplankton is in turn subject to high grazing pressure by mussels and juvenile fish. This is confirmed by our analysis: the coastal area displays lower zooplankton abundance after the late 1980s (**Figure 8**), which in turn can be ascribed to both higher temperature (and thus increased carnivorous losses of herbivores) and lower nutrient concentration propagating to zooplankton production rates.

Historical studies suggest an ecological regime shift in the North Sea in the late 1980s, which involved an increase in phytoplankton biomass (Reid et al., 1998; Beaugrand, 2004; Alheit et al., 2005). In our simulation, we also find a post-1987 biomass increase in the SNS located at coastal to transitional areas. The relative change in costal Chl after the regime shift agrees with the 21% increase according to the long-term chlorophyll data analysis by McQuatters-Gollop et al. (2015). This biological shift coincided with the late 1980s climate regime

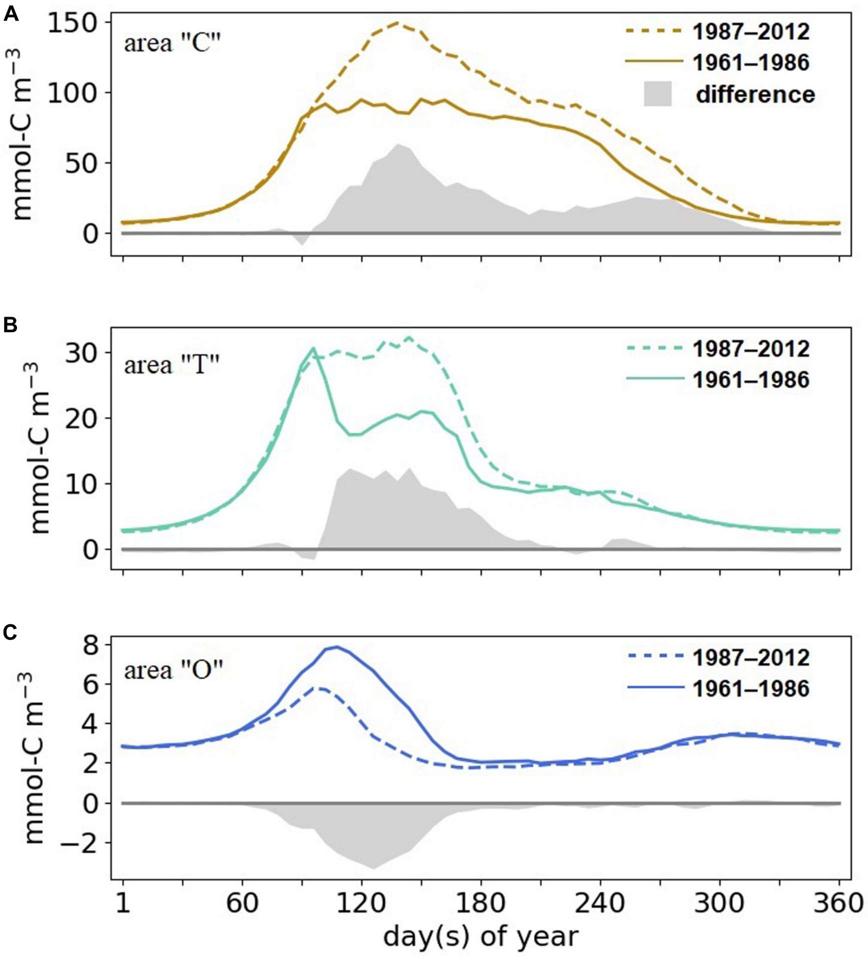

FIGURE 7 | Simulated 6-day mean phytoplankton biomass and changes between 1987–2012 and 1961–1986 (shading) **(A)** in areas "C," **(B)** "T," **(C)** and "O."

shift in the extratropical Northern Hemisphere (Lo and Hsu, 2010), which involved the warming in the North Sea (Edwards et al., 2006; van Aken, 2010; Høyer and Karagali, 2016). This climate regime shift is linked to an increase in the NAO index, which is also evidenced by an increased inflow of relatively warm Atlantic water into the SNS (Edwards et al., 2002; Weijerman et al., 2005; Jaagus et al., 2017).

Beside climatic variations, we also simulated de-eutrophication trends in the SNS (van Beusekom et al., 2009; Burson et al., 2016; Meyer et al., 2018). The long-term time series from Helgoland roads station shows that the variabilities and trends of DIN and DIP (Wiltshire et al., 2010) are consistent with those simulated by our model. Kerimoglu et al. (2018) demonstrated the good skill of our model system in simulating recent decade DIN and DIP by comparing to data from Helgoland and four surrounding monitoring stations in the German Bight.

The North Sea ecosystem is commonly considered as resource-controlled (bottom-up, Beaugrand et al., 2009; Olsen et al., 2011). As a consequence, a decline in Chl or primary production in the SNS should be expected due to the reduced riverine loads of nutrients after the late 1980s. This common view is supported by studies that report decreasing Chl at coastal sites (van Beusekom et al., 2009; Desmit et al., 2019). These studies referred to monitoring stations located at Sylt ("L" in **Supplementary Figure S3**) and very near-shore along the northern (T-10 in **Supplementary Figure S3**) and southern (NW-02, GR-06 in **Supplementary Figure S3**) Dutch coast. Our simulation also reveals a local decrease consistent with the observed trends at the locations NW-02 and GR-06, in contrast to the general increase. Simulated offshore decreases are in accordance with both station observations (i.e., NW-70, **Supplementary Figure S3**) and other model simulations (Daewel and Schrum, 2013; Capuzzo et al., 2018).

The disagreement between the simulation and the station L may be due to the limited model resolution insofar failing to represent physical conditions in the List Tide Basin. The different trends found in station T-10 and in the simulation may indicate the model limitation in resolving differences in BGC processes from the transitional water to offshore as the station is located at the boundary of the two different trends areas. Also, the coarse and parametrized description

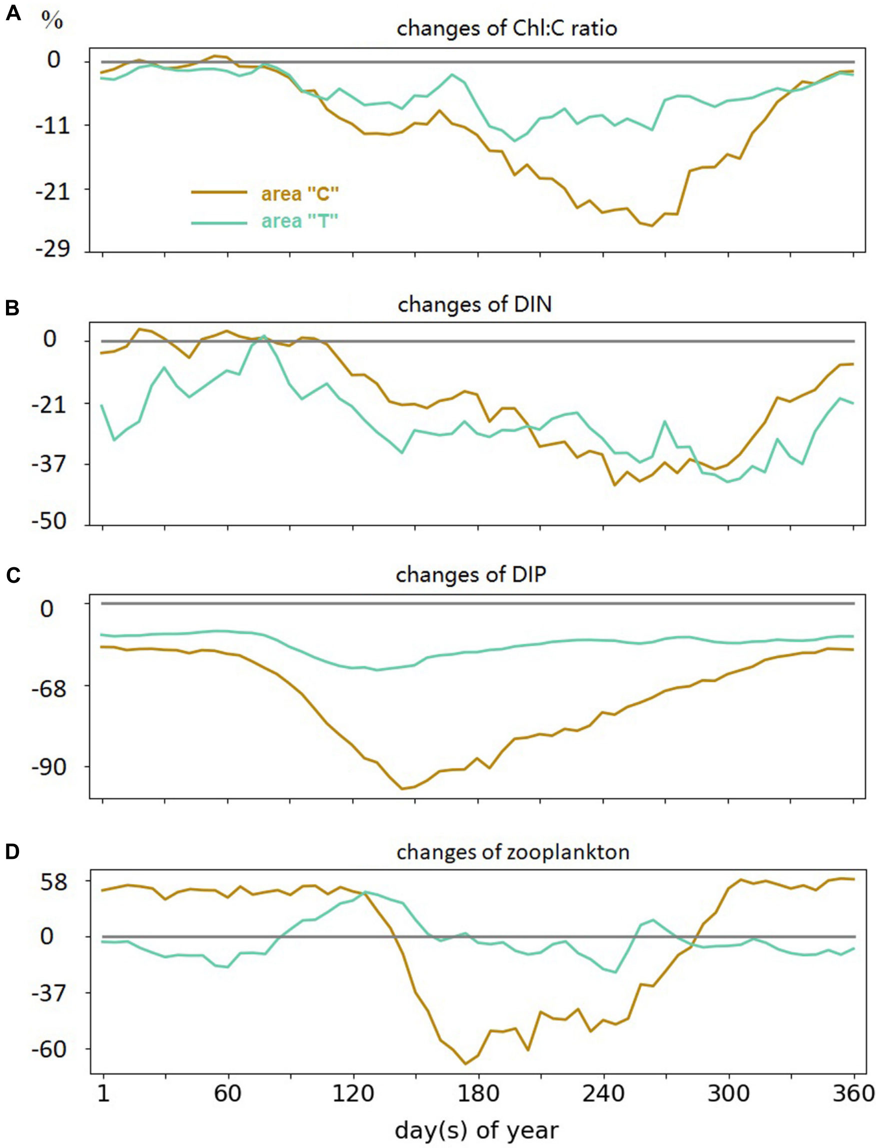

FIGURE 8 | Simulated 6-day variations differences between two periods (1987–2012 – 1961–1982) in panel **(A)** Chl:C ratio, **(B)** DIN concentration, **(C)** DIP concentration, and **(D)** zooplankton; all in areas "C" and "T" in log-10 scale.

of turbidity in the model may fail to capture actual spatial–temporal patterns, which act as an important control of near-shore BGC.

The transitional regions are still affected by the input of optically active constituents such as suspended particulate material and colored dissolved organic matter, which strongly limit the light availability for autotrophic growth (Cadee and Hegeman, 2002). In our long-term simulation, the strengthening of westerly winds after 1986 leads to an elevated transport of more clear offshore water into the "T" area, thereby increasing light availability. In the model simulation, this improvement triggers a decreased Chl:C ratio in "T." Acclimation in Chl:C allows the typically light-limited coastal to transitional phytoplankton to more effectively utilize low nutrient concentration. In addition, the "T" area is located in an intermittently stratified region (van Leeuwen et al., 2015; Capuzzo et al., 2018). The increase in biomass after 1986 occurs mainly in spring, parallel to small changes in stratification intensity. We find a strengthening of stratification (defined as in Lowe et al., 2009) near Helgoland in early spring (**Supplementary Figure S4**), which is related to increased water column stability and better light availability (Bopp et al., 2001), and thus a higher bloom peak. In summer, however, stratification has been suggested to increase only in the northern North Sea, while decreasing in the SNS (Emeis et al., 2015).

The relative increase in simulated phytoplankton biomass at the coast is higher than in the transitional region. The differential trend reflects differences in winter concentration of DIN, which stays invariant at the coast ("C") but decreases in the transitional sea ("T"). This reduction in winter DIN in transitional water partially compensates the effect of the improved light environment and weakens primary production.

These regional differences in trends between models, but also between observations at different locations in the SNS underline the relevance of high-resolution spatial monitoring for assessing trends directly and for validating models. We confirm earlier findings on long-term changes in biomass and productivity for the offshore SNS but reveal a more complex picture for near-shore and transitional waters. The latter host the highest productivity in the SNS (Lemmen, 2018; Slavik et al., 2019) so that the opposing trend here cannot be simply neglected.

The reliability of models and set-ups demonstrated for hindcast studies is critical for making future projections (e.g., Wakelin et al., 2015; Holt et al., 2016; Daewel and Schrum, 2017). Our study has identified benchmarks in terms of relevant spatial–temporal BGC patterns such as Chl accumulation in turbid near-coast waters, or the biomass increase in coastal to transitional waters after the onset of de-eutrophication. If these patterns cannot be reproduced, it may be still too early to generate future scenarios.

A high-resolution physical model set-up that extends into very shallow water and is able to represent areas of the coast that are dry during low tide (such as GETM, in our case) is clearly needed for simulating coastal dynamics. In addition, advanced ecosystem models, which differ from classical NPZD-type models may be required to catch essential response mechanisms. For example, we found as key for simulating highly variable coastal–shelf ecosystems the capability to resolve acclimation in phytoplankton physiology, which has already been demonstrated to be important for the decoupling of the nutrient–biomass dynamics (Kerimoglu et al., 2017, 2018). Other aspects include behavioral changes in vertical swimming of phytoplankton, viral dynamics, and the non-uniform distribution of carnivory, all of which have been shown to be of importance for shaping the coastal gradient (Baschek et al., 2017; Wirtz, 2019). Along with these processes, our results demonstrate that stressors such as changes in temperature, wind, or nutrient reduction do not act in isolation, but may compensate (or amplify) each other. Beside systems modeling, there is currently no alternative approach in sight to analyze and predict responses to multiple stressors at ecosystem scales. Recommendations can also be made for monitoring strategies: Many coastal time-series stations in the SNS area are located in small patches where our model predicts an opposite trend than found for the surrounding waters. This coincidence calls for a strengthening of spatially continuous monitoring techniques such as CPR, satellite remote sensing, ferrybox, gliders, and scanfish as partially realized by the COSYNA system (Baschek et al., 2017).

SUMMARY

We have presented and analyzed a long-term simulation of ecosystem dynamics in the southern North Sea. A major and counterintuitive finding is the increased autotrophic biomass in near-coast and transitional waters against the ongoing de-eutrophication trends. This increase is attributed to compounding factors such as improved light availability caused by a changed wind regime, possible strengthening of trophic cascading at higher temperature, and the acclimative capacity of phytoplankton. These factors are in general neglected in state-of-the-art ecosystem models coupled within an ESM context. Also, *in situ* observations match locally deviating trends in our reconstruction, calling into question the representability of station data for highly variable coastal–shelf ecosystems.

DATA AVAILABILITY STATEMENT

Publicly available datasets were analyzed in this study. This data can be found here: www.coastdat.de, doi: 10.17031/1650.

AUTHOR CONTRIBUTIONS

XX worked on data analysis, figures, and the manuscript. CL worked on the model set up, data analysis, and the manuscript. KW worked on the model simulation and the manuscript.

ACKNOWLEDGMENTS

The work was supported by the program PACES of the Helmholtz society. We thank Pierre Helaouet and David Johns from Continuous Plonkton Recorder Survey who provided the long-term CPR data. We would also like to show our gratitude to to the two reviewers for their comments which help us greatly improved the manuscript.

SUPPLEMENTARY MATERIAL

The Supplementary Material for this article can be found online at: https://www.frontiersin.org/articles/10.3389/fmars.2020.00662/full#supplementary-material

REFERENCES

Alheit, J., Möllmann, C., Dutz, J., Kornilovs, G., Loewe, P., Mohrholz, V., et al. (2005). Synchronous ecological regime shifts in the central Baltic and the North Sea in the late 1980s. *ICES J. Mar. Sci.* 62, 1205–1215. doi: 10.1016/j.icesjms.2005.04.024

Baschek, B., Benavides, I., North, R. P., Smith, G., and Miller, D. (2017). Submesoscale dynamics in the coastal ocean. *J. Acoust. Soc. Am.* 141:3545.

Batten, S. D., Walne, A. W., Edwards, M., and Groom, S. B. (2003). Phytoplankton biomass from continuous plankton recorder data: an assessment of the phytoplankton colour index. *J. Plankton Res.* 25, 697–702. doi: 10.1093/plankt/25.7.697

Beaugrand, G. (2004). The North Sea regime shift: evidence, causes, mechanisms and consequences. *Prog. Oceanogr.* 60, 245–266.

Beaugrand, G., Luczak, C., and Edwards, M. (2009). Rapid biogeographical plankton shifts in the North Atlantic Ocean. *Glob. Change Biol.* 15, 1790–1803. doi: 10.1111/j.1365-2486.2009.01848.x

Bopp, L., Monfray, P., Aumont, O., Dufresne, J. L., LeTreut, H., Madec, G., et al. (2001). Orr, potential impact of climate change on marine export production. *Global Biogeochem. Cycles* 15, 81–100.

Bruggeman, J., and Bolding, K. (2014). A general framework for aquatic biogeochemical models. *Environ. Model. Softw.* 61, 249–265. doi: 10.1016/j.envsoft.2014.04.002

Burchard, H., and Bolding, K. (2002). GETM – a general estuarine transport model. *Sci. Document.*

Burchard, H., Bolding, K., Kühn, W., Meister, A., Neumann, T., and Tand Umlauf, L. (2006). Description of a flexible and extendable physical–biogeochemical model system for the water column. *J. Mar. Syst.* 61, 180–211. doi: 10.1016/j.jmarsys.2005.04.011

Burson, A., Stomp, M., Akil, L., Brussaard, C. P. D., and Huisman, J. (2016). Unbalanced reduction of nutrient loads has created an offshore gradient from phosphorus to nitrogen limitation in the North Sea. *Limnol. Oceanogr.* 61, 869–888. doi: 10.1002/lno.10257

Cadee, G., and Hegeman, J. (2002). Phytoplankton in the Marsdiep at the end of the 20th century; 30 years monitoring biomass, primary production, and phaeocystis blooms. *J. Sea Res.* 48, 97–110. doi: 10.1016/s1385-1101(02)00161-2

Capuzzo, E., Lynam, C. P., Barry, J., Stephens, D., Forster, R. M., Greenwood, N., et al. (2018). A decline in primary production in the North Sea over 25 years, associated with reductions in zooplankton abundance and fish stock recruitment. *Glob. Change Biol.* 24, e352–e364. doi: 10.1111/gcb.13916

Chassot, E., Bonhommeau, S., Dulvy, N. K., Melin, F., Watson, R., Gascuel, D., et al. (2010). Global marine primary production constrains fishery catches. *Ecol. Lett.* 13, 495–505. doi: 10.1111/j.1461-0248.2010.01443.x

Colebrook, J. M., and Robinson, G. A. (1965). Continuous plankton records: seasonal cycles of phytoplankton and copepods in the northeastern Atlantic and the North Sea. *Bull. Mar. Ecol.* 6, 123–139.

Daewel, U., and Schrum, C. (2013). Simulating long-term dynamics of the coupled North sea and Baltic Sea ecosystem with ECOSMO II: model description and validation. *J. Mar. Syst.* 11, 30–49. doi: 10.1016/j.jmarsys.2013.03.008

Daewel, U., and Schrum, C. (2017). Low-frequency variability in North Sea and Baltic Sea identified through simulations with the 3-D coupled physical–biogeochemical model ECOSMO. *Earth Syst. Dyn.* 8, 801–815. doi: 10.5194/esd-8-801-2017

Daewel, U., Schrum, C., and Gupta, A. K. (2015). The predictive potential of early life stage individual-based models (IBMs): an example for Atlantic cod *Gadus morhua* in the North Sea. *Mar. Ecol. Prog. Ser.* 534, 199–219. doi: 10.3354/meps11367

Desmit, X., Nohe, A., Borges, A. V., Prins, T., De Cauwer, K., Lagring, R., et al. (2019). Changes in chlorophyll concentration and phenology in the North Sea in relation to de-eutrophication and sea surface warming. *Limnol. Oceanogr* 9999, 1–20.

Ducrotoy, J. P., Elliott, M., and Jonge, V. N. (2000). The north sea. *Mar. Pollut. Bull.* 41, 5–23.

Edwards, M., Beaugrand, G., Reid, P. C., Rowden, A. A., and Jones, M. B. (2002). Ocean climate anomalies and the ecology of the North Sea. *Mar. Ecol. Prog. Ser.* 239, 1–10. doi: 10.3354/meps239001

Edwards, M., Johns, D. G., Leterme, S. C., Svendsen, E., and Richardson, A. J. (2006). Regional climate change and harmful algal blooms in the northeast Atlantic. *Limnol. Oceanogr* 820–829. doi: 10.4319/lo.2006.51.2.0820

Eisele, A., and Kerimoglu, O. (2015). *MOSSCO River data basis – Riverine Nutrient Inputs*. Germany: Helmholtz-Zentrum Geesthacht Centre for Materials and Coastal Research.

Emeis, K. C., van Beusekom, J., Callies, U., Ebinghaus, R., Kannen, A., Kraus, G., et al. (2015). The North Sea – A shelf sea in the Anthropocene. *J. Marine Syst.* 141, 18–33.

Falkowski, P. G., and Raven, J. A. (eds). (2007). in *Aquatic Photosynthesis*, Princeton: Princeton University Press, 1–43.

Field, C. B., Behrenfeld, M. J., Randerson, J. T., and Falkowski, P. (1998). Primary production of the biosphere: integrating terrestrial and oceanic components. *Science* 281, 237–240. doi: 10.1126/science.281.5374.237

Fock, H. O. (2003). Changes in the seasonal cycles of inorganic nutrients in the coastal zone of the southeastern North Sea from 1960 to 1997: effects of eutrophication and sensitivity to meteoclimatic factors. *Mar. Pollut. Bull.* 46, 1434–1449. doi: 10.1016/s0025-326x(03)00287-x

Ford, D. A., van der Molen, J., Hyder, K., Bacon, J., Barciela, R., Creach, V., et al. (2017). Observing and modelling phytoplankton community structure in the North Sea. *Biogeosciences* 14, 1419–1444. doi: 10.5194/bg-14-1419-2017

Geyer, B. (2014). High-resolution atmospheric reconstruction for Europe 1948–2012: coastDat2. *Earth Syst. Sci. Data* 6, 147–164. doi: 10.5194/essd-6-147-2014

Gräwe, U., Holtermann, P., Klingbeil, K., and Burchard, H. (2015). Advantages of vertically adaptive coordinates in numerical models of stratified shelf seas. *Ocean Model.* 92, 56–68. doi: 10.1016/j.ocemod.2015.05.008

Grosse, F., Greenwood, N., Kreus, M., Lenhart, H. J., Machoczek, D., Pätsch, J., et al. (2016). Looking beyond stratification: a model-based analysis of the biological drivers of oxygen deficiency in the North Sea. *Biogeosciences* 13, 2511–2535. doi: 10.5194/bg-13-2511-2016

Hays, G. C., and Lindley, J. A. (1994). Estimating chlorophyll a abundance from the 'phytoplankton colour' recorded by the Continuous Plankton Recorder survey: validation with simultaneous fluorometry. *Journal of Plankton Research* 16, 23–34. doi: 10.1093/plankt/16.1.23

Hays, G. C., and Warner, A. J. (1993). Consistency of towing speed an sampling depth for the continuous plankton recorder . *J. Mar. Biol. Assoc. U. K.* 73, 967–970. doi: 10.1017/s0025315400034846

Helaouet, P. (2020). *Marine Biological Association of the UK (MBA): 2020 Marine Biological Association of the UK (MBA) CPR Data request Xu Xu Helmholtz-Zentrum Geesthacht*. Geesthacht: DASSH.

Hofmeister, R., Burchard, H., and Beckers, J.-M. (2010). Non-uniform adaptive vertical grids for 3D numerical ocean models. *Ocean Model.* 33, 70–86. doi: 10.1016/j.ocemod.2009.12.003

Hofmeister, R., Lemmen, C., Kerimoglu, O., Wirtz, K. W., and Nasermoaddeli, M. H. (2014). "The predominant processes controlling vertical nutrient and suspended matter fluxes across domains - using the new MOSSCO system form coastal sea sediments up to the atmosphere," in *Proceedings of the 11th International Conference on Hydroscience and Engineering*, eds R. Lehfeldt and R. Kopmann, Hamburg.

Holt, J., Schrum, C., Cannaby, H., Daewel, U., Allen, I., Artioli, Y., et al. (2016). Potential impacts of climate change on the primary productionof regional seas: a comparative analysis of five European seas. *Progress Oceanogr.* 140, 91–115. doi: 10.1016/j.pocean.2015.11.004

Høyer, J. L., and Karagali, I. (2016). Sea surface temperature cli- mate data record for the North Sea and Baltic Sea. *J. Clim.* 29, 2529–2541. doi: 10.1175/jcli-d-15-0663.1

Jaagus, J., Sepp, M., Tamm, T., Järvet, A., and Moisja, K. (2017). Trends and regime shifts in climatic conditions and river runoff in Estonia during 1951–2015. *Earth Syst. Dynam.* 8, 963–976. doi: 10.5194/esd-8-963-2017

Kerimoglu, O., Große, F., Kreus, M., Lenhart, H. J., and van Beusekom, J. E. E. (2018). A model-based projection of historical state of a coastal ecosystem: relevance of phytoplankton stoichiometry. *Sci. Total Environ.* 639, 1311–1323. doi: 10.1016/j.scitotenv.2018.05.215

Kerimoglu, O., Hofmeister, R., Maerz, J., and Wirtz, K. W. (2017). The acclimative biogeochemical model of the southern North Sea. *Biogeosciences* 14, 4499–4531. doi: 10.5194/bg-14-4499-2017

Lemmen, C. (2018). North sea ecosystem-scale model-based quantification of net primary productivity changes by the benthic filter feeder mytilus edulis. *Water* 10:1527. doi: 10.3390/w10111527

Lemmen, C., Hofmeister, R., Klingbei, K., Nasermoaddeli, M. H., Kerimoglu, O., Burchard, H., et al. (2018). "Modular System for Shelves and Coasts (MOSSCO v1.0) – a flexible and multi-component framework for coupled coastal ocean ecosystem modelling. *Geosci. Model. Dev.* 11, 915–935. doi: 10.5194/gmd-11-915-2018

Lenhart, H. J., Mills, D. K., Baretta-Bekker, H., van Leeuwen, S. M., van der Molen, J., Baretta, J. W., et al. (2010). Predicting the consequences of nutrient reduction on the eutrophication status of the North Sea. *J. Mar. Syst.* 81, 148–170. doi: 10.1016/j.jmarsys.2009.12.014

Lo, T. T., and Hsu, H. H. (2010). Change in the dominant decadal patterns and the late 1980 s abrupt warming in the extratropical Northern Hemisphere. *Atmos. Sci. Lett.* 11, 210–215. doi: 10.1002/asl.275

Lowe, J. A., Howard, T. P., Pardaens, A., Tinker, J., Holt, J., Wakelin, S., et al. (2009). *UK Climate Projections Science Report: Marine And Coastal Projections*. Exeter: Met Office Hadley Center, 99.

Lynam, C. P., Llope, M., Möllmann, C., Helaouët, P., Bayliss-Brown, G. A., and Stenseth, N. C. (2017). Interaction between top-down and bottom-up control in marine food webs. *PNAS* 114, 1952–1957. doi: 10.1073/pnas.1621037114

McQuatters-Gollop, A., Edwards, M., Helaouëta, P., Johns, D. G., Owens, N. J. P., Raitsos, D. E., et al. (2015). The continuous plankton recorder survey: how can long-term phytoplankton datasets contribute to the assessment of good environmental status? *Estuar. Coast. Shelf Sci.* 162, 88–97. doi: 10.1016/j.ecss.2015.05.010

Meyer, J., Nehmer, P., Moll, A., and Kröncke, I. (2018). Shifting south-eastern North Sea macrofauna community structure since 1986: a response to de-eutrophication and regionally decreasing food supply? *Estuar. Coast. Shelf Sci.* 213, 115–127. doi: 10.1016/j.ecss.2018.08.010

Müller, D., Krasemann, H., Brewin, R. J. W., Brockmann, C., Deschamps, P.-Y., Doerffer, R., et al. (2015). The Ocean Col- our climate change initiative: I. A methodology for assessing atmospheric correction processors based on in-situ measurements. *Remote Sens. Environ.* 162, 242–256. doi: 10.1016/j.rse.2013.11.026

Nasermoaddeli, M. H., Lemmen, C., Stigge, G., Burchard, H., Klingbeil, K., Hofmeister, R., et al. (2018). A model study on the large-scale effect of macrofauna on the suspended sediment concentration in a shallow shelf sea. *Estuar. Coast. Shelf Sci.* 211, 62–76. doi: 10.1016/j.ecss.2017.11.002

Nezlin, N. P., Sutula, M. A., Stumpf, R. P., and Sengupta, A. (2012). The Ocean col- our climate change initiative: I. A methodology for assessing atmospheric correction processors based on in-situ measurements. *J.Geophys. Res. O.* 162, 242–256. doi: 10.1016/j.ecss.2017.11.002

Olsen, E. M., Ottersen, G., Llope, M., Chan, K.-S., Beaugrand, G., and Stenseth, N. C. (2011). Spawning stock and recruitment in North Sea cod shaped by food and climate. *Proc. Soc, R. B* 278, 504–510. doi: 10.1098/rspb.2010.1465

Painting, S., Foden, J., Forster, R., van der Molen, J., Aldridge, J., Best, M., et al. (2013). Impacts of climate change on nutrient enrichment. *MCCIP Sci. Rev.* 2013, 219–235.

Radach, G., and Pätsch, J. (2007). Variability of continental riverine freshwater and nutrient inputs into the north sea for the years 1977–2000 and its consequences for the assessment of eutrophication. *Estuaries Coasts* 30, 66–81. doi: 10.1007/bf02782968

Raitsos, D. E., Reid, P. C., Lavender, S. J., Edwards, M., and Richardson, A. J. (2005). Extending the SeaWiFS chlorophyll dataset back 50 years in the north-east Atlantic. *Geophy. Res. Lett.* 32:L06603. doi: 10.1029/2005GL022484

Reid, P. C., Edwards, M., Hunt, H. G., and Wamer, J. A. (1998). Phytoplankton change in the North Atlantic. *Nature* 391, 546.

Ribalet, F., Marchetti, A., Hubbard, K. A., Brown, K., Durkin, C. A., Morales, R., et al. (2010). Unveiling a phytoplankton hotspot at a narrow boundary between coastal and offshore waters. *PNAS* 38, 16571–16576. doi: 10.1073/pnas.1005638107

Richardson, A. J., Walne, A. W., John, A. W. G., Jonas, T. D., Lindley, J. A., Sims, D. W., et al. (2006). Using continuous plankton recorder data. *Progress Oceanogr.* 68, 27–74. doi: 10.1016/j.pocean.2005.09.011

Schlüter, M. H., Merico, A., Wiltshire, K. H., Greve, W., and von Storch, H. (2008). A statistical analysis of climate variability and ecosystem response in the German Bight. *Ocean Dyn.* 58, 169–186. doi: 10.1007/s10236-008-0146-5

Slavik, K., Lemmen, C., Zhang, W., Kerimoglu, O., Klingbeil, K., and Wirtz, K. W. (2019). The large scale impact of offshore windfarm structures on pelagic primary production in the southern North Sea. *Hydrobiologia* 845, 35–53. doi: 10.1007/s10750-018-3653-5

Smaal, A. C., Schellekens, T., van Stralen, M. R., and Kromkamp, J. C. (2013). Decrease of the carrying capacity of the Oosterschelde estuary (SW Delta, NL) for bivalve filter feeders due to overgrazing? *Aquaculture* 40, 28–34. doi: 10.1016/j.aquaculture.2013.04.008

Soetaert, K., Herman, P. M., and Middelburg, J. J. (1996). A model of early diagenetic processes from the shelf to abyssal depths. *Geochim Cosmochim Acta* 60, 1019–1040. doi: 10.1016/0016-7037(96)00013-0

Stips, A., Bolding, K., Pohlmann, T., and Burchard, H. (2004). Simulating the temporal and spatial dynamics of the North Sea using the new model GETM (general estuarine transport model). *Ocean Dyn.* 54, 266–283. doi: 10.1007/s10236-003-0077-0

Taylor, A. H., Icarus, A. J., and Clark, P. A. (2000). Extraction of a weak climatic signal by an ecosystem. *Nature* 416, 629–632. doi: 10.1038/416629a

Theurich, G., DeLuca, C., Campbell, T., Liu, F., Saint, K., Vertenstein, M., et al. (2016). the earth system prediction suite: toward a coordinated U.S. modeling capability. *Bull. Am. Meteorol. Soc.* 97, 1229–1247. doi: 10.1175/bams-d-14-00164.1

Truong, C., Oudre, L., and Vayatis, N. (2020). Selective review of offline change point detection methods. *Signal Procedding* 167:107299. doi: 10.1016/j.sigpro.2019.107299

van Aken, H. M. (2010). Meteorological forcing of long-term temperature variations of the Dutch coastal waters. *J. Sea Res.* 63, 143–151. doi: 10.1016/j.seares.2009.11.005

van Beusekom, J. E. E., Loebl, M., and Martens, P. (2009). Distant riverine nutrient supply and local temperature drive the long-term phytoplankton development in a temperate coastal basin. *J. Sea Res.* 61, 26–33. doi: 10.1016/j.seares.2008.06.005

van Leeuwen, S., Tett, P., Mills, D., and van der Molen, J. (2015). Stratified and nonstratified areas in the North Sea: long-term variability and biological and policy implications. *J. Geophy. Res. Oceans* 120, 4670–4686. doi: 10.1002/2014jc010485

Visser, M., Batten, S., Becker, G., Bot, P., Colijn, F., Damm, P., et al. (1996). Time series analysis of monthly mean data of temperature, salinity, nutrients, suspended matter, phyto- and zooplankton at eight locations on the Northwest European shelf. *Deutsche Hydrographische Zeitschrift* 48, 299–323. doi: 10.1007/bf02799376

Wakelin, S. L., Artioli, Y., Butenschön, M., Allen, J. I., and Holt, J. T. (2015). Modelling the combined impacts of climate change and direct anthropogenic drivers on the ecosystem of the northwest european continental shelf. *J. Marine Syst.* 152, 51–63. doi: 10.1016/j.jmarsys.2015.07.006

Weijerman, M., Lindeboom, H., and Zuur, A. F. (2005). Regime shifts in marine ecosystems of the North Sea and Wadden Sea. *Mar. Ecol. Prog. Ser.* 298, 21–39. doi: 10.3354/meps298021

Wiltshire, K. H., Kraberg, A., Bartsch, I., Boersma, M., Franke, H. D., Freund, J., et al. (2010). Helgoland roads, north Sea: 45 years of change. *Estuaries Coasts* 33, 295–310. doi: 10.1007/s12237-009-9228-y

Wirtz, K. W. (2019). Physics or biology? Persistent chlorophyll accumulation in a shallow coastal sea explained by pathogens and carnivorous grazing. *PLoS One* 14:e0212143. doi: 10.1371/journal.pone.0212143

Wirtz, K. W., and Kerimoglu, O. (2016). Autotrophic stoichiometry emerging from optimality and variable co-limitation. *Front. Ecol Evol.*:4:131. doi: 10.3389/fevo.2016.00131

Conflict of Interest: The authors declare that the research was conducted in the absence of any commercial or financial relationships that could be construed as a potential conflict of interest.

frontiers in Marine Science

ORIGINAL RESEARCH
published: 10 September 2020
doi: 10.3389/fmars.2020.00698

Scaling Global Warming Impacts on Ocean Ecosystems: Lessons From a Suite of Earth System Models

Alexis Bahl, Anand Gnanadesikan and Marie-Aude S. Pradal*

Department of Earth and Planetary Sciences, Johns Hopkins University, Baltimore, MD, United States

Edited by:
Darren Pilcher,
University of Washington and
NOAA/PMEL, United States

Reviewed by:
Ivy Frenger,
GEOMAR Helmholtz Center for Ocean
Research Kiel, Germany
Marina Levy,
Institut Pierre Simon Laplace
(IPSL), France

***Correspondence:**
Anand Gnanadesikan
gnanades@jhu.edu

Specialty section:
This article was submitted to
Global Change and the Future Ocean,
a section of the journal
Frontiers in Marine Science

Received: *14 March 2020*
Accepted: *31 July 2020*
Published: *10 September 2020*

Citation:
Bahl A, Gnanadesikan A and
Pradal M-AS (2020) Scaling Global
Warming Impacts on Ocean
Ecosystems: Lessons From a Suite of
Earth System Models.
Front. Mar. Sci. 7:698.
doi: 10.3389/fmars.2020.00698

An important technique used by climate modelers to isolate the impacts of increasing greenhouse gasses on Earth System processes is to simulate the impact of an abrupt increase in carbon dioxide. The spatial pattern of change provides a “fingerprint” that is generally much larger than natural variability. Insofar as the response to radiative forcing is linear (the impact of quadrupling CO_2 is twice the impact of doubling CO_2) this fingerprint can then be used to estimate the impact of historical greenhouse gas forcing. However, the degree to which biogeochemical cycles respond linearly to radiative forcing has rarely been tested. In this paper, we evaluate which ocean biogeochemical fields are likely to respond linearly to changing radiative forcing, which ones do not, and where linearity breaks down. We also demonstrate that the representation of lateral mixing by mesoscale eddies, which varies significantly across climate models, plays an important role in modulating the breakdown of linearity. Globally integrated surface rates of biogeochemical cycling (primary productivity, particulate export) respond in a relatively linear fashion and are only moderately sensitive to mixing. By contrast, the habitability of the interior ocean (as determined by hypoxia and calcite supersaturation) behaves non-linearly and is very sensitive to mixing. This is because the deep ocean, as well as certain regions in the surface ocean, are very sensitive to the magnitude of deep wintertime convection. The cessation of convection under global warming is strongly modulated by the representation of eddy mixing.

Keywords: eddy mixing, climate change, climate sensitivity, primary productivity, export, ocean deoxygenation, calcite undersaturation, oceanic convection

INTRODUCTION

Over the past two decades, Earth System Models (ESMs) have become an important tool for estimating how rising atmospheric carbon dioxide (CO_2) concentrations have impacted global biogeochemical cycling and projecting how it will change in the future (e.g., Bopp et al., 2001, 2013; Fung et al., 2005; Schmittner et al., 2008). One major focus has been the rate of anthropogenic carbon uptake (Frölicher et al., 2009; Heinze et al., 2019), which is important for setting cumulative emissions targets to limit and reduce the risks of rising atmospheric CO_2 levels. Other investigators have focussed on changes in ocean primary and export production (Cabré et al., 2015a; Frölicher et al., 2016) which may have implications for the future of fisheries. Still others are concerned with increasing ocean acidification at and away from the surface (Orr et al., 2005), and the growth of oxygen minimum zones (OMZs; Stramma et al., 2012), both of which have the potential to affect which regions are habitable by a range of species. However, isolating the impact of climate change is complicated by the presence of large-amplitude, long-period natural variability, and by the fact that the surface radiation balance has been changed by both greenhouse gasses and aerosols (Shine et al., 1990; Knutti and Hegerl, 2008). For example, recent trends in Pacific oxygen concentrations are thought to be the result of decadal variability in winds associated with the Pacific Decadal Oscillation rather than part of a long-term trend associated with global warming (Deutsch et al., 2005; Kwon et al., 2016; Duteil et al., 2018).

One method by which climate modelers distinguish climate change forcing from natural variability is by simulating large-step function perturbations in forcing in which CO_2 concentrations are instantaneously quadrupled from pre-industrial concentrations (Friedlingstein et al., 2014). The resulting anthropogenic climate signal is generally much larger than the natural variability within a given model and thus allows for extracting the magnitude of the anthropogenic radiative forcing, for estimating the equilibrium temperature rise and most applicable to this study, for identifying the spatial pattern of climate change, often described as a "fingerprint" (Hegerl and Zwiers, 2011; Andrews et al., 2012). The "fingerprint" is further described by Hasselmann (1993) as an optimal detection method used to first, distinguish the externally generated time-dependent greenhouse warming signal over time from the background noise associated with natural variability and second, extract variables with high signal-to-noise ratio. Such "$4xCO_2$" runs have become a standard part of the Intergovernmental Panel on Climate Change (IPCC) model comparison process.

This method can also be used to distinguish historical changes in biogeochemical processes driven by climate change from those driven by natural variability (Heinze et al., 2019). However, such a separation is only possible if the responses to such forcing are linear. If the fingerprint due to increased radiative forcing has a different pattern when the forcing is large than when it is small, some fraction of the real change at small values of forcing will be erroneously attributed to climate variability. Cao et al. (2014) found differing sensitivities of ocean oxygen in the North Pacific and at a global scale when changing the climate sensitivity in an intermediate-complexity ESM, implying such non-linear behavior. However, there has been limited evaluation of the linearity of global and regional biogeochemical responses to climate change in fully coupled ESMs.

In this paper, we attempt to answer the following three questions about the linearity of biogeochemical responses to climate change:

1. What fields respond linearly to step changes in radiative forcing? Because the radiative response to increasing carbon dioxide is roughly logarithmic (Zhang and Huang, 2014), we examine whether quadrupling CO_2 (denoted as a $4xCO_2$ simulation) produces twice the response of doubling CO_2 (denoted as a $2xCO_2$ simulation). Insofar as it does, it is reasonable to use the magnitude and pattern of the changes in biogeochemical cycling under $4xCO_2$ to estimate how much of a change has already resulted from historical increases in greenhouse gas forcing.
2. What fields do not respond linearly to step changes in radiative forcing? If the change in some field in the $2xCO_2$ simulation is much larger than half the change in the $4xCO_2$ simulation, this would imply that the standard IPCC methodology would underestimate the historical impact of increased greenhouse gasses (Taylor et al., 2011). If the reverse is true, the standard methodology would overestimate the historical impact.
3. What model parameters and processes are implicated when linearity breaks down? It is difficult to answer this question across models (Frölicher et al., 2016). This is partly because simulating biogeochemistry requires understanding changes in environmental conditions such as temperature, stratification, and nutrient supply (Rykaczewski and Dunne, 2010; Taucher and Oschlies, 2011; Chust et al., 2014; Andrews et al., 2017) capturing the sensitivity of oceanic biology to these changes, and simulating how changes in biology feed back on environmental conditions. For example, Andrews et al. (2017) found that the sign and magnitude of oxygen change over the last ∼50 years depended critically on how ocean acidification changes the C:N ratio and calcium carbonate ballasting. The representation of processes like mixing and clouds can also play a big role in modulating model responses.

Because the response of the Earth System is dependent on a multitude of parameterizations a full exploration of the third question is impossible in one manuscript. However, we know from previous work (Palter and Trossman, 2018; Bahl et al., 2019) that the response of oceanic oxygen to global warming is extremely sensitive to the representation of lateral mixing from oceanic mesoscale eddies. While mesoscale eddies dominate both spatial and temporal variability in velocity (Lermusiaux, 2006), they occur at spatial scales that are generally smaller than the grid boxes used in models. Moreover, because of computational cost, high-resolution "eddy-permitting" models are still only run for periods of time much shorter than the many centuries required for biological and chemical fields to come to equilibrium. Thus, simulating long-term biogeochemical cycles will require that the effects of eddy velocity variability on the large-scale tracer field be parameterized for the foreseeable future. In this study we take advantage of key insights gained from Bahl et al. (2019) to examine how this uncertainty is reflected in the linearity of biogeochemical response.

The key variable or parameter used to represent the lateral mixing due to turbulent eddies is the turbulent diffusion coefficient, A_{REDI} (Redi, 1982). In previous work we have shown how the ocean uptake of anthropogenic carbon dioxide (Gnanadesikan et al., 2015a), as well as the patterns and rates of oceanic deoxygenation (Bahl et al., 2019), are impacted by the value and/or spatial distribution of this parameter. However, we have not examined the impact of changing diffusivity on the linearity of response. Here, we build on these previous studies to identify those regions and fields for which linear responses are unlikely to be robust across ESMs.

This paper is structured as follows: section Methodology covers model description, methods used, and experimental design. In section Results, we begin by examining a number of indices of biological cycling that are weakly sensitive to changes in A_{REDI} and respond relatively linearly to climate change. We then demonstrate that the biological cycling in Northern subpolar regions and the habitability of the ocean interior both respond non-linearly to climate change and are sensitive to the mixing coefficient A_{REDI}. Finally, we explore how convection in the subpolar regions connects these results, as it important for surface productivity and deep ventilation and depends on A_{REDI}. A major goal here is to give ecologically-oriented users of ESMs a better sense of what might drive large shifts in ecosystems, and why it is necessary to be cautious about extrapolating results based on large changes in forcing to explain present-day trends.

METHODOLOGY

Overview

We use the GFDL CM2Mc coupled climate model of Galbraith et al. (2011). This model is a coarse-resolution version of the National Oceanic and Atmospheric Administration's (NOAA) Geophysical Fluid Dynamics Laboratory (GFDL) CM2M, which was used in the IPCC's Fourth Assessment report. The coarsened resolution of the atmosphere and oceanic grids in CM2Mc allows for relatively fast simulations and allows us to explore multiple parameter settings.

Physical Model

The atmosphere uses a finite volume dynamical core discussed in Lin (2004) as implemented in CM2.1 (Delworth et al., 2006). The atmosphere model employs an updated M30 grid, with a latitudinal resolution of 3°, a longitudinal resolution of 3.75° and 24 vertical levels (Galbraith et al., 2011). Tracer time steps occur every 1.5 h, dynamical time steps occur every 9 min, and the radiative time step occurs every 3 h, allowing for explicit representation of the diurnal cycle of solar radiation.

Ocean circulation is simulated using a tripolar grid that varies with latitude. A fine latitudinal resolution of 0.6° at the equator allows for an explicit representation of equatorial currents. A total of 28 vertical levels gradually increase in thickness from 10 m near the surface to ∼500 m in the deepest box. Pressure is used as the vertical coordinate and the model is time stepped using an explicit bottom pressure solver that accounts for the transfer of water mass across the ocean surface using real freshwater fluxes. The use of partial bottom cells allows for a representation of topography that is less sensitive to vertical resolution. Exchange across straits is simulated using the cross-land mixing scheme of Griffies et al. (2005). Tracer advection uses the Multidimensional Piecewise Parabolic Method (MDPPM) scheme for temperature and salinity and the Sweby Multidimensional Flux Limited (MDFL) scheme for other tracers (Adcroft et al., 2004; Griffies et al., 2005; Galbraith et al., 2011).

Eddy Mixing

In this paper we focus on one parameter that we already know has the potential to impact the linearity of the biogeochemical response to increased greenhouse gasses. The lateral turbulent mixing coefficient, $A_{REDI,}$ determines the rate at which tracers are stirred horizontally in the mixed layer and laterally along isopycnals (neutral density surfaces) in the ocean interior. This process is represented using a Fickian diffusion approximation (Redi, 1982) such that the flux of tracer with concentration C in direction s (horizontal in the mixed layer or along-isopycnal in the ocean interior as the case may be) F_C^S is given by:

$$F_C^S = -A_{REDI}\frac{\partial C}{\partial s} \tag{1}$$

where A_{REDI} serves as our diffusion coefficient and the flux is down-gradient from high to low values of C.

In addition to stirring tracers along isopycnals, eddies draw their energy from sloping isopycnal surfaces, resulting in a flattening of these surfaces (Gent and McWilliams, 1990). The resulting overturning (shown here for the x-direction alone) results in a transport given by:

$$\left(F_C^x, F_C^z\right) = -C{*}A_{GM}{*}\left(\frac{\partial S_\rho^x}{\partial z}, -\frac{\partial S_\rho^x}{\partial x}\right) \tag{2}$$

where S_ρ^x is the isopycnal slope in the x direction and A_{GM} is a diffusion coefficient. As in CM2.1 Griffies et al. (2005), A_{GM} varies with the horizontal shear between a minimum of 200 m^2 s^{-1} and a maximum of 1,400 m^2 s^{-1}. The maximum slope used to calculate the overturning transport is set to 0.01 to avoid singularity in mixed layers.

Biogeochemical Model

Ocean biogeochemistry is simulated using the Biology-Light-Iron-Nutrients and Gases (BLING) model of Galbraith et al. (2010). BLING has six explicit tracers: dissolved inorganic carbon (DIC), alkalinity (Alk), micronutrient (nominally Fe), macronutrient (nominally PO_4), dissolved organic material, and oxygen, all of which are advected and diffused in the model similarly to temperature and salinity (Galbraith et al., 2010). BLING accounts for shortwave light absorption using a prognostic chlorophyll (Chl) variable, which varies with both biomass and a light and nutrient-dependent Chl:C ratio following Geider et al. (1996). When run in a fully coupled ESM, BLING produces annual mean distributions of Chl and surface macronutrients comparable to those associated with models that run numerous explicit tracers (Galbraith et al., 2015).

The key aspect of BLING is an allometric grazing parameterization [described in Dunne et al. (2005)] that results in phytoplankton biomass being (a) tightly linked to growth rate and (b) showing a much greater sensitivity for large (weakly grazing-controlled) phytoplankton than for small (strongly grazing-controlled) phytoplankton, as appears to be the case in the real ocean.

Growth rates are calculated by:

$$\mu = \mu_0{*}exp(k{*}T) * \min\left(\frac{PO_4}{K_{PO4}+PO_4}, \frac{Fe}{K_{Fe}+Fe}\right){*}\left(1-\exp\left(-\frac{Irr}{Irr_k}\right)\right) \tag{3}$$

where μ_0 is the maximum growth rate at 0°C, k is the Eppley coefficient, PO_4 and Fe are the macro- and micronutrient concentrations, $K_{PO4,Fe}$ are half saturation constants, and Irr_k is a light limitation constant that accounts for a chl:C ratio that depends on nutrient limitation, light supply, and temperature. The growth rate is assumed to come into balance with a grazing rate of:

$$\lambda = \lambda_0 \exp\left(k{*}T\right) * \left(\frac{P}{P_*}\right)^{1/a} \tag{4}$$

where λ_0 is a scaling for grazing rate, P is phytoplankton biomass in a particular size class, P_* is a scaling for this biomass, and a is a size-dependent coefficient. Solving this gives:

$$P = \left\{\left(\frac{\mu_0 P_*}{\lambda_0}\right) * \min\left(\frac{PO_4}{K_{PO4} + PO_4}, \frac{Fe}{K_{Fe} + Fe}\right) * \left(1 - \exp\left(-\frac{Irr}{Irr_k}\right)\right)\right\}^a = \left\{\left(\frac{\mu_0 P_*}{\lambda_0}\right) * Nut_{\lim} {*} Irr_{\lim}\right\}^a \tag{5}$$

where $Nut_{\lim}$ and $Irr_{\lim}$ represent nutrient and light limitation terms, respectively. For small phytoplankton $a = 1$, allowing for the system to approach the equilibrium given by the classic Lotke-Volterra equations and predicting a phytoplankton biomass that depends linearly on the growth rate, and thus on the most limiting nutrient at low concentrations of nutrients. For large phytoplankton, $a = 3$ and biomass is the cube of the growth rate, and thus on the cube of the most limiting nutrient at low concentrations of nutrients. However, because the grazing rates have the same $\exp(k^*T)$ temperature dependence, biomass is only weakly dependent on temperature. As pointed out by Taucher and Oschlies (2011), the relative temperature dependence of grazing and growth rate is poorly known and may be important for projecting future changes in productivity. The disproportionate response of large phytoplankton biomass to environmental changes is supported by observational estimates of the spatial distribution of biomass made via satellite (Kostadinov et al., 2009). However, it is inconsistent with past studies that have shown an increased abundance of small phytoplankton species such as small flagellates coinciding with a decrease of large phytoplankton (Rivero-Calle, 2016; Thomson et al., 2016).

Following Dunne et al. (2005), the export of sinking particles from the ocean surface to the deep (carrying both macro- and micro-nutrient) is parameterized in terms of the phytoplankton size structure and temperature. Grazing of large phytoplankton produces more particulate material than does grazing of small phytoplankton and more of this material sinks at lower temperatures. Organic material sinks with a constant velocity of 16 m/day over the top 80 m, but below 80 m, the sinking velocity decreases by 0.05 m/day/m (Galbraith et al., 2010). The rate of remineralization of organic material depends on the oxygen concentration within the water column resulting in deeper penetration of organic material under OMZs.

Additionally, as described in Galbraith et al. (2011) the model simulates the cycling of radiocarbon. Produced in the upper atmosphere by the interaction of galactic cosmic rays with nitrogen, the bulk of radiocarbon in the ocean-atmosphere system is taken up by the ocean and decays there. In our model, biological sources and sinks of $DI^{14}C$ are identical to those for DIC and thus have little impact on $\Delta^{14}C = \frac{DI^{14}C}{DIC} - 1$. However, air-sea exchange, physical transport and decay lead to different distribution patterns of $DI^{14}C$ and DIC and thus produce spatial patterns in $\Delta^{14}C$. Our model simulations do not include the impact of the 20th century atmospheric nuclear bomb tests and thus must be compared with estimates of the "prebomb" radiocarbon (Key et al., 2004).

Experimental Design

We present runs from six different cases. In four of them A_{REDI} is constant in space and time. These runs are denoted as AREDI-400, AREDI-800 (the case used to spin up ocean state from modern observations), AREDI-1200, and AREDI-2400, with the number denoting the value of the coefficient in $m^2\ s^{-1}$. AREDI-400 and AREDI-800 will often be described in this paper as low-mixing simulations, while AREDI-1200 and AREDI-2400 will be described as high-mixing simulations. As discussed in previous work (Gnanadesikan et al., 2015b) this range is comparable to that found across CMIP5 models. In the remaining two cases, denoted ABER2D and ABERZONAL, A_{REDI} varies in space but not in time. ABER2D uses the distribution found by Abernathey and Marshall (2013), who used velocities derived from altimetric measurements to advect tracers and invert a diffusion coefficient. Maps of this coefficient can be found in previous work (Gnanadesikan et al., 2015a,b; Bahl et al., 2019, Figure 2) and in the **Supplemental Material**.

A key difference between ABER2D and more traditional parametrizations is that the largest values of A_{REDI} (reaching up to 10,000 m^2/s) occur near, but not in, the center of the boundary currents. This is because the relevant length scale for mixing is not the width of the baroclinic zone, but rather the spatial scale over which propagating eddies exchange fluid. When eddies pass through a region rapidly (as they do in boundary currents), water has little time to feel the anomalous pressure of the eddy and is not moved very far (Nikurashin and Ferrari, 2011; Cole et al., 2015). ABERZONAL uses a zonally-averaged version of ABER2D, with low values in high latitudes and high values (exceeding 3,000 m^2/s) in subtropical latitudes. ABERZONAL was run to evaluate whether any signals seen in the ABER2D were primarily due to the large latitudinal changes in the size of the coefficient. If this were the case it would potentially allow a similar parameterization to be used in simulations of paleoclimates.

The AREDI-800 case was spun up starting from modern oceanic temperatures and salinities for 1,500 years with aerosols and greenhouse gases fixed at pre-industrial values. At year 1,500, the five additional cases with different A_{REDI} discussed above were branched off of the main trunk and all six simulations run out for another 500 years with fixed greenhouse gasses. Once the models hit year 1,860 (360 years into the pre-industrial control), two additional perturbations were performed. First, we instantaneously doubled CO_2 concentration from pre-industrial (286 ppmv) to 572 ppmv. Second, we instantaneously quadrupled CO_2 concentration values from the same pre-industrial values to 1,144 ppmv. Both the $2xCO_2$ and $4xCO_2$ simulations were then run out for 140 years.

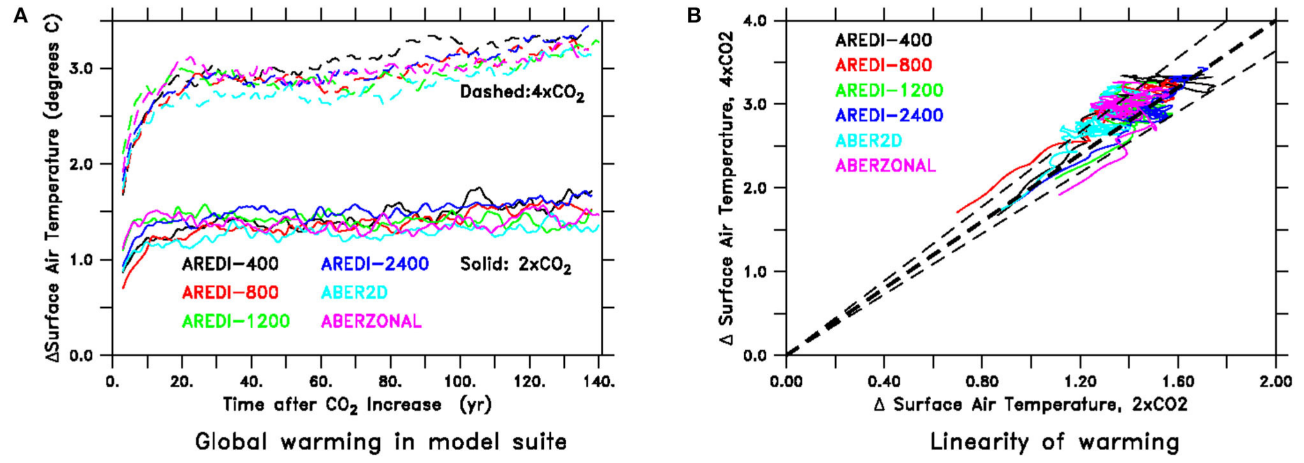

FIGURE 1 | Time-series of temperature response under global warming run for all six A_{REDI} simulations. **(A)** Change in surface air temperature in °C. Solid lines denote simulations under $2xCO_2$, dashed lines show the same simulations under $4xCO_2$. **(B)** Change in surface air temperature under $2xCO_2$ (horizontal axis) vs. change in surface air temperature under $4xCO_2$. 2:1 Line is shown by thick dashed line. Points lying within thin dashed lines are within 10% of a 2:1 relation, meaning that the response under $4xCO_2$ would predict the response under $2xCO_2$ to within about 10%.

RESULTS

Global Temperature Response to Increased CO_2 Is Relatively Insensitive to Eddy Mixing

We start by demonstrating that the standard metrics for global warming behave relatively linearly and are relatively insensitive to the representation of eddy mixing. One of the most important metrics is the climate sensitivity, defined as the response of global mean surface air temperature to a doubling of atmospheric carbon dioxide. As shown in **Figure 1A**, time series of the 5 year smoothed change in surface air temperature are relatively insensitive to the parameterization of mesoscale mixing, with the warming at the end of the 140 year period ranging between ∼1.3–1.6°C for the $2xCO_2$ cases and 3.1–3.5°C for the $4xCO_2$ cases. Note that despite the 5 year smoothing, the warming simulations all show the effects of interannual variability with a peak-to-trough amplitude of around 0.2°C, so that it is important not to overinterpret differences that are smaller than this. Plotting the $2xCO_2$ change against the $4xCO_2$ change (**Figure 1B**), we see that the models initially bracket a 2:1 line (thick dashed line). Over time the $4xCO_2$ cases tend to produce a warming that is slightly more than twice that associated with the $2xCO_2$ cases. The deviation from the 2:1 is generally <10%, as shown by the dashed lines. This means that taking the projected temperature response from the $4xCO_2$ model and dividing it by two would give the projected temperature response in the $2xCO_2$ model to within about 10%.

The relatively weak dependence of the warming on mixing is somewhat surprising, given that the initial climate states differ by up to 1.2°C. We computed the initial radiative forcing F associated with quadrupling CO_2 (ranging between 6.11 and 7.22 W/m^2) by regressing changes in net radiation at the top of the atmosphere against global temperature change (following Gregory et al., 2004). This is consistent with the 6.72 W/m^2 value found by Andrews et al. (2012) for the higher-resolution ESM2M and sits within the 5.85–8.5 W/m^2 found across 11 CMIP5 models. However, the range in initial radiative forcing is balanced by a similar range in how strongly the climate warms in response to that forcing, so that the equilibrium climate sensitivities under doubling range between 1.9 and 2.1°C, on the low end of the CMIP5 range. We defer a more in-depth discussion of these results to a future manuscript. For now, it is sufficient to note that our model has a typical radiative response to increasing CO_2 and that our $4xCO_2$ simulations lie in between the Representative Concentration Pathways (RCP) 6.0 and 8.5 in CMIP5, while our $2xCO_2$ simulations lie between the RCP2.6 and RCP4.5 pathways.

Weak Dependence of Surface Chemistry on Mixing in Control Simulations Outside Northern Subpolar Latitudes

A relatively weak sensitivity of the model to the representation of A_{REDI} is also found when examining the distribution of surface chemistry averaged over the final century of each simulation. As shown in **Figure 2**, the models capture large-scale spatial patterns of zonally-averaged annual mean macronutrient, total alkalinity Alk, and calcite supersaturation compared to observations (observed zonally averaged annual iron is not shown because of data sparsity). The largest disagreements amongst the models, as well as between the models and observations, are found in subpolar latitudes between 40 and 60°N. This is largely driven by the North Pacific subpolar gyre, where iron limitation appears to be much weaker in the model than in the real world (Nishioka, 2007). Increasing mixing produces higher macronutrients, particularly in the northern subpolar latitude band (**Figure 2A**). The low-mixing

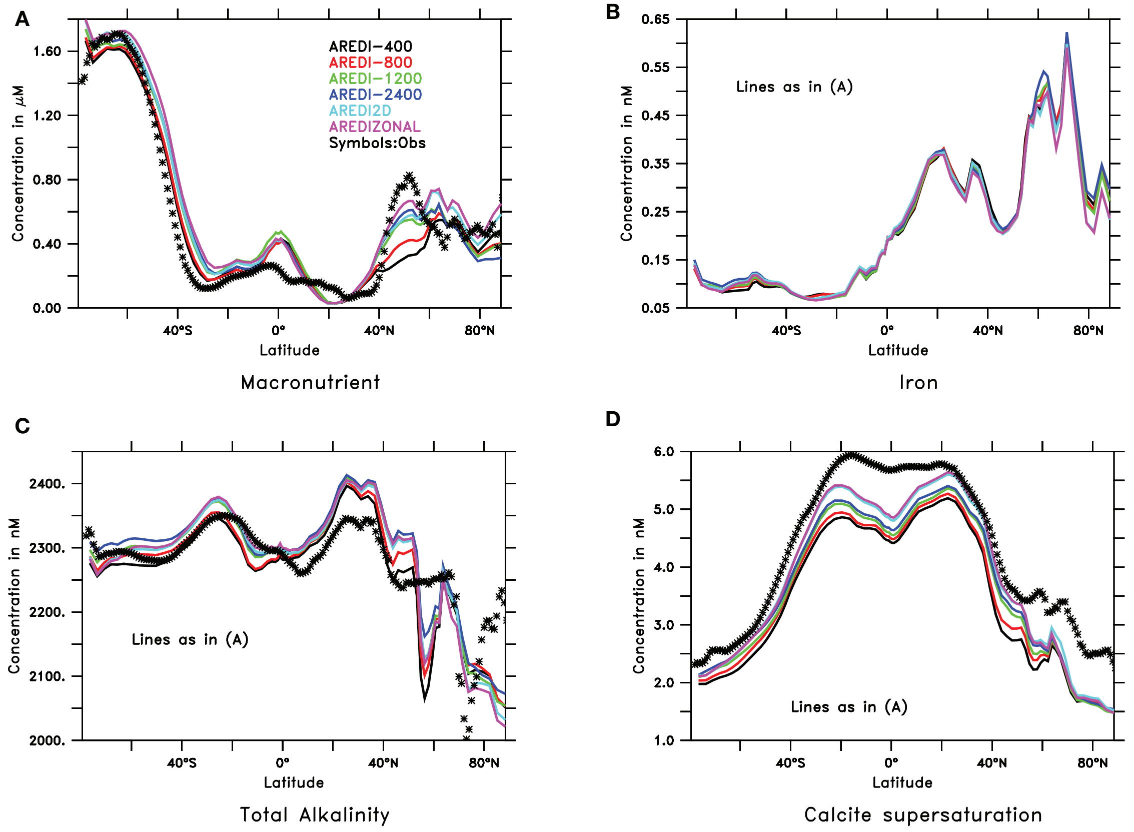

FIGURE 2 | Zonally averaged annual mean surface chemical fields in CM2Mc pre-industrial control run with six different A_{REDI} parameterizations compared to observations (symbols). Iron observations are not included due to a lack of reliable data. **(A)** Phosphate [µM, obs. from WOA09, Garcia et al. (2010)] **(B)** Iron (nM), **(C)** total alkalinity [µM, obs from Lauvset et al. (2016)], and **(D)** calcite supersaturation [non-dimensional, obs from Lauvset et al. (2016)].

simulation, AREDI-400 (black line) has the lowest values, and thus the biggest underestimate relative to observations while ABERZONAL (purple line) produces macronutrient surface estimates closest to observations.

The other hydrographic variables show less sensitivity to mixing. Iron (**Figure 2B**) and alkalinity (**Figure 2C**) both show relatively small differences across models, though Alk appears to increase with greater mixing. All the models simulate the zonal range of calcite supersaturation in surface waters, as seen in **Figure 2D**, however, all models underestimate the degree of calcite supersaturation relative to modern observations.

Dependence of Surface Biological Cycling on Mixing in Control Simulations

Chlorophyll Shows Weak Dependence on Mixing Outside Northern Subtropical Region

We now turn to how our mixing parameterizations affect integrative measures of ecosystem function that can be characterized using remote sensing. Despite major uncertainties in retrieval algorithms, the fact that satellites can monitor such fields with high spatial and temporal resolution allows for detection of global and regional trends. In this paper we consider a number of these variables that have been used to characterize global change. We start with Chl because it is relatively easy to detect from space and has been extensively examined for trends (e.g., Gregg et al., 2005; Henson et al., 2010; Rykaczewski and Dunne, 2011).

As is the case for nutrients, the modeled concentration of Chl in our suite (**Figure 3A**) is only moderately sensitive to the parameterization of A_{REDI}. All models capture the observed contrast between upwelling and downwelling regions and show broad similarities to observations in the Southern Ocean and the tropics. The models all overestimate Chl in the northern subtropics from 30 to 45°N. The largest sensitivity to mixing is found in these latitudes as well, with increasing mixing producing chlorophyll levels up to 50% higher than those seen in AREDI-400.

Biomass Shows Weak Dependence on Mixing Outside Northern Subtropical Region

Chl suffers from one major problem as a measure of ecosystem function. Because phytoplankton can change their chl:C ratio to match the availability of nutrients (Geider et al., 1996), a decline in Chl in response to an increase in light availability may not represent a decline in the total amount of biomass in an ecosystem. For this reason, we

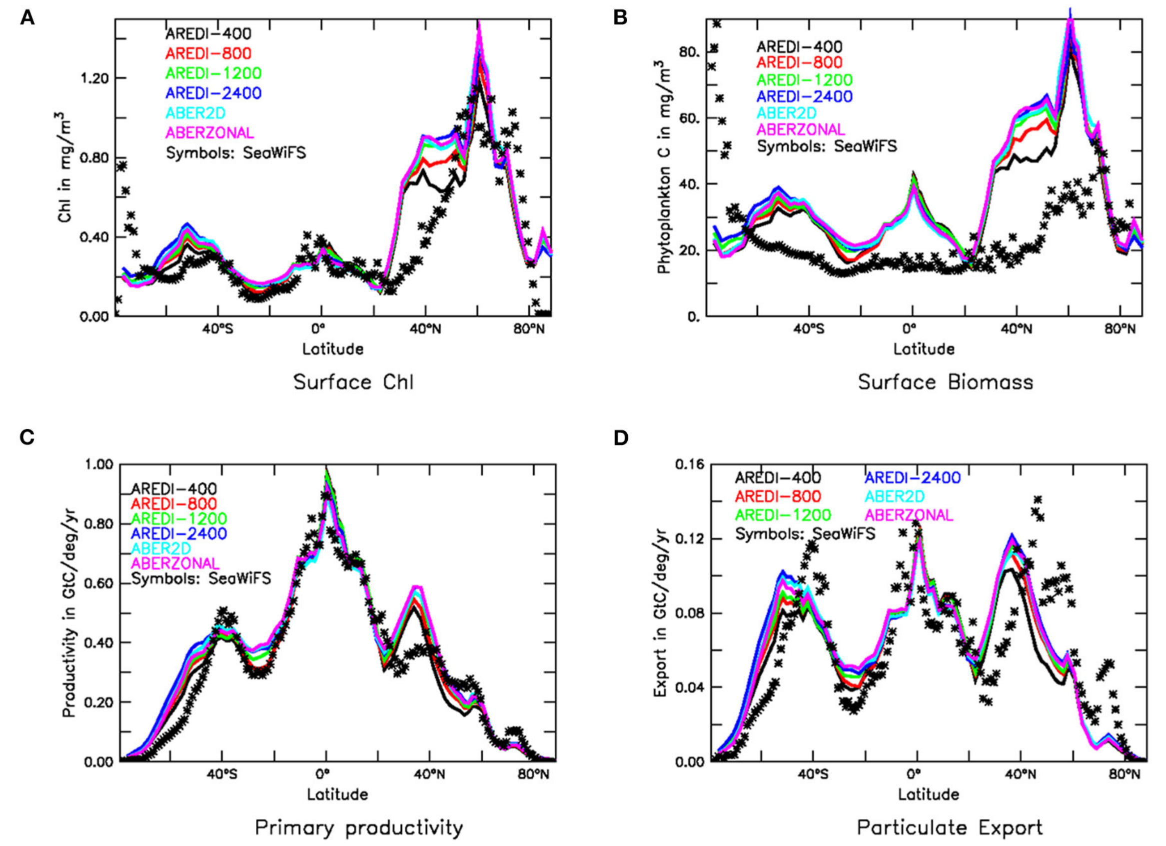

FIGURE 3 | Biological fields in CM2Mc pre-industrial control run with six different A_{REDI} parameterizations (colored lines) compared with satellite-based estimates (symbols). **(A)** Zonally averaged chlorophyll (mg/m^3). **(B)** Zonally averaged particulate carbon (mg/m^3). **(C)** Zonally integrated primary production (GtC/yr/deg) and **(D)** Zonally integrated particle export across 100 m (GtC/yr/deg). Satellite estimates in **(A,C,D)** are taken from Dunne et al. (2007). Particulate carbon in **(B)** is estimated from backscatter following Behrenfeld et al. (2005).

also examine the total phytoplankton biomass, which can be estimated from particulate backscatter (symbols **Figure 3B**). Biomass serves as an index commonly used by fishery experts to monitor ecosystem response to climate change (e.g., Cabré et al., 2015a) and regional trophic interactions (Kwiatkowski et al., 2018). Note that the "observed" biomass in **Figure 3B** does not show a peak in the equatorial zone, which may be due to problems with the retrieval algorithm used to estimate the backscatter [alternative estimates of biovolume such as Kostadinov et al. (2009), show a clear signature of equatorial upwelling].

As seen by the colored lines in **Figure 3B**, zonally averaged phytoplankton biomass is also relatively insensitive to mixing parameterization, except in the northern subtropics from 30 to 45°N. Within this latitude band, macronutrients are not typically overestimated (**Figure 2A**), so it is possible that both the high Chl and biomass concentrations indicate overly high iron concentrations. As with chlorophyll, increasing mixing produces increasing biomass, with the highest mixing models predicting surface biomass in the northern subtropics that is ∼40% higher than in AREDI-400.

Primary Productivity and Particle Export Show Weak Sensitivity to Mixing

Tracing the flow of carbon and nutrients through an ecosystem is generally done using measures of productivity. One such measure is the primary productivity, representing the uptake of carbon by phytoplankton (Chavez et al., 2011), for which many satellite-based estimates exist in the literature (Saba et al., 2011). However, a more appropriate index for detecting bottom-up ecological change on longer timescales may be the particle export (Laufkötter, 2016; Buesseler et al., 2020). This is because export to the deep ocean is more sensitive to grazing from large zooplankton that transfer energy up the food web to fish and also drive the chemistry and biology of the deep ocean (Jones et al., 2014).

Primary productivity and particle export [which are compared with satellite-based estimates from Dunne et al. (2007) in **Figures 3C,D**] are much less sensitive to mixing than chlorophyll and biomass. They are also relatively close to observations. The models all show similar levels of productivity and export as the (relatively uncertain) observations, with peaks in at around 40°S, on the equator and at 40°N. Primary productivity is well-simulated in all the models, with the exception of models

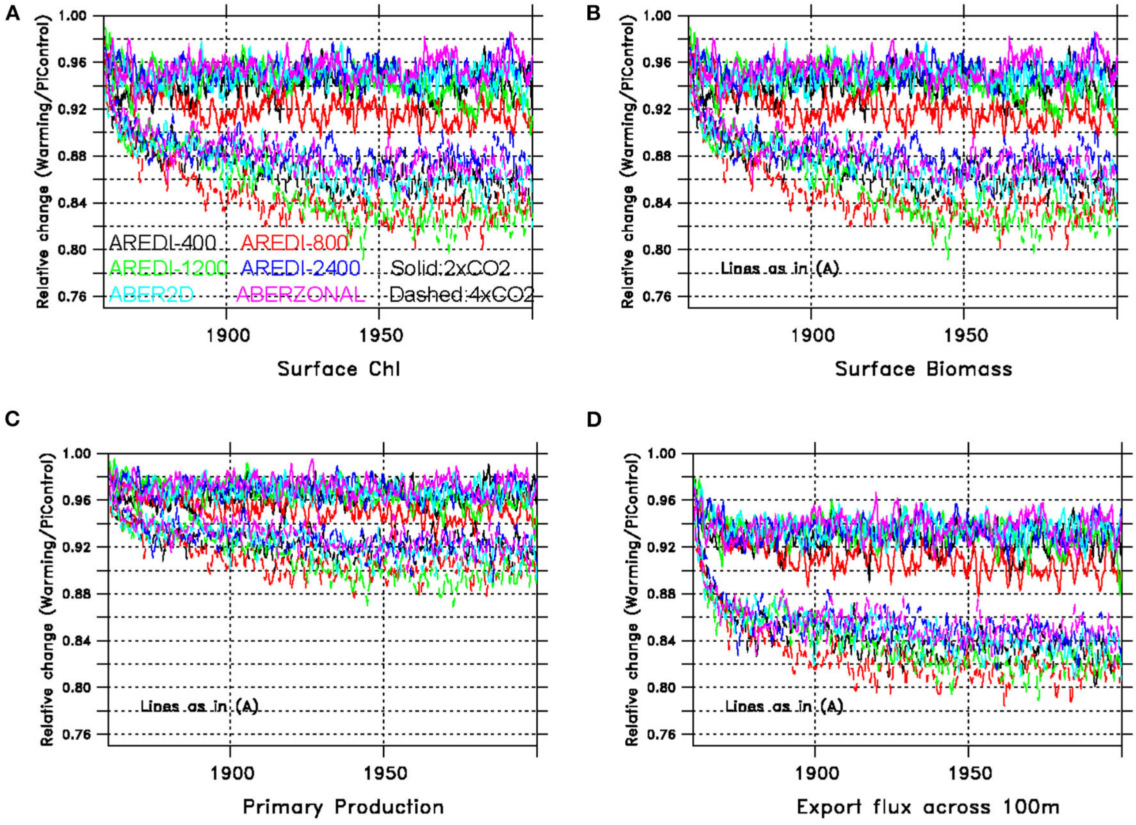

FIGURE 4 | Time series of relative changes in biological variables under doubled and quadrupled CO_2 for the different A_{REDI} parameterizations shown as a ratio of high CO_2/control. Upper group of lines are for doubled CO_2, while lower group shows changes under quadrupled CO_2. **(A)** Global surface chlorophyll change. **(B)** Global surface biomass change. **(C)** Global primary productivity change. **(D)** Global export across 100 m.

overestimating it in the northern subtropics from 30 to 45°N, the same region where chlorophyll and biomass appear to be too high in **Figures 3A,B**. Zonally integrated particle export flux observations peak at 0.12 Gt C/yr/deg of carbon per year in the Southern Hemisphere (SH) and 0.14 Gt C/yr/deg in the NH. The models show peaks that are slightly smaller and shifted southward in both hemispheres. As noted in Bahl et al. (2019), globally integrated values of export production in the model suite (which range from 9.95 GtC yr^{-1} in AREDI-400 to 11.1 GtC yr^{-1} in AREDI-2400) lie well within the range of satellite estimates: of 9.8 GtC yr^{-1} ± 20% estimated by Dunne et al. (2007).

Globally Integrated Biological Responses to Increased CO_2

Different Globally Integrated Indices of Biological Cycling Show Differing Sensitivities to Warming and Mixing

On a global scale all four of the indices of surface biological cycling described in **Figure 3** decrease under global warming. An examination of relative changes in these indices (**Figure 4**) shows that the bulk of the adjustment to the new equilibrium occurs over the first 40–60 years. Further examination of **Figure 4** reveals several important results.

First, although the sign of the decrease is the same across all variables, the magnitude of the decrease is quite different, with primary production (**Figure 4C**) showing much smaller changes than chlorophyll, biomass and export production (**Figures 4A,B,D**). This suggests that some fraction of the declines in biomass are partially compensated by higher temperatures resulting in faster metabolic rates [larger $\exp(k*T)$]. It also points out that using primary productivity as an index of climate change [as in Chavez et al. (2011)] may underestimate potential ecosystem impacts.

Second, there is a greater spread across models for the relative changes in the biological variables than there was for global mean temperatures in **Figure 1**, with much less distinction between the $4xCO_2$ and $2xCO_2$ simulations. Uncertainty about mixing contributes most strongly to uncertainties in surface chlorophyll and primary productivity, where the inter-model range (6 and 4%, respectively) is comparable to the drop due to doubling CO_2. Conversely, uncertainty about mixing contributes less strongly to surface biomass and global export change where a much clearer separation between the $2xCO_2$ and $4xCO_2$ cases is seen.

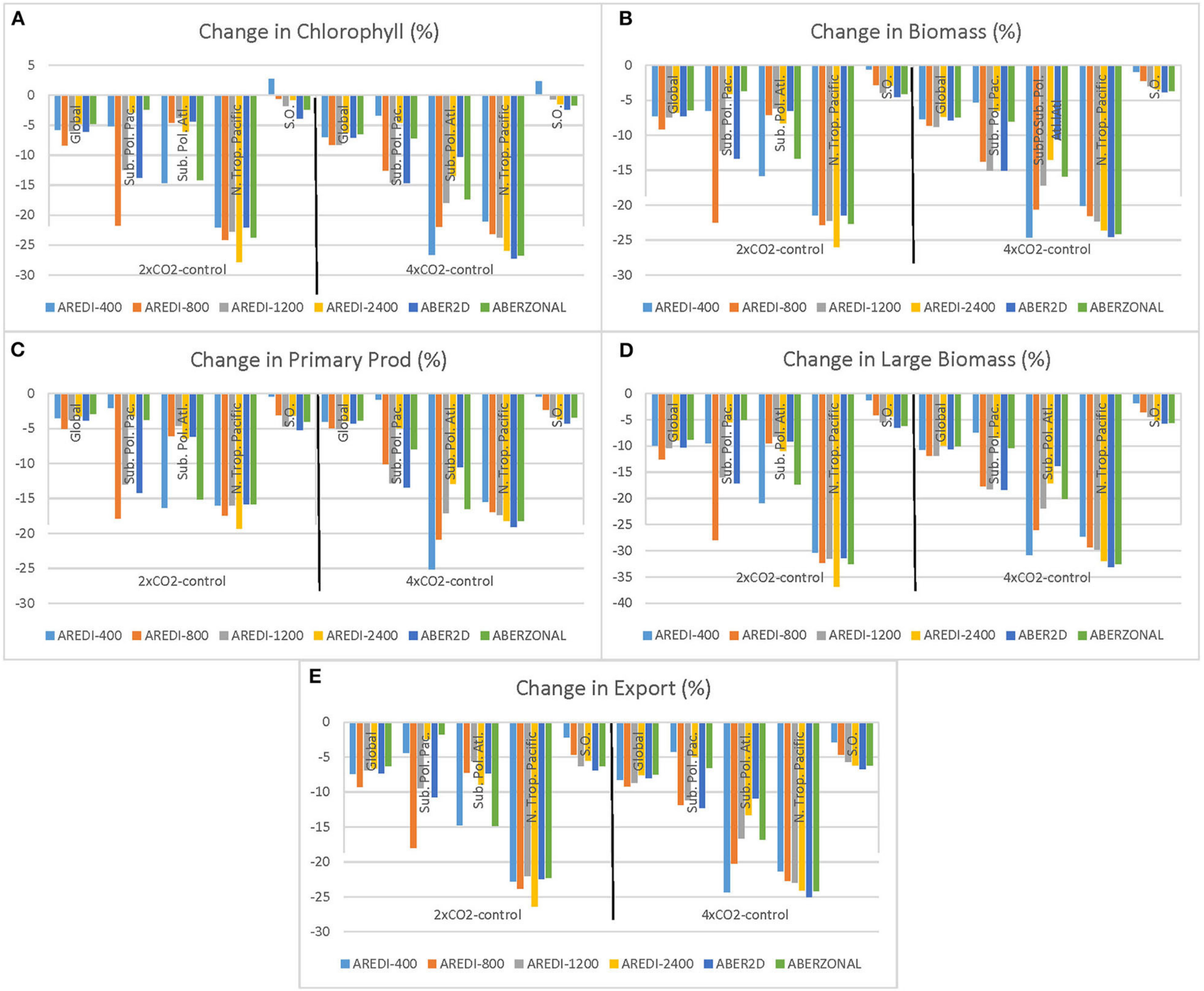

FIGURE 5 | Summary of changes in biological variables across models and scenarios. Each plot shows the relative change in % for **(A)** Chlorophyll, **(B)** Biomass, **(C)** Primary Production, **(D)** Large Biomass, and **(E)** Export. Each plot is divided into results from 2xCO_2 simulations (left half) and ½ the change under the 4xCO_2 simulation (right half). Each cluster of bars shows changes in a particular region across models (colors denote different distributions of A_{REDI}). Clusters from left to right within each half plot show the global integral, the Subpolar North Pacific from 40 to 60°N, the Subpolar North Atlantic from 40 to 60°N, the Northern Tropical Pacific (10-25°N, site of the largest drops in biological variables in **Figure 8**), and the Southern Ocean (70-50°S).

Third, the within-scenario spread across models is consistent across the different variables. Models with a larger relative decrease in chlorophyll have larger decreases in all the other variables as well.

Finally, the size of the changes does not appear to be monotonic with increasing mixing, with the AREDI-800 case showing the largest drop under doubling and AREDI-800 and AREDI-1200 cases showing the largest drops under quadrupling. In general, the ABER2D and ABERZONAL simulations behave more like the high-mixing models than the low-mixing models.

Response of Global Indices Is Relatively Linear, Some Are Moderately Sensitive to Mixing

Because it is difficult to extract patterns from these time series plots, we summarize the results by averaging over years 40–140 and presenting the results as bar plots in **Figure 5**. In each subplot, fractional changes under 2xCO_2 are shown on the left, and ½ of the change under 4xCO_2 is shown on the right. When bars of different colors within a particular region and scenario are of different lengths, this indicates that A_{REDI} (model uncertainty) plays an important role in explaining intermodel variability. If corresponding collections of bars in different scenarios have different lengths this indicates that the linearity assumption used to hindcast historical changes from 4xCO_2 changes is violated. If collection of bars is a perfect rectangle then there is no sensitivity to mixing, whereas if the bars within a cluster have vastly different lengths the sensitivity to mixing is strong. In addition to the four indices used in **Figure 4**, we also look at the changes in the biomass of large phytoplankton which are disproportionately important for feeding energy to higher trophic levels. Some models have suggested that trophic interactions can amplify changes in large phytoplankton biomass to produce relatively larger changes in total biomass (Lotze et al., 2019).

As in **Figure 4**, the magnitude of the decline in biological activity under global warming (**Figure 5**, bars marked "Glob" in each subplot) depends on the index. Primary productivity is the least sensitive of any of the global indices to warming, with declines on the order of 4% under doubling and 8% under quadrupling (**Figures 4C**, **5C**). The biggest changes are seen in large phytoplankton biomass (**Figure 5D**), which drops 8–12% in the $2xCO_2$ case and 20–24% in the $4xCO_2$ case. Chl (4–8% drop under doubling, 12–16% under quadrupling), total biomass (∼8% under doubling, ∼16% under quadrupling), and particle export (∼8% under doubling ∼18% under quadrupling) lie in between these extremes.

In general, the responses of the global indices to increasing radiative forcing is relatively linear. There is some hint of non-linear responses in the global Chl field, with the cluster of bars marked "Glob" on the left-hand side of **Figure 5A** noticeably smaller than those on the right-hand side. This is not the case, however, for the other indices, indicating that the response at $2xCO_2$ is roughly half the response at $4xCO_2$.

There is some sensitivity, however, to the mixing parameterization as each cluster of bars shows intra-cluster variability. As would be expected from **Figure 4**, this is biggest for surface chlorophyll, where the 4% intermodel range under $2xCO_2$ is 2/3 of the ∼6% drop. However, for the other variables, the relative range across the models is smaller. There is also some sense that the relative range across models is smaller for the $4xCO_2$ cases than the $2xCO_2$ cases (each cluster of bars marked "Glob" is more squared off on the right-hand side of each subplot). It is worth noting that the models do not show a monotonic dependence on mixing, with bar lengths sloping down to the left or to the right within each cluster. Instead, all clusters show the strongest sensitivity for AREDI-800 (orange bars) and the weakest for ABERZONAL (green bars).

Regional Response to Increased CO_2 Across Models

Although the global responses are relatively linear and at most moderately sensitive to mixing, this is not always true for regional changes. For instance, relative changes in the zonally averaged biological variables (**Figure 6**, compare with **Figure 3**), reach magnitudes of up to 50% with a strong dependence on mixing. We examine these regional changes in more detail below.

Different Regions Respond Differently to Mixing and Increased CO_2

One latitude band that stands out in **Figure 6** is between ∼40 and 65°N in NH subpolar latitudes. This region exhibits large reductions in Chl, particulate carbon, primary productivity, and particle export that also depend on the mixing parameterization. Under $4xCO_2$, the largest drops are seen in AREDI-400 and AREDI-800, with AREDI-2400 showing the smallest drops and ABER2D and ABERZONAL lying in between. Returning to **Figure 5**, we see that the changes in the zonal mean do not reflect zonal uniformity, as there are large differences between the subpolar North Atlantic (bars marked "SubPolAtl") and the subpolar North Pacific (bars marked "SubPolPac") for all of the variables. Each basin shows quite different sensitivities to mixing, with the largest changes in the $2xCO_2$ simulations in the subpolar North Pacific occurring in the AREDI-800 simulation, but in the AREDI-400 and ABERZONAL simulations in the subpolar North Atlantic.

Northern subpolar indices of biological cycling respond non-linearly to increased CO_2. Changes in the subpolar North Atlantic in the $2xCO_2$ simulations would be greatly overestimated by extrapolating from the $4xCO_2$ simulations for AREDI-800, AREDI-1200, AREDI-2400, and ABER2D, as would changes in the subpolar North Pacific for AREDI-1200. On the other hand, changes in the subpolar North Pacific in AREDI-800 (orange bars, **Figure 5**) in the $2xCO_2$ case would be underestimated by extrapolating from changes in the $4xCO_2$ case.

A second large drop in Chl, biomass, and productivity is found at about 15°N, but in contrast to the changes in the northern subpolar latitudes, the changes in this region are relatively insensitive to the mixing parameterization as the different lines overlay each other. Moreover, although the changes shown in **Figure 6** are larger under $4xCO_2$ than under $2xCO_2$, examination of the bars marked N. Trop. Pacific in **Figure 5** shows that the responses across models are relatively linear and that the changes in the $2xCO_2$ simulations can be relatively well-predicted from changes in the $4xCO_2$ simulations.

In the Southern Ocean, mixing has a big impact on the biological response. The AREDI-400 simulation shows a small increase in Chl and small decreases in total biomass, primary productivity, and export. As the mixing increases, we see a loss of Chl under increased CO_2 and larger decreases in biomass, primary productivity, and export. However, the responses appear to be relatively linear across the $2xCO_2$ and $4xCO_2$ cases (bars marked SOcean in **Figure 5**).

Different Responses of Nutrients to Climate Change by Latitude

In this subsection we examine how climate change produces changes in nutrients. Increasing CO_2 reduces macronutrient (**Figure 7A**) across nearly all latitudes with the $4xCO_2$ scenarios producing larger decreases than the $2xCO_2$ scenarios. Cabré et al. (2015a) show similar declines in nitrate in most biomes across CMIP5 models. The biggest decreases in our suite are seen in the subpolar NH. However, macronutrients rise in the Southern Ocean, most likely due to increased upwelling associated with stronger winds under global warming.

Dissolved iron (**Figure 7B**) shows a very different picture with little variation across models outside the northern subpolar latitudes. Somewhat surprisingly, increasing CO_2 increases iron in the sub-tropics, presumably because with lower nutrients (and export) there is less biological removal. The spatial distribution under $4xCO_2$ is well-correlated with changes under $2xCO_2$. In the subpolar northern hemisphere, iron decreases across scenarios but is strongly modulated by mixing, with an overlap between the $2xCO_2$ and $4xCO_2$ cases.

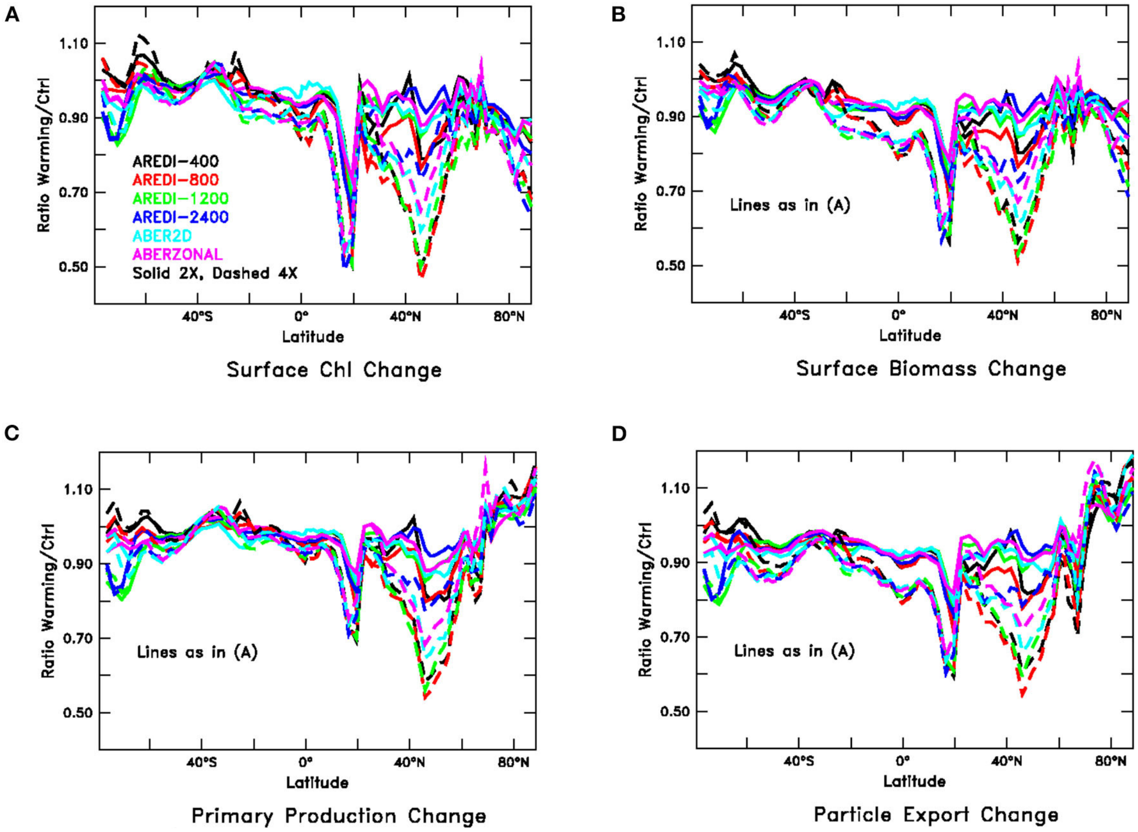

FIGURE 6 | Relative changes in zonally averaged biological fields under global warming (paralleling **Figure 3**), averaged over years 40–140 of high CO_2 simulations. Solid lines show $2xCO_2$, dashed lines $4xCO_2$. **(A)** Chlorophyll, **(B)** Particulate carbon, **(C)** Primary productivity, and **(D)** Particle export across 100 m.

Regional Patterns of Biomass Change in the AREDI-400 and AREDI-2400 Models Involve Changes in Both Light and Nutrient Limitation

As is already clear from looking at basin-averaged changes in the subpolar NH, zonally averaged differences shown in **Figures 6**, **7** are a crude representation of a more complex pattern of changes. These patterns are broadly similar in sign across simulations but have different magnitudes in different regions. This can be seen by looking at **Figure 8**, which shows relative changes in biomass between the $4xCO_2$ simulation and control simulation for the low-mixing AREDI-400 case (top row) and high-mixing AREDI-2400 case (bottom row). Looking at changes in total phytoplankton biomass in **Figures 8A,C**, we see that both simulations project small (<20%) increases in total phytoplankton biomass in the Arctic, Southeast Atlantic Ocean offshore of the Benguela upwelling, the Gulf of Mexico, parts of the Southern Ocean along the coast of East Antarctica, and the Sea of Okhotsk. However, these increases are offset by large decreases in the North Atlantic and Pacific, with a particularly intense band of decrease just south of 20°N (corresponding to where Chl, biomass, and productivity decrease in **Figure 6**). The magnitude of changes is generally larger in AREDI-400 than in AREDI-2400. A few regions (for example the Ross Sea) see opposite-sign changes in biomass.

The impact of quadrupling CO_2 is much greater when we focus on large phytoplankton biomass (**Figures 8B,D**). Both the low- and high-mixing models show steep reductions in large phytoplankton biomass throughout the North. Equatorial current, moving into the Kuroshio current and south into the East Australia Current. The effects can also be seen in the North Atlantic current. However, the low-mixing model appears to project larger reductions in the North Atlantic and the North Pacific, whereas the AREDI-2400 model (**Figure 8D**) projects regional decreases that are smaller due to greater persistence of deep convection. The changes, however, are not found in the center of the convective regions [which Pradal and Gnanadesikan (2014) and Bahl et al. (2019) showed are found in the Northwest Pacific] or the equatorial upwelling zones. Instead, the big drops in biomass in the North Pacific are found at the *edges* of these high nutrient regions. This is consistent with Oschlies (2002), who found the gyre edges experience large relative changes in nutrients.

To better understand these changes, we revisit Equation (5), which shows that the biomass in BLING is regulated by the product of a nutrient limitation term and a light

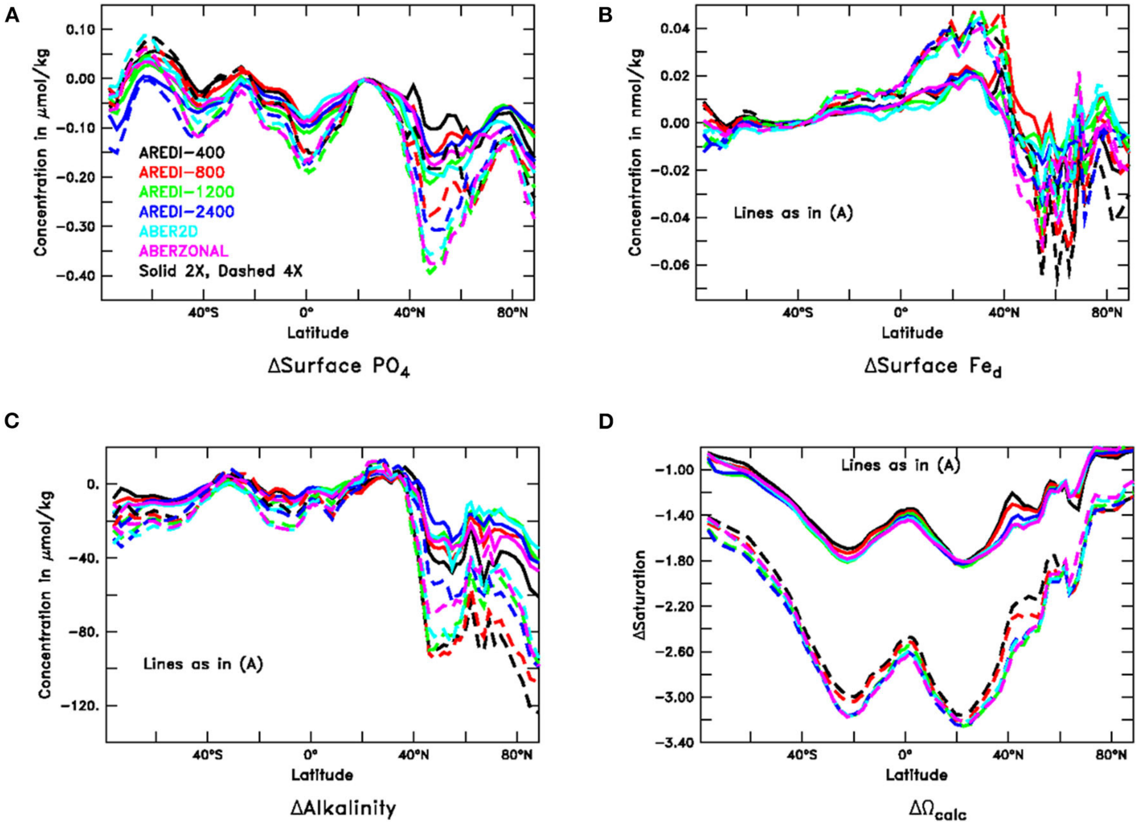

FIGURE 7 | Changes in surface chemical properties for years 40–140 of high CO_2 simulations. Solid lines represent changes under doubled CO_2; dashed lines represent changes under quadrupled CO_2. **(A)** Phosphate (μM). **(B)** Dissolved iron (nM). **(C)** Alkalinity (μM). **(D)** Calcite supersaturation (non-dimensional).

limitation term. The spatial distribution of the changes in these limitation terms under quadrupled CO_2 is shown for AREDI-400 and AREDI-2400 cases in **Figure 9**. Both models show broadly opposite patterns of change for light and nutrient limitation, such that regions with more light limitation have less nutrient limitation and vice-versa. Different biological limitations dominate in different regions. In the Arctic, reduction of light limitation causes biomass and productivity to increase in both models. By contrast, greater nutrient limitation is likely responsible for the decreases in phytoplankton biomass in the North Pacific and subpolar North Atlantic seen in **Figures 5**, **8**.

What gives rise to these different spatial patterns of limitation? In the North Tropical Pacific, greater nutrient limitation is primarily caused by a ∼50% drop in macronutrient concentrations in the equatorial upwelling. Because macronutrients are relatively high along the equator this produces only a small change in nutrient limitation there, but once the nutrients are moved away from the equator they run out much more quickly in the 4xCO_2 simulation. The peak of easterly wind stress to the north of the equator also drops by about 10% in the 4xCO_2 case, resulting in less advection of nutrient-rich water northward and less upwelling of nutrient-rich water from below. These changes are relatively similar across the simulations with different A_{REDI}.

In the subpolar North Pacific, macronutrient is brought up on the northwestern corner of the basin, but is redistributed by the subpolar gyre, with the lowest concentrations in the east. In the AREDI-400 case, quadrupling CO_2 reduces the concentration to the west of the dateline in the latitude band from 40 to 60°N from 0.4 to 0.3 μM (well above the half-saturation coefficient of 0.1 μM). However, to the east of 150°W in the same latitude band quadrupling CO_2 produces a smaller absolute change (from 0.034 to 0.014 μM) but a significant relative change both in nutrient and in the corresponding limitation term. As a result, the relative decline in biomass is much larger here.

By contrast, stronger light limitation (which is driven by more cloudiness–not shown) is responsible for the declines in biomass seen within the Southern Ocean. The somewhat surprising result that nutrient limitation decreases in the Southern Ocean in AREDI-400 is partly attributable to these decreases in light, but also to enhanced winds leading to more upwelling bringing more iron to the surface at around 60°S (see also **Figure 7B**). By contrast in AREDI-2400, decreases in vertical mixing result in a reduced supply of nutrients.

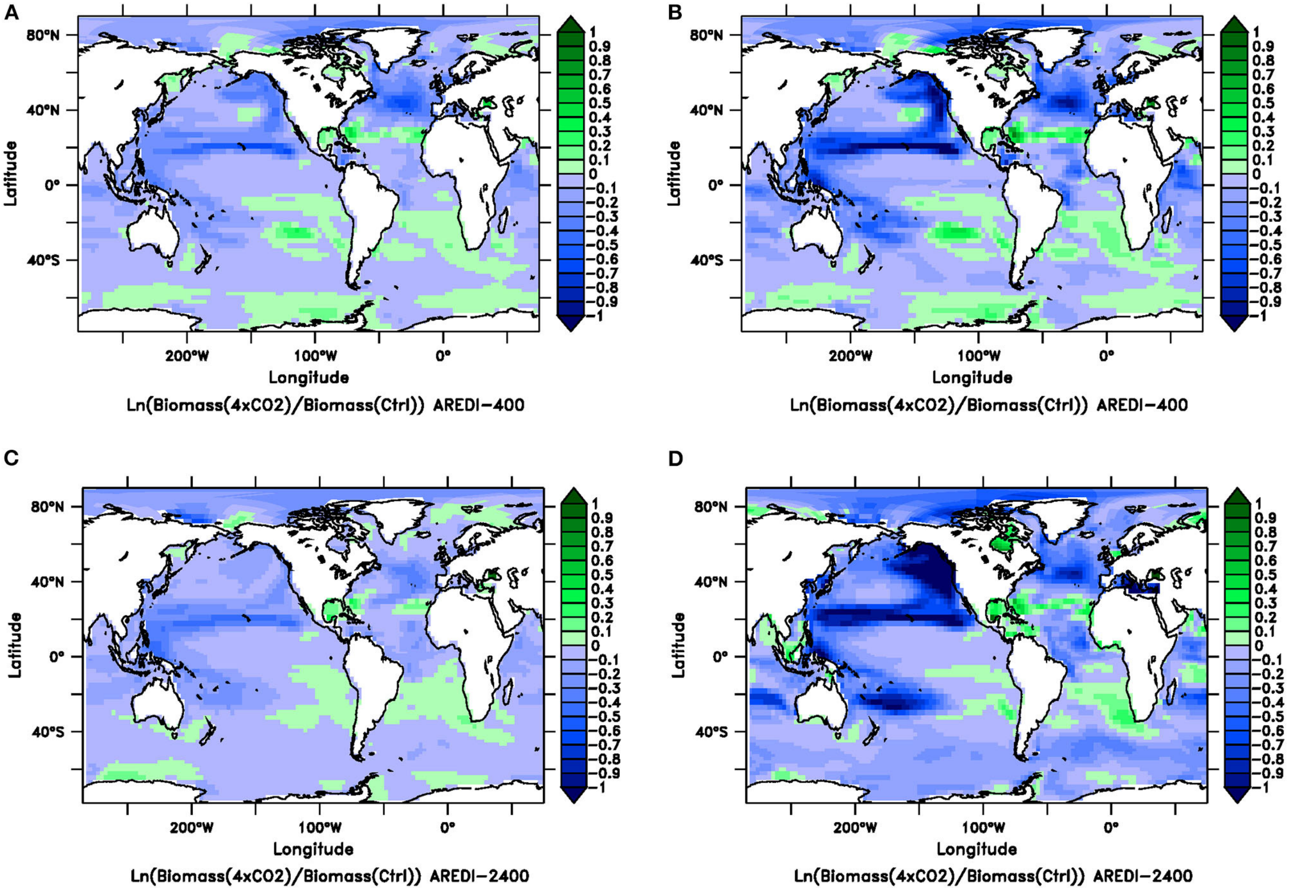

FIGURE 8 | Relative changes (natural log of the quotient of the value in century-long climatology of the 4xCO$_2$ run over the value in a century-long climatology of the Control) in total phytoplankton biomass (left column) and large phytoplankton biomass (right column) for the AREDI-400 case (top row) and AREDI-2400 case (bottom row). **(A)** Relative change in total phytoplankton biomass for the AREDI-400 case, **(B)** Relative change in large phytoplankton biomass for the AREDI-400 case, **(C)** relative change in total phytoplankton biomass for the AREDI-2400 case, and **(D)** relative change in large phytoplankton biomass for the AREDI-2400 case. Small values are effectively fractional changes. The color bar denotes the size of the logarithmic change, so that blue denotes lower biomass; green denotes higher biomass.

Mixing Is Important for Understanding Indices of Interior Habitability in Both the Control and Global Warming Simulations

Although uncertainty in mixing has a relatively small impact on global-scale biological indicators in the surface layers, we know from previous work that this is not necessarily true for the ocean interior. Gnanadesikan et al. (2013) and Bahl et al. (2019) demonstrated that mixing has a big impact on the magnitude and climate sensitivity of oceanic hypoxia (defined here as oxygen concentration >2 ml/l or 88 μM). In this section we extend this work to look at carbonate undersaturation, which like hypoxia, occurs where the products of respired sinking organic material are allowed to accumulate (Gobler and Baumann, 2016). However, in contrast to hypoxia, the calcite saturation state is a function of pressure (Zeebe and Wolf-Gladrow, 2001), and thus will be more strongly affected by small increases in remineralized nutrients and carbon at depth. We also examine the linearity of the response of both parameters, evaluating whether historical changes can be predicted by large-amplitude increases in atmospheric carbon dioxide. Given that the pre-industrial control models show relatively weak sensitivity to mixing in their surface carbonate saturation state (**Figure 2D**), surface concentrations of alkalinity (**Figure 2C**), and particulate export (**Figure 3D**), we might expect that interior differences in hypoxia and calcite undersaturation would also be small across models.

In fact the range of depths experiencing either calcite undersaturation or hypoxia is strongly affected by the value of A$_{\text{REDI}}$. This is particularly clear in the North Pacific where observations (**Figures 10A,B**) show hypoxic waters occupying as much as 2,000 m of the water column, while calcite-undersaturated waters occupy more than 4,000 m in some locations. High levels of calcite undersaturation are expected in the North Pacific where the oldest deep waters with the largest accumulation of acidic remineralized carbon are found. The ability of the models to simulate these environments is not very good and is sensitive to different rates of ventilation. In the AREDI-400 model hypoxic depth ranges up to 4,500 m are found,

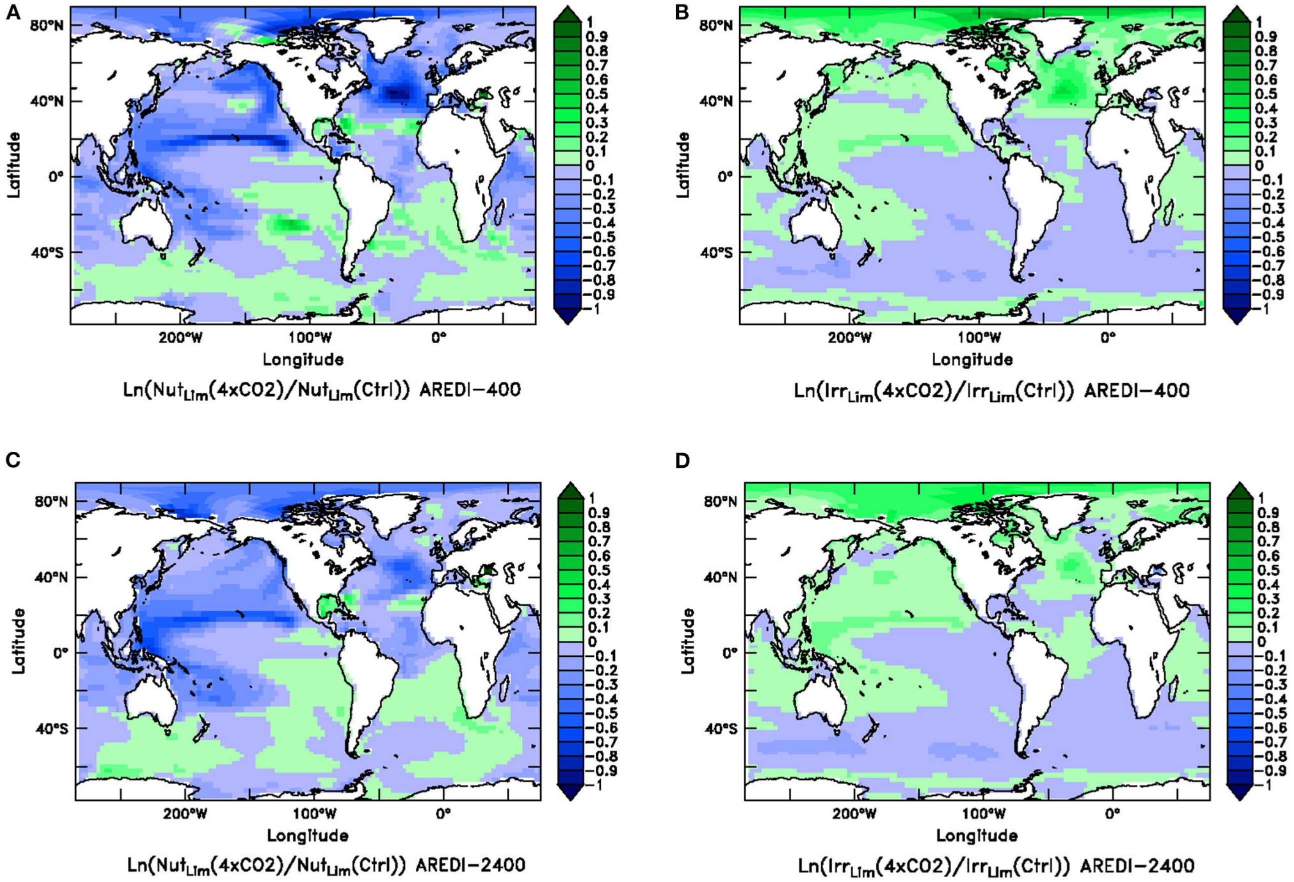

FIGURE 9 | Relative changes (natural log of the quotient of the value in century-long climatology of the $4xCO_2$ run over the value in a century-long climatology of the Control) in the ratio of the quadrupled CO_2 case and the control for the nutrient limitation term (left column) and the light limitation term (right column) for the AREDI-400 case (top row) and AREDI-2400 case (bottom row). **(A)** Nutrient limitation for the AREDI-400 case, **(B)** light limitation term for the AREDI-400 case, **(C)** nutrient limitation for the AREDI-2400 case, and **(D)** light limitation term for the AREDI-2400 case. As the growth rate is the product of these terms, low values mean higher limitation, so that blue denotes lower nutrients or lower light while green denotes higher nutrients or higher light.

but the highest values are found in the Eastern Pacific, as well as a second intense center in the Bay of Bengal. By contrast, the high-mixing case (AREDI-2400) simulates a significantly smaller hypoxic volume with a depth range that does not exceed 2,000 m, shown in **Figure 10E**. This is a somewhat of a common bias amongst models (Gnanadesikan et al., 2013; Cabré et al., 2015b; Bahl et al., 2019). The global volume of calcite-undersaturated waters (**Figures 10D,F**) is somewhat better simulated in AREDI-400, though the volumes in the subpolar North Pacific are too small and those in the equatorial Pacific too large. The AREDI-2400 model also simulates a significantly smaller volume of calcite-undersaturated water in both regions.

Changes in the global volume of hypoxic and calcite-undersaturated waters are very sensitive to the parameterization of mixing, and deviate from perfect linearity. As shown in **Figure 11A**, hypoxic volume expands the most for the AREDI-400 model under $2xCO_2$ and actually contracts in the AREDI-1200 models [also reported in Bahl et al. (2019)]. A novel result in this paper is our finding that changes in hypoxic volume cannot simply be scaled down from the $4xCO_2$ cases. Doing so underestimates the change in hypoxic volume in the $2xCO_2$ case for all the cases other than AREDI-1200 (gray bars in **Figure 11A** are smaller than the blue bars). For AREDI-1200, hypoxia expands slightly in the $4xCO_2$ case but shrinks in the $2xCO_2$ case. The fact that it is difficult for ESMs to consistently reproduce the observed trends of hypoxic water expansion, particularly in the tropical OMZs (Bahl et al., 2019), may in part stem from this underlying non-linearity [though as noted by Andrews et al. (2017), other mechanisms such time-varying stoichiometry may also play a role].

The global volume of calcite-undersaturated water shows a different pattern of change in **Figure 11B**, with undersaturated waters increasing for all of the values of A_{REDI} in both the $2xCO_2$ and $4xCO_2$ simulations. The biggest increases in global calcite undersaturation are seen for AREDI-2400, which predicts 929 Mkm^3 of undersaturated water in the $4xCO_2$ case, an 80% increase from 513 Mkm^3 volume in the pre-industrial control simulation. By contrast, the AREDI-400 case shows an undersaturated water volume of 654.2 Mkm^3 under doubling and 816 Mkm^3 under quadrupling vs. 584 Mkm^3 in the pre-industrial

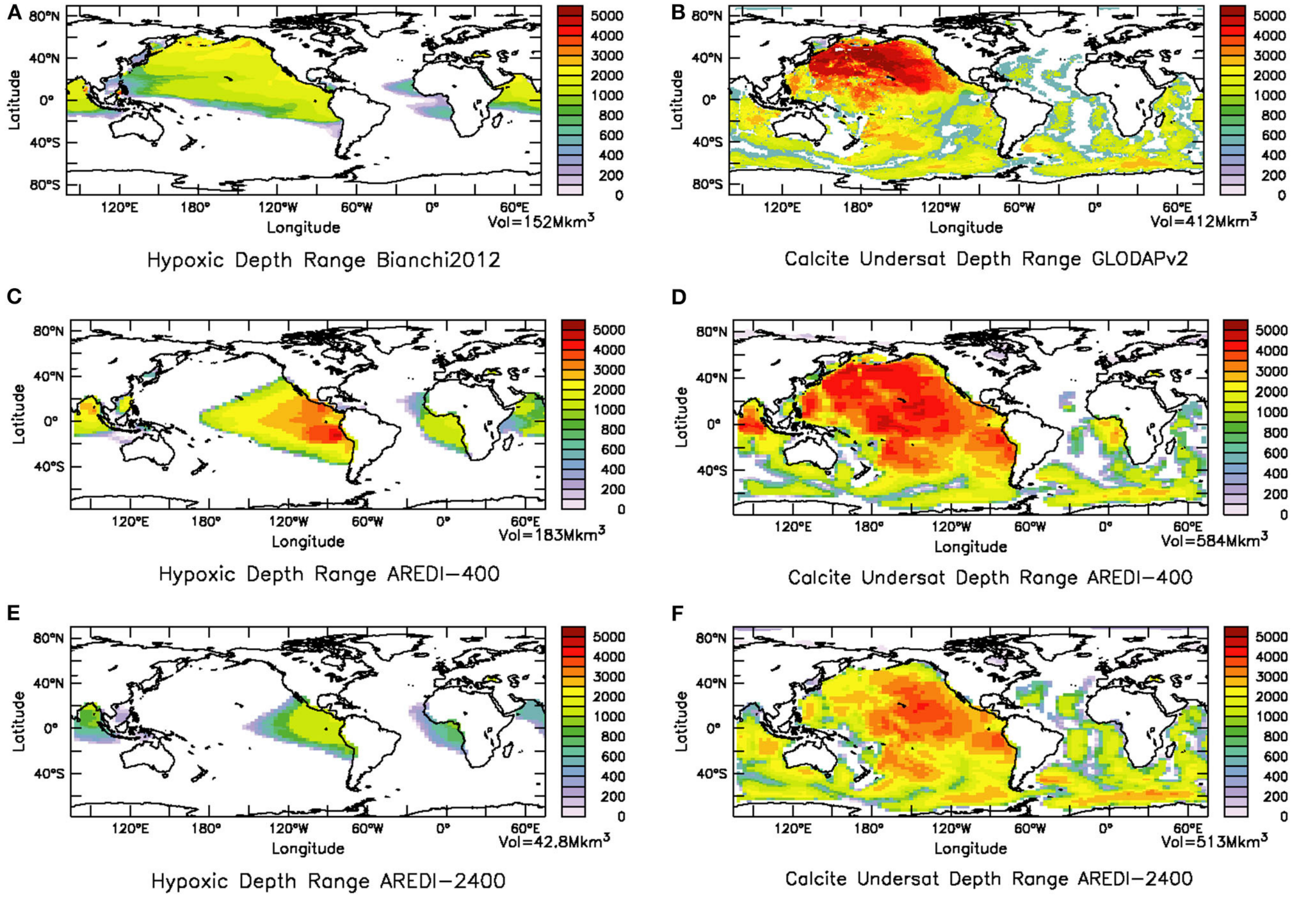

FIGURE 10 | Influence of mixing coefficient on mean-state hypoxia and calcite undersaturation. **(A)** Observations, taken from Bianchi et al. (2012), of depth of water in m column occupied by hypoxic waters and **(B)** observations from GLODAP (Lauvset et al., 2016) of the depth of the water column in m over which calcite undersaturation is found. **(C)** Hypoxic depth range for low-mixing model AREDI-400, **(D)** depth range of calcite undersaturation for low-mixing model AREDI-400, **(E)** Hypoxic depth range for high-mixing model AREDI-2400, and **(F)** depth range of calcite undersaturation for high-mixing model AREDI-2400.

control. Note that in contrast to the hypoxic volume, the 4xCO_2 calcite undersaturation change overpredicts the 2xCO_2 change for all values of mixing.

The spatial pattern of changes in calcite undersaturation are shown in **Figure 12** for the AREDI-400 and AREDI-2400 models. Both models show an increase in the volume of undersaturated water in the North Pacific, qualitatively consistent with recent observational trends (Feely et al., 2004). In AREDI-2400 the impact of a collapse in deep convection is clearly seen, with depths of calcite undersaturation expanding by over 2,000 m. The AREDI-400 model has much smaller changes in the Pacific, but actually shows larger changes in the Southeast Atlantic. Due to a lack of accumulation of respired CO_2 the North Atlantic remains supersaturated in all four runs. In the Indian Ocean, the depths of calcite undersaturation expand as both CO_2 and mixing increase. These differences suggest that calcite undersaturation is one field for which uncertainty in AREDI may contribute strongly to uncertainties in future projection–with important implications for deep-sea organisms (Bach, 2015).

Convection Explains Why Subpolar Gyres and Interior Habitability Behave Non-linearly and Are Sensitive to Mixing

We have seen that in our model suite global measures of surface ecosystem function, in particular chlorophyll, are at most moderately sensitive to changes in mixing and vary relatively linearly with radiative forcing. However, interior measures of habitability such as hypoxia and calcite undersaturation are much more sensitive to mixing and vary non-linearly, just as subpolar changes in ecosystem cycling do. Moreover, we see that the volume of calcite-undersaturated water increases under global warming for all of our models, despite a decrease in export.

We can reconcile these apparently contradictory results by noting that the degree to which interior waters are low in oxygen and carbonate ion is not solely determined by the rate which oxygen and carbonate ion are consumed as a result of remineralization. It is also controlled by the amount of time over which remineralization is allowed to accumulate–the age of the water. The age is inversely related to the rate of vertical exchange in high latitude regions and thus is tightly linked to

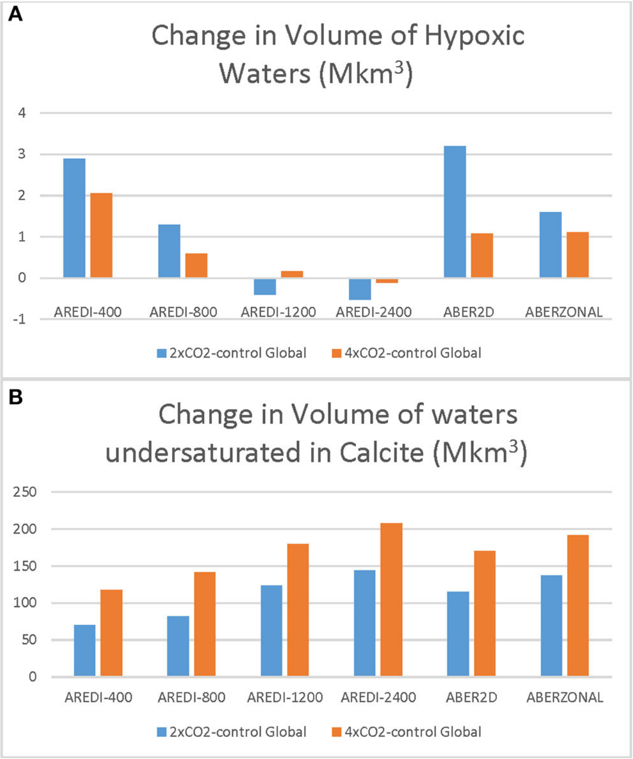

FIGURE 11 | Absolute changes in the volume of hypoxic waters **(A)** and waters undersaturated with respect to calcite **(B)** in Mkm^3. Blue bars show response under 2xCO$_2$. Gray bars show half of the response under 4xCO$_2$-differences from blue bars show lack of linearity.

the magnitude of convection in the subpolar gyres. As discussed in Bahl et al. (2019), the increase in age under global warming explains the changes in interior oxygen under 2xCO$_2$ cases–overwhelming the impact of declining export. **Figure 11B** tells us this must be true for calcite undersaturation as well.

One way of characterizing the changes in age is by looking at $\Delta^{14}C$, which is insensitive to biological cycling. Low gradients in $\Delta^{14}C$ between the surface and 1,500 m imply relatively rapid vertical exchange. As illustrated in **Figure 13A**, the North Pacific in the pre-industrial control simulation looks very different across our model suite. The AREDI-400 model has a vertical gradient over the top 1,000 m that is relatively close to the observed estimate from Key et al. (2004). The higher mixing models (AREDI-1200, AREDI-2400, ABER2D, and ABERZONAL) all simulate very low gradients of radiocarbon, implying unrealistically rapid vertical exchange. The AREDI-800 model (red line, **Figure 13A**) lies in between these two extremes.

Global warming causes increases in the vertical gradient of $\Delta^{14}C$ but does not do so identically across models. In the 2xCO$_2$ simulations (**Figure 13C**), the vertical gradient increases most sharply for the AREDI-800 simulation, which as previously illustrated in **Figure 5** shows the largest relative decline in chlorophyll, biomass, productivity, and export under this scenario. AREDI-1200 and ABER2D show a smaller increase in vertical radiocarbon gradient in the North Pacific in **Figure 13** and a smaller decrease in surface biological cycling in **Figure 5** (gray and blue bars). Under 4xCO$_2$, the biggest changes in the North Pacific radiocarbon gradient are seen in AREDI-1200 and ABER2D, which then also show the biggest relative drops in biological cycling in **Figure 5**. In the North Atlantic, by contrast, the largest changes in vertical radiocarbon gradient between the pre-industrial control and the 2xCO$_2$ case occur in the ABERZONAL and AREDI-400 cases, while AREDI-800 is relatively unchanged. It is thus unsurprising that it is the AREDI-400 and ABERZONAL cases that show the largest relative drops in biological cycling within subpolar North Atlantic (**Figure 5**).

The reasons for the changes in convection are complex and regionally dependent. As discussed in Bahl et al. (2019), an increased hydrological cycle under global warming acts to decrease the density of high latitude surface waters reducing convection. On the other hand, reduction in sea ice (which occurs across all the models for both hemispheres under both scenarios), exposes more open water in the wintertime, leading to more heat loss and increasing the potential for convection. Finally, because the overturning in the North Hemisphere involves a transformation of light to dense water which must balance the transformation of dense to light water in the Southern Hemisphere, the decline in the overturning in the North Pacific can be counterbalanced by the increase in the North Atlantic. A full discussion of these processes is beyond the scope of this paper.

DISCUSSION

A key part of applying ESMs to ecology (a primary goal of this special issue) is understanding where, when and why model responses will be non-linear. This work has focused on the extent to which uncertainty in the parameterization of lateral mixing, which has major impacts on the distribution and sensitivity of deep convection, can propagate into uncertainty in simulating ecosystem functioning and habitat distribution.

Before discussing the impact of mixing in more detail, we show that our estimates of changes in biological cycling are broadly consistent with those seen in the literature, although the decreases under global warming may be significantly larger or smaller than those seen in individual models. On the one hand, our 12–16% drops in Chl under 4xCO$_2$ are much smaller than the projected 50% decline in Chl associated with a 6°C increase in temperatures by Hofmann et al. (2011) in an intermediate complexity ESM. This is true even when the Chl change in Hofmann et al. (2011) is scaled down by a factor of two to match our changes in temperatures. On the other hand, the ~16% drops in surface biomass under 4xCO$_2$ are more extreme than the ~8% drop in biomass seen in two climate models for the RCP8.5 scenario by Lotze et al. (2019). Also using the RCP8.5 scenario, Bopp et al. (2013) reported declines in global primary production ranging from 0.9 to 16.1% (with mean of 8.6%) and Heneghan et al.

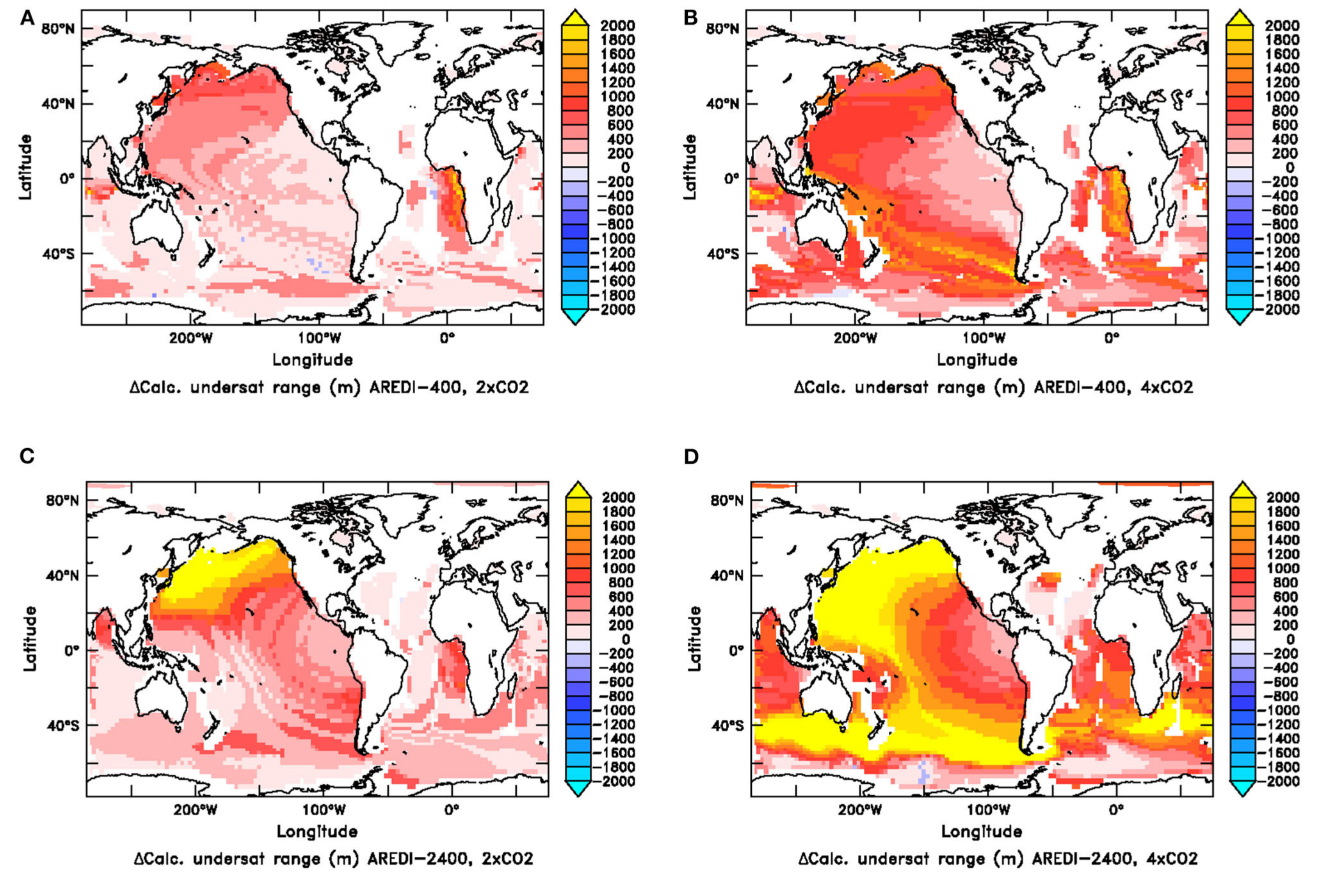

ΔCalc. undersat range (m) AREDI−400, 2xCO2

ΔCalc. undersat range (m) AREDI−400, 4xCO2

ΔCalc. undersat range (m) AREDI−2400, 2xCO2

ΔCalc. undersat range (m) AREDI−2400, 4xCO2

FIGURE 12 | Change in the vertical extent of the water column over which calcite undersaturation is found for the 2xCO_2 **(A,C)** and 4xCO_2 **(B,D)** simulations for the AREDI-400 simulations (top row) and AREDI-2400 simulations (bottom row).

(2019) presents a global decline of 5%. Our changes of 4% under doubling and 8% under quadrupling lie well within this range. Similarly, our changes in particle export of 5–6%/degree lie within the 3–15%/degree warming reported in Cabré et al. (2015a).

The fact that our estimates for the decline in global Chl, biomass, primary production and export cluster around a relatively small range compared to other estimates in the literature suggests that the range of responses in CMIP5 models is due to something other than lateral mixing. Although neglected in our model, one possible driver is the differential metabolic responses of phytoplankton and zooplankton to temperature. Taucher and Oschlies (2011) compared a model in which phytoplankton and zooplankton had the same temperature dependence and one where they had different temperature dependences. Under global warming the change in primary production had different signs in the two models, even though the changes in export were relatively consistent. Kwong and Pakhomov (2017) argue that capturing particle cycling and export may require letting respiration (and thus the effective grazing rate) be dependent on both zooplankton size and temperature and that the effective temperature for vertically migrating zooplankton may differ from that of their phytoplankton prey. Further investigation of such processes is critical.

Regionally, the representation of lateral mixing can make a big difference in the magnitude of change. This is especially apparent for biomass, primary productivity, and export in the subpolar regions. Eddy mixing may help explain the variance (ranging from a small rise of 5% to decline of 20%) in productivity changes found by Cabré et al. (2015b) in subpolar regions within the CMIP5 models under the RCP8.5 scenario. Subpolar regions in the Northern Hemisphere also show a strong non-linear response to warming, with 4xCO_2 simulations failing to capture the response at 2xCO_2. Studies using the output of ESMs to attribute changes in the subpolar gyres need to be aware of these behaviors. While ecologists should always be careful of using projections from a single ESM, this is especially true in such convective regions. Robust fingerprints of global warming impacts on ecosystems could only be found within the tropics. Even here, one can find results within the literature that disagree with our estimates of anthropogenic impacts. For example, Roxy et al. (2016), argued that higher sea surface temperatures have already been associated with a mean decrease of 20% in primary productivity with the Indian Ocean, much larger than the changes we find under 2xCO_2.

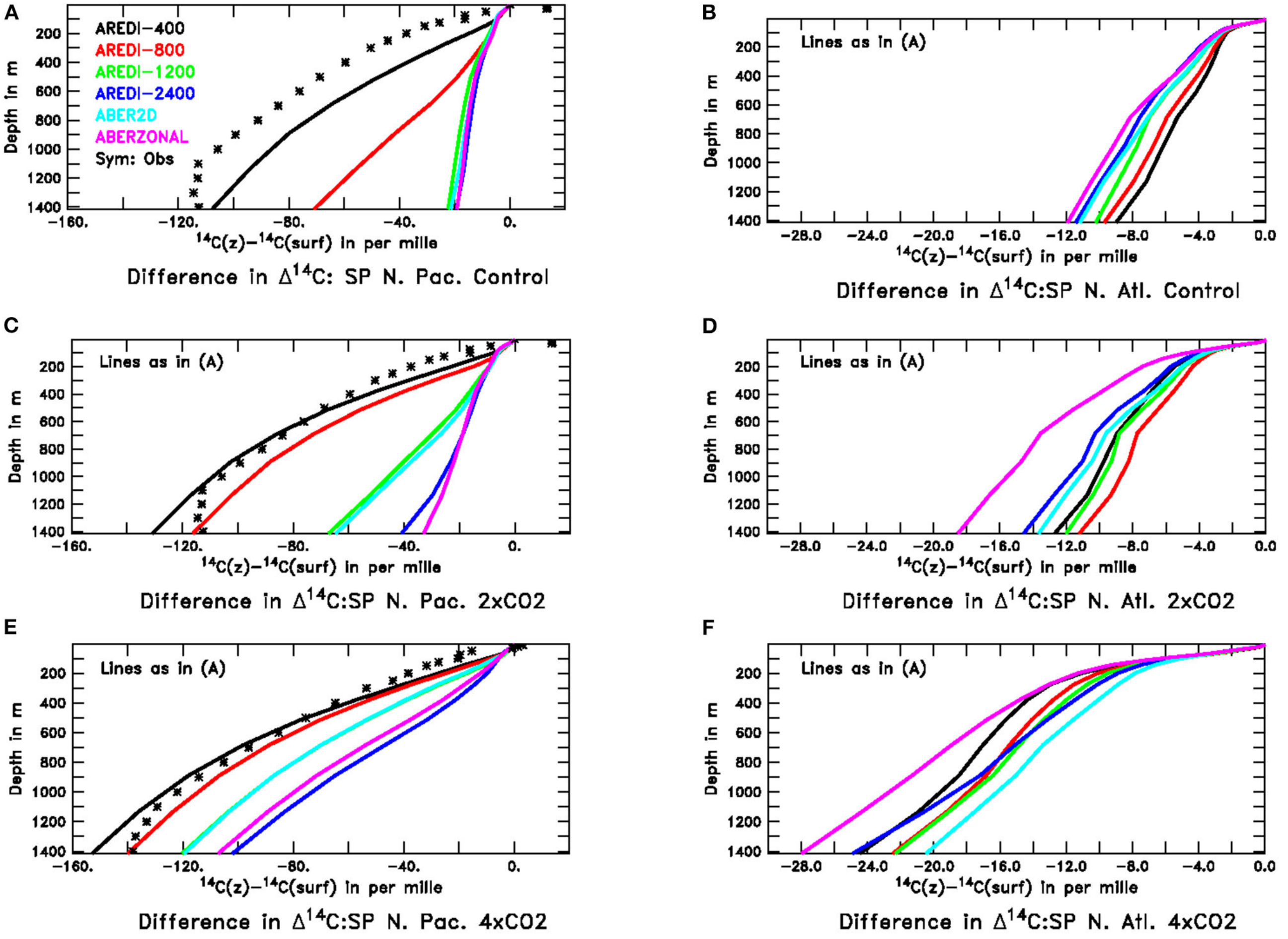

FIGURE 13 | Profiles of radiocarbon relative to its surface value in the subpolar North Pacific and North Atlantic across our model suite. Observational estimates of pre-bomb radiocarbon from Key et al. (2004) are shown for the North Pacific with the symbols. For the North Atlantic the methods used to remove the signal of atmospheric nuclear testing do not work as well, and the deep ocean ends up having a higher radiocarbon concentration than the surface-a physically nonsensical result. For this reason we do not show the Key et al. (2004) estimates for this region. Top row shows the pre-industrial control simulations, middle row the 2xCO_2 simulations and bottom row the 4xCO_2 simulations. All model results are from century-long averages. **(A)** North Pacific, Control **(B)** North Atlantic, Control **(C)** North Pacific, 2xCO_2 **(D)** North Atlantic, 2xCO_2. **(E)** North Pacific, 4xCO_2 **(F)** North Atlantic, 4xCO_2.

The relationship between surface nutrients and zonally averaged biomass is not simple. This is because changes in biomass are much more sensitive to small absolute changes in nutrients at levels that are lower than the half-saturation coefficients for growth than to larger absolute changes at levels higher than these same half saturation coefficient. For example, the average zonally-averaged macronutrient concentrations in the pre-industrial control simulation at ∼40°N are ∼0.4 µM in AREDI-400 and 0.7 µM in AREDI-2400 (**Figure 2**), far higher than the half-saturation coefficient of 0.1 µM. A drop of 0.25 µM under quadrupling in AREDI-400 shifts the modeled phytoplankton into a macronutrient-limited regime, whereas the somewhat larger drop in AREDI-2400 still leaves the macronutrient concentration well above the half-saturation coefficient. As a result larger changes in biomass are seen in AREDI-400 than in AREDI-2400 along the edges of high nutrient zones (**Figure 7B**). This phenomenon is also seen across the CMIP5 models in Cabré et al. (2015a, see their Figure 8).

Similar behavior is found with respect to iron in the Southern Ocean. Described as the largest high nutrient, low chlorophyll (HNLC) province in the world (Deppeler and Davidson, 2017) the Southern Ocean is known to be highly limited by iron (Boyd et al., 2004; Blain et al., 2007). In our model suite, iron follows chlorophyll and biomass by showing a slight increase under global warming in AREDI-400 and AREDI-800, but a decrease in AREDI-1200 and AREDI-2400. Although the differences in dissolved iron within the Southern Ocean in **Figure 7B** are relatively small across the models, the background iron concentrations (**Figure 2B**) are lower than the 0.2 µM half-saturation coefficient K_{Fe}. As a result, these small intermodel differences in the change in iron concentration can help explain the intermodel differences in the change in biomass and productivity.

Deeper within the water column (>300 m) the volume of waters that are hypoxic and/or undersaturated with respect to calcite vary significantly across models, and are very sensitive to the value of A_{REDI}. Larger changes in calcite undersaturation are found in high-mixing models containing excessive deep convection that ceases under global warming as the surface water freshens. Previous work in Bahl et al. (2019) suggests that many CMIP5 models overestimate convection in high-mixing regions such as the North Pacific. However, in our suite such high-mixing models have relatively weak changes in hypoxic water volume under either doubling or quadrupling of CO_2 suggesting that changes in $4xCO_2$ will not produce a robust fingerprint. That carbonate undersaturation and hypoxia behave so differently is particularly interesting as regional particle export declines regardless of the A_{REDI} parameter. The difference between the two fields highlights how variation in A_{REDI} produces different sensitivities of the ventilation at different depths to warming.

Our results also demonstrate that using ESMs to project biogeochemical changes requires constraining the turbulent diffusion coefficient in order to give realistic results. We emphasize that our results do not necessarily define the "correct" values to use. As discussed in Bahl et al. (2019), different models in our suite end up as the "best performers" when compared against different observational metrics. For example, our most "realistic" distribution of A_{REDI} (ABER2D) produces unrealistic deep convection in the Northwest Pacific in its control simulation, leading to an unrealistic simulation of hypoxia and calcite undersaturation, but a more realistic distribution of surface nutrients. This is likely because of compensating errors, the model is only weakly iron-limited in the subpolar gyre relative to observations (e.g., Nishioka, 2007) and thus the more realistically low levels of convection in AREDI-400 result in excessively low surface nutrients.

Efforts to generate dynamically consistent parameterizations of A_{REDI} that vary in space and time are ongoing, but have not yet been incorporated into models actually used for projecting the future evolution of the Earth System. Fox-Kemper et al. (2019) present a summary of some of the issues involved. Major problems include how to limit length scales and thus the mixing coefficient in the presence of ocean boundaries, how to deal with locations where eddies are growing and decaying and how to capture mixing at different spatial scales. Our work does suggest two key features of such parameterizations will be the suppression of isopycnal mixing within the core of currents [as found by Abernathey and Marshall (2013) but not in our version of the model in the North Pacific due to the location of the Kuroshio being offset southward] and how it interacts with convective regions. Moreover, we believe our results demonstrate that one should examine convective mixing and its relationship to A_{REDI} as a key uncertainty that has the potential to explain large differences across ESMs, as the range of constant values used here is comparable to that used in CMIP5.

Despite the complexity of our ESM, a number of caveats are still in order. First, our model suite is run at a relatively coarse resolution relative to CMIP5 and CMIP6 models. As such, while we expect the qualitative sensitivities found in this study to hold in higher-resolution models, it is likely that the exact "tipping points" where convection shuts off may be different. Additionally, as noted by Leblanc et al. (2018), uncertainties relating to how to classify phytoplankton in models have first order implications on projecting long-term impacts to biogeochemical processes–our model has a relatively small number of functional groups. Our model assumes that "a rising tide lifts all phytoplankton." While there is evidence for this from iron fertilization experiments (Barber and Hiscock, 2006) and studies across ecosystems (Brewin et al., 2017), other studies indicate that different functional groups may trade off against each other (Rivero-Calle, 2016). Finally, our model only considers the impact of A_{REDI} in transporting nutrients and affecting physical stratification on the large scale–biogeochemical fields, which are assumed to be homogeneous within each grid box. In real life, eddies may produce small-scale changes associated with frontogenesis and the formation of filaments that are also reflected in biological cycling (Lévy et al., 2012). Further data collection to characterize such small-scale variability remains necessary to improve our understanding of how to link changes in the physical environment to biological cycling and particle export.

DATA AVAILABILITY STATEMENT

Data in support of this paper is archived at the JHU data archive.data.jhu.edu at doi: 10.7281/T1/AUBBJD.

AUTHOR CONTRIBUTIONS

AB contributed to the experimental design, analysis, and writing of the paper. AG participated in running the models, writing and editing the manuscript, and making the figures. M-AP set up and ran the control and $2xCO_2$ scenarios, edited the manuscript, and made several of the figures. All authors contributed to the article and approved the submitted version.

FUNDING

This work was supported by the National Oceanographic and Atmospheric Administration under grant no. NA16OAR4310174, the National Science Foundation under the Frontiers in Earth Systems Dynamics Program under grant no. EAR-1135382, by the Physical Oceanography Program under grant no. OCE-1766568, and by the Department of Energy under proposal DE-SC0019344.

ACKNOWLEDGMENTS

We thank Johns Hopkins Institute for Data Intensive Engineering and Science (IDIES) which hosts the cluster on which the simulations and analysis reported here were performed. We thank Ryan Abernathey and Inga Koszalka for useful discussions.

SUPPLEMENTARY MATERIAL

The Supplementary Material for this article can be found online at: https://www.frontiersin.org/articles/10.3389/fmars.2020.00698/full#supplementary-material

REFERENCES

Abernathey, R. P., and Marshall, J. (2013). Global surface eddy diffusivities derived from satellite altimetry. *J. Geophys. Res. Oceans* 118, 901–916. doi: 10.1002/jgrc.20066

Adcroft, A., Campin, J., Hill, C., and Marshall, J. (2004). Implementation of an atmosphere-ocean general circulation model on the expanded spherical cube. *Mon. Weather Rev*. 132, 2845–2863. doi: 10.1175/MWR2823.1

Andrews, O., Buitenhuis, E., Le Quéré, C., and Suntharalingam, P. (2017). Biogeochemical modelling of dissolved oxygen in a changing ocean. *R. Soc.* 375:328. doi: 10.1098/rsta.2016.0328

Andrews, T., Gregory, J. M., Webb, M. J., and Taylor, K. E. (2012). Forcing, feedbacks and climate sensitivity in CMIP5 couple atmosphere-ocean climate models. *Geophys. Res. Lett*. 39, 1–7. doi: 10.1029/2012GL051607

Bach, L. T. (2015). Reconsidering the role of carbonate ion concentration in calcification by marine organisms. *Biogeosciences* 12, 4939–4951. doi: 10.5194/bg-12-4939-2015

Bahl, A., Gnanadesikan, A., and Pradal, M.-A. (2019). Variations in ocean deoxygenation across earth system models: isolating the role of parameterized lateral mixing. *Global Biogeochem. Cycles* 33, 703–724. doi: 10.1029/2018GB006121

Barber, R. T., and Hiscock, M. R. (2006). A rising tide lifts all phytoplankton: growth response of other phytoplankton taxa in diatom-dominated blooms. *Global Biogeochem. Cycles* 20:GB4S03. doi: 10.1029/2006GB002726

Behrenfeld, M. J., Boss, E., Siegel, D. A., and Shea, D. M. (2005). Carbon-based ocean productivity and phytoplankton physiology from space. *Global Biogeochem. Cycles* 19:GB1006. doi: 10.1029/2004GB002299

Bianchi, D., Dunne, J. P., Sarmiento, J. L., and Galbraith, E. D. (2012). Data-based estimates of suboxia, denitrification and N_2O production in the ocean and their sensitivities to dissolved O_2. *Global Biogeochem. Cycles* 26:GB2009. doi: 10.1029/2011GB004209

Blain, S., Quéguiner, B., Armand, L., Belviso, S., Bombled, B., Bopp, L., et al. (2007). Effect of natural iron fertilization on carbon sequestration in the Southern Ocean. *Nature* 446, 1070–1074. doi: 10.1038/nature05700

Bopp, L., Monfray, P., Aumont, O., Dufresne, J.-L., Le Treut, H., Madec, G., et al. (2001). Potential impact of climate change on marine export production. *Global Biogeochem. Cycles* 15, 81–99. doi: 10.1029/1999GB001256

Bopp, L., Resplandy, L., Orr, J. C., Dunne, J. P., Gehlen, M., Halloran, P., et al. (2013). Multiple stressors of ocean ecosystems in the 21st century: projections with CMIP5 models. *Biogeosciences* 10, 6225–6245. doi: 10.5194/bg-10-6225-2013

Boyd, P. W., Law, C. S., Wong, C. S., Nojiiri, Y., Tsuda, A., Levasseur, M., et al. (2004). The decline and fate of an iron-induced subarctic phytoplankton bloom. *Nature* 428, 549–553. doi: 10.1038/nature02437

Brewin, R. J. W., Ciavatta, S., Sathyendranath, S., Jackson, T., Tilstone, G., Curran, K., et al. (2017). Uncertainty in ocean-color estimates of chlorophyll for phytoplankton groups. *Front. Mar. Sci*. 4:104. doi: 10.3389/fmars.2017.00104

Buesseler, K. O., Boyd, P. W., Black, E. E., and Siegel, D. A. (2020). Metrics that matter for assessing the ocean biological carbon pump. *PNAS* 117, 9679–9687. doi: 10.1073/pnas.1918114117

Cabré, A., Marinov, I., Bernardello, R., and Bianchi, D. (2015b). Oxygen minimum zones in the tropical Pacific across CMIP5 models: mean state differences and climate change trends. *Biogeosciences* 12, 5429–5454. doi: 10.5194/bg-12-5429-2015

Cabré, A., Marinov, I., and Leung, S. (2015a). Consistent global responses of marine ecosystems to future climate change across the IPCC AR5 earth system models. *Clim. Dyn*. 45, 1253–1280. doi: 10.1007/s00382-014-2374-3

Cao, L., Wang, S., Zheng, M., and Zhang, H. (2014). Sensitivity of ocean acidification and oxygen to the uncertainty in climate change. *Environ. Res. Lett*. 9:064055. doi: 10.1088/1748-9326/9/6/064005

Chavez, F. P., Messié, M., and Timothy Pennington, J. (2011). Marine primary production in relation to climate variability and change. *Annu. Rev. Mar. Sci.* 3, 227–260. doi: 10.1146/annurev.marine.010908.163917

Chust, G., Allen, J. I., Bopp, L., Schrum, C., Holt, J., Tsiaras, K., et al. (2014). Biomass changes and trophic amplification of plankton in warmer ocean. *Glob. Chang. Biol*. 20, 2124–2139. doi: 10.1111/gcb.12562

Cole, S. T., Wortham, C., Kunze, E., and Owens, W. B. (2015). Eddy stirring and horizontal diffusivity from Argo float observations: geographic and depth variability. *Geophys. Res. Lett*. 42, 3989–3997. doi: 10.1002/2015GL063827

Delworth, T. L., Broccoli, A. J., Rosati, A., Stouffer, R. J., Balaji, V., Beesley, J. A., et al. (2006). GFDL's CM2 global coupled climate models. Part I: formulation and simulation characteristics. *J. Clim.* 19, 643–674. doi: 10.1175/JCLI3629.1

Deppeler, S. L., and Davidson, A. T. (2017). Southern ocean phytoplankton changing climate. *Front. Mar. Sci*. 4:40. doi: 10.3389/fmars.2017.00040

Deutsch, C., Emerson, S., and Thompson, L. (2005). Fingerprints of climate change in North Pacific oxygen. *Geophys. Res. Lett*. 32:16. doi: 10.1029/2005GL023190

Dunne, J. P., Armstrong, R. A., Gnanadesikan, A., and Sarmiento, J. L. (2005). Empirical and mechanistic models for the partial export ratio. *Global Biogeochem. Cycles* 19:GB4026. doi: 10.1029/2004GB002390

Dunne, J. P., Sarmiento, J. L., and Gnanadesikan, A. (2007). A synthesis of global particle export from the surface ocean and cycling through the ocean interior and on the seafloor. *Global Biogeochem. Cycles* 21:GB4006. doi: 10.1029/2006GB002907

Duteil, O., Oschlies, A., and Böning, C. W. (2018). Pacific Decadal Oscillation and recent oxygen decline in the eastern tropical Pacific Ocean. *Biogeosciences* 15, 7111–7126. doi: 10.5194/bg-15-7111-2018

Feely, R. A., Sabine, C. L., Lee, K., Berelson, W., Kleypas, J., Fabry, V. J., et al. (2004). Impact of anthropogenic CO_2 on the $CaCO_3$ system in the oceans. *Science* 305, 362–366. doi: 10.1126/science.1097329

Fox-Kemper, B., Adcroft, A., Böning, C. W., Chassignet, E. P., Curchitser, E., Danabasoglu, G., et al. (2019). Challenges and prospects in ocean circulation models. *Front. Mar. Sci*. 6:65. doi: 10.3389/fmars.2019.00065

Friedlingstein, P., Meinshausen, M., Arora, V. K., Jones, C. D., Anav, A., Liddicoat, S. K., et al. (2014). Uncertainties in CMIP5 climate projections due to carbon cycle feedbacks. *J. Clim*. 27, 511–526. doi: 10.1175/JCLI-D-12-00579.1

Frölicher, T. L., Joos, F., Plattner, G.-K., Steinacher, M., and Doney, S. C. (2009). Natural variability and anthropogenic trends in oceanic oxygen in a coupled carbon cycle – climate model ensemble. *Global Biogeochem. Cycles*. 23:1. doi: 10.1029/2008GB003316

Frölicher, T. L., Rodgers, K. B., Stock, C. A., and Cheung, W. W. L. (2016). Sources of uncertainties in 21st century projections of potential ocean ecosystem stressors. *Global Biogeochem. Cycles*. 30, 1224–1243. doi: 10.1002/2015GB005338

Fung, I. Y., Doney, S. C., Lindsay, K., and John, J. (2005). Evolution of carbon sinks in a changing climate. *PNAS* 102, 11201–11206. doi: 10.1073/pnas.0504949102

Galbraith, E. D., Dunne, J. P., Gnanadesikan, A., Slater, R. D., Sarmiento, J. L., Dufour, C. O., et al. (2015). Complex functionality with minimal computation: promise and pitfalls of reduced-tracer ocean biogeochemistry models. *J. Adv. Model. Earth Syst*. 7, 2012–2028. doi: 10.1002/2015MS000463

Galbraith, E. D., Gnanadesikan, A., Dunne, J. P., and Hiscock, M. R. (2010). Regional impacts of iron-light colimitation in a biogeochemical model. *Biogeosciences* 7, 1043–1064. doi: 10.5194/bg-7-1043-2010

Galbraith, E. D., Kwon, E. Y., Gnanadesikan, A., Rodgers, K. B., Griffies, S. M., Bianchi, D., et al. (2011). Climate variability and radiocardbon in the CM2Mc earth system model. *J.Clim*. 24, 4230–4254. doi: 10.1175/2011JCLI3919.1

Garcia, H. E., Locarnini, R. A., Boyer, T. P., Antonov, J. I., Zweng, M. M., Baranova, O. K., et al. (2010). "Nutrients (phosphate, nitrate, silicate)," in *World Ocean Atlas 2009, Vol. 4*, ed S. Levitus (Washington, DC: NOAA Atlas NESDIS 71, U.S. Government Printing Office), 398.

Geider, R. J., MacIntyre, H. L., and Kana, T. M. (1996). A dynamic model of photoadaptation in phytoplankton. *Limnol. Oceanogr*. 41, 1–15. doi: 10.4319/lo.1996.41.1.0001

Gent, P. R., and McWilliams, J. (1990). Isopycnal mixing in ocean circulation models. *J. Phys. Oceanogr*. 20, 159–155. doi: 10.1175/1520-0485(1990)020<0150:IMIOCM>2.0.CO;2

Gnanadesikan, A., Bianchi, D., and Pradal, M.-A. (2013). Critical role for mesoscale eddy diffusion in supplying oxygen to hypoxic ocean waters. *Geophys. Res. Lett*. 40, 5194–5198. doi: 10.1002/grl.50998

Gnanadesikan, A., Pradal, M.-A., and Abernathey, R. P. (2015a). Isopycnal mixing by mesoscale eddies significantly impacts oceanic anthropogenic carbon uptake. *Geophys. Res. Lett*. 42, 4249–4255. doi: 10.1002/2015GL064100

Gnanadesikan, A., Pradal, M.-A., and Abernathey, R. P. (2015b). Exploring the isopycnal mixing and helium-heat paradoxes in a suite of Earth System Models. *Ocean Sci*. 11, 591–605. doi: 10.5194/os-11-591-2015

Gobler, C. J., and Baumann, H. (2016). Hypoxia and acidification in ocean ecosystems: coupled dynamics and effects on marine life. *Biol. Lett.* 12:20150976. doi: 10.1098/rsbl.2015.0976

Gregg, W. W., Casey, N. W., and McClain, C. R. (2005). Recent trends in global ocean chlorophyll. *Geophys. Res. Lett.* 32:L03606. doi: 10.1029/2004GL021808

Gregory, J. M., Ingram, W. J., Palmer, M. A., Jones, G. S., Stott, P. A., Thorpe, R. B., et al. (2004). A new method for diagnosing radiative forcing and climate sensitivity. *Geophys. Res. Lett*. 31:L03205. doi: 10.1029/2003GL018747

Griffies, S. M., Gnanadesikan, A., Dixon, K. W., Dunne, J. P., Gerdes, R., Harrison, M. J., et al. (2005). Formulation of an ocean model for global climate simulations. *Ocean Sci*. 1, 45–79. doi: 10.5194/os-1-45-2005

Hasselmann, K. (1993). Optimal fingerprints for the detection of time-dependent climate change. *J. Clim*. 6, 1957–1971. doi: 10.1175/1520-0442(1993)006<1957:OFFTDO>2.0.CO;2

Hegerl, G., and Zwiers, F. (2011). Use of models in detection and attribution of climate change. *WIREs Clim. Change*. 2, 570–591. doi: 10.1002/wcc.121

Heinze, C., Eyring, V., Friedlingstein, P., Jones, C., Balkanski, Y., Collins, W., et al. (2019). ESD reviews: climate feedbacks in the Earth system and prospects for their evaluation. *Earth Syst. Dyn*. 10, 379–452. doi: 10.5194/esd-10-379-2019

Heneghan, R. F., Hatton, I. A., and Galbraith, E. D. (2019). Climate change impacts on marine ecosystems through the lens of the size spectrum. *Emerg. Top. Life Sci*. 3, 233–243. doi: 10.1042/ETLS20190042

Henson, S. A., Sarmiento, J. L., Dunne, J. P., Bopp, L., Lima, I., Doney, S. C., et al. (2010). Detection of anthropogenic climate change in satellite records of ocean chlorophyll and productivity. *Biogeosciences* 7, 621–640. doi: 10.5194/bg-7-621-2010

Hofmann, M., Worm, B., Rahmsdorf, S., and Schellnhuber, H. J. (2011). Declining ocean chlorophyll under unabated atmospheric CO_2 emissions. *Environ. Res. Lett*. 6:034035. doi: 10.1088/1748-9326/6/3/034035

Jones, D. O., Yool, A., Wei, C. L., Henson, S. A., Ruhl, H. A., Watson, R. A., et al. (2014). Global reductions in seafloor biomass in response to climate change. *Global Change Biol*. 20, 1861–1872. doi: 10.1111/gcb.12480

Key, R. M., Kozyr, A., Sabine, C. L., Lee, K., Wanninkhof, R., Bullister, J. L., et al. (2004). A global ocean carbon climatology: results from Global Data Analysis Project (GLODAP). *Global Biogeochem. Cycles* 18:GB4031. doi: 10.1029/2004GB002247

Knutti, R., and Hegerl, G. C. (2008). The equilibrium sensitivity of the Earth's temperature to radiation changes. *Nat. Geosci*. 1, 735–743. doi: 10.1038/ngeo337

Kostadinov, T. S., Siegel, D. A., and Maritorena, S. (2009). Retrieval of the particle size distribution from satellite ocean color observations. *J. Geophys. Res. Oceans* 114:C09015. doi: 10.1029/2009JC005303

Kwiatkowski, L., Aumont, O., and Bopp, L. (2018). Consistent trophic amplification of marine biomass declines under climate change. *Glob. Chang. Biol*. 25, 218–229. doi: 10.1111/gcb.14468

Kwon, E. Y., Deutsch, C., Xie, S., Schmidtko, S., and Cho, Y. (2016). The North Pacific oxygen uptake rates over the past half century. *J. Clim*. 29, 61–76. doi: 10.1175/JCLI-D-14-00157.1

Kwong, L. E., and Pakhomov, E. A. (2017). Assessment of active vertical carbon transport: new methodology. *Uchenye Zapiski Kazanskogo Universiteta Seriya Estestvennye Nauki* 159, 492–509. Available online at: https://kpfu.ru/portal/docs/F_2080971882/159_3_est_13.pdf

Laufkötter, C., et al. (2016). Projected decreases in future marine export production: the role of Carbon flux through the upper ocean ecosystem. *Biogeosciences* 13, 4023–4047. doi: 10.5194/bg-13-4023-2016

Lauvset, S. K., Key, R. M., Olsen, A., van Heuven, S., Velo, A., Lin, X., et al. (2016). A new global interior ocean mapped climatology: the 1× 1 GLODAP version 2. *Earth Syst. Sci. Data* 8, 325–340. doi: 10.5194/essd-8-325-2016

Leblanc, K., Quéguiner, B., Diaz, F., Cornet, V., Michel-Rodriguez, M., Durrieu de Madron, X., et al. (2018). Nanoplanktonic diatoms are globally overlooked but play a role in spring blooms and carbon export. *Nat. Commun*. 9:953. doi: 10.1038/s41467-018-03376-9

Lermusiaux, P. F. J. (2006). Uncertainty estimation and prediction for interdisciplinary ocean dynamics. *J. Comput. Phys*. 217, 176–199. doi: 10.1016/j.jcp.2006.02.010

Lévy, M., Iovino, D., Resplandy, L., Klein, P., Madec, G., Tréguier, A. M., et al. (2012). Large-scale impacts of submesoscale dynamics on phytoplankton: local and remote effects. *Ocean Model*. 43, 77–93. doi: 10.1016/j.ocemod.2011.12.003

Lin, S.-J. (2004). A "vertically Lagrangian" finite-volume dynamical core for global models. *Mon. Weather Rev*. 132, 2293–2307. doi: 10.1175/1520-0493(2004)132<2293:AVLFDC>2.0.CO;2

Lotze, H. K., Tittensor, D. P., Bryndum-Buchholz, A., Eddy, T. D., Cheung, W. W., Galbraith, E. D., et al. (2019). Global ensemble projections reveal trophic amplification of ocean biomass declines with climate change. *Proc. Natl. Acad. Sci. U.S.A.* 116, 12907–12912. doi: 10.1073/pnas.1900194116

Nikurashin, M., and Ferrari, R. (2011). Global energy conversion rate from geostrophic flows into internal waves in the deep ocean. *Geophys. Res. Lett*. 38:L08610. doi: 10.1029/2011GL046576

Nishioka, J., et al. (2007). Iron supply to the western subarctic Pacific: importance of iron export from the Sea of Okhotsk. *J. Geophys. Res.* 112:C10012. doi: 10.1029/2006JC004055

Orr, J. C., Fabry, V. J., Aumont, O., Bopp, L., Doney, S. C., Feely, R. A., et al. (2005). Anthropogenic ocean acidification over the twenty-first century and its impact on calcifying organisms. *Nature* 437, 681–686. doi: 10.1038/nature04095

Oschlies, A. (2002). Can eddies make ocean deserts bloom. *Global Biogeochem. Cycles* 16:1106. doi: 10.1029/2001GB001830

Palter, J. B., and Trossman, D. S. (2018). The sensitivity of future ocean oxygen to changes in ocean circulation. *Global Biogeochem. Cycles* 32, 738–751. doi: 10.1002/2017GB005777

Pradal, M.-A., and Gnanadesikan, A. (2014). How does the Redi parameter for mesoscale mixing impact global climate in an Earth System Model? *J. Adv. Model. Earth Syst*. 6, 586–601. doi: 10.1002/2013MS000273

Redi, M. H. (1982). Oceanic Isopycnal mixing by coordinate rotation. *J. Phys. Oceanogr*. 12, 1154–1158. doi: 10.1175/1520-0485(1982)012<1154:OIMBCR>2.0.CO;2

Rivero-Calle, S. (2016). *Anthropogenic change vs. natural variability: lessons learned from the continuous plankton recorder* (Ph.D. dissertation). Johns Hopkins University, Baltimore, MD, United States. Available online at: http://jhir.library.jhu.edu/handle/1774.2/60651 (accessed August 26, 2020).

Roxy, M. K., A., Modi, R., Murtugudde, V., Valsala, S., Panickal, S., et al. (2016). A reduction in marine primary productivity driven by rapid warming over the tropical Indian Ocean. *Geophys. Res. Lett*. 43, 826–833. doi: 10.1002/2015GL066979

Rykaczewski, R. R., and Dunne, J. P. (2010). Enhanced nutrient supply to the California Current Ecosystem with global warming and increased stratification in an earth system model. *Geophys. Res. Lett*. 37:L21606. doi: 10.1029/2010GL045019

Rykaczewski, R. R., and Dunne, J. P. (2011). A measured look at ocean chlorophyll trends. *Nature* 472, 5–6. doi: 10.1038/nature09952

Saba, V. S., Friedrichs, M. A. M., Antoine, D., Armstrong, R. A., Asanuma, I., Behrenfeld, M. J., et al. (2011). An evaluation of ocean color model estimates of marine primary productivity in coastal and pelagic regions across the globe. *Biogeosciences* 8, 489–503. doi: 10.5194/bg-8-489-2011

Schmittner, A., Oschlies, A., Matthews, H. D., and Galbraith, E. D. (2008). Future changes in climate, ocean circulation, ecosystems, and biogeochemical cycling simulated for a business-as-usual CO2 emission scenario until year 4000AD. *Global Biogeochem. Cycles* 22:GB1013. doi: 10.1029/2007GB002953

Shine, K. P., Wang, W. C., Wuebbles, D., Ding, M., Edmonds, J. A., Fraser, R., et al. (1990). "Radiative forcing of climate," in *Climate Change: The IPCC Scientific Assessment*, 41–68.

Stramma, L., Prine, E. D., Schmidtko, S., Luo, J., Hoolihan, J. P., Visbeck, M., et al. (2012). Expansion of oxygen minimum zones may reduce available habitat for tropical pelagic fishes. *Nat. Clim. Change* 2, 33–37. doi: 10.1038/nclimate1304

Taucher, J., and Oschlies, A. (2011). Can we predict the direction of marine primary production change under global warming? *Geophys. Res. Lett*. 38:L02603. doi: 10.1029/2010GL045934

Taylor, K. E., Stouffer, R. J., and Meehl, G. A. (2011). An overview of CMIP5 and the experiment design. *Am. Meteorol. Soc*. 4, 485–498. doi: 10.1175/BAMS-D-11-00094.1

Thomson, P., Davidson, A., and Maher, L. (2016). Increasing CO_2 changes community composition of pico- and nano-sized protists and prokaryotes at a coastal Antarctic Site. *Mar. Ecol. Prog. Ser*. 554, 51–69. doi: 10.3354/meps11803

Zeebe, R. E., and Wolf-Gladrow, D. A. (2001). *CO2 in Seawater: Equilibrium, Kinetics, Isotopes. Elsevier Oceanography Series, Vol. 65*. Amsterdam: Elsevier.

Zhang, M., and Huang, Y. (2014). Radiative forcing of quadrupling CO_2. *J. Clim*. 27, 2496–2508. doi: 10.1175/JCLI-D-13-00535.1

Conflict of Interest: The authors declare that the research was conducted in the absence of any commercial or financial relationships that could be construed as a potential conflict of interest.

frontiers in Marine Science

ORIGINAL RESEARCH
published: 15 October 2020
doi: 10.3389/fmars.2020.00657

Climate Change-Induced Emergence of Novel Biogeochemical Provinces

Gabriel Reygondeau[1,2], William W. L. Cheung[1], Colette C. C. Wabnitz[1,3], Vicky W. Y. Lam[1], Thomas Frölicher[4,5] and Olivier Maury[6]*

[1] Institute for the Oceans and Fisheries, The University of British Columbia, Vancouver, BC, Canada, [2] Department of Ecology and Evolutionary Biology, Max Planck – Yale Center for Biodiversity Movement and Global Change, Yale University, New Haven, CT, United States, [3] Stanford Center for Ocean Solutions, Stanford University, Stanford, CA, United States, [4] Climate and Environmental Physics, Physics Institute, University of Bern, Bern, Switzerland, [5] Oeschger Centre for Climate Change Research, University of Bern, Bern, Switzerland, [6] Marine Biodiversity, Exploitation and Conservation, Institut de Recherche pour le Développement, Ifremer, Université de Montpellier, CNRS, Sète, France

OPEN ACCESS

Edited by:
Kenneth Alan Rose,
University of Maryland Center for Environmental Science (UMCES), United States

Reviewed by:
Juan José Morrone,
National Autonomous University of Mexico, Mexico
Scott Doney,
University of Virginia, United States
Victoria Janet Coles,
University of Maryland Center for Environmental Science (UMCES), United States

***Correspondence:**
Gabriel Reygondeau
gabriel.reygondeau@gmail.com

Specialty section:
This article was submitted to Global Change and the Future Ocean, a section of the journal Frontiers in Marine Science

Received: *01 March 2020*
Accepted: *20 July 2020*
Published: *15 October 2020*

Citation:
Reygondeau G, Cheung WWL, Wabnitz CCC, Lam VWY, Frölicher T and Maury O (2020) Climate Change-Induced Emergence of Novel Biogeochemical Provinces. Front. Mar. Sci. 7:657. doi: 10.3389/fmars.2020.00657

The global ocean is commonly partitioned into 4 biomes subdivided into 56 biogeochemical provinces (BGCPs) following the accepted division proposed by Longhurst in 1998. Each province corresponds to a unique regional environment that shapes biodiversity and constrains ecosystem structure and functions. Biogeochemical provinces are dynamic entities that change their spatial extent and position with climate and are expected to be perturbated in the near future by global climate change. Here, we characterize the changes in spatial distribution of BGCPs from 1950 to 2100 using three earth system models under two representative concentration pathways (RCP 2.6 and 8.5). We project a reorganization of the current distribution of BGCPs driven mostly by a poleward shift in their distribution (18.4 km in average per decade). Projection of the future distribution of BGCPs also revealed the emergence of new climate that has no analog with past and current environmental conditions. These novel environmental conditions, here named No-Analog BGCPs State (NABS), will expand from 2040 to 2100 at a rate of 4.3 Mkm^2 per decade (1.2% of the global ocean). We subsequently quantified the potential number of marine species and annual volume of fisheries catches that would experience such novel environmental conditions to roughly evaluate the impact of NABS on ecosystem services.

Keywords: physical oceanography, marine biogeography, pelagic environment, novel ocean climate, environmental niche model

INTRODUCTION

The biosphere is partitioned according to well-defined biomes corresponding to unique sets of physical, chemical and biological conditions. On land, biomes such as "desert," "mountain," or "forest" can be delineated by environmental variables such as temperature, precipitation and altitude (Peel et al., 2007; Sayre, 2014). Similarly, the ocean has been subdivided in various ways, using either expert opinion or data driven methods based on both biotic and abiotic components of the marine realm (Kavanagh et al., 2004; Oliver and Irwin, 2008; Reygondeau and Dunn, 2018). The widely accepted system of ocean provinces elaborated originally by Longhurst (2007) covers both open ocean and coastal zones. Two levels structure Longhurst's province system. The first one distinguishes coastal and open ocean areas and subdivides them into temperate, tropical and polar biomes. The second sub-divides each of the coastal and oceanic biomes into oceanographically, ecologically and topographically homogeneous regions. This results in 56 distinct biogeochemical provinces (BGCPs) that have been shown to be closely related to global patterns in marine biodiversity (Pauly, 1999; Beaugrand et al., 2000), ecosystem functions and services such as fisheries productivity (Chassot et al., 2011; Demarcq et al., 2012; Reygondeau et al., 2012).

While the relevance of Longhurst's BGCPs to partition the ocean into homogeneous environmental and ecological regions has been established (Reygondeau et al., 2012), their delineation has been modified to improve their representativeness of the biogeography of diverse biological communities (Reygondeau et al., 2013). Specifically, Reygondeau et al. (2013) have shown how seasonal and inter-annual climate variability – such as such as such as El Niño Southern Oscillation (ENSO) event– modifies BGCPs' boundaries and drives their reorganization.

Climate change is expected to lead to drastic changes in ocean conditions. Oceans have already absorbed more than 93% of the heat resulting from the accumulation of greenhouse gases. They are rapidly getting warmer, less oxygenated (Gattuso et al., 2015) and changes in the seasonality of oceanographic conditions have already been reported. These oceanographic changes will alter the delineation and location of the BGCPs. Notably, some variables are expected to reach levels that are beyond those observed in recorded history (Froelicher et al., 2016). As a result, existing BGCPs might not be able to characterize regions where changes are projected to exceed the range of past observations. Such "novel" climatic zones have already been identified in the terrestrial realm. They have also been reported during marine heatwaves (Frölicher et al., 2018; Oliver et al., 2018).

In this study, we test the hypothesis that climate change might result in a large-scale bio-geographic re-organization of the oceans accompanied by the emergence of novel BGCPs. In particular, we examine the extent to which these novel BGCPs might overlap with marine biodiversity and fisheries (Cheung et al., 2016b; Cheung, 2018). For this purpose, we use the numerical approach described in Reygondeau et al. (2013) to analyze projected ocean conditions from three Earth System Models (ESM; Institut Pierre Simon Laplace, Max plank Institute and Geophysical Fluid Dynamics Laboratory models) under two climate change scenarios (the "strong mitigation" Representative Concentration Pathway, or RCP 2.6, and "business-as-usual" RCP 8.5). For each ESM and RCP scenario we calculate the projected annual average distribution of each BGCP from 1950 to 2100. We then identify regions that are characterized by novel combinations and levels of oceanographic variables and that have therefore never been observed historically. We name these novel BGCPs No Analog Biogeographical State regions (NABS). We quantify the timing of NABS emergence and evaluate the potential consequences on marine biodiversity and key marine ecosystem services.

MATERIALS AND METHODS

Environmental Data

The ocean properties that we used to delineate the BGCPs from 1950 to 2100 were based on outputs from three ESMs. They include annual average surface (average between 0 and 10 m)and bottom sea water temperature (°C), oxygen concentration ($ml.L^{-1}$), salinity, pH, surface net primary production ($mgC.km^2.year^{-1}$),particulate organic carbon concentration ($mgC.km^2.year^{-1}$) and sea ice coverage (%). These data have been simulated by the Geophysical Fluid Dynamics Laboratory Earth System Model (GFDL ESM2M), the Institut Pierre Simon Laplace Climate Model (IPSL-CM5-MR) and the Max Planck Institute for Meteorology Earth System Model (MPI-ESM). They were made available through the Coupled Model Intercomparison Project phase 5 (CMIP5; Taylor et al., 2012). The ESM outputs were re-gridded onto a regular grid of 0.5° of latitude by 0.5° of longitude using the nearest neighbor method and values in coastal cells were extrapolated using bilinear extrapolation. In addition, annual climatologies of euphotic depth (Morel et al., 2007), mixed layer depth (de Boyer Montégut et al., 2004), and bathymetry (Smith and Sandwell, 1997) were also used to delineate BGCP boundaries. These variables were gathered from observations and are here used to optimize the quantification of the environmental envelopes of specific BGCPs such as frontal oceanic systems, coastal regions or boundary of oceanic subtropical gyres.

The ESM outputs for the future period (2006–2100) were simulated under RCP 2.6 and RCP 8.5. The RCP 2.6 is a lower emission "strong mitigation" scenario under which the radiative forcing trajectory peaks at 3 $W.m^{-2}$ before 2100 and then is followed by a decline to 2.6 $W.m^{-2}$ by 2100. The RCP8.5 is a high emission "business-as-usual" scenario with a rising radiative forcing pathway leading to 8.5 $W.m^{-2}$ by 2100.

Modeling the Geography of BGCPs

To delineate the BGCPs' boundaries for each year from 1950 to 2100, we applied the numerical approach described in detail in Reygondeau et al. (2013). The approach quantifies the environmental envelopes of each BGCP based on the variables described above and projecting their future spatial distribution (**Figure 1**). First, the spatial coordinates of the boundaries for each BGCP as defined by Longhurst (2007) were retrieved (**Figure 1A**). Second, to include the monthly variation of each variable and characterize the discrete set of environmental conditions that characterize each BGCP, we obtained monthly values of the ESM outputs for each variable and spatial cell in each BGCP for the time period January 1970 to December 2000. This time period represents the timeframe over which the BGCP delineation was defined originally. We here used all environmental variables (surface and bottom) for BGCP located in the coastal biome and only surface environmental variables for

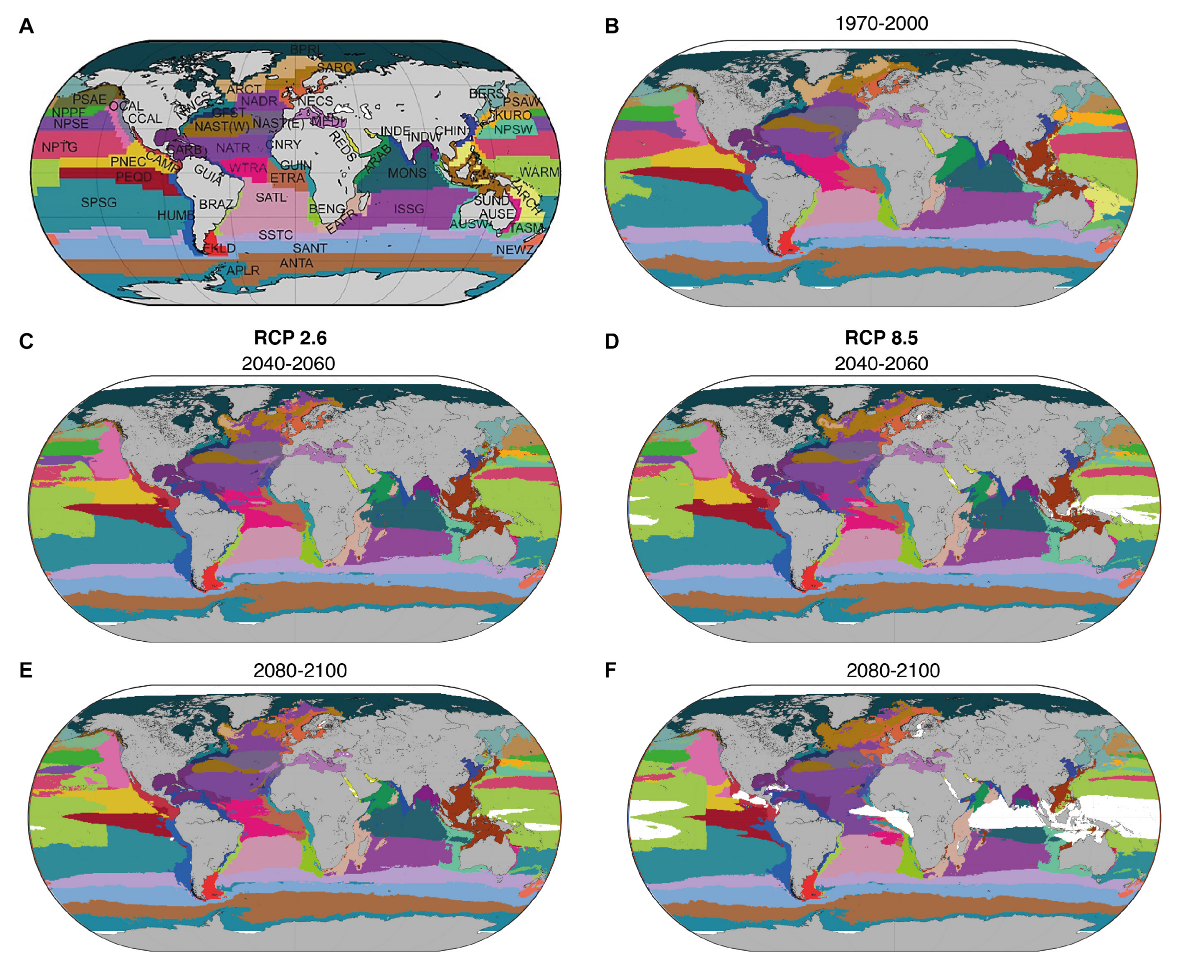

FIGURE 1 | Distribution of the 56 BGCPs: **(A)** according to Longhurst (2007); and for **(B)** the average period 1970–2000, **(C,D)** for 2040–2060, and **(E,F)** 2080–2100 under representative concentration pathway 2.6 and 8.5, respectively. Distributions of each province were averaged across the three Earth System Models and three Environmental Niche Models. Each color represents a BGCP. Color coding refers to panel **(A).** Acronyms of each BGCP can be found in **Supplementary Table 1**.

BGCP located in the tropical, temperate and polar biomes (see **Supplementary Table 1**). We obtained 56 matrices of environmental properties (one for each province) named $X_{n1,p,z}$ (n1 = 360 months, p = x environmental variables, z = number of geographical cells of the selected province). Third, we quantified the environmental envelope of each BGCP using three environmental niche models (ENM): Non-Parametric Probabilistic environmental niche model (Beaugrand et al., 2011), Maxent (Phillips et al., 2004), and boosted Regression Trees (Elith et al., 2008). We treated spatial cells included in each distinct BGCPs as a set of "occurrence records" analogous to species distributions and applied each ENM to model the environmental envelopes of each BGCP. We applied a multi-model ensemble approach to capture the uncertainty associated with the different numerical methods. Finally, we computed the time-dependent spatial distributions of the probability of occurrence (values ranging between 0 and 1) of each BGCP from the annual average ENM outputs for each ESM and each RCP scenario. Global BGCP division is then identified by attributing the geographical cell to the BGCP with the highest probability of occurrence for each year in each geographical cell and year.

Comparing Predictions With Observations

We compared the spatial distribution of and temporal fluctuation in the BGCPs predicted from ESM outputs with the ones gathered using observed environmental variables in Reygondeau et al. (2013). To harmonize the two sets of BGCP predictions, the BGCP distributions were averaged annually over the same period (1998–2007) and regridded using the nearest neighbor method on a 1°×1° spatial grid (original spatial grid used in Reygondeau et al., 2013). We first performed a spatial correlation of the average probability of presence from 1998 and 2007 to evaluate the level of congruence between observed and modeled BGCPs. We then performed a temporal correlation of the standard deviation of the probability of occurrence for the period 1998–2007 for each BGCP. Results from the analyses were used to evaluate the ability of ESM outputs to represent the temporal variability of the probability of a given BGCP (**Supplementary Figure 1**).

Geographical Trends

For each BGCP, we calculated changes in two geographical indices over time and compared the results between climate change scenarios. First, we calculated the annual centroid of each BGCP as the average coordinates of the center of the spatial cell belonging to a BGCP weighted by the value of the probability of occurrence of the same BGCP in the analyzed cell (**Figure 1**). Second, we calculated the total area covered by each BGCP based on the sum of area of the spatial cells belonging to the a given BGCP for each year. We calculated these indices using the ensemble average BGCP distributions across ESM and ENM under each RCP from 1950 to 2100. We then evaluated the latitudinal shifts and changes in total area of the BGCP from 1950 to 2100 (relative to the average of 1970–2000) under RCP 2.6 and RCP 8.5.

Identification of No Analog Biogeographical State

No-Analog BGCPs State (NABS) represents a multi-environmental range of condition that has not been encountered during the training set period (1950–2000) across the BGCPs. More precisely, a NABS set of environmental conditions is significantly different from all possible environmental combinations encountered from 1950 to 2000 and used to inform the multi variable environmental envelopes of the 56 BGCPs. Numerically, NABS are characterized by spatial cells exhibiting a null probability of occurrence for all of the 56 Longhurst BGCPs. We then quantified NABS distribution and coverage by delineating their annual boundaries and total area for each ESM and RCP. We identified the year at which a spatial cell first became a NABS and attributed a confirmed NABS location if the environmental conditions are similar (Null probability of original and spatially surrounding BGCPs) for more than five consecutive years for a given ESM and RCP pathway. We subsequently mapped the distribution of NABS as the 2/3 agreement between the 3 ESMs over time.

Assessing the Potential Impacts of NABS on Biodiversity and Ecosystem Services

The exposure to novel ocean conditions in NABS might seriously challenge the viability of marine species currently inhabiting those areas, thus leading to substantial species turnover, changes in catch composition, and declines in potential fisheries production (Cheung et al., 2016b). To evaluate the risk that the emergence of NABS may pose to marine biodiversity and ecosystems services, we calculated the number of marine species and the annual volume of fisheries catches that will be exposed to NABS conditions. For marine exploited biodiversity, we collated the global gridded marine species richness dataset (Gagné et al., 2020) and added several other exploited species distributions from the Sea Around Us[1] and species used in Asch et al. (2017). This dataset included 1,105 species ranging from invertebrate to top predator. We extracted average annual total fisheries catch (average between 2001 and 2015) from the Sea Around Us database. Both datasets were in the 0.5° latitude × 0.5° longitude grid consistent with the ocean conditions and BGCPs data. We then computed the number of species and total annual catch in spatial cells characterized as NABS for each year between 2000 and 2100 across ESMs and RCPs.

RESULTS

We projected that 26–39% of BGCPs will expand their area, while between 61 and 74% will shrink in size by 2100 under RCP 2.6 and 8.5, respectively (**Figures 1**, **2** and **Supplementary Tables 1, 2**), due to changes in environmental conditions (**Supplementary Figure 2**). Specifically, the tropical BGCPs were projected to expand while the temperate BGCPs were projected to contract by losing area on their tropical side, without compensation via poleward expansion. The two polar BGCPs were projected to shrink in size. This redistribution of BGCPs was moderate by 2050, but projected to be substantial by 2100 under RCP 8.5. The level of such redistribution was found to be more important over the Indo-Pacific basin with a high spatial perturbation located around the warm pool and monsoon provinces (WARM and MONS; **Figure 1** and **Supplementary Table 1**), altering the position of all neighboring BGCPs that tend to move poleward. The change in the distribution can be attributed to changes in SST, pH, salinity and oxygen concentration in the open ocean regions and to mainly NPP and Sea Bottom Temperature in the coastal biome (**Supplementary Figure 2**). Notably, we projected the emergence of a large area of NABS in tropical regions by the end of the 21st century under RCP 8.5 (**Figure 1**).

We projected significantly higher rates of poleward centroid shifts and changes in total area of the BGCPs under RCP 8.5 compared to RCP 2.6 (**Figure 2**). The average projected rate of poleward shift across the 56 BGCPs was 0.36 ± 0.66 km.year^{-1} (average and standard error) and 1.83 ± 1.99 km.year^{-1} under RCP 2.6 and RCP 8.5, respectively. ARAB (Arabian sea, 10.99 ± 0.81 km.year^{-1}), NADR (North Atlantic Drift Region, 6.28 ± 4.72 km.year^{-1}), and SATL (South Atlantic gyral province, 5.63 ± 3.45 km.year^{-1}) were the BGCPs exhibiting the strongest shift in their centroid (**Figure 2**). The ARAB shift would translate into a move north up to a 1,180 km by 2100. In contrast, the ISSG (Indian ocean South Subtropical Gyre province)and BRAZ (Brazilian coastal province) BGCPs did not shift, keeping their centroid locations constant (rate of shift of 0.02–0.05 km.year^{-1}). Biogeochemical provinces that were projected to expand the most were SARC (Sub atlantic ARCtic province; 1.98%.year^{-1}), CNRY (1.52%.year^{-1}) and NECS (NorthEast Atlantic Continental Shelve province, 1.08%.year^{-1}) – effectively doubling or more in size by 2100 – while PEQD (Pacific EQuatorial Divergence province, -1.10%.year^{-1}), ARCT (ARCTic province, -11.09%.year^{-1}) and NADR (North Atlantic Drift Region, -11.09%.year^{-1}) were expected to shrink substantially.

---

[1] www.seaaroundus.org

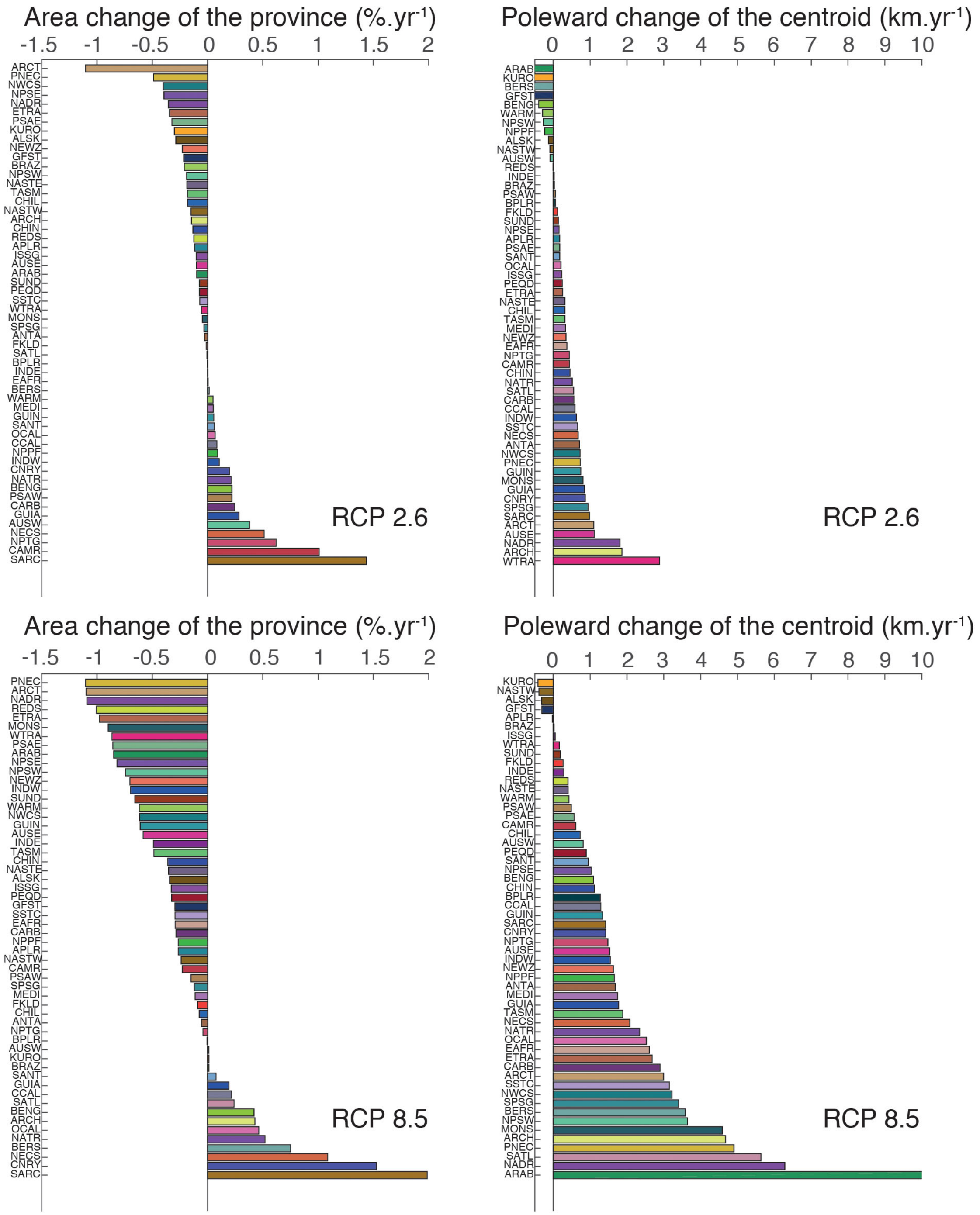

FIGURE 2 | Bar plot of the mean latitudinal change of the BGCPs' centroid (in km.year^{-1}) and percentage of BGCPs area change by 2100 compared to the 1970–2000 reference period (in % .year^{-1}) under RCP 2.6 and 8.5. The color code as well as acronyms are the same as **Figure 1A**.

To highlight the different categories of spatial changes registered by the BGCPs, we describe here examples of the three classes of projected change BGCPs may undergo: (1) poleward shift (North Atlantic Drift Region, NADR), (2) expansion with no spatial shift (North Atlantic Tropical Region, NATR), and (3) no specific change in size or location (Chilean coast, CHIL) (**Figure 3**). The probability of occurrence of the NADR province was projected to decrease sharply at the southern portion of its distribution towards the end of the 21st century under RCP 8.5, with the area between the Greenland Sea and Norwegian Sea displaying more NADR-like conditions over the course of this period. Hence, the overall location of this BGCP is projected to

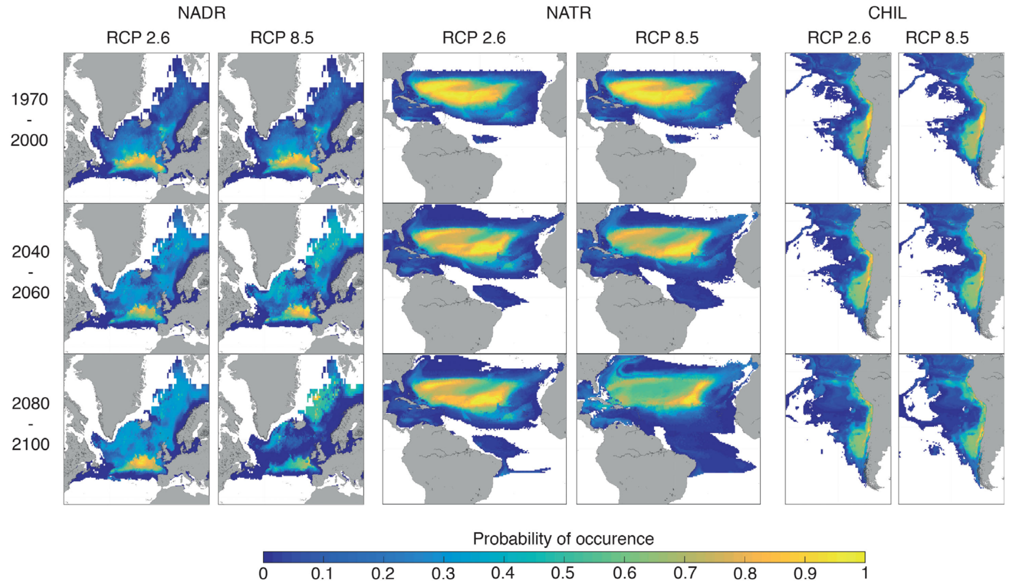

FIGURE 3 | Spatial distribution of the probability of occurrence of the following three BGCPs: North Atlantic Drift region (NADR), North Atlantic Tropical Region (NATR) and Chilean coast (CHIL). Mean ESMs and ENMs distribution of each province for the period 1970–2000, 2040–2060, and 2080–2100 are represented for both RCP 2.6 and 8.5.

shift northward. For NATR (North Atlantic Tropical Region), the BGCP boundary is projected to expand northward and southward into the Atlantic Ocean, while the probability of occurrence of the NATR province shows only a slight decline by the end of the century under RCP 8.5. For the CHIL BGCP, the projected boundary and probability of occurrence remained relatively stable under all scenarios.

We identified the emergence of a NABS in large areas of the western tropical Pacific Ocean, eastern tropical Indian Ocean and eastern tropical Atlantic Ocean (**Figure 4**). The earliest emergence of a NABS region (across all 3 ESMs) was projected to occur in the tropical south Pacific Ocean in the 2040s, under RCP 8.5. This NABS region was projected to grow very rapidly during the 2050s and 2060s, extending into the eastern Indian Ocean and emerging off the coast of tropical west Africa in the 2070s and in the Caribbean in the 2080s. In contrast, under RCP 2.6, the emergence of NABS occurs on average one decade later than under RCP 8.5 in the same general areas. NABS projected size by the end of the 21st century is on average 11.9% of projections under RCP 8.5. NABS regions are characterized by high SST, low oxygen concentration and low NPP or low pH and low NPP conditions compare to the reference period (**Supplementary Figure 3**).

We projected that a substantial proportion of global marine diversity and fisheries catches are presently located in regions where NABS are projected to develop. Under RCP 8.5, 18.97 ± 6.05% in 2050 and 59.49 ± 4,08% in 2100 of the total number of exploited marine species considered here (N = 1,105 species) will be exposed to the expansion of NABS regions. These NABS regions are indeed projected to develop in areas with high seafood dependence [in terms of calories and nutrition (Golden et al., 2016)] with relatively low adaptive capacity (Blasiak et al., 2017) and high exposure to simultaneous losses in terrestrial food production capacity. The proportion of global marine fisheries catches (average between 2001-2011) caught in areas of predicted NABS in 2050 and 2100 are 7.87 ± 3.94% and 30.39 ± 5.32%, respectively, under RCP 8.5. The projected exposure to NABS was much lower under RCP 2.6, with only 15% of exploited species and 5% of total catch in NABS areas by the end of the 21st century. The difference in trajectories in regards to NABS between RCP 2.6 and RCP 8.5 became significantly larger than the inter-ESM variability after the end of the 2040s.

DISCUSSION

This study supports the hypotheses that climate change will deeply affect the biogeography of the global ocean, and lead to the emergence of biomes with no historical analog. At the global scale, we predict that trade wind provinces will expand (Staten et al., 2018), with the distribution of several westerly wind provinces migrating poleward. This evolution will be driven mostly by the poleward extension of warm surface waters, pH, oxygen concentration, and NPP (**Supplementary Figure 2**). Warming of the tropics will drive a poleward migration of the BGCPs (**Figure 1** and **Supplementary Figure 2**) with the polar provinces progressively shrinking over time and being concentrated at the highest latitudes. These biogeographical changes appear to be corroborated by the rapid modifications in biogeochemical processes, species composition and food web dynamics already documented for these regions (Beaugrand et al., 2002; Dulvy et al., 2008; Polovina et al., 2008; Stramma et al., 2012; Fossheim et al., 2015). Such patterns are also in accordance with other projections performed using modeled distributions of

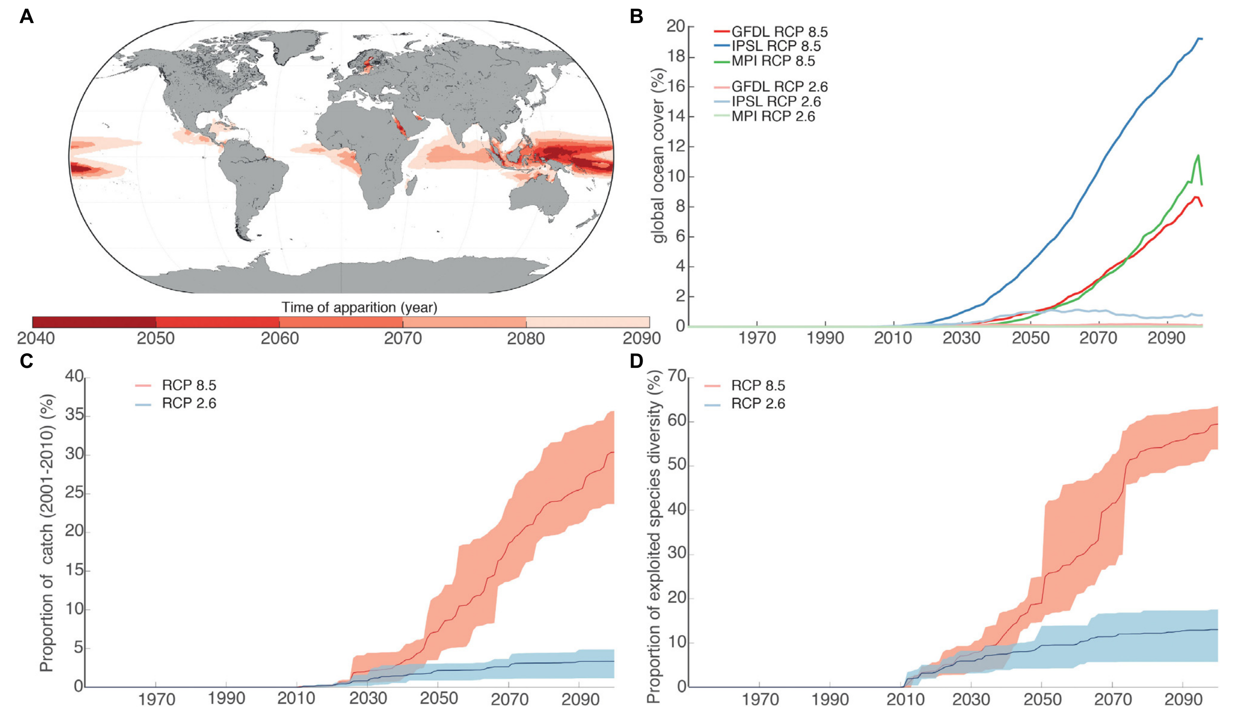

FIGURE 4 | (A) Spatial distribution of the average time of appearance of the NABS across ESMs under RCP 8.5. **(B)** Evolution of the global coverage of the NABS for the three ESMs and two RCPs. **(C)** Proportion of global fisheries catches (sum of catch between 2001 and 2010) located in the NABS regions for the period 1970–2100. Interval of confidence computed using the three different ESMs. Thick line represents the median across ESMs. **(D)** Proportion of the number of species in the NABS for the period 1970–2100. Interval of confidence computed using the three different ESMs. Thick line represents the median across ESMs.

marine species (Cheung et al., 2009; Lenoir et al., 2011), biomes (Sarmiento et al., 2004) and climate velocity computed using only SST(Burrows et al., 2011). However, in areas where province boundaries are constrained by the presence of land, we expect a significant decline in the original area of several provinces (ARAB, GUIN, GUIA, CARB, CHIN), with the potential to significantly impact the ecological assemblages characterizing those provinces.

Our results show that NABS regions will cover areas where a substantial proportion of global marine biodiversity presently occurs and with a crucial dependence on seafood production. The emergence of wide NABS areas in the tropical ocean will exacerbate the high vulnerability of populations living in developing coastal nations and small island states (Lam et al., 2016; Blasiak et al., 2017). Biodiversity, structure and function of marine ecosystems, and fisheries catches are closely related to the characteristics of the BGCPs (Reygondeau et al., 2013). The climate-induced changes to BGCPs that we project provide additional support to the idea that climate change will deeply alter the distribution and function of marine ecosystems as well as the benefits derived from them by people. Predicting the evolution of marine biodiversity in the NABS areas raises significant challenges, as the knowledge we currently hold regarding the organization of ecosystems in existing biomes is likely to be invalidated in no-analog environmental conditions (Fitzpatrick and Hargrove, 2009). While we cannot definitively state that no species stand to benefit from these new conditions, as the NABS predominantly occur in tropical regions where many species are already close to physiological maxima (Walther et al., 2002; Sunday et al., 2011, 2012), it is likely the emergence of NABS will substantially elevate the risk of impacts on marine biodiversity and fisheries.

The NABS were characterized by very warm mean annual temperatures, high salinity, low oxygen concentration and low NPP compared to the reference period (**Supplementary Figure 3**). Most marine species will be physiologically stressed under such conditions, which could impact their survival rate (Sunday et al., 2012). This explains the high rate of local extinction predicted by previous studies in the regions where NABS environmental conditions will not fit the environmental tolerance range of the majority of endemic species (Beaugrand et al., 2015; Jones and Cheung, 2015). Paleontological records have shown that the apparition of novel types of climate increases the rate of migration impacting the local biodiversity pool (Jablonski, 2008). Also, such changes in the local environmental condition will impact the biological processes of marine species. In NABS regions, we therefore expect a decrease in the size of endemic species as well as a decline in local biomass, as suggested by the literature. However, it is possible that some species will manage to survive in NABS-like environments, particularly small organisms with high turnover rates, such as microbes, that have good potential for rapid adaptation, as well as species that are physiologically more flexible, such as widely distributed marine species that occur in the Pacific Warm Pool. However, species that prove capable of adapting in NABS may only represent a small fraction of the currently high biological diversity occurring in these regions (Donelson et al., 2019; Palumbi et al., 2019).

Our results can be linked to recent studies on marine extreme events (Frölicher et al., 2018; Oliver et al., 2018) that have shown, using satellite observations, that recurring and permanent marine heatwaves already occur in the regions where we expect NABS to appear by the middle of the 21st century. We can reasonably expect that the impacts that these marine heatwaves already have had on marine life (Le Nohaïc et al., 2017; Oliver et al., 2017) will be similar or even amplified under NABS conditions. The emergence of NABS would be limited in most regions of the global ocean if CO_2 emissions can be held to the level required to achieve RCP 2.6 (**Figure 1**). However, if this is not the case (which currently appears likely), we expect the earliest NABS to emerge in about twenty years from 2010 in the tropical Pacific region and a decade later in the Indo-Pacific basin. There is therefore an urgent need to develop adaptation policies anticipating the risk of rapid ecosystem collapses in these regions, in addition to supporting efforts for strong mitigation.

The original methodology developed in Reygondeau et al. (2013) was applied on observed environmental data and used the ocean partition proposed by Longhurst (2007) as framework to quantify the environmental envelopes of BGCPs. Consequently, the application of the methodology to ESM have large uncertainty in correctly representing the ocean properties in several regions of the Ocean and hence distribution of BGCPs. The natural provinces (or regions of similar environmental conditions) derived from the models may not spatially match the prescribed boundaries found in Reygondeau et al. (2013). We subsequently tested the spatial and temporal agreement between our predictions based on different ESM projections and results from Reygondeau et al. (2013) (**Supplementary Figure 1**). Overall, the spatial division and internal variation of BGCPs are well captured in ESM outputs (**Supplementary Figure 1**), but several regions need to be considered with caution. First, the dynamic of coastal regions are not well captured by this generation of ESMs in the CMIP5 repository (Stock et al., 2011; Cheung et al., 2016a) and consequently, the distribution and dynamics of coastal BGCPs are not well represented for current or future projection. Second, semi enclosed sea (Red sea, Persian Gulf, Baltic sea, Mediterranean sea) have similar biases as coastal regions and results for these areas need to be taken with caution. Third, while the division of the southern ocean is well captured by the methodology using ESM outputs, several biases in the representation of the region biogeochemical dynamics are known (Bindoff et al., 2019). Consequently, future projection of the BGCPs in the southern Ocean are sensitive to thse biases. We hope that the finer resolution of the new generation of ESM models that are under development may resolve these issues in a future re-analysis.

Our results indicate that the environmental changes that would occur in the global ocean along a "no mitigation" RCP 8.5 scenario would lead to a drastic reorganization of global marine biogeography, associated biodiversity and trophic networks. These changes would include the emergence of wide regions with no environmental analog compared to current observations. If the global climate is not kept below 2°C warming, NABS areas can be expected to emerge, as early as 20 years from the 2010s. It would affect 19% of the total number of exploited species in 2050 and 59% in 2100 and would cover regions that are currently responsible for 8% of global marine fisheries catch in 2050 and 30% in 2100, under RCP 8.5. These numbers would change to only 15% of exploited species and 5% of total fisheries catches in NABS areas by the end of the 21st century under the RCP 2.6 scenario. Mitigating anthropogenic pressures at a level sufficient to reach the Paris agreement targets would therefore substantially reduce the risk of emergence of large NABS regions in the global ocean, and the dramatic consequences that such large-scale ecological changes would entail for tropical marine biodiversity, associated fisheries and the human communities that they support.

DATA AVAILABILITY STATEMENT

The datasets generated for this study are available on request to the corresponding author.

AUTHOR CONTRIBUTIONS

GR performed all the analyses and wrote the original of the manuscript. Idea originated from OM and GR. All other co-authors contributed to data sharing, idea, analysis, and writing of the manuscript. All authors contributed to the article and approved the submitted version.

FUNDING

WC, GR, CW, and VL acknowledge funding support from the Nippon Foundation-the University of British Columbia Nereus Program. WC acknowledges support from the Natural Sciences and Engineering Research Council of Canada. OM acknowledges the support of the French ANR project CIGOEF (grant ANR-17-CE32-0008-01). TF thanks the Swiss National Science Foundation (PP00P2_170687) and the European Union's Horizon 2020 Research and Innovation Programme under grant agreement no. 820989 (project COMFORT, Our common future ocean in the Earth system – quantifying coupled cycles of carbon, oxygen, and nutrients for determining and achieving safe operating spaces with respect to tipping points) for financial support.

ACKNOWLEDGMENTS

This study is dedicated by GR to the memory of Madeleine Remy.

SUPPLEMENTARY MATERIAL

The Supplementary Material for this article can be found online at: https://www.frontiersin.org/articles/10.3389/fmars.2020.00657/full#supplementary-material

REFERENCES

Asch, R. G., Cheung, W. W. L., and Reygondeau, G. (2017). Future marine ecosystem drivers, biodiversity, and fisheries maximum catch potential in Pacific Island countries and territories under climate change. *Mar. Policy.* 88, 285–294. doi: 10.1016/j.marpol.2017.08.015

Beaugrand, G., Edwards, M., Raybaud, V., Goberville, E., and Kirby, R. R. (2015). Future vulnerability of marine biodiversity compared with contemporary and past changes. *Nat. Clim. Chang* 5, 695–701. doi: 10.1038/nclimate2650

Beaugrand, G., Lenoir, S., Ibañez, F., and Manté, C. (2011). A new model to assess the probability of occurrence of a species, based on presence-only data. *Mar. Ecol. Prog. Ser.* 424, 175–190. doi: 10.3354/meps08939

Beaugrand, G., Reid, P., Ibañez, F., and Planque, B. (2000). Biodiversity of North Atlantic and North Sea calanoid copepods. *Mar. Ecol. Prog. Ser.* 204, 299–303. doi: 10.3354/meps204299

Beaugrand, G., Reid, P. C., Ibañez, F., Lindley, J. A., and Edwards, M. (2002). Reorganization of North Atlantic marine copepod biodiversity and climate. *Science* 296, 1692–1694. doi: 10.1126/science.1071329

Bindoff, N. L., Cheung, W. W. L., Kairo, J. G., Arístegui, J., Guinder, V. A., Hallberg, R., et al. (2019). "Changing ocean, marine ecosystems, and dependent communities," in *IPCC Special Report on the Ocean and Cryosphere in a Changing Climate*, eds H.-O. Pörtner, D. C. Roberts, V. Masson-Delmotte, P. Zhai, M. Tignor, E. Poloczanska, et al. Available online at: https://www.researchgate.net/publication/341281995_Changing_Ocean_Marine_Ecosystems_and_Dependent_Communities_09_SROCC_Ch05_FINAL-1 (accessed September 28, 2020).

Blasiak, R., Spijkers, J., Tokunaga, K., Pittman, J., Yagi, N., and Österblom, H. (2017). Climate change and marine fisheries: Least developed coutries top global index of vulnerability. *PLoS One.* 12:e0179632. doi: 10.1371/journal.pone.0179632

Burrows, M. T., Schoeman, D. S., Buckley, L. B., Moore, P., Poloczanska, E. S., Brander, K. M., et al. (2011). The pace of shifting climate in marine and terrestrial ecosystems. *Science* 334, 652–655. doi: 10.1126/science.1210288

Chassot, E., Bonhommeau, S., Reygondeau, G., Nieto, K., Polovina, J. J., Huret, M., et al. (2011). Satellite remote sensing for an ecosystem approach to fisheries management. *ICES J. Mar. Sci. J. du Cons.* 68:651.

Cheung, W. W. L. (2018). The future of fishes and fisheries in the changing oceans. *J. Fish Biol.* 92, 790–803. doi: 10.1111/jfb.13558

Cheung, W. W. L., Jones, M. C., Reygondeau, G., Stock, C. A., Lam, V. W. Y., and Frölicher, T. L. (2016a). Structural uncertainty in projecting global fisheries catches under climate change. *Ecol. Modell.* 325, 57–66. doi: 10.1016/j.ecolmodel.2015.12.018

Cheung, W. W. L., Reygondeau, G., and Frölicher, T. L. (2016b). Large benefits to marine fisheries of meeting the 1.5°*C global warming target*. *Science* 354, 1591–1594. doi: 10.1126/science.aag2331

Cheung, W. W. L., Lam, V. W. Y., Sarmiento, J. L., Kearney, K., Watson, R., and Pauly, D. (2009). Projecting global marine biodiversity impacts under climate change scenarios. *Fish Fish.* 10, 235–251. doi: 10.1111/j.1467-2979.2008.00315.x

de Boyer Montégut, C., Madec, G., Fischer, A. S., Lazar, A., and Ludicone, D. (2004). Mixed layer depth over the global ocean: An examination of profile data and a profile-based climatology. *J. Geophys. Res. C* 109, C12003.

Demarcq, H., Reygondeau, G., Alvain, S., and Vantrepotte, V. (2012). Monitoring marine phytoplankton seasonality from space. *Remote Sens. Environ.* 117, 211–222. doi: 10.1016/j.rse.2011.09.019

Donelson, J. M., Sunday, J. M., Figueira, W. F., Gaitán-Espitia, J. D., Hobday, A. J., Johnson, C. R., et al. (2019). Understanding interactions between plasticity, adaptation and range shifts in response to marine environmental change. *Philosoph. Transact. Royal Soc. B* 374:20180186.

Dulvy, N. K., Rogers, S. I., Jennings, S., Stelzenmller, V., Dye, S. R., and Skjoldal, H. R. (2008). Climate change and deepening of the North Sea fish assemblage: a biotic indicator of warming seas. *J. Appl. Ecol.* 45, 1029–1039. doi: 10.1111/j.1365-2664.2008.01488.x

Elith, J., Leathwick, J. R., and Hastie, T. (2008). A working guide to boosted regression trees. *J. Anim. Ecol.* 77, 802–813. doi: 10.1111/j.1365-2656.2008.01390.x

Fitzpatrick, M. C., and Hargrove, W. W. (2009). The projection of species distribution models and the problem of non-analog climate. *Biodivers. Conserv.* 18:2255. doi: 10.1007/s10531-009-95849588

Fossheim, M., Primicerio, R., Johannesen, E., Ingvaldsen, R. B., Aschan, M. M., and Dolgov, A. V. (2015). Recent warming leads to a rapid borealization of fish communities in the Arctic. *Nat. Clim. Chang.* 5, 673–677. doi: 10.1038/nclimate2647

Froelicher, T. L., Rodgers, K. B., Stock, C. A., and Cheung, W. W. L. (2016). Sources of uncertainties in 21st century projections of potential ocean ecosystem stressors. *Global Biogeochem. Cycles.* 30, 1224–1243. doi: 10.1002/2015GB005338

Frölicher, T. L., Fischer, E. M., and Gruber, N. (2018). Marine heatwaves under global warming. *Nature* 560, 383–389. doi: 10.1038/s41586-018-0383389

Gagné, T. O., Reygondeau, G., Jenkins, C. N., Sexton, J. O., Bograd, S. J., Hazen, E. L., et al. (2020). Towards a global understanding of the drivers of marine and terrestrial biodiversity. *PLoS One* 15:e0228065. doi: 10.1371/journal.pone.0228065

Gattuso, J. P., Magnan, A., Billé, R., Cheung, W. W. L., Howes, E. L., Joos, F., et al. (2015). Contrasting futures for ocean and society from different anthropogenic CO2emissions scenarios. *Science* 349:aac4722. doi: 10.1126/science.aac4722

Golden, C. D., Allison, E. H., Cheung, W. W. L., Dey, M. M., Halpern, B. S., McCauley, D. J., et al. (2016). Nutrition: Fall in fish catch threatens human health. *Nature* 534, 317–320. doi: 10.1038/534317a

Jablonski, D. (2008). Extinction and the spatial dynamics of biodiversity. *Proc. Natl. Acad. Sci.* 1, 11528–11535. doi: 10.1073/pnas.0801919105

Jones, M. C., and Cheung, W. W. L. (2015). Multi-model ensemble projections of climate change effects on global marine biodiversity. *ICES J. Mar. Sci.* 72, 741–752. doi: 10.1093/icesjms/fsu172

Kavanagh, P., Newlands, N., Christensen, V., and Pauly, D. (2004). Automated parameter optimization for Ecopath ecosystem models. *Ecol. Modell.* 172, 141–149.

Lam, V. W. Y., Cheung, W. W. L., Reygondeau, G., and Rashid Sumaila, U. (2016). Projected change in global fisheries revenues under climate change. *Sci. Rep.* 6:32607. doi: 10.1038/srep32607

Le Nohaïc, M., Ross, C. L., Cornwall, C. E., Comeau, S., Lowe, R., McCulloch, M. T., et al. (2017). Marine heatwave causes unprecedented regional mass bleaching of thermally resistant corals in northwestern Australia. *Sci. Rep.* 7:14999. doi: 10.1038/s41598-017-14794-y

Lenoir, S., Beaugrand, G., and Lécuyer, E. (2011). Modeled spatial distribution of marine fish and projected modifications in the North Atlantic Ocean. *Glob. Chang. Biol.* 17, 115–129. doi: 10.1111/j.1365-2486.2010.02229.x

Longhurst, A. (2007). *Ecological Geography of the Sea*. Cambridge, MA: Academic Press.

Morel, A., Huot, Y., Gentili, B., Werdell, P. J., Hooker, S. B., and Franz, B. A. (2007). Examining the consistency of products derived from various ocean color sensors in open ocean (Case 1) waters in the perspective of a multi-sensor approach. *Remote Sens. Environ.* 111, 69–88. doi: 10.1016/j.rse.2007.03.012

Oliver, E. C. J., Benthuysen, J. A., Bindoff, N. L., Hobday, A. J., Holbrook, N. J., Mundy, C. N., et al. (2017). The unprecedented 2015/16 Tasman Sea marine heatwave. *Nat. Commun.* 8, 1–12. doi: 10.1038/ncomms16101

Oliver, E. C. J., Donat, M. G., Burrows, M. T., Moore, P. J., Smale, D. A., Alexander, L. V., et al. (2018). Longer and more frequent marine heatwaves over the past century. *Nat. Commun.* 9:1324. doi: 10.1038/s41467-018-037323739

Oliver, M. J., and Irwin, A. J. (2008). Objective global ocean biogeographic provinces. *Geophys. Res. Lett.* 35:L15601.

Palumbi, S. R., Evans, T. G., Pespeni, M. H., and Somero, G. N. (2019). Present and future adaptation of marine species assemblages. *Oceanography* 32, 82–93.

Pauly, D. (1999). Longhurst Areas. *Trends Ecol. Evol.* 14:118. doi: 10.1016/S0169-5347(99)015861584

Peel, M. C., Finlayson, B. L., and Mcmahon, T. A. (2007). Updated world map of the Koppen-Geiger climate classification. *Hydrol. Earth Syst. Sci. Discuss.* 11, 1633–1644. doi: 10.1127/0941-2948/2006/0130

Phillips, S. J., Dudík, M., and Schapire, R. E. (2004). "A maximum entropy approach to species distribution modeling," in *Proceedings of the twenty-first international conference on Machine learning*, (New York: ACM), 83.

Polovina, J. J., Howell, E. A., and Abecassis, M. (2008). Ocean's least productive waters are expanding. *Geophys. Res. Lett.* 35, 1–5.

Reygondeau, G., and Dunn, D. (2018). *Encyclopedia of Ocean Sciences*. Netherland: Elsevier Ltd.

Reygondeau, G., Longhurst, A., Martinez, E., Beaugrand, G., Antoine, D., and Maury, O. (2013). Dynamic biogeochemical provinces in the global ocean. *Global. Biogeochem. Cycles* 27, 1046–1058.

Reygondeau, G., Maury, O., Beaugrand, G., Fromentin, J. M., Fonteneau, A., and Cury, P. (2012). Biogeography of tuna and billfish communities. *J. Biogeogr.* 39, 114–129. doi: 10.1111/j.1365-2699.2011.02582.x

Sarmiento, J. L., Slater, R., Barber, R., Bopp, L., Doney, S. C., Hirst, A. C., et al. (2004). Response of ocean ecosystems to climate warming. *Global Biogeochem. Cycles.* 18:GB3003. doi: 10.1029/2003GB002134

Sayre, R., Dangermond, J., Frye, C., Vaughan, R., Aniello, P., Breyer, S., et al. (2014). *A New Map of Global Ecological Land Units – An Ecophysiographic Stratification Approach*. Washington, DC: Association of American Geographers, 46.

Smith, W. H. F., and Sandwell, D. T. (1997). Global Sea Floor Topography from Satellite Altimetry and Ship Depth Soundings. *Science* 277, 1956–1962.

Staten, P. W., Lu, J., Grise, K. M., Davis, S. M., and Birner, T. (2018). Re-examining tropical expansion. *Nat. Clim. Chang.* 8, 768–775. doi: 10.1038/s41558-018-0246242

Stock, C. A., Alexander, M. A., Bond, N. A., Brander, K. M., Cheung, W. W. L., Curchitser, E. N., et al. (2011). On the use of IPCC-class models to assess the impact of climate on living marine resources. *Prog. Oceanogr.* 88, 1–27.

Stramma, L., Prince, E. D., Schmidtko, S., Luo, J., Hoolihan, J. P., Visbeck, M., et al. (2012). Expansion of oxygen minimum zones may reduce available habitat for tropical pelagic fishes. *Nat. Clim. Chang.* 2, 33–37. doi: 10.1038/nclimate1304

Sunday, J. M., Bates, A. E., and Dulvy, N. K. (2011). Global analysis of thermal tolerance and latitude in ectotherms. *Proc. R. Soc. B Biol. Sci.* 278, 1823–1830. doi: 10.1098/rspb.2010.1295

Sunday, J. M., Bates, A. E., and Dulvy, N. K. (2012). Thermal tolerance and the global redistribution of animals. *Nat. Clim. Chang.* 2, 686–690. doi: 10.1038/nclimate1539

Taylor, K. E., Stouffer, R. J., and Meehl, G. A. (2012). An overview of CMIP5 and the experiment design. *Bull. Am. Meteorol. Soc.* 93, 485–498. doi: 10.1175/BAMS-D-11-00094.1

Walther, G. R., Post, E., Convey, P., Menzel, A., Parmesan, C., Beebee, T. J. C., et al. (2002). Ecological responses to recent climate change. *Nature* 416, 389–395. doi: 10.1038/416389a

Conflict of Interest: The authors declare that the research was conducted in the absence of any commercial or financial relationships that could be construed as a potential conflict of interest.

frontiers in Marine Science

ORIGINAL RESEARCH
published: 26 November 2020
doi: 10.3389/fmars.2020.588482

Large Pelagic Fish Are Most Sensitive to Climate Change Despite Pelagification of Ocean Food Webs

Colleen M. Petrik[1]*, Charles A. Stock[2], Ken H. Andersen[3], P. Daniël van Denderen[3] and James R. Watson[4]

[1] Department of Oceanography, Texas A&M University, College Station, TX, United States, [2] Geophysical Fluid Dynamics Laboratory, National Oceanic and Atmospheric Administration, Princeton, NJ, United States, [3] Centre for Ocean Life, DTU Aqua, Technical University of Denmark, Lyngby, Denmark, [4] College of Earth, Ocean and Atmospheric Sciences, Oregon State University, Corvallis, OR, United States

Edited by:
*Kenneth Alan Rose,
University of Maryland Center
for Environmental Science (UMCES),
United States*

Reviewed by:
*Eric D. Galbraith,
McGill University, Canada
Jeroen Gerhard Steenbeek,
Ecopath International Initiative
Research Association, Spain*

***Correspondence:**
*Colleen M. Petrik
cpetrik@tamu.edu*

Specialty section:
*This article was submitted to
Global Change and the Future Ocean,
a section of the journal
Frontiers in Marine Science*

Received: *29 July 2020*
Accepted: *03 November 2020*
Published: *26 November 2020*

Citation:
*Petrik CM, Stock CA,
Andersen KH, van Denderen PD and
Watson JR (2020) Large Pelagic Fish
Are Most Sensitive to Climate Change
Despite Pelagification of Ocean Food
Webs. Front. Mar. Sci. 7:588482.
doi: 10.3389/fmars.2020.588482*

Global climate change is expected to impact ocean ecosystems through increases in temperature, decreases in pH and oxygen, increased stratification, with subsequent declines in primary productivity. These impacts propagate through the food chain leading to amplified effects on secondary producers and higher trophic levels. Similarly, climate change may disproportionately affect different species, with impacts depending on their ecological niche. To investigate how global environmental change will alter fish assemblages and productivity, we used a spatially explicit mechanistic model of the three main fish functional types reflected in fisheries catches (FEISTY) coupled to an Earth system model (GFDL-ESM2M) to make projections out to 2100. We additionally explored the sensitivity of projections to uncertainties in widely used metabolic allometries and their temperature dependence. When integrated globally, the biomass and production of all types of fish decreased under a high emissions scenario (RCP 8.5) compared to mean contemporary conditions. Projections also revealed strong increases in the ratio of pelagic zooplankton production to benthic production, a dominant driver of the abundance of large pelagic fish vs. demersal fish under historical conditions. Increases in this ratio led to a "pelagification" of ecosystems exemplified by shifts from benthic-based food webs toward pelagic-based ones. The resulting pelagic systems, however, were dominated by forage fish, as large pelagic fish suffered from increasing metabolic demands in a warming ocean and from declines in zooplankton productivity that were amplified at higher trophic levels. Patterns of relative change between functional types were robust to uncertainty in metabolic allometries and temperature dependence, though projections of the large pelagic fish had the greatest uncertainty. The same accumulation of trophic impacts that underlies the amplification of productivity trends at higher trophic levels propagates to the projection spread, creating an acutely uncertain future for the ocean's largest predatory fish.

Keywords: climate change, fish and fisheries, functional types, marine ecosystem model, metabolism, secondary production, trait-based model, trophic amplification

INTRODUCTION

Anthropogenic greenhouse gas emissions are increasing global ocean temperatures, altering stratification and mixed layer depths, and decreasing pH and dissolved oxygen (Stocker et al., 2013). Centennial-scale projections with coupled climate-ocean-biogeochemistry Earth system models (ESMs) show global increases in temperature, and most project decreases in primary productivity (Bopp et al., 2013; Stocker et al., 2013). Ocean temperature and productivity exert strong controls on marine fish biomasses and distributions. Temperature directly impacts physiological rates and thus energy supply and demand. As a consequence, cooler habitats can support greater biomasses per unit of energy supply than warmer ones (Brown et al., 2004). Additionally, temperature indirectly affects ecosystem structure through the effects of stratification on primary production. Thermal stratification maintains phytoplankton in the euphotic zone while it impedes the upward movement of nutrients from below the mixed layer. Regionally, the temporally evolving interplay between access to light and nutrients shapes both the total amount of primary production, its seasonality, and the size of primary producers (e.g., Behrenfeld and Boss, 2014). Beyond temperature, fish abundances are also related to measures of ecosystem productivity. The total amount of energy available at the base of the ecosystem and phytoplankton size affect the number of trophic steps between primary producers and fish, and thus the amount of energy available to upper trophic levels (Ryther, 1969; Pauly and Christensen, 1995).

The combined effect of decreased energy at the base of the food web and increased energy demand from higher temperatures leads to projections of decreased fish biomasses (Cheung et al., 2010; Blanchard et al., 2012; Bryndum-Buchholz et al., 2019; Carozza et al., 2019; Lotze et al., 2019) and smaller individual sizes (Blanchard et al., 2012; Audzijonyte et al., 2013; Cheung et al., 2013; Lefort et al., 2015; Lotze et al., 2019) under climate change. However, many of these models rely on net primary production (NPP) as a forcing variable, yet there is a large degree of uncertainty in NPP across ESM projections (Bopp et al., 2013). Furthermore, the connections between primary productivity and fish catches are complex. Empirical studies have found that NPP alone is a weak predictor of regional variations in total fish biomass (Ryther, 1969; Friedland et al., 2012; Stock et al., 2017). Rather, the production of fish biomass is closely tied to the separation of NPP into pelagic and benthic secondary production and the total amounts of these two types (Friedland et al., 2012; Stock et al., 2017). van Denderen et al. (2018) expanded this work by hypothesizing that the ratio of the two pathways from NPP to fishes influences which fish functional type dominates. The ratio of the fraction of NPP that remained in the pelagic to the fraction that was exported to the seafloor explained the majority of the deviance in the relative biomass of large pelagic fish vs. demersal fish in commercial landings (van Denderen et al., 2018). When the amounts of pelagic and benthic resources are similar, the generalist demersals are able to outcompete the large pelagic specialists by feeding on both resource pools while the large pelagics only have access to one. Mechanistic food web models have also verified this statistical relationship between the fraction of pelagic and benthic resources (van Denderen et al., 2018; Petrik et al., 2019). Global simulations of the Fisheries Size and Functional Type (FEISTY) model using a recent historic climatology indicated that large-scale spatial differences in the dominance of large pelagic vs. demersal fishes is strongly related to the ratio of pelagic zooplankton production to benthic production (Petrik et al., 2019).

The partitioning of production between pelagic and benthic pathways also helps explain latitudinal patterns in the distributions of large pelagic fish and demersal fish. In oligotrophic waters, like the continuously stratified subtropical gyres, the majority of NPP is recycled within the mixed layer via microbial pathways that support microzooplankton grazers in the pelagic zone. In contrast, the light-limited high latitudes experience strong but short blooms in NPP with high interannual variability. The variability in bloom timing can lead to a mismatch between phytoplankton and the zooplankton grazer population, which has been reduced to low levels via deep winter mixing, resulting in an ungrazed fraction of NPP that is available for export (e.g., Lutz et al., 2007). The degree of zooplankton-phytoplankton coupling, quantified as the fraction of NPP grazed by zooplankton, is projected to increase in the more stratified conditions produced by climate change (Stock et al., 2014a). Direct temperature effects reinforce bloom-driven latitudinal patterns in pelagic vs. benthic resources, and introduce additional sensitivities to climate change. Increasing particle remineralization rates under warmer temperatures during export may reduce the amount of organic carbon that reaches the seafloor (Pomeroy and Deibel, 1986; Laws et al., 2000; Laufkötter et al., 2017), though remineralization is also modulated by oxygen and biogenic and lithogenic minerals (Armstrong et al., 2002; Klaas and Archer, 2002).

The diverse pathways connecting ocean productivity and fisheries and their myriad susceptibilities to climate change underscores the need for models capable of resolving these pathways and resolving the fish functional type-specific responses to the climate-driven changes in them. Furthermore, to integrate climate drivers, global fish models such as those considered by Lotze et al. (2019) often rely on emergent regularities between physiological/ecological rates and organism size and temperature (e.g., von Bertalanffy, 1960; Perrin, 1995). These relationships are subject to significant uncertainties (e.g., Clarke and Johnston, 1999; Rall et al., 2012) whose impacts on projected changes in fish abundance and production have not been systematically explored, to the best of our knowledge.

In this paper, we contribute to addressing these limitations by assessing the impacts of changing energy flow pathways between phytoplankton and fish by projecting the changes in global production of three primary commercial fisheries functional types, forage, large pelagic, and demersal fishes, under IPCC RCP 8.5 through 2100. We use the FEISTY model (Petrik et al., 2019), which resolves trophic interactions and basic life cycle processes for each of the functional types of interest (**Figure 1**). We focus on patterns of trophic amplification, contrasts in the response of fish functional types, and the sensitivity of both these critical processes to uncertainties in widely applied metabolic allometries and temperature dependences in fisheries models.

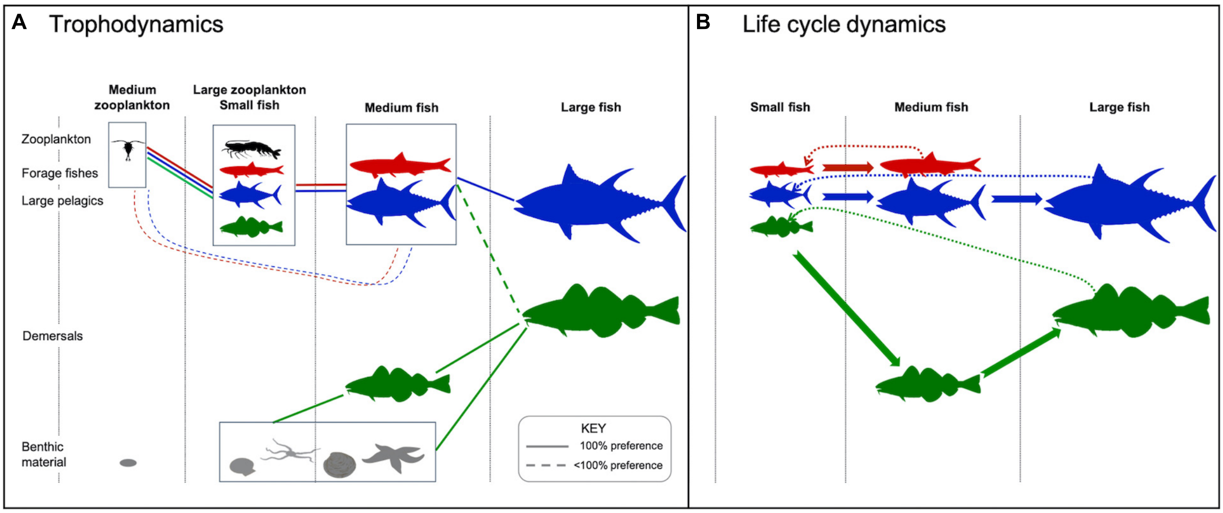

FIGURE 1 | Model structure denoting the two zooplankton size classes, three fish size classes, three functional types, two habitats, and two prey categories. **(A)** Size-based feeding interactions. Dashed line denotes feeding preference of <100%. For demersal fish (green), feeding in the pelagic only occurs in regions ≤200 m deep. **(B)** Life cycle dynamics including growth into a different stage/size class (solid arrows) and reproduction (dotted arrows). Fauna silhouettes courtesy of the Integration and Application Network, University of Maryland Center for Environmental Science (ian.umces.edu/symbols/).

MATERIALS AND METHODS

The projections integrate three model complexes that span physics, biogeochemistry, lower trophic level production, and fish production. In the following sections, we present an overview of the fish production (FEISTY) model (section "FEISTY: A Global Fisheries Model"), details on the Earth system model (ESM2M-COBALT) that provides the physics, biogeochemistry, and lower trophic level production (section "Ocean and Biogeochemical Projections"), a description of how parameter uncertainty was incorporated into projections (section "Projection Uncertainty"), and specifications on the simulations that were run and their analysis (section "Simulations and Analyses").

FEISTY: A Global Fisheries Model

The fish community in FEISTY describes the three main commercially harvested fish functional types. Each type resolves the life cycle from eggs to adults, with growth and reproduction depending on consumed food. The model is based on the physiology of an individual fish of a given size: its prey encounter, ingestion, and assimilation, its metabolic costs, and its allocation of net energy between somatic growth and reproduction. The scaling from individuals to the fish community is done by respecting mass balance. A detailed description of the fish model is given in Petrik et al. (2019).

The three functional types are forage fish, large pelagic fish, and (large) demersal fish. Each functional type is defined by its maximum body size (medium for forage fish; large for large pelagics and demersals), its habitat, and its prey preference. Within each group the size structure is represented by 2–3 life stages from 1 mg to 0.25 kg (all types) and to 125 kg (only large pelagics and demersals) (**Table 1**). The prey preference changes with body size. Fish eat prey that is smaller than themselves, either zooplankton, other fish, or benthos, and that live in the same habitat (**Figure 1A**). The habitat is either benthic or pelagic and changes with ontogeny. All larvae (fish in the first size group) are pelagic. Forage fish and large pelagics are also pelagic in the one or two next size groups. Demersal fish transition to benthic feeding in the medium (juvenile) size group. The adults are fully benthic in areas where the water column is >200 m, while in shallower areas they may feed in both the benthic and pelagic zones. This difference in habitat means that the forage and large pelagic fishes feed only on the pelagic energy pathway, while the demersal fish act as generalists that also feed on benthos. Benthic invertebrates are modeled separately from the fish functional types. They are represented by a biomass pool with no explicit size that is governed by additions via the detrital flux to the seafloor multiplied by a transfer efficiency and losses to predation by demersal fish.

The energy budget of an individual fish is described through ingestion with a Type II functional response. There is a constant fraction lost in the assimilation process and another loss to metabolism. The rate of biomass-specific available energy assimilation is:

$$v_i = aI_i - M_i \tag{1}$$

where M_i (d^{-1}) is the metabolic rate of size group i, a is the assimilation efficiency, and I (d^{-1}) is the ingestion rate. The available energy is used for somatic growth and reproduction, with reproduction only by the last size class (**Figure 1B**). Metabolism and all components of ingestion (encounter rate and maximum consumption rate) scale with body size via empirically determined allometric relationships of the form:

$$\exp(k(T - T_0))aw^b \tag{2}$$

TABLE 1 | Model parameters and simulated variables referenced in the main text (see **Table 2** and Petrik et al., 2019 for full list).

Symbol	Description	Value	Units
Parameters			
β	Transfer efficiency from detritus to benthic invertebrates	0.075	–
dt	Time step	1	d
ε	Reproductive efficiency	0.01	–
F	Fishing mortality rate	8.22E-04	d^{-1}
k	Temperature sensitivity of most rates	0.063	$°C^{-1}$
μ_{nat}	Natural mortality rate constant	2.74E-04	d^{-1}
T_0	Metabolic rates reference temperature	10	°C
w_L	Weight of large size class individual	250–125,000 (mean 5,600)	g
w_M	Weight of medium size class individual	0.5–250 (mean 11.2)	g
w_S	Weight of small size class individual	0.001–0.5 (mean 0.02)	g
Simulated			
B	Biomass of fish or benthic invertebrates	–	$g\ m^{-2}$
I	Mass-specific consumption rate	–	$g\ g^{-1}\ d^{-1}$
M	Mass-specific basal metabolic rate	–	$g\ g^{-1}\ d^{-1}$
ν	Rate of assimilation of total energy available for growth and reproduction	–	$g\ g^{-1}\ d^{-1}$

Means are geometric means. Parameter values are those in the baseline set. Simulated quantities are those derived from the model-governing equations, given a specified set of parameters and forcing. Note that these simulated variables are in addition to the core model state variables summarized in ***Figure 1****.*

where k governs temperature sensitivity by comparing habitat temperature, T, to the reference, T_0, w is weight, b is the size scaling exponent, and a is a constant factor. The exponential increase with temperature is akin to other forms such as the Arrhenius equation, based on Boltzmann activation energy, or the Q_{10} function, representing the rate of change with an increase of 10°C. Similar temperature- and mass-dependent functions are broadly applied in fisheries and marine ecosystem models (e.g., Tittensor et al., 2018), and sensitivity of trophic amplification and functional type-specific responses to these scalings will be a key facet of the analyses herein (see section "Projection Uncertainty"). Natural mortality, which represents mortality from sources other than piscivory, is independent of size and temperature and set at the constant value of 0.1 y^{-1} for all fish.

Scaling from the available energy to the group level is done as a size structured model (Andersen et al., 2016) based on a simple numerical scheme that reduces each size group to an ordinary differential equation coupled to the other size groups (De Roos et al., 2008). In this way the entire fish community is represented by 2+3+3 = 8 ordinary differential equations. Each spatial grid cell is comprised of this set of 8 equations and is independent of its neighbors. At this time there is no movement of the fishes or invertebrates, though the ESM inputs used to drive the model (see section "Ocean and Biogeochemical Projections") reflect the effects of temporally varying horizontal and vertical velocities. The model is advanced in time with a forward-Euler scheme integrated with a daily time step, which is stable at these temporal and spatial scales (Watson et al., 2015; Petrik et al., 2019).

The structure of FEISTY shares many characteristics with other size-based fish community models (Maury, 2010; Blanchard et al., 2011; Jennings and Collingridge, 2015; Carozza et al., 2016; Andersen, 2019): it is based upon predation fueling growth and reproduction while inflicting mortality on the prey. The model differs from others in three ways. For one, production of new offspring directly relies on energy available for reproduction without any other density dependent effects or carrying capacity. Further, it represents the difference between pelagic and benthic energy pathways (as in Blanchard et al., 2011) by representing pelagic and demersal fish functional groups. Finally, FEISTY is mass-balanced with respect to its coupling with zooplankton and benthic resources. By using the zooplankton mortality rates from the ESM to limit the ingestion of zooplankton, fishes never consume more than what is lost to upper trophic levels in the independent ESM (see section "Ocean and Biogeochemical Projections").

Ocean and Biogeochemical Projections

As described above, FEISTY requires estimates of mesozooplankton biomass, mesozooplankton production, the flux of organic matter to the benthos, and depth-resolved temperature. For this analysis, we used outputs from GFDL's ESM2M (Dunne et al., 2012, 2013) integrated with the Carbon, Ocean Biogeochemistry, and Lower Trophics (COBALT) ecosystem model (Stock et al., 2014b). This coupled climate-atmosphere-ocean model includes the CM2.1 climate model (Delworth et al., 2006), the AM2 atmospheric model (Anderson et al., 2004; Lin, 2004), and the MOM4p1 ocean model (Griffies, 2009). The horizontal resolution in the ocean submodel is 1° that decreases down to 1/3° at the equator and is tripolar in the Arctic above 65°N (Griffies et al., 2005), while the atmospheric submodel is 2° × 2.5°. There are 50 vertical layers in the ocean, with 10 m vertical resolution over the top 200 m. The minimum depth is 40 m, which treats all locations <40 m as if they are 40 m deep.

COBALT resolves cycles of carbon, nitrogen, phosphate, silicate, iron, calcium carbonate, oxygen, and lithogenic material at the global scale using 33 state variables (Stock et al., 2014b). The planktonic food web within COBALT is better-resolved than most global ESMs (Laufkötter et al., 2015; Séférian et al., 2020) and includes interactions between bacteria, small and large phytoplankton, diazotrophs, and small, medium, and large zooplankton. Trophic interactions are rooted in allometric and bioenergetic relationships and use mean predator to prey size ratios (Hansen et al., 1994). The model was parameterized to be quantitatively accordant with observed large-scale planktonic food web dynamics, including primary production, zooplankton production, and export fluxes (Stock et al., 2014b). Detritus is produced via phytoplankton aggregation and zooplankton egestion, with a larger fraction of egested material contributing to the sinking flux for larger organisms. The near surface e-folding depth for the remineralization of sinking material is consistent with Martin et al. (1987), with biogenic and lithogenic minerals inhibiting remineralization for an increasing "protected fraction" as particles sink (Armstrong et al., 2002; Klaas and Archer, 2002; Dunne et al., 2005).

A primary shortcoming of ESM2M-COBALT, and other global climate models and ESMs (Stock et al., 2011), is its coarse ocean resolution. This degrades the capacity of general circulation models to simulate coastal regions (e.g., Liu et al., 2019). We addressed this in the initial FEISTY development by using a simulation from a prototype high-resolution ESM (GFDL-ESM2.6; Stock et al., 2017), which featured 10 km ocean resolution. The computational costs of such models, however, prevents the hundreds to thousands of years required for a full climate change projection, forcing global fisheries projections to rely on the large-scale patterns revealed by global general circulation models (e.g., Lotze et al., 2019). However, we found that the FEISTY simulation characteristics were similar at coarse and high-resolution, and the model's capacity to capture observed catch patterns across functional types lessened only slightly (**Supplementary Appendix A1**).

We recognize that there are differences between ESMs in the projected changes in the plankton ecosystem properties required to drive fisheries projections with FEISTY (Bopp et al., 2013; Frölicher et al., 2016). We chose to focus our uncertainty analysis on the relatively unexplored spread in projections related to uncertainty in allometric relationships defining the environmental dependence of the fisheries relationships (see section "Projection Uncertainty"), leaving exploration of uncertainty routed in different ESMs and climate scenarios to other work (Lotze et al., 2019). Projected changes in plankton productivity in ESM2M-COBALT are described in detail in Stock et al. (2014a). Projected global NPP changes of –3.6% by the latter half of the twenty-first century are consistent with declines projected in the majority of global ESMs and near the mid-point of the simulated range (Bopp et al., 2013; Laufkötter et al., 2015; Kwiatkowski et al., 2020). ESM2M-COBALT's simulated amplification of projected changes for mesozooplankton (–7.9%) rests on first-order trophodynamic principles, and has now been shown to be a robust feature across ESMs (Kwiatkowski et al., 2019).

ESM2M-COBALT is linked to FEISTY by an "offline" coupling with no feedbacks of the fish on the plankton dynamics, but in a way that ensures fish do not have more food available than is produced. As described in Stock et al. (2014b), higher predation losses are imposed on medium and large zooplankton in COBALT. Feeding rates are determined by extrapolating the relationship of Hansen et al. (1997) and assuming that the biomass of unresolved predators scales in proportion to the biomass of prey (e.g., Steele and Henderson, 1992). This approach results in simulated mesozooplankton biomass and productivity that are consistent with observations, with just over half of mesozooplankton production ($\sim$1 Pg C yr^{-1}) being routed to higher trophic levels (Stock et al., 2014b). This rate of biomass loss by higher predators sets an upper bound on ingestion of zooplankton by fish in FEISTY. Specifically, FEISTY is forced by the COBALT outputs: medium and large zooplankton biomass integrated over the top 100 m (biomass m^{-2}), the rate of biomass loss by higher predators of medium and large zooplankton integrated over the top 100 m (biomass m^{-2} s^{-1}), the flux of detrital matter to the ocean floor (biomass m^{-2} s^{-1}), the mean temperature in the upper 100 m, and the bottom temperature. All biomasses and fluxes from COBALT were converted from moles of nitrogen (molN) to grams wet weight (gWW) assuming Redfield (1934) stoichiometry and the wet weight to carbon ratio (9:1) of Pauly and Christensen (1995). Henceforth, all biomasses are expressed as wet weight (i.e., g signifies gWW). A daily time-step was used for FEISTY, with plankton and ocean forcing interpolated from monthly values.

Projection Uncertainty

A previous parameter perturbation analysis of FEISTY exposed multiple ways of regulating the relative abundance of different functional types and their latitudinal distribution (Petrik et al., 2019). In order to encompass the sensitivity and uncertainty of these parameter choices into projections of fish biomass, we constructed an ensemble of simulations with multiple parameter sets that maintained (1) low squared deviation from/high correlation with estimated fish catch by functional type and (2) coexistence between forage fish and large pelagic fish in high productivity areas. The second condition was imposed to prevent globally skillful ensemble members that nonetheless produced highly unrealistic results in a small number of regions. This was enforced by increasing the weight (i.e., the misfit penalty) associated with forage fish in upwelling systems.

For catch comparisons, we used a global catch reconstruction that includes estimates of industrial fisheries, small-scale fisheries, and discards from the Sea Around Us (SAU) project (Pauly and Zeller, 2015; v43). We compared SAU catches to those simulated by the model under contemporary ocean conditions at the spatial level of large marine ecosystems (LMEs). Model simulations were evaluated with the Akaike Information Criterion (AIC) and model misfits from SAU catches were calculated by functional type by LME for the 45 LMEs that have not been identified as low-catch and/or low-effort regions (c.f., Stock et al., 2017). As a baseline, we considered simulations generated with the parameter values described in Petrik et al. (2019), which we will refer to as our "baseline parameter values." These values produced moderate matches with total, large pelagic, and demersal catches, including reproduction of observed spatial variations in fish catch spanning two orders of magnitude across LMEs (Petrik et al., 2019). A similar methodology for selecting ensemble members that combines comparison to SAU catch peaks at the LME level with other ecologically meaningful constraints has also been used by Carozza et al. (2017).

We restricted the search of parameter space to the 5 most influential parameters, defined by the total magnitude of the combined five indicator metrics (**Supplementary Table A2-1**) of Petrik et al. (2019). The most critical parameters were the assimilation efficiency and the coefficients controlling the ingestion and respiration allometry (α, b_M, b_E, a_M, a_E). We added the temperature scaling of metabolism (k_M) to this parameter set due to its potential importance in a warming ocean. We tested all permutations of high, mid, and low values of literature ranges for each variable (**Table 2**), yielding 729 potential combinations. From this set, we considered 43 parameter sets (**Supplementary Table A2-2**) with AIC values equal to or better than our baseline parameter values (Petrik et al., 2019) and that also satisfied co-existence conditions (see **Supplementary Appendix A2**). We did not apply any further weighting to the ensemble members based on AIC differences (e.g., Burnham and Anderson, 2002), as the intent here was to elucidate the basic characteristics of the parameter sensitivity characteristics and the magnitude of the uncertainty generated by this under-explored aspect of model uncertainty.

The temperature dependence of respiration rates exceeded that of the ingestion rates in the baseline parameter set, which was replicated in the above ensemble. While this is justified by several lines of evidence (Perrin, 1995; Rall et al., 2012; Carozza et al., 2017), there is also support for similar scalings (Brown et al., 2004). Thus, to further examine the role of the temperature dependence in the simulation results, we generated a separate set of parameters where all rates used the same value (see Appendix A2). The same permutations of the five most critical parameters were combined with the temperature sensitivities of physiological rates $k = k_M$ = 0.0630, 0.0793, and 0.0955 C^{-1} (equivalent Q_{10} = 1.88, 2.21, and 2.60), which are low, mid, and high values bounded by the temperature dependence of ingestion rates in the baseline set and the highest temperature dependence of respiration rate tested. Of this set of 729, 15 were skillful (**Supplementary Table A2-3**). This parameter set is referred to as the "equal temperature dependence ensemble" to distinguish it from the "varying temperature dependence ensemble" described above.

Simulations and Analyses

FEISTY was run from 1860 to 2100 using offline forcing of the ESM2M-COBALT Historical (1860–2005) and RCP 8.5 Projection (2006–2100) conditions. Simulations with the baseline parameter set were used to illustrate the basic characteristics of the response of fish production, fisheries yield, food web structure, and environmental conditions. Production is the biomass generated via growth and/or reproduction and was quantified as the product of biomass, B (g m^{-2}), and the biomass-specific assimilation rate of energy available for growth and reproduction, ν (d^{-1}; Eq. 1). We performed a global area-integration of production (g m^{-2} d^{-1}) to produce total production in units of mass per time (g d^{-1} or g y^{-1}). Fishing effort was represented by a fishing mortality rate F (**Table 1**). In reality, fishing effort varies globally and across the three functional groups. In the absence of a coherent assessment of these differences, both historically and under future scenarios, and to isolate the bottom-up effects of climate change on fish production, we used the same constant fishing mortality on all functional groups. We set $F = 0.3$ y^{-1} to roughly correspond with the fishing effort that gives the maximum sustainable yield (Andersen and Beyer, 2015). This leads to a fisheries yield (MT y^{-1}) that is proportional to abundance and a decent estimate of the maximum fisheries production. Analyses of fisheries yield present the total area-integrated biomass harvested in LMEs. Food web structure was quantified as the relative fractions of production of the different fish functional types. Transfer efficiency between different trophic levels of the food web was calculated as in Petrik et al. (2019) by examining the ratio of production of secondary production (medium zooplankton, large zooplankton, benthos) to net primary production (NPP), of the highest trophic level (HTL; pelagics and demersals in the large size class) fish production to secondary production, and of HTL production to NPP. Our results focused on time series from 1951 to 2100. Spatial results present the mean conditions of the last 50 years of the Projection (2051–2100) compared to the 50-year period from the century prior (1951–2000), whereas time series results are changes relative to 1951 conditions. In addition to the analyses performed on the baseline set, the varying temperature dependence ensemble simulations were used to identify the parameter sets that resulted in

TABLE 2 | Parameters varied in ensemble simulations from their baseline value used in the baseline set.

Parameter	Description	Baseline value	Units	Low	Mid	High
a_E	Encounter intercept	0.1918^a	m^2 g^{bE-1} d^{-1}	0.1370	0.2055	0.2740
a_M	Metabolism intercept	0.0110	g^{bM-1} d^{-1}	0.0082	0.0110	0.0137^b
α	Assimilation efficiency	0.700^c	–	0.600^d	0.675	0.750
b_E	Encounter slope	–0.20	–	–0.15	$–0.20^d$	–0.25
b_M	Metabolism slope	$–0.175^a$	–	–0.15	–0.175	–0.20
k_M	Metabolism Temperature Sensitivity	0.0855^e	$°C^{-1}$	0.0755	0.0855	0.0955

Values shown represent the low, middle, and high end of literature values. [a]*Modifed from* Hartvig et al. (2011), [b]Hartvig and Andersen (2013), [c]Watson et al. (2015), [d]Hartvig et al. (2011), [e]*Modified from* Stock et al. (2014b).

maximum and minimum changes relative to 1951 in total fish production and for each functional type. These ensemble simulations of the 1+43+15 = 59 total parameter sets provided estimates of minimum and maximum fish production, as well as measures of uncertainty.

RESULTS

Historic Patterns

Historic simulations of ESM2M-COBALT reproduce established large-scale patterns of primary and secondary production, with high net primary production and mesozooplankton production in upwelling regions as well as temperate and subpolar areas, and high seafloor detritus in shallow shelf environments (**Figures 2A–C**). Global distributions of forage fish and large pelagic fish largely mimic those of primary and mesozooplankton production (**Figures 2E,F**), whereas demersal distributions (**Figure 2G**) reflect benthic production (**Figure 2D**). Primary production rates span <1 order of magnitude (90% range: 1.13–7.85 g m^{-2} d^{-1}) whereas the rates of mesozooplankton, detritus, and benthos span 1.5–2 orders of magnitude (0.05–1.09; $7.13{\cdot}10^{-3}$–$4.35{\cdot}10^{-1}$; $5.35{\cdot}10^{-4}$–$3.26{\cdot}10^{-2}$ g m^{-2} d^{-1}). Fish production rates vary over 4 orders of magnitude. The smaller bodied forage fish cover a 90% range of $6.71{\cdot}10^{-5}$–$1.07{\cdot}10^{-1}$ g m^{-2} d^{-1}. The bottom dwelling demersal fish span a smaller range ($9.38{\cdot}10^{-5}$–$1.59{\cdot}10^{-2}$ g m^{-2} d^{-1}) owing to the lower and more stable temperatures outside of coastal areas. Production of large pelagic fish varies greatly ($4.26{\cdot}10^{-12}$–$4.91{\cdot}10^{-2}$ g m^{-2} d^{-1}), with rates that exceed those of the equally large demersal fish, but also experiencing diminished production in oligotrophic regions. Reductions in absolute production occur moving up trophic levels

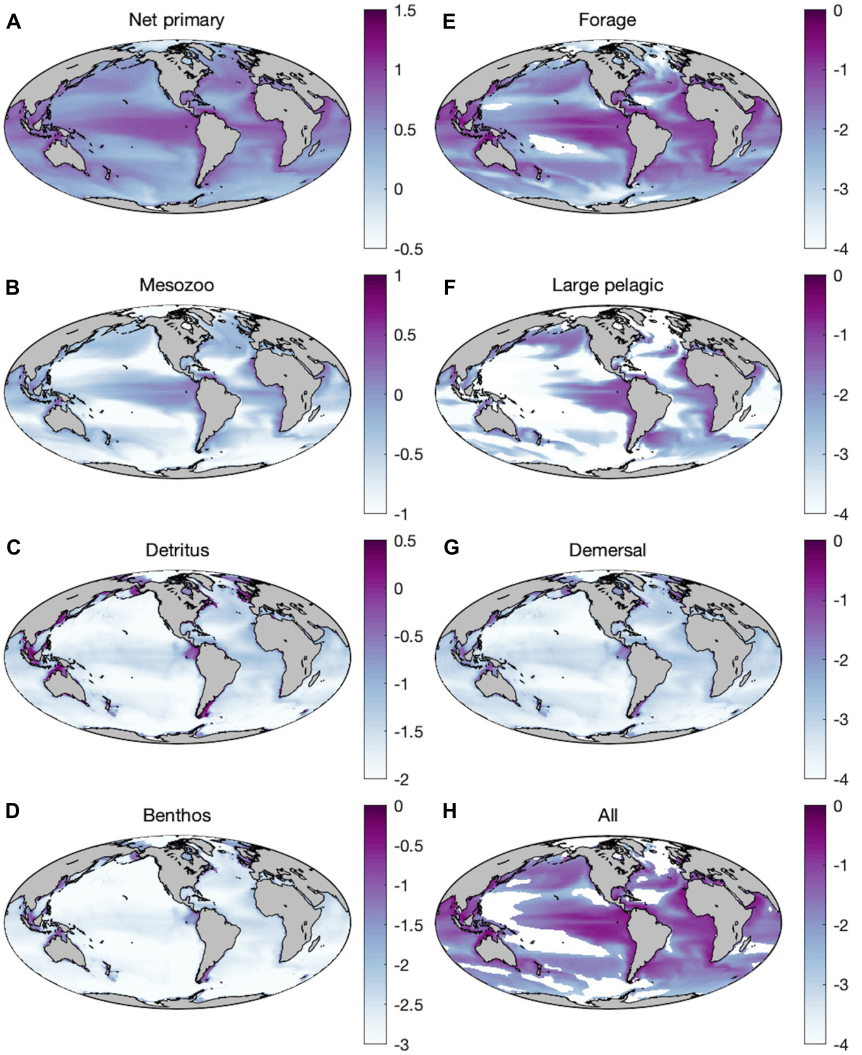

FIGURE 2 | Mean historic (1951–2000) distributions of production ($\log_{10}$ g WW m^{-2} d^{-1}) of **(A)** net primary producers, **(B)** mesozooplankton (medium + large), **(C)** seafloor detritus, **(D)** benthic invertebrates, **(E)** forage fish, **(F)** large pelagic fish, **(G)** demersal fish, and **(H)** all fishes combined with the baseline parameterization.

(**Figure 2**) as expected from the efficiency of trophic transfers up the food chain.

Trophic Amplification

Changes in production of primary producers, secondary producers, and fish consumers over the last 50 years of the twenty-first century (2051–2100) compared to the last 50 years of the twentieth century exhibit regional variations with decreases in the subtropics and the majority of low-latitude regions (**Figure 3**). Plankton and forage fish experience increases in production in polar areas, and scattered areas of enhanced productivity elsewhere (**Figures 3A,B,E**). Plankton productivity trends and forage fish trends are generally well correlated, but there are regions where forage fish production increases despite declining zooplankton production due to changes in predation on forage fish. Forage fish productivity, for example, increases across much of the northern sub-polar Atlantic and Pacific despite mixed trends in NPP and mesozooplankton productivity. The production of large pelagic fish, in contrast, is less well correlated with local plankton productivity changes and exhibits sharp declines in many regions, including across the Arctic (**Figure 3F**). The correspondence of several areas of sharp large pelagic declines with areas of forage increase (e.g., the sub-polar North Atlantic) is indicative of top-down control on some productivity trends. Conversely, production of seafloor detritus and demersal fish decreases nearly globally, with the exception of the Arctic and sub-Arctic, and two localized spots in southeast Pacific and southeast Atlantic near the Humboldt and Benguela upwelling systems, respectively (**Figure 3D,G**). Such regional "hot-spots" are often associated with shifts in physical and biogeochemical boundaries, and their locations are generally not robust across ESMs (e.g., Bopp et al., 2013; Laufkötter et al., 2015). Their

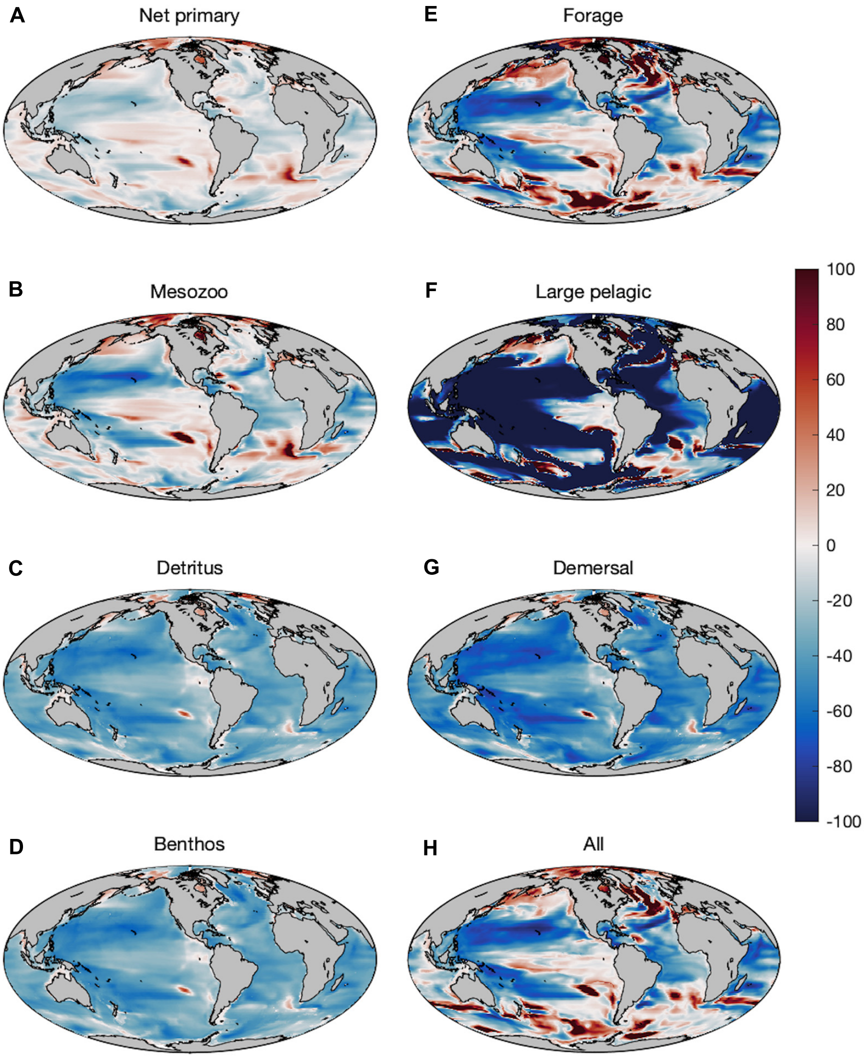

FIGURE 3 | Percent change in production in the Projection (2051–2100) compared to the Historic (1951–2000) time period of **(A)** net primary producers, **(B)** mesozooplankton (medium + large), **(C)** seafloor detritus, **(D)** benthic invertebrates, **(E)** forage fish, **(F)** large pelagic fish, **(G)** demersal fish, and **(H)** all fishes combined.

presence is thus indicative of the potential for limited regional increases, but not strong evidence for increases in the exact locations where they occur.

Fractional increases and decreases in production generally become greater for larger organisms higher in the food chain, consistent with "trophic amplification," in both the pelagic and benthic ecosystems (**Figure 3**). This is clearly illustrated in the increasing magnitude of global declines of each size class of organisms, with a mean decline of 13.1% (±1.1%) across all medium fishes and a decline of 19.2% (±1.5%) across all large fishes in the varying temperature dependence ensemble (**Figure 4A**). Both decreases are substantially greater than the primary production (3.6%) and mesozooplankton production (7.2%) declines that underlie them (**Figure 4**). The magnitude of these changes in fish production are smaller in the equal temperature dependence ensemble, at 9.6% (±1.2%) and 12.1% (±2.1%) for medium and large fish, respectively, but the amplification pattern is consistent (**Figure 4B**).

Community Reorganization

In addition to changes in the magnitude of plankton productivity available to fish, the end of the twenty-first century also exhibits a near-global increase in the ratio of zooplankton production to seafloor detritus flux (**Figure 5A**). Increases are especially large in upwelling and temperate/subpolar regions of the North and Equatorial Pacific, the Humboldt Current, south of Greenland, and in the Argentine Basin (**Figure 5A**). Despite area-integrated declines in both zooplankton production and detritus flux, this ratio increases in future projections due to the greater reductions of detritus over time compared to mesozooplankton (**Figure 5B**), denoting a "pelagification" of food resources. It is notable that the strong pelagification in deep ocean areas (**Figure 5A**) often occurs where the flux of material to the benthos is quite low. For example, regions with a change >15 have a mean depth of 4,591 m, historic mean detrital flux of 0.02 g m^{-2} d^{-1}, and historic mean Zoo:Det ratio of 33.2. However, consideration of the temporally evolving ratio of the globally integrated zooplankton production to the globally integrated benthic flux (which includes outsized contributions from coastal areas) reveals the same pelagification trend (**Figure 5B**). This pelagification is evidenced in areas shallower than 1,000 m where the mean change in Zoo:Det is 0.13 and the projected mean Zoo:Det is 1.25.

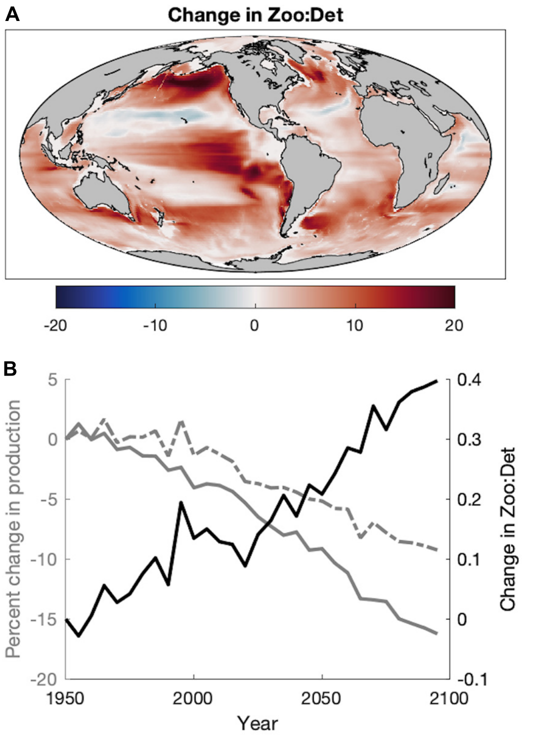

FIGURE 5 | (A) The absolute change in the ratio of zooplankton production to seafloor detrital flux (Zoo:Det) as the difference of the Projection (2051–2100) from the Hindcast (1951–2000). **(B)** Time series of the percent change in the global area-integrated mean zooplankton production (dashed gray), the percent change in the global area-integrated mean flux of detritus to the seafloor (solid gray), and the absolute change in the ratio of their global area-integrated means (Zoo:Det) during the Historic and Projection time periods relative to 1951.

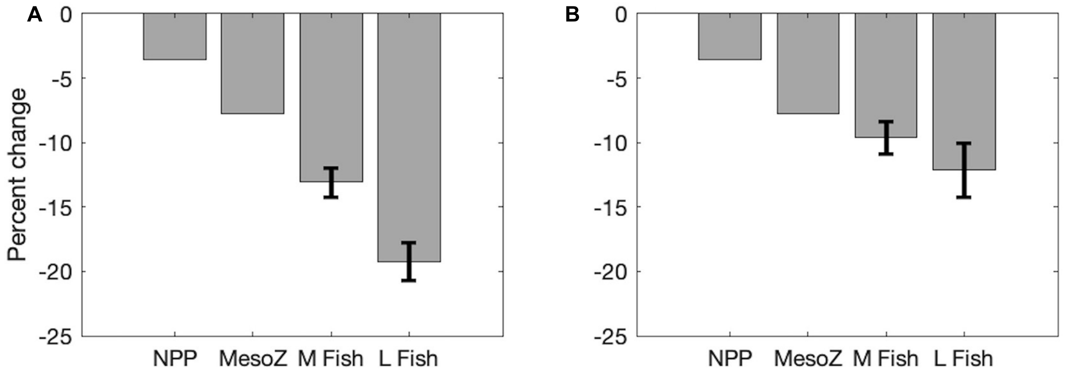

FIGURE 4 | Area-integrated changes in production in the Projection (2051–2100) compared to the Historic (1951–2000) time period illustrating trophic amplification of net primary production (NPP), mesozooplankton (MesoZ = medium + large zooplankton) production, all medium (M) fishes, and all large (L) fishes. Mean (± 1 SD) of **(A)** varying temperature dependence parameter ensembles and **(B)** equal temperature dependence parameter ensembles.

Though the ratio of zooplankton to detritus production explains a large proportion of the historic spatial variance in the dominance of large pelagic fish compared to demersal fish (van Denderen et al., 2018; Petrik et al., 2019), future changes in the fraction of large pelagic fish do not mirror the regional patterns of the zooplankton:detritus production ratio (**Figure 6A**). Rather, the fraction of all fishes that is composed of large pelagics decreases out to 2100 despite the pelagification of food resources (**Figures 6A,D**). Any positive impact of the pelagification of food resources on large pelagics is overwhelmed by the negative impacts of global productivity reductions and warming-driven increased respiratory demands that act to amplify productivity reductions at higher trophic levels. There is, however, a marked shift toward forage fishes (**Figures 6B,D**) that leads to an overall increase in the fraction of total pelagic fish production (forage + large pelagic) at 2100 (**Figure 6D**) and large regional increases in the fraction of total pelagic fish in the subpolar and polar oceans (**Figure 6C**), areas with a historically large fraction of demersal fish.

Ensemble Results

The predominant projected changes in the functional types were robust to parameter uncertainty (**Figure 7**). When globally averaged, forage fish production decreased the least with the least variation (**Table 3** and **Figure 7A**). Demersal fish had intermediate levels of production decline and uncertainty, while large pelagic fish had the greatest mean change and variance (**Table 3** and **Figure 7A**). Simulated fisheries yield, calculated as a fraction of stock of biomass rather than production, exhibited slightly different patterns (**Figure 7B**). The yield of forage fish experienced the smallest changes with a moderate degree of uncertainty (**Table 3** and **Figure 7B**). On average, demersal fish suffered greater losses than the forage fish, though the uncertainty bounds of the ensemble simulations (±1 SD) overlapped (**Table 3** and **Figure 7B**). Similar to percent changes in production, yield of large pelagic fish fell by the greatest extent with the largest degree of uncertainty out of all functional types (**Table 3** and **Figure 7B**). Despite the high uncertainty in projected changes in large pelagic production and fishing yield, declines exceeded those of the other functional types after 2070 at the latest (**Figure 7**). The degree of uncertainty in both production and fishing yield of each functional type increased over time in ensemble simulations (**Figure 7**). Changes to production and yield in projections under equal temperature dependence were qualitatively similar (**Supplementary Table A2-4** and **Supplementary Figure A2-1**).

Of the parameter sets that produced viable solutions, those producing the largest declines for the total fish productivity and the productivity of each functional type all featured the highest temperature dependence of metabolic costs (**Table 4** and **Supplementary Table A2-5**). Similarly, the most resilient projections for all fish, large pelagic fish, and demersal fish all featured the lowest temperature dependence of metabolic costs (**Table 4** and **Supplementary Table A2-5**). Other aspects of the response differed by functional type and highlight competitive and/or predatory interactions. For example, the least perturbed forage fish projection valued steep allometric penalties on the encounter rate and a large temperature dependence for the metabolic rate. Both of these characteristics are associated with the steepest declines in large pelagic fish, suggesting decreased top-down control is an essential element for the resilience of forage fish in these simulations. In contrast, the least impaired large pelagic and demersal fish projections value weak allometric penalties on the encounter rate. Surprisingly, resilient large pelagic and demersal projections also feature low assimilation efficiency and, in the case of demersals, low overall encounter rates. These seemingly counter-intuitive results emphasize the importance of interactions with forage fish: parameter combinations that hinder forage fish more than demersals and large pelagics lead to less vulnerable projections for these larger functional types. Resilient projections for large pelagic and demersal also both favored small allometric penalties and the most unchanged patterns for forage fish favored large ones in the equal temperature dependence ensemble (**Supplementary Table A2-5**).

DISCUSSION

Our work contributes to a growing set of projected changes in global fish production and biomass distribution under climate change. Our results move beyond species-based and size-based models by examining climate change effects on the food web structure of global marine ecosystems, the fish functional types composing them, and the sensitivity of responses to uncertainties in critical allometric and temperature scalings broadly applied in fish and fisheries modeling. Additionally, many other fish models use net primary production (NPP) from ocean biogeochemistry models and earth system models (ESMs) as the input at the base of the food chain. Unfortunately, NPP estimates are highly variable across ESMs (Bopp et al., 2013), thereby introducing uncertainty in the fish projections based on which ESM was used as forcing. A significant fraction of this uncertainty, however, is linked to differences in the response of recycled production within plankton food webs (e.g., Taucher and Oschlies, 2011). These fluxes are not available to fish. Following Dugdale and Goering (1967), the NPP available to higher trophic levels is more accurately assessed by NPP supported by the supply of "new" nutrients to the euphotic zone. Over time, this supply of new nutrients must be balanced by export from the euphotic zone. There is greater agreement on export production trends across ESMs (Bopp et al., 2013; Fu et al., 2016), reducing uncertainty relative to projections based on NPP alone. In the present study, this reduction in uncertainty was achieved through explicit representation of the plankton food web processes that determine recycled and new production and subsequent pathways of energy flow between phytoplankton and fish (Ryther, 1969; Friedland et al., 2012; Stock et al., 2017). While far from perfect, the underlying plankton food web dynamics simulation used in this study accurately captures observed variations in mesozooplankton biomass and productivity and export fluxes across ocean biomes (Stock and Dunne, 2010; Stock et al., 2014b). Thus, by using zooplankton and seafloor detritus as resources rather than deriving secondary production from NPP, FEISTY may be considered a more robust indicator of

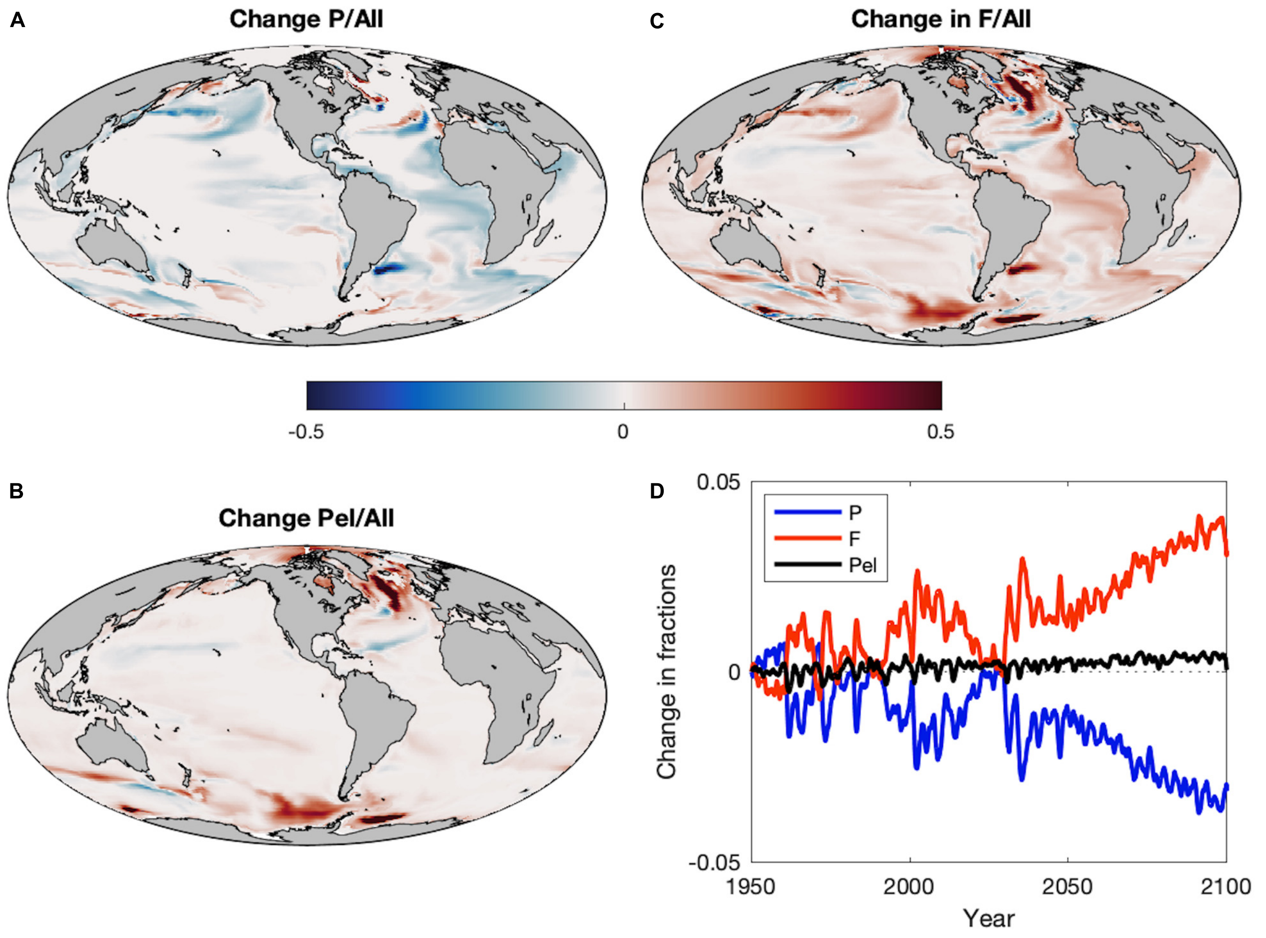

FIGURE 6 | The change in the fractions of **(A)** large pelagics (P), **(B)** all pelagics (Pel = F+P), and **(C)** forage fish (F) out of all fish during Projection (2051–2100) period compared to the Historic (1951–2000) period. **(D)** Time series of the area-integrated mean fractions of large pelagics (P: blue), all pelagics (Pel = F+P: black), and forage fish (F: red) out of all fishes during the Historic and Projection time periods relative to 1951.

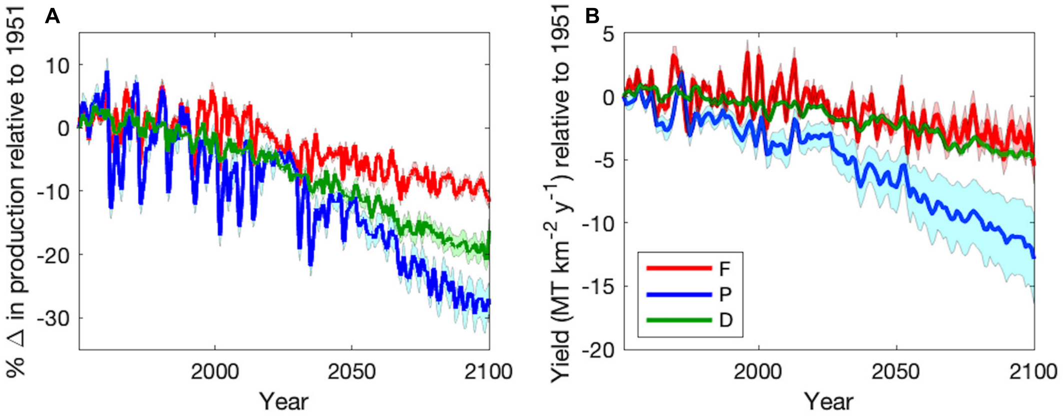

FIGURE 7 | Time series of varying temperature dependence ensemble mean (±1 SD) **(A)** percent change in production relative to 1951 and **(B)** total change in fishing yield (MT km^{-2} y^{-1}) relative to 1951 of forage fish (red), large pelagic fish (blue), and demersal fish (green) during the Historic (1951–2000) and Projection (2051–2100) time periods. Monthly values in **(A)** were smoothed with a 12-month moving mean. Yield in **(B)** reflects harvest of adults only.

TABLE 3 | The difference and percent change in production (g y^{-1}) and fisheries yield (MT y^{-1}) of the 2051–2100 mean from the 1951–2000 mean of each functional type and all fishes combined across the 44 member varying temperature dependence parameter ensemble.

	Production				**Fisheries yield**			
	Difference		**Percent change**		**Difference**		**Percent change**	
	Mean	***SD***	**Mean**	***SD***	**Mean**	***SD***	**Mean**	***SD***
F	−1.12E+12	1.12E+11	−10.2	0.8	−3.07	0.98	−7.3	2.0
P	−6.47E+11	2.31E+11	−20.8	1.6	−8.02	2.12	−19.7	1.2
D	−1.53E+11	2.66E+10	−15.8	1.3	−3.65	0.24	−8.5	0.4
All	−1.92E+12	3.16E+11	−12.8	1.0	−14.73	1.71	−11.8	0.3
B	−2.52E+11	–	−12.3	–	–	–	–	–

F, forage; P, large pelagic; D, demersal; All: F+P+D, B: benthos. Yield reflects harvest of adults only.

TABLE 4 | Parameter sets in the varying temperature dependence ensemble that resulted in maximum and minimum percent changes in production relative to 1951 of each functional type and all fishes combined.

		%Δ production	α	b_M	b_E	a_M	a_E	k_M
All	Max	13.6%	0.600	−0.175	−0.150	0.0082	0.274	0.0955
	Min	9.0%	0.750	−0.150	−0.150	0.0110	0.274	0.0755
F	Max	9.0%	0.600	−0.175	−0.150	0.0082	0.274	0.0955
	Min	5.8%	0.750	−0.150	−0.200	0.0082	0.205	0.0955
P	Max	28.2%	0.675	−0.150	−0.200	0.0082	0.274	0.0955
	Min	17.2%	0.600	−0.150	−0.150	0.0082	0.274	0.0755
D	Max	21.1%	0.675	−0.150	−0.150	0.0082	0.274	0.0955
	Min	13.3%	0.600	−0.150	−0.150	0.0082	0.137	0.0755
B	Max	31.9%	0.750	−0.150	−0.150	0.0110	0.274	0.0755
	Min	−13.9%	0.675	−0.150	−0.150	0.0082	0.274	0.0955

*Parameters described in **Table 2**. F, forage fish; P, large pelagic fish; D, demersal fish.*

future changes in the dynamics between pelagic and demersal components of food webs.

Trophic Amplification

When grouped by trophic level, the amplification of projected productivity declines from primary producers to fishes is apparent in the results of FEISTY, despite differences in feeding preferences and habitats of the three functional types. Projections of primary and secondary production across ESMs have previously been examined in the literature. The ESM2M-COBALT decline in NPP of 3.6% is moderate with respect to other CMIP5 ESMs (Bopp et al., 2013), while the approximate doubling of production changes from net primary producers to mesozooplankton from 3.6 to 7.9% using ESM2M-COBALT (Stock et al., 2014a) is similar to the doubling of biomass changes that occur in the IPSL ESM (Chust et al., 2014) and ensembles of 12 CMIP5 ESMs (Kwiatkowski et al., 2019). That is, there is "negative amplification" as defined by Kwiatkowski et al. (2019).

Earth system model intercomparison of the flux of detritus to the seafloor has not been assessed, though export production out of the euphotic zone has. Studies have found differing ranges of decrease that span 1–18% based on the ESMs used in the comparison (Bopp et al., 2013; Fu et al., 2016; Laufkötter et al., 2016). The 12.3% drop in seafloor detritus flux in ESM2M-COBALT simulations comparing 2051–2100 to 1951–2000 is in the center of 7–18% range in export flux of Fu et al. (2016) who compared 2091–2100 to 1991–2000. Variations across ESMs are due to the number of size classes of phytoplankton and differences in aggregation and sinking formulations (Fu et al., 2016; Laufkötter et al., 2016). Larger projected declines in export from the euphotic zone relative to projected primary productivity declines within it is consistent with a shift toward smaller plankton sizes as stratification increases. This shift leads to more effective recycling and, as deep winter mixing is reduced, more efficient coupling between phytoplankton and grazers (Behrenfeld and Boss, 2014; Stock et al., 2014a). Reductions in export at the base of the euphotic zone can be further amplified by increased remineralization in warming waters at depth (Marsay et al., 2015; Laufkötter et al., 2017) or decreased ballast minerals due to acidification (e.g., Gehlen et al., 2007; Gangstø et al., 2008).

Though processes governing benthic biomass in FEISTY are less detailed than those that dictate fish biomass, projected changes in biomass are consistent with past results. Jones et al. (2014) used the empirical relationship of Wei et al. (2010) between benthic biomass and carbon export to estimate changes in benthic biomass from carbon flux to 500 m above seafloor derived from 8 CMIP5 ESMs. They found a global decrease of 5.2%, which was an attenuation of the 11.4% average drop in seafloor carbon flux. Conversely, Yool et al. (2017) achieved an amplified decline of 17.6% using a size-based model of benthic invertebrates forced by the coupled ocean-biogeochemistry model NEMO-MEDUSA under RCP 8.5, which displayed 3.9% decreases in seafloor carbon flux. The FEISTY decrease estimates of 9.0 ± 4.6% fell within the low end of these values and exhibited analogous patterns of spatial change to both models (**Supplementary Figure S1A**). Similar to the results of Jones et al. (2014), simulated benthic biomass did not amplify the changes in seafloor detrital flux. The effect of the decline in detrital flux on benthic biomass was counteracted by increases in the benthic biomass as a result of release from top-down predation mortality by the large demersal fish. Combined with the results of Jones et al. (2014), the FEISTY simulations suggest that considerations of size and respiration, as in Yool et al. (2017), are necessary to produce trophic amplification in benthic organisms.

Unsurprisingly, increases in metabolic demands with size and temperature are drivers of modeled trophic amplifications up through fishes. Firstly, increases in temperature lead to greater basal metabolic demands, which are more difficult to meet given decreases in net primary production. This mechanism contributes the greatest amount to trophic amplification from phytoplankton to zooplankton in ESM2M-COBALT (Stock et al., 2014a). Secondly, marine predator-prey relationships tend to be size-structured, whereby decreases in plankton size lead to longer food chains with more transfers between trophic levels (c.f., Ryther, 1969). For instance, in a food chain consisting of diatoms, copepods, and forage fish, the forage fish at trophic level (TL) 3 would receive a fraction of NPP equal to TE^2, where TE (transfer efficiency) is the fraction of production that is transferred between trophic levels and the exponent is determined by the number of transfers (TL-1). If the primary production shifted to smaller phytoplankton (but did not change in amount) such that the phytoplankton had to be consumed by microzooplankton before it could be eaten by copepods, the forage fish would move to TL4 and would only receive $NPP \cdot TE^3$. Though trophic levels are semi-fixed in FEISTY, change in trophic level is another mechanism responsible for trophic amplification in ESM2M-COBALT, though of lesser importance than metabolism (Stock et al., 2014a). Finally, decreases in transfer efficiency with climate change have been revealed in mesocosm studies (Ullah et al., 2018) and both empirical (Moore et al., 2018) and mechanistic (du Pontavice et al., 2020*)* models forced by ESMs. Thusly, fish would likely receive a reduced fraction of NPP with increasing temperature without any underlying changes to NPP or TL. Similar reductions in TE are demonstrated with climate change projections of FEISTY (**Supplementary Figure A2-3**). With varying temperature dependence, decreases in transfers between consumers (TL2 to TL4) are greater than the decline from primary to secondary producers (TL1 to TL2; **Supplementary Figure A2-3**). Since fish production is controlled by the balance of metabolic needs with assimilated energy from ingestion, which are functions of size, temperature, and prey abundance, it was the greater temperature-dependence of the metabolic rate compared to feeding rates that caused the strong decrease in high trophic level TE. The decline in high trophic level TE was similar to that of low trophic levels under equal temperature-dependence (**Supplementary Figure A2-3**), suggesting that there are other mechanisms involved in TE declines.

Trophic amplification of fish production in FEISTY was consistent with multi-model ensembles of 5 global fisheries and marine ecosystem models forced by 2 ESMs (GFDL-ESM2M and IPSL-CM5A-LR) that spanned −5 to −28% under RCP 8.5 when all groups of consumers at trophic levels higher than zooplankton were combined (Lotze et al., 2019). The spatial distribution of percent biomass change of all fishes (**Supplementary Figure S1F**) agreed well with the multi-model mean of Lotze et al. (2019), displaying increases in polar regions and declines in subtropical and temperate areas. The only area of disagreement was in the central North Atlantic, a region of higher inter-model variability and lower model agreement (Lotze et al., 2019), where FEISTY projected increases in fish biomass while the multi-model mean projected decreases.

Community Reorganization

Projections of lower trophic levels and fishes show a "pelagification" of marine food webs. The ratio of zooplankton production to the seafloor detritus flux increased in nearly all marine ecosystems. When averaged globally, both types of secondary production decreased in the future, but seafloor detritus experienced greater reductions. At a regional level, increases in this ratio were the result of either (I) an increase in zooplankton production and decrease in seafloor detritus flux, (II) an increase in zooplankton production greater than the increase in seafloor detritus flux, or (III) a decrease in zooplankton production less than the decrease in seafloor detritus flux. Type I was responsible for the increased ratio in the central Arctic, Northwest Pacific, upwelling areas, the eastern Caribbean, and the Southern Ocean. Unequal increases were the least common and accounted for the increased ratio in the coastal Arctic and two localized spots southwest of the Humboldt and Benguela upwelling regions. On the other hand, the strong increases in the zooplankton to detritus production ratio south of Greenland and in the Argentine Basin were on account of unequal decreases in production, which was the most prevalent cause of an increase in the ratio.

Despite a large proportion of the spatial variance in historic observed and simulated catches of large pelagic fish compared to demersal fish being explained by the ratio of zooplankton to detritus production (van Denderen et al., 2018; Petrik et al., 2019), it was the fraction of forage fish (**Figures 6C,D**), rather than the fraction of large pelagic fish, that best mimicked the projected regional patterns of alteration in the zooplankton:detritus production ratio (**Figure 5**). The degree of change in the fraction of forage fish did not necessarily match that of the zooplankton:detritus ratio, but the directions of change did. In general, the projected variations in demersal fish biomass reflected the modifications in the seafloor detrital flux, whereas the relative fraction of demersal fish was approximately the inverse of the relative fraction of forage fishes. This could be of particular concern in coastal regions of temperate and subpolar oceans that have historically hosted large populations of demersal fishes that support valuable fisheries. Recent observations of these demersal fisheries have detected poleward shifts (Fossheim et al., 2015), which also arose in model results via increases in biomass in polar regions and declines in temperate and subpolar areas

(**Supplementary Figure S1E**). Demersal fish biomass increased in most coastal regions of the Arctic, but decreased in the central Arctic. The areas with reduced demersal biomass experienced a concomitant increase in all pelagic fishes, mostly forage fish, with the exception of the Faroe Plateau where all fishes suffered losses. Though not directly comparable, simulations of the size-based model of Blanchard et al. (2012) at 2050 under the SREASA1B scenario displayed decreases in benthic biomass in nearly all 28 non-arctic Large Marine Ecosystems studied and increases in pelagic biomass in several northern ecosystems. The Blanchard et al. (2012) model does not include the interactions between pelagic and demersal fish, so the similarity of the results to FEISTY indicates that the major pattern of pelagification is driven by the changes in primary and secondary production.

While copious research suggest that large-scale patterns in fish biomass and catch reflect patterns in ocean productivity (i.e., bottom-up drivers; Ryther, 1969; Friedland et al., 2012; Stock et al., 2017), "trophic cascades" associated with strong fishing pressure have also been observed (e.g., Pauly et al., 1998). In some cases, evidence suggests that these cascades have extended to plankton communities (e.g., Frank et al., 2005). While our simulations did not consider sharp increases in fishing pressure implicated in such cascades, pronounced shifts in forage fish dominance could produce similar effects on plankton communities. Resolving such feedbacks, however, would require a "two-way" coupling between fish and plankton models (e.g., Maury, 2010; Kearney et al., 2012) that was beyond the scope of this work. This should be addressed in future efforts, though we note that doing so will make parameter uncertainty investigations far more difficult. A further complication is to represent climate change-driven shifts in geographical range (Pinsky et al., 2013). It is not clear, though, whether geographical range expansions (or contractions) on the level of functional group requires a specific description of migration (see section "Assumptions and Limitations") or whether just representing demographical change, as in the current model, is sufficient. In this respect a particular focus should be the large pelagic fish whose migrations span oceanic basins and have a considerable predation impact during feeding migrations (Watson et al., 2015; Mariani et al., 2017). Increased understanding of fisheries responses to climate change will thus ultimately need combinations of sensitivity studies in the one-way coupled context (such as those presented herein) and targeted two-way coupled experiments to explore trophic cascades and assess the higher predation closures used by biogeochemical models.

Ensemble Results

The ensemble of diverse parameter sets was used to quantify uncertainty and understand the sensitivity of the physiological dimensions underlying the model structure. Parameter sets varied in terms of assimilation efficiency, weight-dependence of prey encounter rates, and temperature and weight dependence of metabolic rates. These are comparable to the parameters governing trophic scaling, growth rates, and mortality rates of Carozza et al. (2017), who also identified their importance in generating parameter ensembles that simulated fish biomasses and catches in accordance with ecological constraints and observed catches. Though it was too computationally expensive to search the full parameter space, over 700 parameter sets were explored, resulting in the 59 sets used in this analysis. As expected, parameter sets with the highest temperature sensitivity of metabolism resulted in the greatest percent reductions in production of all fish functional types and all fishes combined. However, this pattern was not seen in the equal temperature dependence ensemble. Resilient projections of large pelagic and demersal production favored small allometric penalties (e.g., metabolism that declines more rapidly with size than prey encounter, $b_M < b_E$) while those for forage fish production favored large penalties on size in both ensembles. The differential responses of the functional types emphasize the importance of their competitive and predatory interactions in addition to their life history traits. To some extent, the emergent combinations of parameters represent the physiological constraints on simulating contemporary fish catches and producing coexistence between forage fish and large pelagic fish in high productivity regions. It is likely that a very limited area of parameter space meets these conditions and that this hinders identification of clear relationships between parameter combinations and the magnitude of projected changes.

Regardless, parameter sets produced variability between end members and ensemble projections yielded robust results of the response of fish productivity under climate change. The forage fish experienced lesser declines in production compared to the other, larger functional types. Large pelagic fish suffered the greatest reductions in both production and fisheries yield, and with the highest degree of uncertainty. Even when factoring in parameter uncertainty, these changes were substantially larger than those of forage and demersal fish when the temperature dependence of metabolism exceeded that of ingestion rates. With rates of equal temperature dependence, all results were qualitatively similar, with the exception of the mean percent change in large pelagic fish production being comparable to that of demersal fish. The difference between simulations with varying vs. equal temperature dependence is effectively demonstrated by a simpler analysis of the fish community with a 0-dimensional model of FEISTY. With equal temperature dependence of respiration, encounter, and maximum consumption rates, warming above the reference temperature of 10°C leads to a drop in large pelagic biomass, even with high prey resources (**Supplementary Figures A2-4A,B**). This illustrates that the baseline parameters related to the size dependence of rates disadvantage the large fish, as was necessary to achieve coexistence between large pelagic fish and forage fish (Petrik et al., 2019). When metabolic rates are more sensitive to temperature, large fish are doubly hit by their maximum size and warming, resulting in larger biomass declines and a greater minimum level of prey production needed to support large pelagic fish (**Supplementary Figures A2-4C,D**). A similar shrinking under warming was seen in simulations of fish communities when metabolism was more sensitive to temperature than assimilated ingestion (Guiet et al., 2016).

Our lack of knowledge on the temperature dependence of these physiological rates does not compromise the qualitative predictions. Though our simulations are able to robustly predict the directionality of change in production, they are poor at estimating the magnitude, which is driven by some largely unknown set of temperature-scaling parameters. The strong temperature dependence of metabolic rates is well-known (e.g., von Bertalanffy, 1960). In contrast, the temperature dependence of encounter and consumption rates are less certain, though both theoretical (Rall et al., 2012) and empirical (Perrin, 1995) studies suggest that they are lower than basal metabolism. Unequal temperature sensitivity of metabolism and other rates is adopted by some global fish models (e.g., Cheung et al., 2010; Jennings and Collingridge, 2015; Guiet et al., 2016; Carozza et al., 2017), but not all, thereby making it one of many factors contributing to inter-model variability. The ensemble results of FEISTY reveal the importance of better constraining estimates of the temperature sensitivity of physiological rates, especially for projecting the impacts of climate change on large pelagic fishes. Furthermore, interactions between temperature and oxygen (e.g., Deutsch et al., 2015; Pauly and Cheung, 2018) and ontogenetic variations in thermal tolerance (e.g., Dahlke et al., 2020) advocate the need for thorough examinations of marine ecosystems under a warming climate.

Impacts on Fisheries

To predict the bottom-up effects of climate change on ecosystem productivity, we used a simple representation of fishing (constant in space and time) that captured the main basin-scale patterns under contemporary conditions. Thus, results of simulated fisheries yield reflect the isolated bottom-up effects of environmental change on fish communities rather than the effects of changes in human behavior such as a redistribution of effort in amount, space, time, or toward different functional types. In this case, total fisheries yield declined by 11.8% (±0.3%; **Table 3**) with decreases of 7.4% (±2.0%) at TL3 and 13.9% (±0.7%) at TL4. These estimates were greater than the 5.7% and 6.8% losses in fisheries yield of TL3 and TL4, respectively, estimated by Moore et al. (2018) who used an empirical model of fish catch as a function of zooplankton biomass from an ESM. Our changes in total fisheries yield are more in line with the "no conservation" fishing scenario of Carozza et al. (2019) who found a 15% (12, 20%) change at 2081–2100 under RCP 8.5 from 1851 to 1900 conditions in the IPSL ESM. The decrease in the yield of large pelagic fish (19.7 ± 1.2%; **Table 3**) at 2100 with FEISTY was closer to their change of 32% with fishing rates "optimized for human food" (Carozza et al., 2019), and similar to the >20% decline of Moore et al. (2018) that did not occur until 2300. While other marine ecosystem models have employed reconstructions of historical fishing effort, more work is needed on developing scenarios of plausible projections of fishing effort like those of Carozza et al. (2019). As such, the FEISTY levels of uncertainty in fisheries yields should be considered underestimates, as future changes in fishing effort and technology will further increase uncertainty. The FEISTY results highlight the importance of considering the non-uniform effect of climate change on the three different functional types of fish. The projected pelagification of ecosystems will promote some parts of the fisheries sector and weaken others, which could require large structural changes. Though fishers can switch gears and participate in multiple fisheries (e.g., Fuller et al., 2017), and boats can move (e.g., Watson et al., 2018), previously unfished regions will require management plans, while old ones will need to be renegotiated (Pinsky et al., 2018). In addition to affecting fishing communities, the shifts toward pelagic food webs could impact the ecology of populations not represented in the model, such as marine mammals and sea birds.

Assumptions and Limitations

We note that the structure of FEISTY and how it was implemented for this study makes certain assumptions and presents limitations. These include, but are not limited to, simplistic fishing (addressed above), the representation of only three fish functional types, no movement, and environmental forcing. There are numerous factors that may influence the productivity of fish, especially under a changing climate. This analysis focused on the effects of temperature and secondary production, while climate-induced changes to oxygen (e.g., Deutsch et al., 2015), pH (Branch et al., 2013), and nutrient content of prey [such as lipid density (e.g., Heintz et al., 2013; Peterson et al., 2013) or iron content (Galbraith et al., 2019)] should be considered in future studies.

The current COBALT configuration does not include vertical migrations of zooplankton, which results in most of the zooplankton biomass, and thus energy available to fish, being located in the upper 100 m of the water column. As such, we expect that the FEISTY predictions of forage fish biomass incorporates both epi- and mesopelagic fish. How the biomass is distributed between the two groups will depend on the vertical migration behavior of these fish types, their prey, and their predators (Pinti and Visser, 2019). This work is currently under investigation.

Our model makes the case that large pelagics are fundamentally disadvantaged in warm water. This is a result of the high temperature scaling of standard metabolism. However, large pelagics are most commonly observed in warmer tropical regions, which appears at odds with the model. We discussed this issue at length in Petrik et al. (2019). First, large pelagics experience competition from demersal fish, thriving in regions where the demersals do not have support from benthic production (van Denderen et al., 2018), most notably in the low export, oligotrophic tropics. Second, the relationship between growth and temperature is lower for large pelagic fish than for small pelagic fishes (van Denderen et al., 2020), which could arise from metabolic rates that increase with temperature at a rate greater than the feeding rates and supports our parameterization. Third, basin-wide migrations of large pelagics across oligotrophic regions are often in search of favorable larval environments (e.g., Bakun, 2013; Reglero et al., 2014) during which adults feed advantageously at mesoscale features (e.g., Polovina et al., 2001; Nieblas et al., 2014) that are not represented in our global model with a 1° resolution. Horizontal movement has the potential to rectify some of the discrepancy between simulated and observed catches of large pelagic fish, particularly in the western tropics (Watson et al., 2015; Petrik et al., 2019). Our simulations that exclude movement capture the first-order spatio-temporal patterns of energy flow in marine food webs. Future work that incorporates swimming behavior will add value to these initial results, particularly on the stabilizing potential of movement (Murdoch, 1977; Briggs and Hoopes, 2004) that may reduce some of the negative climate change impacts on large pelagic fish. We recognize the many advantages of the FEISTY framework, while its limitations promote the value obtained by using a diversity of model approaches, each with their own strengths and weaknesses, rather than promising one correct single model (Tittensor et al., 2018).

CONCLUSION

Projections under the business-as-usual carbon emissions scenario (RCP 8.5) of fish functional types with FEISTY resulted in trophic amplification of the decreases in primary and secondary production seen in GFDL-ESM2M-COBALT. The biomass and production of all fish decreased globally, though with differences between functional types. Large pelagic fish suffered the greatest declines but also with the highest degree of projection uncertainty. The reduction in large pelagic fish occurred despite a pelagification of the food webs. Pelagification was a result of unequal decreases in secondary production, leading to increases in the ratio of pelagic zooplankton production to seafloor detritus production, which shifted benthic-based ecosystems historically dominated by demersal fish toward pelagic-based ones dominated by forage fish.

DATA AVAILABILITY STATEMENT

The raw data supporting the conclusions of this article will be made available by the authors, without undue reservation.

AUTHOR CONTRIBUTIONS

CP and CS developed the initial conceptualization of research and established the manuscript structure and key figures. KA, PD, and JW further refined analyses. CP performed simulations and analyses and wrote the initial draft. All authors contributed to the interpretation of results and editing of the manuscript.

FUNDING

CP was funded by the Nereus Program. KA and PD were funded by the "Ocean Life" VKR center of excellence supported by the Villum foundation.

ACKNOWLEDGMENTS

We would like to thank Vicky Lam for the Sea Around Us data, and Hyung-Gyu Lim and Jessica Luo for helpful reviews of earlier drafts. Portions of this research were conducted with the advanced computing resources and consultation provided by Texas A&M High Performance Research Computing.

SUPPLEMENTARY MATERIAL

The Supplementary Material for this article can be found online at: https://www.frontiersin.org/articles/10.3389/fmars.2020.588482/full#supplementary-material

REFERENCES

Andersen, K. H. (2019). *Fish Ecology, Evolution, and Exploitation*. Princeton: Princeton University Press.

Andersen, K. H., and Beyer, J. E. (2015). Size structure, not metabolic scaling rules, determines fisheries reference points. *Fish Fish.* 16, 1–22. doi: 10.1111/faf.12042

Andersen, K. H., Jacobsen, N. S., and Farnsworth, K. D. (2016). The theoretical foundations for size spectrum models of fish communities. *Can. J. Fish. Aquat. Sci.* 73, 575–588. doi: 10.1139/cjfas-2015-0230

Anderson, J. L., Balaji, V., Broccoli, A. J., Cooke, W. F., Delworth, T. L., Dixon, K. W., et al. (2004). The new GFDL global atmosphere and land model AM2-LM2: evaluation with prescribed SST simulations. *J. Clim.* 17, 4641–4673. doi: 10.1175/jcli-3223.1

Armstrong, R. A., Lee, C., Hedges, J. I., Honjo, S., and Wakeham, S. G. (2002). A new, mechanistic model for organic carbon fluxes in the ocean based on the quantitative association of POC with ballast minerals. *Deep Sea Res. II* 49, 219–236. doi: 10.1016/s0967-0645(01)00101-1

Audzijonyte, A., Kuparinen, A., Gorton, R., and Fulton, E. A. (2013). Ecological consequences of body size decline in harvested fish species: positive feedback loops in trophic interactions amplify human impact. *Biol. Lett.* 9:20121103. doi: 10.1098/rsbl.2012.1103

Bakun, A. (2013). Ocean eddies, predator pits and bluefin tuna: implications of an inferred 'low risk–limited payoff' reproductive scheme of a (former) archetypical top predator. *Fish Fish.* 14, 424–438. doi: 10.1111/faf.12002

Behrenfeld, M. J., and Boss, E. S. (2014). Resurrecting the ecological underpinnings of ocean plankton blooms. *Annu. Rev. Mar. Sci.* 6, 167–208. doi: 10.1146/annurev-marine-052913-021325

Blanchard, J. L., Jennings, S., Holmes, R., Harle, J., Merino, G., Allen, J. I., et al. (2012). Potential consequences of climate change for primary production and fish production in large marine ecosystems. *Philos. Trans. R. Soc. B* 367, 2979–2989. doi: 10.1098/rstb.2012.0231

Blanchard, J. L., Law, R., Castle, M. D., and Jennings, S. (2011). Coupled energy pathways and the resilience of size-structured food webs. *Theor. Ecol.* 4, 289–300. doi: 10.1007/s12080-010-0078-9

Bopp, L., Resplandy, L., Orr, J. C., Doney, S. C., Dunne, J. P., Gehlen, M., et al. (2013). Multiple stressors of ocean ecosystems in the 21st century: projections with CMIP5 models. *Biogeosciences* 10, 6225–6245. doi: 10.5194/bg-10-6225-2013

Branch, T. A., DeJoseph, B. M., Ray, L. J., and Wagner, C. A. (2013). Impacts of ocean acidification on marine seafood. *Trends Ecol. Evol.* 28, 178–186. doi: 10.1016/j.tree.2012.10.001

Briggs, C. J., and Hoopes, M. F. (2004). Stabilizing effects in spatial parasitoid–host and predator–prey models: a review. *Theor. Popul. Biol.* 65, 299–315. doi: 10.1016/j.tpb.2003.11.001

Brown, J. H., Gillooly, J. F., Allen, A. P., Savage, V. M., and West, G. B. (2004). Toward a metabolic theory of ecology. *Ecology* 85, 1771–1789. doi: 10.1890/03-9000

Bryndum-Buchholz, A., Tittensor, D. P., Blanchard, J. L., Cheung, W. W., Coll, M., Galbraith, E. D., et al. (2019). Twenty-first-century climate change impacts on marine animal biomass and ecosystem structure across ocean basins. *Glob. Change Biol.* 25, 459–472.

Burnham, K. P., and Anderson, D. R. (2002). *Model Selection Multimodel Inference A Practical Information-Theoretic Approach*, 2nd Edn. New York, NY: Springer.

Carozza, D. A., Bianchi, D., and Galbraith, E. D. (2016). The ecological module of BOATS-1.0: a bioenergetically constrained model of marine upper trophic levels suitable for studies of fisheries and ocean biogeochemistry. *Geosci. Model Dev.* 9, 1545–1565. doi: 10.5194/gmd-9-1545-2016

Carozza, D. A., Bianchi, D., and Galbraith, E. D. (2017). Formulation, general features and global calibration of a bioenergetically-constrained fishery model. *PLoS One* 12:e0169763. doi: 10.1371/journal.pone.0169763

Carozza, D. A., Bianchi, D., and Galbraith, E. D. (2019). Metabolic impacts of climate change on marine ecosystems: implications for fish communities and fisheries. *Glob. Ecol. Biogeogr.* 28, 158–169. doi: 10.1111/geb.12832

Cheung, W. W., Sarmiento, J. L., Dunne, J., Frölicher, T. L., Lam, V. W., Palomares, M. D., et al. (2013). Shrinking of fishes exacerbates impacts of global ocean changes on marine ecosystems. *Nat. Clim. Chang.* 3, 254–258. doi: 10.1038/nclimate1691

Cheung, W. W. L., Lam, V. W. Y., Sarmiento, J. L., Kearney, K., Watson, R., Zeller, D., et al. (2010). Large-scale redistribution of maximum fisheries catch potential in the global ocean under climate change. *Glob. Change Biol.* 16, 24–35. doi: 10.1111/j.1365-2486.2009.01995.x

Chust, G., Allen, J. I., Bopp, L., Schrum, C., Holt, J., Tsiaras, K., et al. (2014). Biomass changes and trophic amplification of plankton in a warmer ocean. *Glob. Change Biol.* 20, 2124–2139. doi: 10.1111/gcb.12562

Clarke, A., and Johnston, N. M. (1999). Scaling of metabolic rate with body mass and temperature in teleost fish. *J. Anim. Ecol.* 68, 893–905. doi: 10.1046/j.1365-2656.1999.00337.x

Dahlke, F. T., Wohlrab, S., Butzin, M., and Pörtner, H. O. (2020). Thermal bottlenecks in the life cycle define climate vulnerability of fish. *Science* 369, 65–70. doi: 10.1126/science.aaz3658

De Roos, A. M., Schellekens, T., Van Kooten, T., Van De Wolfshaar, K., Claessen, D., and Persson, L. (2008). Simplifying a physiologically structured population model to a stage-structured biomass model. *Theor. Popul. Biol.* 73, 47–62. doi: 10.1016/j.tpb.2007.09.004

Delworth, T. L., Broccoli, A. J., Rosati, A., Stouffer, R. J., Balaji, V., Beesley, J. A., et al. (2006). GFDL's CM2 global coupled climate models, Part I: formulation and simulation characteristics. *J. Clim.* 19, 643–674.

Deutsch, C., Ferrel, A., Seibel, B., Pörtner, H. O., and Huey, R. B. (2015). Climate change tightens a metabolic constraint on marine habitats. *Science* 348, 1132–1135. doi: 10.1126/science.aaa1605

du Pontavice, H., Gascuel, D., Reygondeau, G., Maureaud, A., and Cheung, W. W. L. (2020). Climate change undermines the global functioning of marine food webs. *Glob. Change Biol.* 26, 1306–1318. doi: 10.1111/gcb.14944

Dugdale, R. C., and Goering, J. J. (1967). Uptake of new and regenerated forms of nitrogen in primary productivity 1. *Limnol. Oceanogr.* 12, 196–206. doi: 10.4319/lo.1967.12.2.0196

Dunne, J. P., Armstrong, R. A., Gnanadesikan, A., and Sarmiento, J. L. (2005). Empirical and mechanistic models for the particle export ratio. *Glob. Biogeochem. Cycles* 19:GB4026.

Dunne, J. P., John, J. G., Adcroft, A. J., Griffies, S. M., Hallberg, R. W., Shevliakova, E., et al. (2012). GFDL's ESM2 global coupled climate-carbon earth system models, Part I: physical formulation and baseline simulation characteristics. *J. Clim.* 25, 6646–6665. doi: 10.1175/Jcli-D-11-00560.1

Dunne, J. P., John, J. G., Shevliakova, E., Stouffer, R. J., Krasting, J. P., Malyshev, S. L., et al. (2013). GFDL's ESM2 global coupled climate-carbon earth system models, Part II: carbon system formulation and baseline simulation characteristics. *J. Clim.* 26, 2247–2267. doi: 10.1175/Jcli-D-12-00150.1

Fossheim, M., Primicerio, R., Johannesen, E., Ingvaldsen, R. B., Aschan, M. M., and Dolgov, A. V. (2015). Recent warming leads to a rapid borealization of fish communities in the Arctic. *Nat. Clim. Chang.* 5, 673–677. doi: 10.1038/nclimate2647

Frank, K. T., Petrie, B., Choi, J. S., and Leggett, W. C. (2005). Trophic cascades in a formerly cod-dominated ecosystem. *Science* 308, 1621–1623. doi: 10.1126/science.1113075

Friedland, K. D., Stock, C., Drinkwater, K. F., Link, J. S., Leaf, R. T., Shank, B. V., et al. (2012). Pathways between primary production and fisheries yields of large marine ecosystems. *PLoS One* 10:e0133794. doi: 10.1371/journal.pone.0028945

Frölicher, T. L., Rodgers, K. B., Stock, C. A., and Cheung, W. W. (2016). Sources of uncertainties in 21st century projections of potential ocean ecosystem stressors. *Glob. Biogeochem. Cycles* 30, 1224–1243. doi: 10.1002/2015gb005338

Fu, W., Randerson, J. T., and Moore, J. K. (2016). Climate change impacts on net primary production (NPP) and export production (EP) regulated by increasing stratification and phytoplankton community structure in the CMIP5 models. *Biogeosciences* 13, 5151–5170. doi: 10.5194/bg-13-5151-2016

Fuller, E. C., Samhouri, J. F., Stoll, J. S., Levin, S. A., and Watson, J. R. (2017). Characterizing fisheries connectivity in marine social–ecological systems. *ICES J. Mar. Sci.* 74, 2087–2096. doi: 10.1093/icesjms/fsx128

Galbraith, E. D., Le Mézo, P., Solanes Hernandez, G., Bianchi, D., and Kroodsma, D. (2019). Growth limitation of marine fish by low iron availability in the open ocean. *Front. Mar. Sci.* 6:509. doi: 10.3389/fmars.2019.00509

Gangstø, R., Gehlen, M., Schneider, B., Bopp, L., Aumont, O., and Joos, F. (2008). Modeling the marine aragonite cycle: changes under rising carbon dioxide and its role in shallow water CaCO3 dissolution. *Biogeosciences* 5, 1057–1072. doi: 10.5194/bg-5-1057-2008

Gehlen, M., Gangstø, R., Schneider, B., Bopp, L., Aumont, O., and Ethe, C. (2007). The fate of pelagic CaCO3 production in a high CO 2 ocean: a model study. *Biogeosciences* 4, 505–519. doi: 10.5194/bg-4-505-2007

Griffies, S. M. (2009). *Elements of MOM4p1*. Princeton: NOAA/GFDL.

Griffies, S. M., Gnanadesikan, A., Dixon, K. W., Dunne, J. P., Gerdes, R., Harrison, M. J., et al. (2005). Formulation of an ocean model for global climate simulations. *Ocean Sci.* 1, 45–79. doi: 10.5194/os-1-45-2005

Guiet, J., Aumont, O., Poggiale, J. C., and Maury, O. (2016). Effects of lower trophic level biomass and water temperature on fish communities: a modelling study. *Prog. Oceanogr.* 146, 22–37. doi: 10.1016/j.pocean.2016.04.003

Hansen, B. W., Bjornsen, P. K., and Hansen, P. J. (1994). The size ratio between planktonic predators and their prey. *Limnol. Oceanogr.* 39, 395–402. doi: 10.4319/lo.1994.39.2.0395

Hansen, P. J., Bjornsen, P. K., and Hansen, B. W., (1997). Zooplankton grazing and growth: scaling within the 2–2000-mm body size range. *Limnol. Oceanogr.* 42, 687–704. doi: 10.4319/lo.1997.42.4.0687

Hartvig, M., and Andersen, K. H. (2013). Coexistence of structured populations with size-based prey selection. *Theor. Popul. Biol.* 89, 24–33. doi: 10.1016/j.tpb.2013.07.003

Hartvig, M., Andersen, K. H., and Beyer, J. E. (2011). Food web framework for size-structured populations. *J. Theor. Biol.* 272, 113–122. doi: 10.1016/j.jtbi.2010.12.006

Heintz, R. A., Siddon, E. C., Farley, E. V. Jr., and Napp, J. M. (2013). Correlation between recruitment and fall condition of age-0 walleye pollock (*Theragra chalcogramma*) from the eastern Bering Sea under varying climate conditions. *Deep Sea Res. II* 94, 150–156. doi: 10.1016/j.dsr2.2013.04.006

Jennings, S., and Collingridge, K. (2015). Predicting consumer biomass, size-structure, production, catch potential, responses to fishing and associated uncertainties in the world's marine ecosystems. *Mar. Ecol. Prog. Ser.* 410, 233–244.

Jones, D. O., Yool, A., Wei, C. L., Henson, S. A., Ruhl, H. A., Watson, R. A., et al. (2014). Global reductions in seafloor biomass in response to climate change. *Glob. Change Biol.* 20, 1861–1872. doi: 10.1111/gcb.12480

Kearney, K. A., Stock, C., Aydin, K., and Sarmiento, J. L. (2012). Coupling planktonic ecosystem and fisheries food web models for a pelagic ecosystem: description and validation for the subarctic Pacific. *Ecol. Modell.* 237, 43–62. doi: 10.1016/j.ecolmodel.2012.04.006

Klaas, C., and Archer, D. E. (2002). Association of sinking organic matter with various types of mineral ballast in the deep sea: implications for the rain ratio. *Glob. Biogeochem. Cycles* 16:1116.

Kwiatkowski, L., Aumont, O., and Bopp, L. (2019). Consistent trophic amplification of marine biomass declines under climate change. *Glob. Change Biol.* 25, 218–229. doi: 10.1111/gcb.14468

Kwiatkowski, L., Olivier Torres, O., Bopp, L., Aumont, O., Chamberlain, M., Christian, J., et al. (2020). Twenty-first century ocean warming, acidification, deoxygenation, and upper ocean nutrient decline from CMIP6 model projections. *Biogeosciences* 17, 3439–3470. doi: 10.5194/bg-2020-16

Laufkötter, C., John, J. G., Stock, C. A., and Dunne, J. P. (2017). Temperature and oxygen dependence of the remineralization of organic matter. *Glob. Biogeochem. Cycles* 31, 1038–1050. doi: 10.1002/2017gb005643

Laufkötter, C., Vogt, M., Gruber, N., Aita-Noguchi, M., Aumont, O., Bopp, L., et al. (2015). Drivers and uncertainties of future global marine primary production in marine ecosystem models. *Biogeosciences* 12, 6955–6984. doi: 10.5194/bg-12-6955-2015

Laufkötter, C., Vogt, M., Gruber, N., Aumont, O., Bopp, L., Doney, S. C., et al. (2016). Projected decreases in future marine export production: the role of carbon fluxes through the upper ocean ecosystem. *Biogeosci. Discuss.* 12, 19941–19998. doi: 10.5194/bgd-12-19941-2015

Laws, E. A., Falkowski, P. G., Smith, W. O., Ducklow, H., and McCarthy, J. J. (2000). Temperature effects on export production in the open ocean. *Glob. Biogeochem. Cycles* 14, 1231–1246. doi: 10.1029/1999gb001229

Lefort, S., Aumont, O., Bopp, L., Arsouze, T., Gehlen, M., and Maury, O. (2015). Spatial and body-size dependent response of marine pelagic communities to projected global climate change. *Glob. Change Biol.* 21, 154–164. doi: 10.1111/gcb.12679

Lin, S. J. (2004). A "vertically lagrangian" finite-volume dynamical core for global models. *Mon. Weather Rev.* 132, 2293–2307. doi: 10.1175/1520-04932004132<2293:Avlfdc<2.0.Co;2

Liu, X., Dunne, J. P., Stock, C. A., Harrison, M. J., Adcroft, A., and Resplandy, L. (2019). Simulating water residence time in the coastal ocean: a global perspective. *Geophys. Res. Lett.* 46, 13910–13919. doi: 10.1029/2019gl085097

Lotze, H. K., Tittensor, D. P., Bryndum-Buchholz, A., Eddy, T. D., Cheung, W. W., Galbraith, E. D., et al. (2019). Global ensemble projections reveal trophic amplification of ocean biomass declines with climate change. *Proc. Natl. Acad. Sci. U.S.A.* 116, 12907–12912.

Lutz, M. J., Caldeira, K., Dunbar, R. B., and Behrenfeld, M. J. (2007). Seasonal rhythms of net primary production and particulate organic carbon flux to depth describe the efficiency of biological pump in the global ocean. *J. Geophys. Res.* 112:C10011.

Mariani, P., Andersen, K. H., Lindegren, M., and MacKenzie, B. R. (2017). Trophic impact of Atlantic bluefin tuna migrations in the North Sea. *ICES J. Mar. Sci.* 74, 1552–1560. doi: 10.1093/icesjms/fsx027

Marsay, C. M., Sanders, R. J., Henson, S. A., Pabortsava, K., Achterberg, E. P., and Lampitt, R. S. (2015). Attenuation of sinking particulate organic carbon flux through the mesopelagic ocean. *Proc. Natl. Acad. Sci. U.S.A.* 112, 1089–1094. doi: 10.1073/pnas.1415311112

Martin, J. H., Knauer, G. M., Karl, D. M., and Broenkow, W. W., (1987). VERTEX: carbon cycling in the Northeast Pacific. *Deep-Sea Res.* 34, 267–285. doi: 10.1016/0198-0149(87)90086-0

Maury, O. (2010). An overview of APECOSM, a spatialized mass balanced "Apex Predators ECOSystem Model" to study physiologically structured tuna population dynamics in their ecosystem. *Prog. Oceanogr.* 84, 113–117. doi: 10.1016/j.pocean.2009.09.013

Moore, J. K., Fu, W., Primeau, F., Britten, G. L., Lindsay, K., Long, M., et al. (2018). Sustained climate warming drives declining marine biological productivity. *Science* 359, 1139–1143. doi: 10.1126/science.aao6379

Murdoch, W. W. (1977). Stabilizing effects of spatial heterogeneity in predator-prey systems. *Theor. Popul. Biol.* 11, 252–273. doi: 10.1016/0040-5809(77)90028-4

Nieblas, A. E., Demarcq, H., Drushka, K., Sloyan, B., and Bonhommeau, S. (2014). Front variability and surface ocean features of the presumed southern bluefin tuna spawning grounds in the tropical southeast Indian Ocean. *Deep Sea Res. Part II* 107, 64–76. doi: 10.1016/j.dsr2.2013.11.007

Pauly, D., and Cheung, W. W. (2018). Sound physiological knowledge and principles in modeling shrinking of fishes under climate change. *Glob. Change Biol.* 24, e15–e26.

Pauly, D., and Christensen, V. (1995). Primary production required to sustain global fisheries. *Nature* 374, 255–257. doi: 10.1038/374255a0

Pauly, D., Christensen, V., Dalsgaard, J., Froese, R., and Torres, F. (1998). Fishing down marine food webs. *Science* 279, 860–863. doi: 10.1126/science.279.5352.860

Pauly, D., and Zeller, D. (2015). "Reconstructing marine fisheries catch data," in *Catch Reconstructions: Concepts, Methods and Data Sources*, eds D. Pauly and D. Zeller. (Vancouver: Sea Around Us).

Perrin, N. (1995). About Berrigan and Charnov's life-history puzzle. *Oikos* 73, 137–139. doi: 10.2307/3545737

Peterson, W. T., Morgan, C. A., Peterson, J. O., Fisher, J. L., Burke, B. J., and Fresh, K. (2013). *Ocean Ecosystem Indicators of Salmon Marine Survival in the Northern California Current.* Seattle, WA: Northwest Fisheries Science Center, 77.

Petrik, C. M., Stock, C. A., Andersen, K. H., van Denderen, P. D., and Watson, J. R. (2019). Bottom-up drivers of global patterns of demersal, forage, and pelagic fishes. *Prog. Oceanogr.* 176:102124. doi: 10.1016/j.pocean.2019.102124

Pinsky, M. L., Reygondeau, G., Caddell, R., Palacios-Abrantes, J., Spijkers, J., and Cheung, W. W. (2018). Preparing ocean governance for species on the move. *Science* 360, 1189–1191. doi: 10.1126/science.aat2360

Pinsky, M. L., Worm, B., Fogarty, M. J., Sarmiento, J. L., and Levin, S. A. (2013). Marine taxa track local climate velocities. *Science* 341, 1239–1242. doi: 10.1126/science.1239352

Pinti, J., and Visser, A. W. (2019). Predator-prey games in multiple habitats reveal mixed strategies in diel vertical migration. *Am. Nat.* 193, E65–E77.

Polovina, J. J., Howell, E., Kobayashi, D. R., and Seki, M. P. (2001). The transition zone chlorophyll front, a dynamic global feature defining migration and forage habitat for marine resources. *Prog. Oceanogr.* 49, 469–483. doi: 10.1016/s0079-6611(01)00036-2

Pomeroy, L. R., and Deibel, D. O. N. (1986). Temperature regulation of bacterial activity during the spring bloom in Newfoundland coastal waters. *Science* 233, 359–361. doi: 10.1126/science.233.4761.359

Rall, B. C., Brose, U., Hartvig, M., Kalinkat, G., Schwarzmüller, F., Vucic-Pestic, O., et al. (2012). Universal temperature and body-mass scaling of feeding rates. *Phil. Trans. R. Soc. B* 367, 2923L–2934.

Redfield, A. C. (1934). "On the proportions of organic derivations in sea water and their relation to the composition of plankton," in *James Johnstone Memorial Volume*, ed. R. J. Daniel (Liverpool: University Press of Liverpool), 176–192.

Reglero, P., Tittensor, D. P., Álvarez-Berastegui, D., Aparicio-González, A., and Worm, B. (2014). Worldwide distributions of tuna larvae: revisiting hypotheses on environmental requirements for spawning habitats. *Mar. Ecol. Prog. Ser.* 501, 207–224. doi: 10.3354/meps10666

Ryther, J. H. (1969). Photosynthesis and fish production in the sea. *Science* 166, 72–76. doi: 10.1126/science.166.3901.72

Séférian, R., Berthet, S., Yool, A., Palmieri, J., Bopp, L., Tagliabue, A., et al. (2020). Tracking improvement in simulated marine biogeochemistry between CMIP5 and CMIP6. *Curr. Clim. Change* 18, 1–25.

Steele, J. H., and Henderson, E. W. (1992). "The significance of interannual variability," in *Towards a Model of Ocean Biogeochemical Processes*, eds G. T. Evans and M. J. R. Fasham (Heidelberg: Springer-Verlag), 227–260.

Stock, C., and Dunne, J. (2010). Controls on the ratio of mesozooplankton production to primary production in marine ecosystems. *Deep Sea Res. I* 57, 95–112. doi: 10.1016/j.dsr.2009.10.006

Stock, C. A., Alexander, M. A., Bond, N. A., Brander, K. M., Cheung, W. W., Curchitser, E. N., et al. (2011). On the use of IPCC-class models to assess the impact of climate on living marine resources. *Prog. Oceanogr.* 88, 1–27. doi: 10.1016/j.pocean.2010.09.001

Stock, C. A., Dunne, J. P., and John, J. G. (2014a). Drivers of trophic amplification of ocean productivity trends in a changing climate. *Biogeosciences* 11, 7125–7135. doi: 10.5194/bg-11-7125-2014

Stock, C. A., Dunne, J. P., and John, J. G. (2014b). Global-scale carbon and energy flows through the marine planktonic food web: an analysis with a coupled physical-biological model. *Prog. Oceanogr.* 120, 1–28. doi: 10.1016/j.pocean.2013.07.001

Stock, C. A., John, J. G., Rykaczewski, R. R., Asch, R. G., Cheung, W. W. L., Dunne, J. P., et al. (2017). Reconciling fisheries catch and ocean productivity. *Proc. Natl. Acad. Sci. U.S.A.* 114, E1441–E1449. doi: 10.1073/pnas.1610238114

Stocker, T. F., Qin, D., Plattner, G., Tignor, M., Allen, S. K., Boschung, J., et al. (eds) (2013). *IPCC, 2013: Summary for Policymakers in Climate Change 2013: the Physical Science Basis, Contribution of Working Group I to the Fifth Assessment Report of the Intergovernmental Panel On Climate Change*. Cambridge: Cambridge University Press.

Taucher, J., and Oschlies, A. (2011). Can we predict the direction of marine primary production change under global warming? *Geophys. Res. Lett.* 38:L02603.

Tittensor, D. P., Eddy, T. D., Lotze, H. K., Galbraith, E. D., Cheung, W., Barange, M., et al. (2018). A protocol for the intercomparison of marine fishery and ecosystem models: fish-MIP v1.0. *Geosci. Model Dev.* 11, 1421–1442.

Ullah, H., Nagelkerken, I., Goldenberg, S. U., and Fordham, D. A. (2018). Climate change could drive marine food web collapse through altered trophic flows and cyanobacterial proliferation. *PLoS Biol.* 16:e2003446. doi: 10.1371/journal.pbio.2003446 van Denderen, D., Gislason, H., van den Heuvel, J., and Andersen, K. H., (2020). Global analysis of fish growth rates shows weaker responses to temperature than metabolic predictions. *Glob. Ecol. Biogeogr.* doi: 10.1111/geb.13189

van Denderen, D., Lindegren, M., MacKenzie, B. R., Watson, R. A., and Andersen, K. H. (2018). Global patterns in marine predatory fish. *Nat. Ecol. Evol.* 2, 65–70. doi: 10.1038/s41559-017-0388-z

von Bertalanffy, L. (1960). "Fundamental aspects of normal and malignant growth," in *Fundamental Aspects of Normal and Malignant Growth*, ed. W. W. Nowinski (Amsterdam: Elsevier), 137–259. doi: 10.1016/b978-0-408-10638-2.50012-4

Watson, J. R., Fuller, E. C., Castruccio, F. S., and Samhouri, J. F. (2018). Fishermen follow fine-scale physical ocean features for finance. *Front. Mar. Sci.* 5:46. doi: 10.3389/fmars.2018.00046

Watson, J. R., Stock, C. A., and Sarmiento, J. L. (2015). Exploring the role of movement in determining the global distribution of marine biomass using a coupled hydrodynamic-size-based ecosystem model. *Prog. Oceanogr.* 138, 521–532. doi: 10.1016/j.pocean.2014.09.001

Wei, C.-L., Rowe, G. T., Escobar-Briones, E., Boetius, A., Soltwedel, T., Caley, M. J., et al. (2010). Global patterns and predictions of seafloor biomass using random forests. *PLoS One* 5:e15323. doi: 10.1371/journal.pone.0015323

Yool, A., Martin, A. P., Anderson, T. R., Bett, B. J., Jones, D. O., and Ruhl, H. A. (2017). Big in the benthos: future change of seafloor community biomass in a global, body size-resolved model. *Glob. Change Biol.* 23, 3554–3566. doi: 10.1111/gcb.13680

Conflict of Interest: The authors declare that the research was conducted in the absence of any commercial or financial relationships that could be construed as a potential conflict of interest.

frontiers
in Marine Science

ORIGINAL RESEARCH
published: 16 March 2021
doi: 10.3389/fmars.2021.602991

Future Changes in Oceanography and Biogeochemistry Along the Canadian Pacific Continental Margin

Amber M. Holdsworth[1]*, **Li Zhai**[2], **Youyu Lu**[2] **and James R. Christian**[1,3]

[1] Fisheries and Oceans Canada, Institute of Ocean Sciences, Sidney, BC, Canada, [2] Fisheries and Oceans Canada, Bedford Institute of Oceanography, Dartmouth, NS, Canada, [3] Canadian Centre for Climate Modelling and Analysis, Victoria, BC, Canada

Edited by:
Darren Pilcher,
University of Washington and
NOAA/PMEL, United States

Reviewed by:
Mercedes Pozo Buil,
University of California, Santa Cruz,
United States
Elizabeth Joan Drenkard,
Geophysical Fluid Dynamics
Laboratory (GFDL), United States

***Correspondence:**
Amber M. Holdsworth
amber.holdsworth@dfo-mpo.gc.ca

Specialty section:
This article was submitted to
Global Change and the Future Ocean,
a section of the journal
Frontiers in Marine Science

Received: 04 September 2020
Accepted: 15 February 2021
Published: 16 March 2021

Citation:
Holdsworth AM, Zhai L, Lu Y and
Christian JR (2021) Future Changes in
Oceanography and Biogeochemistry
Along the Canadian Pacific
Continental Margin.
Front. Mar. Sci. 8:602991.
doi: 10.3389/fmars.2021.602991

Model projections of ocean circulation and biogeochemistry are used to investigate large scale climate changes under moderate mitigation (RCP 4.5) and high emissions (RCP 8.5) scenarios along the continental shelf of the Canadian Pacific Coast. To reduce computational cost, an approach for dynamical downscaling of climate projections was developed that uses atmospheric climatologies with augmented winds to simulate historical (1986–2005) and future (2046–2065) periods separately. The two simulations differ in initial and lateral open boundary conditions. For each simulation, the daily climatology of surface winds in the driving model was augmented with high-frequency variability from an atmospheric reanalysis product. The "time-slice" approach was able to reproduce the observed climate state for the historical period. Sensitivity tests confirmed that the high frequency wind variability plays an essential role in freshwater distribution in this region. Projections suggest that sea surface temperature will increase by 1.8–2.4°C and surface salinity will decrease between -0.08 and -0.23 depending on whether a moderate or high emissions scenario is used. Stratification increases throughout the region and there is some evidence of nutrient limitation near the surface. Primary production and phytoplankton productivity (chlorophyll) also increase. Density surfaces are relocated deeper in the water column and this change is mainly driven by surface heating and freshening. Changes in saturation state are mainly due to anthropogenic CO_2 with minor contributions from solubility, remineralization and advection. There is little difference between RCP 4.5 and RCP 8.5 with regard to projections of deoxygenation and acidification. The depths of the aragonite saturation state and the oxygen minimum zone are projected to become shallower by $\simeq 100$ and $\simeq 75$ m respectively. Extreme states of temperature, oxygen and acidification are projected to become more frequent and more extreme, with the frequency of occurrence of $[O_2] < 60\,\mathrm{mmol\,m^{-3}}$ expected to approximately double under either scenario.

Keywords: modeling, biogeochemistry, acidification, deoxygenation, Pacific ocean, projection, climate-change

1. INTRODUCTION

Increasing atmospheric greenhouse gas (GHG) concentrations affect marine ecosystems worldwide through a variety of mechanisms, notably ocean acidification due to dissolution of atmospheric CO_2 and declining oxygen concentrations (deoxygenation). Canadian Pacific coastal waters are often considered to be particularly vulnerable because waters rich in dissolved inorganic carbon (DIC) and low in oxygen are naturally present at relatively shallow depths on the continental slope (e.g., Feely et al., 2008). Warming of the surface ocean results in both declining surface oxygen concentrations, and increased stratification that leads to reduced ventilation of the subsurface ocean. Rising temperature, acidification, and declining oxygen are three important stressors that affect marine biodiversity and ecosystem health both individually and synergistically (Gruber, 2011; Pörtner et al., 2014). Climate change may also result in changes to the upwelling- and downwelling-favorable winds that play a major role in the oceanography of the Canadian Pacific continental margin (Merryfield et al., 2009; Foreman et al., 2014).

Episodes of extremely hypoxic or corrosive water have already led to extensive die offs of marine life in the region (Barton et al., 2015; Chan et al., 2019). To manage marine ecosystems under a changing climate and plan potential strategies for adaptation, projections of how physical, chemical, and biological characteristics of the ocean ecosystem will change are needed. Regional ocean downscaling of climate projections from global Earth System models are the only available source of information beyond the very limited time scales on which forecasting is possible (e.g., Li et al., 2019).

Estimates of projected changes in ocean state can be used, in combination with species observations, to estimate impacts on marine ecosystems. By identifying habitat changes, potential hot-spots and refugia, climate projections can be used to inform marine conservation and spatial planning. Additionally, projected ocean changes are a precursor to investigations of climate impacts on the goods and services that these ecosystems provide including, for example, the catch potential for various marine species (Cheung et al., 2010).

We present here a high-resolution regional projection of future climate for the Canadian Pacific continental margin. The point of departure for this work is Foreman et al. (2014) which examined changes in the physical oceanography of the British Columbia (BC) Continental Shelf. Our model includes biogeochemistry, has a higher resolution and uses an approach to dynamically downscaling climate projections that reduces computational costs. This work will evaluate the model's ability to reproduce the observed state of the ocean in the historical-climate simulation, present projections of the future ocean biogeochemical state, and evaluate the mechanisms underlying the projected changes.

2. MATERIALS AND METHODS

This study uses a multi-stage downscaling approach to dynamically downscale global climate projections at a 1/36° $(1.5-2.25\,\mathrm{km})$ resolution. We chose to use the second-generation Canadian Earth System model (CanESM2) because high-resolution downscaled projections of the atmosphere over the region of interest are available from the Canadian Regional Climate Model version 4 (CanRCM4). We used anomalies from CanESM2 with a resolution of about 1° at the open boundaries, and the regional atmospheric model, CanRCM4 (Scinocca et al., 2016) for the surface boundary conditions. CanRCM4 is an atmosphere only model with a 0.22° resolution and was used to downscale climate projections from CanESM2 over North America and its adjacent oceans.

The model used is computationally expensive. This is due to the relatively high number of points in the domain $(715 \times 1,021 \times 50)$ and the relatively complex biogeochemical model (19 tracers). Therefore, rather than carrying out interannual simulations for the historical and future periods, we implemented a new method that uses atmospheric climatologies with augmented winds to force the ocean. We show that augmenting the winds with hourly anomalies allows for a more realistic representation of the surface freshwater distribution than using the climatologies alone.

Section 2.1 describes the ocean model that is used to estimate the historical climate and project the ocean state under future climate scenarios. The time periods are somewhat arbitrary; 1986–2005 was chosen because the Coupled Model Intercomparison Project Phase 5 (CMIP5) historical simulations end in 2005 as no community-accepted estimates of emissions were available beyond that date (Taylor et al., 2009); 2046–2065 was chosen to be far enough in the future that changes in 20 year mean fields are unambiguously due to changing GHG forcing (as opposed to model internal variability) (e.g., Christian, 2014), but near enough to be considered relevant for management purposes.

While it is true that 30 years rather than 20 is the canonical value for averaging over natural variability, in practice the difference between a 20 and a 30 year mean is small (e.g., if we average successive periods of an unforced control run, the variance among 20 year means will be only slightly larger than for 30 year means). Also, there is concern that longer averaging periods are inappropriate in a non-stationary climate (Livezey et al., 2007; Arguez and Vose, 2011). We chose 20 year periods because they are adequate to give a mean annual cycle with little influence from natural variability, while minimizing aliasing of the secular trend into the means. As the midpoints of the two time periods are separated by 60 years, the contribution of natural variability to the differences between the historical and future simulations is negligible e.g., (Hawkins and Sutton, 2009; Frölicher et al., 2016).

Section 2.2 describes how climatologies derived from observations were used for the initialization and open boundary conditions for the historical simulations and pseudo-climatologies were used for the future scenarios. The limited availability of observations means that the years used for these climatologies differs somewhat from the historical and future periods. Section 2.3 details the atmospheric forcing fields and the method that we developed to generate winds with realistic high-frequency variability while preserving the daily climatological means from the CanRCM4 data. Section

2.4 shows the equilibration of key modeled variables to the forcing conditions.

2.1. Northeast Pacific Model Description and Forcing Fields

The regional model is based on the Nucleus for European Modeling of the Ocean (NEMO) numerical framework version 3.6 (Madec, 2008). The North–Eastern Pacific (NEP) model domain spans the Canadian Pacific Ocean east of $\simeq$ 140°W and north of 45°N (**Figure 1A**). The horizontal resolution is nominally 1/36° latitude and longitude which gives a variable grid spacing between 1.5 and 2.25 km (**Figure 1A**).

The model, referred to as NEP36, is an update of the model developed by Lu et al. (2017) based on NEMO version 3.1 and uses the same bathymetry (**Figure 1B**). The sea-ice module was not used because of negligible presence of sea-ice in the model domain. Water temperatures below the freezing point were set to the freezing temperature.

The vertical discretization includes 50 levels with thickness varying from approximately 1 m at the surface to 450 m at 5,000 m with partial cells at the bottom. The minimum thickness of the partial cell at a particular location is set to be the minimum of 6 m or 20% of the full thickness of the cell near the bottom. The thickness of the vertical levels varies slightly with changes in sea surface elevation (Levier et al., 2007).

The NEP36 physical ocean model used in this study has the same 50-level setup as the version validated by Lu et al. (2017). A 75-level version of the NEP36, based on NEMO 3.6, is used in an operational prediction system. For each version of NEP36, the parameterizations of vertical and lateral mixing are tuned based on model validation. Specifically, in the current version the vertical eddy diffusivity and viscosity are computed using the General Length Scale scheme (Umlauf and Burchard, 2003). The bottom friction is parameterized using a quadratic law, with a fixed drag coefficient of 5×10^{-3}. The horizontal diffusivity and viscosity are parameterized by a Laplacian scheme along isopycnal and horizontal levels, respectively. The horizontal viscosity is related to the strength of the horizontal shear of the velocity according to Smagorinsky (1963), with the constant parameter set to 0.7. The eddy horizontal Prandtl number (the ratio of eddy diffusivity to viscosity) is set to 0.1. The background horizontal eddy diffusivity and viscosity are set to be $20\text{m}^2\ \text{s}^{-1}$. In order to compare the performance of the current version with the 2017 version, a short hindcast test was run using the same Climate Forecast Reanalysis (CFSR) (Saha et al., 2010) forcing. The results were substantially close (not shown).

The ocean biogeochemistry module is called the Canadian Ocean Ecosystem model (CanOE). It was developed for the Canadian Earth System Model v.5 (CanESM5, Swart et al., 2019), which is based on NEMO 3.4.1, and was adapted to run within NEMO 3.6. CanOE is fully integrated within the physical circulation model through NEMO's Tracers in the Ocean Paradigm (TOP) module. The model consists of 19 tracers including dissolved inorganic carbon (DIC), total alkalinity (TA), oxygen (O_2), nitrate (NO_3), ammonium (NH_4), dissolved iron (dFe), large (P_L), and small (P_S) phytoplankton, large (Z_L) and small (Z_S) zooplankton, and large (D_L) and small (D_S) detritus. Each phytoplankton group has four state variables: nitrogen, carbon, iron, and chlorophyll. Iron limitation was turned off, as BC shelf waters are rich in iron (Johnson et al., 2005). A schematic diagram of the ecosystem model and a more detailed description can be found in Hayashida et al. (2019).

The time-step of the physical model (baroclinic mode) was 60 s and each physical step covers 4 ecosystem model time-steps. The computational cost was reduced by removing the land-only tiles using the land-processor elimination tool within NEMO. Unless otherwise stated, model outputs were derived from five day averages and the analysis presented will use fields that are averaged over the last 3 years for historical (1986–2005) and future (2046–2065) simulations. While only three averaging years are used, each year represents the climate over the entire 20 year period because the model is forced with climatologies except that the winds are augmented with high frequency variability.

To project future climate, models make use of scenarios of how technology, population, economics, policy, and land-use will change over time (e.g., Moss et al., 2010). This study examines a "moderate mitigation" scenario, Representative Concentration Pathway (RCP) 4.5, and a "no mitigation" (high emissions) scenario, RCP 8.5.

2.2. Ocean Initialization and Forcing

For the historical simulation, the physical ocean model was initialized using potential temperature (T), salinity (S), sea surface height (SSH) and zonal (u) and meridional (v) velocities from climatological conditions in January, and the lateral open boundary conditions (OBC) use the climatologies for each month. For ocean T and S, monthly climatologies (1985–2004) were constructed from a combination of the North East Pacific (NEP) and the Northern North Pacific (NNP) regional climatologies on a $1/10^\circ \times 1/10^\circ$ grid with 57 depth levels from 0 to 1,500 m (Seidov et al., 2017). The World Ocean Atlas (WOA 2013) 1/4° data was used to fill in any gaps in our domain for salinity (Zweng et al., 2013) and temperature (Locarnini et al., 2013). Monthly climatologies for SSH and velocities were created from Ocean ReAnalysis System 4 (ORAS4) (1986–2005) (Balmaseda et al., 2013). Where necessary, SOSIE[1] was used to re-grid the data. The OBC also included tidal SSH and depth-averaged currents for 8 constituents (K1, O1, P1, Q1, M2, S2, N2, and K2) that were obtained from WebTide[2], with the solution for the Northeast Pacific Ocean based on Foreman et al. (2000).

Pseudo-climatologies for DIC and TA were constructed from the Global Ocean Data Analysis Project (GLODAP) version 2 (Key et al., 2015) and Lauvset et al. (2016) (only annual data are available so monthly data files were created with the same data in each month). Monthly climatologies ($1981 - 2010$) for oxygen and nitrate were taken from WOA 2013 (Garcia et al., 2014a,b). River runoff was defined according to Morrison et al. (2012) and the concentrations of dissolved inorganic carbon and total alkalinity in river water were set to 10^{-3} mol/L.

---

[1] http://sosie.sourceforge.net/

[2] http://www.bio.gc.ca/science/research-recherche/ocean/webtide/index-en.php

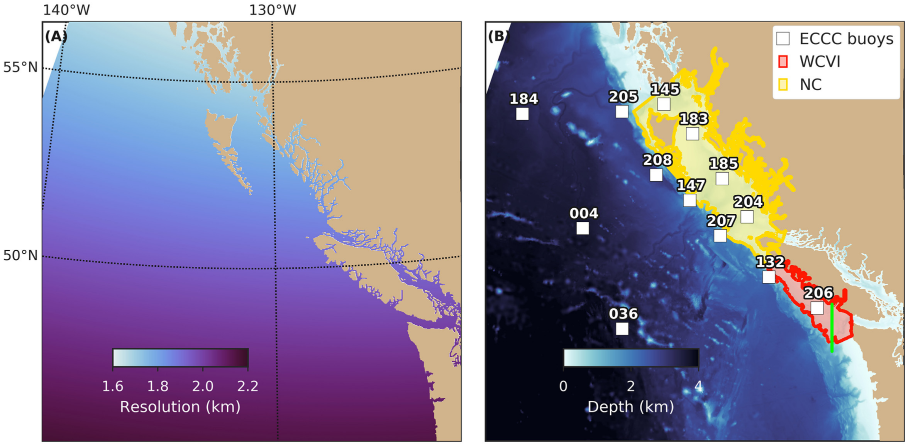

FIGURE 1 | Maps of the **(A)** NEP36 model domain and resolution and **(B)** the model bathymetry. **(B)** Shows the focus regions of West Coast Vancouver Island (WCVI) and the Northern Coast (NC) as well as the positions of weather buoys maintained by Environment and Climate Change Canada. The green line shows the location where a vertical cross-section was extracted.

Similar to Foreman et al. (2014), future initial conditions and OBC were constructed using the Pseudo-Global-Warming method (Hara et al., 2008; Morrison et al., 2012) by adding a monthly anomaly generated from CanESM2 (Arora et al., 2011) to the historical fields. CanESM2 has a $1-2^{\circ}$ horizontal resolution with 40 vertical levels and uses the Canadian Model of Ocean Carbon (CMOC) which is a precursor to CanOE with 6 passive tracers. The monthly anomalies were calculated as the difference between climatologies for historical (1986–2005) and future periods (2046–2065) for T, S, u, v, TA, DIC, and NO_3. Because CanESM2 did not have O_2, the O_2 anomaly was estimated as a solubility term calculated from T and S and a remineralization contribution calculated from NO_3 assuming Redfield stoichiometry. The sea surface height remains unchanged from the historical simulation. Atmospheric CO_2 concentration was assumed to be a constant 360 ppmv for the historical simulation and 496 ppmv (576 ppmv) for RCP 4.5 (RCP 8.5) (Meinshausen et al., 2011).

2.3. Atmospheric Forcing

Rather than running the model forward in time from e.g., 2000 to 2070, this study uses prescribed atmospheric climatologies. This “time-slice” approach generates outputs of the modeled variables that represent the climate of the “historical” (1986–2005) period and “future” (2046–2065) scenarios. While similar approaches have been used to investigate climate change between past and future periods the simulations were run inter-annually and then averaged to produce the analyzed climatology (Cannaby et al., 2015; Peña et al., 2018). Most studies using atmospheric climatologies to force the ocean do not augment the winds with high-frequency variability (i.e., Penduff et al., 2011). However, studies show that high frequency wind variability is essential to maintaining a realistic ocean state (Holdsworth and Myers, 2015; Wu et al., 2016; Jamet et al., 2019). We introduce a new method for dynamically downscaling climate projections using an ocean only model that uses prescribed atmospheric climatologies and augments the winds with high frequency variability from the historical climate.

The CanRCM4 climatologies project increases in atmospheric temperatures throughout all of the seasons with an annual increase of 2.3°C (2.9°C) under RCP 4.5 (RCP 8.5). Projected changes in precipitation imply wetter winters and dryer summers. The strongest increases occurring during winter and fall are up to $2.4\,\mathrm{mm\,d^{-1}}$ ($2.5\,\mathrm{mm\,d^{-1}}$) under RCP 4.5 (RCP 8.5). Average summer decreases are as high as $-1.0\,\mathrm{mm\,d^{-1}}$ ($-1.5\,\mathrm{mm\,d^{-1}}$) under RCP 4.5 (RCP 8.5).

Each simulation was run for $\simeq$ 10 years or until it approached an internal equilibrium, at least for the upper ocean. Because the model is run for a relatively short time, this method substantially reduces the computational costs and model drift.

Daily climatologies for surface air temperature (SAT), total precipitation, specific humidity, sea level pressure, and incident long-wave radiation were constructed from downscaling simulations with the $\simeq$ 22 km CanRCM4. CanRCM4 was used to downscale global climate model (CanESM2) simulations for the atmosphere over North America; the physical process parameterizations in the CanRCM and the CanESM atmosphere are generally the same. For surface solar irradiance (shortwave radiation) an observation-based climatology was used. Data from 1983 to 1991 (Bishop et al., 1997) were averaged for each day of the year. These data were interpolated to the NEP36 grid online using the weight files generated with the NEMO TOOLS.

Climatologies of the zonal and meridional wind velocities were constructed by computing the wind direction and speed separately using the daily CanRCM4 output. For the wind speed, $\bar{s} = \frac{1}{n_k}\sum_{k=1}^{n_k}\sqrt{(u_k^2+v_k^2)}$ where n_k is the number of years in the climatological period. Wind directions were computed using $\bar{\theta} = \tan^{-1}(\bar{v}/\bar{u})$ for each day from the averaged wind vectors (e.g., $\bar{u} = \frac{1}{n_k}\sum_{k=1}^{n_k} u_k$). Then, $u = \bar{s}\cos\bar{\theta}$ and $v = \bar{s}\sin\bar{\theta}$ define the vector components of the climatological winds. The scalar averaged winds, u and v, preserve the wind speed magnitude and are generally greater than vector averaged quantities $\bar{u}$ and $\bar{v}$ especially for locations with large variance in the wind direction.

The climatological winds exclude high frequency ($\lesssim$ 2 days) variability that, due to the nonlinear dependence of turbulent surface fluxes on the wind speed, plays an important role in ocean mixing and circulation (Wu et al., 2016). Daily forcing frequencies cannot provide any information about variations that occur over time-scales of $<$24 h. Therefore, we developed a new method to generate hourly winds with realistic high-frequency variability that preserves the daily climatological means from the CanRCM4 data.

To construct the historical winds, hourly wind speed anomalies were added to the daily means from CanRCM4 ($\bar{s}$). The anomalies were calculated based on the hourly winds of the United States National Centers for Environmental Prediction Climate Forecast System Reanalysis (CFSR) (Saha et al., 2010). To compute the anomaly, a daily climatology of the CFSR wind speeds (1986–2005) was subtracted from the hourly CFSR wind speeds for a selected year of the CFSR data. By adding this hourly wind speed anomaly to $\bar{s}$, and keeping the daily wind direction ($\bar{\theta}$) unchanged, the hourly wind velocities (u, v) were obtained. Years were randomly selected from the CFSR to avoid biasing the model toward any particular year; linear interpolation is applied over the last day of each year. The randomly selected years were run in the following order 2005, 1994, 1997, 2002, 1986, 1999, 1993, 1998, 1989, 1990, 1988, and 2004 (the last year was only used for interpolation in December).

Augmenting the winds with hourly anomalies was necessary for an accurate representation of the wind speed distribution. The distribution of wind speeds for the historical winds is similar to the ECCC weather buoy data, while the distribution of the climatological winds (without including the hourly anomalies) is dominated by weaker winds with speeds $<5\,\mathrm{m\,s^{-1}}$ (**Figure 2A**). Here, the model data was extracted from the nearest grid cell to the buoy locations. For comparison, we created daily winds augmented with daily anomalies from the CanRCM4 data (CanRCM4 historical). The year 1995 was selected (arbitrarily) to facilitate direct comparison. We found that the dominant wind speeds are within the range of $5\,\mathrm{m\,s^{-1}} - 10\,\mathrm{m\,s^{-1}}$, and strong (weak) winds with speed larger (smaller) than $10\,\mathrm{m\,s^{-1}}$ ($5\,\mathrm{m\,s^{-1}}$) are still mostly missing (**Figure 2A**). Only the historical winds (CanRCM4 climatological augmented with hourly CFSR) were able to accurately represent the wind speed distribution exhibited by the buoy time-series.

A sensitivity test was conducted using the climatological winds. While this test provides some insight into the influence of high frequency winds, we caution that this was completed during model development and there are small differences in the initial conditions between this run and the historical run. Moreover, we are comparing 1 year of the climatological simulation with a 3 year average from the historical simulation. More details of model validation with shipboard data will be given in section 3.1. For the analysis of the sensitivity test, we binned the vertical profiles at each station into the means above and below 10 m so that the error bars represent the variability across the stations. The solution of the climatological simulation exhibited larger biases in the ocean state compared with the solution of the historical simulation (using the augmented hourly winds) (**Figure 2B**). In particular, the salinity bias for depths $<$10 m was significantly reduced (diamond markers) for all of the seasons when high frequency winds were included (**Figure 2B**). For greater depths, the only significant difference was in fall, however, this cannot be directly attributed to changes in the surface winds because of differences in the initial conditions (**Figure 2C**). These results suggest that including high frequency wind anomalies is important for an accurate representation of upper ocean mixing.

Some interannual variability is introduced to the wind fields from the CFSR wind speed anomalies. Examining the standard deviation among these 3 years indicates which variables are strongly influenced by upper ocean mixing due to the wind variability. But more carefully conducted model studies are needed to better understand the role that high frequency wind variability plays in setting oceanic conditions for this region. More details of the year-over-year variability for key variables in the 10 year historical simulation are given in section 2.4.

For the future simulations, the same technique of randomly shuffling years for the wind speed anomalies was implemented, but the full range of years from the CFSR data set 1979 − 2010 was used. The randomly selected years used for the wind patterns in RCP 4.5 are 1991, 2003, 2005, 2007, 1979, 1985, 1988, 1999, 1994, 1980, 1987, 2000, and 2008 and for RCP 8.5 they are 1985, 2001, 1998, 2005, 1982, 1989, 2009, 1986, 1993, 1990, 1997, 2002, and 1991.

While the hourly wind frequency is adequate to capture localized wind events, future changes in the frequency, duration, and pathways for these storms are not considered. It is widely accepted that storms tracks will shift poleward in the future as a result of increasing mean ocean temperatures (Yin, 2005). But there is no generally accepted theory about how they will change at regional scales (Shaw et al., 2016; Mbengue and Schneider, 2017), so assessing the impact of changes in weather extremes is beyond the scope of this study.

The magnitude of the wind speeds for the historical simulation (with the CFSR anomaly from 2005) are consistent with climatologies calculated from weather buoy data. The locations of the buoys are shown in **Figure 1** and a more complete description of these data is given in the **Supplementary Material**. The corresponding wind directions are more consistent with the buoys over the open ocean and shelf than near shore (**Figure 3**). Near the shelf break, winds are typically northward in winter (downwelling-favorable) and to the east or south-east in summer (upwelling-favorable). The wind field is broadly consistent with the observations in terms of the timing of upwelling, but the winds turn too early during the fall transition and too late during the spring transition. Nearer to shore (e.g., buoys 204, 185, 183, 145), the model wind direction has errors of 20–30° (rotated clockwise relative to the observations). The historical winds exhibit more accurate wind speeds and directions than those of the North American Regional Climate Change Assessment Program (NARCCAP) Regional Climate Model (RCM) ensemble (c.f. Figure 5 of Morrison et al., 2014) which were typically rotated counter-clockwise relative to the

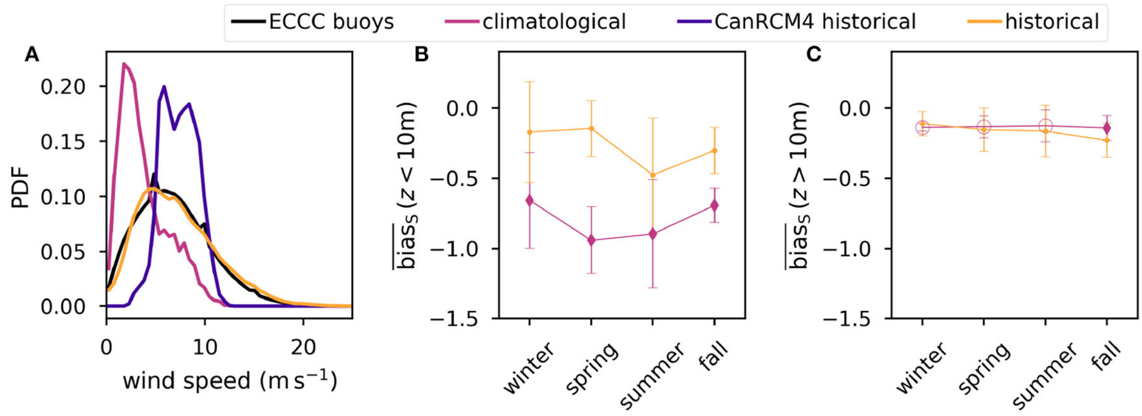

FIGURE 2 | (A) The frequency distribution of wind speeds for the historical period for the daily CanRCM4 climatology (climatological), the CanRCM4 climatology augmented with the daily CanRCM4 anomalies (CanRCM4 historical), and the CanRCM4 climatology augmented with CFSR hourly anomalies (historical). **(B,C)** Seasonal bias in salinity averaged over all stations at depths **(B)** < 10 m and **(C)** > 10 m for a simulations forced with the historical winds and the CanRCM4 climatology. The error-bars represent the standard deviation over the seasonal averages. The diamond markers indicate significant ($p < 0.05$) differences from the historical simulation (Welch's *t*-test).

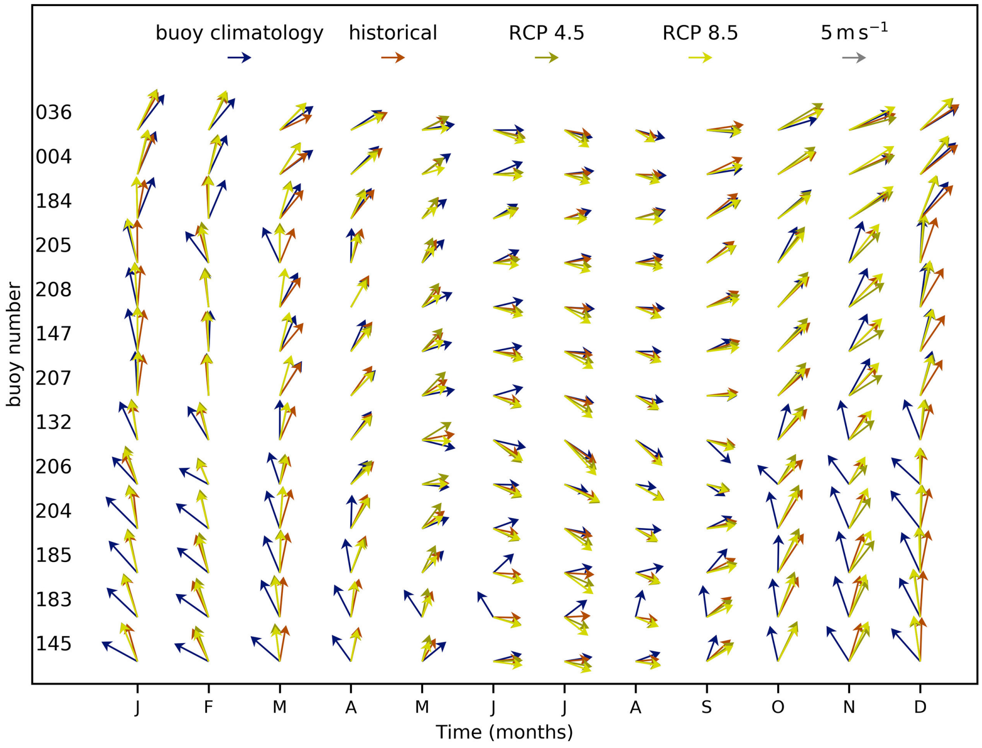

FIGURE 3 | Monthly mean wind vectors for the ECCC buoy climatologies (shown in **Figure 1**) along with the future and historical wind fields (CanRCM4 and CFSR from 2005).

buoy winds and did not turn sufficiently south during the upwelling season.

The year 2005 was used for our comparisons with the future winds because it was common to the random selections for future and historical wind anomalies; the year chosen to provide the high-frequency variability is, however, arbitrary and does not affect the results. Future winds along the shelf begin the spring transition later than the historical winds with a more southward direction during the summer upwelling season (i.e., 204, 206, 207, 132). With the exception of the buoys over the open ocean (004, 036, 184), winds turn earlier in the future during the fall transition (**Figure 3**).

2.4. Model Spinup

Although the model does not start from rest, it takes some time to adjust to the forcing. Since a different randomly chosen wind anomaly was used for each year, the model was not expected to converge to a perfectly repeating annual cycle. To determine whether the model had equilibrated, the domain was divided into nine different regions and the evolution of essential model variables was evaluated. The spin-up was examined over the entire domain, but we show only the two example regions which are the focus of our study as described below (**Figure 1B**).

The model resolution varies laterally and vertically. To avoid any biases associated with the variable grid cell volume regional averages for the study regions were normalized using a volume V weighted integral $\bar{F} = \int_V F(x, y, z)\frac{dV}{V}$. The freshwater content is defined by the volume weighted integral of $\frac{S_r - S(x,y,z)}{S_r}$ with a reference salinity $S_r = 32.5$ and heat content is defined by the volume weighted integral of $\rho c_p(T(x, y, z) - T_r)$ where $c_p = 4,184\,\mathrm{J\,kg^{-1}\,K^{-1}}$ is the heat capacity of water, $\rho = 1,020\,\mathrm{kg\,m^{-3}}$ is a reference density, and $T_r = 0^\circ\mathrm{C}$ is the reference temperature). Both quantities took several years to equilibrate before a regular seasonal cycle was achieved (**Figures 4A,B**). This adjustment period is most apparent for fresh water (**Figure 4B**) especially for near surface waters (solid lines).

The biogeochemical model was initialized late in year six of the physical model spinup. Volume weighted mean concentrations of NO_3, and the salinity-normalized DIC (nDIC) are shown in **Figures 4C,D**. Both NO_3 and nDIC undergo substantial adjustments over the first few years before a relatively regular seasonal cycle begins to emerge (**Figures 4C,D**).

The future simulation was initialized with 3D velocity fields constructed from the ORAS4 data used for the historical simulation, plus CanESM2 anomalies. This simulation exhibited a pattern of convergence for the physical and biogeochemical variables that was similar to the historical simulation (not shown).

3. RESULTS

The analysis focuses on the West Coast of Vancouver Island (WCVI) region and the Northern Coast (NC) region shown by shaded areas in **Figure 1B**. Both of these regions are bounded by the 500 m isobath on the continental slope. They meet at Brooks Peninsula near the northwestern tip of Vancouver Island. The WCVI region extends south to 47.7° and across the mouth of Juan de Fuca Strait. It is an important region for wind-driven upwelling, and forms the northernmost part of the California Current system.

The NC region substantially overlaps the Pacific North Coast Integrated Management Area (PNCIMA) (Lucas et al., 2007; Irvine and Crawford, 2011), extending to the Alaska/Canada border at the northern edge. The region between Vancouver Island and Haida Gwaii, known as Queen Charlotte Sound, is unique because of its complex bathymetry, with deep troughs along the continental slope and shallow banks that form important habitat for marine ecological communities.

3.1. Model Validation

The model ocean represents a climatology of the historical period (1986–2005) rather than any particular year because it is forced with climatologies of the atmospheric fields (with augmented winds). Therefore, the resulting ocean fields are validated against climatologies estimated from observations over the same period. Generally, the model is in agreement with the observations. The comparisons with the shipboard observations are described in detail and, for brevity, only a summary is given for light-station data, buoy data, and satellite SST analysis, which are further described in the **Supplementary Material**.

For locations near the coast where the bathymetry is not well resolved, we expected large biases. However, comparisons with the light station data indicate an annual average fresh bias in SSS of about 0.5 ± 0.6 and an average warm bias of around $0.3 \pm 0.8^\circ\mathrm{C}$ (Fisheries and Oceans Canada , DFO). The bias for each station and each month are shown in **Supplementary Figure 4**.

The model exhibits a cold bias in SST of less than $1^\circ\mathrm{C}$ during the winter months transitioning to a warm bias of up to $2^\circ\mathrm{C}$ throughout the summer compared to a climatology of NOAA $1/4^\circ$ daily Optimum Interpolation Sea Surface Temperature (OISST) (Banzon et al., 2016). The biases appear to be fairly uniform across the domain, whereas we would expect a more spatially variable pattern if the biases were primarily dynamically driven, e.g., the bias would be larger in regions with strong upwelling-favorable winds, which are a small part of the total area. Comparisons with the ECCC buoy SST and SAT suggest that these biases are largely driven by biases in the CanRCM4 surface air temperature (shown in **Supplementary Figure 5**).

For validation of modeled fields, vertical profiles were compared to shipboard observations at model locations for which there were at least 10 observed vertical profiles within a 5 km radius for each season (winter-DJF, spring-MAM, summer -JJA, fall-SON). To eliminate any overlap, the stations were separated by at least 10 km. The observations were binned to the vertical model levels. For each location and season, model grid points within a 5 km radius were averaged for each z level.

The locations of shipboard observations of ocean temperature and salinity are shown in **Supplementary Figure 2**. Most of the observations are from the West Coast of Vancouver Island. For all seasons, the model is generally biased cold (**Figures 5A–D**), with biases typically less than $1^\circ\mathrm{C}$ in summer, fall and winter and slightly larger biases in spring (annual average bias is $-0.4 \pm 0.6^\circ\mathrm{C}$). There is a relatively small fresh bias for all of the seasons, with an average bias of -0.2 ± 0.2 (**Figures 5E–H**).

The locations of the climatologies for O_2 profiles are primarily focused around WCVI with few in Queen Charlotte Sound. The bias in O_2 is positive for all seasons, with largest values in spring and fall (**Figures 5J–M**). The mean bias over all of the seasons is about $20\,\mathrm{mmol\,m^{-3}}$ with an average standard deviation of $21\,\mathrm{mmol\,m^{-3}}$.

For NO_3, the locations of available observations were in the WCVI region. The mean bias in NO_3 over all of the seasons is about $-3.3\,\mathrm{mmol\,m^{-3}}$ with an average standard deviation of $3.5\,\mathrm{mmol\,m^{-3}}$.

The near-surface salinity bias averaged over all of the stations was significantly reduced by augmenting the climatological

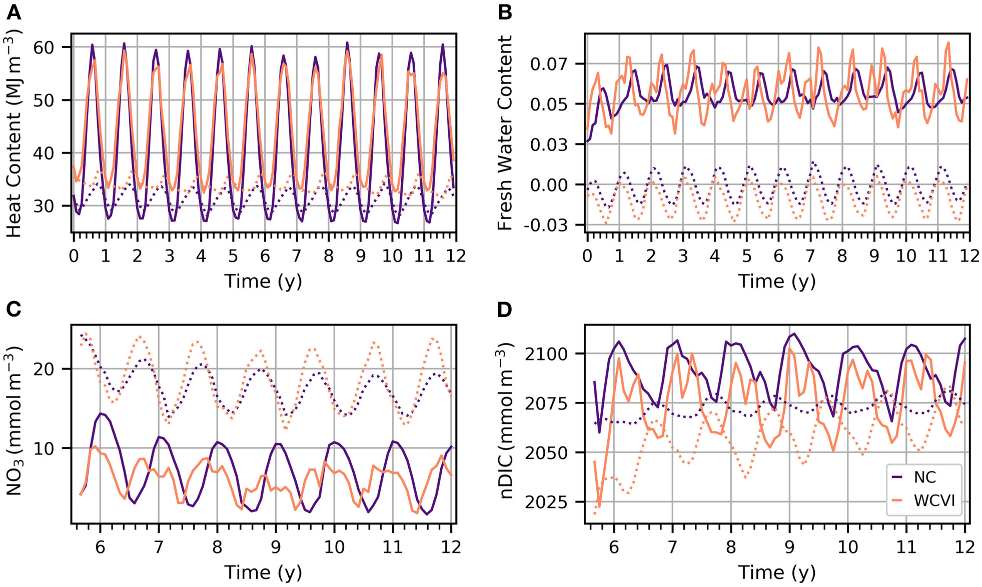

FIGURE 4 | For the historical run, model spinup for the regions shown in **Figure 1** (NC, North Coast; WCVI, west Coast Vancouver Island) for depths < 10 m (solid lines) and > 10 m (dotted lines). **(A)** Ocean heat content, **(B)** freshwater content and volume weighted mean concentrations of **(C)** NO$_3$, and **(D)** mean DIC concentration normalized to a salinity of $S_r = 32.5$.

winds with high frequency variability from the CFSR winds (**Figure 2A**). Because randomly selected years were used for the CFSR wind anomaly, this result indicates that exact knowledge of the high-frequency variability is not required to substantially reduce model bias. It is evident from the sensitivity test that the nonlinear response of ocean surface currents and mixing/stirring to high-frequency wind forcing is important to accurately simulating the freshwater distribution in this region.

3.2. Broad Changes Across the Continental Shelf

Both the NC and WCVI regions are projected to experience substantial changes. To illustrate the annual changes along the Northeastern Pacific continental shelf in the 2055 climate, **Figure 6** shows the volume weighted averages for several model variables. Error bars correspond to the standard deviation across the 3 years averaged (which is due to the variability in the winds).

The regionally averaged SST is projected to increase by 1.8°C for the NC and 2.0°C for WCVI under RCP 4.5 and by 2.4°C for both regions under RCP 8.5 (**Figure 6A**). These increases correspond to a change between 3°C and 4°C per century which is more rapid than the 0.9°C per century increase reported by Cummins and Masson (2014) for BC lightStations over the historical record (60–70 years).

The average SSS decreases by -0.14 in the NC region and by -0.23 in WCVI for RCP 4.5, yet for RCP 8.5, SSS decreases by -0.10 for the NC and -0.08 for WCVI (**Figure 6B**). While the change appears to be greater in RCP 4.5, the difference is smaller than the interannual variability associated with the augmented wind forcing which strongly influences the freshwater distribution. The variability among model years due to augmented wind forcing is considerably larger for SSS than for SST, but still smaller than the change. While the future projections all indicate freshening which is likely due to increases in precipitation, the magnitude of the difference is less well-constrained due to uncertainties in the projected wind speed distributions for 2046–2065.

The only clear change in mixed layer depth (**Figure 6C**) is a projected increase for WCVI under RCP 8.5; year-to-year variability due to the wind anomaly is substantial. The overall stratification of the water column increases. The convective energy (CE), the amount of energy required to mix the column to a given depth (100 m), is projected to strengthen for both regions with a greater increase in the NC compared with WCVI (**Figure 6D**). This increase of about 50 J m^{-3} is relatively small, yet it represents an $\simeq$ 10% increase in stratification. The static stability of the water column is controlled primarily by the salinity in all of the simulations (not shown). The increase in stratification does not appear to inhibit phytoplankton growth, as total chlorophyll and primary productivity increase for both of the regions (**Figures 6E,F**).

The minimum oxygen and average aragonite saturation state (Ω_A) below 100 m decreases for both regions indicative of more corrosive (lower Ω_A) and less oxygenated waters on the continental shelf (**Figures 6G,H**). Error bars confirm that the wind anomaly influences minimum oxygen concentration on the shelf as highly oxygenated near-surface waters are mixed downward, but has little effect on Ω_A.

There is a relatively low amount of hypoxic (< 60 mmol m^{-3}) water in the study regions on the continental shelf, but the volume (weighted by the volume of each grid cell) increases

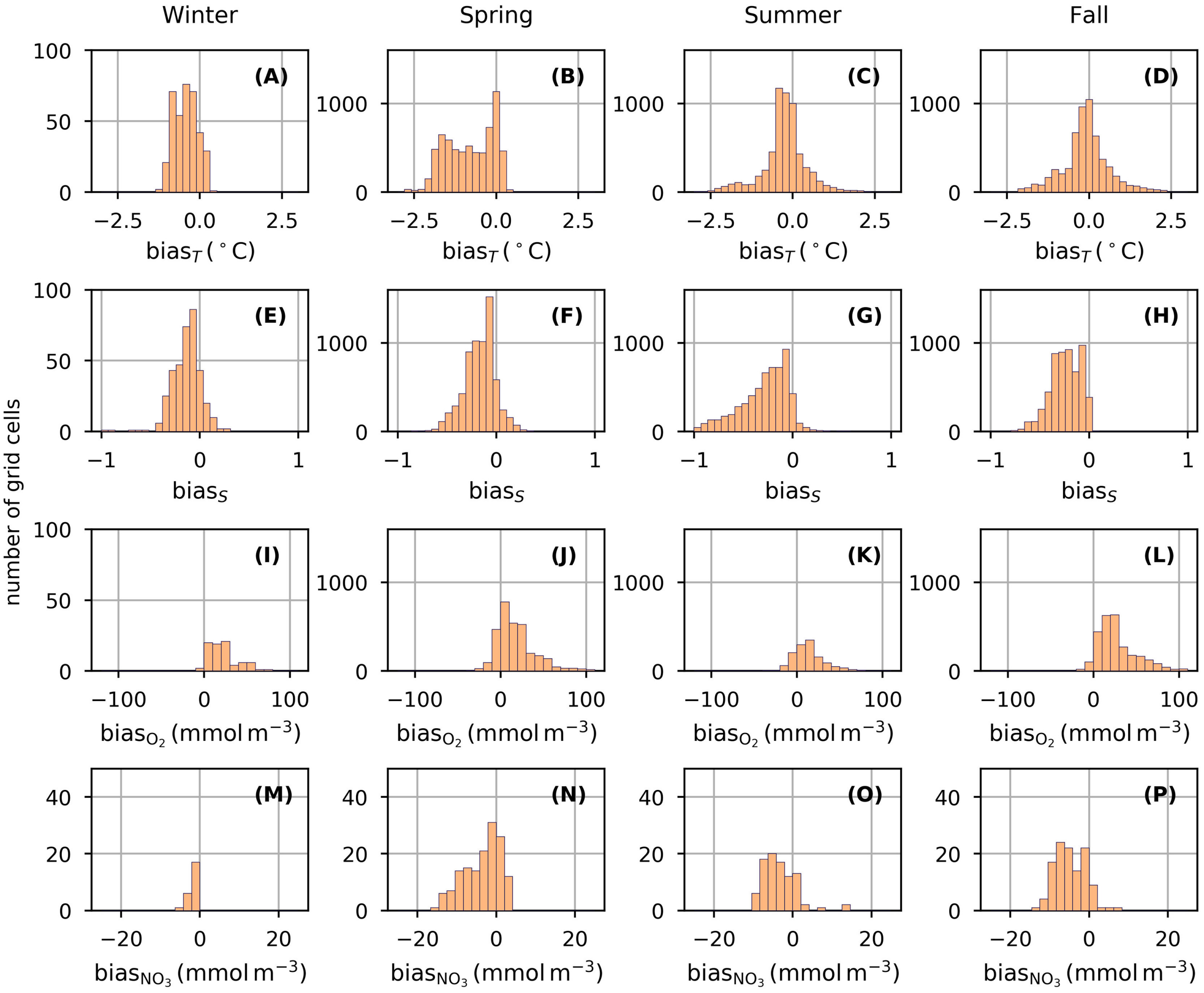

FIGURE 5 | For the historical run, model bias (model-observations) in temperature **(A–D)**, salinity **(E–H)**, oxygen **(I–L)**, and nitrate **(M–P)** concentration calculated from climatologies of shipboard observations (1986–2005) for each of the seasons as indicated at the top of each column. For *T*, *S*, and O_2 the y-axis limits differ for the winter column as there are fewer observations. Relatively few observations of DIC are available so these data were validated using the empirical relationships derived by D. Ianson using the methods and data from Lara-Espinosa (2012) (D. Ianson (Fisheries and Oceans Canada) private communication, 2019) and shown in the **Supplementary Material**.

from around 5 km^3 in the historical simulation to around 50 km^3 by the 2050s (**Supplementary Figure 6**). The volume of undersaturated waters is much higher ($\simeq$ 1,000 km^3). Throughout the year, the largest volume of corrosive water is in the NC region, while the largest volume of low-oxygen water is in the WCVI region. The oxygen minimum zone is deeper in the northern part of the domain (discussed in section 3.3) so less of the low-oxygen water flows onto the shelf. Since the saturation horizon is higher in the water column than the oxygen minimum zone, corrosive water flows into the deep submarine canyons of the NC more than in the WCVI region (see **Supplementary Figure 1**).

During summer upwelling, the aragonite saturation state of shelf waters is generally lower than the other seasons (**Supplementary Figure 6**). Maps of the minimum summer Ω_A illustrate that while minimum Ω_A does not change very much in the open ocean, the shelf regions are becoming undersaturated ($\Omega_A < 1$) (**Figure 7**) even for the moderate mitigation scenario RCP 4.5. Hotspots of change include the near shore regions of WCVI and the banks of the NC (**Figure 7C**). For RCP 8.5, the magnitude of the change is greater, but the locations of greatest change remain similar to RCP 4.5. While the maps illustrate changes east of Vancouver Island (the Salish Sea), we have neglected this region because even 2−3 km resolution is not adequate there (cf. Peña et al., 2016; Soontiens and Allen, 2017).

The key factors influencing phytoplankton growth and primary productivity are light, temperature, availability of nutrients (in this region principally N), and stratification

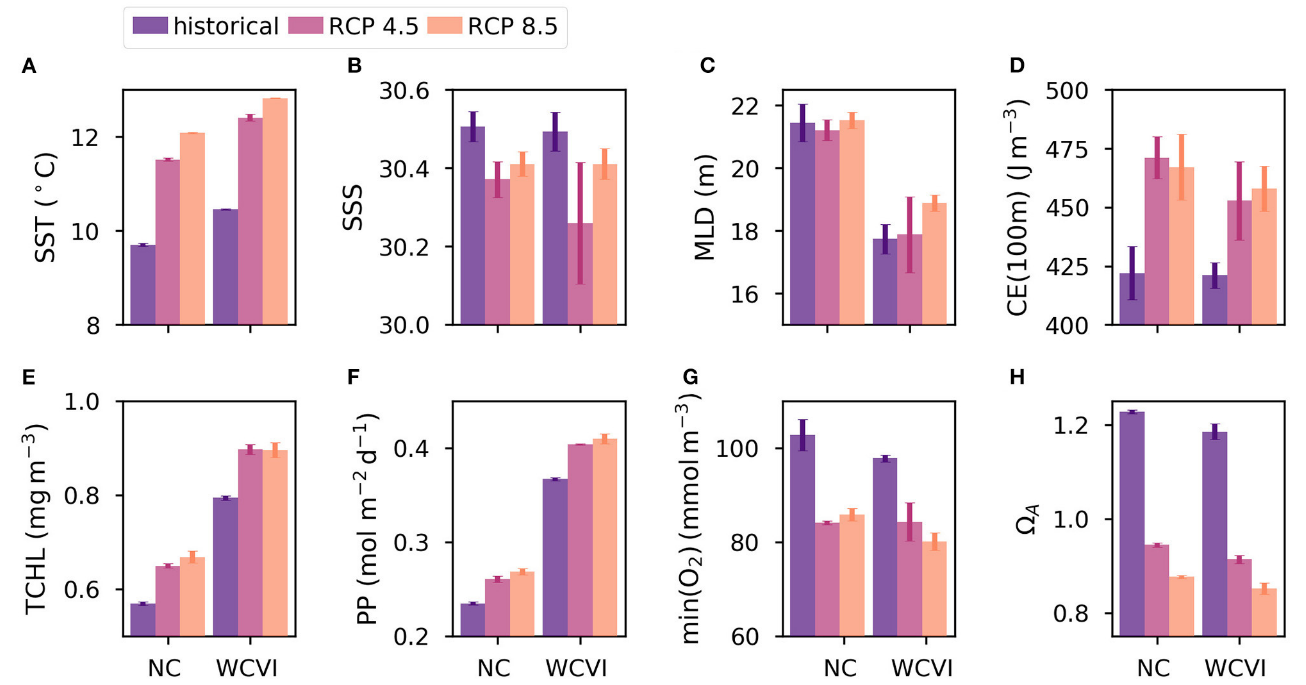

FIGURE 6 | Annual average **(A)** sea surface temperature, **(B)** sea surface salinity, **(C)** mixed layer depth, **(D)** convective energy, **(E)** total chlorophyll, **(F)** primary productivity, and volume weighted averages over the bottom 100 m for **(G)** minimum oxygen, and **(H)** aragonite saturation state for historical (1986-2005) and future (2045-2065) simulations. Error bars represent the year-to-year variability due to the wind stress anomaly.

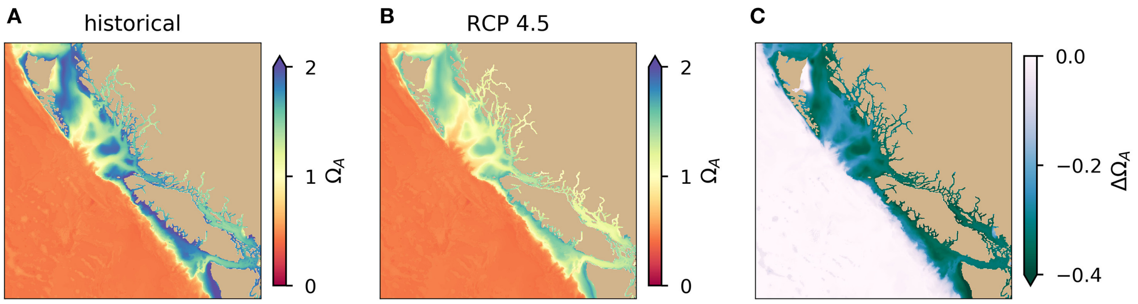

FIGURE 7 | Maps of the minimum aragonite saturation state in summer for the **(A)** historical period, **(B)** future (RCP 4.5), and the **(C)** difference between the two. Here the 5-day averages were used to compute Ω_A and the minimum was taken over all depths.

of the water column. There is a notable increase in Total Chlorophyll (TCHL) in the top 10 m across the continental shelf. For example, **Figures 8A,B** shows the volume averaged change in TCHL for RCP 4.5. Surface chlorophyll is strongly affected by wind variability (shaded regions showing standard deviation due to the wind anomaly) especially during the spring over WCVI. Fewer nutrients reach the euphotic zone in the future scenarios, but subsurface nitrate is projected to increase during the upwelling season (**Figures 8C,D**) which may be a consequence of stronger upwelling winds. The non-dimensional nitrogen limitation term (N_{lim}) is based on the cell N quota; it ranges between 0 and 1 with larger values corresponding to increased growth rates (Hayashida et al., 2019). Although the stratification is increasing, nitrogen limitation does not appear to be a major factor limiting productivity along the continental shelf in the 2050s (**Figures 6F,G**). Since nutrient concentrations are generally sufficient to support phytoplankton growth, increases in productivity across the continental shelf could be due to temperature dependent metabolic rate, changes in the mixed layer depth, or changes in circulation. More work is needed to understand these mechanisms.

3.3. Changes Along the Continental Slope

Figure 9 shows a vertical cross-section across WCVI (the green line in **Figure 1**). Each column corresponds to a different

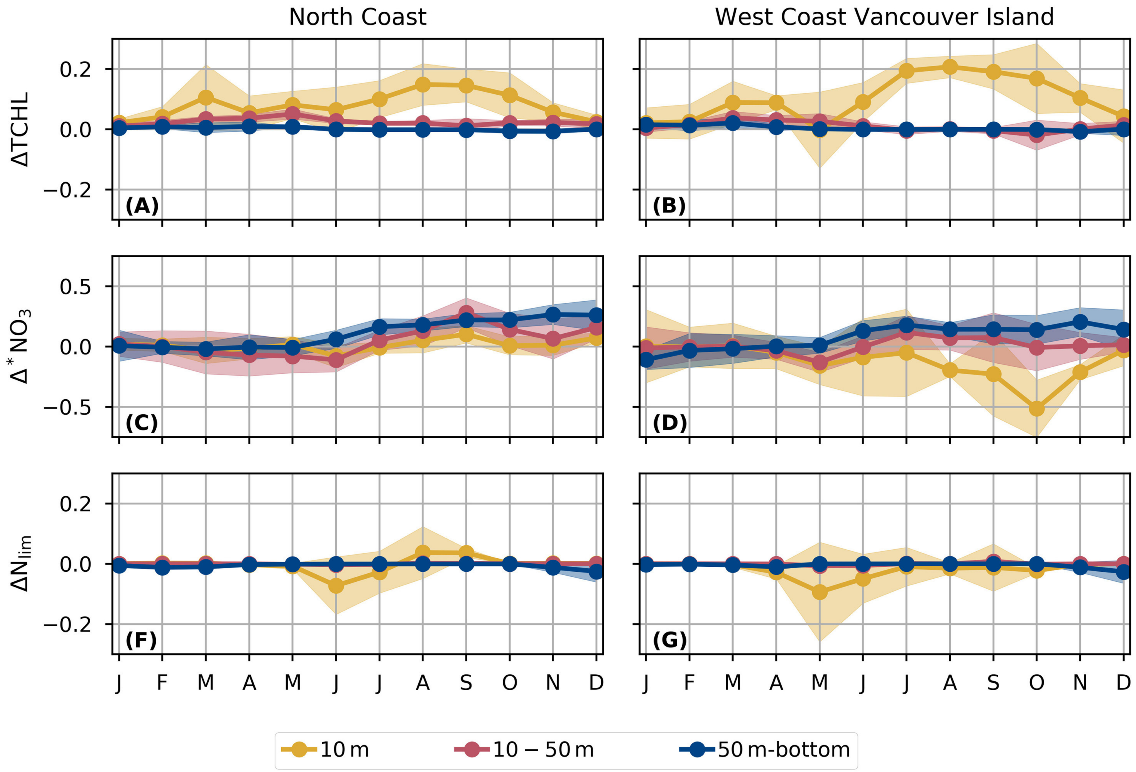

FIGURE 8 | Regionally averaged changes between 1986 – 2005 and 2046 – 2065 (RCP 4.5) for **(A)**, **(B)** total chlorophyll **(C)**, **(D)** nitrate concentration (normalized by the range of values in the historical period) and **(F)**, **(G)** nitrogen limitation of phytoplankton based on cell nitrogen quotas. Shaded regions correspond to the standard deviation among the years averaged due to wind variability as in **Figure 6**. Nitrogen limitation is a non-dimensional index ranging from 0 (cell quota at its minimum) to 1 (cell quota at its maximum).

simulation. Qualitatively, impacts are similar for both scenarios from the continental shelf to the shore; isopycnal surfaces are deepening, while corrosive, deoxygenated water is rising. For RCP 8.5 the effect is more pronounced with corrosive waters moving to shallower depths in the water column (**Figure 9** row 2 and 3). While the oxygen content is declining for the bottom waters across the continental shelf, maps of the spatial extent indicate that hypoxic waters remain largely confined to the continental slope (not shown).

To estimate the projected changes along the continental margin, we first located the 300 m isobath for both focus regions, then moved approximately 100 km along the model grid toward the open ocean (purple markers in **Figure 10A**). Seasonally averaged fields were extracted along this vertical cross-section and interpolated to a uniform 1 m vertical grid.

Isopycnal surfaces (binned at a resolution of $0.1\sigma_\theta$) are projected to deepen with increased temperature and salinity at a given density (e.g., **Figure 10B**). In summer, isopycnals are located deeper in the water column by as much as 100 m depending on the isopycnal (**Figure 10C**). For all of the seasons, the most pronounced changes in isopycnal depth are from $26\sigma_\theta$ to $27\sigma_\theta$ (i.e., below the pycnocline), where the vertical density gradient is small. Nearer to the surface, there are seasonal differences in the *T-S* plots. In summer and fall warming isopycnals deepen by between 15 and 25 m, while increased precipitation in winter and spring results in near-surface isopycnals that are warmer and fresher with deepening by 15–60 m (not shown).

A likely mechanism driving the apparent downward "shift" of isopycnal surfaces is warming and freshening from the surface downward, which decreases the density at a specific depth horizon causing a downward relocation of the isopycnal. That this mechanism is responsible for the relocation is evident from, for example, the average temperature and salinity profiles for summer (**Figure 11**). Anthropogenic warming produces a warmer atmosphere with higher levels of precipitation in the 2050s. The warming signal propagates downward through the water column, with warming up to 2°C near the surface tapering off to 1°C at 500 m depth (**Figure 11A**) increasing the stratification. Substantial freshening due to increases in precipitation reduces the density at the surface, and the salinity anomaly is mixed down into the upper water column (**Figure 11B**). In effect, both future scenarios have lighter density waters near the surface than the historical simulation which results in the "movement" of denser isopycnals to greater depth (**Figure 11C**). This result is consistent with observations of

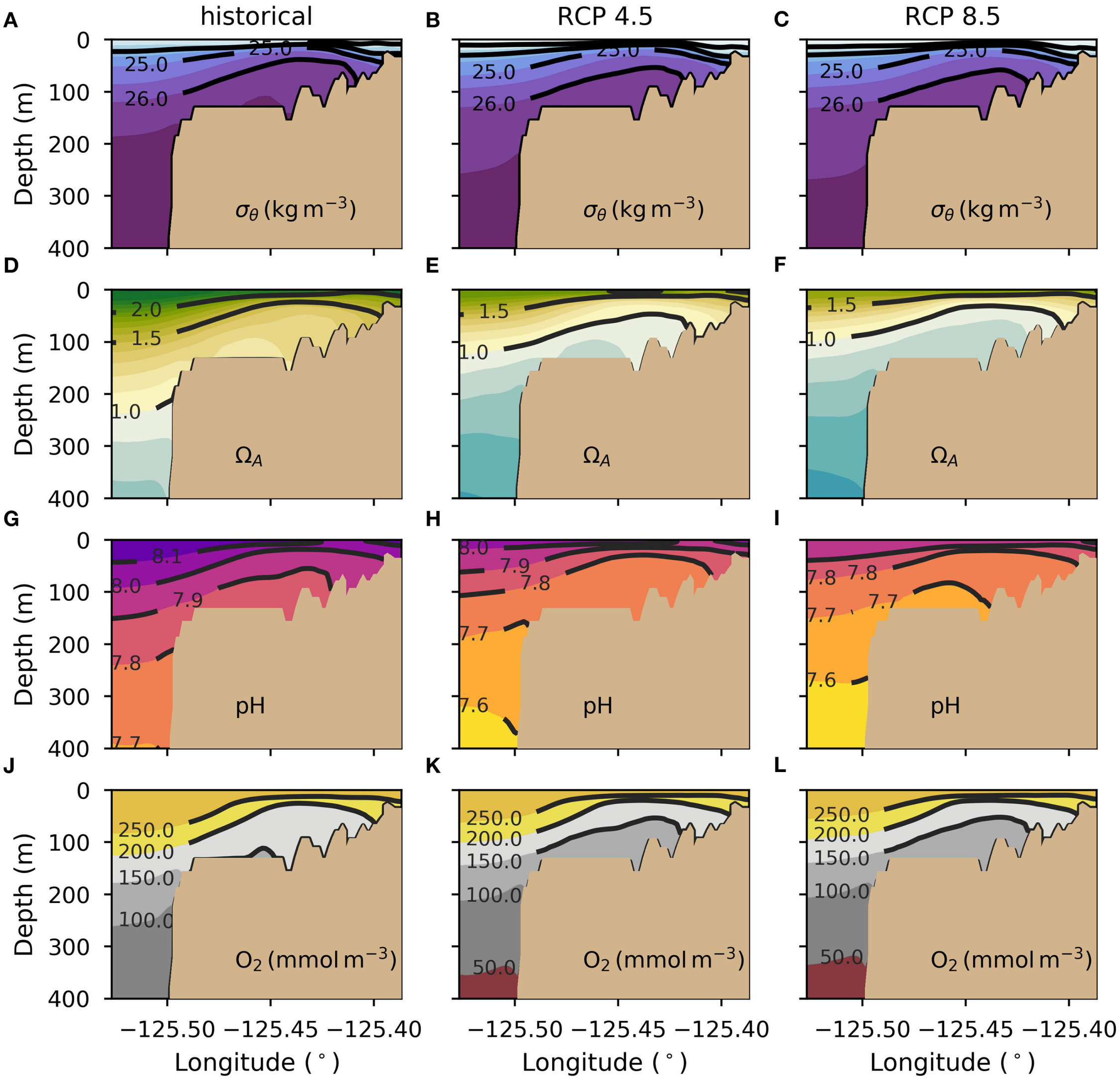

FIGURE 9 | Vertical cross-sections taken across WCVI (green line in **Figure 1B**) of the summer climatology for **(A–C)** potential density (color contours every 0.5σ_θ), **(D–F)** aragonite saturation state (color contours separated by 0.1), **(G–I)** pH and **(J–L)** dissolved oxygen. Each column corresponds to the simulation indicated on the top panel (historical, RCP 4.5 and RCP 8.5).

T, *S*, and *P* from the 1970s to 1990s which show a downward displacement of density surfaces at latitudes between 45° and 50° (Helm et al., 2011).

The change in oxygen near the surface can be attributed mainly to changes in solubility (controlled primarily by temperature), while changes along deeper isopycnals are primarily due to changes in remineralization and circulation. The apparent oxygen utilization was calculated by subtracting the actual concentration from the saturation value of oxygen (i.e., $\text{AOU} = [\text{O}_2]_{\text{sat}} - [\text{O}_2]$). Assuming the non-solubility fraction is entirely due to remineralization ($\text{remin} = -\text{AOU}$), the remineralization component for DIC and NO_3 were also estimated (Sarmiento and Gruber, 2006). For example, **Figure 12** shows the change along isopycnal surfaces for summer climatologies near the continental slope (locations shown in **Figure 10A**). The change due to solubility is relatively small for the near-surface isopycnals ($\sigma_\theta < 25$), but this figure excludes isopycnals that are not present in the historical climate because of substantial decreases in surface density (i.e., **Figure 11C**). If, instead, the solubility fraction is calculated based on depth levels (e.g., inset panel of **Figure 12**), it accounts for about 84% (94%) of the total in the upper 100 m and 21% (28%) over all depths for RCP 4.5 (RCP 8.5). These values are larger than the observed oxygen decline due to solubility since the 1960s of $\simeq$ 15% for the global ocean (Helm et al., 2011; Schmidtko et al., 2017).

The largest declines in oxygen occur for isopycnals between 26 σ_θ and 27σ_θ because that is where the most substantial relocation occurs. For example, in summer under RCP 4.5, the

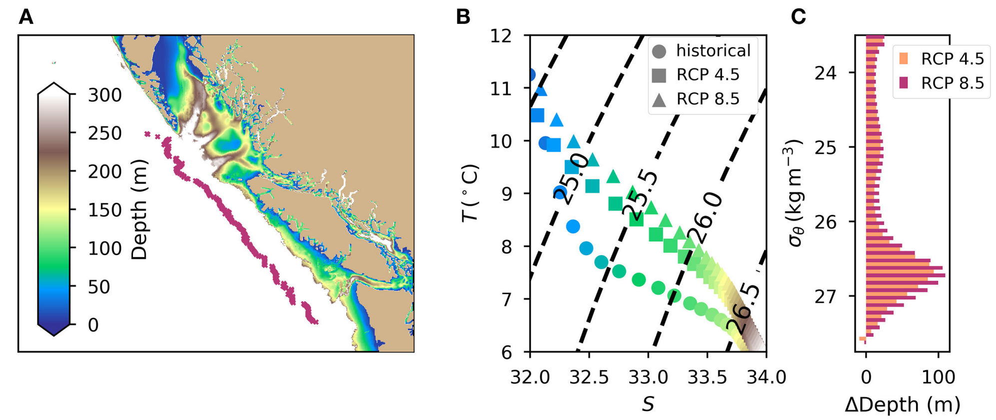

FIGURE 10 | Changes in the depths of isopycnal surfaces for a series of locations (100 km seaward of the 300 m isobath. **(A)** Locations of vertical profiles and bathymetry for depth < 300 m. **(B)** *T*-*S* plots for present and future with depth of isopycnal indicated by color (same colorbar as **A**), and **(C)** change in the depth of isopycnals between present and future simulations. All results are summer climatologies, averaged over all of the locations shown in **(A)**.

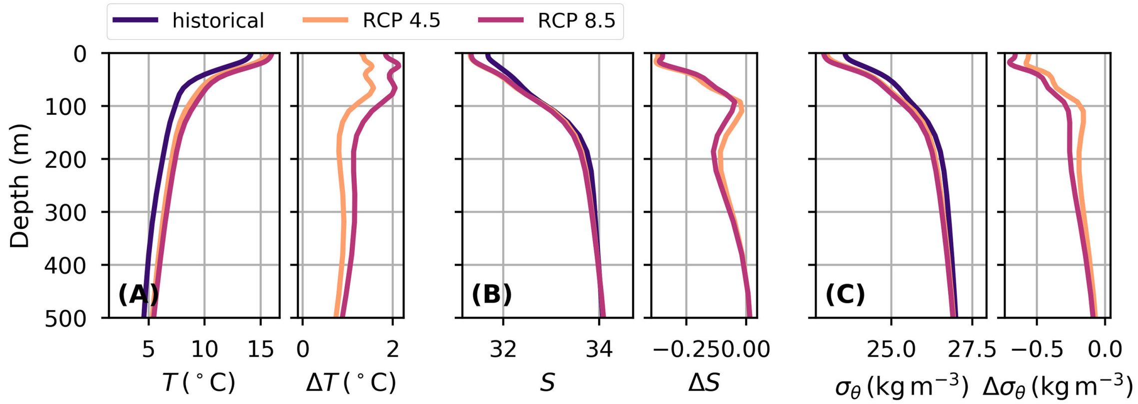

FIGURE 11 | Using the same summer-averaged vertical profiles that were used in **Figure 10** the average profiles are shown for each simulation with differences (future-historical) on the right panel for **(A)** temperature, **(B)** salinity, and **(C)** density.

greatest changes in concentration occur for $\sigma_\theta = 26.5$ with $\Delta O_2 = -54\,\mathrm{mmol\,m^{-3}}$ and correspond to a depth change of $\simeq 70$ m. Comparing this to the vertical gradient of O_2 in the historical climate, we find that if $\sigma_\theta = 26.5$ were to be displaced downward by the same distance then $\Delta O_2 \simeq -55\,\mathrm{mmol\,m^{-3}}$. This simple example demonstrates that the magnitude of the change in concentration on specific isopycnals experience is broadly consistent with the downward displacement of the isopycnal surfaces.

Crawford and Peña (2013) examined the decline off of WCVI for $\sigma_\theta = 26.6$ from 1981 to 2011. While direct comparisons with their observations are not possible because of differences in sampling and model bias, examining the same isopycnal provides insight into the change in O_2 for the region. On average, the $\sigma_\theta = 26.6$ isopycnal sits at a depth between 186 m and 296 m in the historical simulation with an average oxygen concentration of $122\,\mathrm{mmol\,m^{-3}}$. The change of about $-0.9\,\mathrm{mmol\,m^{-3}\,y^{-1}}$ ($-1.0\,\mathrm{mmol\,m^{-3}\,y^{-1}}$) for RCP 4.5 (RCP 8.5) (estimated from the two time-slices) is broadly consistent with the declines (Crawford and Peña, 2013) estimated over the historical period.

The downward penetration of atmospheric CO_2 into the water column is responsible for most of the change in the DIC. The change due to remineralization, estimated from AOU ($\mathrm{DIC_{rem}}$), is small relative to the total projected change especially near the surface (**Figure 12B**). $\mathrm{DIC_{rem}}$ only approaches half of the total change at the isopycnals where O_2 change is greatest (**Figure 12**). The change in DIC due to anthropogenic CO_2 is likely to be primarily local, because it declines approximately monotonically from the surface down, because it is consistent across the region (not shown), and because vertical penetration will be generally slower in oceanic waters, making an explanation based on subsurface advection of such waters unlikely. The remineralization fraction may be partly local and partly advective (given the horizontal gradients in concentration, it would take only a fairly small change in mean circulation to explain the changes in concentration, and the stoichiometry of O_2 loss / DIC

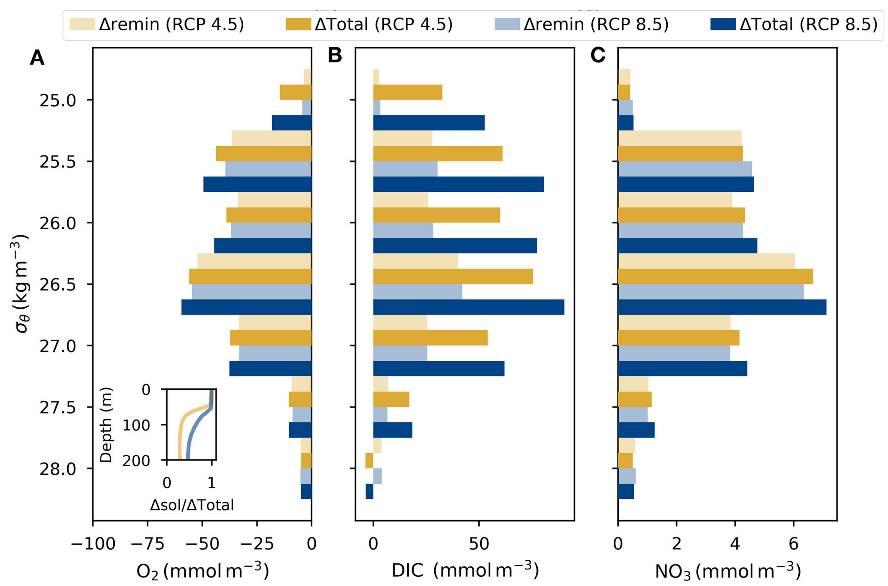

FIGURE 12 | For isopycnals (binned at a resolution of 0.5σ_θ), the **(A)** total change in [O_2] and the change that is not attributable to solubility (remin = −AOU). The inset panel shows the fraction of the change in [O_2] that is due to solubility for each depth. Total change and estimated changes due to remineralization for **(B)** DIC and **(C)** nitrate. The remineralization fraction was calculated from AOU assuming 1O_2 : 1C :(16/106)N. All results are based on summer climatologies averaged over all of the locations shown in **Figure 10A**.

and NO_3 gain would be similar). However, a primarily advective mechanism is unlikely because of the small change in salinity at the levels where the greatest change occurs (**Figures 10**, **11**), and because, as noted above, the change in O_2 on e.g., 26.5 is consistent with the downward displacement of the isopycnal by surface warming and freshening. To the extent that the change in salinity is not monotonic with depth, the deviation occurs at much shallower depths (**Figure 11**) and is most plausibly explained by shoreward advection of more oceanic water due to slightly stronger upwelling-favorable winds.

For nitrate, most of the change is associated with remineralization (**Figure 12C**). The increase in remineralization is attributed primarily to the relocation of the isopycnal surfaces, as DIC and nitrate both increase monotonically with depth.

Corrosive (undersaturated) waters are projected to encroach substantially on the continental shelf. The average aragonite saturation state decreases by 0.2 (0.3) in RCP 4.5 (RCP 8.5) (**Figure 14A**) becoming consistently undersaturated throughout the year.

The oxygen minimum zone is projected to rise up in the water column by about 75 m. For example, **Figure 13** shows the change in the depth of the 60 mmol m^{-3} isopleth (locations in **Figure 10A**) under RCP 4.5. The dashed line marks Brooks Peninsula which separates the WCVI and NC regions as discussed above. The depths vary seasonally, particularly for the NC region; deeper during winter downwelling and shallower during summer upwelling. The isopleth shoals more in the south than in the north. Qualitatively similar results were found along the 300 m isobath (parallel to those shown in **Figure 10A**), but there was much more variability along the transect (not shown). Shaded regions indicate the variability associated with the wind anomaly was ±27 m.

The annual change in potential temperature for a transect along the 300 m isobath is 0.9°C (1.8°C) in RCP 4.5 (RCP 8.5) which represents an average change of about 1.5° C (2° C) per century. The depth of the saturation horizon along that transect shoals by about 100 m across all seasons (**Figure 14B**) while exhibiting the same seasonal cycle of a shallower (deeper) horizon during the upwelling (downwelling) seasons. The encroachment projected over the next 50 years is substantially larger than the change observed since the preindustrial period of 30–50 m (Feely et al., 2016).

In summer in the future simulation, corrosive waters reach into the top 100 m of the water column along the continental slope. Stronger summer upwelling is not the primary driver of the change in acidification as isopycnal surfaces are deeper in the future relative to the historical period. Instead the change is driven primarily by downward mixing of anthropogenic DIC.

3.4. Extreme States

Because extreme states are known to have important biological impacts that can be overlooked by looking only at mean states, we recorded the maximum and minimum values within the 5 day averaging period. A series of vertical profiles are extracted along the 300 m isobath of the continental slope (parallel to the locations in **Figure 10**) to examine how extreme states are changing. For each grid cell, the minimum (maximum) value for each season is used in the histogram. Broadly, extreme states of corrosive and deoxygenated water are becoming more frequent and more extreme, and extremely cold temperatures

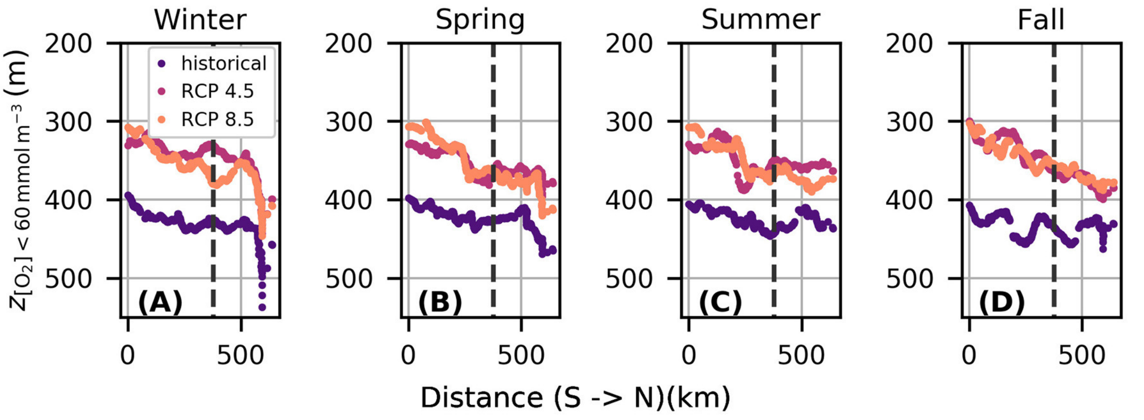

FIGURE 13 | Depth of the $[O_2] = 60\,mmol\,m^{-3}$ isopleth for historical and future simulations in **(A)** winter, **(B)** spring, **(C)** summer, and **(D)** fall for a series of vertical profiles along the 300 m isobath of the continental shelf (parallel to the locations in **Figure 10**).

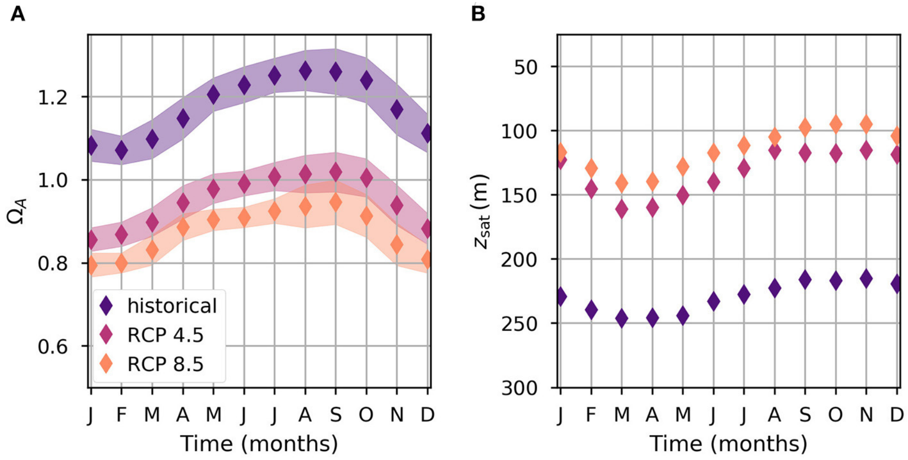

FIGURE 14 | For a series of vertical profiles along the 300 m isobath of the continental shelf (parallel to the locations in **Figure 10**), the average **(A)** aragonite saturation state and **(B)** saturation horizon for each month.

are becoming rare (**Figure 15**). The peak of the pH histogram is shifting to more acidic conditions, with a noticeably greater effect in RCP 8.5 than RCP 4.5. For oxygen, **Figure 15B** is truncated to emphasize hypoxic states, but the mode for the historical simulation is around 290 $mmol\,m^{-3}$, which declines by 13 − 20 $mmol\,m^{-3}$ in the future scenarios. Roughly 6% of the $[O_2]$ data are below the canonical hypoxic threshold of 60 $mmol\,m^{-3}$, whereas in RCP 4.5 (RCP 8.5) more than 11% (12%) are below this threshold (**Figure 15B**). The modal minimum temperature in the historical simulation is 7 °C increasing by between 1.9 °C and 2.4 °C by the 2050s. In the historical simulation around half of the temperatures are below 7 °C, but this declines to less than 23% (21%) in RCP 8.5 (RCP 4.5) (**Figure 15C**).

States of extremely warm temperatures are increasing in magnitude and frequency (**Figure 15D**). The maximum temperature in the historical climate was 17.8°C increasing to 18.9°C (19.9°C) by the 2050s in RCP 4.5 (RCP 8.5). At that time, about 4% (15%) of maximum temperatures will be above the historical extreme maximum temperature of 17.8°C.

4. DISCUSSION

Warming and freshening at the ocean surface will propagate throughout the water column on the continental shelf as these waters are mixed vertically by winter storms and tidal currents. Increased carbon dioxide absorbed from the atmosphere is also mixed throughout the water column, moving the $CaCO_3$ saturation horizon upward and onto the continental shelf. pH declines substantially, with corrosive bottom waters present in both study regions. Beyond the continental shelf, there is gradual downward penetration of excess heat and DIC that results in shoaling of the isopleths of oxygen concentration and $CaCO_3$ saturation state (e.g., **Figure 9**). Shoaling of corrosive and oxygen poor waters gives rise to new potential impacts, as these waters

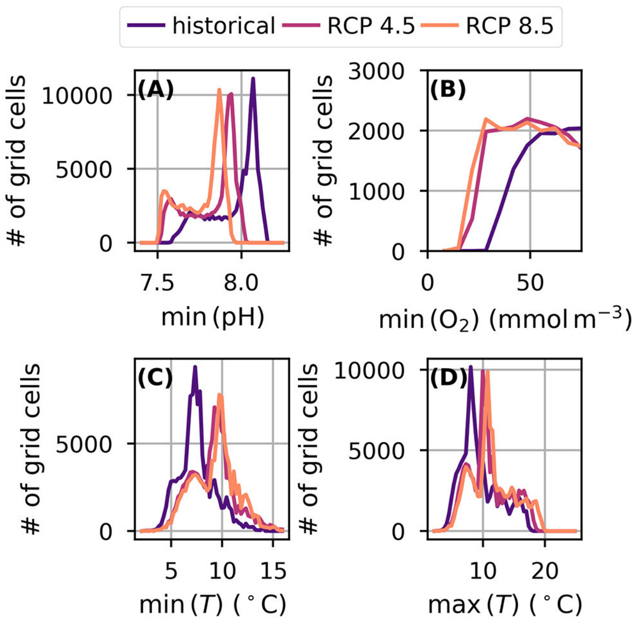

FIGURE 15 | Annual minimum **(A)** pH, **(B)** oxygen concentration, and **(C)** temperature and **(D)** annual maximum temperature for vertical profiles along the 300 m isobath parallel to those shown in **Figure 10A**. For oxygen, the x-axis has been truncated to emphasize the increase in frequency of concentrations below 60 mmol m^{-3}.

can affect the biota of the continental shelf, especially during upwelling events and storms.

Our experiments help to elucidate a dominant mechanism by which changes in thermocline biogeochemistry along the continental slope occur. There is no evidence of enhanced "uplift" of isopycnal surfaces due to changes in wind stress. Rather, the isopycnal surfaces are relocated to greater depths as warm and fresh surface inputs are mixed downward, reducing the density at each depth stratum. This mechanism is thermodynamic rather than dynamic and changes the biogeochemistry associated with each isopycnal.

This study provides an overview of the projected climate impacts for the continental shelf focusing on general impacts for a large geographical area that has complex bathymetric features (**Supplementary Figure 1**) and circulation. Projected changes in advection, upwelling, and downwelling have variable impacts across the continental slope so the analysis presented here does not preclude changes in the circulation for the region. Further study of the localized impacts using higher resolution coastal models is warranted.

By examining the change in oxygen concentration and its deviation from that expected from saturation concentration alone, we can estimate the remineralization contribution to changes in nitrate and DIC. Remineralization dominates changes in nitrate concentration on specific isopycnal surfaces, mainly because the concentration increases with depth and there is a relocation of isopycnal surfaces. Changes in DIC are dominated by the downward penetration of anthropogenic CO_2. As previously noted by Feely et al. (2008), whatever other changes in circulation or remineralization occur that affect e.g., the $CaCO_3$ saturation state, will be exacerbated by the contribution of anthropogenic CO_2.

An important limitation of this study is that runoff data for the future climate simulations were not available. Changes in surface freshwater flux are therefore solely due to evaporation and precipitation. This bias is likely to be small along the WCVI during the summer upwelling season, as runoff is mostly precipitation driven and is low in summer. It is potentially larger in the NC where runoff from melting snowpack plays a larger role. If summer runoff declines substantially, it could make the water column more unstable and lead to entrainment of deeper oxygen poor or low pH into the surface layer in some regions. In our experiments, the change is toward slightly greater stratification (**Figure 6**), but this is a broad regional average. Less springtime runoff along the WCVI region could result in a less stable water column as the near-surface salinity is lowest during spring (**Figure 4**).

Because of the augmented winds, this study provides evidence that the high-frequency variability in the wind stress is essential to realistically distributing the freshwater sources throughout the model domain (e.g., **Figure 2**). Variations in the annual pattern of high frequency wind stress, such as gale force winds and storms, modify mixed layer depths, and the near surface stratification (e.g., **Figure 6**) and affect the amount of nutrients reaching the surface (e.g., **Figure 8**). The variability of the winds also influences the depth of the oxygen minimum zone along the continental shelf through its influence on the ocean circulation (e.g., **Figure 13**), but has little effect on ocean acidification despite its influence on gas exchange (e.g., **Figure 14**).

On the whole, total chlorophyll and primary productivity increase (**Figures 6**, **8**), and this is universally the case over a larger set of smaller averaging regions (not shown). But we caution that the biological model was developed for the global domain and was applied to these simulations with no parameter tuning. The main influence on phytoplankton production is increased temperature, as the region is relatively replete with nutrients and has shallow mixed layers. Again, we generally expect stratification to increase, although the opposite may occur locally in some runoff-dominated regions. There is a slight increase in N stress in some seasons (**Figure 8**). In general, we do not expect any decline in productivity over the time scale considered here, although we can not rule out changes in species composition. Any increase in N limitation is of concern in a region dominated by diatoms adapted to nutrient-rich environments.

This study has shown that future climate under either scenario exhibits more frequent and more extreme states of warm temperature, hypoxia and acidification. While changes in each of these stressors individually have important consequences for ecosystem health, simultaneous shifts in these three stressors can result in synergistic effects that greatly exceed the effect of each in isolation (Gruber, 2011). Together they threaten marine biodiversity and ecosystem health by inhibiting growth, respiration, reproduction, and immune response as well as causing epigenetic changes in organisms (Haigh et al., 2015; Breitburg et al., 2018). More work is needed to understand the durations, magnitudes, and locations of extreme events and their impacts on ecosystems.

Our results are constrained between the bounds of the two scenarios examined. While RCP 8.5 is the scenario with the least mitigation, RCP 4.5 provides a more conservative estimate of the extent of changes to marine ecosystems that will occur by the 2050s. RCP 2.6 has even lower emissions than RCP4.5, but it is unlikely to be achieved given the amount of CO_2 that has already accumulated in the atmosphere (Arora et al., 2011). A newer set of scenarios, and simulations conducted with them, are now available via CMIP6, but are unlikely to substantially alter the results shown.

This study has explored scenario uncertainty by looking at RCP 4.5 and RCP 8.5. After scenario uncertainty, model uncertainty is the next largest source of error (Frölicher et al., 2016). To minimize this uncertainty, a range of climate models (in addition to CanESM/CanRCM) should be explored; we are presenting initial results from a single-model downscaling study because the cost of ensembles is presently prohibitive. The third source of uncertainty is natural variability (Deser et al., 2012; Cheung et al., 2016); because our experimental design uses climatological forcing for each time period, the differences are almost entirely due to anthropogenic forcing with little effect of natural variability. However, we caution that our experimental design does not permit us to address the effects that physical processes underlying natural climate variability in this region may have on future changes in ocean state.

The method for downscaling atmospheric climatologies presented here introduced high frequency variability to the climatological winds. Consequently, a relatively small amount of interannual variability was also introduced to the model solution through the wind fields. Examining the standard deviation among these years is a useful hueristic for exploring the role of the high frequency wind variability in the setting the physical and biogeochemical oceanographic properties for the North-Eastern Pacific continental margin. To analyze the projected changes for the region we averaged the last 3 years of the model solution. The historical simulation represents the climate from (1986 to 2005) with an acceptable bias (**Figure 5**). All of the model solutions converge toward a repeating annual cycle after several years of spinup (**Figure 4**). Therefore, the difference between the historical and future climates is much larger than the interannual variability introduced through the high frequency wind speed variability.

Forcing the model with climatological means (time-slice approach) instead of running the model continuously through the historical and future period reduces computational expense, but it also limits the breadth of climate information that can be provided. Estimates of "the rate of change" for modeled variables presented in this paper are broad estimates using only two points in time.

5. CONCLUSIONS

This paper has examined climate change projections along the continental shelf of the Canadian Pacific Coast by dynamically downscaling using the North-Eastern Pacific Canadian Ocean Ecosystem Model (NEP36-CanOE). To circumvent computational constraints, a new approach was introduced that downscales using atmospheric climatologies (with augmented winds) to project ocean circulation and biogeochemistry under moderate mitigation (RCP 4.5) and high emissions (RCP 8.5) scenarios.

Comparisons with available observations showed that the time-slice approach was able to reproduce the observed climate state for the historical period. The model exhibited a cold bias that was typically less than 1°C (annual average bias is $-0.4 \pm 0.6°C$) and a freshwater bias of -0.2 ± 0.2 when compared to shipboard observations. Including high-frequency wind forcing reduces the salinity bias substantially and does not require specific knowledge of how this component may change.

Over the 60 year period between the historical and future climates, surface ocean temperatures will increase across the NC and WCVI by between 1.8°C and 2.4°C depending on whether a moderate or high emissions scenario is used. The projected surface freshening is between -0.08 and -0.23, however future changes in fresh water content will be strongly affected by changes in wind stress. Changes in wind stress have a substantial influence on freshwater distribution, and wind speeds may change in the future in ways not fully captured by the RCM.

Stratification, primary production and total chlorophyll are increasing along the continental margin and across the continental shelf. There is some evidence of increased nutrient limitation in summer and changes in species composition are possible (e.g., a shift from diatoms to dinoflagellates, including harmful algal bloom species), but our results suggest that changes in overall productivity will be small over this time scale.

Low $CaCO_3$ saturation state (corrosive) and low oxygen waters are projected to rise up the continental shelf. In the 2055 climate, the saturation horizon and oxygen minimum zone are projected to rise by $\simeq$ 100m and $\simeq$ 75m, respectively, relative to the historical simulation. With corrosive and hypoxic waters nearer to the surface, episodes of extremely acidic and deoxygenated water become more likely along shorelines and in regions important to fisheries and aquaculture and other marine life.

By examining the maximum and minimum values within the 5 day averaging period, we showed that extreme states of hypoxic, corrosive and warm water are projected to become more frequent and more extreme. In addition, extremely cold temperatures are becoming rare.

The increase in temperature and acidity projected by the 2050s for both scenarios is substantially greater than the change observed over the historical record (Cummins and Masson, 2014; Feely et al., 2016) because increasing GHGs in the atmosphere are accelerating the rate of change. Over this time-scale, there is little difference in ocean acidification or deoxygenation between the moderate mitigation scenario (RCP 4.5) and the high emissions scenario (RCP 8.5).

DATA AVAILABILITY STATEMENT

The data associated with this work is publicly accessible using the following link: Northeastern Pacific Canadian Ocean Ecosystem Model (NEP36-CanOE) Climate Projections – https://open.canada.ca/data/en/dataset/a203a06d-9c1f-4bb1-a908-fc52912ff658.

AUTHOR CONTRIBUTIONS

AH adapted the biogeochemical model for use in NEMO 3.6, developed the forcing fields including the downscaling methodology (augmented winds), conducted the climate simulations, validated the model, developed analysis methodology and completed analysis, interpreted results, and wrote the manuscript. LZ developed and tuned the physical model, assisted with debugging for the BGC model, contributed to the final version of the manuscript. YL led the development of the physical model, contributed to the final version of the manuscript (particularly with refining the write up for the methodology). JC principle investigator for the project, had the initial idea for the project and supervised the work, advised on the development of methodology, contributed to the interpretation of the results, and edited the manuscript. All authors contributed to the article and approved the submitted version.

FUNDING

This work was supported by the Fisheries and Oceans Canada's (DFO) Aquatic Climate Change Adaptation Services Program (ACCASP).

ACKNOWLEDGMENTS

We are grateful to all of the DFO and ECCC staff who have collected at-sea observations, and other observational data sets such as the weather buoys and lighthouse stations, over many years, and to those responsible for the CanRCM model output. We also thank the originators of all of the public-domain data products used, including GLODAP, WOA, OISST, and CFSR. Thanks to Adam H. Monahan, for useful discussions about the augmented wind forcing.

SUPPLEMENTARY MATERIAL

The Supplementary Material for this article can be found online at: https://www.frontiersin.org/articles/10.3389/fmars.2021.602991/full#supplementary-material

REFERENCES

Arguez, A., and Vose, R. S. (2011). The definition of the standard [WMO] climate normal: the key to deriving alternative climate normals. *Bull. Am. Meteorol. Soc.* 92, 699–704. doi: 10.1175/2010BAMS2955.1

Arora, V. K., Scinocca, J. F., Boer, G. J., Christian, J. R., Denman, K. L., Flato, G. M., et al. (2011). Carbon emission limits required to satisfy future representative concentration pathways of greenhouse gases. *Geophys. Res. Lett.* 38:L05805. doi: 10.1029/2010GL046270

Balmaseda, M. A., Mogensen, K., and Weaver, A. T. (2013). Evaluation of the ECMWF ocean reanalysis system ORAS4. *Q. J. R. Meteorol. Soc.* 139, 1132–1161. doi: 10.1002/qj.2063

Banzon, V., Smith, T. M., Chin, T. M., Liu, C., and Hankins, W. (2016). A long-term record of blended satellite and *in situ* sea-surface temperature for climate monitoring, modeling and environmental studies. *Earth Syst. Sci. Data* 8, 165–176. doi: 10.5194/essd-8-165-2016

Barton, A., Waldbusser, G. G., Feely, R. A., Weisberg, S. B., Newton, J. A., Hales, B., et al. (2015). Impacts of coastal acidification on the Pacific Northwest shellfish industry and adaptation strategies implemented in response. *Oceanography* 28, 146–159. doi: 10.5670/oceanog.2015.38

Bishop, J. K. B., Rossow, W. B., and Dutton, E. G. (1997). Surface solar irradiance from the international satellite cloud climatology project 1983-1991. *J. Geophys. Res.* 102, 6883–6910. doi: 10.1029/96JD03865

Breitburg, D., Levin, L. A., Oschlies, A., Grégoire, M., Chavez, F. P., Conley, D. J., et al. (2018). Declining oxygen in the global ocean and coastal waters. *Science* 359:6371. doi: 10.1126/science.aam7240

Cannaby, H., Fach, B. A., Arkin, S. S., and Salihoglu, B. (2015). Climatic controls on biophysical interactions in the black sea under present day conditions and a potential future (A1B) climate scenario. *J. Mar. Syst.* 141, 149–166. doi: 10.1016/j.jmarsys.2014.08.005

Chan, F., Barth, J.A., Kroeker, K. J., Lubchenco J., and Menge, B. A. (2019). The dynamics and impact of ocean acidification and hypoxia: insights from sustained investigations in the Northern California Current Large Marine Ecosystem. *Oceanography* 32, 62–71. doi: 10.5670/oceanog.2019.312

Cheung, W. W., Frölicher, T. L., Asch, R. G., Jones, M. C., Pinsky, M. L., Reygondeau, G., et al. (2016). Building confidence in projections of the responses of living marine resources to climate change. *ICES J. Mar. Sci.* 73, 1283–1296. doi: 10.1093/icesjms/fsv250

Cheung, W. W., Lam, V. W., Sarmiento, J. L., Kearney, K., Watson, R., Zeller, D., et al. (2010). Large-scale redistribution of maximum fisheries catch potential in the global ocean under climate change. *Glob. Change Biol.* 16, 24–35. doi: 10.1111/j.1365-2486.2009.01995.x

Christian, J. R. (2014). Timing of the departure of ocean biogeochemical cycles from the preindustrial state. *PLoS ONE* 9:e109820. doi: 10.1371/journal.pone.0109820

Crawford, W. R., and Pe na, M. A. (2013). Declining oxygen on the British Columbia continental shelf. *Atmos. Ocean* 51, 88–103. doi: 10.1080/07055900.2012.753028

Cummins, P. F., and Masson, D. (2014). Climatic variability and trends in the surface waters of coastal British Columbia. *Prog. Oceanogr.* 120, 279–290. doi: 10.1016/j.pocean.2013.10.002

Deser, C., Knutti, R., Solomon, S., and Phillips, A. S. (2012). Communication of the role of natural variability in future North American climate. *Nat. Clim. Change* 2, 775–779. doi: 10.1038/nclimate1562

Feely, R. A., Alin, S. R., Carter, B., Bednaršek, N., Hales, B., Chan, F., et al. (2016). Chemical and biological impacts of ocean acidification along the west coast of North America. *Estuar. Coast. Shelf Sci.* 183, 260–270. doi: 10.1016/j.ecss.2016.08.043

Feely, R. A., Sabine, C. L., Hernandez-Ayon, J. M., Ianson, D., and Hales, B. (2008). Evidence for upwelling of corrosive "acidified" water onto the continental shelf. *Science* 320, 1490–1492. doi: 10.1126/science.1155676

Fisheries and Oceans Canada (DFO) (2019). *British Columbia Lightstation Sea-Surface Temperature and Salinity Data (Pacific), 1914-present.* Available online at: https://open.canada.ca/data/en/dataset/719955f2-bf8e-44f7-bc26-6bd623e82884 (accessed May 15, 2019).

Foreman, M., Crawford, W., Cherniawsky, J., Henry, R., and Tarbotton, M. (2000). A high-resolution assimilating tidal model for the northeast Pacific Ocean. *J. Geophys. Res.* 105, 28629–28651. doi: 10.1029/1999JC000122

Foreman, M. G. G., Callendar, W., Masson, D., Morrison, J., and Fine, I. (2014). A model simulation of future oceanic conditions along the British Columbia continental shelf. Part II: Results and analyses. *Atmos. Ocean* 52, 20–38. doi: 10.1080/07055900.2013.873014

Frölicher, T. L., Rodgers, K. B., Stock, C. A., and Cheung, W. W. (2016). Sources of uncertainties in 21^{s}t century projections of potential ocean ecosystem stressors. *Glob. Biogeochem. Cycles* 30, 1224–1243. doi: 10.1002/2015GB005338

Garcia, H. E., Locarnini, R. A., Boyer, T. P., Antonov, J. I., Baranova, O. K., Zweng, M., et al. (2014a). *World Ocean Atlas 2013. Volume 3: Dissolved Oxygen, Apparent Oxygen Utilization, and Oxygen Saturation.* ed S. Levitus. A. Mishonov Technical Ed.

Garcia, H. E., Locarnini, R. A., Boyer, T. P., Antonov, J. I., Baranova, O. K., Zweng, M., et al. (2014b). *World Ocean Atlas 2013. Volume 4: Dissolved Inorganic Nutrients (Phosphate, Nitrate, Silicate).* ed A. Levitus. Mishonov Technical Ed.

Gruber, N. (2011). Warming up, turning sour, losing breath: ocean biogeochemistry under global change. *Philos. Trans. R. Soc. A Math. Phys. Eng. Sci*. 369, 1980–1996. doi: 10.1098/rsta.2011.0003

Haigh, R., Ianson, D., Holt, C. A., Neate, H. E., and Edwards, A. M. (2015). Effects of ocean acidification on temperate coastal marine ecosystems and fisheries in the Northeast Pacific. *PLoS ONE* 10:e117533. doi: 10.1371/journal.pone.0117533

Hara, M., Yoshikane, T., Kawase, H., and Kimura, F. (2008). Estimation of the impact of global warming on snow depth in Japan by the pseudo-global-warming method. *Hydrol. Res. Lett*. 2, 61–64. doi: 10.3178/hrl.2.61

Hawkins, E., and Sutton, R. (2009). The potential to narrow uncertainty in regional climate predictions. *Bull. Am. Meteorol. Soc*. 90, 1095–1108. doi: 10.1175/2009BAMS2607.1

Hayashida, H., Christian, J. R., Holdsworth, A. M., Hu, X., Monahan, A. H., Mortenson, E., et al. (2019). CSIB v1 (Canadian Sea-Ice Biogeochemistry): a sea-ice biogeochemical model for the NEMO community ocean modelling framework. *Geosci. Model Dev*. 12, 1965–1990. doi: 10.5194/gmd-12-1965-2019

Helm, K. P., Bindoff, N. L., and Church, J. A. (2011). Observed decreases in oxygen content of the global ocean. *Geophys. Res. Lett*. 38:L23602. doi: 10.1029/2011GL049513

Holdsworth, A. M., and Myers, P. G. (2015). The influence of high-frequency atmospheric forcing on the circulation and deep convection of the Labrador Sea. *J. Clim*. 28, 4980–4996. doi: 10.1175/JCLI-D-14-00564.1

Irvine, J. R., and Crawford, W. R. (2011). *State of the Ocean Report for the Pacific North Coast Integrated Management Area (PNCIMA). Fisheries and Oceans*. Canadian Manuscript Report of Fisheries and Aquatic Sciences, 2971.

Jamet, Q., Dewar, W., Wienders, N., and Deremble, B. (2019). Fast warming of the surface ocean under a climatological scenario. *Geophys. Res. Lett*. 46, 3871–3879. doi: 10.1029/2019GL082336

Johnson, W. K., Miller, L. A., Sutherland, N. E., and Wong, C. S. (2005). Iron transport by mesoscale Haida eddies in the Gulf of Alaska. *Deep Sea Res. Part II* 52, 933–953. doi: 10.1016/j.dsr2.2004.08.017

Key, R. M., Olsen, A., van Heuven, S., Lauvset, S. K., Velo, A., Lin, X., et al. (2015). *Global Ocean Data Analysis Project, Version 2 (GLODAPv2), ORNL/CDIAC-162, ND-P093*. Oak Ridge, TN: Carbon Dioxide Information Analysis Center, Oak Ridge National Laboratory, US Department of Energy. Available online at: https://www.glodap.info/wp-content/uploads/2017/08/NDP_093.pdf

Lara-Espinosa, A. (2012). *Determination of the acidification state of canadian pacific coastal waters using empirical relationships with hydrographic data* (Master's thesis). University of Victoria, Victoria, BC, Canada.

Lauvset, S. K., Key, R. M., Olsen, A., van Heuven, S., Velo, A., Lin, X., et al. (2016). A new global interior ocean mapped climatology: the $1^\circ \times 1^\circ$ GLODAP version 2. *Earth Syst. Sci. Data* 8, 325–340. doi: 10.5194/essd-8-325-2016

Levier, B., Tréguier, A., Madec, G., and Garnier, V. (2007). Free surface and variable volume in the NEMO code. *Zenodo* doi: 10.5281/zenodo.3244182

Li, H., Ilyina, T., Müller, W. A., and Landschützer, P. (2019). Predicting the variable ocean carbon sink. *Sci. Adv*. 5:6471. doi: 10.1126/sciadv.aav6471

Livezey, R. E., Vinnikov, K. Y., Timofeyeva, M. M., Tinker, R., and van den Dool, H. M. (2007). Estimation and extrapolation of climate normals and climatic trends. *J. Appl. Meteorol. Climatol*. 46, 1759–1776. doi: 10.1175/2007JAMC1666.1

Locarnini, R. A., Mishonov, A. V., Antonov, J. I., Boyer, T. P., Garcia, H. E., Baranova, O. K., et al. (2013). "Volume 1: temperature," in *World Ocean Atlas 2013*, eds S. Levitus and A. Mishonov (NOAA Atlas NESDIS), 40

Lu, Y., Li, J., Lei, J., and Hannah, C. (2017). Impacts of model resolution on simulation of meso-scale eddies in the Northeast Pacific Ocean. *Satellite Oceanogr. Meteorol*. 2:328.

Lucas, B., Verrin, S. M., and Brown, R. (2007). *Ecosystem overview: Pacific North Coast Integrated Management Area (PNCIMA). Number 2667*. Fisheries and Oceans Canada.

Madec, G. (2008). *NEMO Ocean Engine. Note du Pôle de modélisation*. Institut Pierre-Simon Laplace (IPSL).

Mbengue, C., and Schneider, T. (2017). Storm-track shifts under climate change: toward a mechanistic understanding using baroclinic mean available potential energy. *J. Atmos. Sci*. 74, 93–110. doi: 10.1175/JAS-D-15-0267.1

Meinshausen, M., Smith, S. J., Calvin, K., Daniel, J. S., Kainuma, M. L. T., Lamarque, J.-F., et al. (2011). The RCP greenhouse gas concentrations and their extensions from 1765 to 2300. *Clim. Change* 109:213. doi: 10.1007/s10584-011-0156-z

Merryfield, W. J., Pal, B., and Foreman, M. G. G. (2009). Projected future changes in surface marine winds off the west coast of Canada. *J. Geophys. Res*. 114:C06008. doi: 10.1029/2008JC005123

Morrison, J., Callendar, W., Foreman, M. G. G., Masson, D., and Fine, I. (2014). A model simulation of future oceanic conditions along the British Columbia continental shelf. Part I: Forcing fields and initial conditions. *Atmosphere-Ocean* 52, 1–19. doi: 10.1080/07055900.2013.868340

Morrison, J., Foreman, M. G. G., and Masson, D. (2012). A method for estimating monthly freshwater discharge affecting British Columbia coastal waters. *Atmosphere-Ocean* 50, 1–8. doi: 10.1080/07055900.2011.637667

Moss, R. H., Edmonds, J. A., Hibbard, K. A., Manning, M. R., Rose, S. K., Van Vuuren, D. P., et al. (2010). The next generation of scenarios for climate change research and assessment. *Nature* 463, 747–756. doi: 10.1038/nature08823

Peña, A., Fine, I., and Masson, D. (2018). *13. Towards Climate Change Projections of Biogeochemical Conditions Along the British Columbia Coast*. Report of Working Group 29 on Regional Climate Modeling, 114.

Peña, M. A., Masson, D., and Callendar, W. (2016). Annual plankton dynamics in a coupled physical-biological model of the Strait of Georgia, British Columbia. *Prog. Oceanogr*. 146, 58–74. doi: 10.1016/j.pocean.2016.06.002

Penduff, T., Juza, M., Barnier, B., Zika, J., Dewar, W. K., Treguier, A.-M., et al. (2011). Sea level expression of intrinsic and forced ocean variabilities at interannual time scales. *J. Clim*. 24, 5652–5670. doi: 10.1175/JCLI-D-11-00077.1

Pörtner, H.-O., Karl, D. M., Boyd, P. W., Cheung, W., Lluch-Cota, S. E., Nojiri, Y., et al. (2014). "Ocean systems," in *Climate Change 2014: Impacts, Adaptation, and Vulnerability. Part A: Global and Sectoral Aspects. Contribution of Working Group II to the Fifth Assessment Report of the Intergovernmental Panel on Climate Change* (Cambridge University Press), 411–484.

Saha, S., Moorthi, S., Pan, H., Wu, X., Wang, J., Nadiga, S., et al. (2010). *NCEP Climate Forecast System Reanalysis (CFSR) Selected Hourly Time-Series Products, January 1979 to December 2010*. Research Data Archive at the National Center for Atmospheric Research. Computational and Information Systems Laboratory. doi: 10.5065/D6513W89

Sarmiento, J. L., and Gruber, N. (2006). *Ocean Biogeochemical Dynamics*. Princeton University Press. doi: 10.1515/9781400849079

Schmidtko, S., Stramma, L., and Visbeck, M. (2017). Decline in global oceanic oxygen content during the past five decades. *Nature* 542, 335–339. doi: 10.1038/nature21399

Scinocca, J. F., Kharin, V. V., Jiao, Y., Qian, M. W., Lazare, M., Solheim, L., et al. (2016). Coordinated global and regional climate modeling. *J. Clim*. 29, 17–35. doi: 10.1175/JCLI-D-15-0161.1

Seidov, D., Baranova, O., Boyer, T., Cross, S., Mishonov, A., and Parsons, A. (2017). *Northeast Pacific Regional Climatology (NCEI Accession 0163799). Version 1.1*. NOAA National Centers for Environmental Information.

Shaw, T. A., Baldwin, M., Barnes, E. A., Caballero, R., Garfinkel, C. I., Hwang, Y.-T., et al. (2016). Storm track processes and the opposing influences of climate change. *Nat. Geosci*. 9:656. doi: 10.1038/ngeo2783

Smagorinsky, J. (1963). General circulation experiments with the primitive equations: I. the basic experiment. *Month. Weath. Rev*. 91, 99–164. doi: 10.1175/1520-0493(1963)091<0099:GCEWTP>2.3.CO;2

Soontiens, N., and Allen, S. E. (2017). Modelling sensitivities to mixing and advection in a sill-basin estuarine system. *Ocean Model*. 112, 17–32. doi: 10.1016/j.ocemod.2017.02.008

Swart, N. C., Cole, J. N., Kharin, V. V., Lazare, M., Scinocca, J. F., Gillett, N. P., et al. (2019). The Canadian earth system model version 5 (CanESM5.0.3). *Geosci. Model Dev*. 12, 4823–4873. doi: 10.5194/gmd-12-4823-2019

Taylor, K. E., Stouffer, R. J., and Meehl, G. A. (2009). *A Summary of the CMIP5 Experiment Design*.

Umlauf, L., and Burchard, H. (2003). A generic length-scale equation for geophysical turbulence models. *J. Mar. Res*. 61, 235–265. doi: 10.1357/002224003322005087

Wu, Y., Zhai, X., and Wang, Z. (2016). Impact of synoptic atmospheric forcing on the mean ocean circulation. *J. Clim*. 29, 5709–5724. doi: 10.1175/JCLI-D-15-0819.1

Yin, J. H. (2005). A consistent poleward shift of the storm tracks in simulations of 21st century climate. *Geophys. Res. Lett*. 32:L18701. doi: 10.1029/2005GL023684

Zweng, M. M., Reagan, J. R., Antonov, J. I., Locarnini, R. A., Mishonov, A. V., Boyer, T. P., et al. (2013). "Volume 2: salinity," in *World Ocean Atlas 2013*, eds S. Levitus and A. Mishonov (Atlas NESDIS), 39.

Conflict of Interest: The authors declare that the research was conducted in the absence of any commercial or financial relationships that could be construed as a potential conflict of interest.

frontiers in Marine Science

ORIGINAL RESEARCH
published: 07 April 2021
doi: 10.3389/fmars.2021.612874

A Dynamically Downscaled Ensemble of Future Projections for the California Current System

Mercedes Pozo Buil[1,2]*, Michael G. Jacox[1,2,3], Jerome Fiechter[4], Michael A. Alexander[3], Steven J. Bograd[1,2], Enrique N. Curchitser[5], Christopher A. Edwards[4], Ryan R. Rykaczewski[6] and Charles A. Stock[7]

[1] Institute of Marine Science, University of California, Santa Cruz, Santa Cruz, CA, United States, [2] NOAA Southwest Fisheries Science Center, Monterey, CA, United States, [3] NOAA Earth System Research Laboratory, Boulder, CO, United States, [4] Ocean Sciences Department, University of California, Santa Cruz, Santa Cruz, CA, United States, [5] Department of Environmental Sciences, Rutgers University, New Brunswick, NJ, United States, [6] NOAA Pacific Islands Fisheries Science Center, Honolulu, HI, United States, [7] NOAA Geophysical Fluid Dynamics Laboratory, Princeton, NJ, United States

Edited by:
Sara Rivero-Calle,
University of Georgia, United States

Reviewed by:
Vincent Michel Echevin,
UMR 7159, Laboratoire d'Océanographie et du Climat Expérimentations et Approches Numériques (LOCEAN), France
Ana Franco,
University of British Columbia, Canada

***Correspondence:**
Mercedes Pozo Buil
mercedes.pozo@ucsc.edu

Specialty section:
This article was submitted to Global Change and the Future Ocean, a section of the journal Frontiers in Marine Science

Received: *01 October 2020*
Accepted: *15 March 2021*
Published: *07 April 2021*

Citation:
Pozo Buil M, Jacox MG, Fiechter J, Alexander MA, Bograd SJ, Curchitser EN, Edwards CA, Rykaczewski RR and Stock CA (2021) A Dynamically Downscaled Ensemble of Future Projections for the California Current System. Front. Mar. Sci. 8:612874. doi: 10.3389/fmars.2021.612874

Given the ecological and economic importance of eastern boundary upwelling systems like the California Current System (CCS), their evolution under climate change is of considerable interest for resource management. However, the spatial resolution of global earth system models (ESMs) is typically too coarse to properly resolve coastal winds and upwelling dynamics that are key to structuring these ecosystems. Here we use a high-resolution (0.1°) regional ocean circulation model coupled with a biogeochemical model to dynamically downscale ESMs and produce climate projections for the CCS under the high emission scenario, Representative Concentration Pathway 8.5. To capture model uncertainty in the projections, we downscale three ESMs: GFDL-ESM2M, HadGEM2-ES, and IPSL-CM5A-MR, which span the CMIP5 range for future changes in both the mean and variance of physical and biogeochemical CCS properties. The forcing of the regional ocean model is constructed with a "time-varying delta" method, which removes the mean bias of the ESM forcing and resolves the full transient ocean response from 1980 to 2100. We found that all models agree in the direction of the future change in offshore waters: an intensification of upwelling favorable winds in the northern CCS, an overall surface warming, and an enrichment of nitrate and corresponding decrease in dissolved oxygen below the surface mixed layer. However, differences in projections of these properties arise in the coastal region, producing different responses of the future biogeochemical variables. Two of the models display an increase of surface chlorophyll in the northern CCS, consistent with a combination of higher nitrate content in source waters and an intensification of upwelling favorable winds. All three models display a decrease of chlorophyll in the southern CCS, which appears to be driven by decreased upwelling favorable winds and enhanced stratification, and, for the HadGEM2-ES forced run, decreased nitrate content in upwelling source waters in nearshore regions. While trends in the downscaled models reflect those in the ESMs that force them, the ESM and downscaled solutions differ more for biogeochemical than for physical variables.

Keywords: downscaled ensemble projections, California Current System, future coastal changes, eastern boundary upwelling system, climate change

INTRODUCTION

The California Current System (CCS) is one of the four global eastern boundary upwelling systems (EBUSs) characterized by extraordinary biological productivity that supports a variety of human uses including tourism, fisheries, and recreation (e.g., Checkley and Barth, 2009). As in other EBUS, the high level of primary productivity in the CCS is primarily attributed to wind-driven coastal upwelling, which delivers nutrient-rich deep waters to the surface. However, upwelled waters also have low pH, contain high concentrations of respired carbon, and are moderately oxygen-poor, making this region prone to hypoxia and acidification, conditions that can threaten both benthic and pelagic marine life (e.g., Gruber et al., 2012; Turi et al., 2014; Feely et al., 2016). Simulations of changes in the CCS that affect those processes are therefore key to evaluate the direct ecological and economic impact of the future climate on this dynamic ecosystem (Vecchi et al., 2006; Bakun et al., 2010; Sydeman et al., 2014; Rykaczewski et al., 2015; Howard et al., 2020b).

Under future climate scenarios, projected physical changes in the CCS include enhanced stratification, shifts in the timing and intensity of upwelling, and alteration of the properties and relative contributions of source waters advected into the region (e.g.,Rykaczewski and Dunne, 2010; Doney et al., 2012; Rykaczewski et al., 2015; Bograd et al., 2019). Ocean warming generally results in increased water column stability (Capotondi et al., 2012), reducing vertical mixing, nutrient supply, and primary productivity in the euphotic zone of subtropical regions (Hoegh-Guldberg and Bruno, 2010). In EBUS regions, however, it has been proposed that heterogeneous warming of the land and ocean could intensify the surface atmospheric pressure gradient and consequently enhance equatorward winds and coastal upwelling (i.e., the Bakun hypothesis; Bakun, 1990; Bakun et al., 2015). Global climate models suggest that the Bakun hypothesis is overly simplified; projected changes in upwelling are likely to be season- and latitude-dependent, with intensification of CCS upwelling during spring, especially in the southern CCS, followed by a significant weakening of upwelling during the summer months, especially in the northern region of the CCS (e.g., García-Reyes et al., 2015; Rykaczewski et al., 2015; Wang et al., 2015). These anthropogenic trends in upwelling are not likely to be emergent until mid-century (∼2050) in the southern CCS and even later (∼2080) in the northern CCS (Brady et al., 2017), as strong decadal variability remains the dominant signal on shorter time horizons.

In the biogeochemical realm, reduced ventilation and circulation of the North Pacific may increase nutrient concentrations, lower pH, and decrease oxygen concentrations in the deep source waters of the CCS (Rykaczewski and Dunne, 2010; Van Oostende et al., 2018; Xiu et al., 2018). These source water changes could result in increased primary productivity over the continental shelf, which, when the increased organic matter is subsequently remineralized and combined with reduced oxygen in source waters, would result in a significant expansion of hypoxic areas (Dussin et al., 2019). Similarly, Hauri et al. (2013) projected that, by 2050, the nearshore mean surface pH of the CCS will move outside the envelope of present-day variability and the aragonite saturation horizon of the central CCS will shoal into the upper 75 m, causing near-permanent undersaturation in subsurface waters. However, many of these biogeochemical projections describe results from individual climate models; biogeochemical responses to climate change in the CCS vary considerably across models (Frölicher et al., 2016) and the robustness of projected changes must be determined.

Earth system models (ESMs) are essential tools for future climate studies. ESMs are atmosphere-ocean-land-sea ice general circulation models (GCMs) that have been coupled to biogeochemical models (Taylor et al., 2012). While the initial motivation for global ESM development was resolving the partitioning of anthropogenic carbon emissions between the land, ocean, and atmosphere (e.g., Friedlingstein et al., 2006; Arora et al., 2013, 2020), the inclusion of ocean biogeochemical components provided new insights into ocean acidification, deoxygenation, and productivity changes (Bopp et al., 2013; Kwiatkowski et al., 2020). However, the utility of ESMs on regional scales and especially in upwelling systems is limited by their coarse resolution (Boville and Gent, 1998; Mote and Mantua, 2002; Palmer, 2014). The ocean component in most GCMs is too coarse to resolve fine-scale processes including coastal upwelling, mesoscale eddy activity, and coastal trapped waves (Stock et al., 2011). Their atmosphere component is also too coarse to resolve nearshore structure in the winds, which can exert a strong influence on the physical and biogeochemical signature of coastal upwelling (e.g., Mote and Mantua, 2002; Capet et al., 2004; Jacox and Edwards, 2012; Small et al., 2015; Renault et al., 2016; Franco et al., 2018). Dynamical downscaling (i.e., using coarse global fields to force a high-resolution regional model) is one commonly used approach to produce high-resolution ocean projections at regional scale (Drenkard et al., in review). This approach has been used in other EBUS (Benguela Upwelling, e.g., Machu et al., 2015; Humboldt Upwelling, e.g., Echevin et al., 2012, 2020; Iberian Upwelling, Miranda et al., 2013), and in the CCS (Auad et al., 2006; Li et al., 2014; Xiu et al., 2018; Arellano and Rivas, 2019; Dussin et al., 2019; Howard et al., 2020a). For the CCS, these previous high-resolution projections were conducted by downscaling single climate projections forced by just one ESM, analyzed short future periods (10–30-year time-slices), or applied idealized perturbations in some variables that did not account for all physical and biogeochemical forcing. They often do not consider inherent present-climate bias in ESMs or capture the full envelope of future climate uncertainties, which in the case of biogeochemistry projections significant contribution comes from model uncertainties (Cheung et al., 2016; Frölicher et al., 2016).

Dynamically downscaled projections allow us to recover important regional-scale features that are missing or poorly represented in their coarse-resolution parents models. But, the high-resolution projection is tied to the large-scale forcing from the ESMs, including their biases, and performing a bias correction on the ESM forcing has the potential to significantly improve dynamical downscaling simulations (Bruyère et al., 2014; Machu et al., 2015; Xu et al., 2019; Drenkard et al., in review). Here we use a high-resolution regional ocean-biogeochemical coupled model and apply a "time-varying" delta approach to dynamically downscale three different ESMs. The selected ESMs span a wide range of potential future changes in both the mean and variance of physical and biogeochemical properties for the CCS. Our objectives are to produce and present downscaled projections of climate change in the CCS at 0.1 degree. (i.e., mesoscale resolving) horizontal resolution from 1980 until 2100 under the Representative Concentration Pathway (RCP) 8.5 scenario. We examine a range of ecosystem-relevant variables including sea surface temperature (SST), chlorophyll, and subsurface nitrate and oxygen. We analyze changes in those variables for the middle and end-of century and the plausible mechanisms associated with those changes. The remainder of the paper is organized as follows: section "Materials and Methods" describes the regional modeling approach, the ESM output used and the bias correcting method applied to construct the forcing of the regional model. Section "Results" describes the projected changes in ecosystem-relevant variables, and discussion of the results and conclusion are presented in sections "Discussion" and "Concluding Remarks," respectively.

MATERIALS AND METHODS

Coupled Physical-Biogeochemical Model: ROMS-NEMUCSC

To produce the high-resolution future projections in the CCS, we use the Regional Ocean Modeling System (ROMS) coupled with a biogeochemical model (NEMUCSC) based on the North Pacific Ecosystem Model for Understanding Regional Oceanography (NEMURO). ROMS is a free-surface, hydrostatic, primitive equation ocean model that uses stretched, terrain-following coordinates in the vertical and orthogonal curvilinear coordinates in the horizontal (Shchepetkin and McWilliams, 2005; Haidvogel et al., 2008). The model configuration, developed by the University of California Santa Cruz, covers the region 30–48°N and 115.5–134°W (midway down Baja California to just south of Vancouver Island) with 0.1° (∼10 km) horizontal resolution and 42 vertical sigma levels (Veneziani et al., 2009[1]). NEMURO is a medium complexity nutrient-phytoplankton-zooplankton (NPZ) model specifically developed and parameterized for the North Pacific (Kishi et al., 2007). The model includes three limiting macro-nutrients (i.e., nitrate, ammonium, and silicate), two phytoplankton groups (nanophytoplankton and diatoms), three zooplankton groups (micro-, meso-, and predatory zooplankton) and three detritus pools (DON, PON, and opal). Here, we use a customized version of NEMURO, called NEMUCSC, which is specifically parameterized for the CCS and augmented with oxygen and carbon cycling (Cheresh and Fiechter, 2020; Fiechter et al., 2018, 2020). The coupled ocean-biogeochemistry regional model will be hereafter referred to as "ROMS-NEMUCSC."

We first use ROMS-NEMUCSC to perform a historical control simulation (CTRL) for 1980–2010. Initial and ocean lateral boundary conditions are derived from the Simple Ocean Data Assimilation version 2.1.6 (SODA; Carton and Giese, 2008) at monthly resolution. The atmospheric surface forcing is derived from the global atmospheric reanalysis from European Centre for Medium-Range Weather Forecasts version 5 (ERA-5; Hersbach et al., 2020) at 1-h and ∼30 km resolution, with the exception of surface winds, which were obtained from ERA-5 for 1980–1987 and from the 0.25° (∼25 km) Cross-Calibrated Multi-Platform wind product (CCMP1; Atlas et al., 2011) for 1988–2010 at 6-h resolution. In the nearshore region of the CCS, especially off northern California and Oregon, we have found that CCMP1 more closely reproduces the observed magnitude of summertime winds and leads to better representation of biogeochemical processes near the coast. Air-sea fluxes are computed in ROMS internally using bulk formulae (Fairall et al., 1996a,b; Liu et al., 1979). Physical variables are stored daily and used to force the biogeochemical component "offline" (i.e., NEMUCSC is run independently and driven by daily surface atmospheric fluxes and oceanic fields from ROMS). Initial and boundary conditions are derived from the 2009 World Ocean Atlas (WOA) climatology (Garcia et al., 2010a,b) for nutrients and oxygen, from the Global Ocean Data Analysis Project (Key et al., 2004) for total alkalinity, and from the empirical relationship of Alin et al. (2012) for DIC using monthly temperature and oxygen. Initial and boundary conditions for ammonium, phytoplankton, zooplankton, and detritus are set to a small value (0.1 mmol N m^{-3}), noting that the evolution of these quantities is dominated by surface ocean dynamics that adjust rapidly to simulated macronutrients in the interior of the model domain.

Earth System Models

For the regional downscaling, we select three ESMs, from a total of nineteen from phase 5 of the Coupled Model Intercomparison Project (CMIP5) archive: the Geophysical Fluid Dynamics Laboratory (GFDL) ESM2M, Institut Pierre Simon Laplace (IPSL) CM5A-MR, and the Hadley Center HadGEM2-ES (HAD). Key characteristics of the selected ESMs are summarized in **Table 1**. We downscaled each ESM for the period from 1980 to 2100 using historical forcing (1980–2005) and the RCP8.5 climate change scenario (2006–2100). We focus on the RCP8.5 scenario since model uncertainty dominates scenario uncertainty for biogeochemical (and to a lesser degree, physical) changes in the CCS. Indeed, for biogeochemical variables in the CCS the range of projections under the RCP2.6 and RCP4.5 scenarios is fully contained within the model uncertainty under the RCP8.5 scenario (**Supplementary Figure 1** same as **Figure 8** in Drenkard et al., in review).

The question of which ESMs to include in a multi-model ensemble is an active research area. The models that best match the observed historical climate are not necessarily the ones that will most faithfully represent future climate sensitivity, and more process-based model selection methods (e.g., with emerging constraints) are being developed (Eyring et al., 2019; Hall et al., 2019). Given the lack of definitive selection criteria, we chose three ESMs that capture the CMIP5 range of projected future changes in both the mean and variance of physical and biogeochemical CCS properties. While they show agreement in the sign of the projected SST change in the CCS, they differ in the magnitude of warming and disagree on the sign of the primary

---

[1] https://oceanmodeling.ucsc.edu

TABLE 1 | Characteristics of the ESMs selected for regional downscaling.

Modeling center ESM model	Atmospheric model resolution	Ocean model resolution	Biogeochemical model	References
NOAA Geophysical Fluid Dynamics Laboratory, United States, GFDL-ESM2M (GFDL)	2.5° longitude 2° latitude 24 levels Monthly	MOM4p1 1° longitude ∼0.3–1° latitude 50 levels Monthly	TOPAZ2 (3Phyto, 3Zoo, N, P, Si, Fe, O_2) Annual	Dunne et al., 2012
Institut Pierre-Simon Laplace, France, IPSL-CM5A-MR (IPSL)	2.5° longitude 1.25° latitude 39 levels Monthly	NEMOv3.2 2° longitude ∼0.5–2° latitude 31 levels Monthly	PISCES (2Phyto, 2Zoo, N, P, Si, Fe, O_2) Annual	Dufresne et al., 2013
Met Office Hadley Center, United Kingdom, HadGEM2-ES (HAD)	1.25° longitude 1.875° latitude 24 levels Monthly	UM 1° longitude ∼0.3–1° latitude 40 levels Monthly	Diat-HadOCC (2Phyto, 1Zoo, N, P, Si, Fe, O_2) Annual	Collins et al., 2011

production (PP) change (**Figure 1**). HAD projects the warmest SST anomalies by 2100 and a sharp decline in PP by around 2050. Relative to the CMIP5 ensemble mean, GFDL and IPSL project weak and moderate increases in SST, respectively, and both project increased PP by 2100 (**Figure 1**), counter to the declining PP trend in the CMIP5 ensemble mean (Bopp et al., 2013). Similarly, these three models have different projections for changes in the magnitude of interannual variability under climate change. The three models span the range of potential changes in physical and biogeochemical variance, which may increase, decrease, or remain unchanged depending on the variable and model (**Supplementary Figure 2**).

Downscaling Approach

Output from the selected ESMs provide the surface and ocean boundary conditions for ROMS-NEMUCSC in a one-way downscaling approach. To reduce biases exhibited in the ESMs historical simulations, we apply a "time-varying delta" bias-correction method prior to downscaling the ESMs output. We first estimate time-varying deltas (DELTA) for a forcing atmospheric variable (ATM) by subtracting the ESM's historical monthly climatology (ESM_{CLM}; years 1980–2010) from the whole period of interest (i.e., 1980–2100).

$$\mathrm{DELTA}_{1980-2100} = \mathrm{ESM}_{1980-2100} - \mathrm{ESM}_{\mathrm{CLM},1980-2010} \quad (1)$$

These monthly time-varying deltas are first bilinearly interpolated in space and time to the resolution of the reanalysis data used to force the control run (REAN), and then added to the monthly reanalysis climatology ($REAN_{CLM}$). Finally, we add high-frequency variability from the reanalysis ($REAN_{HF}$), computed as the residual after removing a 30-day running mean, as the absence of this high-frequency variability and associated damping of upwelling can lead to a biased ecosystem state (Gruber et al., 2006, 2011). The climatology and high-frequency component from the reanalysis (i.e., $REAN_{CLM}$ and $REAN_{HF}$) are repeated (∼4 times) to cover the whole period of interest. Thus, for each ATM, the bias-corrected forcing ATM′ is computed as:

$$\mathrm{ATM}'_{1980-2100} = \mathrm{REAN}_{\mathrm{CLM},\,1980-2010} + \mathrm{REAN}_{\mathrm{HF},\,1980-2010} + \mathrm{DELTA}_{1980-2100} \quad (2)$$

Bias correction for the ocean and biogeochemical variables is handled similarly, but with several adjustments for the lower frequency of available ESM output. The high-frequency component ($REAN_{HF}$) is excluded, since the available ESM output for 3D physical and biogeochemical variables have monthly and annual temporal resolution, respectively. In addition, the time-varying deltas for the biogeochemical variables are calculated annually, again because the ESM biogeochemical outputs are available at annual resolution (**Table 1**). Model initialization is handled similarly to the ocean boundaries by applying deltas from the year 1980 to our CTRL initial conditions.

The time-varying delta method for downscaling retains the observed historical climatology and high-frequency (sub-monthly) variability while inheriting the long-term change and interannual variability of the parent ESM. Relative to a "fixed delta" method that compares a historical period to a future one (e.g., Alexander et al., 2019; Shin and Alexander, 2020), the time-varying delta method has advantages of capturing projected changes in interannual variability, and resolving the full climate change evolution, including potentially non-linear impacts that would be missed when the transient response is excluded. An alternative method for prescribing the high-frequency variability would be to use the daily ESM forcing, which may be modulated by low-frequency variability (e.g., El Niño Southern Oscillation events alter storm tracks in the CCS). We retain the observed historical high-frequency variability from the reanalysis for several reasons. First, it allows us to force the model with high-resolution temporal forcing (6-hourly for the winds and hourly for the rest of ATMs), which resolves the daily cycle and is consistent with the historical forcing. Second, high frequency variability is likely to differ substantially within the space of a single ESM grid cell, particularly near the coast, and will not be resolved by the ESMs. In other EBUS, previous works applied statistical downscaling methods in the wind forcing to overcome the limitation of the coarse resolution models (e.g.,Goubanova et al., 2011; Machu et al., 2015; Bonino et al., 2019). While future changes in high frequency atmospheric forcing is not the focus of this study, it should be a topic of further research.

We refer to the downscaled simulations from ROMS-NEMUCSC, driven by GFDL, IPSL, and HAD as ROMS-GFDL, ROMS-IPSL, and ROMS-HAD, respectively, in the following sections and figures.

Observation Data for Model Evaluation

To evaluate the CTRL and the historical period of the downscaled simulations (i.e., ROMS-GFDL, ROMS-IPSL, and ROMS-HAD), we use the Optimum Interpolation

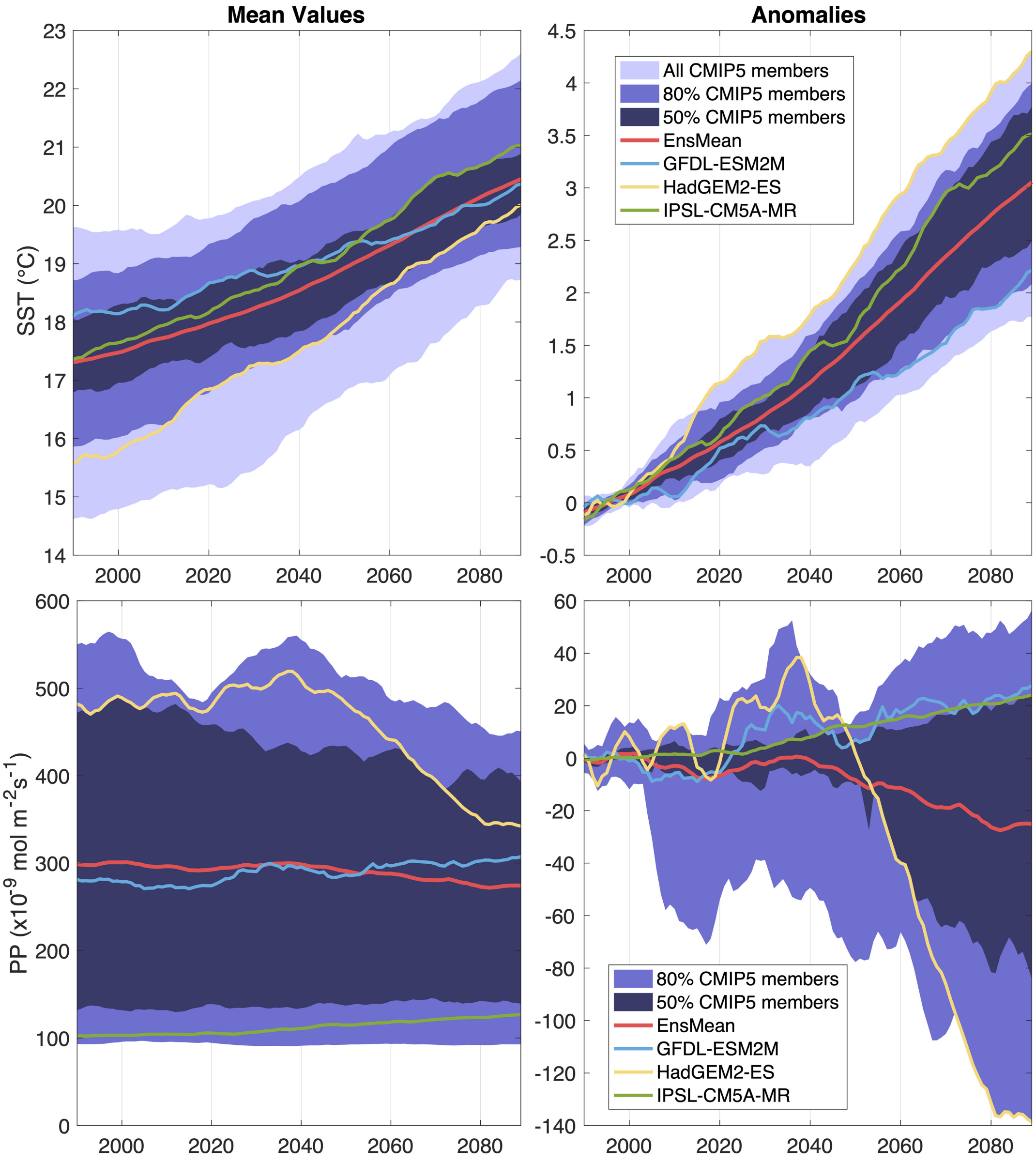

FIGURE 1 | Time series of yearly averages of the California Current sea surface temperature (SST, first row) and primary production (PP, second row) for the 1976–2099 period, averaged over the California Current Large Marine Ecosystem. The simulations are forced using historical emissions (1976 to 2005) and the RCP8.5 scenario for future projection (2006 to 2099). Left panels show the mean values and right panels show the anomalies relative to the 1976–2005 climatology. A 20-year running mean is applied. The figure is adapted from the NOAA climate website (https://www.psl.noaa.gov/ipcc).

SST data set, which combines *in situ* and satellite-based observations, from the National Oceanic and Atmospheric Administration (NOAA OISST v2; Reynolds et al., 2007) at 0.25° from 1982 to 2010 and for surface chlorophyll (chl), we use data from the Sea-viewing Wide Field-of-view Sensor (SeaWiFS) obtained from the National Aeronautics and Space Administration (NASA) Ocean Color Website (NASA Goddard Space Flight Center, Ocean Ecology Laboratory, Ocean Biology Processing Group; 2014) at ∼0.1° resolution from 2000 to 2010. In addition, we evaluate simulated physical and biogeochemical fields with climatological data from the WOA derived from the World Ocean Database (oxygen, Garcia et al., 2013a; nitrate, Garcia et al., 2013b; temperature,Locarnini et al., 2013).

RESULTS

In the following sections, we describe projected changes in the future physical and biogeochemical states of the CCS, first for the long-term mean changes for the 2070–2100 period with respect to the historical period (1980–2010) (i.e., Future − Historical) and then the time-dependent changes for the full transient runs (1980–2100).

Model Evaluation

The historical CTRL reproduces many aspects of the CCS physical and biogeochemical variability (**Supplementary Figures 3**, **4**). The simulated annual mean SST has a weak warm bias over most of the domain and a weak cold bias along the northern boundary. The Southern California Bight (SCB) shows the largest SST bias (∼1.4°C), which is comparable with other numerical simulations of the CCS (e.g., Veneziani et al., 2009; Renault et al., 2016) and is likely due to the poor representation of cloud cover and the cross-shore gradient in alongshore winds resulting from coarse spatial resolution in the forcing reanalysis data (Renault et al., 2020). The annual mean subsurface patterns of nitrate and dissolved oxygen in the CTRL simulation are also well represented compared to climatological values from the WOA. Although the observed and simulated values of nitrate and oxygen differ near the coast, which cannot be resolved by the coarse horizontal resolution of the WOA grid (1° × 1°), the model reasonably reproduces the offshore spatial gradient and variability of climatological subsurface nitrate and dissolved oxygen (**Supplementary Figures 3**, **4**). The observed and simulated annual mean chlorophyll exhibits similar onshore-offshore gradients. However, the main differences are located in the nearshore regions, where the model overestimates chlorophyll between the northern San Francisco Bay (SFB) and Cape Blanco, and underestimates it in the northern coastal domain (>44°N), SFB, and the SCB (**Supplementary Figure 3**).

Long-Term Mean Changes

Alongshore Wind Stress and Vertical Velocity

We use meridional wind stress as a proxy for the alongshore or upwelling favorable winds. In general, the three ESM-driven ROMS simulations exhibit an overall intensification (i.e., more negative) and a northern displacement (>39°N) of the meridional wind stress (**Figure 2**), consistent with prior analysis (Rykaczewski et al., 2015; Xiu et al., 2018). These equatorward wind stress anomalies oppose the mean wind stress (poleward) at the northern latitudes. However, there are some notable inter-model differences in the spatial variability. ROMS-GFDL and ROMS-IPSL show a strong increase centered in the northern nearshore regions (<200 km from the coast) of the CCS, while ROMS-HAD shows the center of this intensification offshore and in the northwest corner of the domain. While ROMS-GFDL exhibits the strongest intensification across the CCS domain, ROMS-IPSL exhibits a weaker intensification that is confined along the coastal domain, and ROMS-HAD shows this intensification confined to the northern part of the CCS. A strong decrease in alongshore wind stress over the southern part of the domain is projected in both ROMS-IPSL and ROMS-HAD, offshore in the former and nearshore in the latter.

We use vertical velocity at 50 m as a measure for upwelling (**Figure 2**). The projected increase in the equatorward meridional wind stress over the northern coastal region of the CCS enhances coastal upwelling (upward and positive vertical velocity changes) in the three ESM-driven downscaled ROMS simulations. While ROMS-GFDL and ROMS-IPSL projections show an overall upward velocity all along the coast of the domain, the intense weakening of the alongshore-wind stress projected by ROMS-HAD reduces coastal upwelling in the southern part of the domain.

Sea Surface Temperature

The SST response to projected climate change includes warming over the entire domain in all three ESM-driven ROMS simulations (**Figure 2**). Although the three ROMS simulations agree on the warming of the CCS region, the magnitude of change differs considerably among simulations. ROMS-GFDL exhibits the weakest projected warming (<2.5°C), ROMS-IPSL a moderate warming (>3°C), and the ROMS-HAD the strongest warming (>3.5°C). In addition to the differences in overall climate sensitivity, there are differences among the spatial warming patterns: in the ROMS-IPSL the warming offshore of the SCB is relatively smaller, while ROMS-HAD presents a more homogeneous warming pattern. In ROMS-IPSL, this weaker warming extends north along the coast up to ∼43°N. In ROMS-GFDL, the warming is lessened in the northern coastal waters (>39°N), suggesting that increased wind-driven upwelling may partially mitigate the warming locally, while the strongest warming occurs in the offshore waters of the SCB.

Subsurface Nitrate

The ecological effects of upwelling critically depend on the biogeochemical properties and composition of upwelled source waters. To explore the subsurface biogeochemical properties, we select a depth of 150 m (Chhak and Di Lorenzo, 2007), which is deeper than the seasonal historical mixed layer depth (MLD) which ranges from 30 to 100 m in the whole domain. All three downscaled simulations project an increase of the subsurface nitrate concentration in the offshore waters (>100 km from the coast), with a larger increase by the end of the 21st century in ROMS-GFDL (∼5 mmol/m^3) than in the other two simulations (∼2.5–3 mmol/m^3) (**Figure 3**). However, the projections differ in the coastal waters (<100 km from the coast). While ROMS-GFDL shows a coastwide nitrate increase, the nitrate increase in ROMS-IPSL is much weaker and limited to the southern and northern CCS, and ROMS-HAD projects a decrease in subsurface nitrate along the coast, which is strongest in the southern part of the domain (**Figure 3**).

Subsurface Oxygen

Below the seasonal pycnocline, upwelling systems are characterized by both high nutrient concentrations and low oxygen concentrations. The projected dissolved oxygen changes at 150 m depth mirror the nitrate changes described above – all three models exhibit large-scale oxygen declines. ROMS-HAD diverges from the others with a weak increase in dissolved oxygen that extends in the coastal waters from the southern boundary up to ∼40°N (**Figure 3**). Other ecologically important measures of the oxygen environment – bottom oxygen concentration and depth of the hypoxic boundary – show similar changes. While ROMS-GFDL and ROMS-IPSL projections feature a decline of bottom dissolved oxygen on the shelf, which is more intense

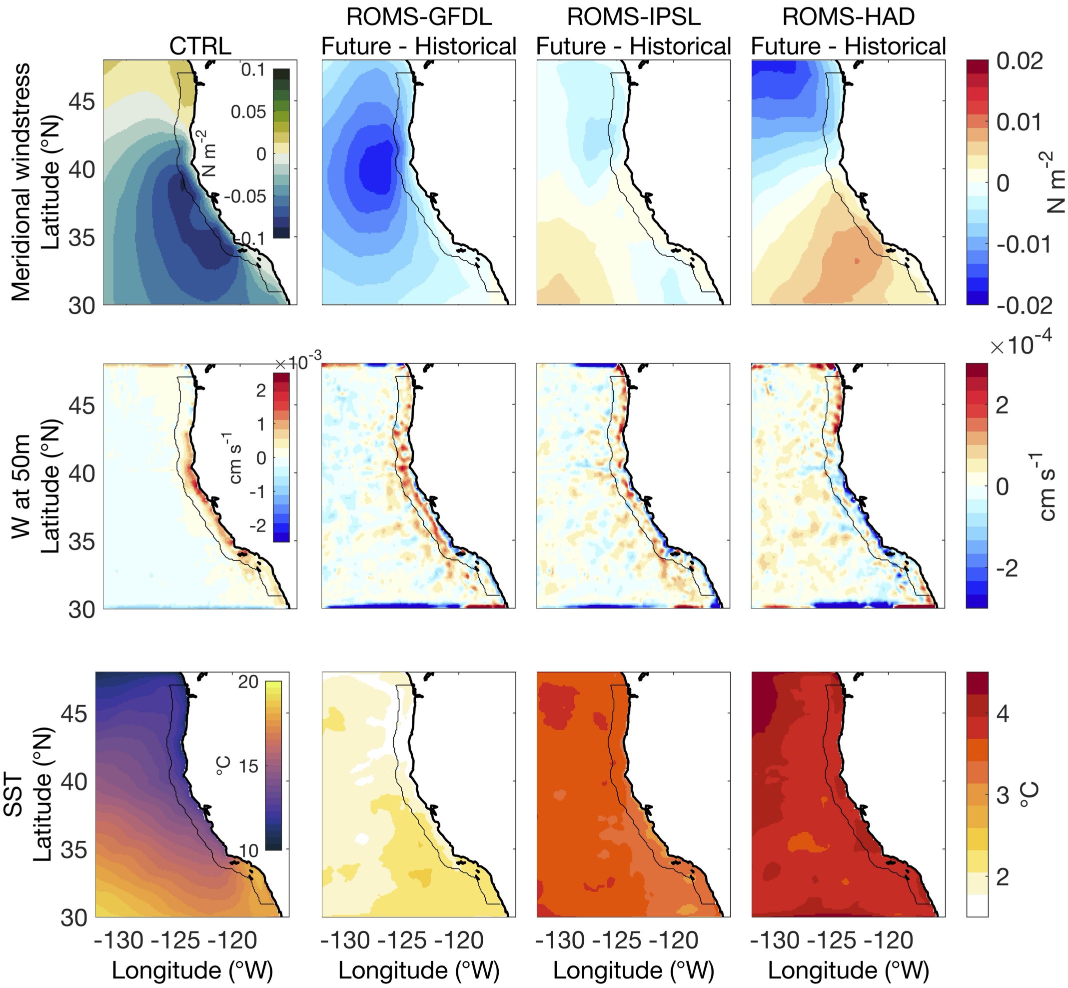

FIGURE 2 | Control run (1980–2010) mean and future changes (2070–2100 relative to historical) for the physical variables. Rows show from top to bottom: meridional wind stress, vertical velocity at 50 m depth (w), and sea surface temperature (SST). Columns show data for the historical period in the control simulation (CTRL, first column) and the future changes from the high-resolution downscaled projections: ROMS-GFDL (second column), ROMS-IPSL (third column), and ROMS-HAD (fourth column). Negative values of wind stress changes correspond to an increase in equatorward wind stress. Black contour marks 100 km from shore. Vertical velocity field has been spatially smoothed out for better representation.

(~50 mmol m^3) in the northern and southern coastal waters, ROMS-HAD projects a weak increase (~25 mmol m^3) of the bottom dissolved oxygen that extends from the southern coastal waters up to 40°N (**Figure 3**). Future changes in depth of the hypoxic boundary layer have a similar spatial pattern as the O_2 at 150 m. The hypoxic boundary, defined here as the depth at which dissolved oxygen = 1.43 ml/l (i.e., 63.86 mmol/m^3), is projected to shoal by up to ~150 m in the offshore waters. Along the coast there is a weak shoaling, up to ~60–70 m, in ROMS-GFDL and ROMS-IPSL, while ROMS-HAD projects changes of similar magnitude but opposite sign off southern and central California (**Figure 3**).

Phytoplankton Biomass

We present total phytoplankton biomass – the sum of NEMUCSC's small (nanophytoplankton) and large (diatoms) phytoplankton groups – in units of chlorophyll concentration, which is estimated from NEMUCSC's nitrogen units using fixed ratios for C:N (106:16) and C:Chl (50:1 and 100:1 for small and large phytoplankton, respectively, Goebel et al., 2010). By the end of the century, ROMS-HAD projects a decrease of surface chlorophyll along the entire coast; ROMS-IPSL projects a weaker decrease along most of the coast but a slight increase in the northern regions; and in contrast, ROMS-GFDL projects an increase centered in in the northern CCS (>39°–45°N), coincident with the region of most pronounced increases in upwelling favorable winds (**Figure 4**). Offshore, ROMS-IPSL and ROMS-HAD project a decrease in surface chlorophyll everywhere, while in ROMS-GFDL surface chlorophyll change is mostly positive north of 35°N. For ROMS-GFDL and ROMS-HAD, projected changes in vertically integrated chlorophyll over the upper 50 m exhibit similar patterns to surface chlorophyll changes. However, for ROMS-IPSL the slight increase in surface chlorophyll in the nearshore northern CCS is offset

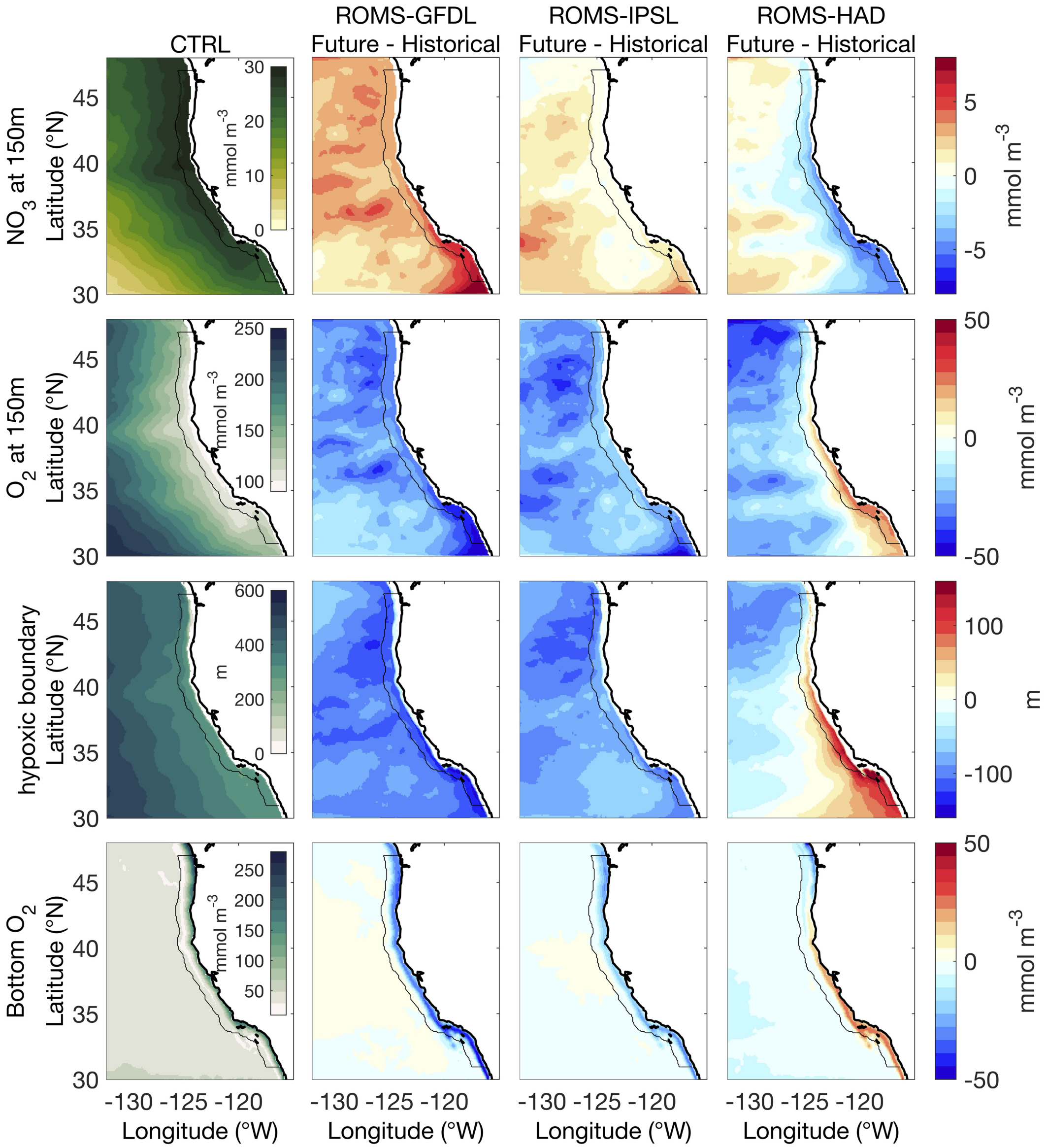

FIGURE 3 | Control run (1980–2010) mean and future changes (2070–2100 relative to historical) for the subsurface biogeochemical variables. Rows show from top to bottom: nitrate (NO_3) and dissolved oxygen at 150 m depth (O_2), depth of 1.43 ml/l (i.e., 63.86 mmol/m^3) O_2 layer, and bottom oxygen. Columns show data for the historical period in the control simulation (CTRL, first) and the future changes from the high-resolution downscaled projections: ROMS-GFDL (second column), ROMS-IPSL (third column), and ROMS-HAD (fourth column). Black contour marks 100 km from shore.

by subsurface chlorophyll decrease such that the upper 50 m integrated chlorophyll is projected to decline (**Figure 4**). In sum, phytoplankton biomass is projected to decline throughout the study domain with the exception of the northern CCS, where enhanced biomass is projected in ROMS-GFDL and ROMS-IPSL, though only for a shallow nearshore layer in the latter.

Vertical Sections

All three downscaled simulations show an overall increase in temperature in the subsurface, with the warming being surface-intensified such that there is also an increase in stratification (i.e., more tightly packed potential density contours or isopycnals) by the end of the century (**Figure 5**). ROMS-HAD and ROMS-IPSL project warming changes up to ∼2°C at 300 m depth, and warming of ∼1°C extends to 500 m or more. As for SST, ROMS-GFDL indicates less subsurface warming than the other two projections, with weak warming in the northern latitudes, almost no change in the southern latitudes, and even a slight cooling of ∼0.5°C around ∼150 m depth in the nearshore southern CCS (32°N; **Figure 5**).

The inter-model consistency of the projected nitrate changes is spatially dependent. All three projections show subsurface increases in nitrate concentration offshore, though ROMS-GFDL shows a stronger increase with greater horizontal and vertical

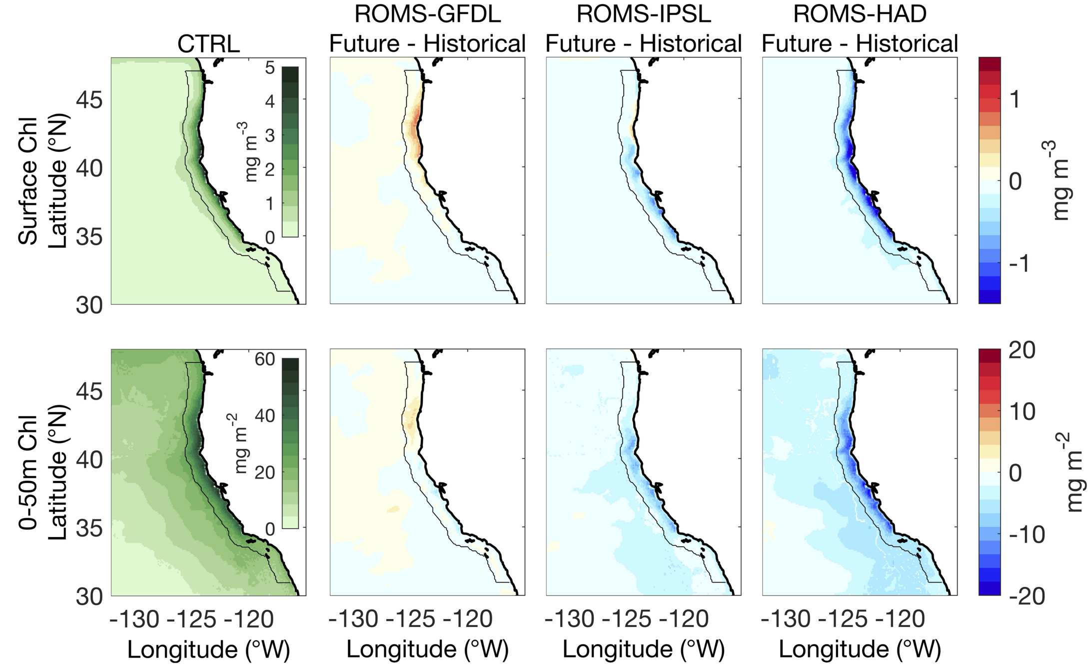

FIGURE 4 | Control run (1980–2010) mean and future changes (2070–2100 relative to historical) for the surface **(top)** and integrated (0–50 m, **bottom**) chlorophyll (Chl). Columns show data for the historical period in the control simulation (CTRL, first) and the future changes from the high-resolution downscaled projections: ROMS-GFDL (second column), ROMS-IPSL (third column), and ROMS-HAD (fourth column). Black contour marks 100 km from shore.

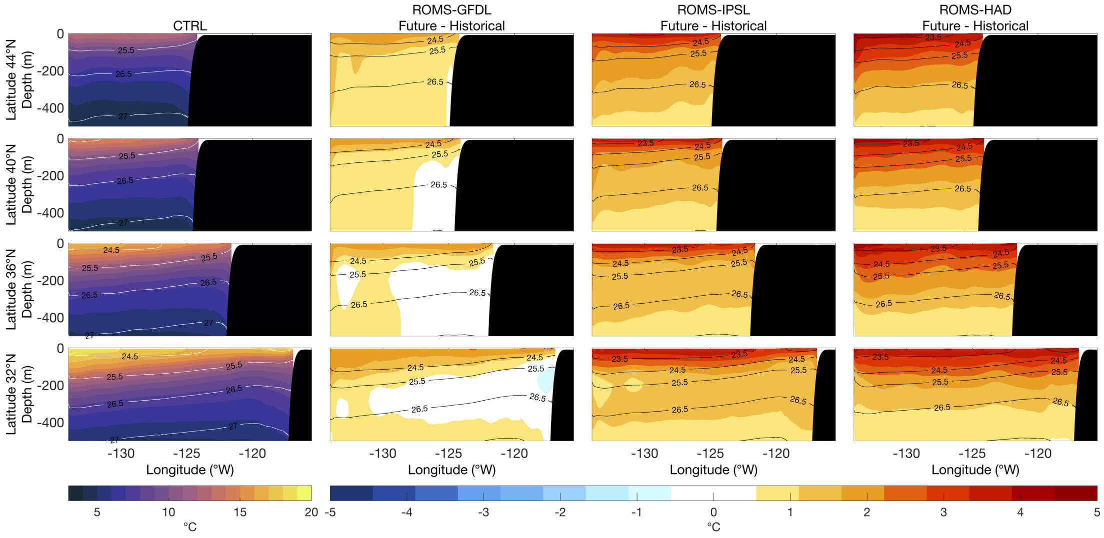

FIGURE 5 | Vertical sections of mean temperature (1980–2010) from the control run (CTRL, first column) and of future temperature changes (2070–2100 relative to historical) from the high-resolution downscaled projections: ROMS-GFDL (second column), ROMS-IPSL (third column), and ROMS-HAD (fourth column). Black contours are potential density (kg m^{-3}) relative to sea surface.

extent compared to the other models (**Figure 6**). However, the changes diverge near the coast. At 32°N and ∼200 m depth, in the core of the California Undercurrent (CU; i.e., ∼26.5 kg m^{-3}), there is an increase of nitrate concentration in ROMS-GFDL but a decrease in ROMS-HAD. In both models, the inshore change in concentration extends north of 32°N, but with reduced magnitude (**Figure 6**). In contrast, ROMS-IPSL exhibits no discernible change in nearshore nitrate concentrations.

The future changes of spatial patterns of dissolved oxygen generally follow those of nitrate concentration with opposite signs (**Figure 7**), though the oxygen declines are more pronounced and widespread than the nitrate increases. There is

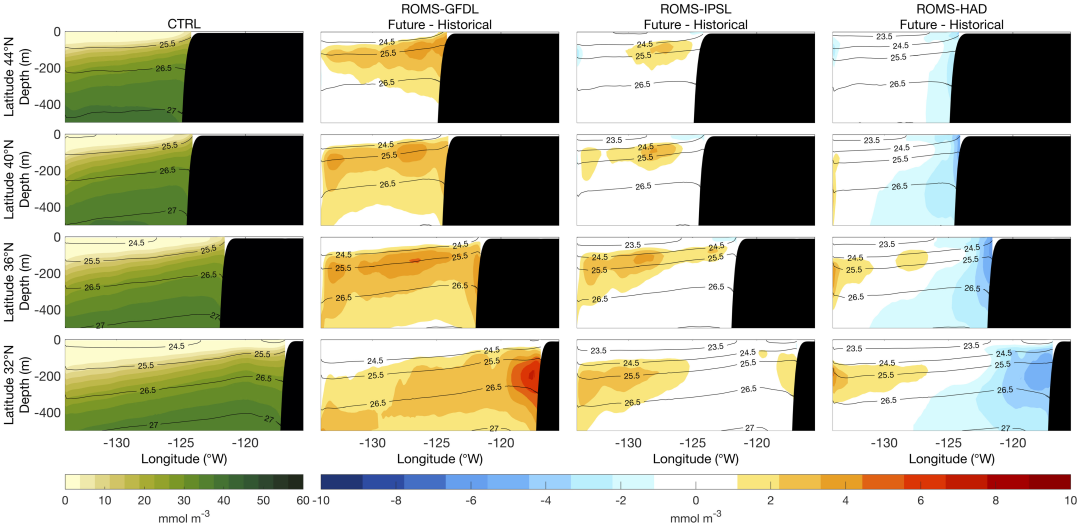

FIGURE 6 | Vertical sections of mean nitrate (1980–2010) from the control run (CTRL, first column) and of future nitrate changes (2070–2100 relative to historical) from the high-resolution downscaled projections: ROMS-GFDL (second column), ROMS-IPSL (third column), and ROMS-HAD (fourth column). Black contours are potential density (kg m^{-3}) relative to sea surface.

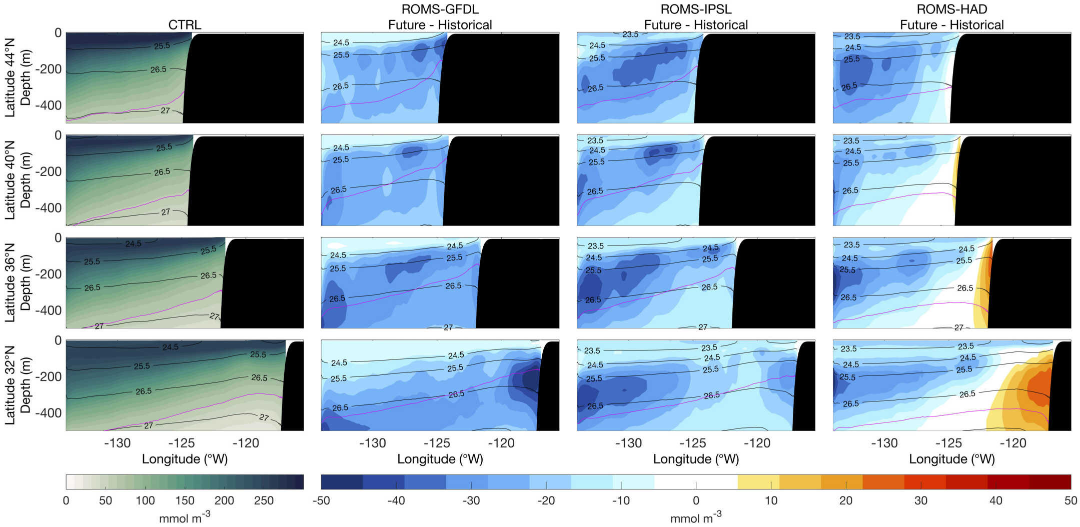

FIGURE 7 | Vertical sections of mean dissolved oxygen (1980–2010) from the control run (CTRL, first column) and of future nitrate changes (2070–2100 relative to historical) from the high-resolution downscaled projections: ROMS-GFDL (second column), ROMS-IPSL (third column), and ROMS-HAD (fourth column). Black contours are potential density (kg m^{-3}) relative to sea surface. Magenta contour corresponds to the hypoxic boundary layer (1.43 ml/l or 63.86 mmol/m^3 O_2).

a strong decrease in dissolved oxygen nearly everywhere in all of the projections, with the most pronounced decreases occurring slightly deeper in the south than in the north. Accompanying the nitrate concentration changes around the core of the CU, ROMS-GFDL and ROMS-IPSL project a decrease in oxygen, which is again stronger in ROMS-GFDL, while ROMS-HAD projects an increase of oxygen in the CU core at 32°N that vanishes quickly to the north. The association of enhanced nitrate and decreased oxygen is consistent with "older" subsurface waters adjacent to the California Current upwelling (e.g., Rykaczewski and Dunne, 2010; waters adjacent to the California Current upwelling have been isolated from the ocean surface for a longer period, allowing more nitrate to accumulate and more oxygen to be lost through aerobic remineralization of sinking organic material).

Coastal Trends and Long-Term Variability

Alongshore Wind Stress

Projections of wind stress across the three simulations share a common meridional pattern with intensification of equatorward (upwelling-favorable) wind stress in the northern CCS and unchanged or slightly weakened winds in the southern and central CCS (**Figure 8**). This pattern is consistent with previous

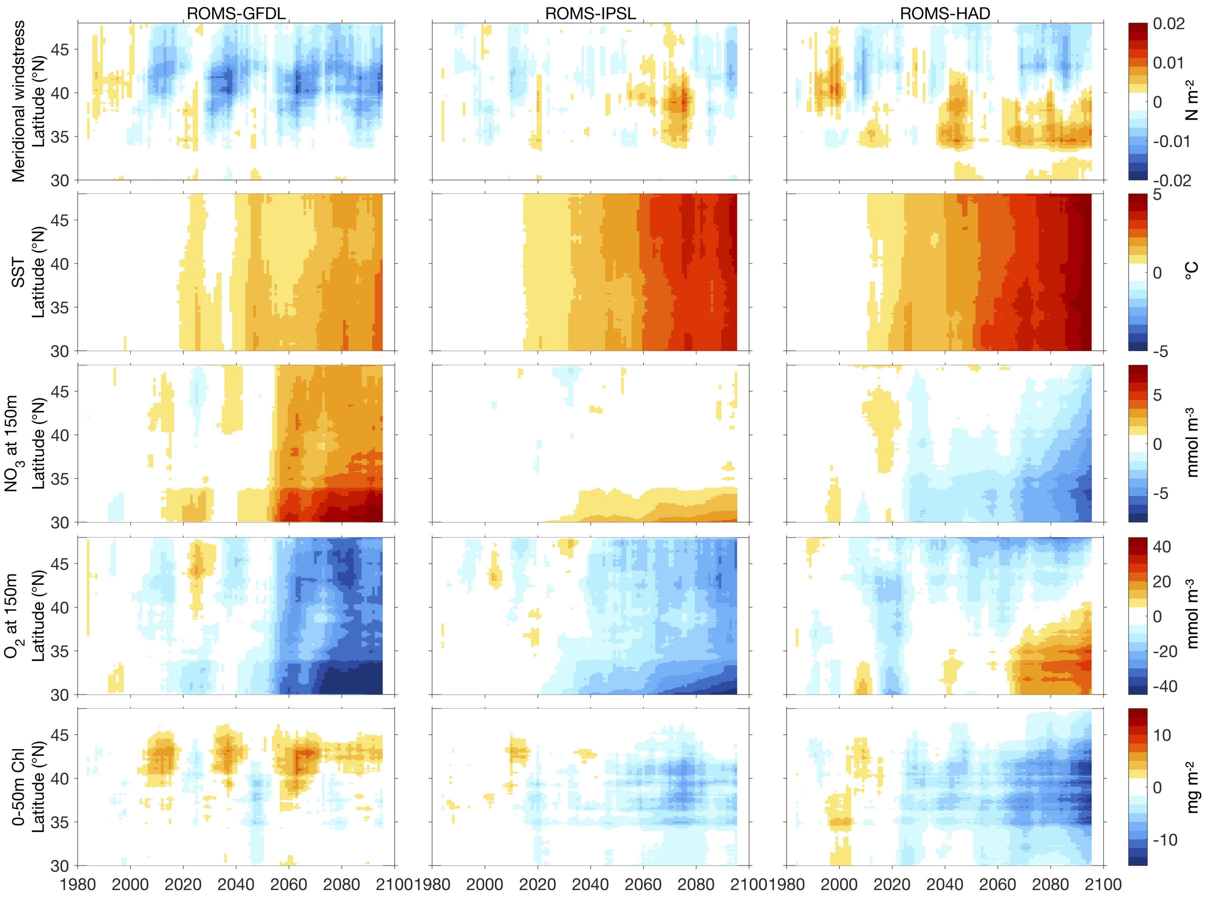

FIGURE 8 | Hovmöller diagrams of 10-year running mean annual anomalies averaged from the coast to 100 km offshore of meridional wind stress (top row), SST (second row), nitrate (third row) and dissolved oxygen (fourth row) at 150 and 0–50 m integrated chlorophyll (bottom row) with respect to the historical period (1980–2010), from the high-resolution downscaled projections: ROMS-GFDL **(left)**, ROMS-IPSL **(center)**, and ROMS-HAD **(right)**.

analysis of CMIP5 models (Rykaczewski et al., 2015), but there are noticeable differences between simulations in the magnitude and timing of change throughout the 21st century. In ROMS-GFDL, the strongest intensification in upwelling favorable winds, centered between 40 and 45°N, becomes apparent by 2030 and persists through the end of the century. ROMS-IPSL shows low frequency variability without strong linear trends; in particular there is a period of considerably weakened upwelling favorable winds north of 35°N from approximately 2060–2080 followed by an intensification from 2080 through the end of the century. The prominence of these signals throughout the projections suggests the influence of decadal variability in this system, which can delay the emergence of anthropogenic upwelling trends until the late 21st century (Brady et al., 2017). ROMS-HAD has a consistent trend of equatorward wind stress intensification in northern latitudes and weakening in southern latitudes, with the division between increasing and decreasing upwelling favorable winds at ∼40°N.

Sea Surface Temperature

Surface ocean warming is one of the most robust ocean responses to climate change, and all three simulations project increases in SST across all latitudes (**Figure 8**). SST continues to increase with time in all simulations, with ROMS-GFDL projecting the weakest increase (∼2.5°C by 2090), ROMS-IPSL projecting a stronger increase (∼4°C by 2090), and ROMS-HAD projecting the strongest increase (∼5°C by 2090). ROMS-GFDL projects slightly stronger warming at southern latitudes, while ROMS-IPSL and ROMS-HAD project nearly uniform warming across the meridional extent of the coastal domain.

Subsurface Nitrate Concentration

Regional Ocean Modeling System-Geophysical Fluid Dynamics Laboratory projects a strong increase in subsurface nitrate concentration, with a trend that emerges from the natural variability (i.e., exceeds 1 standard deviation of the historical variability) by ∼2050 and is strongest from 30° to 35°N (**Figure 8**). ROMS-IPSL exhibits a similar spatial pattern, but with a reduced trend that exceeds decadal variability only in the southern part of the domain and that is inherited from the parent ESM. The nearshore decrease in nitrate concentration in ROMS-HAD emerges clearly in roughly 2060 in the southern latitudes and spreads northward across most of the domain by the end of the century (**Figure 8**).

Subsurface Dissolved Oxygen

Projected dissolved oxygen concentrations generally follow those of the nitrate concentrations, with opposite signs, across all three models (**Figure 8**). The tight coupling between nitrate and oxygen is evident both in the decadal variability and in the long-term trends, though the oxygen trends are even more pronounced. While all three models project a strong decrease in dissolved oxygen, particularly in the northern latitudes, the time when the dissolved oxygen changes becomes prominent differs among models. Trends emerge from the natural variability across all latitudes by ∼2060 and ∼2040 in ROMS-GFDL and ROMS-IPSL, respectively. In ROMS-HAD, an oxygen decrease has already emerged in the northern latitudes (>43°N), while decadal variability remains the dominant signal in the rest of the domain, and beyond 2070, a weak increase in dissolved oxygen emerges in the southern part of the domain, consistent with the decrease of nitrate there.

Vertically Integrated Phytoplankton Biomass

All three models project the main changes in chlorophyll, vertically integrated over 0–50 m, along a latitude band between 35 and 45°N, the most productive portion of the CCS (**Figure 8**). ROMS-HAD and ROMS-IPSL project a chlorophyll decrease starting in ∼2040 and ∼2050, respectively, near 37°N, which strengthens and extends across most of the coastal domain by the end of the century in ROMS-HAD. In contrast, ROMS-GFDL projects an increase of vertically integrated chlorophyll (∼8 mg m^2 that becomes distinct ∼2050), off Northern California and Oregon (∼40–45°N) and a decrease off Central California (∼35–37°N). These changes in ROMS-GFDL are likely driven by both the intensification of the alongshore winds, which increase the upwelling between 40° and 45°N, and the strong increase of the subsurface nitrate concentration. In ROMS-HAD, the negative trends in vertically integrated chlorophyll are largely consistent with trends in the weakening of the upwelling-favorable wind stress and the decrease of subsurface nitrate concentration along the southern (<39°N) CCS coast. However, along the northern (>39°N) CCS coast, these negative trends in chlorophyll indicate that the intensification of alongshore winds cannot offset the depletion of subsurface nitrate. However, the dynamics driving chlorophyll changes are not necessarily straightforward, as phytoplankton biomass can be influenced by changes in upwelling strength, subsurface nutrients, upper ocean stratification, and top-down control by grazers. The relative influence of these potentially competing drivers under historic and future forcing continues to be a topic of interest, which we discuss more in the following section.

Coastal Trends ESMs Comparisons

To highlight the impact of the downscaling process, we compare coastal trends of key ecosystem variables with those of the ESMs (**Figure 9**). All projections show a strong warming of the coastal CCS. SST increases rapidly in the ROMS-IPSL and in ROMS-HAD from the late 2020s, and late 2030s. By the end of the century, SST increases in ROMS-IPSL reach ∼4°C and >3.5°C in the northern and southern CCS, respectively, while in ROMS-HAD warming reaches >4.5°C in both the northern and southern regions. ROMS-GFDL shows a moderate increase in SST, starting later (∼2040), and reaching ∼2°C and >2.5°C, in the northern and southern CCS, respectively, by the end of the century. SST trends in the downscaled projections strongly followed those from the ESMs, resulting in no significant spread between the downscaled projections and their ESMs counterparts. Compared to the evolution of the ROMS-ESM SST means, the SST ESMs exhibit an offset of the trends due to their different bias with respect to the historical period (∼1–2°C, **Supplementary Figure 5**).

Biogeochemical variables in ROMS-ESMs show different signs in the trends along the CCS coast. These changes and their meridional differences in magnitude are consistent with those from ESMs (**Figures 9**, **10**). In ROMS-GFDL and ROMS-HAD, the evolution of subsurface nitrate and oxygen agree more closely with their ESM counterparts. However, the evolution of these anomalies in ROMS-IPSL separate from those in the IPSL, showing a significant intra-model spread especially in the southern coastal region.

Regional Ocean Modeling System-Institut Pierre Simon Laplace and ROMS-HAD depict a moderate and a strong decline of coastal chlorophyll along the coast, reaching −0.5 and −10 mg m^{-2} by the end of the century, respectively. Meanwhile, ROMS-GFDL depicts a moderate increase of chlorophyll in the northern CCS coast. The evolution of the ROMS-GFDL chlorophyll trends agrees more closely with those from GFDL, showing a pronounced decadal variability. However, ROMS-IPSL and ROMS-HAD show a larger spread in chlorophyll with respect to their counterparts. While anomalies of chlorophyll in IPSL remain unchanged during the century, the chlorophyll in ROMS-ISPL declines, showing larger variability than the chlorophyll projection in IPSL (**Figure 9**).

Because of the inherent ESM bias with respect to the historical period, the evolution of the mean values of the biogeochemical variables also exhibit an offset compared to those in the ROMS-ESMs. Offset magnitudes are larger in subsurface nitrate and oxygen in GFDL and IPSL, while chlorophyll offset is larger in HAD (**Supplementary Figure 5**).

DISCUSSION

We used a coupled physical-biogeochemical model (ROMS-NEMUCSC) at 0.1-degree (∼10 km) resolution to produce downscaled projections of climate change in CCS from 1980 to 2100 under the high emissions RCP8.5 scenario. To capture the spread of projections, we selected three ESMs, GFDL-ESM2M, HadGEM2-ES, and IPSL-CM5A-MR, that span the CMIP5 range for future changes in both the mean and variance of physical and biogeochemical CCS properties. The downscaled runs provide information on potential future physical and biogeochemical states in the CCS at higher resolution than those available from current generation ESMs. More importantly, they provide insight into which future changes are robust (i.e., with different projections agreeing on the sign of change, if not the magnitude) and which are uncertain even in a qualitative sense (i.e., when models diverge on the sign of changes). They also illustrate

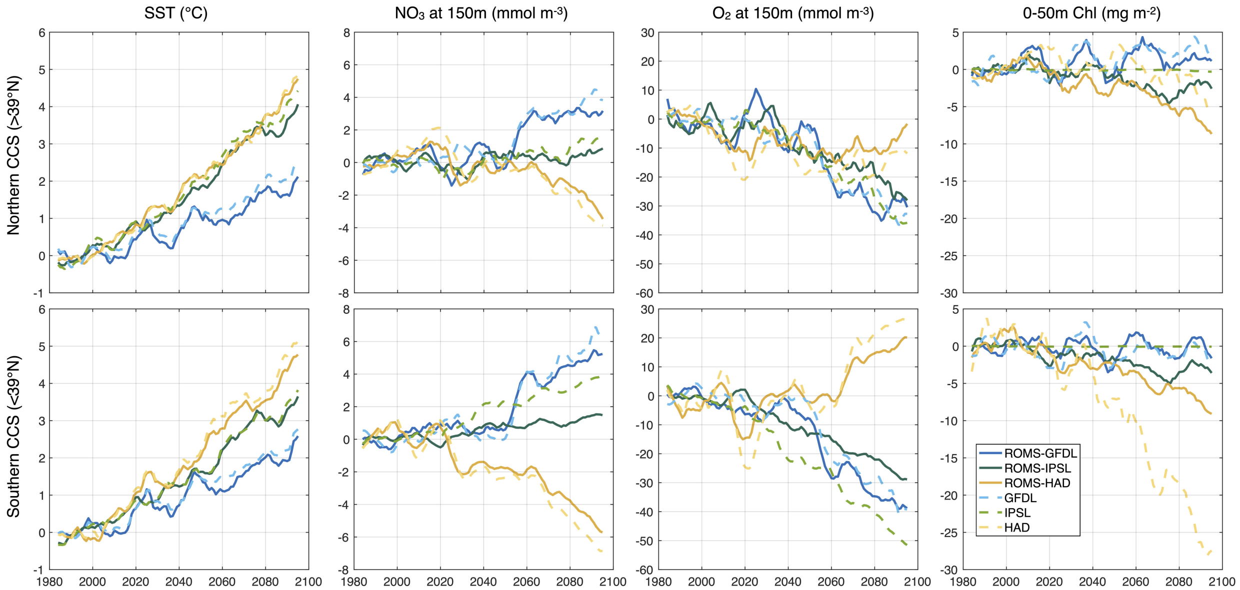

FIGURE 9 | From left to right time series of yearly averaged anomalies with respect to the historical period averaged from the coast to 100 km offshore of SST, NO_3 and O_2 at 150 and 0–50 m vertically integrated chlorophyll for the northern (**top**, >39°N) and southern (**bottom**, <39°N) CCS.

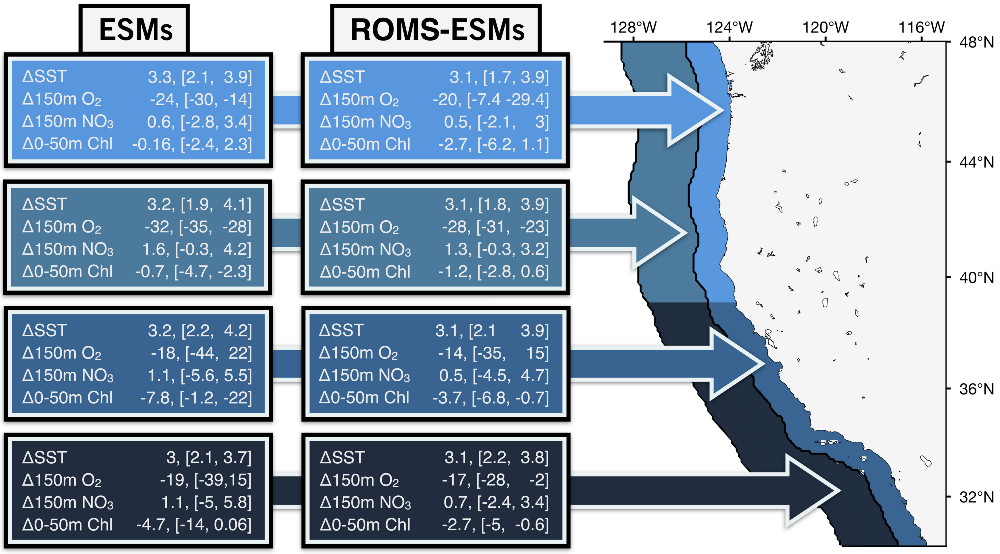

	ESMs	ROMS-ESMs
ΔSST	3.3, [2.1, 3.9]	3.1, [1.7, 3.9]
Δ150m O_2	-24, [-30, -14]	-20, [-7.4 -29.4]
Δ150m NO_3	0.6, [-2.8, 3.4]	0.5, [-2.1, 3]
Δ0-50m Chl	-0.16, [-2.4, 2.3]	-2.7, [-6.2, 1.1]
ΔSST	3.2, [1.9, 4.1]	3.1, [1.8, 3.9]
Δ150m O_2	-32, [-35, -28]	-28, [-31, -23]
Δ150m NO_3	1.6, [-0.3, 4.2]	1.3, [-0.3, 3.2]
Δ0-50m Chl	-0.7, [-4.7, -2.3]	-1.2, [-2.8, 0.6]
ΔSST	3.2, [2.2, 4.2]	3.1, [2.1 3.9]
Δ150m O_2	-18, [-44, 22]	-14, [-35, 15]
Δ150m NO_3	1.1, [-5.6, 5.5]	0.5, [-4.5, 4.7]
Δ0-50m Chl	-7.8, [-1.2, -22]	-3.7, [-6.8, -0.7]
ΔSST	3, [2.1, 3.7]	3.1, [2.2, 3.8]
Δ150m O_2	-19, [-39,15]	-17, [-28, -2]
Δ150m NO_3	1.1, [-5, 5.8]	0.7, [-2.4, 3.4]
Δ0-50m Chl	-4.7, [-14, 0.06]	-2.7, [-5, -0.6]

FIGURE 10 | Schematic table summarizing the main physical and biogeochemical variables future changes for the period (2070–2100), from the ESMs **(left)** and ROMS-ESMs **(right)** projections for the nearshore (from a distance of 100 km to the coast) and offshore (from 100 to 300 km) for the northern and southern CCS coast. The variables listed are: SST (°C), NO_3 and O_2 at 150 (mmol/m^3) and 0–50 m vertically integrated chlorophyll (mg/m^2). For each variable, the mean change and inter-model range change during the period are shown.

benefits and limitations of dynamical downscaling in the context of climate change projection. We discuss these points below.

Similarities and Differences Among ESM-Driven ROMS Projections

All three downscaled models show an overall intensification of the meridional wind stress (i.e., equatorward wind stress or upwelling-favorable winds) in the northern part of the domain (>40°N), consistent with previous work (Rykaczewski et al., 2015; Wang et al., 2015; Xiu et al., 2018), with ROMS-IPSL showing the weakest intensification and ROMS-GFDL the strongest. In the southern region, ROMS-GFDL and ROMS-IPSL show a weaker intensification of the upwelling-favorable wind stress, while ROMS-HAD projects a weakening wind stress. Although, ROMS-GFDL and ROMS-IPSL simulations project an intensification of the upwelling-favorable wind stress for the last thirty years of the end of the century, ROMS-IPSL projects a weakening of the meridional wind stress in coastal waters from approximately 2060–2080. Since low frequency variability in the dynamically downscaled surface winds remains dependent on the overlying larger-scale wind, this period of winds stress relaxation along the CCS coast in ROMS-IPSL may reflect variability in the North Pacific represented by the ESM model parent IPSL. Further analysis demonstrates that decadal-scale variability in upwelling-favorable wind stress in all three models is correlated with basin-scale climate oscillations (i.e., the Pacific Decadal Oscillation, PDO; Mantua et al., 1997). For example, weakened upwelling-favorable wind stress in ROMS-IPSL during 2050–2080 occurs during a positive phase of the PDO (**Supplementary Figures 6, 7**, and **Supplementary Table 1**). Without careful assessment, an analysis of the projections from ROMS-IPSL for this particular and short period of time (i.e., 2060–2080) could lead to misattributing this signal to anthropogenic climate change instead of natural climate variability (e.g., Deser et al., 2012). Thus, it is important to consider the simulation's full transient period, or longer time-scales projections, as recommended in the downscaling protocols by Drenkard et al. (in review). It also justifies our approach of using a time-varying delta method to generate the downscaled projections.

In the subsurface offshore, the three ESM-driven ROMS simulations project similar enrichment of nitrate and a decrease in dissolved oxygen as well as a shoaling of the hypoxic boundary layer, all of which follow their ESM counterparts. In the coastal regions, ROMS-GFDL and ROMS-IPSL biogeochemical responses are similar in sign and aligned to those off the coast, featuring an average of ∼30–40% increase/decrease of subsurface nitrate/dissolved oxygen, ∼25% reduction of bottom oxygen on the shelf, and a ∼50 m shallower hypoxic boundary layer. ROMS-HAD projects a different response featuring a decrease of subsurface nitrate (∼20%) that by 2070 extends along the entire coast, an increase of subsurface oxygen (30%) in the southern region that extends to the bottom of the shelf, and a deepening of the hypoxic boundary layer by ∼30 m. Changes in subsurface nitrate and oxygen in our ROMS projections are largely consistent with recent downscaling studies that include these ESMs (Xiu et al., 2018; Howard et al., 2020a). One exception is subsurface oxygen in ROMS-HAD along the coast, for which we find an increase in oxygen coupled to the decrease in subsurface nitrate. Howard et al. (2020a) find that subsurface oxygen decreases in their downscaled HAD projection, though that decrease is much weaker than in their GFDL and IPSL projections. A plausible explanation for this may be associated with the downscaling method and/or the specific ensemble member from HAD used to force the high-resolution projections.

Changes in nutrient concentrations and nutrient ratios have already been observed in upwelling source waters of the CCS (e.g., Bograd et al., 2015). ROMS-GFDL and ROMS-IPSL projected trends in nitrate enrichment and deoxygenation are consistent with previous studies that suggest that biogeochemical changes in upwelling source waters could be a first order effect in changes in the biogeochemistry of the CCS, with the decrease in ventilation of North Pacific interior waters, increase in stratification and the subsequent deepening of the isopycnals, being the proposed driving mechanisms (Rykaczewski and Dunne, 2010; Xiu et al., 2018; Dussin et al., 2019; Howard et al., 2020a). Moreover, deoxygenation of the upwelling source waters is the main driver of changes in hypoxia and expansion of hypoxic areas on the shelf (Dussin et al., 2019). Under the future RCP8.5 scenario, HAD and IPSL project relatively small changes of Equatorial Undercurrent (EUC) transport compared to GFDL, accompanied by a slight compression of the oxygen minimum zones (OMZ) in the former and expansion in the latter (Shigemitsu et al., 2017). These models' biases (i.e., representation of the EUC) and discrepancies in the future projections of the complex equatorial dynamics and the OMZ (Cabré et al., 2015; Busecke et al., 2019) could explain the diverse trends in the downscaled projections. The strong decrease of subsurface oxygen near the southern boundary projected by ROMS-GFDL might be associated with the weakening of the EUC and transport of older waters (i.e., less oxygen and higher nutrient concentrations) into the CCS from the south. In contrast, the increase of subsurface oxygen in the projected ROMS-HAD might be related to the compression of the OMZ and the transport of younger waters to the CCS. Future changes in the equatorial dynamics and their connections to the CCS source waters will be explored in future work.

The projected enrichment of nutrients in subsurface waters, combined with increased upwelling caused by the intensification of the meridional wind stress, could be the driving mechanisms for increases in the phytoplankton biomass of ∼50% in ROMS-GFDL. Enrichment of nutrients near the depth of upwelled source waters may increase primary productivity in the CCS (Rykaczewski and Dunne, 2010), but our results suggest that the increase in productivity is reinforced by the intensification of upwelling favorable winds projected to occur in the northern coastal CCS in ROMS-GFDL. Conversely, nutrient-poor source waters combined with the weakening of upwelling winds (15–18%) likely drive the projected strong decrease of chlorophyll (∼50%) in the coastal CCS by ROMS-HAD. This differing response of ROMS-HAD could come from inheriting the large-scale biogeochemical changes in HAD that propagate through the CCS boundaries.

All the models show that future ocean warming in the CCS is surface intensified, indicating enhanced stratification (**Figure 5** and **Supplementary Figure 8**). In the coastal domain, ROMS-GFDL and ROMS-IPSL project the larger stratification and reduced (i.e., shallower) MLD around ∼34–40°N (between Point Conception and Cape Mendocino), while ROMS-HAD projects a weaker stratification and less shoaling of the MLD in that region (**Supplementary Figure 8**). Increased stratification can potentially counteract the effect of intensifying winds and source water nutrient enrichment by limiting the nutrient flux to the mixed layer and decreasing PP (Di Lorenzo et al., 2005; García-Reyes et al., 2015; Jacox et al., 2015). Thus, enhanced stratification, in combination with weakened upwelling-favorable winds, could explain why phytoplankton biomass decreases are projected in the southern CCS by ROMS-GFDL and along most of the coast by ROMS-IPSL despite increasingly nutrient-rich subsurface waters. The uncertainty related to the interplay between the thermal stratification and intensification of upwelling winds should be explored further.

Impact of Regional Downscaling

Given the added effort, computational cost, and storage required associated with dynamical downscaling, it is worth considering the added benefit relative to the uncertainties in the parent model forcing. We compared the ROMS projections with those from their ESM counterparts and showed that both SST and chlorophyll trends are qualitatively consistent between ROMS simulations and their ESM parents (**Figure 9**). ROMS-ESM SST changes follow those of their ESM parents closely in magnitude, producing a similar range of the uncertainties. From the ESM parent models, GFDL and IPSL agree on the sign of the NPP and surface chlorophyll change (i.e., increasing through the century), while the CMIP5 ensemble mean projects declines in NPP in this region with the same sign trend as HadGEM2-ES, but with much smaller magnitude (**Figure 1**). Along the CCS coast, ROMS-GFDL and ROMS-HAD also agree on the trend sign and the latitudinal expressions of the chlorophyll changes compared to their ESM parents, but not in the magnitude in the latter. On the other hand, ROMS-IPSL projects a clear negative trend in chlorophyll while the trend in IPSL is weaker (**Figure 9** and **Supplementary Figure 9**). Differences in the sign and magnitude of the trends might be related to non-linear interactions in the biogeochemistry as a response to the upwelling dynamics that are better resolved in the downscaled models. Compared to the SST changes, some ROMS-ESM biogeochemical changes largely differ in magnitude from their ESM parents, producing larger intra-model spread in particular between ROMS-HAD and HAD in chlorophyll, and ROMS-IPSL and IPSL in subsurface nitrate and oxygen. However, there is an overall reduction of the uncertainty of the biogeochemistry projections in the ROMS-ESMs, likely due to using the same biogeochemical model and parameterization for all three downscaled simulations. A summary of these main physical and biogeochemical changes in the CCS is shown in **Figure 10**.

The larger biogeochemical differences between ROMS simulations and their ESM parent models illustrate the impact of regional downscaling's ability to resolve local processes impacting productivity (Echevin et al., 2020). Various factors may explain why biogeochemical variables are more sensitive to regional downscaling than physical variables: (1) high-spatial resolution for the circulation is needed to simulate upwelling dynamics and their ecosystem responses; (2) complex nonlinear interactions occur between the physical changes and ecosystem responses; and (3) the formulation of the biogeochemical component varies among ESMs and is different than NEMUCSC, which has been specifically calibrated for the CCS.

CONCLUDING REMARKS

The high-resolution downscaled projections presented here belong to a broader end-to-end modeling project (Future Seas[2]) that integrates climate, biogeochemical, ecosystem, and socioeconomic models to evaluate the impacts of climate change in the CCS and evaluate fisheries management strategies under projected future conditions. The regional ocean models provide the physical and biogeochemical foundation for higher trophic level models of various types, including individual based models and species distribution models (Smith et al., 2021), highlighting the utility of high-resolution projections for regional marine resource applications. However, given that differences between downscaled models and their ESM parents can be small relative to the differences between ESMs, any specific application should consider the value of dynamical downscaling in the context of other sources of uncertainty. Until large ensembles of eddy-resolving global or regional models are computationally feasible, we suggest that a fruitful approach is to combine coarser resolution large ensembles with dynamical downscaling of select runs informed by analyses like the one presented here to assess how representative basin-scale changes are translated to shelf-scale responses.

DATA AVAILABILITY STATEMENT

The regional model output is available on request from the corresponding author. CMIP5 model output is available through a distributed data archive developed and operated by the Earth System Grid Federation data portal (ESGF, https://esgf-node.llnl.gov/search/cmip5/). ERA-5, the fifth generation of ECMWF atmospheric reanalyses of the global climate, is available from the Copernicus Climate Change Service Climate Data Store website (https://cds.climate.copernicus.eu/cdsapp#!/home). The Cross-Calibrated Multi-Platform (CCMP) wind vector analysis product version 1.1 is available from (http://www.remss.com/measurements/ccmp/). NOAA High Resolution SST data by the NOAA/OAR/ESRL PSL, Boulder, Colorado, USA is available from their website https://psl.noaa.gov/. Sea-viewing Wide Field-of-view Sensor (SeaWiFS) chlorophyll data from the NASA Goddard Space Flight Center, Ocean Ecology Laboratory, Ocean Biology Processing Group is available from their website https://oceancolor.gsfc.nasa.gov/data/seawifs/. Finally, World Ocean Atlas database series are derived from the Word Ocean Database, and are available from https://www.nodc.noaa.gov/OC5/indprod.html.

AUTHOR CONTRIBUTIONS

MPB and MGJ designed the research. MPB and MAA downscaled the ESM models. MPB conducted the physical

---

[2] https://future-seas.com

variables projections, and analyzed the data. JF produced the biogeochemical variables projections. MPB, MGJ, JF, MAA, SJB, ENC, CAE, RRR, and CAS wrote the manuscript.

FUNDING

This work was supported by a grant from the National Atmospheric and Oceanic Administration (NOAA) CPO Coastal and Climate Applications (COCA) program and the NOAA Fisheries Office of Science and Technology (NA17OAR4310268).

ACKNOWLEDGMENTS

Many thanks to Isaac Schroeder and Liz Drenkard for helpful comments on an earlier version of the manuscript.

SUPPLEMENTARY MATERIAL

The Supplementary Material for this article can be found online at: https://www.frontiersin.org/articles/10.3389/fmars.2021.612874/full#supplementary-material

REFERENCES

Alexander, M. A., Shin, S. -i., Scott, J. D., Curchitser, E., and Stock, C. (2019). The response of the northwest atlantic ocean to climate change. *J. Climate* 33, 405–428. doi: 10.1175/jcli-d-19-0117.1

Alin, S. R., Feely, R. A., Dickson, A. G., Hernández-Ayón, J. M., Juranek, L. W., Ohman, M. D., et al. (2012). Robust empirical relationships for estimating the carbonate system in the southern California current system and application to CalCOFI hydrographic cruise data (2005–2011). *J. Geophys. Res.* 117:C05033. doi: 10.1029/2011jc007511

Arellano, B., and Rivas, D. (2019). Coastal upwelling will intensify along the Baja California coast under climate change by mid-21st century: insights from a GCM-nested physical-NPZD coupled numerical ocean model. *J. Mar. Syst.* 199:103207. doi: 10.1016/j.jmarsys.2019.103207

Arora, V. K., Boer, G. J., Friedlingstein, P., Eby, M., Jones, C. D., Christian, J. R., et al. (2013). Carbon–Concentration and carbon–climate feedbacks in CMIP5 earth system models. *J. Climate* 26, 5289–5314. doi: 10.1175/jcli-d-12-00494.1

Arora, V. K., Katavouta, A., Williams, R. G., Jones, C. D., Brovkin, V., Friedlingstein, P., et al. (2020). Carbon–concentration and carbon–climate feedbacks in CMIP6 models and their comparison to CMIP5 models. *Biogeosciences* 17, 4173–4222. doi: 10.5194/bg-17-4173-2020

Atlas, R., Hoffman, R. N., Ardizzone, J., Leidner, S. M., Jusem, J. C., Smith, D. K., et al. (2011). A cross-calibrated, multiplatform ocean surface wind velocity product for meteorological and oceanographic applications. *Bull. Am. Meteorol. Soc.* 92, 157–174. doi: 10.1175/2010bams2946.1

Auad, G., Miller, A., and Di Lorenzo, E. (2006). Long-term forecast of oceanic conditions off California and their biological implications. *J. Geophys. Res.* 111:C09008. doi: 10.1029/2005jc003219

Bakun, A. (1990). Global climate change and intensification of coastal ocean upwelling. *Science* 247, 198–201. doi: 10.1126/science.247.4939.198

Bakun, A., Black, B. A., Bograd, S. J., Garcia-Reyes, M., Miller, A. J., Rykaczewski, R. R., et al. (2015). Anticipated effects of climate change on coastal upwelling ecosystems. *Curr. Climate Change Rep.* 1, 85–93. doi: 10.1007/s40641-015-0008-4

Bakun, A., Field, D. B., Redondo-Rodriguez, A., and Weeks, S. J. (2010). Greenhouse gas, upwelling-favorable winds, and the future of coastal ocean upwelling ecosystems. *Global Change Biol.* 16, 1213–1228. doi: 10.1111/j.1365-2486.2009.02094.x

Bograd, S. J., Buil, M. P., Lorenzo, E. D., Castro, C. G., Schroeder, I. D., Goericke, R., et al. (2015). Changes in source waters to the Southern California Bight. *Deep Sea Res. Part II Top. Stud. Oceanogr.* 112, 42–52. doi: 10.1016/j.dsr2.2014.04.009

Bograd, S. J., Schroeder, I. D., and Jacox, M. G. (2019). A water mass history of the Southern California current system. *Geophys. Res. Lett.* 46, 6690–6698. doi: 10.1029/2019gl082685

Bonino, G., Di Lorenzo, E., Masina, S., and Iovino, D. (2019). Interannual to decadal variability within and across the major Eastern Boundary Upwelling Systems. *Sci. Rep.* 9:19949. doi: 10.1038/s41598-019-56514-8

Bopp, L., Resplandy, L., Orr, J. C., Doney, S. C., Dunne, J. P., Gehlen, M., et al. (2013). Multiple stressors of ocean ecosystems in the 21st century: projections with CMIP5 models. *Biogeosciences* 10, 6225–6245. doi: 10.5194/bg-10-6225-2013

Boville, B. A., and Gent, P. R. (1998). The NCAR climate system model, version One*. *J. Climate* 11, 1115–1130. doi: 10.1175/1520-04421998011<1115:Tncsmv<2.0.Co;2

Brady, R. X., Alexander, M. A., Lovenduski, N. S., and Rykaczewski, R. R. (2017). Emergent anthropogenic trends in California current upwelling. *Geophys. Res. Lett.* 44, 5044–5052. doi: 10.1002/2017gl072945

Bruyère, C. L., Done, J. M., Holland, G. J., and Fredrick, S. (2014). Bias corrections of global models for regional climate simulations of high-impact weather. *Clim. Dyn.* 43, 1847–1856. doi: 10.1007/s00382-013-2011-6

Busecke, J. J. M., Resplandy, L., and Dunne, J. P. (2019). The equatorial undercurrent and the oxygen minimum zone in the Pacific. *Geophys. Res. Lett.* 46, 6716–6725. doi: 10.1029/2019gl082692

Cabré, A., Marinov, I., Bernardello, R., and Bianchi, D. (2015). Oxygen minimum zones in the tropical Pacific across CMIP5 models: mean state differences and climate change trends. *Biogeosciences* 12, 5429–5454. doi: 10.5194/bg-12-5429-2015

Capet, X. J., Marchesiello, P., and McWilliams, J. C. (2004). Upwelling response to coastal wind profiles. *Geophys. Res. Lett.* 31:L13311. doi: 10.1029/2004gl020123

Capotondi, A., Alexander, M. A., Bond, N. A., Curchitser, E. N., and Scott, J. D. (2012). Enhanced upper ocean stratification with climate change in the CMIP3 models. *J. Geophys. Res. Oceans* 117:C04031. doi: 10.1029/2011jc007409

Carton, J. A., and Giese, B. S. (2008). A reanalysis of Ocean climate using simple Ocean data assimilation (SODA). *Month. Weath. Rev.* 136, 2999–3017. doi: 10.1175/2007mwr1978.1

Checkley, D. M., and Barth, J. A. (2009). Patterns and processes in the California current system. *Progr. Oceanogr.* 83, 49–64. doi: 10.1016/j.pocean.2009.07.028

Cheresh, J., and Fiechter, J. (2020). Physical and biogeochemical drivers of alongshore pH and oxygen variability in the California current system. *Geophys. Res. Lett.* 47:e2020GL089553. doi: 10.1029/2020gl089553

Cheung, W. W. L., Frölicher, T. L., Asch, R. G., Jones, M. C., Pinsky, M. L., Reygondeau, G., et al. (2016). Building confidence in projections of the responses of living marine resources to climate change. *ICES J. Mar. Sci.* 73:fsv250. doi: 10.1093/icesjms/fsv250

Chhak, K., and Di Lorenzo, E. (2007). Decadal variations in the California Current upwelling cells. *Geophys. Res. Lett.* 34:203. doi: 10.1029/2007gl030203

Collins, W. J., Bellouin, N., Doutriaux-Boucher, M., Gedney, N., Halloran, P., Hinton, T., et al. (2011). Development and evaluation of an Earth-System model – HadGEM2. *Geosci. Model Dev.* 4, 1051–1075. doi: 10.5194/gmd-4-1051-2011

Deser, C., Knutti, R., Solomon, S., and Phillips, A. S. (2012). Communication of the role of natural variability in future North American climate. *Nat. Climate Change* 2, 775–779. doi: 10.1038/nclimate1562

Di Lorenzo, E., Miller, A. J., Schneider, N., and McWilliams, J. C. (2005). The warming of the California current system: dynamics and ecosystem implications. *J. Phys. Oceanogr.* 35, 336–362. doi: 10.1175/jpo-2690.1

Doney, S. C., Ruckelshaus, M., Emmett Duffy, J., Barry, J. P., Chan, F., English, C. A., et al. (2012). Climate change impacts on marine ecosystems. *Ann. Rev. Mar. Sci.* 4, 11–37. doi: 10.1146/annurev-marine-041911-111611

Dufresne, J. L., Foujols, M. A., Denvil, S., Caubel, A., Marti, O., Aumont, O., et al. (2013). Climate change projections using the IPSL-CM5 Earth System Model: from CMIP3 to CMIP5. *Clim. Dyn.* 40, 2123–2165. doi: 10.1007/s00382-012-1636-1

Dunne, J. P., John, J. G., Adcroft, A. J., Griffies, S. M., Hallberg, R. W., Shevliakova, E., et al. (2012). GFDL's ESM2 global coupled climate–carbon earth system models. Part I: physical formulation and baseline simulation characteristics. *J. Climate* 25, 6646–6665. doi: 10.1175/jcli-d-11-00560.1

Dussin, R., Curchitser, E. N., Stock, C. A., and Van Oostende, N. (2019). Biogeochemical drivers of changing hypoxia in the California current ecosystem. *Deep Sea Res. Part II Top. Stud. Oceanogr.* 169–170:104590. doi: 10.1016/j.dsr2.2019.05.013

Echevin, V., Gévaudan, M., Espinoza-Morriberón, D., Tam, J., Aumont, O., Gutierrez, D., et al. (2020). Physical and biogeochemical impacts of RCP8.5 scenario in the Peru upwelling system. *Biogeosciences* 17, 3317–3341. doi: 10.5194/bg-17-3317-2020

Echevin, V., Goubanova, K., Belmadani, A., and Dewitte, B. (2012). Sensitivity of the Humboldt Current system to global warming: a downscaling experiment of the IPSL-CM4 model. *Clim. Dyn.* 38, 761–774. doi: 10.1007/s00382-011-1085-2

Eyring, V., Cox, P. M., Flato, G. M., Gleckler, P. J., Abramowitz, G., Caldwell, P., et al. (2019). Taking climate model evaluation to the next level. *Nat. Clim. Change* 9, 102–110. doi: 10.1038/s41558-018-0355-y

Fairall, C. W., Bradley, E. F., Godfrey, J. S., Wick, G. A., Edson, J. B., and Young, G. S. (1996a). Cool-skin and warm-layer effects on sea surface temperature. *J. Geophys. Res. Oceans* 101, 1295–1308. doi: 10.1029/95jc03190

Fairall, C. W., Bradley, E. F., Rogers, D. P., Edson, J. B., and Young, G. S. (1996b). Bulk parameterization of air-sea fluxes for tropical Ocean-global atmosphere coupled-ocean atmosphere response experiment. *J. Geophys. Res. Oceans* 101, 3747–3764. doi: 10.1029/95jc03205

Feely, R. A., Alin, S. R., Carter, B., Bednaršek, N., Hales, B., Chan, F., et al. (2016). Chemical and biological impacts of ocean acidification along the west coast of North America. *Estuar. Coast. Shelf Sci.* 183, 260–270. doi: 10.1016/j.ecss.2016.08.043

Fiechter, J., Edwards, C. A., and Moore, A. M. (2018). Wind, circulation, and topographic effects on alongshore phytoplankton variability in the California current. *Geophys. Res. Lett.* 45, 3238–3245. doi: 10.1002/2017gl076839

Fiechter, J., Santora, J. A., Chavez, F., Northcott, D., and Messié, M. (2020). Krill hotspot formation and phenology in the california current ecosystem. *Geophys. Res. Lett.* 47:e2020GL088039. doi: 10.1029/2020gl088039

Franco, A. C., Gruber, N., Frölicher, T. L., and Kropuenske Artman, L. (2018). Contrasting impact of future CO2 emission scenarios on the extent of CaCO3 mineral undersaturation in the humboldt current system. *J. Geophys. Res. Oceans* 123, 2018–2036. doi: 10.1002/2018jc013857

Friedlingstein, P., Cox, P., Betts, R., Bopp, L., von Bloh, W., Brovkin, V., et al. (2006). Climate–carbon cycle feedback analysis: results from the C4MIP model intercomparison. *J. Clim.* 19, 3337–3353. doi: 10.1175/jcli3800.1

Frölicher, T. L., Rodgers, K. B., Stock, C. A., and Cheung, W. W. L. (2016). Sources of uncertainties in 21st century projections of potential ocean ecosystem stressors. *Glob. Biogeochem. Cycles* 30, 1224–1243. doi: 10.1002/2015gb005338

Garcia, H. E., Boyer, T. P., Locarnini, R. A., Antonov, J. I., Mishonov, A. V., Baranova, O. K., et al. (2013a). *World Ocean Atlas 2013. Volume 3, Dissolved Oxygen, Apparent Oxygen Utilization, and Oxygen Saturation [Atlas]. (NOAA Atlas NESDIS; 75)*. Washington, DC: U.S. Government Printing Office. doi: 10.7289/V5XG9P2W

Garcia, H. E., Locarnini, R. A., Boyer, T. P., Antonov, J. I., Baranova, O. K., Zweng, M. M., et al. (2013b). *World Ocean Atlas 2013. Volume 4, Dissolved Inorganic Nutrients (Phosphate, Nitrate, Silicate) [Atlas].(NOAA Atlas NESDIS; 76)*. Washington, DC: U.S. Government Printing Office. doi: 10.7289/V5J67DWD

Garcia, H., Locarnini, R., Boyer, T., Antonov, J., Baranova, O., Zweng, M., et al. (2010a). Dissolved oxygen, apparent oxygen utilization, and oxygen saturation. Vol. 3, World Ocean Atlas 2009. *NOAA Atlas Nesdis* 70:28.

Garcia, H., Locarnini, R., Boyer, T., Antonov, J., Zweng, M., Baranova, O., et al. (2010b). *World Ocean Atlas 2009, Volume 4: Nutrients (Phosphate, Nitrate, Silicate), NOAA Atlas NESDIS 71* Ed. S. Levitus). Washington, DC: U.S. Government Printing Office.

García-Reyes, M., Sydeman, W. J., Schoeman, D. S., Rykaczewski, R. R., Black, B. A., Smit, A. J., et al. (2015). Under pressure: climate change, upwelling, and eastern boundary upwelling ecosystems. *Front. Mar. Sci.* 2:109. doi: 10.3389/fmars.2015.00109

Goebel, N. L., Edwards, C. A., Zehr, J. P., and Follows, M. J. (2010). An emergent community ecosystem model applied to the California current system. *J. Mar. Syst.* 83, 221–241. doi: 10.1016/j.jmarsys.2010.05.002

Goubanova, K., Echevin, V., Dewitte, B., Codron, F., Takahashi, K., Terray, P., et al. (2011). Statistical downscaling of sea-surface wind over the Peru–Chile upwelling region: diagnosing the impact of climate change from the IPSL-CM4 model. *Clim. Dyn.* 36, 1365–1378. doi: 10.1007/s00382-010-0824-0

Gruber, N., Frenzel, H., Doney, S. C., Marchesiello, P., McWilliams, J. C., Moisan, J. R., et al. (2006). Eddy-resolving simulation of plankton ecosystem dynamics in the California current system. *Deep Sea Res. Part I Oceanogr. Res. Pap.* 53, 1483–1516. doi: 10.1016/j.dsr.2006.06.005

Gruber, N., Hauri, C., Lachkar, Z., Loher, D., Frölicher, T. L., and Plattner, G.-K. (2012). Rapid progression of Ocean acidification in the California current system. *Science* 337, 220–223. doi: 10.1126/science.1216773

Gruber, N., Lachkar, Z., Frenzel, H., Marchesiello, P., Münnich, M., McWilliams, J. C., et al. (2011). Eddy-induced reduction of biological production in eastern boundary upwelling systems. *Nat. Geosci.* 4, 787–792. doi: 10.1038/ngeo1273

Haidvogel, D. B., Arango, H., Budgell, W. P., Cornuelle, B. D., Curchitser, E., Di Lorenzo, E., et al. (2008). Ocean forecasting in terrain-following coordinates: formulation and skill assessment of the Regional Ocean modeling system. *J. Comput. Phys.* 227, 3595–3624. doi: 10.1016/j.jcp.2007.06.016

Hall, A., Cox, P., Huntingford, C., and Klein, S. (2019). Progressing emergent constraints on future climate change. *Nat. Clim. Change* 9, 269–278. doi: 10.1038/s41558-019-0436-6

Hauri, C., Gruber, N., Vogt, M., Doney, S. C., Feely, R. A., Lachkar, Z., et al. (2013). Spatiotemporal variability and long-term trends of ocean acidification in the California current system. *Biogeosciences* 10, 193–216. doi: 10.5194/bg-10-193-2013

Hersbach, H., Bell, B., Berrisford, P., Hirahara, S., Horányi, A., Muñoz-Sabater, J., et al. (2020). The ERA5 global reanalysis. *Q. J. R. Meteorol. Soc.* 146, 1999–2049. doi: 10.1002/qj.3803

Hoegh-Guldberg, O., and Bruno, J. F. (2010). The impact of climate change on the world's marine ecosystems. *Science* 328, 1523–1528. doi: 10.1126/science.1189930

Howard, E. M., Frenzel, H., Kessouri, F., Renault, L., Bianchi, D., McWilliams, J. C., et al. (2020a). Attributing causes of future climate change in the california current system with multimodel downscaling. *Global Biogeochem. Cycles* 34:6646. doi: 10.1029/2020gb006646

Howard, E. M., Penn, J. L., Frenzel, H., Seibel, B. A., Bianchi, D., Renault, L., et al. (2020b). Climate-driven aerobic habitat loss in the California current system. *Sci. Adv.* 6:eaay3188. doi: 10.1126/sciadv.aay3188

Jacox, M. G., and Edwards, C. A. (2012). Upwelling source depth in the presence of nearshore wind stress curl. *J. Geophys. Res. Oceans* 117:C05008. doi: 10.1029/2011jc007856

Jacox, M. G., Bograd, S. J., Hazen, E. L., and Fiechter, J. (2015). Sensitivity of the California Current nutrient supply to wind, heat, and remote ocean forcing. *Geophys. Res. Lett.* 42, 5950–5957. doi: 10.1002/2015gl065147

Key, R. M., Kozyr, A., Sabine, C. L., Lee, K., Wanninkhof, R., Bullister, J. L., et al. (2004). A global ocean carbon climatology: results from Global Data Analysis Project (GLODAP). *Global Biogeochem. Cycles* 18, 1–23. doi: 10.1029/2004gb002247

Kishi, M. J., Kashiwai, M., Ware, D. M., Megrey, B. A., Eslinger, D. L., Werner, F. E., et al. (2007). NEMURO—a lower trophic level model for the North Pacific marine ecosystem. *Ecol. Model.* 202, 12–25. doi: 10.1016/j.ecolmodel.2006.08.021

Kwiatkowski, L., Torres, O., Bopp, L., Aumont, O., Chamberlain, M., Christian, J. R., et al. (2020). Twenty-first century ocean warming, acidification, deoxygenation, and upper-ocean nutrient and primary production decline from CMIP6 model projections. *Biogeosciences* 17, 3439–3470. doi: 10.5194/bg-17-3439-2020

Li, H., Kanamitsu, M., Hong, S.-Y., Yoshimura, K., Cayan, D. R., Misra, V., et al. (2014). Projected climate change scenario over California by a regional ocean–atmosphere coupled model system. *Climatic Change* 122, 609–619. doi: 10.1007/s10584-013-1025-8

Liu, W. T. L., Katsaros, K., and Businger, J. (1979). Bulk parameterization of air-sea exchanges of heat and water vapor including the molecular constraints at the interface. *J. Atmosph. Sci.* 36, 1722–1735. doi: 10.1175/1520-04691979036<1722:BPOASE<2.0.CO;2

Locarnini, R., Mishonov, A., Antonov, J., Boyer, T., Garcia, H., Baranova, O., et al. (2013). World Ocean Atlas 2013, Volume 1: temperature. *NOAA Atlas NESDIS* 73:40.

Machu, E., Goubanova, K., Le Vu, B., Gutknecht, E., and Garçon, V. (2015). Downscaling biogeochemistry in the Benguela eastern boundary current. *Ocean Model.* 90, 57–71. doi: 10.1016/j.ocemod.2015.01.003

Mantua, N. J., Hare, S. R., Zhang, Y., Wallace, J. M., and Francis, R. C. (1997). A Pacific interdecadal climate oscillation with impacts on salmon production. *Bull. Am. Meteorol. Soc.* 78, 1069–1079. doi: 10.1175/1520-04771997078<1069: apicow<2.0.co;2

Miranda, P. M. A., Alves, J. M. R., and Serra, N. (2013). Climate change and upwelling: response of Iberian upwelling to atmospheric forcing in a regional climate scenario. *Clim. Dyn.* 40, 2813–2824. doi: 10.1007/s00382-012-1442-9

Mote, P. W., and Mantua, N. J. (2002). Coastal upwelling in a warmer future. *Geophys. Res. Lett.* 29, 53-51–53-54. doi: 10.1029/2002gl016086

Palmer, T. (2014). Climate forecasting: build high-resolution global climate models. *Nat. News* 515:338. doi: 10.1038/515338a

Renault, L., Deutsch, C., McWilliams, J. C., Frenzel, H., Liang, J.-H., and Colas, F. (2016). Partial decoupling of primary productivity from upwelling in the California current system. *Nat. Geosci.* 9, 505–508. doi: 10.1038/ngeo2722

Renault, L., McWilliams, J. C., Jousse, A., Deutsch, C., Frenzel, H., Kessouri, F., et al. (2020). *The Physical Structure and Behavior of the California Current System*. Cold Spring Harbor, NY: Cold Spring Harbor Laboratory. doi: 10.1101/2020.02.10.942730

Reynolds, R. W., Smith, T. M., Liu, C., Chelton, D. B., Casey, K. S., and Schlax, M. G. (2007). Daily high-resolution-blended analyses for sea surface temperature. *J. Clim.* 20, 5473–5496. doi: 10.1175/2007jcli1824.1

Rykaczewski, R. R., and Dunne, J. P. (2010). Enhanced nutrient supply to the California current ecosystem with global warming and increased stratification in an earth system model. *Geophys. Res. Lett.* 37:L21606. doi: 10.1029/2010gl045019

Rykaczewski, R. R., Dunne, J. P., Sydeman, W. J., García-Reyes, M., Black, B. A., and Bograd, S. J. (2015). Poleward displacement of coastal upwelling-favorable winds in the ocean's eastern boundary currents through the 21st century. *Geophys. Res. Lett.* 42, 6424–6431. doi: 10.1002/2015gl064694

Shchepetkin, A. F., and McWilliams, J. C. (2005). The regional oceanic modeling system (ROMS): a split-explicit, free-surface, topography-following-coordinate oceanic model. *Ocean Model.* 9, 347–404. doi: 10.1016/j.ocemod.2004.08.002

Shigemitsu, M., Yamamoto, A., Oka, A., and Yamanaka, Y. (2017). One possible uncertainty in CMIP5 projections of low-oxygen water volume in the Eastern Tropical Pacific. *Global Biogeochem. Cycles* 31, 804–820. doi: 10.1002/2016gb005447

Shin, S.-I., and Alexander, M. A. (2020). Dynamical Downscaling of future hydrographic changes over the northwest Atlantic Ocean. *J. Clim.* 33, 2871–2890. doi: 10.1175/jcli-d-19-0483.1

Small, R. J., Curchitser, E., Hedstrom, K., Kauffman, B., and Large, W. G. (2015). The benguela upwelling system: quantifying the sensitivity to resolution and coastal wind representation in a global climate model*. *J. Clim.* 28, 9409–9432. doi: 10.1175/jcli-d-15-0192.1

Smith, J. A., Muhling, B., Sweeney, J., Tommasi, D., Pozo Buil, M., Fiechter, J., et al. (2021). The potential impact of a shifting Pacific sardine distribution on U.S. West Coast landings. *Fish. Oceanogr.* 1–18. doi: 10.1111/fog.12529 [Epub ahead of print].

Stock, C. A., Alexander, M. A., Bond, N. A., Brander, K. M., Cheung, W. W. L., Curchitser, E. N., et al. (2011). On the use of IPCC-class models to assess the impact of climate on Living Marine Resources. *Progr. Oceanogr.* 88, 1–27. doi: 10.1016/j.pocean.2010.09.001

Sydeman, W. J., García-Reyes, M., Schoeman, D. S., Rykaczewski, R. R., Thompson, S. A., Black, B. A., et al. (2014). Climate change and wind intensification in coastal upwelling ecosystems. *Science* 345, 77–80. doi: 10.1126/science.1251635

Taylor, K. E., Stouffer, R. J., and Meehl, G. A. (2012). An Overview of CMIP5 and the Experiment Design. *Bull. Am. Meteorol. Soc.* 93, 485–498. doi: 10.1175/bams-d-11-00094.1

Turi, G., Lachkar, Z., and Gruber, N. (2014). Spatiotemporal variability and drivers of CO2 and air–sea CO2 fluxes in the California current system: an eddy-resolving modeling study. *Biogeosciences* 11, 671–690. doi: 10.5194/bg-11-671-2014

Van Oostende, N., Dussin, R., Stock, C. A., Barton, A. D., Curchitser, E., Dunne, J. P., et al. (2018). Simulating the ocean's chlorophyll dynamic range from coastal upwelling to oligotrophy. *Progr. Oceanogr.* 168, 232–247. doi: 10.1016/j.pocean.2018.10.009

Vecchi, G. A., Soden, B. J., Wittenberg, A. T., Held, I. M., Leetmaa, A., and Harrison, M. J. (2006). Weakening of tropical Pacific atmospheric circulation due to anthropogenic forcing. *Nature* 441, 73–76. doi: 10.1038/nature04744

Veneziani, M., Edwards, C. A., Doyle, J. D., and Foley, D. (2009). A central California coastal ocean modeling study: 1. Forward model and the influence of realistic versus climatological forcing. *J. Geophys. Res.* 114:4774. doi: 10.1029/2008jc004774

Wang, D., Gouhier, T. C., Menge, B. A., and Ganguly, A. R. (2015). Intensification and spatial homogenization of coastal upwelling under climate change. *Nature* 518, 390–394. doi: 10.1038/nature14235

Xiu, P., Chai, F., Curchitser, E. N., and Castruccio, F. S. (2018). Future changes in coastal upwelling ecosystems with global warming: the case of the California current system. *Sci. Rep.* 8:21247. doi: 10.1038/s41598-018-21247-7

Xu, Z., Han, Y., and Yang, Z. (2019). Dynamical downscaling of regional climate: a review of methods and limitations. *Sci. China Earth Sci.* 62, 365–375. doi: 10.1007/s11430-018-9261-5

Conflict of Interest: The authors declare that the research was conducted in the absence of any commercial or financial relationships that could be construed as a potential conflict of interest.

frontiers
in Marine Science

ORIGINAL RESEARCH
published: 19 July 2021
doi: 10.3389/fmars.2021.685241

Projected Shifts in 21st Century Sardine Distribution and Catch in the California Current

Jerome Fiechter[1]*, Mercedes Pozo Buil[2,3], Michael G. Jacox[3,4], Michael A. Alexander[4] and Kenneth A. Rose[5]

[1] Ocean Sciences Department, University of California, Santa Cruz, Santa Cruz, CA, United States, [2] Institute of Marine Sciences, University of California, Santa Cruz, Santa Cruz, CA, United States, [3] Environmental Research Division, Southwest Fisheries Science Center (NOAA), Monterey, CA, United States, [4] Physical Sciences Laboratory, National Oceanic and Atmospheric Administration (NOAA), Boulder, CO, United States, [5] Horn Point Laboratory, University of Maryland Center for Environmental Science, Cambridge, MD, United States

OPEN ACCESS

Edited by:
Chih-hao Hsieh,
National Taiwan University, Taiwan

Reviewed by:
Evan Howard,
University of Washington,
United States
Chen-Yi Tu,
Institute for National Defense
and Security Research, Taiwan

***Correspondence:**
Jerome Fiechter
fiechter@ucsc.edu

Specialty section:
This article was submitted to
Global Change and the Future Ocean,
a section of the journal
Frontiers in Marine Science

Received: *24 March 2021*
Accepted: *16 June 2021*
Published: *19 July 2021*

Citation:
Fiechter J, Pozo Buil M, Jacox MG, Alexander MA and Rose KA (2021) Projected Shifts in 21st Century Sardine Distribution and Catch in the California Current. Front. Mar. Sci. 8:685241. doi: 10.3389/fmars.2021.685241

Predicting changes in the abundance and distribution of small pelagic fish species in response to anthropogenic climate forcing is of paramount importance due to the ecological and socioeconomic importance of these species, especially in eastern boundary current upwelling regions. Coastal upwelling systems are notorious for the wide range of spatial (from local to basin) and temporal (from days to decades) scales influencing their physical and biogeochemical environments and, thus, forage fish habitat. Bridging those scales can be achieved by using high-resolution regional models that integrate global climate forcing downscaled from coarser resolution earth system models. Here, "end-to-end" projections for 21st century sardine population dynamics and catch in the California Current system (CCS) are generated by coupling three dynamically downscaled earth system model solutions to an individual-based fish model and an agent-based fishing fleet model. Simulated sardine population biomass during 2000–2100 exhibits primarily low-frequency (decadal) variability, and a progressive poleward shift driven by thermal habitat preference. The magnitude of poleward displacement varies noticeably under lower and higher warming conditions (500 and 800 km, respectively). Following the redistribution of the sardine population, catch is projected to increase by 50–70% in the northern CCS and decrease by 30–70% in the southern and central CCS. However, the late-century increase in sardine abundance (and hence, catch) in the northern CCS exhibits a large ensemble spread and is not statistically identical across the three downscaled projections. Overall, the results illustrate the benefit of using dynamical downscaling from multiple earth system models as input to high-resolution regional end-to-end ("physics to fish") models for projecting population responses of higher trophic organisms to global climate change.

Keywords: climate projection, dynamical downscaling, California Current, sardine fishery, end-to-end ecosystem model, upwelling system

INTRODUCTION

In eastern boundary current upwelling regions, such as the California Current System (CCS), sardines and other small pelagic fish play a key role in the transfer of energy between planktonic organisms and higher trophic levels species, such as seabirds and marine mammals (Cury et al., 2000; Peck et al., 2021). Healthy sardine populations also account for a substantial fraction of the global fish catch (Fréon et al., 2005) and support important commercial fishing activities worldwide, yielding multimillion dollars ex-vessel revenues (i.e., revenues from landed catch) off the west coast of the United States alone (Pacific Fishery Management Council (PFMC), 2011). The ecological and economic significance of sardines in upwelling regions make them a prime candidate to explore how populations may respond to changing climate conditions (Cheung et al., 2015; Morley et al., 2018) and to identify potential drivers (e.g., warming and prey availability) and uncertainty sources (Frölicher et al., 2016) associated with shifts in distribution and abundance.

Environmental variability in the CCS occurs over a wide range of spatiotemporal scales and is seasonally driven by coastal upwelling of cool, nutrient rich waters in response to prevailing alongshore winds (Checkley and Barth, 2009). The combination of coastal and curl-driven upwelling produces elevated levels of new production along most of the west coast of the United States and contributes to shaping the habitats of planktonic organisms and forage fish (Rykaczewski and Checkley, 2008; Zwolinski et al., 2011; Fiechter et al., 2020). Physical, biogeochemical and ecosystem states in the CCS are further modulated by basin-scale variability associated with ocean-atmosphere couplings, such as the El Niño Southern Oscillation (Lynn and Bograd, 2002), Pacific Decadal Oscillation (Mantua et al., 1997) and North Pacific Gyre Oscillation (Di Lorenzo et al., 2008). These decadal changes in environmental conditions have been postulated as the main drivers of low-frequency variability of sardine and anchovy populations in the region (Chavez et al., 2003; Lindegren et al., 2013).

The combined effects of basin-scale forcing, regional processes, and local upwelling patterns on small pelagic fish habitat pose a significant challenge for predicting how sardine population dynamics will be affected by changing climate conditions in the CCS and in other eastern boundary current upwelling systems. Global projections from Earth System Models (ESMs) typically lack the necessary atmospheric and oceanic horizontal resolution to reproduce the full spectrum of processes associated with wind-driven coastal upwelling (Stock et al., 2011; Small et al., 2015). Higher-resolution regional models can resolve finer-scale physical and biogeochemical coastal dynamics but must be driven by realistic localized representations of future climate forcing. Dynamical downscaling of low-resolution (∼1° × 1°) ESM solutions has emerged as a valuable method for producing higher-resolution (∼0.1° × 0.1°) regional projections of environmental and ecosystem variability in eastern boundary current upwelling systems under anticipated future conditions (Echevin et al., 2012; Machu et al., 2015; Howard et al., 2020a; Pozo Buil et al., 2021).

The focus of this study is to extend the dynamical downscaling approach of Pozo Buil et al. (2021) to sardine population dynamics and catch in the CCS by integrating a full life-cycle individual-based model (IBM) for sardine and an agent-based model for its fishing fleet into the projections. By nature, the IBM allows for a mechanistic interpretation of environmental drivers regulating growth, reproduction, survival, and behavior of sardine (Fiechter et al., 2015; Rose et al., 2015), and it is thus well-suited to explore which and how underlying physical and biological processes will likely cause changes in sardine abundance and distribution over the course of the 21st century. While anthropogenic warming will undoubtedly play an important role (Cheung et al., 2015; Morley et al., 2018), the IBM projections can shed light on the relative extent to which future temperatures will affect sardine population dynamics through metabolism (growth, reproduction, and early life survival rates) and movement behavior (shift in thermal habitat). The IBM also offers insight into the possible influence on sardine of other bottom-up drivers, such as coastal upwelling intensity and prey availability, which may exhibit more subtle local and regional responses to climate change (Rykaczewski et al., 2015; Checkley et al., 2017) or whose trends have not yet emerged from natural variability (Brady et al., 2017). Since climate models have inherent physical and biogeochemical uncertainty (Frölicher et al., 2016), the robustness of sardine population and catch projections are assessed by downscaling three representative members of the CMIP5 ensemble (Bopp et al., 2013).

MATERIALS AND METHODS

End-to-End Ecosystem Model

The numerical framework is an existing end-to-end ecosystem model that has already been successfully implemented to study historical sardine and anchovy population variability and their environmental drivers in the CCS (Fiechter et al., 2015; Rose et al., 2015; Politikos et al., 2018; Nishikawa et al., 2019) and in the Canary Current upwelling system (Sánchez-Garrido et al., 2018, 2021). The end-to-end model includes a regional ocean circulation component, a nutrient-phytoplankton-zooplankton (NPZ) component, a sardine population dynamics IBM component, and an agent-based fishing fleet component. Since detailed descriptions of the model can be found in Rose et al. (2015) and Fiechter et al. (2015), only an abbreviated overview of the different model components is provided here.

The ocean circulation model is an implementation of the Regional Ocean Modeling System (ROMS) (Shchepetkin and McWilliams, 2005; Haidvogel et al., 2008) for the broader California Current region (30°N to 48°N and 116°W to 134°W), with a horizontal grid resolution of 1/10° (ca. 10 km) and 42 non-uniform terrain-following vertical levels. The NPZ model is a customized version of the North Pacific Ecosystem Model for Understanding Regional Oceanography (NEMURO) (Kishi et al., 2007) specifically parameterized for the CCS (Fiechter et al., 2018, 2020). Physical transport of NPZ tracers is achieved by solving an advection-diffusion equation at every time step using archived daily velocities and mixing coefficients from ROMS. The

IBM tracks sardine individuals on the ROMS grid in continuous (Lagrangian) space and over their full life cycle.

Scaling from individuals to the population level is done using a super-individual approach (Scheffer et al., 1995), where each super-individual in the IBM represents a larger number of individuals (called worth) with identical attributes (a super-individual can be envisioned as a school of identical fish). Super-individuals remain in the simulation until they either reach their oldest allowed age (10 years) or mortality sources reduce their worth to zero. All output from the IBM is scaled by the worths of super-individuals (for example, population abundance is the sum of the worths over all super-individuals, and mean length is a weighted average of the lengths of super-individuals with the weighting factors being their worths).

The IBM explicitly includes formulations for growth from bioenergetics and feeding on zooplankton prey (from NPZ component), reproduction, and natural and fishing mortality for the following life stages (as appropriate): eggs, yolk-sac larvae, feeding larvae, juveniles, non-mature adults, and mature adults. The development of eggs and yolk-sack larvae is determined uniquely by temperature; larvae transition to juveniles based on a weight threshold; juveniles become non-mature adults on January 1 of each model year; and adults reach maturity based on a length threshold. Since mature adults produce eggs which become the next spawning adults, recruitment is an emergent property in the model (as opposed to being imposed annually or defined *a priori* via a spawner-recruit relationship). Behavioral movement for juveniles and adults includes temperature and consumption cues using a kinesis approach that combines inertial and random displacements based on a proximity to optimal conditions (Humston et al., 2004; Watkins and Rose, 2013). When temperature and feeding conditions experienced by an individual are within a prescribed suitable range (defined here as within one standard deviation from the optimal value), the inertial component is weighted more heavily than the random component, thereby allowing the individual to maintain itself within a suitable thermal and foraging habitat by conserving its current heading and slowing down.

The fishing fleet model simulates daily fishing trips of boats out of 4 United States west coast ports (San Pedro, Monterey, Astoria and Westport). Choice of fishing locations and associated daily sardine catch are based on a simplified multinomial logit, agent-based approach where boats maximize their expected net revenue for each trip (e.g., Eales and Wilen, 1986). While the fleet model incorporates effort in the sense that no fishing occurs on a given day if a boat does not have access to fishing locations yielding a positive revenue, it does not account for specific fisheries management actions that have been imposed historically. For example, the simulations do not include the regulatory quotas imposed on the fishery during 1986–1991 following the sardine moratorium in California (Wolf, 1992) or the lack of a recent commercial fishery in the Pacific Northwest until 1999 (Emmett et al., 2005).

The version of the end-to-end model used here differs from its earlier implementation in several ways. (i) For computational efficiency, each component of the system is run in successive steps (i.e., offline coupling), starting with the physical circulation, then the NPZ component, and finally the fish and fleet components. When using archived daily fields, the offline approach yields a solution virtually identical to that of the fully coupled model, yet it allows for larger time steps for the NPZ (dt = 30 min) and fish and fleet (dt = 6 h) components compared to that of the physical and, hence fully coupled model (dt = 10 min); (ii) The fish IBM component includes only one coastal pelagic species, sardine, and no migratory predator. Earlier results from Rose et al. (2015) demonstrated that sardine and anchovy had small direct effects on each other in the simulations (i.e., dynamics were quasi-independent and therefore separable) and that predatory mortality was small compared to the other sources of mortality represented in the model; (iii) The diet for adult sardine has been adjusted to include higher feeding preferences on copepods and euphausiids. This modification yields a more realistic offshore extent of the sardine population (food is one of the movement cues) compared to that calculated in earlier implementations of the model where adult sardine favored microzooplankton. The new parameterization also leads to an emergent northward summer feeding migration (albeit of reduced amplitude and limited to older fish), thereby alleviating the need of a prescribed seasonal migration as in Rose et al. (2015) and Fiechter et al. (2015). (iv) The parameterization of the NPZ component was revisited to improve the representation of key phytoplankton and zooplankton functional groups in the CCS, especially euphausiids (Fiechter et al., 2018, 2020). Specific parameter values for the NPZ, sardine IBM, and fishing fleet models are provided as supplementary material and references for parameter sources are available in Rose et al. (2015).

Historical Simulation and Climate Projections

Four different numerical simulations of the end-to-end model were performed: a historical run for 1983–2010 and three downscaled climate projections for 1983–2100 based on the GFDL-ESM2M (Dunne et al., 2012), IPSL-CM5A-MR (Dufresne et al., 2013), and Hadley-GEM2-ES (Collins et al., 2011) earth system models under the Representative Concentration Pathway (RCP) 8.5 emission scenario. These models were selected for their inclusion of marine biogeochemical fields and to represent the spread of physical and biogeochemical futures in the CMIP5 ensemble: GFDL has a low rate of warming and increased primary production; Hadley has a high rate of warming and decreased primary production; and IPSL corresponds to a moderate scenario (Bopp et al., 2013; Pozo Buil et al., 2021). The primary purpose of the historical simulation was to generate a reference solution for the calibration and evaluation of the sardine IBM and fishing fleet model.

For the historical simulation, initial and open boundary conditions for physical variables are derived from the Simple Ocean Data Assimilation (SODA) reanalysis (Carton and Giese, 2008), and surface atmospheric fields are based on version 1 of the Cross-Calibrated Multi-Platform (CCMP1) winds (Atlas et al., 2011) and version 5 of the European Centre for Medium-Range Weather Forecasts (ERA5) reanalysis (Hersbach et al., 2020). Initial and boundary conditions for nitrate and silicic acid are derived from the World Ocean Atlas (WOA) (Conkright and Boyer, 2002), while other biogeochemical tracers are set to a small value (0.1 mmol N m^{-3}) for lack of better information. Total sardine population biomass is initialized so that the biomass contributed by mature (age-2 and older) adult individuals at the beginning of the simulation roughly matched the mean spawning stock biomass estimated for 1985–1999 (∼0.35 million metric tons) (Hill et al., 2010). Sardine super-individuals are randomly initialized within a subregion of the model between 30–35°N and within 100 km of the coast where surface temperatures and food availability on 1 January 1983 are within one standard deviation of their respective optimal values for kinesis.

For the downscaled projections, a "time-varying delta" method is used to generate open boundary and surface atmospheric forcing. For each ESM, time-varying deltas (representing monthly open boundary and surface atmospheric anomalies) are calculated relative to their respective 1980–2010 climatology and added to their corresponding climatology in the historical simulation (SODA and WOA for physical and biogeochemical open boundary conditions, and CCMP1 and ERA5 for surface atmospheric forcing) (Pozo Buil et al., 2021). The downscaled projections are generated for 1983–2100 using historical forcing for 1983–2005 and the RCP8.5 emission scenario for 2006–2100. The main advantage of using a time-varying delta method is that it corrects for inherent biases in the earth model solutions and produces continuous projections reflecting climate change effects in the CCS throughout the 21st century (as opposed to the more common "fixed delta" method that considers only a specific period of the future climate, e.g., 2070–2100). The initial location and biomass of sardine individuals for the projections is determined using the same approach as for the historical simulation.

Analysis

Evaluation of the end-to-end historical simulation includes sea surface temperatures and surface chlorophyll concentrations from the ROMS and NPZ models; sardine spawning stock biomass, age-class structure, recruitment, and egg distribution from the IBM; and regional annual catch from the fishing fleet model. Simulated sea surface temperatures and chlorophyll concentrations are respectively compared to NOAA's OISST AVHRR dataset[1] and NASA's SeaWiFS dataset.[2] Simulated sardine spawning stock biomass (age-2 and older individuals), age-class structure and recruitment are compared to stock assessment estimates from Table 10 in Hill et al. (2010); egg distribution patterns are evaluated against *in situ* observations of egg presence from Zwolinski et al. (2011); and simulated catch is compared to reported regional United States west coast landings from Table 1 in Hill et al. (2010). Recruitment is an emergent property in the IBM and represents the number of eggs that survive to enter the adult stage on January 1 of each year.

Analysis of the end-to-end model projections includes: (1) total annual adult sardine biomass from each downscaled solution and multi-model mean, as well as multi-model spread calculated as the standard deviation between the three projections and the multi-model mean, (2) spatial distributions of adult sardine abundance and egg production, (3) spatial maps of suitable thermal and feeding habitats, and (4) total annual catch in the southern (San Pedro), central (Monterey) and northern (Astoria and Westport) CCS. Since sardines in the model consume multiple prey types from the NPZ component, a functional response is applied to combine them into a single index (Rose et al., 2015). The functional response uses the prey biomasses, and after accounting for feeding preferences and efficiencies of sardine, generates the fraction of maximum possible consumption rate that would be achieved (hereafter referred to as "P"). The identification of thermal and feeding habitats is purposedly based on the parameters used in kinesis to weight inertial and random movement, so spatial changes in projected sardine distributions are directly relatable to future availability of suitable conditions in the CCS as perceived by individuals in the IBM. Suitable thermal and feeding habitats are thus defined as grid cell locations where temperature and P values are, respectively, within one standard deviation of their optimal value, (i.e., 11–16°C for temperature and greater than 0.75 for P). For these ranges, habitat quality is highest and inertial movement (indicative of good habitat) outweighs random behavior (indicative of poor habitat) in kinesis.

Total biomass is calculated by multiplying the body weight by the worth of a super-individual and summing over all super individuals representing mature adult sardines; worth is the number of actual fish represented by a super-individual and body weight is identical for all fish within a super-individual. Spawning stock biomass is further calculated by summing only over super-individuals representing age-2 and older mature adult sardines. Spatial distributions of abundance are calculated as yearly averages of instantaneous (every 5 days) summed adult worth in each grid cell, and egg production is determined by annually summing the number of eggs spawned (scaled up for the worths of spawners) in each grid cell. Adult abundance and egg production are subsequently mapped to a coarser 30 km resolution grid, which helps smooth out spatial variability in the model output not associated with coherent circulation features. Total annual catch is calculated by summing daily catch over all boats and all days of the year for each port. An unpaired, two-sample Student's *t*-test is also performed on sardine abundances at each grid cell location to determine if the means of the distributions are statistically identical across the three downscaled solutions over the analysis period (2000–2100). The projections are considered statistically "robust" at a grid cell location if the pairwise (GFDL-Hadley, GFDL-IPSL, and Hadley-IPSL) *t*-tests support the hypothesis of identical means at the 95% confidence level.

RESULTS

Model Evaluation

The evaluation of the ROMS and NPZ models focuses on sea surface temperatures and chlorophyll concentrations, as

---

[1] https://www.ncdc.noaa.gov/oisst

[2] https://oceancolor.gsfc.nasa.gov/data/seawifs

these two variables are intimately related to the presence of suitable thermal and feeding habitats for sardine individuals in the IBM. Despite a slight warm bias (∼0.5°C or less), simulated surface temperatures adequately reproduce observed spatial patterns and temporal variability, including the transition from a warmer to a colder regime in the northeast Pacific Ocean in 1999 associated with a phase change of the Pacific Decadal Oscillation (Peterson and Schwing, 2003) (**Figure 1**, upper panels). Simulated surface chlorophyll concentrations also demonstrate reasonable agreement with observed values in the spatial extent of the coastal upwelling zone and in their interannual variability and trend (**Figure 1**, lower panels).

Historical sardine spawning stock biomass from the IBM exhibits low-frequency variability comparable to stock assessment estimates, with a rapid increase in biomass starting in the early 1990s, a period of peak biomass during the late 1990s and early 2000s, and a decline in the late 2000s (**Figure 2**, upper left panel). However, simulated values greatly underestimate the difference between high and low biomass periods. Over the 28 years, simulated values vary by a factor of about 1.5 times compared to an order of magnitude difference for observed biomass. This discrepancy is partly explained by lower average recruitment values (∼4,200 vs. ∼7,400 million individuals during 1990–2010) and smaller interannual variability. The model predicts a factor of 2–3 times between high and low recruitment years, whereas the factor is 5–10 times for recruitment reported in the stock assessment (**Figure 2**, lower left panel). However, the IBM reasonably replicates periods of high and low recruitment in the stock assessment, with correlation coefficients of 0.41 based on annual values and 0.71 based on 3-year running mean values. Furthermore, the IBM provides an acceptable representation of the observed age-class structure of the population, and adequately reproduces the observed latitudinal range (33–36°N) and offshore extent of sardine spawning based on *in situ* egg presence reported by Zwolinski et al. (2011) for 1998–2009 (**Figure 2**, right panels).

The cause for the order of magnitude discrepancy between the model and stock assessment during periods of higher and lower spawning stock biomass is difficult to pinpoint exactly, but prey availability and density-dependent mortality could both play a role. The quadratic natural mortality term in the NPZ component prevents large fluctuations in phytoplankton and zooplankton biomasses [as identified for simulated krill in Fiechter et al. (2020)], which could in turn have a stabilizing effect on recruitment via larval and juvenile growth, and on egg production via adult growth. Introducing density-dependent processes (either via mortality such as predation or crowding effects on prey availability and growth) would presumably improve the IBM's ability to reproduce observed population-level patterns in spawning stock biomass. However, density-dependence was ultimately not included in the IBM to maximize simulated responses to variation in environmental variables and prey availability, thereby enabling more easily interpretable results in the projections. Including density-dependence would dampen responses and, given the uncertainty in how to formulate the density-dependence among processes and life stages (see Rose et al., 2001), would require extensive testing of alternative formulations of differing strength. An option for additional analyses would be to calibrate the density-dependence to match the historical spawner-recruit relationship (e.g., from stock assessment estimates), but it is not clear how this relationship may change under future conditions. Furthermore, since relative changes in simulated sardine abundance and distribution are comparable over an order of magnitude change in initial population biomass (**Supplementary Figure 1**), discrepancies in historical spawning stock biomass and recruitment should not fundamentally alter the qualitative spatial and temporal patterns identified in the IBM projections.

Comparing simulated catch to observed landings is obscured by the fact that the fleet model does not account for the sardine moratorium (1974–85) and subsequent period of limited fishing quotas (1986–1991) in California (Wolf, 1992) and for the lack of a recent commercial fishery in the Pacific Northwest until 1999 (Emmett et al., 2005). Excluding those periods and ramp-up phase of the fishery, simulated catch reasonably reproduces the magnitude and temporal variability of reported landings in the southern CCS during 2000–2010 and northern CCS during 2002–2010 (**Supplementary Figure 2**). However, the model exhibits significantly less similarity with landings in the central CCS, both in amplitude and year-to-year variation. The agreement between simulated catch and landings (at least for San Perdo, Astoria, and Westport) during the period of high sardine abundance suggests that, despite the factor 2–3 difference between simulated spawning stock biomass and stock assessment estimates, the model results are informative with careful interpretation and caveats.

Downscaled Projections

All three downscaled climate projections display substantial low-frequency variability in sardine biomass over the course of the 21st century, with a notable decrease in adult biomass during 2020–2040 and a rapid increase in adult biomass starting in the 2070s (**Figure 3**). However, the importance of the mid-century low biomass period and the magnitude of the end of the century increase differ markedly between the three projections. Based on the multi-model mean, sardine biomass decreases by about 40% between historical (2000–2020) and mid-century (2040–2060) values, with GFDL projecting a smaller decrease (∼15%) than the multi-model mean, and Hadley and IPSL projecting a larger decrease (up to 70% for IPSL). Comparatively, the change in sardine biomass during the second half of the century is more substantial, as evidenced by the 2.5–3 times increase in the multi-model mean between mid-century and end of the century values. Individual projections also exhibit greater spread, with GFDL and Hadley projecting a lower increase (closer to doubling), and IPSL projecting a much larger increase (∼7 times increase).

The projected changes in total biomass are also accompanied by a regional redistribution of the sardine population over the course of the 21st century, as illustrated by the poleward shift in the multi-model mean between 2000–2020, 2040–2060, and 2080–2100 (**Figure 3**). While the poleward displacement of the sardine population is a common feature of all three downscaled projections, the timing and magnitude of the shift

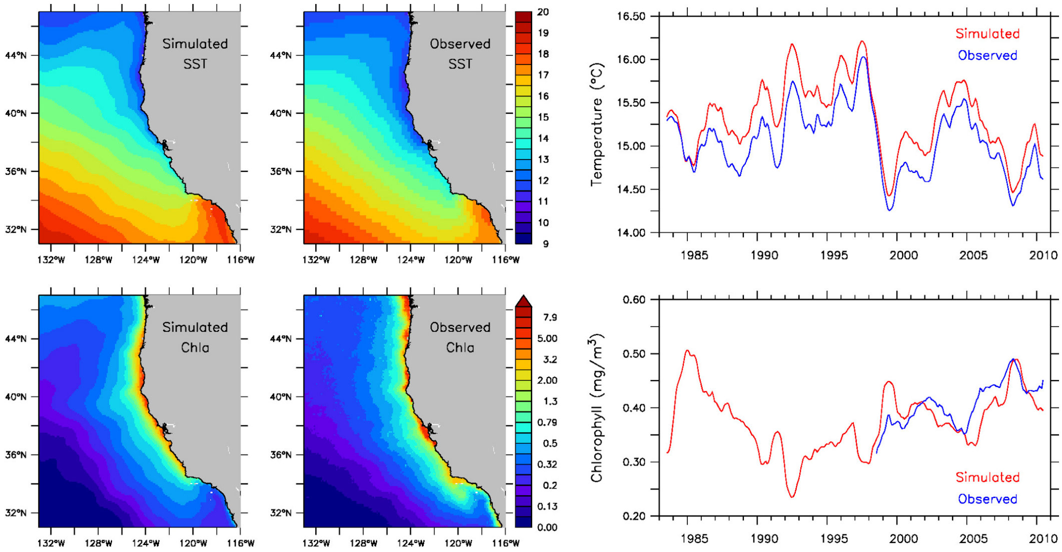

FIGURE 1 | Historical surface temperatures (°C) **(top)** and chlorophyll concentrations (mg/m^3) **(bottom)** from the ROMS and NPZ models for 1983–2010. **Left panels:** simulated and observed annual means. **Right panel:** monthly simulated (red) and observed (blue) spatial means. Observed temperatures are from NOAA's OISST AVHRR dataset (https://www.ncdc.noaa.gov/oisst) and chlorophyll concentrations are from NASA's SeaWiFS dataset (https://oceancolor.gsfc.nasa.gov/data/seawifs).

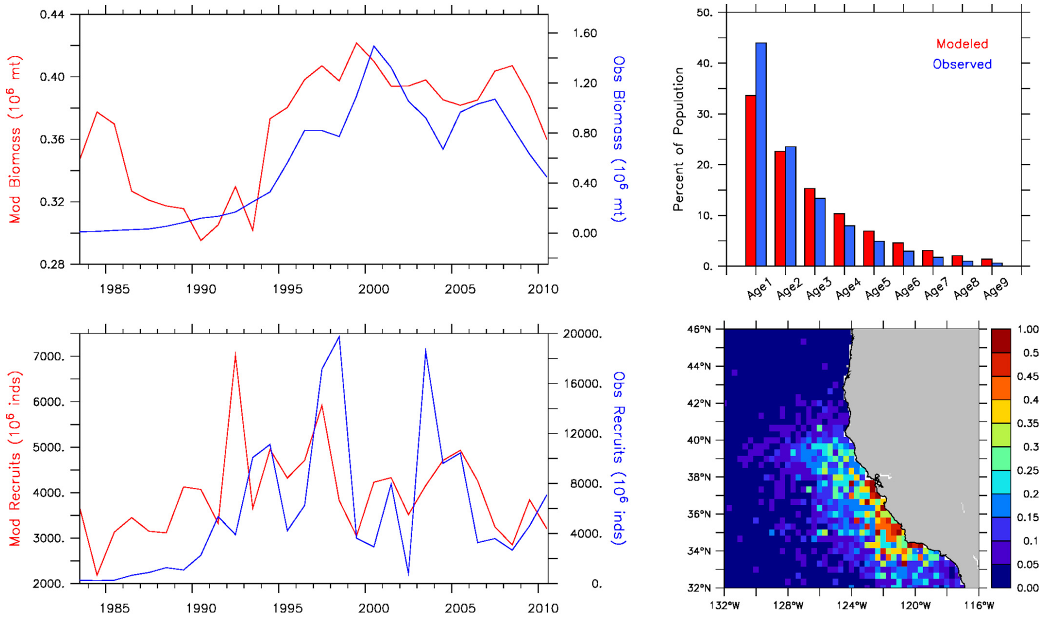

FIGURE 2 | Historical sardine population dynamics from the IBM for 1983–2010. **Top left:** simulated (red) and observed (blue) spawning stock biomass (adults age-2 and older) (10^3 metric tons). **Top right:** simulated (red) and observed (blue) age-class distribution (percent of population). **Bottom left:** simulated (red) and observed (blue) recruitment (millions of individuals). **Bottom right:** Annual mean simulated egg distribution (percent of total production contained in each grid cell). Observed values are from Hill et al. (2010) stock assessment estimates.

differ substantially between the GFDL, Hadley and IPSL solutions (**Figure 4**, upper panels). By mid-century, Hadley projects a region of peak abundance (~37–46°N) on average 2° farther north than those in the GFDL and IPSL projections (~35–44°N). In contrast, by the end of the century, Hadley and IPSL project that peak sardine abundance is limited to the northern CCS (north of 40°N), whereas GFDL suggests higher sardine abundance still occurs in the central CCS between 37–40°N. This poleward shift in sardine abundance over the course of the 21st century is accompanied by a similar displacement of peak egg production (i.e., primary spawning grounds) (**Figure 4**, lower panels).

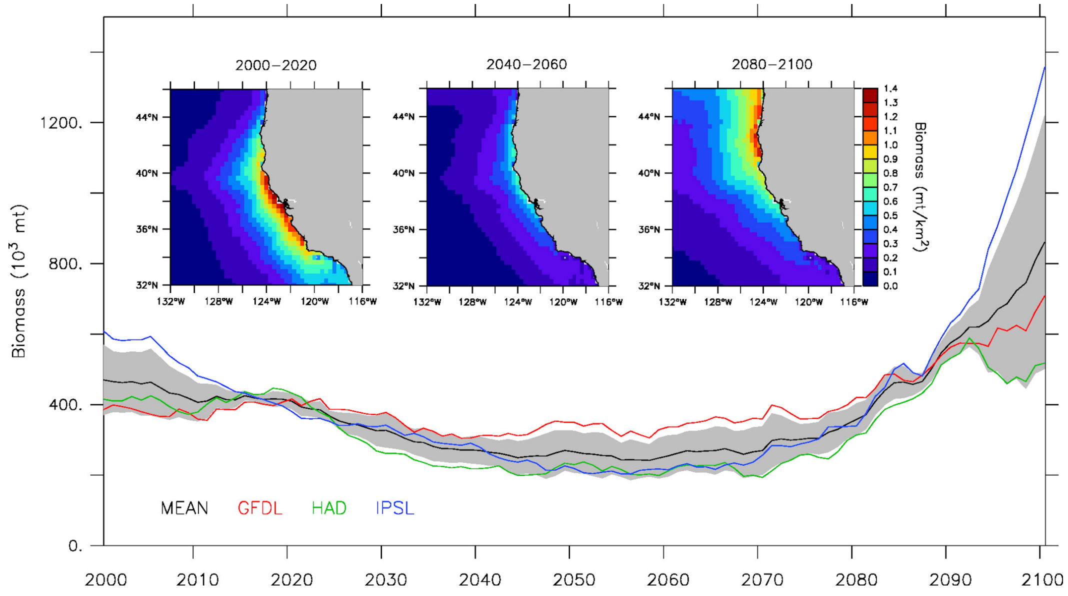

FIGURE 3 | Projected sardine spawning stock biomass (10^3 metric tons) for 2000–2100. The time series represent CCS-wide annual adult (age-2 and older) biomass from the ensemble mean (black) and individual GFDL (red), Hadley (green) and IPSL (blue) solutions (gray shading denotes ensemble spread). Insets represent the ensemble mean spatial biomass distribution (metric tons per km^2) for 2000–2020 **(left)**, 2040–2060 **(center)**, and 2080–2100 **(right)**.

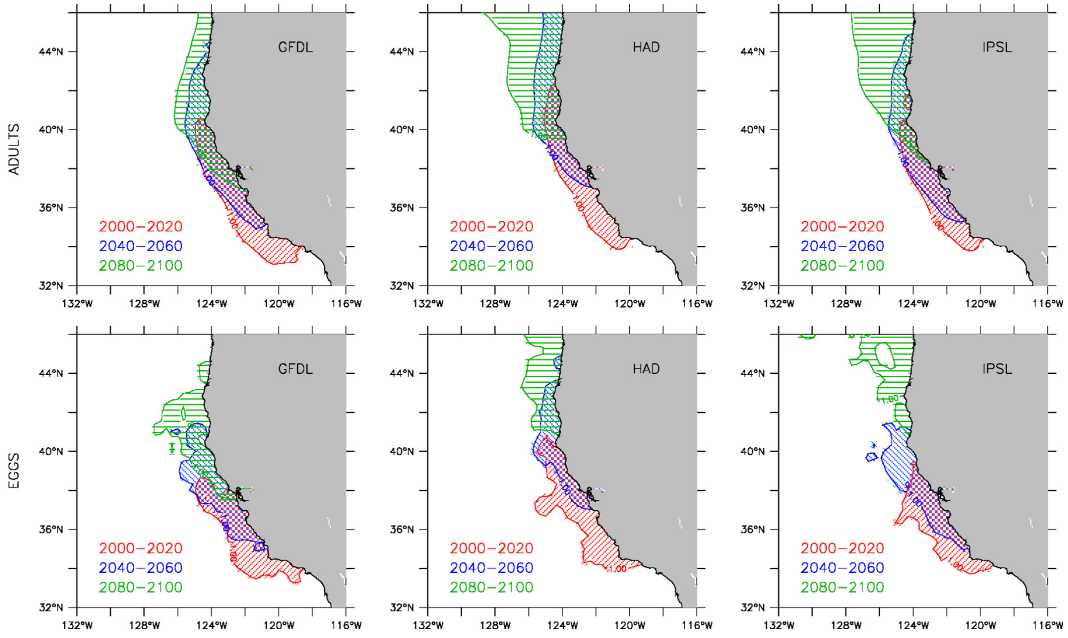

FIGURE 4 | Projected spatial distributions of peak adult sardine abundance **(top)** and egg production **(bottom)** for 2000–2020 (red), 2040–2060 (blue), and 2080–2100 (green) from GFDL **(left)**, Hadley **(center)**, and IPSL **(right)** solutions. Regions of peak adult abundance and egg production are defined as locations where individual and egg counts are greater than one standard deviation above the mean (based on all locations where individuals and eggs were present).

The cues for behavioral movement in kinesis are used to identify whether temperature or food availability is the primary driver for the projected poleward shift of the sardine population (**Figure 5**). All three model solutions indicate that prey availability, and thus consumption, remain optimal throughout the 21st century in most coastal regions where sardines would normally be found. In contrast, simulated optimal temperatures for sardines become progressively limited in the southern and central CCS. By 2100, the GFDL projection (lowest rate of warming) retains a narrow coastal region of optimal temperature conditions in the central CCS (as far south as 34°N), while the Hadley projection (highest rate of warming) has virtually no suitable thermal habitat for sardines equatorward of 40°N. Hence, the poleward shift of the sardine population in the end-to-end model is primarily associated with a substantial reduction of thermal habitat in the southern and central CCS by the end of the century.

The progressive displacement of simulated peak sardine abundance from the southern to the northern CCS has clear implications for projected catch (**Figure 6**). All three model solutions indicate a substantial decrease of total catch in the southern and central CCS by the end of the century. The decrease is more pronounced and occurs more rapidly in the Hadley and IPSL projections, with catch in the southern and central CCS being 50–70% lower by mid-century (2040–2060) relative to historical conditions (2000–2020). Catch changes more gradually in the GFDL projection, with a decrease of ∼20% by mid-century (2040–2060) and another ∼10% by the end of the century (2080–2100) in both the southern and central CCS. In contrast, catch in the northern CCS consistently increases, reaching a factor of 2–3 times higher by the end of the century relative to historical values for all three projections. On aggregate across the entire CCS, simulated decadal variability in catch aligns closely with changes in total sardine population biomass, as evidence by a steady decrease during the first half of the 21st century, followed by a sharper increase starting around 2070. This pattern is least pronounced in the GFDL projection due to its reduced low-frequency sardine biomass variability (notably the mid-century minimum and end of the century maximum).

DISCUSSION

While the GFDL, Hadley, and IPSL projections each provide a plausible outcome for climate change impacts on sardine biomass and catch in the CCS, it is worth discussing their robustness by considering whether the three downscaled solutions describe statistically identical mean sardine populations. In general, mean abundances are statistically "robust" in the southern and central CCS, but not in the northern CCS where the downscaled solutions predict a large increase in sardine biomass late in the century (**Supplementary Figure 3**). The results also suggest that the mid-century decline in abundance is confined to the southern and central CCS and robustly predicted across the three projections. Furthermore, the spread of the multi-model ensemble over the entire domain is primarily determined by the model spread associated with "robust" locations in the southern and central CCS, until about 2090 when "non-robust" contributions from the northern CCS become an equally important source of uncertainty. The emergence of statistically different mean abundances underscores the need to understand not only physical and biological sources of uncertainty in the downscaled projections, but also how they may lead to diverging predictions of sardine population dynamics under future climate conditions in the CCS. For instance, the lack of robustness in the northern CCS could be associated with different representations of the latitudinal position and poleward displacement of the North Pacific Current bifurcation in the three ESM solutions (**Supplementary Figure 4**). It is therefore conceivable that the timing and magnitude of the simulated poleward shift of the sardine population in the IBM is influenced by both anthropogenic warming and basin-scale circulation patterns, with the latter having a stronger impact on the robustness of the projections.

The underlying physical, NPZ, and IBM models used here are obviously not perfect, and the downscaled solutions are only as valid as the assumptions made in the development and implementation of each component. Uncertainty in the physical response of the climate system to greenhouse gases occurs due the emissions scenario used for anthropogenic forcing, differences in the model physics (e.g., resolution, numerical methods, parameterizations), and internal variability (Hawkins and Sutton, 2009). Internal variability, caused by non-linear processes, can lead to substantially different evolutions of the climate system, even on long time scales (Deser et al., 2012a, 2020). Large ensembles of simulations using the same model and scenario but different initial conditions, indicate that natural variability could strongly influence regional trends, especially for dynamic variables such as sea level pressure and upwelling along the United States west coast (Deser et al., 2012b; Brady et al., 2017). While uncertainty in environmental variability is in part inherited from the earth system model solutions, some is generated locally, such as the lack of large amplitude fluctuations in phytoplankton and zooplankton biomass in the NPZ model.

Ignoring density-dependent processes in the sardine IBM represents another source of uncertainty for adequately reproducing the amplitude of historical and future fluctuations in sardine abundance in the CCS. While density-dependent mortality or crowding effects on food limitation may help improve the accuracy of future projections, such additions to the model would significantly increase uncertainty because of alternative ways to combine larval and juvenile processes to mimic the historical spawner-recruit relationship. Furthermore, the historical spawner-recruit relationship for forage species like sardine has its own uncertainties about how it affects population dynamics (Canales et al., 2020), and the sardine relationship for the CCS exhibits high variability, reflects past management actions, and will likely change under future conditions. The possibility of density-dependence in the adult stage must also be considered (Lorenzen, 2008; Andersen et al., 2017). The choice made here was to sacrifice some realism offered by including density-dependence to the benefit of generating clear responses to climate-induced environmental variation and avoiding over-constraining the model solution based on historical conditions (e.g., using density-dependent mortality to match observed spawner-recruit relationships). Hence, the model results should be considered as an exploratory interpretation about how climate change can propagate through the physics and lower trophic levels and affect sardine at the population level.

The degree of agreement between the IBM results and empirical data for the historical period was sufficient to support the analysis of the downscaled projections, as the IBM reproduces periods of relatively higher and lower sardine abundance and recruitment without density-dependent

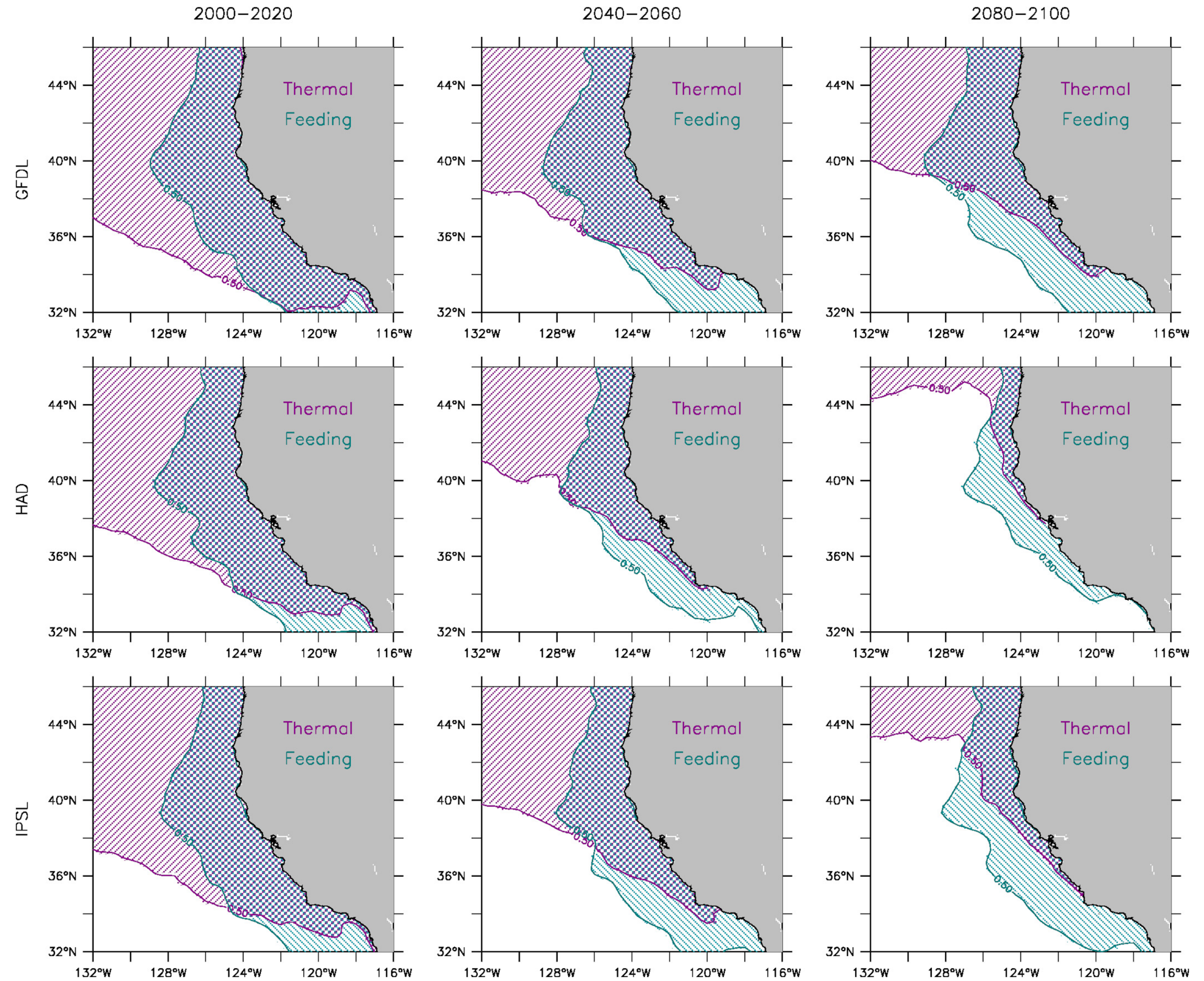

FIGURE 5 | Feeding and thermal habitat suitability for adult sardines during 2000–2020 **(left)**, 2040–2060 **(center)**, and 2080–2100 **(right)** from GFDL **(top)**, Hadley **(middle)**, and IPSL **(bottom)** solutions. Shading denotes locations where temperature (magenta) and fraction of maximum consumption (P) (cyan) are within one standard deviation of their respective optimal values (as defined in kinesis for horizontal behavior) at least 50% of the time.

processes (**Figure 2**). A sensitivity study was also performed to confirm that the spatial and temporal patterns identified in the projections are mostly unaffected by initial sardine population biomass (**Supplementary Figure 1**). However, the model-data discrepancies in the historical comparisons of spawning stock biomass and recruitment are important to consider when interpreting the implications of the projections. The IBM results should be viewed in a relative sense as the magnitude of change (trend) is likely overestimated, while the amplitude of change (interannual variability) is presumably underestimated.

The projected decadal variability of the multi-model mean sardine population during the 21st century is to some extent consistent with known changes that have occurred during the 20th century between 1930 and 2010 (Schwartzlose et al., 1999), with a 10–20-year decline (1940–1950 vis-à-vis 2020–2040) followed by a low abundance period of ~40 years (1950–1990 vis-à-vis 2040–2080) and a subsequent 10–20-year increase (1990–2010 vis-à-vis 2080–2100). In the projections, sardine biomass initially declines in response to a decrease in prey availability (i.e., zooplankton concentrations) affecting adult growth and reproductive output. This decline is eventually compensated, and outweighed toward the end of the century, by an increase in recruitment associated with enhanced early life survival (primarily eggs and yolk-sac larvae) caused by increasing near-surface ocean temperatures. Hence, the results underscore the fact that, while thermal tolerance primarily drives the spatial redistribution of sardines in the IBM, interannual and decadal variability in prey availability within a region of suitable habitat still contribute to temporal fluctuations in population abundance.

The overall poleward shift of the sardine population occurring in all three downscaled projections (albeit with different

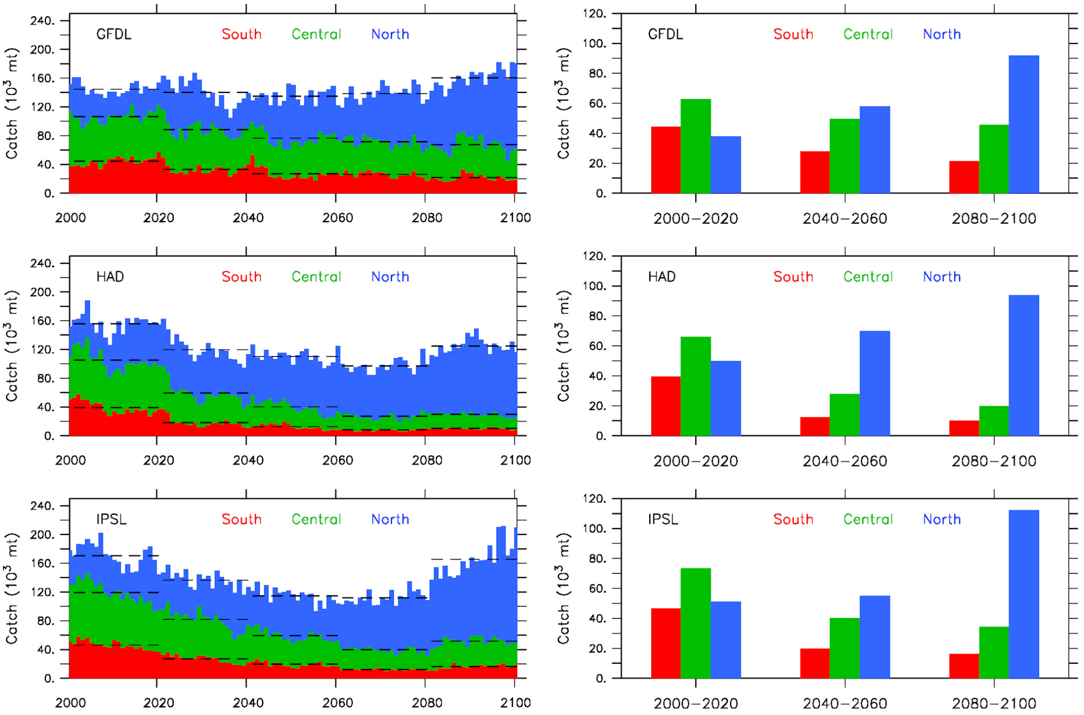

FIGURE 6 | Projected sardine catch (10^3 metric tons) for 2000–2100 in southern (red), central (green) and northern (blue) CCS from GFDL **(top)**, Hadley **(middle)**, and IPSL **(bottom)** solutions. **Left:** cumulative annual catch (bars) and 20-year averages (dashed lines). **Right:** 20-year average catch by region during 2000–2020, 2040–2060, 2080–2100. The three subregions correspond to catch originating from Long Beach (southern CCS), Monterey (central CCS) and Astoria + Westport (northern CCS).

magnitudes and spatial details) is generally consistent with thermal displacements identified for marine heatwaves where intensities of 1–3°C resulted in 500–1,000 km poleward shifts of species distributions in the CCS (Jacox et al., 2020). This range of thermal heatwave intensities closely approximates the projected range of sea surface temperature warming in the CCS by GFDL (∼2°C), Hadley (∼4°C) and IPSL (∼3°C) for the end of the 21st century (Pozo Buil et al., 2021), which led to poleward population displacements in the sardine IBM of ∼500 km for GFDL (36 → 41°N) and ∼800 km for Hadley and IPSL (36 → 44°N) based on regions of peak abundance (**Figure 4**). The associated shift in sardine catch is also in agreement with the findings of Smith et al. (2021) derived from the same set of downscaled projections but using a different modeling framework based on a species distribution model for sardine and a more realistic fisheries model tuned to historical landings in the CCS. The results presented here suggest a 30–70% decrease in the southern and central CCS and a 50–70% increase in the northern CCS, which is comparable to the 20–50% decrease and up to 50% increase by 2080 projected by Smith et al. (2021). The agreement between the two studies is primarily due to catch being overwhelmingly affected by the projected poleward redistribution of the sardine population, a predominant feature emerging in both the IBM and species distribution model.

The exact magnitude of the thermal displacement sardines will experience in the CCS is dictated by the amount of warming that will occur during the 21st century and the results presented here for the Hadley model under the RCP8.5 scenario likely portray an upper bound. This shift could be dramatically reduced under mitigation scenarios (Morley et al., 2018) and fall closer to the GFDL solution which represents a relatively low rate of warming under RCP8.5 conditions. However, it should also be recognized that "optimal" thermal conditions are identified here based on fixed movement parameters from the IBM and, thus, do not account for phenotypic plasticity, which could reduce temperature constraints and expand habitat suitability. The geographical extent of suitable sardine habitat could also be further constrained by the expected decrease of oxygen levels in the CCS (Bograd et al., 2008; Rykaczewski et al., 2015). The mechanistic structure of the sardine IBM provides a valuable framework to determine the compounding effects that other stressors, such as hypoxia and hypercapnia, may have on metabolic rates and behavioral movement (McNeil and Sasse, 2016; Howard et al., 2020b). Such studies would not only yield a better understanding of the relative impacts of co-drivers associated with the redistribution of pelagic forage fish species in the California Current region under changing climate conditions, but also lead to more constrained estimates of uncertainty sources which, ultimately, determine the value of regional climate projections for marine ecosystem services to coastal communities.

DATA AVAILABILITY STATEMENT

The raw data supporting the conclusions of this article will be made available by the authors, without undue reservation. The model output is deposited on Dryad at https://doi.org/10.7291/D1QQ3H.

AUTHOR CONTRIBUTIONS

JF designed the numerical experiments, analyzed the model results, and wrote the manuscript. MP, MJ, and MA implemented the time-varying delta method and generated the physical downscaled solutions. KR assisted with the implementation of the IBM and fishing fleet models. All authors contributed to manuscript editing.

FUNDING

This work was supported by a grant from the National Atmospheric and Oceanic Administration (NOAA) CPO Coastal and Climate Applications (COCA) program and the NOAA Fisheries Office of Science and Technology (NA17OAR4310268).

SUPPLEMENTARY MATERIAL

The Supplementary Material for this article can be found online at: https://www.frontiersin.org/articles/10.3389/fmars.2021.685241/full#supplementary-material

REFERENCES

Andersen, K. H., Jacobsen, N. S., Jansen, T., and Beyer, J. E. (2017). When in life does density dependence occur in fish populations?. *Fish Fish.* 18, 656–667. doi: 10.1111/faf.12195

Atlas, R., Hoffman, R. N., Ardizzone, J., Leidner, S. M., Jusem, J. C., Smith, D. K., et al. (2011). A Cross-calibrated, Multiplatform Ocean Surface Wind Velocity Product for Meteorological and Oceanographic Applications. *Bull. Am. Meteorol. Soc.* 92, 157–174. doi: 10.1175/2010bams2946

Bograd, S. J., Castro, C. G., Di Lorenzo, E., Palacios, D. M., Bailey, H., Gilly, W., et al. (2008). Oxygen declines and the shoaling of the hypoxic boundary in the California Current. Geophys. *Res. Lett.* 35:L12607. doi: 10.1029/2008GL034185

Bopp, L., Resplandy, L., Orr, J. C., Doney, S. C., Dunne, J. P., Gehlen, M., et al. (2013). Multiple stressors of ocean ecosystems in the 21st century: projections with CMIP5 models. *Biogeosciences* 10, 6225–6245. doi: 10.5194/bg-10-6225-2013

Brady, R. X., Alexander, M. A., Lovenduski, N. S., and Rykaczewski, R. R. (2017). Emergent anthropogenic trends in California Current upwelling. *Geophys. Res. Lett.* 44, 5044–5052. doi: 10.1002/2017gl072945

Canales, T. M., Delius, G. W., and Law, R. (2020). Regulation of fish stocks without stock–recruitment relationships: the case of small pelagic fish. *Fish Fish.* 21, 857–871. doi: 10.1111/faf.12465

Carton, J. A., and Giese, B. S. (2008). A Reanalysis of Ocean Climate Using Simple Ocean Data Assimilation (SODA). *Mon. Weather Rev.* 136, 2999–3017. doi: 10.1175/2007mwr1978

Chavez, F. P., Ryan, J., Lluch-Cota, S. E., and Òiquen, M. (2003). From anchovies to sardines and back: multidecadal change in the Pacific Ocean. *Science* 299, 217–221. doi: 10.1126/science.1075880

Checkley, D. M. Jr., Asch, R. G., and Rykaczewski, R. R. (2017). Climate, anchovy, and sardine. *Annu. Rev. Mar. Sci.* 9, 469–493. doi: 10.1146/annurev-marine-122414-033819

Checkley, D. M., and Barth, J. A. (2009). Patterns and processes in the California Current System. *Prog. Oceanogr.* 83, 49–64. doi: 10.1016/j.pocean.2009.07.028

Cheung, W. W. L., Brodeur, R. D., Okey, T. A., and Pauly, D. (2015). Projecting future changes in distributions of pelagic fish species of Northeast Pacific shelf seas. *Prog. Oceanogr.* 130, 19–31. doi: 10.1016/j.pocean.2014.09.003

Collins, W. J., Bellouin, N., Doutriaux-Boucher, M., Gedney, N., Halloran, P., Hinton, T., et al. (2011). Development and evaluation of an Earth-System model – HadGEM2. *Geosci. Model Dev.* 4, 1051–1075. doi: 10.5194/gmd-4-1051-2011

Conkright, M. E., and Boyer, T. P. (2002). *World Ocean Atlas 2001: Objective Analyses, Data Statistics, and Figures, CD-ROM Documentation*. Silver Spring, MD: National Oceanographic Data Center.

Cury, P., Bakun, A., Crawford, R. J. M., Jarre-Teichmann, A., Quinones, R. A., Shannon, L. J., et al. (2000). Small pelagics in upwelling systems: patterns of interaction and structural changes in "wasp-waist" ecosystems. *ICES J. Mar. Sci.* 57, 603–618. doi: 10.1006/jmsc.2000.0712

Deser, C., Knutti, R., Solomon, S., and Phillips, A. S. (2012a). Communication of the role of natural variability in future North American climate. *Nat. Clim. Change* 2, 775–779. doi: 10.1038/nclimate1562

Deser, C., Phillips, A., Bourdette, V., and Teng, H. (2012b). Uncertainty in climate change projections: the role of internal variability. *Clim. Dyn.* 38, 527–546. doi: 10.1007/s00382-010-0977-x

Deser, C., Lehner, F., Rodgers, K. B., Ault, T., Delworth, T. L., DiNezio, P. N., et al. (2020). Insights from earth system model initial-condition large ensembles and future prospects. *Nat. Clim. Change* 10, 277–286. doi: 10.1038/s41558-020-0731-2

Di Lorenzo, E., Schneider, N., Cobb, K. M., Chhak, K., Franks, P. J. S., Miller, A. J., et al. (2008). North Pacific Gyre Oscillation links ocean climate and ecosystem change. *Geophys. Res. Lett.* 35:L08607. doi: 10.1029/2007GL032838

Dufresne, J. L., Foujols, M. A., Denvil, S., Caubel, A., Marti, O., Aumont, O., et al. (2013). Climate change projections using the IPSL-CM5 Earth System Model: from CMIP3 to CMIP5. *Clim. Dyn.* 40, 2123–2165. doi: 10.1007/s00382-012-1636-1

Dunne, J. P., John, J. G., Adcroft, A. J., Griffies, S. M., Hallberg, R. W., Shevliakova, E., et al. (2012). GFDL's ESM2 Global Coupled Climate–Carbon Earth System Models. Part I: physical Formulation and Baseline Simulation Characteristics. *J. Clim.* 25, 6646–6665. doi: 10.1175/jcli-d-11-00560.1

Eales, J., and Wilen, J. E. (1986). An examination of fishing location choice in the pink shrimp fishery. *Mar. Resour. Econ.* 4, 331–351. doi: 10.1086/mre.2.4.42628909

Echevin, V., Goubanova, K., Belmadani, A., and Dewitte, B. (2012). Sensitivity of the Humboldt Current system to global warming: a downscaling experiment of the IPSL-CM4 model. *Clim. Dyn.* 38, 761–774. doi: 10.1007/s00382-011-1085-2

Emmett, R. L., Brodeur, R. D., Miller, T. W., Pool, S. S., Bentley, P. J., Krutzikowsky, G. K., et al. (2005). Pacific sardine (Sardinops sagax) abundance, distribution, and ecological relationships in the Pacific Northwest. *CalCOFI Rep.* 46:122.

Fiechter, J., Edwards, C. A., and Moore, A. M. (2018). Wind, Circulation, and Topographic Effects on Alongshore Phytoplankton Variability in the California Current. *Geophys. Res. Lett.* 45, 3238–3245. doi: 10.1002/2017gl076839

Fiechter, J., Rose, K. A., Curchitser, E. N., and Hedstrom, K. (2015). The role of environmental controls in determining sardine and anchovy population cycles in the California Current: analysis of an end-to-end model. *Prog. Oceanogr.* 138, 381–398. doi: 10.1016/j.pocean.2014.11.013

Fiechter, J., Santora, J. A., Chavez, F., Northcott, D., and Messié, M. (2020). Krill Hotspot Formation and Phenology in the California Current Ecosystem. *Geophys. Res. Lett.* 47:e2020GL088039. doi: 10.1029/2020gl088039

Fréon, P., Curry, P., Shannon, L., and Roy, C. (2005). Sustainable exploitation of small pelagic fish stocks challenged by environmental and ecosystem changes: a review. *Bull. Mar. Sci.* 76, 385–462.

Frölicher, T. L., Rodgers, K. B., Stock, C. A., and Cheung, W. W. L. (2016). Sources of uncertainties in 21st century projections of potential ocean ecosystem stressors. *Global Biogeochem. Cycles* 30, 1224–1243. doi: 10.1002/2015gb005338

Haidvogel, D. B., Arango, H., Budgell, W. P., Cornuelle, B. D., Curchitser, E., Di Lorenzo, E., et al. (2008). Ocean forecasting in terrain-following coordinates:

formulation and skill assessment of the Regional Ocean Modeling System. *J. Comput. Phys.* 227, 3595–3624. doi: 10.1016/j.jcp.2007.06.016

Hawkins, E., and Sutton, R. (2009). The potential to narrow uncertainty in regional climate predictions. *Bull. Am. Meterol. Soc.* 90, 1095–1107. doi: 10.1175/2009bams2607.1

Hersbach, H., Bell, B., Berrisford, P., Hirahara, S., Horányi, A., Muñoz-Sabater, J., et al. (2020). The ERA5 global reanalysis. *Q. J. R. Meteorol. Soc.* 146, 1999–2049. doi: 10.1002/qj.3803

Hill, K. T., Lo, N. C. H., Macewicz, B. J., Crone, P. R., and Felix-Uraga, R. (2010). *Assessment of the Pacific sardine resource in 2009 for U.S. management in 2010. NOAA-TM-NMFS-SWFSC-4452*. California: NOAA Southwest Fisheries Science Center.

Howard, E. M., Frenzel, H., Kessouri, F., Renault, L., Bianchi, D., McWilliams, J. C., et al. (2020a). Attributing Causes of Future Climate Change in the California Current System with Multimodel Downscaling. *Global Biogeochem. Cycles* 34:e2020GB006646. doi: 10.1029/2020gb006646

Howard, E. M., Penn, J. L., Frenzel, H., Seibel, B. A., Bianchi, D., Renault, L., et al. (2020b). Climate-driven aerobic habitat loss in the California Current System. *Sci. Adv.* 6:eaay3188. doi: 10.1126/sciadv.aay3188

Humston, R., Olson, D. B., and Ault, J. S. (2004). Behavioral assumptions in models of fish movement and their influence on population dynamics. *Trans. Am. Fish. Soc.* 133, 1304–1328. doi: 10.1577/t03-040.1

Jacox, M. G., Alexander, M. A., Bograd, S. J., and Scott, J. D. (2020). Thermal displacement by marine heatwaves. *Nature* 584, 82–86. doi: 10.1038/s41586-020-2534-z

Kishi, M. J., Kashiwai, M., Ware, D. M., Megrey, B. A., Eslinger, D. L., Werner, F. E., et al. (2007). NEMURO - a lower trophic level model for the North Pacific marine ecosystem. *Ecol. Modell.* 202, 12–25. doi: 10.1016/j.ecolmodel.2006.08.021

Lindegren, M., Checkley, D. M., Rouyer, T., MacCall, A. D., and Stenseth, N. C. (2013). Climate, fishing, and fluctuations of sardine and anchovy in the California Current. *Proc. Natl. Acad. Sci. U. S. A.*110, 13672–13677. doi: 10.1073/pnas.1305733110

Lorenzen, K. (2008). Fish population regulation beyond "stock and recruitment": the role of density-dependent growth in the recruited stock. *Bull. Mar. Sci.* 83, 181–196.

Lynn, R. J., and Bograd, S. J. (2002). Dynamic evolution of the 1997-1999 El-Niño - La-Niña cycle in the southern California Current System. *Prog. Oceanogr.* 54, 59–75.

Machu, E., Goubanova, K., Le, Vu, B., Gutknecht, E., and Garçon, V. (2015). Downscaling biogeochemistry in the Benguela eastern boundary current. *Ocean Model.* 90, 57–71. doi: 10.1016/j.ocemod.2015.01.003

Mantua, N. J., Hare, S. R., Zhang, Y., Wallace, J. M., and Francis, R. C. (1997). A Pacific interdecadal climate oscillation with impacts on salmon production. *Bull. Am. Meteorol. Soc.* 78, 1069–1079. doi: 10.1175/1520-0477(1997)078<1069:apicow>2.0.co;2

McNeil, B., and Sasse, T. (2016). Future ocean hypercapnia driven by anthropogenic amplification of the natural CO_2 cycle. *Nature* 529, 383–386. doi: 10.1038/nature16156

Morley, J. W., Selden, R. L., Latour, R. J., Frölicher, T. L., Seagraves, R. J., and Pinsky, M. L. (2018). Projecting shifts in thermal habitat for 686 species on the North American continental shelf. *PLoS One* 13:e0196127. doi: 10.1371/journal.pone.0196127

Nishikawa, H., Curchitser, E. N., Fiechter, J., Rose, K. A., and Hedstrom, K. (2019). Using a climate-to-fishery model to simulate the influence of the 1976–1977 regime shift on anchovy and sardine in the California Current System. *Prog. Earth Planet. Sci.* 6, 1–20.

Pacific Fishery Management Council (PFMC) (2011). *Status of the Pacific Coast Coastal Pelagic Species Fishery and Recommended Acceptable Biological Catches. Stock Assessment and Fishery Evaluation - 2011*. Portland: Pacific Fishery Management Council.

Peck, M. A., Alheit, J., Bertrand, A. I, Catalán, A., Garrido, S., Moyano, M., et al. (2021). Small pelagic fish in the new millennium: a bottom-up view of global research effort. *Prog. Oceanogr.* 191:102494. doi: 10.1016/j.pocean.2020.102494

Peterson, W. T., and Schwing, F. B. (2003). A new climate regime in northeast pacific ecosystems. *Geophys. Res. Lett.* 30:1896. doi: 10.1029/2003GL017528

Politikos, D. V., Curchitser, E. N., Rose, K. A., Checkley, D. M. Jr., and Fiechter, J. (2018). Climate variability and sardine recruitment in the California Current: a mechanistic analysis of an ecosystem model. *Fish. Oceanogr.* 27, 602–622. doi: 10.1111/fog.12381

Pozo Buil, M., Jacox, M., Fiechter, J., Alexander, M. A., Bograd, S. J., Curchister, E. N., et al. (2021). A dynamically downscaled ensemble of future projections for the California Current System. *Front. Mar. Sci.* 8:612874. doi: 10.3389/fmars.2021.612874

Rose, K. A., Cowan, J. H. Jr., Winemiller, K. O., Myers, R. A., and Hilborn, R. (2001). Compensatory density dependence in fish populations: importance, controversy, understanding and prognosis. *Fish Fish.* 2, 293–327. doi: 10.1046/j.1467-2960.2001.00056.x

Rose, K. A., Fiechter, J., Curchitser, E. N., Hedstrom, K., Bernal, M., Creekmore, S., et al. (2015). Demonstration of a fully-coupled end-to-end model for small pelagic fish using sardine and anchovy in the California Current. *Prog. Oceanogr.* 138, 348–380.

Rykaczewski, R. R., and Checkley, D. M. Jr. (2008). Influence of ocean winds on the pelagic ecosystem in upwelling regions. *Proc. Natl. Acad. Sci. U. S. A.* 105, 1965–1970. doi: 10.1073/pnas.0711777105

Rykaczewski, R. R., Dunne, J. P., Sydeman, W. J., García-Reyes, M., Black, B. A., and Bograd, S. J. (2015). Poleward displacement of coastal upwelling-favorable winds in the ocean's eastern boundary currents through the 21st century. *Geophys. Res. Lett.* 42, 6424–6431. doi: 10.1002/2015gl064694

Sánchez-Garrido, J. C., Werner, F. E., Fiechter, J., Ramos, A., Curchitser, E., Rose, K. A., et al. (2018). Decadal-scale variability of sardine and anchovy simulated with an end-to-end coupled model of the Canary Current ecosystem. *Prog. Oceanogr.* 171, 212–230. doi: 10.1016/j.pocean.2018.12.009

Sánchez-Garrido, J. C., Fiechter, J., Rose, K. A., Werner, F. E., and Curchitser, E. N. (2021). Dynamics of anchovy and sardine populations in the Canary Current off NW Africa: responses to environmental and climate forcing in a climate-to-fish ecosystem model. *Fish. Oceanogr.* 30, 232–252. doi: 10.1111/fog.12516

Scheffer, M., Baveco, J. M., DeAngelis, D. L., Rose, K. A., and van Nes, E. H. (1995). Super-individuals a simple solution for modelling large populations on an individual basis. *Ecol. Model.* 80, 161–170. doi: 10.1016/0304-3800(94)00055-m

Schwartzlose, R. A., Alheit, J., Bakun, A., Baumgartne, T. R., Cloete, R., Crawford, R. J. M., et al. (1999). Worldwide large-scale fluctuations of sardine and anchovy populations. *Afr. J. Mar. Sci.* 21, 289–347. doi: 10.2989/025776199784125962

Shchepetkin, A. F., and McWilliams, J. C. (2005). The regional oceanic modeling system (ROMS): a split-explicit, free-surface, topography-following-coordinate oceanic model. *Ocean Model.* 9, 347–404. doi: 10.1016/j.ocemod.2004.08.002

Small, R. J., Curchitser, E., Hedstrom, K., Kauffman, B., and Large, W. G. (2015). The Benguela Upwelling System: quantifying the Sensitivity to Resolution and Coastal Wind Representation in a Global Climate Model*. *J. Clim.* 28, 9409–9432. doi: 10.1175/jcli-d-15-0192.1

Smith, J. A., Muhling, B., Sweeney, J., Tommasi, D., Pozo Buil, M., Fiechter, J., et al. (2021). The potential impact of a shifting Pacific sardine distribution on US West Coast landings. *Fish. Oceanogr.* 30, 437–454. doi: 10.1111/fog.12529

Stock, C. A., Alexander, M. A., Bond, N. A., Brander, K. M., Cheung, W. W. L., Curchitser, E. N., et al. (2011). On the use of IPCC class models to assess the impact of climate on Living Marine Resources. *Prog. Oceanogr.* 88, 1–27. doi: 10.1016/j.pocean.2010.09.001

Watkins, K. S., and Rose, K. A. (2013). Evaluating the performance of individual-based animal movement models in novel environments. *Ecol. Model.* 250, 214–234. doi: 10.1016/j.ecolmodel.2012.11.011

Wolf, P. A. (1992). Recovery of the Pacific sardine and the California sardine fishery. *CalCOFI Rep.* 33, 76–86.

Zwolinski, J. P., Emmett, R. L., and Demer, D. A. (2011). Predicting habitat to optimize sampling of Pacific sardine (Sardinops sagax). *ICES J. Mar. Sci.* 68, 867–879. doi: 10.1093/icesjms/fsr038

Conflict of Interest: The authors declare that the research was conducted in the absence of any commercial or financial relationships that could be construed as a potential conflict of interest.

frontiers in Marine Science

ORIGINAL RESEARCH
published: 12 August 2021
doi: 10.3389/fmars.2021.669951

Climate Change Induced Trends and Uncertainties in Phytoplankton Spring Bloom Dynamics

Lőrinc Mészáros[1,2]*, *Frank van der Meulen*[2], *Geurt Jongbloed*[2] *and Ghada El Serafy*[1,2]

[1] *Marine and Coastal Systems, Deltares, Delft, Netherlands,* [2] *Applied Mathematics, Delft University of Technology, Delft, Netherlands*

Spring phytoplankton blooms in the southern North Sea substantially contribute to annual primary production and largely influence food web dynamics. Studying long-term changes in spring bloom dynamics is therefore crucial for understanding future climate responses and predicting implications on the marine ecosystem. This paper aims to study long term changes in spring bloom dynamics in the Dutch coastal waters, using historical coastal *in-situ* data and satellite observations as well as projected future solar radiation and air temperature trajectories from regional climate models as driving forces covering the twenty-first century. The main objective is to derive long-term trends and quantify climate induced uncertainties in future coastal phytoplankton phenology. The three main methodological steps to achieve this goal include (1) developing a data fusion model to interlace coastal *in-situ* measurements and satellite *chlorophyll-a* observations into a single multi-decadal signal; (2) applying a Bayesian structural time series model to produce long-term projections of chlorophyll-a concentrations over the twenty-first century; and (3) developing a feature extraction method to derive the cardinal dates (beginning, peak, end) of the spring bloom to track the historical and the projected changes in its dynamics. The data fusion model produced an enhanced chlorophyll-a time series with improved accuracy by correcting the satellite observed signal with *in-situ* observations. The applied structural time series model proved to have sufficient goodness-of-fit to produce long term chlorophyll-a projections, and the feature extraction method was found to be robust in detecting cardinal dates when spring blooms were present. The main research findings indicate that at the study site location the spring bloom characteristics are impacted by the changing climatic conditions. Our results suggest that toward the end of the twenty-first century spring blooms will steadily shift earlier, resulting in longer spring bloom duration. Spring bloom magnitudes are also projected to increase with a 0.4% $year^{-1}$ trend. Based on the ensemble simulation the largest uncertainty lies in the timing of the spring bloom beginning and -end timing, while the peak timing has less variation. Further studies would be required to link the findings of this paper and ecosystem behavior to better understand possible consequences to the ecosystem.

Keywords: regional climate model, climate change, uncertainty quantification, phytoplankton phenology, Bayesian model, data fusion, non-parametric regression

OPEN ACCESS

Edited by:
Sara Rivero-Calle,
University of Georgia, United States

Reviewed by:
Fernando Gonzalez Taboada,
Princeton University, United States
Yuntao Wang,
Ministry of Natural Resources, China

***Correspondence:**
Lőrinc Mészáros
lorinc.meszaros@deltares.nl

Specialty section:
This article was submitted to
Global Change and the Future Ocean,
a section of the journal
Frontiers in Marine Science

Received: *19 February 2021*
Accepted: *14 July 2021*
Published: *12 August 2021*

Citation:
Mészáros L, van der Meulen F, Jongbloed G and El Serafy G (2021) Climate Change Induced Trends and Uncertainties in Phytoplankton Spring Bloom Dynamics.
Front. Mar. Sci. 8:669951.
doi: 10.3389/fmars.2021.669951

1. INTRODUCTION

Phytoplankton and their seasonally occurring blooms are vital to marine ecosystems as they are a major source of energy input for higher trophic levels (Smayda, 1997). Phytoplankton blooms are natural phenomena occurring when phytoplankton growth exceeds the losses (mortality, respiration, feeding, sinking, and dispersive losses) and rapid accumulation takes place when optimal abiotic and biotic conditions are present for the growth. An early account of the bloom phenomenon is given by Sverdrup (1953). Phytoplankton blooms can be identified through chlorophyll-a concentration, which is an indicator for algal biomass, though concerns were raised (Alvarez-Fernandez and Riegman, 2014) about using chlorophyll as phytoplankton biomass proxy in the North Sea. In the Dutch coastal zone, phytoplankton mass seasonality is described by a prominent spring bloom (diatom dominated) and a less pronounced late summer bloom. This is partly driven by increased riverine nutrient loads (melting snow and spring rains) and intensified mixing by seasonal winds blowing over the shallow shelf sea. The onset of spring blooms is usually initiated by correlated changes in water temperature and the light availability (Winder and Sommer, 2012) but coupled to and controlled by thermal stratification, resource dynamics (e.g., nutrient availability) and predator-prey interactions (e.g., grazing) (Behrenfeld and Boss, 2018). Temperate marine environments, such as the Dutch coastal waters, are particularly sensitive to changes in spring bloom initiation due to the fact that higher trophic levels are greatly dependent on synchronized planktonic production (Edwards and Richardson, 2004).

When studying the functioning of continental shelf ecosystems, such as the southern North Sea, one should consider various influencing elements. Regarding the hydrodynamics, the southern North Sea is a tidally mixed region where tidal fronts occur across the English Channel. The variability in the tidal fronts influence stratification and mixing regimes and have ecological consequences, or may even be the driving force of regime shifts in the North Sea ecosystem (Longhurst, 2007). In addition to tidal fronts, along the Dutch coast, other shallow water (e.g., Wadden Sea), coastal, and estuarine fronts are impacting the system dynamics. These fronts are characterized by turbidity and salinity gradients. Since the study location is situated at the boundary of the North Sea and the shallower Wadden Sea, in the Mardiep tidal inlet, the coastal influence is an important factor. In the Dutch coastal zone the observed gradients of phytoplankton biomass are very steep and there is considerable natural variability in the chlorophyll-a concentration. In these shallower coastal waters the concentration of suspended inorganic matter, which influences the extinction of light, is relatively high and dynamically varying. According to Los and Blaas (2010) in Dutch coastal waters 25–75% of the light extinction is caused by suspended matter. Further coastal influencing factor affecting the spring bloom is the riverine nutrient loads. In the North Sea rivers provide a significant portion of the total nitrogen and phosphorus load (Los et al., 2014). Although the study site is not situated at a river outflow, there are nine major rivers that affect the Dutch coastal waters based on the nutrient composition matrix derived by Los et al. (2014). The plumes of these major effluents, especially the Rhine, are significant influencing factors to phytoplankton dynamics.

Available climate models offer us a range of (atmospheric) climate variables that could be considered as external drivers influencing phytoplankton seasonality. The climate variables include air temperature, precipitation, solar radiation, eastward and northward wind, air pressure, humidity, and cloud cover. In this study we focus on air temperature and solar radiation that were found to be the most influential atmospheric variables affecting coastal chlorophyll-a concentrations in the Dutch coastal waters, along with wind speed (in shallow systems). This conclusion was reached by applying various statistical techniques to explore temporal, spatial, and functional correlations from the historical atmospheric and chlorophyll-a time series at this location.

In its recent comprehensive study of the Wadden Sea eutrophication trends, van Beusekom et al. (2019) lists the phytoplankton governing factors, both bottom-up (light, nutrient) and top-down (grazing, filter feeding). Through the review of various studies, it was concluded that light is the dominating limiting factor, which is present all year long, while nutrient limitation occurs during summer and toward the end of the growth season. Moreover, a cross correlation analysis was conducted by Blauw et al. (2018) in the North Sea between environmental variables (tidal mixing, wind mixing, solar radiation, air temperature, SST, salinity, turbidity) and chlorophyll-a hourly time series, including various lags. At the site with dynamics similar to our study area, the highest correlations were found with solar radiation, air temperature, turbidity, and tidal mixing. Additionally, Irwin and Finkel (2008) reports that sea surface temperature is the best predictor of chlorophyll-a concentration in the North Atlantic. In their climate impact study, Richardson and Schoeman (2004) also opted to use only mean annual sea surface temperature as an environmental driver since it acts as a useful proxy for other physical processes and influences seasonal and regional changes in vertical stratification, nutrients, and winds. We should also note that there is relationship between air temperature, solar radiation, and mixing. Blauw et al. (2018) indicated that in the North Sea air temperature and solar radiation influences phytoplankton biomass through diurnal variation in convective mixing and diurnal vertical migration of motile phytoplankton. Supporting this, Van Haren et al. (1998) reported that the diurnal variation in convective mixing is attributed to the sinking of phytoplankton during daytime (thermal micro-stratification) and resuspension at night (surface cooling). Irwin and Finkel (2008) also confirmed that temperature is correlated with stratification, mixed layer depth, and nutrient availability and their temporal changes.

The thermal structure of the North Sea as a whole is characterized by a well-developed thermocline during summer and well-mixed water column during winter (Gräwe et al., 2014). Nevertheless, there are important regional differences. In the central North Sea the water column can be strongly stratified and the tidal-induced mixing is less important. In these regions wind-driven mixing and convective cooling have a greater impact on phytoplankton biomass (Blauw et al., 2018). This seasonally stratified condition is in stark contrast with the highly dynamic coastal systems where tidal mixing is the most dominant physical factor. McQuatters-Gollop and Vermaat (2011) also documented important differences between the offshore and coastal North Sea regarding the impact of climatic conditions and nutrient availability. It was found that inter-annual variability in phytoplankton dynamics of the offshore regions was mainly regulated by temperature, Atlantic inflow, as well as co-varying wind stress and North Atlantic Oscillation (NAO). Contrarily, in coastal waters solar radiation and sea surface temperature, as well as Si availability was dominant (McQuatters-Gollop and Vermaat, 2011). In addition to the regional differences, the influence of environmental drivers of phytoplankton biomass also differs at different temporal scales (Blauw et al., 2018). At short time scales, the physical transport of phytoplankton cells by wind-driven or tidal mixing is the dominant. On the other hand, focusing on the seasonal time scales it is solar radiation and air temperature, together with associated changes in thermal stratification, nutrient availability and grazing, that dominate phytoplankton dynamics (Sverdrup, 1953; Sommer et al., 2012; Blauw et al., 2018). Finally, at longer inter-annual and decadal time scales climatic variation and long-term human impacts on the eutrophication status will become influential (Richardson and Schoeman, 2004; Blauw et al., 2018). Consequently, we acknowledge that in other regions physical processes play a dominant role in coastal chlorophyll-a concentrations, especially through the mixing (e.g., wind-driven) of nutrients into the euphotic layer during stratified conditions. Although this is particularly important in oligotrophic regions where solar energy is abundant and phytoplankton dynamics is mainly limited by nutrient availability (Yu et al., 2019), it is less influential in our case.

Our study is motivated by the fact that climate-induced regime shifts reportedly took place in the North Sea (Alvarez-Fernandez et al., 2012; Beaugrand et al., 2014). Consequently, seasonal variability of phytoplankton biomass in relation to light and temperature is particularly important aspect in the North West Shelf Seas (Tulp et al., 2006; Llope et al., 2009). The interactive effects of temperature and solar irradiance on phytoplankton have been extensively studied without clear consensus. This may be partly due to the fact that phytoplankton response to temperature change greatly varies between individual and aggregate level. Considering the individual level phytoplankton responses to temperature are exponentially or linearly increasing until the optimum, and declining above that (Edwards et al., 2016). On the other hand, looking at the aggregate level, species can replace one another along a temperature gradient via competition resulting in monotonically increasing growth rates. However, temperature also influences predator-prey interactions, not only phytoplankton growth. The intensity of grazing (or zooplankton ingestion) is partly determined by temperature, along with the available phytoplankton biomass and the zooplankton biomass (Townsend et al., 1994).

Due to the complex interactions of physical forcing conditions with food web processes, phenological responses of phytoplankton to climate change are not trivial to estimate. Nevertheless, according to Rolinski et al. (2007), focusing on the spring season may help to reduce the complexity. It was suggested that in temperate marine systems the impact of physical environment and the response of the biological system can be best studied in spring. During spring, the physical limiting factors like temperature, light availability, and mixing are more prominent than the non-physical ones, such as trophic interactions (e.g., grazing). While in the spring period trophic interactions may not be limiting, later on in the year, they become more important and may dominate over the physical factors (Sommer et al., 1986, 2012). Thus, we acknowledge the complexity of physical and trophic interactions and do not dismiss their influence on the phytoplankton phenology. Nevertheless, this study aims to focus on the physical drivers, or more precisely on the climatic ones. Consequently, to limit the masking effect of trophic interactions, as far as this may be possible, we focus on the spring phytoplankton bloom to study the impact of changing climatic conditions in the Dutch coastal zone.

Changing climatic conditions directly affect the photosynthetic metabolism of phytoplankton, but also indirectly impact them by modifying their physical environment (D'Alelio et al., 2020). Climate change impacts on phytoplankton are manifested as shifts in seasonal dynamics, species composition, and population size structure (Winder and Sommer, 2012). Since in the current study we only use chlorophyll-a concentration as response variable, we can only draw conclusions on the seasonal dynamics of the aggregate level, not on species composition or population structure. As an indicator of climate change impacts on seasonal phytoplankton dynamics, we selected the long term changes in spring bloom dynamics. There is, however, no single definition of phytoplankton blooms in the literature or in policies, for instance based on the rate of change or the threshold of concentration, as this is highly dependent on the type of ecosystems (e.g., inland or marine, local species, climate, bathymetry). In this study we describe the spring bloom dynamics by their cardinal dates (bloom initiation, -peak, and -ending) using log-concave regression. Alternatives methods of deriving cardinal dates and the benefits of using log-concave regression are presented in the section 2.4.

A range of studies investigating climate change induced shifts in phytoplankton bloom dynamics in the North Sea already exist. Most of these studies derive their findings from historical chlorophyll-a data, measured either by *in-situ* sensors or remote sensing (Edwards and Richardson, 2004; Philippart et al., 2010; Friedland et al., 2015; Hjerne et al., 2019; Desmit et al., 2020), or from laboratory experiments (Lewandowska and Sommer, 2010; Winder et al., 2012). Climate impact studies which focus on future developments of phytoplankton bloom dynamics generally use few climate change scenarios from global or regional climate models and traditionally use physically-based models (Friocourt et al., 2012; Holt et al., 2014, 2016; Pushpadas et al., 2015; Schrum et al., 2016). We acknowledge that previous papers already introduced ways to characterize phytoplankton blooms (Rolinski et al., 2007; Wiltshire et al., 2008; Lewandowska and Sommer, 2010; Philippart et al., 2010;

Hjerne et al., 2019). Nevertheless, uncertainty quantification in the shift of phytoplankton dynamics in these studies is not a central topic.

There are, however, existing studies that address uncertainty in bloom detection. Cole et al. (2012) investigates the impact of missing data on phytoplankton phenology metrics (threshold-based definition) using satellite observed chlorophyll-a; Ferreira et al. (2014) compares the accuracy and precision of three bloom metrics (biomass-based threshold method, cumulative biomass-based threshold method, rate of change) on biogeochemical model outputs and satellite observed chlorophyll-a; while González Taboada and Anadón (2014) performs probabilistic phytoplankton phenology characterization using Bayesian harmonic regression and a threshold-based definition of bloom metrics based on satellite observed chlorophyll-a. Major advantage of these studies is the quantification of errors or uncertainties in the computation of the bloom metrics. Our research deviates from these studies in that we do not focus on historical data but aim to quantify future projected uncertainties in spring bloom dynamics. In fact, in our analysis the bloom detection algorithm is the only step where "model uncertainties" are not quantified and instead all other steps involve uncertainty estimates. The reason for this is that in future climate change studies the main source of uncertainty does not arise from the derivation of the bloom metrics but from the climate forcings and from the projection of the chlorophyll-a signal. Our method does provide uncertainty ranges for the bloom metrics but that is derived from the ensemble of generated chlorophyll-a projections. The benefit of reconstructing a range ($>$ 100) of full seasonal cycles is therefore to obtain predictive uncertainty estimates on bloom metrics from the input data rather than from the bloom detection itself.

Considering the above, the novelty of our work lies in the following features. In our research we make use of both *in-situ* and satellite observations jointly by applying a data fusion algorithm to get a more complete, more accurate, and longer data record. While a range of possibilities already exist to describe phytoplankton blooms, in our research we propose a new way of extracting the cardinal dates of the phytoplankton spring blooms. We use non-parametric shape constrained (log-concave) regression, which provides a flexible formulation without tuning parameters and assumptions on the distribution patterns and can be directly applied on the annual bi-modal time series without any pre-processing. Consequently, our proposed method is less sensitive to bloom amplitude, missing data, and observational noise.

Moreover, we augment existing climate change scenarios with synthetically generated ones, thus supplying numerous ($>$ 100) trajectories for air temperature and solar radiation development. In addition to this, our proposed method complements the computationally expensive numerical models for chlorophyll-a simulation with a data driven approach, using a Bayesian structural time series model. Complementing physically-based prediction models with statistical ones allows us to compute a large number of simulations and achieve better characterization of predictive uncertainties. These methodological advances enable the combination of different chlorophyll-a data sources, the incorporation of climate covariates and the propagation of uncertainty from observations to nonlinear estimates of projected changes in spring bloom metrics under an enriched number of climate change scenarios (associated to future development and emission pathways).

2. MATERIALS AND METHODS

In this chapter we describe the data sources and introduce the main methods that were developed and/or applied within the framework of this study. When new methods are proposed, such as the data fusion model and the shape constraint model to derive bloom metrics, we aim to sufficiently document those to allow replication studies.

Figure 1 presents the methodological framework and summarizes the connections between elements. Our research aims to study changes in phytoplankton phenology based on historical data and future climate projections. Given the historical records of chlorophyll-a concentrations obtained from various data sources, one can extract the cardinal dates of the spring bloom for the past decades using the proposed feature extraction technique. Furthermore, changes in the spring blooms may be projected for the future by utilizing the correlation between climatic factors, represented by air temperature and solar radiation, and the ecological response, indicated by the chlorophyll-a concentration. This correlation can be inferred from past records since air temperature and solar radiation were measured by field sensors for the past decades. Though future chlorophyll-a concentrations are not available to us, we attempt to make projections using the trends and seasonality from historical observations and taking into account the correlations with projected air temperature and solar radiation, produced by regional climate models. While this methodological framework allows us to investigate past and projected spring bloom dynamics, we note that there are several sources of uncertainties, both data and model related ones, which are propagated through the steps. These uncertainty sources ($\pm$U) are marked in **Figure 1**. In order to address this issue, we aim to use transparent statistical approaches that allow us to quantify intrinsic uncertainties. Noting that the projected trends in bloom metrics constitute the main findings of the research, the importance of the uncertainty quantification framework should also be emphasized, which should always go hand-in-hand with climate change impact studies.

2.1. Data Sources

This research is based on a multitude of data sources from sensors and numerical models of various types. The environmental and climate variables in this study are chlorophyll-a concentration, air temperature, and solar radiation. In order to investigate past trends and obtain the correlation between these variables, we make use of historical measurements, whereas to anticipate future climate change impacts, climate model outputs are used.

2.1.1. Chlorophyll-a Concentration Measurements

Available historical chlorophyll-a data includes field observations at Marsdiep Noord station (see **Figure 2**), from the Dutch

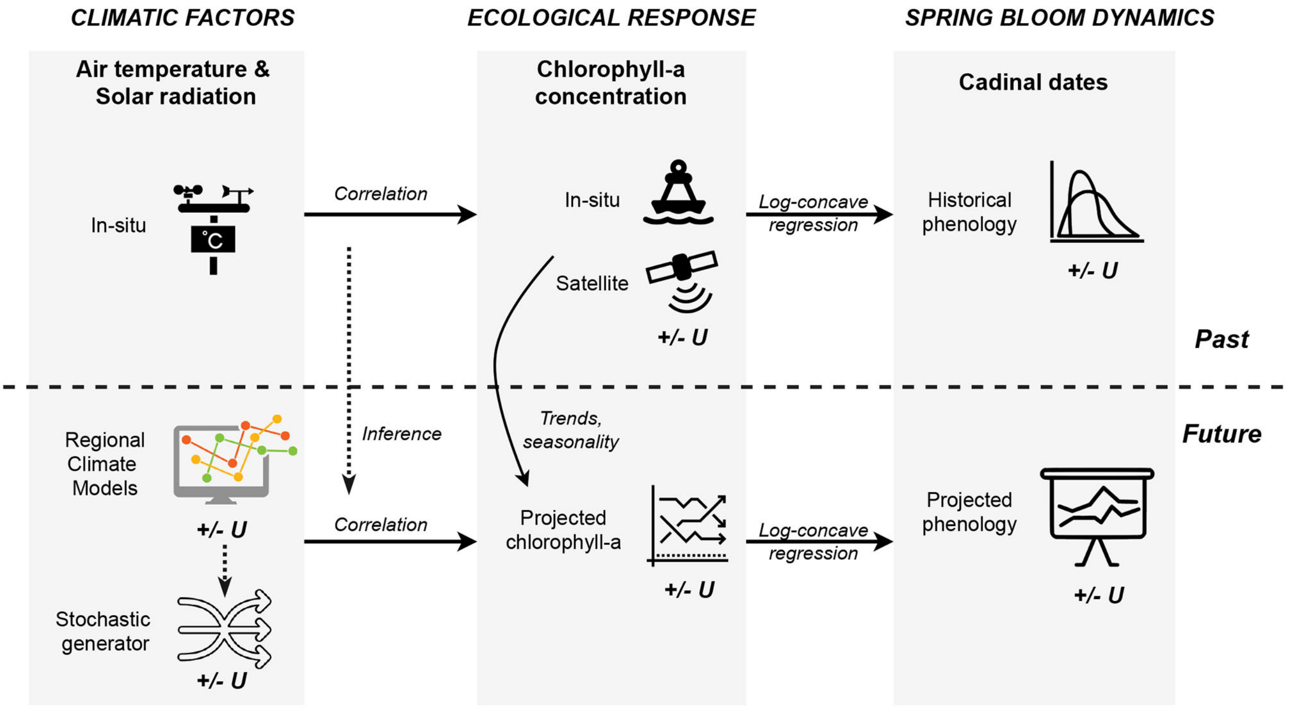

FIGURE 1 | Methodological framework including three main elements with causal and temporal relations: (1) climatic factors, (2) ecological response, and (3) spring bloom dynamics.

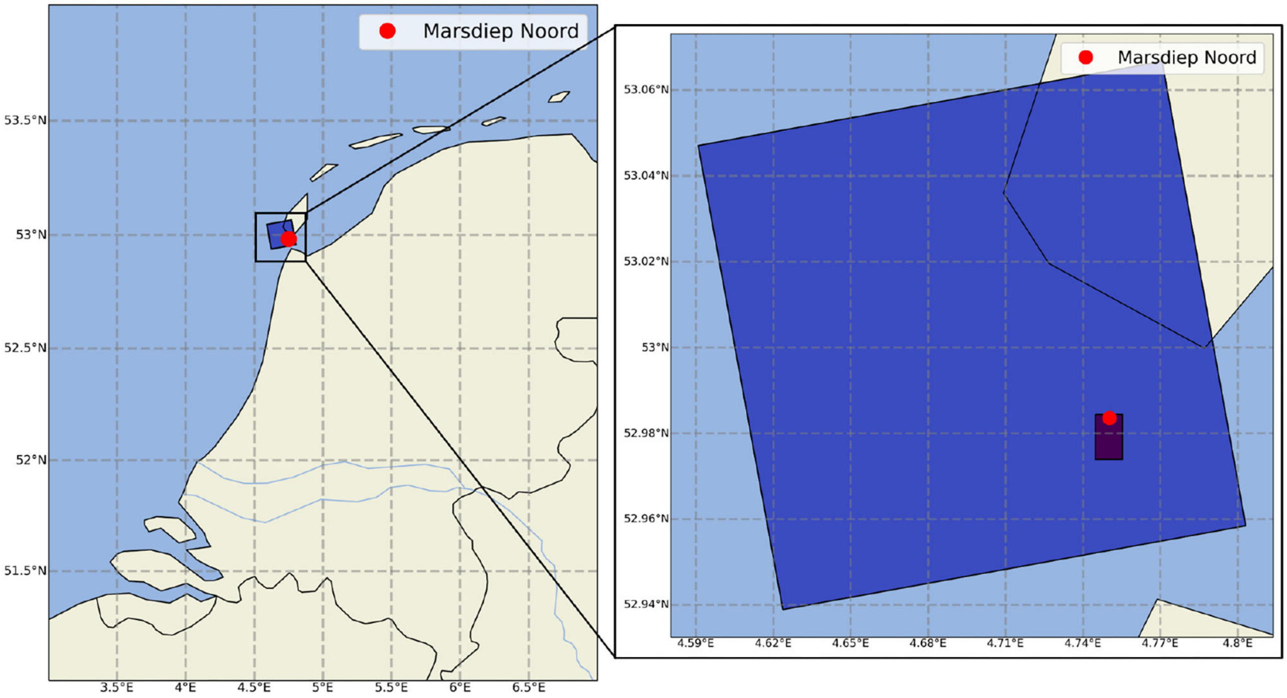

FIGURE 2 | Location of the study area and the monitoring point together with the pixels of the matching Euro-CORDEX climate model output and CMEMS satellite measured chlorophyll-a.

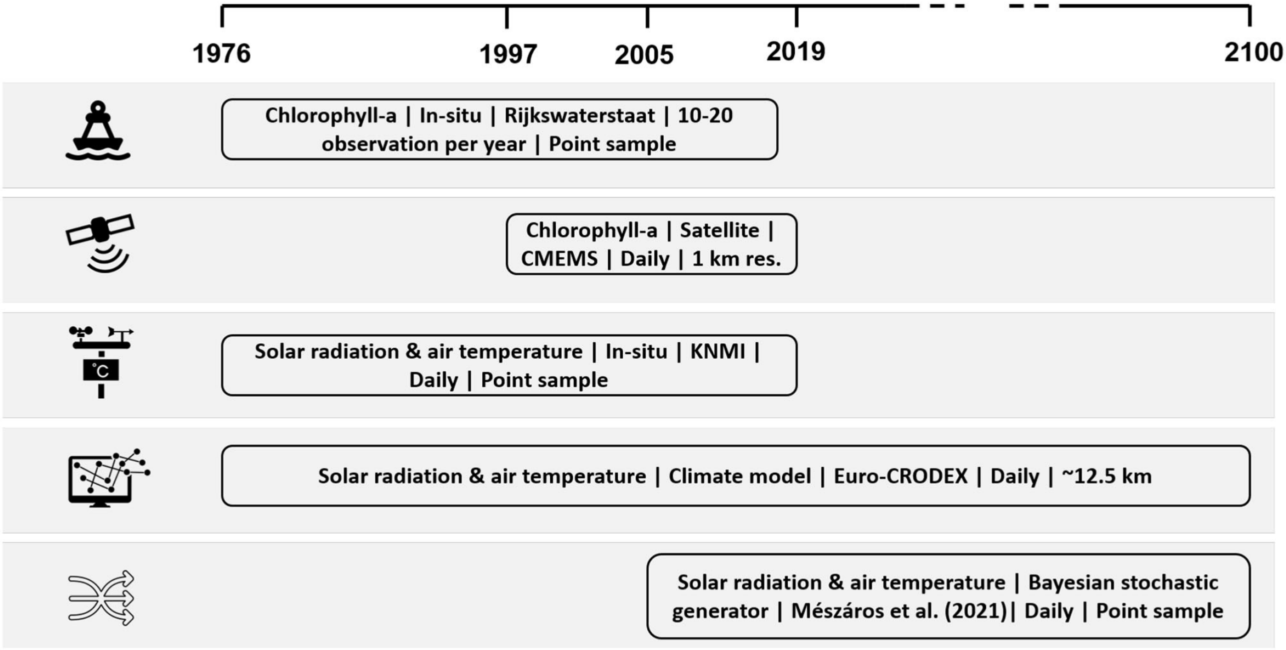

FIGURE 3 | Overview of data sources. The description includes variable name, data type, data source, data frequency, and spatial resolution.

Directorate-General for Public Works and Water Management (Rijkswaterstaat), covering more than 40 years from 1976 to 2018, but measured rather sparsely. To complement these field measurements, processed, and validated satellite observed chlorophyll-a concentration (extracted at the same location) was used from the Copernicus Marine Environment Monitoring Service (CMEMS) from 1997 to 2019 (see **Figure 3**). We should note that satellite observation of phytoplankton biomass in the Dutch coastal waters is complex since the chlorophyll-a signal may be mixed with the relative distribution of suspended matter and CDOM instead of phytoplankton biomass (Longhurst, 2007).

The specific product in use is the North Atlantic Chlorophyll-a, daily interpolated and reprocessed product with one km spatial resolution (OCEANCOLOUR_ATL_CHL_L4_REP_OBSERVATIONS_009_098). The satellite product is limited to the surface depth. This chlorophyll-a product is produced using multiple sensors (multi-sensor product), multiple chlorophyll-a algorithms and a daily space-time interpolation scheme (Saulquin et al., 2019). The interpolation scheme includes a combination of a water-typed merge of chlorophyll-a estimates and kriging interpolation method with regional anisotropic covariance models at the shore, as described in Saulquin et al. (2019). This product uses the Copernicus-GlobColor processor and it is obtained by merging the following sensors: SeaWIFS, MODIS Aqua, MODIS Terra, MERIS, VIIRS NPP, VIIRS-JPSS1 OLCIS3A, and S3B. For coastal waters the product uses the standard OC3-OC4 (Antoine and Morel, 1996; O'Reilly et al., 1998, 2000) and OC5 (Gohin et al., 2002) algorithms. The latest product validation results against *in-situ* measurements show an r^2 of 0.73 with $N = 11,502$ data points (Garnesson et al., 2020). For a more in-depth description of this satellite product the reader is referred to the QUality Information Document (QUID) (Garnesson et al., 2020).

The chlorophyll-a concentration seasonality from *in-situ* observation is shown in **Figure 4A**, and from satellite observations in **Figure 4B**. Naturally these data sources have different sampling methods and associated uncertainties. The *in-situ* observations are point samples taken by the Dutch national *in-situ* monitoring programme (MWTL) https://waterinfo-extra.rws.nl/monitoring/. It should be noted that the samples are taken close to the water surface, usually in the upper 3–5 m of the water column. These observations are often considered as ground truth and are the most reliable, however, in the case of chlorophyll-a concentration the temporal frequency of the observations is relatively low, around 10-20 observations per year. This amount of field observations poses a limitation to assess annual phytoplankton bloom cycles (Winder and Cloern, 2010). Thus, the more frequently sampled satellite images are also used to complement the *in-situ* measurements for a better assessments of bloom characteristics. This complementary data source is used noting that satellite derived chlorophyll-a is only available at the water surface (lack of vertical resolution), has a coarse 1 km resolution and suffers from algorithmic and interpolation errors, consequently having a higher level of associated uncertainty.

Since the two types of chlorophyll-a measurements describe the same underlying process, we propose a data fusion model to combine them. This data fusion model interlaces the *in-situ* and satellite observations into a single chlorophyll-a concentration signal, which is more complete then the individual observations

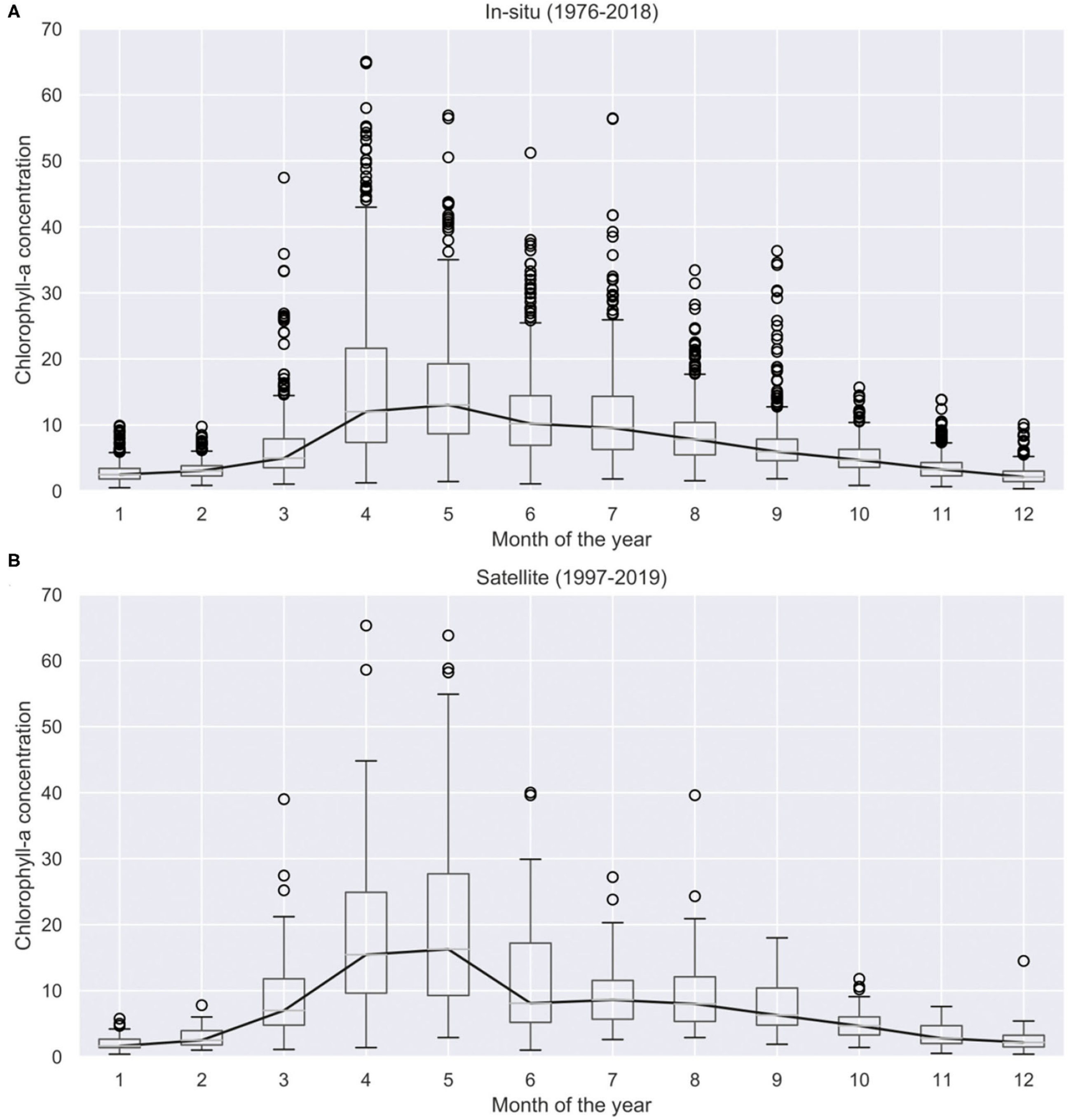

FIGURE 4 | Historical chlorophyll-a concentrations measured in the Dutch Wadden Sea using *in-situ* data between 1976 and 2018 **(A)** and satellite images between 1997 and 2019 **(B)**. Climatological median (solid black line) per calendar is also shown.

and covers a longer time period. The data fusion model is described in section 2.2.

2.1.2. Solar Radiation and Air Temperature Measurements

The historical daily solar radiation and air temperature records are obtained at the nearest weather station (De Kooy) from the Royal Netherlands Meteorological Institute (KNMI) for the matching period (1976–2019). Apart from historical data, future projected values of air temperature and solar radiation are acquired from the high resolution 0.11° (∼ 12.5 km) EURO-CORDEX Coordinated Regional Downscaling Experiment (Jacob et al., 2014), which uses the Swedish Meteorological and Hydrological Institute Rossby

Centre regional atmospheric model (SMHI-RCA4). In order to produce various regionally downscaled scenarios, EURO-CORDEX applies a range of General Circulation Models (GCMs) to drive the above mentioned Regional Climate Model (RCM). In addition to the driving models, further scenarios are obtained by considering different socio-economic changes described in the Representative Concentration Pathways (RCPs). RCPs are labeled according to their specific radiative forcing pathway in 2100 relative to pre-industrial values. The EURO-CORDEX scenario simulations use the RCPs defined for the Fifth Assessment Report of the IPCC. In this study we include RCP8.5 (high), and RCP4.5 (medium-low) (van Vuuren et al., 2011) and four driving GCMs.

In the upcoming Sixth Assessment Report new scenarios and pathways will also be included, which are called Shared Socioeconomic Pathways (SSPs) (Abram et al., 2019). SSPs describe five alternative socioeconomic pathways (SSP1–SSP5) for future society enhancing the existing RCPs with socioeconomic challenges to adaptation and mitigation. Such socioeconomic challenges are population, economic growth, urbanization, or technological development for instance (O'Neill et al., 2017). It should be emphasized that SSPs are not replacing but complementing RCPs. In the Sixth Assessment Report the RCP-based climate projections and SSP-based socioeconomic scenarios are combined to achieve an integrative framework for climate impact and policy analysis (Abram et al., 2019). From the SSP scenarios SSP5-8.5 corresponds to RCP8.5 and represents the high end of the range of future forcing pathways, while SSP2-4.5 represents the medium part and corresponds to RCP4.5 (Abram et al., 2019).

Together the four different driving GCMs and two RCPs that are applied in this study provide us with an ensemble of eight future solar radiation and temperature trajectories. Since the RCM simulations are subject to climate model structural error and boundary errors from the driving GCMs (Navarro-Racines et al., 2020), they should be bias corrected before applying them in impact studies (Luo, 2016). For this reason, quantile mapping bias correction (Amengual et al., 2012) was applied using the RCM simulations for the reference period (1976–2005) and daily historical field measurements from KNMI for the same period, as described in Mészáros et al. (2021). The quantile-quantile mapping transfer functions were established for the reference period and separately for each RCM simulation. The transfer functions were then applied for the bias correction of each future projections (2006–2100) separately.

This ensemble of climate trajectories is used to simulate a range of possible phytoplankton seasonality shifts and the associated uncertainty described by the predictive distribution of the phytoplankton bloom cardinal dates. It should be noted that applying only eight climate projections reduces the ability to adequately resolve the unknown predictive distribution that one tries to estimate, hence, higher number of climate trajectories providing sufficient resolution in terms of probabilities is required (Leutbecher, 2019). Consequently, to better characterize uncertainties, an enriched set of climate change projections is employed. This set of air temperature and solar radiation projections was produced using a Bayesian stochastic generator (Mészáros et al., 2021), which builds on the above mentioned Regional Climate Model scenarios provided by the EURO-CORDEX experiment and generates further synthetic scenarios using a hierarchical Bayesian model. The generated ensemble of air temperature and solar radiation projections include 120 members and their statistical properties are similar to the input projections. Both the EURO-CORDEX and synthetic projections are shown for air temperature in **Figure 5A** and for solar radiation in **Figure 5B**. At this specific location we can observe a consistently increasing temperature trend over the twenty-first century and a slightly decreasing solar radiation trend. While increasing air temperatures are in line with expectations, decreasing solar radiation trends may need further explanation. The main cause of this negative trend is the fact that total cloud cover at this site is projected by EURO-CORDEX to increase, hence, limiting surface downwelling shortwave radiation. This is a region specific feature, and the difficulty of projecting cloud cover and solar radiation changes in coastal areas with sea-land-atmosphere boundaries, such as the study site, has been previously highlighted by Bartók et al. (2017), along with discrepancy between RCMs and their driving GCMs in their solar radiation projections over Europe.

2.2. Data Fusion of Chlorophyll-a Measurements

2.2.1. Statistical Model

In order to describe the chlorophyll-a concentration, we assume that there is a continuously evolving latent signal ($X_t,\ t \in [0, T]$) that satisfies the stochastic differential equation (sde)

$$\mathrm{d}X_t = -\alpha(X_t - \mu(t))\,\mathrm{d}t + \sigma\,\mathrm{d}W_t. \tag{1}$$

The underlying idea is to model a stochastic process that is mean reverting (with strength α) toward the deterministic signal $t \mapsto \mu(t)$. We will take μ to be periodic with period 1. We start off from a continuous time description as *in-situ* measurements are not collected at regular times. Observations can be of three types

1. $Y_i \sim N(X_{t_i}, \psi_1)$;
2. $Y_i \sim N(X_{t_i}, \psi_2)$;
3. $Y_i \sim N_2\left(\begin{bmatrix}1\\1\end{bmatrix} X_{t_i}, \begin{bmatrix}\psi_1 & 0\\ 0 & \psi_2\end{bmatrix}\right)$.

This reflects having two types of measurements (*in-situ* and satellite) with different accuracies. Sometimes one measurement is obtained, sometimes the other one, and sometimes both are available. We take Y_i to be the log of the measured concentration (component-wise) to ensure the model only predicts non-negative concentrations. While we acknowledge that there are other mapping functions to achieve non-negativity, taking the log of chlorophyll-a concentration is often used in practice (Campbell, 1995).

Assuming successive observations are obtained closely in time, i.e., $\Delta_i := t_i - t_{i-1}$ being small for all i, we have

$$X_{t_i} \approx X_{t_{i-1}} - \alpha(X_{t_{i-1}} - \mu(t_{i-1}))\Delta_i + \sigma\sqrt{\Delta_i}\epsilon_i,$$

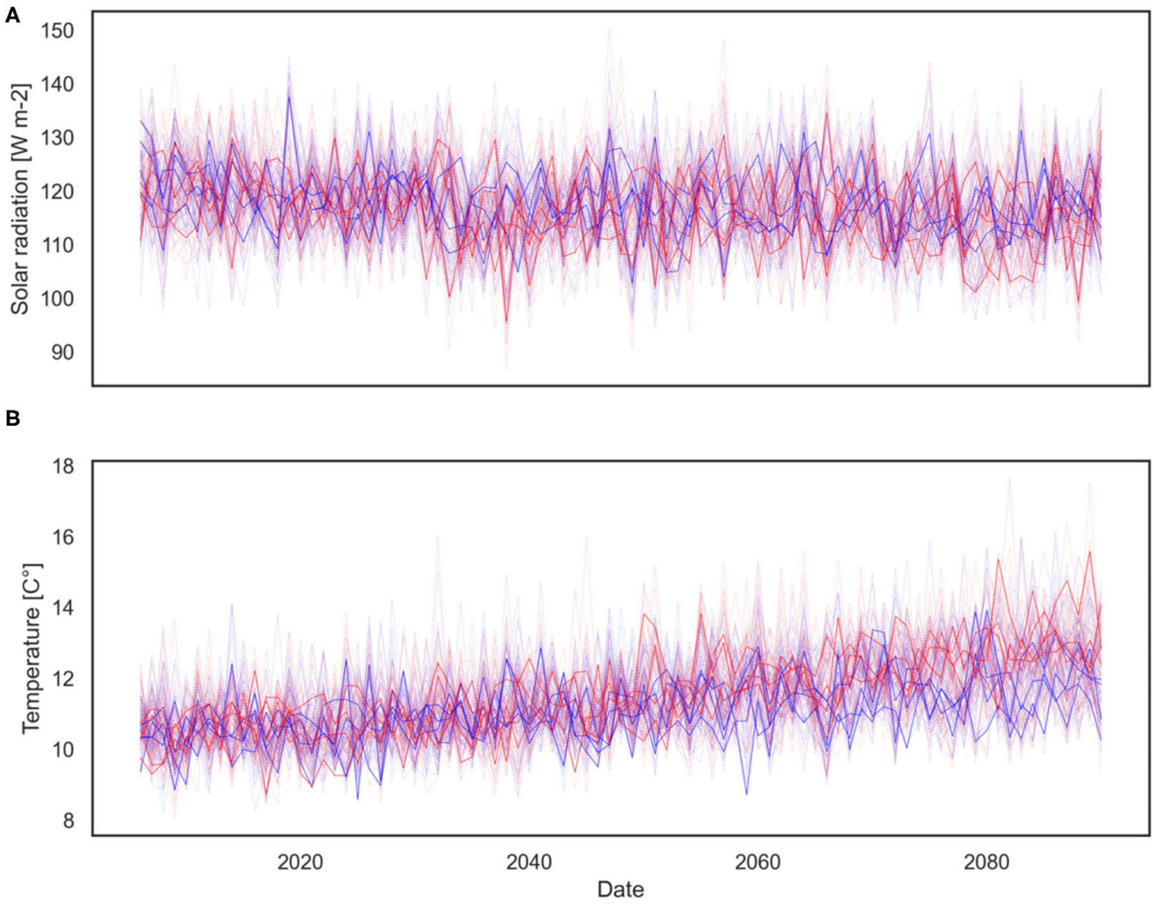

FIGURE 5 | Eight EURO-CORDEX (darker solid line) and 120 generated synthetic (shaded dashed line) climate change projections for solar radiation **(A)** and air temperature **(B)**, grouped by RCP scenarios (blue—RCP4.5, red—RCP8.5). Plot of the yearly averages based on the daily data.

where $\{\epsilon_i\}_i$ is a sequence of independent standard Normal random variables. Ignoring discretization error, the resulting equation can be rewritten and combined with the observation scheme:

$$\begin{aligned} X_i &= (1-\alpha\Delta_i)X_{i-1} + \alpha\mu(t_{i-1})\Delta_i + \sigma\sqrt{\Delta_i}\epsilon_i \\ Y_i &= N(L_iX_i, \Upsilon_i), \end{aligned}$$

where $X_i \equiv X_{t_i}$. For numerical stability, it is better to discretize (1) using an implicit scheme on the deterministic part. This leads to the dynamical system

$$\begin{aligned} X_i &= \frac{X_{i-1} + \alpha\mu(t_i)\Delta_i}{1+\alpha\Delta_i} + \sigma\sqrt{\Delta_i}\epsilon_i \\ Y_i &= N(H_iX_i, R_i), \end{aligned}$$

We write the model in state-space form, sticking to the notation in Särkkä (2013),

$$\begin{aligned} X_i &= A_{i-1}X_{i-1} + a_{i-1} + N(0, Q_{i-1}) \\ Y_i &= H_iX_i + N(0, R_i) \end{aligned} \tag{2}$$

Here

$$A_{i-1} = (1+\alpha\Delta_i)^{-1} \qquad a_{i-1} = \frac{\alpha\Delta_i}{1+\alpha\Delta_i}\mu(t_i) \qquad Q_{i-1} = \sigma^2\Delta_i,$$

$$R_i = \begin{cases} \psi_1 & \text{if only } \textit{in-situ} \text{ measurement} \\ \psi_2 & \text{if only satellite measurement} \\ \begin{bmatrix} \psi_1 & 0 \\ 0 & \psi_2 \end{bmatrix} & \text{both } \textit{in-situ} \text{ and satellite measurements} \end{cases}$$

and

$$H_i = \begin{cases} \begin{bmatrix} 1 \end{bmatrix} & \text{if only 1 measurement is available at time } t_i \\ \begin{bmatrix} 1 & 1 \end{bmatrix}' & \text{if both measurements are available at time } t_i \end{cases}.$$

Note that (2) specifies a linear Gaussian state-space model. The equation for Y is the observation equation, that for X the state-equation. We will parameterize ψ_1, ψ_2 by taking

$$\psi_1 = \eta\bar{\psi}\psi \qquad \psi_2 = \psi,$$

where $\eta \in (0,1)$ is fixed and $\bar{\psi}$ will get assigned a prior distribution supported on $(0,1)$. This reflects *apriori* knowledge that the *in-situ* measurements are believed to be more accurate. The *in-situ* chlorophyll-a observations are obtained from sampling campaigns (bucket water samples from a sampling jetty) and therefore considered as the true values (ground truth). While the satellite product is calibrated with many *in-situ* observations in the North Sea, it does not produce perfect match with the *in-situ* observations at the study location. Moreover, the number of satellite observations is much higher than the *in-situ* observations. This over-representation is counter balanced by the fusion model otherwise the reconstruction would be mostly determined by the satellite measurements.

We model the mean trend using the series expansion of the form

$$\mu(x) = \sum_{k=1}^{K} \xi_k \varphi_k(x),$$

where K is fixed, and $\boldsymbol{\xi} := (\xi_1, \dots, \xi_K) \sim N_K(0, \sigma_\xi^2 I)$. This term allows us to account for a varying shape of the seasonal cycle. The functions φ_k are taken as follows: $\varphi_1 = \mathbf{1}_{[0,1]}$ and for $j \in \{1, \dots, J\}$

$$\varphi_{jk}(x) = j^{-1}\varphi_0(2^{j-1}x - k), \qquad \text{with } k \in \{0, \dots, 2^{j-1} - 1\}.$$

We take

$$\varphi_0(x) = \frac{9}{2}x^2 \mathbf{1}_{[0,1/3]}(x) + \left(\frac{3}{4} - 9(x - 1/2)^2\right) \mathbf{1}_{[1/3,2/3]}(x)$$

$$+\frac{9}{2}(1-x)^2 \mathbf{1}_{[2/3,1]}(x),$$

which is the quadratic *B*-spline function scaled to have support $[0, 1]$. Note that φ_0 is continuously differentiable. The hierarchical structure of the basis is exactly like the Schauder basis, but uses a smoother basic element than the traditional "hat"-function.

2.2.2. Inference

Let $\theta = (\alpha, \xi, \sigma^2, \psi, \bar{\psi})$. Inference can be carried out by initializing θ and iterating the following steps (Robert and Casella, 2004):

1. conditional on $\theta, Y_1, \dots, Y_n$, run the Forward Filtering Backwards Sampling (FFBS)-algorithm (see Appendix) to reconstruct $X_1, \dots, X_n$;
2. draw from the posterior of θ, conditional on $X_1, \dots, X_n$, and $Y_1, \dots, Y_n$ (note that the likelihood is simple, once we know the latent path $X_1, \dots, X_n$).

For updating parameters we use Gibbs sampling. Note that the updates for $\bar{\psi}$ and ψ only depend on $Y_1, \dots, Y_n$, and updates for all other parameters only depend on $X_1, \dots, X_n$.

- The updates steps for σ^2 and ψ are trivial when using independent InverseGamma distributions as prior due to partial conjugacy.
- For $\bar{\psi}$ we assume the $Unif(0, 1)$-prior. A Metropolis-Hastings step is implemented where we use random-walk type proposals (Robert and Casella, 2004) of the form

  $$\log \frac{\bar{\psi}^\circ}{1 - \bar{\psi}^\circ} := \log \frac{\bar{\psi}}{1 - \bar{\psi}} + N(0, \tau_{\bar{\psi}}^2),$$

  which implies that the proposal ratio equals

  $$\frac{q(\bar{\psi} \mid \bar{\psi}^\circ)}{q(\bar{\psi}^\circ \mid \bar{\psi})} = \frac{\bar{\psi}^\circ(1 - \bar{\psi}^\circ)}{\bar{\psi}(1 - \bar{\psi})}.$$

  Note that $\bar{\psi}^\circ = \bar{\psi}/(\bar{\psi} + (1 - \bar{\psi})\tau_{\bar{\psi}} Z)$, where $Z \sim N(0, 1)$.
- For updating α we use a Metropolis-Hastings step of the form $\log \alpha^\circ := \log \alpha + N(0, \tau_\alpha^2)$.
- The "full" conditional density for $\boldsymbol{\xi}$ is proportional to

  $$\exp\left(-\frac{1}{2\sigma_\xi^2}\|\boldsymbol{\xi}\|^2 - \frac{1}{2\sigma^2}\sum_{i=2}^{n} \Delta_i^{-1}\left(X_i - A_{i-1}X_{i-1}\right.\right.$$
  $$\left.\left. - \frac{\alpha\Delta_i}{1 + \alpha\Delta_i}\sum_{k=1}^{K}\xi_k\varphi_k(t_i)\right)^2\right)$$
  $$= \exp\left(-\frac{1}{2\sigma_\xi^2}\|\boldsymbol{\xi}\|^2 - \frac{1}{2\sigma^2}\sum_{i=2}^{n}\left(U_i - \bar{\alpha}_i\sum_{k=1}^{K}\xi_k\varphi_k(t_i)\right)^2\right),$$

  where

  $$U_i = \Delta_i^{-1/2}(X_i - A_{i-1}X_{i-1}) \qquad \bar{\alpha}_i = \frac{\alpha\sqrt{\Delta_i}}{1 + \alpha\Delta_i}.$$

  This is proportional to

  $$\exp\left(\left(-\frac{1}{2}\boldsymbol{\xi}'(\sigma^{-2}V + \sigma_\xi^{-2}I_K)\boldsymbol{\xi} + \sigma^{-2}\boldsymbol{v}'\boldsymbol{\xi}\right)\right)$$

  with

  $$\boldsymbol{v}_k = \sum_{i=2}^{n} U_i\bar{\alpha}_i\varphi_k(t_i) \qquad V_{k\ell} = \sum_{i=2}^{n}\bar{\alpha}_i^2\varphi_k(t_i)\varphi_\ell(t_i).$$

  Hence, the update step for $\boldsymbol{\xi}$ boils down to sampling from a multivariate normal distribution with precision $\sigma^{-2}V + \sigma_\xi^{-2}I_K$ and potential vector $\sigma^{-2}\boldsymbol{v}$ (the potential vector is the product of the precision matrix with the mean vector).

Details on the prior specification: for both σ^2 and ψ we took (independently) InverseGamma priors, parameterized with shape and scale, with both parameters equal to 0.1. For α we took the Exponential distribution with mean 10. We took $\sigma_\xi^2 = 10$ and tuned the step-sizes τ_ψ and τ_α such that the corresponding random-walk Metropolis-Hastings steps were accepted with probability in between 25 and 50%. In the series expansion we took a fixed value for K = 5. We took $\eta = 658/8,005$, which is the ratio of the *in-situ* and satellite measurements.

2.3. Long Term Projection Using Bayesian Structural Time Series Models

After the fused historical chlorophyll-a concentration signal has been derived, it is used to train the time series model for scenario analysis. It was previously argued that variability in the spring bloom dynamics occur due to changing environmental conditions. Consequently, apart from historical trends and seasonality in the observed chlorophyll-a concentration time series, projected solar radiation and air temperature are also used to drive future chlorophyll-a concentration trajectories. These simulated trajectories are then utilized to extract the bloom characteristics applying the feature extraction methodology described in section 2.4.

In this study an existing Bayesian structural time series modeling framework is customized to our purpose, which is the Prophet forecasting model (Taylor and Letham, 2017). This is a decomposable time series model with trend, seasonality, and additional regressor component, as well as error term as the main model components:

$$y(t) = g(t) + l(t) + \epsilon(t).$$

where, at time t, $y(t)$ is the response variable (chlorophyll-a concentration), $g(t)$ is a piecewise linear trend model, $l(t)$ is a linear component representing seasonality and additional regressors, and $\epsilon(t)$ is the error term (independent and identically distributed noise). In order to avoid negatively predicted values, the natural logarithm of the response variable was taken in the model, and the prediction was then transformed back to its original scale by using the exponential function. An advantage of the Prophet model is that it can handle irregular intervals, which is important as our fused chlorophyll-a observations are not regularly spaced. Prohpet is similar to other decomposition based approaches to time-series forecasting except that it uses generalized additive models instead of a state-space representation to describe each component. Using state space models would offer a more generic model formulation, whereas this approach explicitly models features common to the chlorophyll-a time series at hand, such as multi-period seasonality. The structural time series model could alternatively be put into state-space format, but rewriting it into that form would not alter the results.

Bayesian structural time series models possess further key features for modeling time series data that are favorable for long-term chlorophyll-a scenario analysis studies. The main feature is uncertainty quantification, as they allows us to quantify the posterior uncertainty of the individual components, control the variance of the components, and impose prior beliefs on the model. This is crucial as uncertainties increase over time in the future, especially in long-term projections. The second key feature is transparency, since the model is decomposed into simple time series components, which can be visually inspected. Moreover, they do not rely on differencing or moving averages, which make them more transparent than other autoregressive moving average models. The third key feature is the ability to incorporate regressors (covariates) as explanatory variables in the model. This feature is beneficial to include climate change impacts on chlorophyll-a trajectories from solar radiation and air temperature.

Here we briefly introduce the model without aiming completeness; for the full model formulation the reader is referred to Taylor and Letham (2017). We use a piecewise linear model with a constant rate of growth and change points. Suppose there are S change points, over a history of T points, at times $s_j, j = 1, \ldots, S$. We define a vector of rate adjustments $\delta \in \mathbb{R}^S$, where δ_j is the change in rate that occurs at time s_j. The rate at any time t is then the base rate k, plus all of the adjustments up to that point, which is represented by a vector $\boldsymbol{a}(t) \in \{0, 1\}^S$ such that

$$a_j(t) = \begin{cases} 1, & \text{if } t \geq s_j, \\ 0, & \text{otherwise.} \end{cases}$$

The piecewise linear trend model with change points is then

$$g(t) = \left(k + \boldsymbol{a}(t)^T \boldsymbol{\delta}\right) t + \left(m + \boldsymbol{a}(t)^T \boldsymbol{\gamma}\right)$$

where k is the growth rate, $\boldsymbol{a}(t)$ is a change point indicator as defined above, $\boldsymbol{\delta}$ is the vector of rate adjustments, m is the offset parameter, and to make the function continuous, γ_j is set to $-s_j\delta_j$. We employ the following prior on $\boldsymbol{\delta} = (\delta_1, \ldots, \delta_S)$.

$$\delta_j \sim \text{Laplace}\,(0, \tau)$$

where τ controls the flexibility of the model in alternating its rate. While the model automatically detects change points and allows the trend to adapt appropriately, we have control over the trend flexibility by adjusting the strength of the sparse prior using the change point prior scale τ. In this application trend flexibility is significantly reduced by decreasing the change point prior scale to one fifth of its default value. The value was fined tuned by balancing between the training error (which is lower with more flexibility) and the prediction error, while keeping the width of the projected uncertainty interval reasonable.

When the model is used for forecasting, the trend has constant rate and the uncertainty in the forecast trend is estimated. Future rate changes are simulated that emulate those of the past. In a fully Bayesian framework this can be done with a hierarchical prior on τ to obtain its posterior. In long-term projections, which is our purpose, one of the most influential factors is the uncertainty in the future trend. In this model, the uncertainty in the forecast trend is estimated by assuming that in the future the same average frequency and magnitude of rate changes will occur as observed in the past:

$$\text{for all j} > T, \begin{cases} \delta_j = 0 & \text{with probability } \frac{T-S}{T} \\ \delta_j \sim \text{Laplace}\,(0, \lambda) & \text{with probability } \frac{S}{T}. \end{cases}$$

Once λ has been inferred from the data, we use this model to simulate possible future trends and to compute uncertainty intervals. Due to the assumptions in the trend forecasting (matching historical frequency and magnitude) the trend intervals may not be exact, nevertheless they provide an indication of the level of uncertainty and also reveals trend model overfitting.

In the seasonality model we approximate seasonal effects with a standard Fourier series expansion with chosen periodicity P, and Fourier order n. The seasonality model is:

$$s(t) = \sum_{n=1}^{N} \left(a_n \cos\left(\frac{2\pi nt}{P}\right) + b_n \sin\left(\frac{2\pi nt}{P}\right) \right).$$

In this model the following periods are used, $P = 3652.5$ for decadal periodicity, $P = 365.25$ for yearly periodicity, $P = 182.625$ for half-yearly periodicity, and $P = 91.3125$ for quarterly periodicity (in days). The Fourier order was chosen as $N = 10$ after tuning such that under-fitting and over-fitting is avoided by minimizing the test error. The linear component then becomes

$$l(t) = X(t)\boldsymbol{\beta}$$

where $X(t) = [\cos\left(\frac{2\pi 1t}{P}\right), \sin\left(\frac{2\pi 1t}{P}\right), \ldots, \cos\left(\frac{2\pi Nt}{P}\right), \sin\left(\frac{2\pi Nt}{P}\right), R_1(t), \ldots, R_J(t)]$ is a matrix of seasonal components $s(t)$ and additional vectors of regressors, while $\boldsymbol{\beta} = \left[a_1, b_1, \ldots, a_N, b_N, r_1, \ldots, r_J\right]^T$ includes the $2N$ parameters of the Fourier series expansion and the R regression coefficients of the additional explanatory variables. The following $\boldsymbol{\beta} \sim N(0, \sigma^2)$ prior is imposed independently on each component of β. By default the linear component of the model only contains features for modeling seasonality but through specifying covariates ("regressors") we can include additional arbitrary vectors to $X(t)$ whose regression coefficients will be inferred. Combining the trend, seasonality, and error components the final model becomes:

$$y(t)\,|\,m, \delta, \beta, \sigma \sim N\left(g(t) + l(t), \sigma\right)$$

In order to construct an appropriate structural time series model, the selection of model components was facilitated by exploratory analysis steps, such as seasonal shape extraction, investigating the correlation of explanatory and response variables (**Figure 6**), produce periodogram and wavelet analysis to explore periodicity, and perform time series decomposition. Apart from chlorophyll-a, the solar radiation regressor data is also log transformed, since that produces a correlation structure to log chlorophyll, which is closer to linearity (see **Figure 6**). The temperature data could not be log transformed as it contains negative values. The continuous wavelet power spectrum revealed a persistent 12-month periodicity, which explained the largest amount of variability over the sampling period, while the rest of the variability is attributed to 6 and 3 month periodicity. This is in line with previous research findings of wavelet analysis for the same observation station (Winder and Cloern, 2010).

In the current structural time series model implementation the following components are used. Linear trend with change points (change point prior scale is defined), multi-period seasonality: decadal, yearly, half-yearly, and quarterly (periodicity, Fourier order, and prior scale are defined), as well as four additional regressors (air temperature, solar radiation, and their lag1). It should be noted, that adding more than lag1 of the regressors did not improve the prediction further. The parameter inference can be either done by optimization, using Limited-memory Broyden-Fletcher-Goldfarb-Shanno algorithm (L-BFGS) to find a maximum a posteriori estimate, or through full posterior inference to include model parameter uncertainty in the forecast uncertainty.

2.4. Tracking Phytoplankton Spring Bloom Dynamics

In order to track phytoplankton spring bloom dynamics, the last step of the methodological framework focuses on deriving spring bloom metrics obtained from the chlorophyll-a concentration time series. We must emphasize that uncertainty in the previous methodological steps (data fusion and long term projection) is being propagated to the estimates of cardinal dates and bloom magnitude. Although efforts have been dedicated to quantify these uncertainties, propagated uncertainty carries implications for the accuracy of the calculated cardinal dates.

Several existing methods are available to characterize phytoplankton blooms. Ji et al. (2010) provides an exhaustive list of timing indices for quantifying phytoplankton phenology with advantages and disadvantages. These can be classified as biomass-based threshold methods, rate of change methods, and cumulative biomass-based threshold methods (Brody et al., 2013). One might use the number of consecutive days that exceed a given threshold (elevated assessment level) defined by the literature. In the case of Dutch coastal waters this is around 12–15 and 22–24 mg/m^3 for the Wadden Sea (Peters et al., 2005). Alternatively, a low-pass method could be used for determining the start of the bloom (Wiltshire et al., 2008), which is a temporal averaging algorithm acting as a low-pass filter, reducing the short-term fluctuations. Philippart et al. (2010) suggested using the date of the maximum and minimum values of daily change rates in the interpolated chlorophyll-a concentrations for the timing of the annual onset and breakdown of the phytoplankton bloom. The timing of the bloom can also be represented by another quantity, the center of gravity (COG) of the carbon content within the typical spring bloom period (Hjerne et al., 2019). Another possibility to characterize the spring bloom is to derive the cardinal dates of the mass development (Rolinski et al., 2007). The cardinal dates are the beginning of the spring phytoplankton mass development, the maximum of the spring bloom (bloom peak), and the end of the spring mass development. Mathematical methods of describing cardinal dates were proposed by Rolinski et al. (2007), such as finding the points of inflexion in the smoothed, log transformed, and differenced (1-week lag) data, deriving them from four linear segments (constant–increasing–decreasing–constant) fitted to the logarithmic values, or extracting the cardinal dates from the quantiles of a fitted parametric function (Weibull function). Similarly, Lewandowska and Sommer (2010) transformed phytoplankton biomass according to standard normal variation and took the first and third quartiles as cardinal dates, the beginning and the end of the spring bloom, respectively.

Several of the above mentioned methods (or listed by Ji et al., 2010) cannot properly deal with bi-modal data

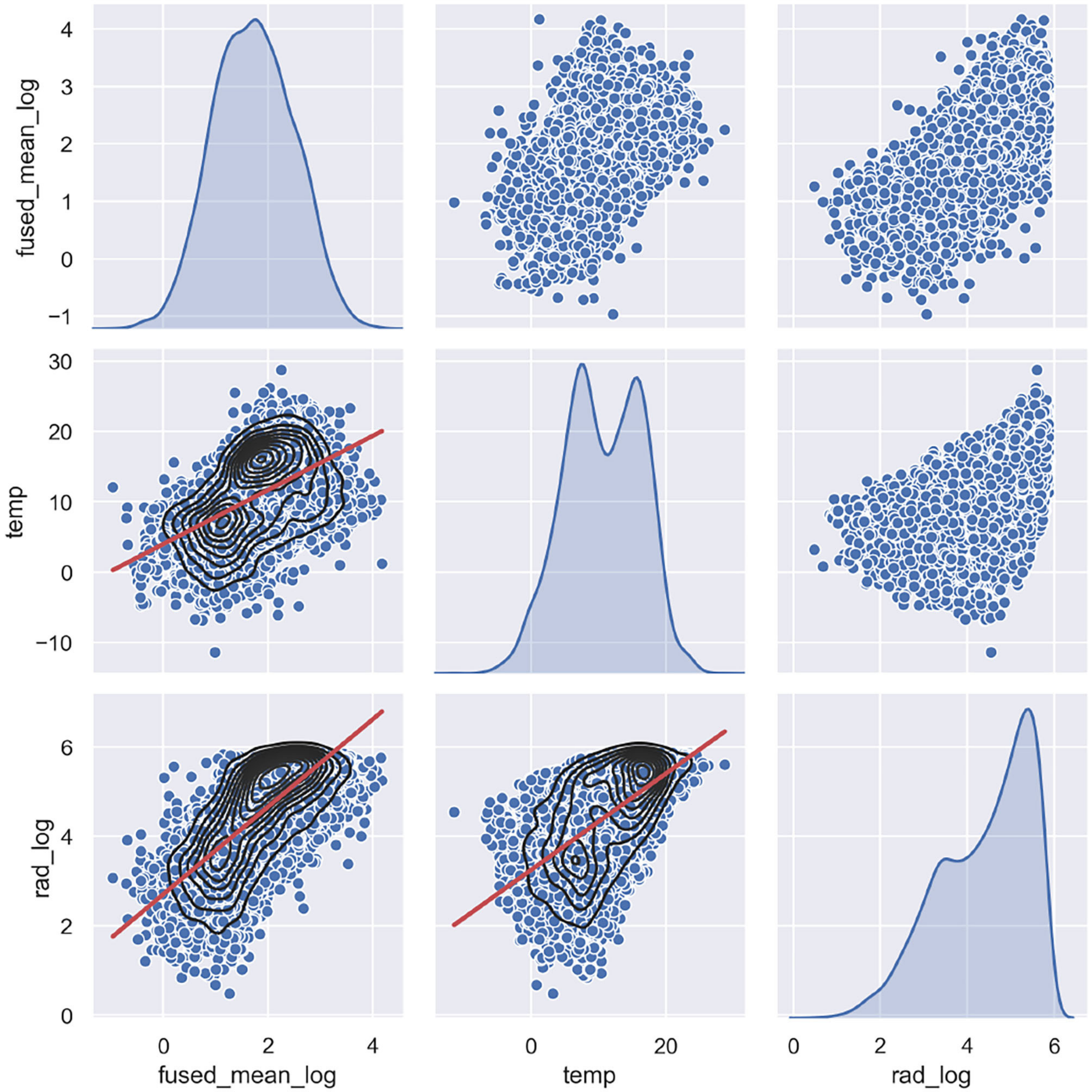

FIGURE 6 | Pair plots of the log transformed response variable (fused chlorophyll-a), and the explanatory variables (log transformed radiation and temperature). Scatter plots are shown together with Kernel Density Estimates (black) and linear regression (red).

(require separation of the spring bloom) or large fluctuations in amplitude, some methods need parametric fitting (e.g., Vargas et al., 2009), and most methods cannot deal with noisy data, hence require smoothing to pre-process the seasonal data before deriving the cardinal dates. As summarized by Ji et al. (2010) if the seasonal time series is uni-modal, from densely sampled and without noise, most methods will perform well. This is rarely the case, unless the data is interpolated and denoised. If that is not the case, more flexible approaches perform better which use less assumption on distribution patterns. For this reason to track long term changes in phytoplankton spring blooms we propose to derive the cardinal dates using a non-parametric shape constrained method, namely log-concave regression (Groeneboom et al., 2001; Groeneboom and Jongbloed, 2014; Doss, 2019). Log-concave regression meets this flexibility requirement as it does not require any tuning parameters and can be directly applied on the annual bi-modal time series without any pre-processing. Consequently, our proposed method is less sensitive to bloom amplitude, missing data, and observational noise.

In summary, determining a mode of a unimodal (part of a) function, sometimes called "bump hunting" is classically done using smoothing techniques, assuming some level of smoothness (which is reasonable) of the function. The advantage of using log-concave regression compared to techniques based on smoothing, is that it does not require tuning parameters (such as bandwidths) that heavily influence the outcome of the analysis. An alternative method one could use, would be unimodal regression, where no smoothness is used at all, resulting in discontinuous unimodal step functions as estimate of the regression function. The large class of log-concave functions contains unimodal functions that are continuous. Moreover, estimation of these can be done in a stable manner.

In order to track long term changes in phytoplankton spring blooms we propose to derive the cardinal dates using a non-parametric shape constrained method, namely concave regression (Groeneboom et al., 2001; Groeneboom and Jongbloed, 2014; Doss, 2019). The concave or convex regression setup for a data set of size $\{n:(x_i, y_i): i = 1, \ldots, n\}$ where $x_1 < x_2 < \ldots < x_n$ is the following:

$$Y_i = r_0(x_i) + \epsilon_i$$

for a concave function r_0 on $\mathbb{R}$, where $\{\epsilon_i : i = 1, \ldots, n\}$ are independent and identically distributed random variables and Y_i is the log chlorophyll-a concentration. Then, we apply concave regression on the log chlorophyll-a concentration data. We assume that the target of the estimation, $r_0 : \mathbb{R} \to \mathbb{R}$, is concave. Writing $\mathcal{K}$ for the set of concave functions on $\mathbb{R}$, the least squares estimate of r_0 is

$$\operatorname*{argmin}_{r \in \mathcal{K}} \Phi(r), \quad \text{where} \quad \Phi(r) = \frac{1}{2} \sum_{i=1}^{n} \left(y_i - r(x_i)\right)^2$$

Utilizing this concave regression setup, the following two methodological steps are taken to identify the spring bloom cardinal dates (see **Figure 7**). The cardinal dates are the spring bloom beginning (B), -peak (P), and -end (E) dates expressed as the day of the year.

2.4.1. Isolating the Spring Bloom

We take yearly time series of log chlorophyll-a concentrations (y_t), and assume that it is bi-modal separated by a boundary point t_b. In order to reduce computation time of the first step, we omit the first 2 months ($t_1 = 60$) and last 2 months ($t_2 = 300$) of the dataset since we know that the boundary that separates the spring and summer bloom will not be found there. It should be noted that omitting a portion of the yearly time series is only done in the first step during the identification of the boundary point. In the latter step, during the derivation of the spring bloom cardinal dates all dates on the "left side" of the boundary point are used $[0, t_b^{opt}]$. Omitting a portion of the yearly time series is optional. Then we fit $\Phi(t)$ on the data:

$$\Phi(t) = \begin{cases} \varphi_{t_b}(t) & t \le t_b \\ \tilde{\varphi}_{t_b}(t) & t > t_b \end{cases}$$

where $\varphi_{t_b}(t)$ is the concave regression of $(x_i, y_i) : x_i \le t_b$ on $[t_1, t_b]$, the "left side," and $\tilde{\varphi}_{t_b}(t)$ is the concave regression of $(x_i, y_i) : x_i > t_b$ on $[t_b + 1, t_2]$, the "right side." Therefore, both $\varphi_{t_b}(t)$ and $\tilde{\varphi}_{t_b}(t)$ are concave. The optimal boundary t_b^{opt} is found where the mean squared error of $\Phi(t)$ is minimal:

$$t_b^{opt} \to \operatorname*{argmin}_{t_b} MSE_{t_b} + M\tilde{S}E_{t_b}$$

$$MSE_{t_b} = \frac{1}{t_b} \sum_{j=t_1}^{t_b} \left(y_j - \varphi_{t_b}(t_j)\right)^2$$

$$M\tilde{S}E_{t_b} = \frac{1}{t_2 - t_b} \sum_{j=t_b+1}^{t_2} \left(y_j - \tilde{\varphi}_{t_b}(t_j)\right)^2$$

This process of determining the boundary of spring and summer bloom is visually depicted in **Figures 7A,B**.

2.4.2. Derive Cardinal Dates of the Spring Bloom

After finding the boundary (t_b^{opt}) only the spring bloom ("left side") of the data is considered for further analysis where $t \in [0, t_b^{opt}]$. Then we take a continuous function $\Phi^*(t)$ which is defined as follows:

$$\Phi^*(t) = \begin{cases} c_l = \text{mean}\left(y_t : t \in [0, t_l]\right) & t \le t_l \\ \varphi(t) & t_l < t \le t_r \\ c_r = \text{mean}\left(y_t : t > t_r\right) & t > t_r \end{cases}$$

where c_l and c_r are constant and $\varphi(t)$ is the concave regression of $(x_i, y_i) : t_l < x_i \le t_r$. The points where the left constant function ends and the right constant function starts (t_l and t_r) will become the beginning and the end of the bloom (cardinal dates B and E). The third cardinal date, the peak of the bloom, is where $\varphi(t)$ takes its maximum. The points t_l and t_r are found where the mean squared error of $\Phi^*(t)$ is minimal:

$$(t_l, t_r) \to \operatorname*{argmin}_{t_l, t_r} MSE_{c_l} + MSE_{c_r} + MSE_{\varphi}$$

$$MSE_{c_l} = \frac{1}{t_l} \sum_{j=0}^{t_l} \left(y_j - c_l(t_j)\right)^2$$

$$MSE_{c_r} = \frac{1}{t_J - t_r} \sum_{j=t_r}^{t_J} \left(y_j - c_r(t_j)\right)^2$$

$$MSE_{\varphi} = \frac{1}{t_r - t_l} \sum_{j=t_l}^{t_r} \left(y_j - \varphi(t_j)\right)^2$$

This final methodological step to identify t_l and t_r is shown in **Figures 7C,D**. Finally, the cardinal dates together with the concave regression and the chlorophyll-a time series (transformed back to original values by taking their exponential function) are depicted in **Figure 7E**.

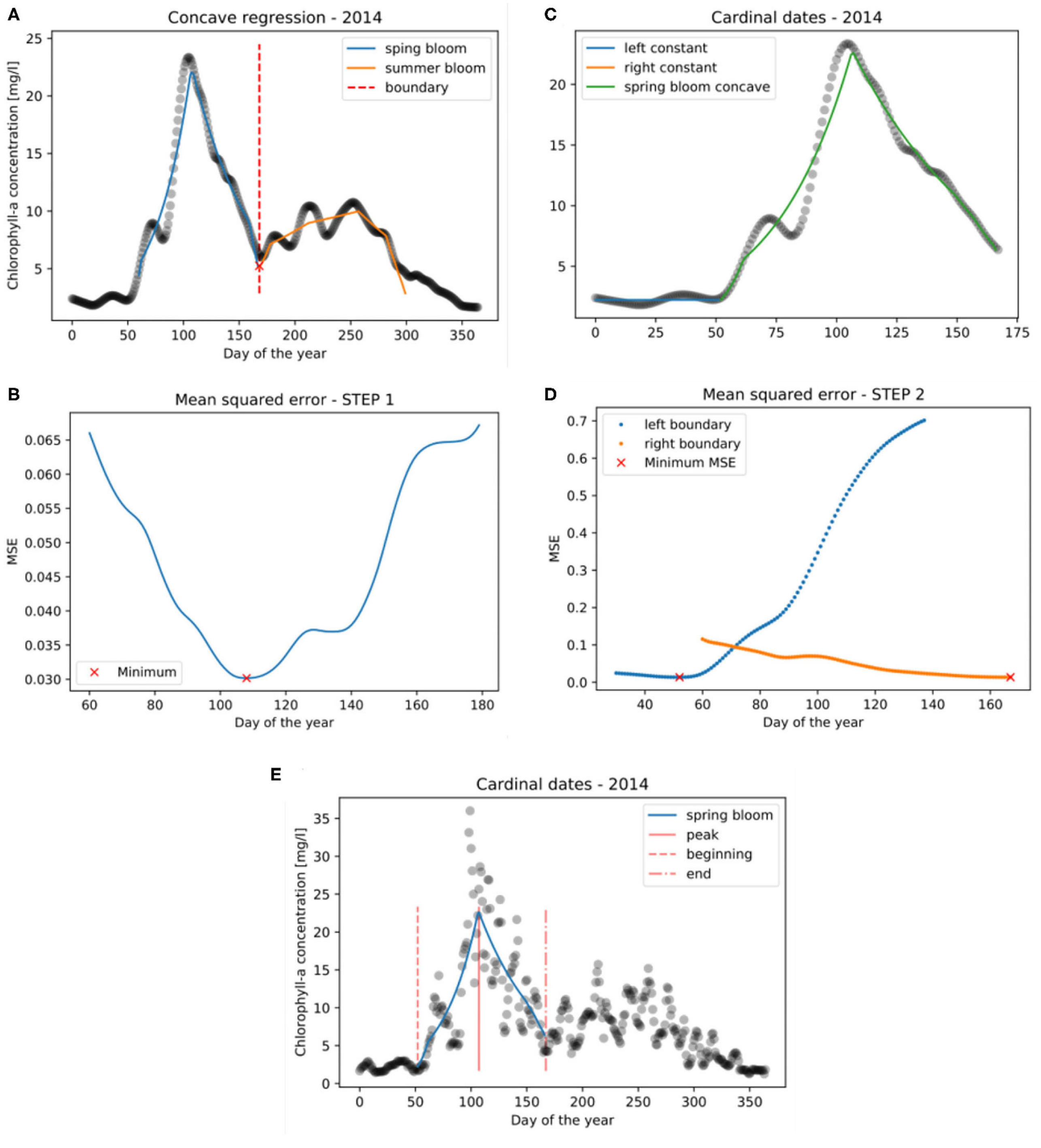

FIGURE 7 | Steps to derive the cardinal dates of phytoplankton spring blooms: (1) Determining the boundary (t_b) for isolating the spring bloom **(A,B)**, and (2) concave regression to spring bloom **(C,D)**. The cardinal dates of the spring bloom are shown in **(E)**.

3. RESULTS

3.1. Fused Chlorophyll-a Concentration Signal

The fused chlorophyll-a concentration signal, together with satellite observations, is depicted in **Figure 8A** and with *in-situ* observations in **Figure 8B**. One can observe that the fused signal almost perfectly follows the *in-situ* ("water") observations over the period in which only that type of measurements are available. From the moment that both *in-situ* and satellite date are available (1998), the fused signal lies between the two types but being closer to the *in-situ* observations according to the model formulation,

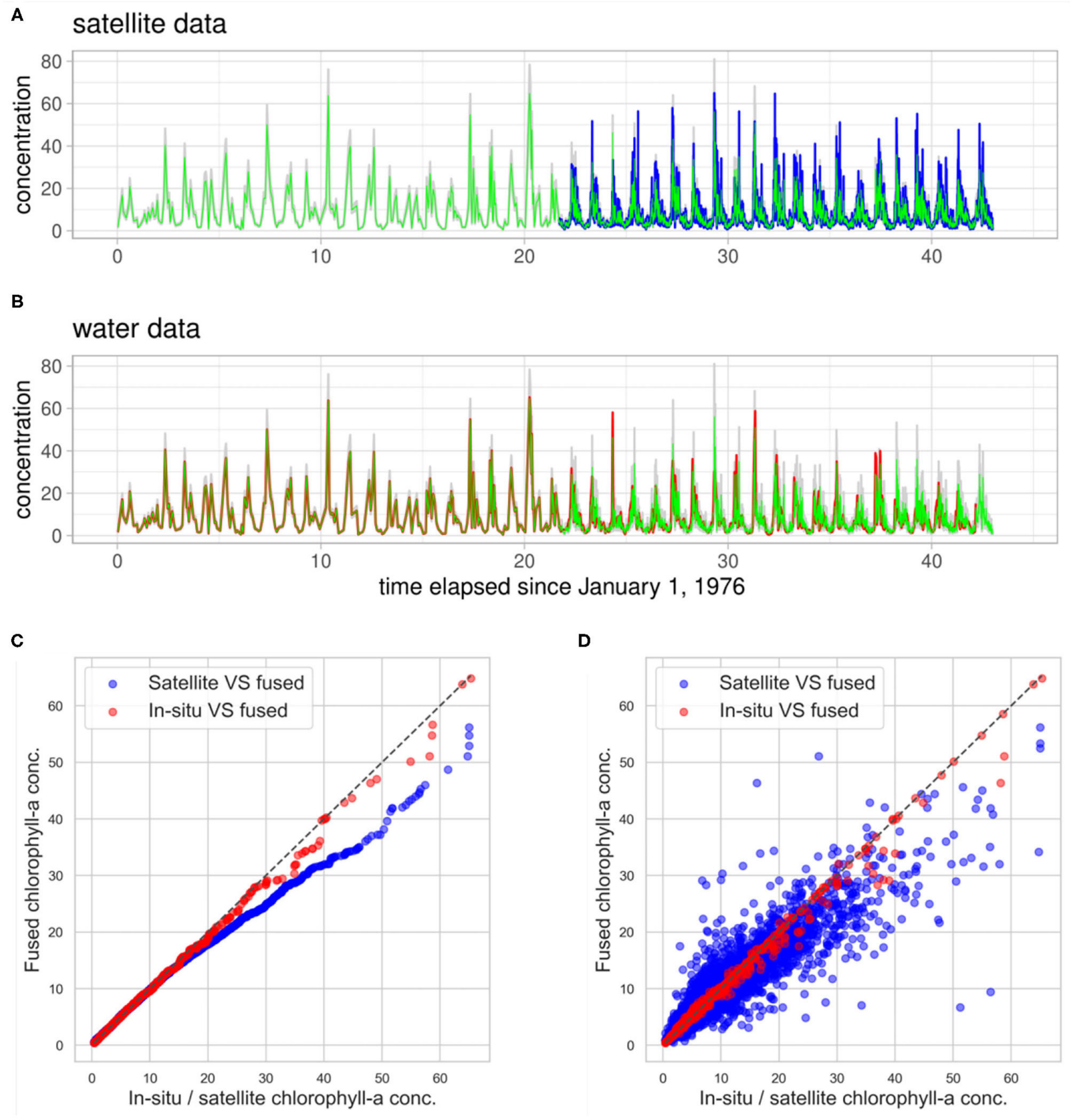

FIGURE 8 | Data fusion results. The mean fused chlorophyll-a concentration signal (green) with uncertainty (gray) compared with satellite observations (blue) in **(A)**, and *in-situ* "water" observations (red) in **(B)**. Quantile-quantile plot of the fused signal compared to both *in-situ* and satellite observations in **(C)** and scatter plot in **(D)**.

since we have higher confidence in the field data. This is also reflected in the quantile-quantile plot and scatter plot of the fused signal compared to the *in-situ* data in **Figures 8C,D**, which lies almost perfectly on the diagonal, whereas the plot of the fused signal against the satellite observations deviates more from the diagonal. This enhancement of the historical chlorophyll-a signal has benefits for the projection step. Since the long-term projection is largely based on the observed correlations, if the input chlorophyll-a concentration time series is less accurate the statistical model will misrepresent the processes.

3.2. Long Term Chlorophyll-a Projection

The Bayesian structural time series model (introduced in section 2.3) was trained (1976–2010) and tested (2010–2018) on the fused

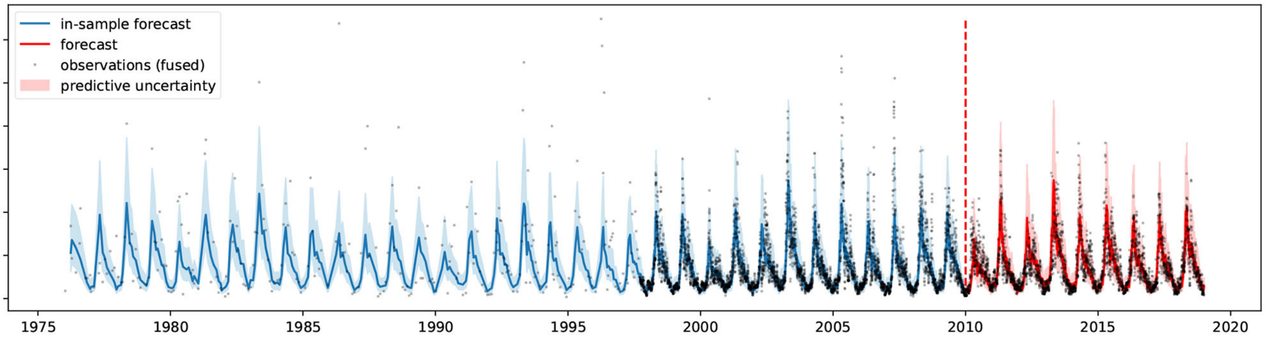

FIGURE 9 | Time series forecasting validation against fused observations. Model fit between 1976 and 2010 (blue) and forecast between 2010 and 2018 (red). Predictive uncertainties in shaded area.

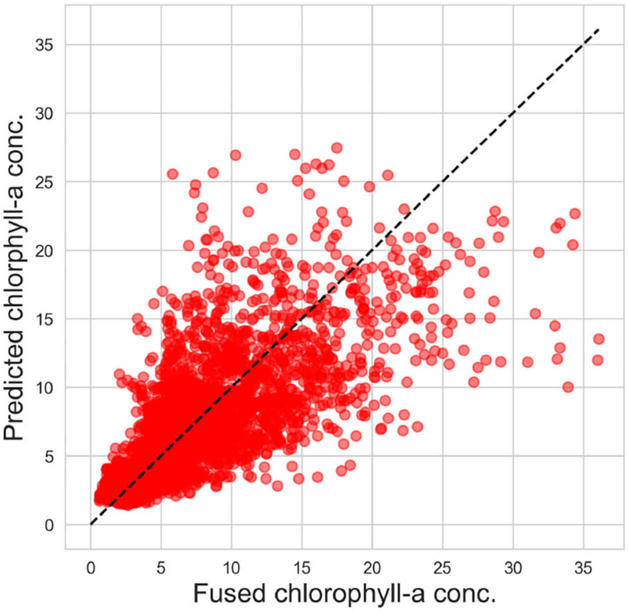

FIGURE 10 | Scatter plot of predicted chlorophyll-a concentration against fused observations. Model forecast between 2010 and 2018 with *N* = 3,287 data points.

chlorophyll-a concentration signal and the historical measured solar radiation and air temperature data. **Figure 9** visually depicts the validation of the in-sample forecast (1976–2010) and the forecast (2010–2018) against the fused data. The figure shows that most measurements (75%) lie within the predictive uncertainty band, indicating the model's reliability. The scatter plot of predictions is shown in **Figure 10** whereas the performance metrics can be found in **Table 1**.

While long-term data driven chlorophyll-a concentration prediction for climate impact assessment is not widespread, there have been few studies conducted on both inland water systems (Cho et al., 2018; Keller et al., 2018; Liu et al., 2019; Luo et al., 2019) and marine systems (Irwin and Finkel, 2008; Blauw et al., 2018; Krasnopolsky et al., 2018; de Amorim et al., 2021) that performed short term predictions. Blauw et al. (2018) predicted chlorophyll-a in the North Sea at different sites applying Generalized Additive Models (GAMs) with accuracies (R^2 values) ranging from 0.25 to 0.51 for hourly time scale, 0.15–0.22 for daily time scale, and 0.27–0.63 for bi-weekly time scale. Higher accuracy ($R^2 = 0.83$) was obtained in the North Atlantic, using a spatial GAM to predict month-to-month variation (Irwin and Finkel, 2008) or in a recent study by de Amorim et al. (2021) where an R^2 value of more than 0.7 was achieved for a longer-term prediction (multi-year) with three different algorithms: Support Vector Machine Regressor (SVR), Random Forest, and Multi-layer Perceptron Regressor (MLP). SVR performed the best ($R^2 = 0.78$) with 17 predictor variables. Similar accuracies (R^2 values) were achieved in short-term prediction studies for lakes or reservoirs using Random Forest algorithm on monthly (0.2–0.6) and daily (0.6–0.8) data (Liu et al., 2019), as well as using Multiple-Layer Perceptron Neural Network (MLPNN) and Adaptive Network-based Fuzzy Inference System (ANFIS) 0.52–0.85 (Luo et al., 2019). In comparison with these studies, we conclude that our model has acceptable accuracy, especially considering that we predict on a daily scale and 8 years ahead, while most of the cited work focuses on much shorter prediction time frame. It should be noted that model comparability with other studies is hampered not only by the differences in ecosystem types (fresh water or open ocean instead of coastal waters) but also due to the fact that the predictor variables differ, and so as the experimental setup such as data splitting strategies, and prediction time frames.

After the calibration of hyperparameters and initial validation, the time series model was retrained using the entire historical period (1976–2018), to better capture historical trends, and used for long-term chlorophyll-a concentration projection (2019–2089). Since the model contains log transformed solar radiation and air temperature as regressors, they need to be provided for the entire projection period. Consequently, after 2019 the bias corrected climate change projections are applied instead of the field observations. Given the numerous generated climate change projections (120 were used), the same number of future chlorophyll-a concentration trajectories were simulated,

TABLE 1 | Time series forecasting validation metrics against fused observations.

Performance metric	Value
N	3287.00
MAPE	0.38
RMSE	3.78
R2	0.51
% of obs in uncertainty band	75.63

Model forecast between 2010 and 2018 with N = 3,287 data points.

as shown in **Figure 11**. One can observe that the predictive uncertainty increases over time as we get farther from the projection start date. This predictive uncertainty originates from the trend component as explained in section 2.3, and the modeling choices (e.g., changepoint prior scale) will influence it. We should emphasize that such long term projection is only a simplified approximation of the future chlorophyll-a signal, which follows a piecewise linear trend and continues to repeat its multi-seasonal behavior, learnt from the past data, moreover includes linear effects of the two climate variables. These assumptions guarantee fast computation time, thus allowing numerous simulations for uncertainty quantification, which is the objective of this study. Nonetheless, it does not replace complex physically-based numerical models that are capable of simulating a wide range of ecological processes.

3.3. Changes in Phytoplankton Bloom Dynamics

The feature extraction step to derive the spring bloom cardinal dates (see section 2.4) is first applied to the mean fused chlorophyll-a data to obtain the historical changes in spring bloom dynamics. Unfortunately, the cardinal dates could only be derived starting from 1998. This is due to the fact that between 1976 and 1998 only *in-situ* measurements were available which had a sparse temporal sampling frequency (10–20 per year). As previously argued, this number of yearly data points is insufficient to extract the cardinal dates. The historical phytoplankton bloom dynamics from 1998 to 2018 is depicted in **Figure 12**. The figure displays the three cardinal dates (beginning—green, peak—red, end—blue), the bloom duration (shaded blue area), and the bloom duration anomaly from the long-term mean bloom duration (bar chart). It can be observed that for certain years (2002, 2012, 2013) the bloom peak and bloom end cardinal dates lie very close to each other. These instances were visually confirmed. It was found that for 2002 and 2012 the feature extraction algorithm was accurate as a fast decay followed the bloom peak. On the other hand, in 2013 there was visibly no spring bloom observed, only a dominant summer bloom. This led the algorithm to falsely identify the spring bloom peak and end. This finding suggests that years where no spring bloom is observed should be removed from the dataset prior to applying the spring bloom cardinal detection algorithm. A possible extension of the method could be to report the type of seasonality (spring bloom, summer bloom, bi-modal, no bloom) (González Taboada and Anadón, 2014) since changes in the type of seasonality are of interest, nevertheless, this is not part of the current implementation.

The feature extraction steps are then repeated on the projected future chlorophyll-a concentration between 2019 and 2089. The projected future spring bloom cardinal dates are depicted as boxplots in **Figure 13A** and as histograms in **Figure 13B**. The results indicate a relatively small variation, ∼ 6 days, in the projected bloom peak timing (see **Figure 14B**), while a much higher level of uncertainty is observed for the bloom beginning, ∼ 25 days, (see **Figure 14A**) and end timing, ∼ 20 days (see **Figure 14C**). Bloom beginning and -peak resemble normal distributions, in the case of the bloom peak with a lower variance (higher peakedness). On the other hand, the bloom end resembles a right skewed log-normal distribution with relatively heavy tale due to the high number of outliers.

The bloom beginning is projected to slightly but consistently shift earlier, resulting in longer bloom duration toward the end of the century (see **Figure 15A**). The earlier spring bloom as an effect of climate change is in line with previous findings by Lewandowska and Sommer (2010) and Winder et al. (2012) in laboratory trials (mesocosm experiments), by Desmit et al. (2020), Hjerne et al. (2019), Philippart et al. (2010), and Edwards and Richardson (2004) using historical data, or by Friocourt et al. (2012) using numerical (hydrodynamic and ecological) prediction models forced by future climate change scenarios. Many of these studies found an even higher rate of spring bloom forward shift but in our case the accelerating effect of temperature rise might be moderated by the decreasing solar radiation trend. Despite the considerable uncertainty in the bloom end timing, no apparent trend can be observed. We emphasize that the actual day of the year of the derived cardinal dates may not be comparable to other findings in literature, since we used another method to obtain these cardinal dates. Thus, the projected trends and uncertainties carry the most value. We should also point out that the projected earlier spring blooms may not be a simple climatic response but could be the result of complex processes (physical and non-physical). Further investigation of these processes is necessary to fully understand the underlying mechanisms causing shifts in phytoplankton dynamics (Hjerne et al., 2019).

Apart from the cardinal dates, the chlorophyll-a concentration magnitude was also investigated. As **Figure 15B** shows, at the end of the twenty-first century higher spring bloom peak magnitude can be expected. Considering the ensemble mean values, a $0.4\% year^{-1}$ trend is projected. This trend magnitude is comparable with the latest findings on chlorophyll-a historical trends in the North-West Shelf regions (0.4–0.96% year^{-1}) Hammond et al. (2020), noting that this estimate was considering offshore marine waters, not coastal zones. It is also comparable to Xu et al. (2020) who found nearly 20–30% chlorophyll increase in the same study area between 1987 and 2012. Various numerical studies using climate models also project moderate increase in daily mean net primary production between 1980–1999 and 2080–2099 in the shallower southern North Sea (Holt et al., 2014, 2016; Pushpadas et al., 2015). We must emphasize that increasing chlorophyll concentration due to climate change is highly region specific (only occurring in some coastal areas) and

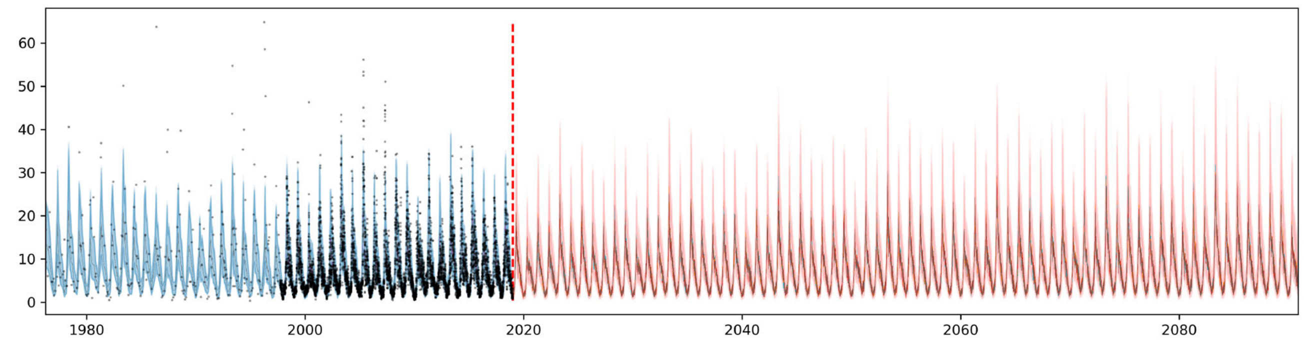

FIGURE 11 | Long term chlorophyll-a concentration time series projection with radiation and temperature explanatory variables from generated climate projections (based on EURO-CORDEX). One hundred and twenty solar radiation and air temperature projection scenarios were used to produce the 120 chlorophyll-a trajectories. Model fit between 1976 and 2018 (blue) and projection between 2019 and 289 (red). Predictive uncertainty in shaded area.

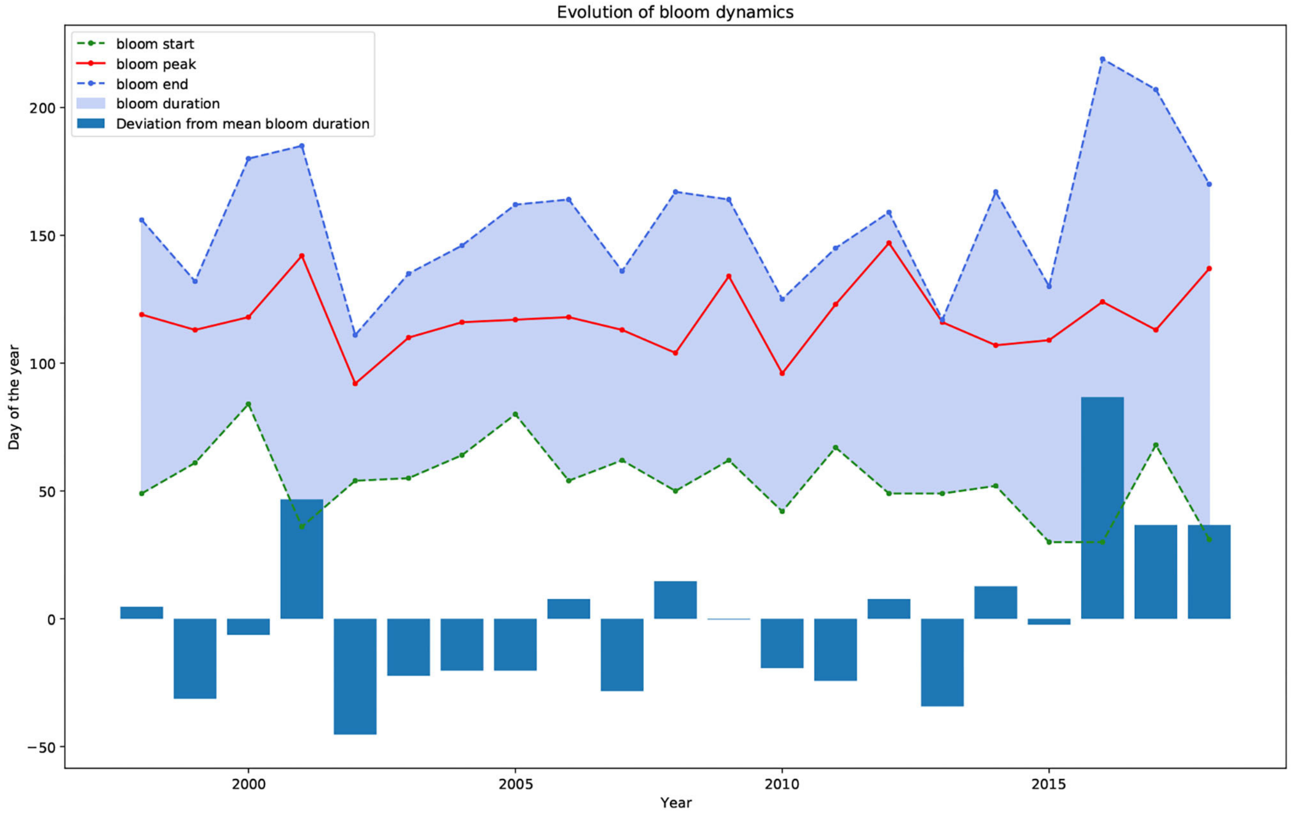

FIGURE 12 | Historical spring bloom cardinal dates (beginning—green, peak—red, end—blue) and bloom duration (shaded blue area). The bar chart shows the yearly deviation (anomaly) from the long-term mean bloom duration.

very much debated (Xu et al., 2020). In fact, some studies only report shift in spring bloom timing and species composition, but not in magnitude. In our study the projected positive trend is most probably driven by the linear trend component of the time series model and the rising air temperature as regressor, which have positive correlation to chlorophyll, based on the historical data. It should be noted, that in reality the correlation between air temperature and chlorophyll-a is non-linear and seasonally varying, moreover, it is different on a species or aggregate level. As the time series model could not incorporate non-linear correlations, it is assumed linear, hence, simulated interactions are only approximations of the real conditions. Nevertheless, in the season of interest (spring), when air temperature and solar radiation values did not reach their peak, this correlation is positive and the linearity assumption is a good approximation (see **Figure 6**). Furthermore, with chlorophyll-a concentration

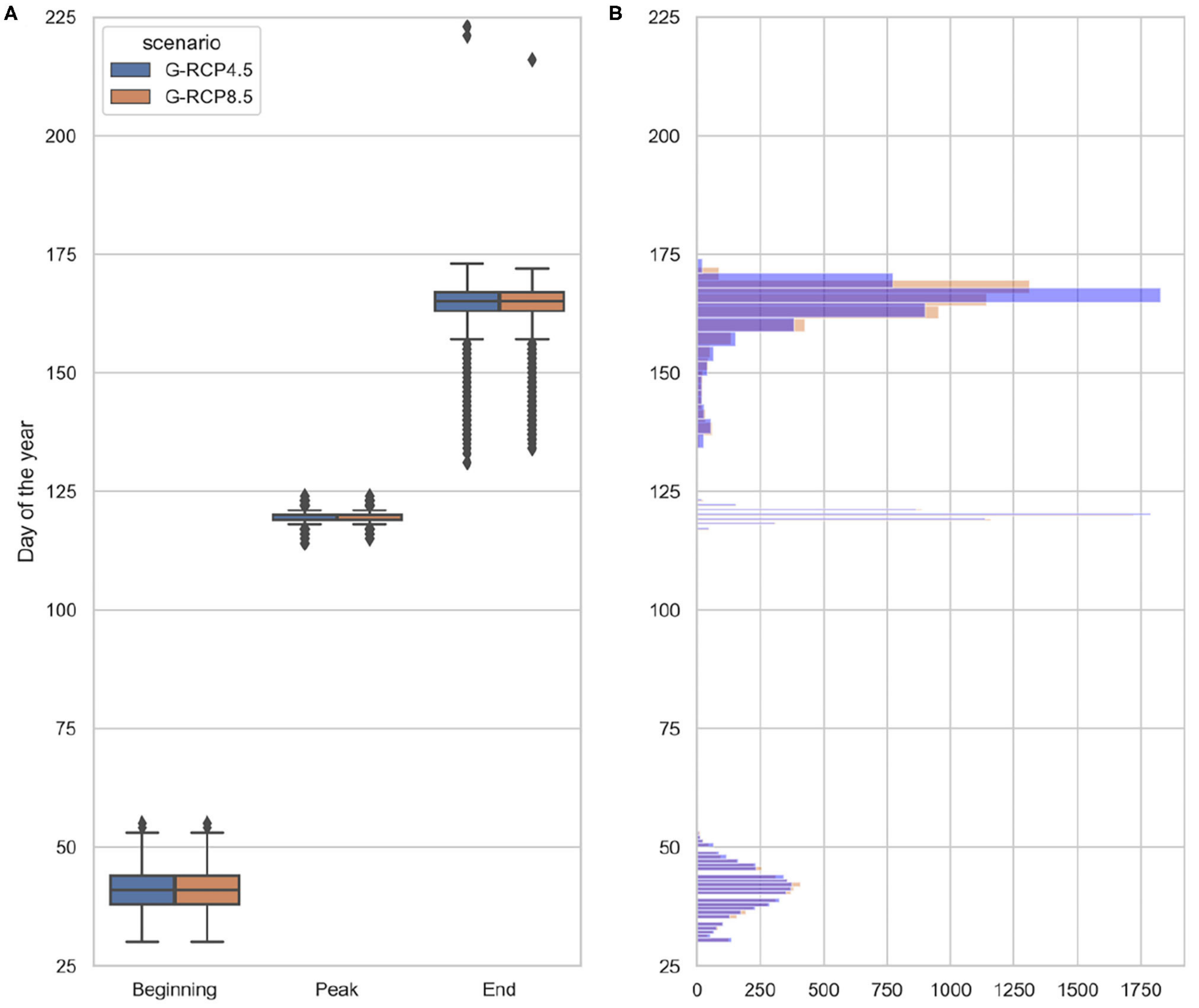

FIGURE 13 | Range of projected future bloom cardinal dates **(A)** and their distributions **(B)** under 120 generated radiation and temperature projections (based EURO-CORDEX) (2019–2089). The statistics are grouped based on the generated projections corresponding to RCP scenarios (G-RCP4.5 and G-RCP8.5).

as a proxy we aim to describe aggregate level response, rather than species level response. We also emphasize that bloom magnitude is heavily influenced by nutrient concentration in the mixed layer depth (Sverdrup, 1953; Behrenfeld, 2010). Although nutrient concentration was not used as an explanatory variable in this study we may expect that the correlation between air temperature and chlorophyll-a captured in historical data may include indirect effects such as thermal stratification, which influences nutrient availability in the mix layer depth.

The projected cardinal dates in **Figures 13–15** are also grouped based on the generated projections corresponding to RCP scenarios. One observed difference is that in the last two decades bloom peak magnitudes are somewhat higher for RCP8.5. Perhaps counter intuitively, no other structural differences are visible between the RCP scenarios. The similarity between projected cardinal dates corresponding to RCP scenarios could be attributed to few reasons. Firstly, we must investigate the differences in solar radiation and air temperature projections between the RCP scenarios from Euro-CORDEX. As **Figure 5** depicts, these differences for solar radiation are not apparent. For air temperature projections we see similar behavior until the end of the century and differences in the last two decades become more articulate (RCP8.5 being higher), although few GCMS from both RCPs remain entangled and only one GCM from the RCP8.5 scenarios presents more extreme behavior. This leads us to the second reason which might explain the lack of difference in cardinal dates between RCPs. The generated scenarios have been produced with a Bayesian stochastic generator introduced in Mészáros et al. (2021). This model assumes that Euro-CORDEX scenarios are exchangeable rather

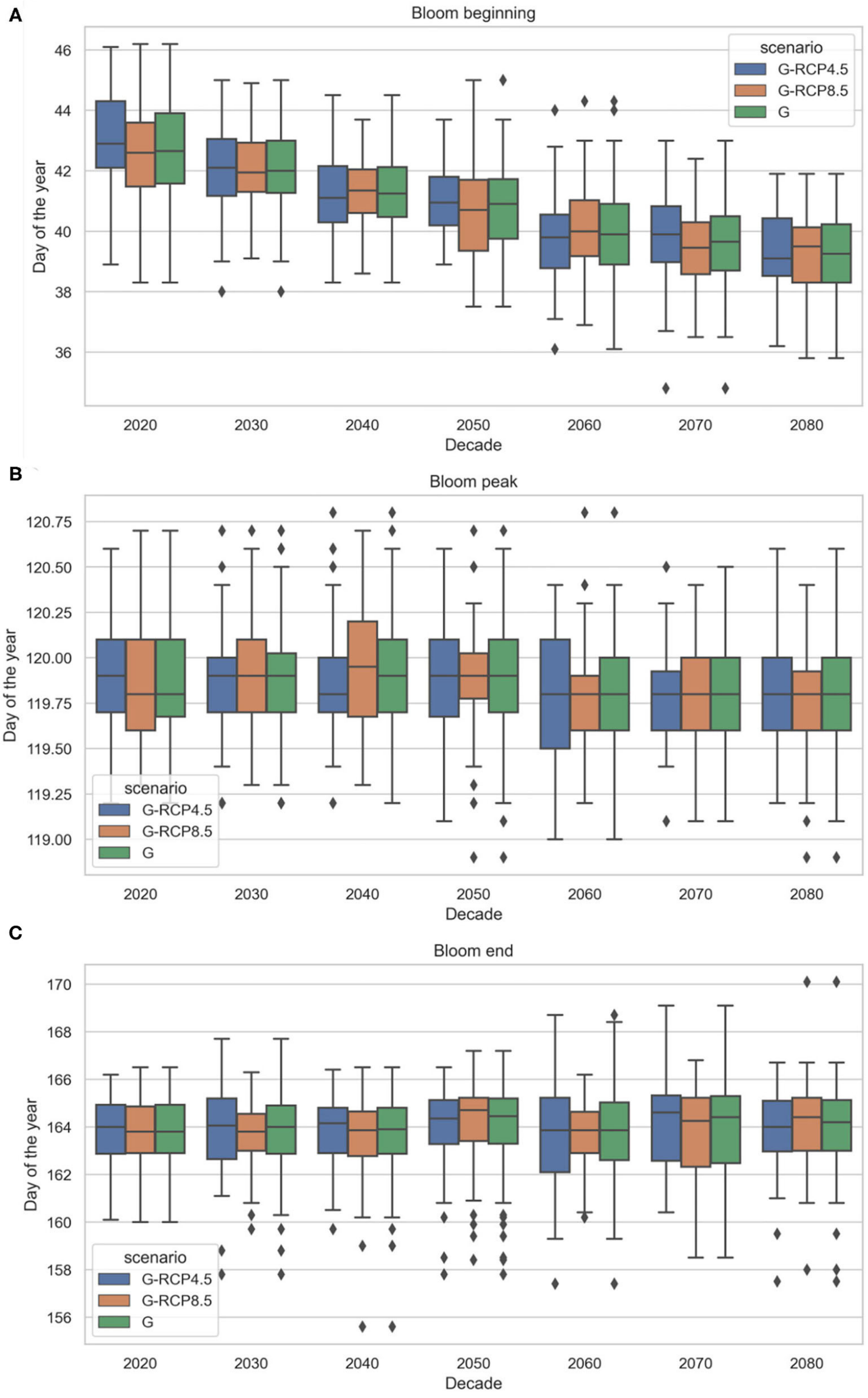

FIGURE 14 | Projected future phytoplankton spring bloom beginning **(A)**, peak timing **(B)**, and end **(C)** under generated (G) radiation and temperature projections (based EURO-CORDEX) (2019–2089). The cardinal dates are grouped based on all generated projections (G), and generated projections corresponding to RCP scenarios (G-RCP4.5 and G-RCP8.5).

than independent, due to the fact that they originate from a common genealogy (Steinschneider et al., 2015). Consequently, the model formulation induces the phenomenon of "borrowing strength" where estimates for parameters over different scenarios are combined ("pooled"). This can correct outlier-like behavior and makes the estimates statistically more robust (Gamerman and Lopes, 2006; Gelman and Hill, 2006). Thus, synthetic projections from this stochastic generator relax some of the distinct characteristics that input Euro-CORDEX RCP scenarios had. Although, new synthetic scenarios are generated per Euro-CORDEX scenario, due to the intentionally propagated uncertainty, the differences between synthetic scenarios of different RCP "families" may be less prominent. Additionally, the lack of clear response to the evident temperature difference increase in the past two decades may be attributed to a delayed feedback caused by ecosystem resilience (Atkinson et al., 2015). Finally, and perhaps most importantly, it should be emphasized that generated scenarios serve as input into the structural time series model, which then feeds into log-concave regression step to derive the bloom metrics. As mentioned above, this adds further layers of uncertainties and the impacts of the various non-linear transformations may not be easily explained.

4. DISCUSSION

This paper presents an approach to study observed past and projected future marine phytoplankton phenology making use of statistical techniques, rather than physically-based models. The Bayesian setup in the data fusion and time series prediction models offer flexibility in model formulation and allow characterization of predictive uncertainties, which is crucial in climate change impact studies. In addition, for the extraction of phytoplankton cardinal dates we proposed a non-parametric regression model under shape constraints which has not been used before for such purposes, to our knowledge. Regarding the applied data, we aimed to make best use of the cross-disciplinary and multi-sourced measurements, covering marine biogeochemistry and atmospheric variables from field measurements, satellite imagery, numerical models, and synthetic generated scenarios.

We acknowledge the various sources of uncertainties in the data and models, which are considered and statistically quantified where possible. Firstly, uncertainty in the fusion of chlorophyll-a observations is quantified by the posterior distributions obtained through Bayesian parameter inference. Secondly, uncertainties in the climate projections are addressed using a large ensemble of generated stochastic scenarios, which cover numerous possible trajectories. Thirdly, in the Bayesian time series model we quantify uncertainties in two ways. On the one hand, uncertainty intervals of the future trend are computed individually for each projection, and on the other hand, this is repeated for a large number of projections, resulting in predictive uncertainty bands for each trajectory and for the entire ensemble. Lastly, uncertainty quantification in the feature extraction step is not possible explicitly, nevertheless, thanks to the ensemble approach a range of potential phytoplankton phenologies are simulated over the course of the twenty-first century.

The main findings regarding phytoplankton phenology, the projected uncertainties in the beginning and the end of the spring bloom, as well as the prolonged bloom duration, increased peak magnitude and its forward shift (earlier bloom), may have repercussions on the marine food web. Friedland et al. (2015) found the same trends and attributed them to phenological mismatch between bloom timing and grazing pressure. When grazing pressure is shifted and predator-prey interactions are perturbed the phytoplankton loss by grazing is reduced resulting in higher bloom magnitude (van Beusekom et al., 2009). The forward shift in phytoplankton bloom phenology may also be explained by several other factors. These include increased early spring temperatures that accelerate phytoplankton cell division rates (Beaugrand and Reid, 2003; Tulp et al., 2006; Hunter-Cevera et al., 2016), change in stratification driven by temperature and/or wind trends, or change in the underwater light climate. Although, in our study slightly negative radiation trends are projected light availability can also be influenced by turbidity.

A consequence of these projected trends could be that energy transfer to higher trophic levels is disrupted as there is a tight coupling between the plankton trophic levels in marine pelagic ecosystems (Richardson and Schoeman, 2004). Such consequences are often described with the trophic match-mismatch hypothesis of Cushing (1990). Based on this hypothesis the reproductive success of higher trophic levels will be best when the phytoplankton phenology matches their requirements. Phenological shifts may therefore cause a temporal mismatch between zooplankton consumption (grazing) and phytoplankton production peak leading to higher mortality of the zooplankton, causing cascading effects toward the higher members of the food web (Richardson and Schoeman, 2004; Tulp et al., 2006; Sommer et al., 2012; Blauw et al., 2018). This has been documented in the North Sea (Beaugrand et al., 2003), and other parts of the North Atlantic (Platt et al., 2003; Koeller et al., 2009). The severity of these adverse effects in temperate productive systems is, however, debated (Atkinson et al., 2015). Due to already high natural variability in the timing of predator consumption and its prey in temperate marine systems, compensating mechanisms may exist that could potentially reduce the impact of the projected planktonic phenological shift (Atkinson et al., 2015; Desmit et al., 2020).

Our study aimed to quantify how uncertainty in environmental forcing, that influences the formation mechanism of spring blooms (through thermal stratification, mixed-layer temperatures, phytoplankton metabolic rates, and grazing) will impact the uncertainty in spring blooms dynamics. Since uncertainties in the spring bloom dynamics (especially timing; Townsend et al., 1994) are closely tied to uncertainties in secondary production, in the survival of larval populations, and ultimately in the recruitment to the adult stock (Longhurst, 2007), our results can inform further studies that attempt to propagate phytoplankton phenology related uncertainties to ecosystem response in higher trophic levels. An enhanced understanding of the variability of phytoplankton blooms

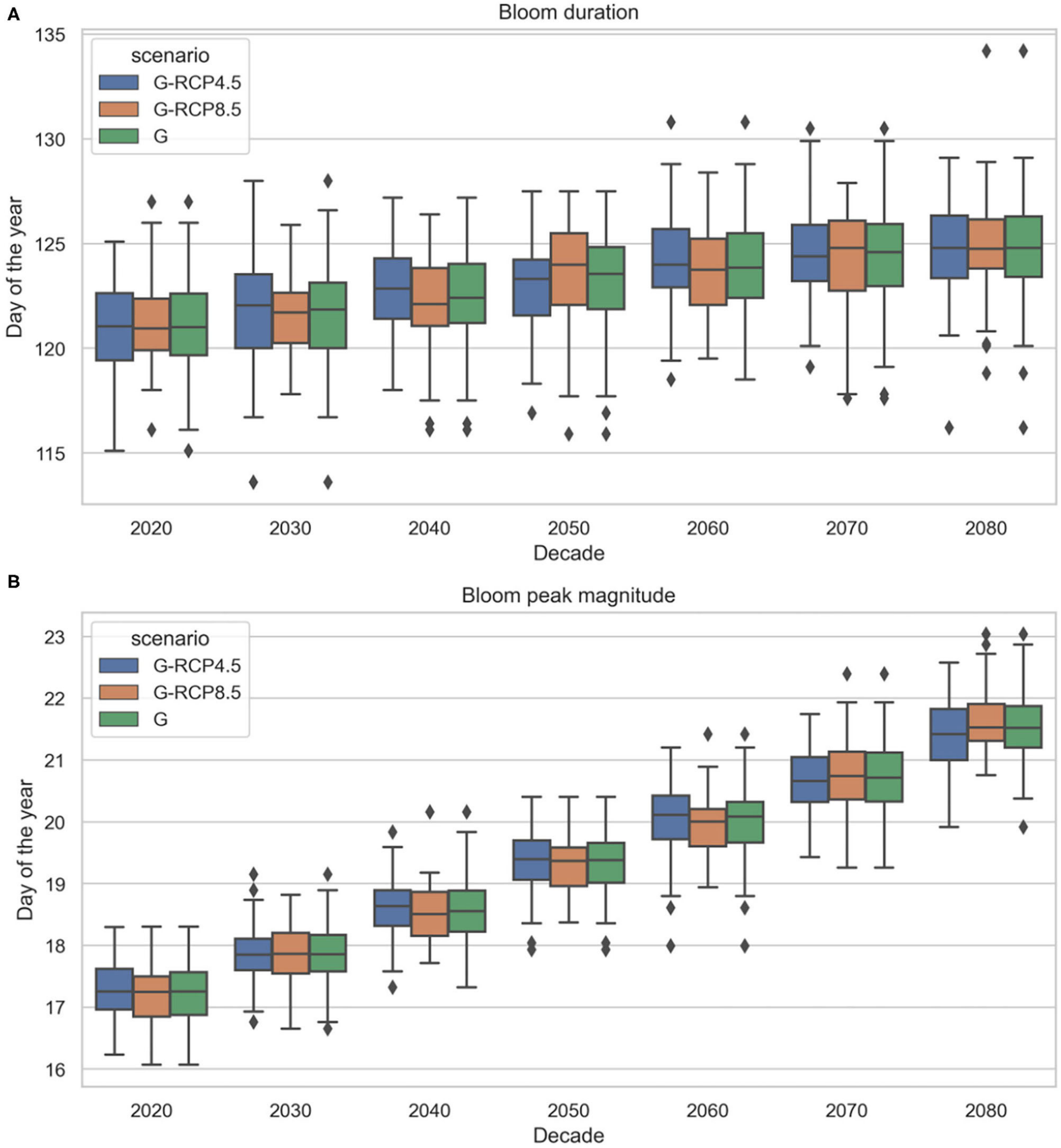

FIGURE 15 | Projected future phytoplankton spring bloom duration **(A)** and peak magnitude **(B)** under generated radiation and temperature projections (based EURO-CORDEX) (2019–2089).

is therefore a crucial step to estimate the impact on marine ecosystem functioning (Winder and Cloern, 2010).

For future research the authors recommend to merge three components of the methodological framework into a single model. Integrating the Bayesian stochastic climate generator, the Bayesian data fusion model, and the Bayesian structural time series model would provide a consistent Bayesian hierarchical model that eliminates redundancies and offers a more elegant solution. It is worth noting that this integrated solution would be harder to re-use for researchers who are interested to take advantage of only a part of the model (stochastic generator, data fusion, or projection) rather than the full chain. A further recommendation is to extend the approach to include spatial correlations, since currently only one location is considered. Extending the methodology in this way would allow us to make better use of the multi-dimensional data structure and include spatial gradients from coast to offshore locations.

As previously mentioned, chlorophyll-a concentration may not be an accurate proxy of phytoplankton biomass in the Southern North Sea (Alvarez-Fernandez and Riegman, 2014). In order to address this shortcoming, a potential avenue would be to apply novel satellite-derived products that consider phytoplankton functional types (Xi et al., 2020) or use phytoplankton carbon (Bellacicco et al., 2020) instead of chorophyll-a. Although less frequently measured phytoplankton historical *in-situ* data is available in the North Sea, that could complement satellite derived indicators. In future research it should be evaluated if these indicators could better assess phytoplankton response to climate change. Another natural extension of the research is to further propagate uncertainties in spring bloom metrics to ecosystem behavior. This could be achieved using statistical techniques or numerical models for predictive habitat distribution modeling (e.g., artificial neural networks, classification, and regression trees).

An important limitation of the study is to only use air temperature and solar radiation as environmental covariates. Even though we confirmed that air temperature and solar radiation are the most dominant predictors for the study area and for the targeted temporal scale, inclusion of additional environmental factors impacting vertical mixing and bloom formation, such as nutrients, wind, salinity, dissolved oxygen, or mixed layer depth could improve the scenario analysis. Noting that the availability of long-term climate projections of any additional covariate is a prerequisite. Precipitation as a process related to ocean salinity has not been included for the following reason. According to van Aken (2008) the salinity in the Wadden Sea is determined by fresh water input and its mixing with the North Sea and the influence of local climatic variations in precipitation can be ignored. Long-term variability of the salinity in our study area is in fact due to climatic variations in the precipitation over the river catchment areas (particularly the river Rhine) along with other human induced changes and operation of waterways and sluices. Therefore, precipitation data at this site was not considered. Nevertheless, the air temperature and solar radiation variables indirectly impact ocean salinity through evaporation rates. Excluding vertical mixing processes such as wind can also be justified. While vertical mixing indeed affect nutrient conditions for phytoplankton blooms, the impacts depend on whether the area is already stratified (Tulp et al., 2006). According to Groeskamp et al. (2011), at the study location the water column is usually vertically well-mixed due to strong tidal mixing processes (strong flood and ebb currents) and persistent wind, which is a common feature here. This makes wind less relevant at this particular location. This was confirmed by both literature and our own data analysis.

Along with these points, we should also mention another important source of uncertainty in future climate studies focusing on the coastal zone, which is the role of anthropogenic interventions. Such interventions in the southern North Sea include coastal zone management efforts, aquaculture activities, sand mining, oil drilling, or fishing. Especially, large dredging and replenishment activities, like the major extension of the Port of Rotterdam (Maasvlakte 2) cause resuspension of buried inorganic nutrients into the water column and alter phytoplankton seasonality. In shallow coastal locations these uncertainties from anthropogenic impacts may outweigh the climate change induced ones, while moving toward transitional and offshore waters the effects are less prominent. Nonetheless, in this research human impacts are not addressed, only climatic ones.

Finally and most importantly, we recognize that our results related to climate change impacts on spring bloom dynamics will not resolve the ongoing debate on the complex and often contradictory findings. Especially, given the fact that the proposed data driven approach neglects the complicated and often non-linear ecological processes on species level. We reduced the marine biogeochemical response to climate change into a simple cause-effect relationship between two climate variables and chlorophyll-a concentration. As a consequence, our results are only an extrapolation of the observed correlations given projected changes in the climate using statistical models and giving appropriate attention to uncertainty quantification.

Despite the limitations, we believe that our proposed approach contributes to an integrated understanding of ecological responses to variable climate change through expressing future likelihoods of projected spring bloom dynamics and through the enhanced characterization of uncertainties associated to data and statistical methods.

DATA AVAILABILITY STATEMENT

The datasets presented in this study can be found in online repositories. The names of the repository/repositories and accession number(s) can be found at: https://marine.copernicus.eu/; http://projects.knmi.nl/klimatologie/; https://waterinfo.rws.nl/; http://data.dta.cnr.it/ecopotential/wadden_sea/; https://github.com/fmeulen/DataFusion; https://github.com/lorincmeszaros/spring-bloom-dynamics.

AUTHOR CONTRIBUTIONS

The study was conducted within the Ph.D. research of LM. LM led the data collection, data and results analysis, and manuscript preparation. FM is the author of section 2.2 on data fusion, he developed the data fusion algorithm and executed the computations. GJ provided advice on the use of concave regression for spring bloom cardinal date extraction and contributed to its mathematical formulation in section 2.4. GE advised on the ecological aspects and helped to refine the research objective in order to ensure its applicability to the journal. All authors contributed to the study conception, design and the discussion of results, recommendations, and read and approved the final manuscript.

FUNDING

This research has received funding from the European Union's Horizon 2020 research and innovation programme under grant agreement No 727277. The work was supported by Deltares Theme Enabling Technologies, funded by Deltares—Strategic Research Budget from the Ministry of Economic Affairs and Climate Policy.

ACKNOWLEDGMENTS

We are grateful to the reviewers for their thorough reviews and insightful comments, which significantly improved the quality of the manuscript.

REFERENCES

Abram, N., Gattuso, J.-P., Cheng, L., Paz Chidichimo, M., Crate, S., Enomoto, H., et al. (2019). "Framing and context of the report," in *IPCC Special Report on the Ocean and Cryosphere in a Changing Climate*, IPCC.

Alvarez-Fernandez, S., Lindeboom, H., and Meesters, E. (2012). Temporal changes in plankton of the North Sea: community shifts and environmental drivers. *Mar. Ecol. Prog. Ser*. 462, 21–38. doi: 10.3354/meps09817

Alvarez-Fernandez, S., and Riegman, R. (2014). Chlorophyll in North Sea coastal and offshore waters does not reflect long term trends of phytoplankton biomass. *J. Sea Res*. 91, 35–44. doi: 10.1016/j.seares.2014.04.005

Amengual, A., Homar, V., Romero, R., Alonso, S., and Ramis, C. (2012). A statistical adjustment of regional climate model outputs to local scales: application to Platja de Palma, Spain. *J. Clim*. 25, 939–957. doi: 10.1175/JCLI-D-10-05024.1

Antoine, D., and Morel, A. (1996). Oceanic primary production: 1. Adaptation of a spectral light-photosynthesis model in view of application to satellite chlorophyll observations. *Glob. Biogeochem. Cycles* 10, 43–55. doi: 10.1029/95GB02831

Atkinson, A., Harmer, R. A., Widdicombe, C. E., McEvoy, A. J., Smyth, T. J., Cummings, D. G., et al. (2015). Questioning the role of phenology shifts and trophic mismatching in a planktonic food web. *Prog. Oceanogr*. 137, 498–512. doi: 10.1016/j.pocean.2015.04.023

Bartók, B., Wild, M., Folini, D., Lüthi, D., Kotlarski, S., Schär, C., et al. (2017). Projected changes in surface solar radiation in CMIP5 global climate models and in EURO-CORDEX regional climate models for Europe. *Clim. Dyn*. 49, 2665–2683. doi: 10.1007/s00382-016-3471-2

Beaugrand, G., Brander, K. M., Lindley, J. A., Souissi, S., and Reid, P. C. (2003). Plankton effect on cod recruitment in the North Sea. *Nature* 426, 661–664. doi: 10.1038/nature02164

Beaugrand, G., Harlay, X., and Edwards, M. (2014). Detecting plankton shifts in the North Sea: a new abrupt ecosystem shift between 1996 and 2003. *Mar. Ecol. Prog. Ser*. 502, 85–104. doi: 10.3354/meps10693

Beaugrand, G., and Reid, P. C. (2003). Long-term changes in phytoplankton, zooplankton and salmon related to climate. *Glob. Change Biol*. 9, 801–817. doi: 10.1046/j.1365-2486.2003.00632.x

Behrenfeld, M. J. (2010). Abandoning sverdrup's critical depth hypothesis on phytoplankton blooms. *Ecology* 91, 977–989. doi: 10.1890/09-1207.1

Behrenfeld, M. J., and Boss, E. S. (2018). Student's tutorial on bloom hypotheses in the context of phytoplankton annual cycles. *Glob. Change Biol*. 24, 55–77. doi: 10.1111/gcb.13858

Bellacicco, M., Pitarch, J., Organelli, E., Martinez-Vicente, V., Volpe, G., and Marullo, S. (2020). Improving the retrieval of carbon-based phytoplankton biomass from satellite ocean colour observations. *Remote Sens*. 12, 1–13. doi: 10.3390/rs12213640

Blauw, A. N., Benincá, E., Laane, R. W., Greenwood, N., and Huisman, J. (2018). Predictability and environmental drivers of chlorophyll fluctuations vary across different time scales and regions of the North Sea. *Prog. Oceanogr*. 161, 1–18. doi: 10.1016/j.pocean.2018.01.005

Brody, S. R., Lozier, M. S., and Dunne, J. P. (2013). A comparison of methods to determine phytoplankton bloom initiation. *J. Geophys. Res*. 118, 2345–2357. doi: 10.1002/jgrc.20167

Campbell, J. W. (1995). The lognormal distribution as a model for bio-optical variability in the sea. *J. Geophys. Res*. 100, 13237–13254. doi: 10.1029/95JC00458

Carter, C. K., and Kohn, R. (1994). On gibbs sampling for state space models. *Biometrika* 81:541. doi: 10.1093/biomet/81.3.541

Cho, H., Choi, U. J., and Park, H. (2018). Deep learning application to time-series prediction of daily chlorophyll-a concentration. *WIT Trans. Ecol. Environ*. 215, 157–163. doi: 10.2495/EID180141

Cole, H., Henson, S., Martin, A., and Yool, A. (2012). Mind the gap: the impact of missing data on the calculation of phytoplankton phenology metrics. *J. Geophys. Res*. 117:C08030. doi: 10.1029/2012JC008249

Cushing, D. H. (1990). Plankton production and year-class strength in fish populations: an update of the match/mismatch hypothesis. *Adv. Mar. Biol*. 26, 249–293. doi: 10.1016/S0065-2881(08)60202-3

D'Alelio, D., Rampone, S., Cusano, L. M., Morfino, V., Russo, L., Sanseverino, N., et al. (2020). Machine learning identifies a strong association between warming and reduced primary productivity in an oligotrophic ocean gyre. *Sci. Rep*. 10:3287. doi: 10.1038/s41598-020-59989-y

de Amorim, F., Rick, J., Lohmann, G., and Wiltshire, K. H. (2021). Evaluation of Machine Learning predictions of a highly resolved time series of Chlorophyll-a concentration. *Cold Spring Harbor Lab*. doi: 10.1101/2021.05.12.443749

Desmit, X., Nohe, A., Borges, A. V., Prins, T., De Cauwer, K., Lagring, R., et al. (2020). Changes in chlorophyll concentration and phenology in the North Sea in relation to de-eutrophication and sea surface warming. *Limnol. Oceanogr*. 65, 828–847. doi: 10.1002/lno.11351

Doss, C. R. (2019). Concave regression: value-constrained estimation and likelihood ratio-based inference. *Math. Program*. 174, 5–39. doi: 10.1007/s10107-018-1338-5

Edwards, K. F., Thomas, M. K., Klausmeier, C. A., and Litchman, E. (2016). Phytoplankton growth and the interaction of light and temperature: a synthesis at the species and community level. *Limnol. Oceanogr*. 61, 1232–1244. doi: 10.1002/lno.10282

Edwards, M., and Richardson, A. J. (2004). Impact of climate change on marine pelagic phenology and trophic mismatch. *Nature* 430:7002. doi: 10.1038/nature02808

Ferreira, A. S., Visser, A. W., MacKenzie, B. R., and Payne, M. R. (2014). Accuracy and precision in the calculation of phenology metrics. *J. Geophys. Res*. 119, 8438–8453. doi: 10.1002/2014JC010323

Friedland, K. D., Leaf, R. T., Kane, J., Tommasi, D., Asch, R. G., Rebuck, N., et al. (2015). Spring bloom dynamics and zooplankton biomass response on the US Northeast Continental Shelf. *Contin. Shelf Res*. 102, 47–61. doi: 10.1016/j.csr.2015.04.005

Friocourt, Y. F., Skogen, M., Stolte, W., and Albretsen, J. (2012). Marine downscaling of a future climate scenario in the North Sea and possible effects on dinoflagellate harmful algal blooms. *Food Addit. Contam*. 29, 1630–1646. doi: 10.1080/19440049.2012.714079

Gamerman, D., and Lopes, H. F. (2006). *Markov Chain Monte Carlo: Stochastic Simulation for Bayesian Inference, 2nd Edn, Vol. 1*. New York, NY: Taylor & Francis. doi: 10.1201/9781482296426

Garnesson, P., Mangin, A., and Bretagnon, M. (2020). *Ocean Colour Production Centre Satellite Observation Copernicus-GlobColour Products*. Technical report, Copernicus Marine Environemnt Monitoring Service.

Gelman, A., and Hill, J. (2006). *Data Analysis Using Regression and Multilevel/Hierarchical Models. Analytical Methods for Social Research*. Cambridge: Cambridge University Press. doi: 10.1017/CBO9780511790942

Gohin, F., Druon, J. N., and Lampert, L. (2002). A five channel chlorophyll concentration algorithm applied to Sea WiFS data processed by SeaDAS in coastal waters. *Int. J. Remote Sens*. 23, 1639–1661. doi: 10.1080/01431160110071879

González Taboada, F., and Anadón, R. (2014). Seasonality of North Atlantic phytoplankton from space: impact of environmental forcing on a changing phenology (1998-2012). *Glob. Change Biol*. 20, 698–712. doi: 10.1111/gcb.12352

Gräwe, U., Burchard, H., Müller, M., and Schuttelaars, H. M. (2014). Seasonal variability in M2 and M4 tidal constituents and its implications for the coastal residual sediment transport. *Geophys. Res. Lett*. 41, 5563–5570. doi: 10.1002/2014GL060517

Groeneboom, P., and Jongbloed, G. (2014). *Nonparametric Estimation Under Shape Constraints: Estimators, Algorithms and Asymptotics*. Cambridge: Cambridge University Press. doi: 10.1017/CBO9781139020893

Groeneboom, P., Jongbloed, G., and Wellner, J. A. (2001). Estimation of a convex function: characterizations and asymptotic theory. *Ann. Stat*. 29, 1653–1698. doi: 10.1214/aos/1015345958

Groeskamp, S., Nauw, J. J., and Maas, L. R. M. (2011). Observations of estuarine circulation and solitary internal waves in a highly energetic tidal channel. *Ocean Dyn*. 61, 1767–1782. doi: 10.1007/s10236-011-0455-y

Hammond, M. L., Beaulieu, C., Henson, S. A., and Sahu, S. K. (2020). Regional surface chlorophyll trends and uncertainties in the global ocean. *Sci. Rep*. 10:15273. doi: 10.1038/s41598-020-72073-9

Hjerne, O., Hajdu, S., Larsson, U., Downing, A. S., and Winder, M. (2019). Climate driven changes in timing, composition and magnitude of the Baltic sea phytoplankton spring bloom. *Front. Mar. Sci*. 6:482. doi: 10.3389/fmars.2019.00482

Holt, J., Schrum, C., Cannaby, H., Daewel, U., Allen, I., Artioli, Y., et al. (2014). Physical processes mediating climate change impacts on regional sea ecosystems. *Biogeosci. Discuss*. 11, 1909–1975. doi: 10.5194/bgd-11-1909-2014

Holt, J., Schrum, C., Cannaby, H., Daewel, U., Allen, I., Artioli, Y., et al. (2016). Potential impacts of climate change on the primary production of regional seas: a comparative analysis of five European seas. *Prog. Oceanogr*. 140, 91–115. doi: 10.1016/j.pocean.2015.11.004

Hunter-Cevera, K. R., Neubert, M. G., Olson, R. J., Solow, A. R., Shalapyonok, A., and Sosik, H. M. (2016). Physiological and ecological drivers of early spring blooms of a coastal phytoplankter. *Science* 354, 326–329. doi: 10.1126/science.aaf8536

Irwin, A. J., and Finkel, Z. V. (2008). Mining a sea of data: Deducing the environmental controls of ocean chlorophyll. *PLoS ONE* 3:3836. doi: 10.1371/journal.pone.0003836

Jacob, D., Petersen, J., Eggert, B., Alias, A., Christensen, O. B., Bouwer, L. M., et al. (2014). Euro-cordex: new high-resolution climate change projections for European impact research. *Region. Environ. Change* 14, 563–578. doi: 10.1007/s10113-013-0499-2

Ji, R., Edwards, M., MacKas, D. L., Runge, J. A., and Thomas, A. C. (2010). Marine plankton phenology and life history in a changing climate: current research and future directions. *J. Plank. Res*. 32, 1355–1368. doi: 10.1093/plankt/fbq062

Keller, S., Maier, P. M., Riese, F. M., Norra, S., Holbach, A., Börsig, N., et al. (2018). Hyperspectral data and machine learning for estimating CDOM, chlorophyll a, diatoms, green algae and turbidity. *Int. J. Environ. Res. Publ. Health* 15:1881. doi: 10.3390/ijerph15091881

Koeller, P., Fuentes-Yaco, C., Platt, T., Sathyendranath, S., Richards, A., Ouellet, P., et al. (2009). Basin-scale coherence in phenology of shrimps and phytoplankton in the North Atlantic Ocean. *Science* 324, 791–793. doi: 10.1126/science.1170987

Krasnopolsky, V., Nadiga, S., Mehra, A., and Bayler, E. (2018). Adjusting neural network to a particular problem: neural network-based empirical biological model for chlorophyll concentration in the upper ocean. *Appl. Comput. Intell. Soft Comput*. 2018:7057363. doi: 10.1155/2018/7057363

Leutbecher, M. (2019). Ensemble size: how suboptimal is less than infinity? *Quart. J. R. Meteorol. Soc*. 145, 107–128. doi: 10.1002/qj.3387

Lewandowska, A., and Sommer, U. (2010). Climate change and the spring bloom: a mesocosm study on the influence of light and temperature on phytoplankton and mesozooplankton. *Mar. Ecol. Prog. Ser*. 405, 101–111. doi: 10.3354/meps08520

Liu, X., Feng, J., and Wang, Y. (2019). Chlorophyll a predictability and relative importance of factors governing lake phytoplankton at different timescales. *Sci. Tot. Environ*. 648, 472–480. doi: 10.1016/j.scitotenv.2018.08.146

Llope, M., Chan, K.-S., Ciannelli, L., Reid, P. C., Stige, L. C., and Stenseth, N. C. (2009). Effects of environmental conditions on the seasonal distribution of phytoplankton biomass in the North Sea. *Limnol. Oceanogr*. 54, 512–524. doi: 10.4319/lo.2009.54.2.0512

Longhurst, A. R. (2007). *Ecological Geography of the Sea*. San Diego, CA: Elsevier Inc. doi: 10.1016/B978-012455521-1/50002-4

Los, F. J., and Blaas, M. (2010). Complexity, accuracy and practical applicability of different biogeochemical model versions. *J. Mar. Syst*. 81, 44–74. doi: 10.1016/j.jmarsys.2009.12.011

Los, F. J., Troost, T. A., and Van Beek, J. K. L. (2014). Finding the optimal reduction to meet all targets-Applying Linear Programming with a nutrient tracer model of the North Sea. *J. Mar. Syst*. 131, 91–101. doi: 10.1016/j.jmarsys.2013.12.001

Luo, Q. (2016). Necessity for post-processing dynamically downscaled climate projections for impact and adaptation studies. *Stochast. Environ. Res. Risk Assess*. 30, 1835–1850. doi: 10.1007/s00477-016-1233-7

Luo, W., Zhu, S., Wu, S., and Dai, J. (2019). Comparing artificial intelligence techniques for chlorophyll-a prediction in US lakes. *Environ. Sci. Pollut. Res*. 26, 30524–30532. doi: 10.1007/s11356-019-06360-y

McQuatters-Gollop, A., and Vermaat, J. E. (2011). Covariance among North Sea ecosystem state indicators during the past 50-years–Contrasts between coastal and open waters. *J. Sea Res*. 65, 284–292. doi: 10.1016/j.seares.2010.12.004

Mészáros, L., van der Meulen, F., Jongbloed, G., and El Serafy, G. (2021). A Bayesian stochastic generator to complement existing climate change scenarios: supporting uncertainty quantification in marine and coastal ecosystems. *Stoch. Environ. Res. Risk Assess*. 35, 719–736. doi: 10.1007/s00477-020-01935-5

Navarro-Racines, C., Tarapues, J., Thornton, P., Jarvis, A., and Ramirez-Villegas, J. (2020). High-resolution and bias-corrected CMIP5 projections for climate change impact assessments. *Sci. Data* 7, 1–14. doi: 10.1038/s41597-019-0343-8

O'Neill, B. C., Oppenheimer, M., Warren, R., Hallegatte, S., Kopp, R. E., Pörtner, H. O., et al. (2017). IPCC reasons for concern regarding climate change risks. *Nat. Clim. Change* 7, 28–37. doi: 10.1038/nclimate3179

O'Reilly, J., Maritorena, S., Mitchell, B., Siegel, D., Carder, K., Garver, S., et al. (1998). Ocean color chlorophyll algorithms for SeaWiFS. *J. Geophys. Res. Atmos*. 103, 24937–24953. doi: 10.1029/98JC02160

O'Reilly, J., Maritorena, S., Siegel, D., O'Brien, M., Toole, D., Mitchell, B., et al. (2000). "Ocean chlorophyll-a Algorithms for Sea WiFS, OC2 and OC4: version 4," in *Sea WiFS Postlaunch Calibration and Vali-dation Analyses*, Part 3. NASA Tech. Memo. 2000-206892(11). eds S. B. Hooker, and E. R. Firestone. (Greenbelt, Maryland: NASA Goddard Space Flight Center), 9–23. Available online at: https://www.researchgate.net/publication/284044296_Ocean_color_chlorophyll_a_algorithms_for_SeaWiFS_OC2_and_OC4_Version_4

Peters, S., Eleveld, M., Pasterkamp, R., van der Woerd, H., DeVolder, M., Jans, S., et al. (2005). *Atlas of Chlorophyll-a Concentration for the North Sea (Based on MERIS Imagery of 2003). Number E-05/01*. Instituut voor Milieuvraagstukken.

Philippart, C. J. M., van Iperen, J. M., Cadée, G. C., and Zuur, A. F. (2010). Long-term field observations on seasonality in chlorophyll-a concentrations in a shallow coastal marine ecosystem, the Wadden Sea. *Estuar. Coasts* 33, 286–294. doi: 10.1007/s12237-009-9236-y

Platt, T., Fuentes-Yaco, C., and Frank, K. T. (2003). Marine ecology: spring algal bloom and larval fish survival. *Nature* 423, 398–399. doi: 10.1038/423398b

Pushpadas, D., Schrum, C., and Daewel, U. (2015). Projected climate change impacts on North Sea and Baltic Sea: CMIP3 and CMIP5 model based scenarios. *Biogeosci. Discuss*. 12, 12229–12279. doi: 10.5194/bgd-12-12229-2015

Richardson, A. J., and Schoeman, D. S. (2004). Climate impact on plankton ecosystems in the northeast Atlantic. *Science* 305, 1609–1612. doi: 10.1126/science.1100958

Robert, C. P., and Casella, G. (2004). *Monte Carlo Statistical Methods. Springer Texts in Statistics*. New York, NY: Springer New York. doi: 10.1007/978-1-4757-4145-2

Rolinski, S., Horn, H., Petzoldt, T., and Paul, L. (2007). Identifying cardinal dates in phytoplankton time series to enable the analysis of long-term trends. *Oecologia* 153, 997–1008. doi: 10.1007/s00442-007-0783-2

Särkkä, S. (2013). *Bayesian Filtering and Smoothing. Institute of Mathematical Statistics Textbooks*. Cambridge University Press.

Saulquin, B., Gohin, F., and Fanton d'Andon, O. (2019). Interpolated fields of satellite-derived multi-algorithm chlorophyll-a estimates at global and European scales in the frame of the European Copernicus-Marine Environment Monitoring Service. *J. Operat. Oceanogr*. 12, 47–57. doi: 10.1080/1755876X.2018.1552358

Schrum, C., Lowe, J., Meier, H. E. M., Grabemann, I., Holt, J., Mathis, M., et al. (2016). *Projected Change-North Sea*. Cham: Springer. doi: 10.1007/978-3-319-39745-0_6

Smayda, T. J. (1997). What is a bloom? A commentary. *Limnol. Oceanogr*. 42(5 Pt 2), 1132–1136. doi: 10.4319/lo.1997.42.5_part_2.1132

Sommer, U., Adrian, R., Domis, L. D. S., Elser, J. J., Gaedke, U., Ibelings, B., et al. (2012). Beyond the plankton ecology group (PEG) model: mechanisms driving plankton succession. *Annu. Rev. Ecol. Evol. Syst*. 43, 429–448. doi: 10.1146/annurev-ecolsys-110411-160251

Sommer, U., Gliwicz, Z. M., Lampert, W., and Duncan, A. (1986). The PEG-model of seasonal succession of planktonic events in fresh waters. *Arch. Hydrobiol*. 106, 433–471.

Steinschneider, S., McCrary, R., Mearns, L. O., and Brown, C. (2015). The effects of climate model similarity on probabilistic climate projections and the implications for local, risk-based adaptation planning. *Geophys. Res. Lett*. 42, 5014–5044. doi: 10.1002/2015GL064529

Sverdrup, H. U. (1953). On conditions for the vernal blooming of phytoplankton. *ICES J. Mar. Sci*. 18, 287–295. doi: 10.1093/icesjms/18.3.287

Taylor, S. J., and Letham, B. (2017). *Forecasting at Scale*. San Diego, CA: PeerJ Inc. doi: 10.7287/peerj.preprints.3190

Townsend, D. W., Cammen, L. M., Holligan, P. M., Campbell, D. E., and Pettigrew, N. R. (1994). Causes and consequences of variability in the timing of spring phytoplankton blooms. *Deep Sea Res. Part I* 41, 747–765. doi: 10.1016/0967-0637(94)90075-2

Tulp, I., van Hal, R., and Rijnsdorp, A. (2006). *Effects of Climate Change on North Sea Fish and Benthos*. Technical report, Wageningen: IMARES.

van Aken, H. M. (2008). Variability of the water temperature in the western Wadden Sea on tidal to centennial time scales. *J. Sea Res*. 60, 227–234. doi: 10.1016/j.seares.2008.09.001

van Beusekom, J. E., Loebl, M., and Martens, P. (2009). Distant riverine nutrient supply and local temperature drive the long-term phytoplankton development in a temperate coastal basin. *J. Sea Res*. 61, 26–33. doi: 10.1016/j.seares.2008.06.005

van Beusekom, J. E. E., Carstensen, J., Dolch, T., Grage, A., Hofmeister, R., Lenhart, H., et al. (2019). Wadden sea eutrophication: long-term trends and regional differences. *Front. Mar. Sci*. 6:370. doi: 10.3389/fmars.2019.00370

Van Haren, H., Mills, D. K., and Wetsteyn, L. P. (1998). Detailed observations of the phytoplankton spring bloom in the stratifying central North Sea. *J. Mar. Res*. 56, 655–680. doi: 10.1357/002224098765213621

van Vuuren, D. P., Edmonds, J., Kainuma, M., Riahi, K., Thomson, A., Hibbard, K., et al. (2011). The representative concentration pathways: an overview. *Clim. Change* 109:5. doi: 10.1007/s10584-011-0148-z

Vargas, M., Brown, C. W., and Sapiano, M. R. (2009). Phenology of marine phytoplankton from satellite ocean color measurements. *Geophys. Res. Lett*. 36:L01608. doi: 10.1029/2008GL036006

Wiltshire, K. H., Malzahn, A. M., Wirtz, K., Greve, W., Janisch, S., Mangelsdorf, P., et al. (2008). Resilience of North Sea phytoplankton spring bloom dynamics: an analysis of long-term data at Helgoland Roads. *Limnol. Oceanogr*. 53, 1294–1302. doi: 10.4319/lo.2008.53.4.1294

Winder, M., Berger, S. A., Lewandowska, A., Aberle, N., Lengfellner, K., Sommer, U., et al. (2012). Spring phenological responses of marine and freshwater plankton to changing temperature and light conditions. *Mar. Biol*. 159, 2491–2501. doi: 10.1007/s00227-012-1964-z

Winder, M., and Cloern, J. E. (2010). The annual cycles of phytoplankton biomass. *Philos. Trans. R. Soc. B Biol. Sci*. 365, 3215–3226. doi: 10.1098/rstb.2010.0125

Winder, M., and Sommer, U. (2012). Phytoplankton response to a changing climate. *Hydrobiologia* 698, 5–16. doi: 10.1007/s10750-012-1149-2

Xi, H., Losa, S. N., Mangin, A., Soppa, M. A., Garnesson, P., Demaria, J., et al. (2020). Global retrieval of phytoplankton functional types based on empirical orthogonal functions using CMEMS GlobColour merged products and further extension to OLCI data. *Remote Sens. Environ*. 240:111704. doi: 10.1016/j.rse.2020.111704

Xu, X., Lemmen, C., and Wirtz, K. W. (2020). Less nutrients but more phytoplankton: long-term ecosystem dynamics of the Southern North Sea. *Front. Mar. Sci*. 7:662. doi: 10.3389/fmars.2020.00662

Yu, Y., Xing, X., Liu, H., Yuan, Y., Wang, Y., and Chai, F. (2019). The variability of chlorophyll-a and its relationship with dynamic factors in the basin of the South China Sea. *J. Mar. Syst*. 200:103230. doi: 10.1016/j.jmarsys.2019.103230

Conflict of Interest: The authors declare that the research was conducted in the absence of any commercial or financial relationships that could be construed as a potential conflict of interest.

5. APPENDIX

The Forward Filtering Backwards Sampling (FFBS)-algorithm steps (Carter and Kohn, 1994; Särkkä, 2013) are defined as follows, where the dynamic and measurement models are:

$$\begin{aligned} x_k &= A_{k-1}x_{k-1} + a_{k-1} + N(0, Q_{k-1}) \\ y_k &= H_k x_k + N(0, R_k) \end{aligned}$$

where $x_k \in R^n$ is the state, $y_k \in R^m$ is the measurement, $N(0, Q_{k-1})$ is the process noise, $N(0, R_k)$ is the measurement noise, A_{k-1} is the transition matrix of the dynamic model, H_k is the measurement model matrix, and the prior Gaussian $x_0 \sim N(m_0, P_0)$. The model can be written in probabilistic terms:

$$\begin{aligned} p(x_k \,|\, x_{k-1}) &= N(x_k \,|\, A_{k-1}x_{k-1} + a_{k-1}, Q_{k-1}) \\ p(y_k \,|\, x_k) &= N(y_k \,|\, H_k x_k, R_k). \end{aligned}$$

This implies that there exist vectors m_k^- and m_k, and matrices P_k^-, P_k, S_k^- such that

$$\begin{aligned} p(x_k \,|\, y_{1:k-1}) &= N(x_k \,\big|\, m_k^-, P_k^-) \\ p(x_k \,|\, y_{1:k}) &= N(x_k \,|\, m_k, P_k) \\ p(y_k \,|\, y_{1:k-1}) &= N(y_k \,\big|\, H_k m_k^-, S_k^-) \end{aligned}$$

Then the prediction and update steps are the following, where the the recursion is started from the prior mean m_0 and covariance P_0.

For $k \geq 1$ Prediction steps

$$\begin{aligned} m_k^- &= A_{k-1}m_{k-1} + a_{k-1} \\ P_k^- &= A_{k-1}P_{k-1}A_{k-1}^T + Q_{k-1} \end{aligned}$$

Update steps

$$\begin{aligned} v_k &= y_k - H_k m_k^- \\ S_k &= H_k P_k^- H_k^T + R_k \\ K_k &= P_k^- H_k^T S_k^{-1} \\ m_k &= m_k^- + K_k v_k \\ P_k &= P_k^- - K_k S_k K_k^T \end{aligned}$$

Backward sampling:

$$\begin{aligned} G_k &= P_k A_k^T [P_{k+1}^-]^{-1} \\ m_k^s &= m_k + G_k[y_{k+1} - m_{k+1}^-] \\ P_k^s &= P_k - G_k P_{k+1}^- G_k^T \end{aligned}$$

Advantages of publishing in Frontiers

OPEN ACCESS
Articles are free to read
for greatest visibility
and readership

FAST PUBLICATION
Around 90 days
from submission
to decision

HIGH QUALITY PEER-REVIEW
Rigorous, collaborative,
and constructive
peer-review

TRANSPARENT PEER-REVIEW
Editors and reviewers
acknowledged by name
on published articles

Frontiers
Avenue du Tribunal-Fédéral 34
1005 Lausanne | Switzerland

Visit us: www.frontiersin.org
Contact us: frontiersin.org/about/contact

REPRODUCIBILITY OF RESEARCH
Support open data
and methods to enhance
research reproducibility

DIGITAL PUBLISHING
Articles designed
for optimal readership
across devices

FOLLOW US
@frontiersin

IMPACT METRICS
Advanced article metrics
track visibility across
digital media

EXTENSIVE PROMOTION
Marketing
and promotion
of impactful research

LOOP RESEARCH NETWORK
Our network
increases your
article's readership